Deep Underground Neutrino Experiment (DUNE)
Far Detector Technical Design Report

Volume II
DUNE Physics

arXiv:2002.03005v1 [hep-ex] 7 Feb 2020

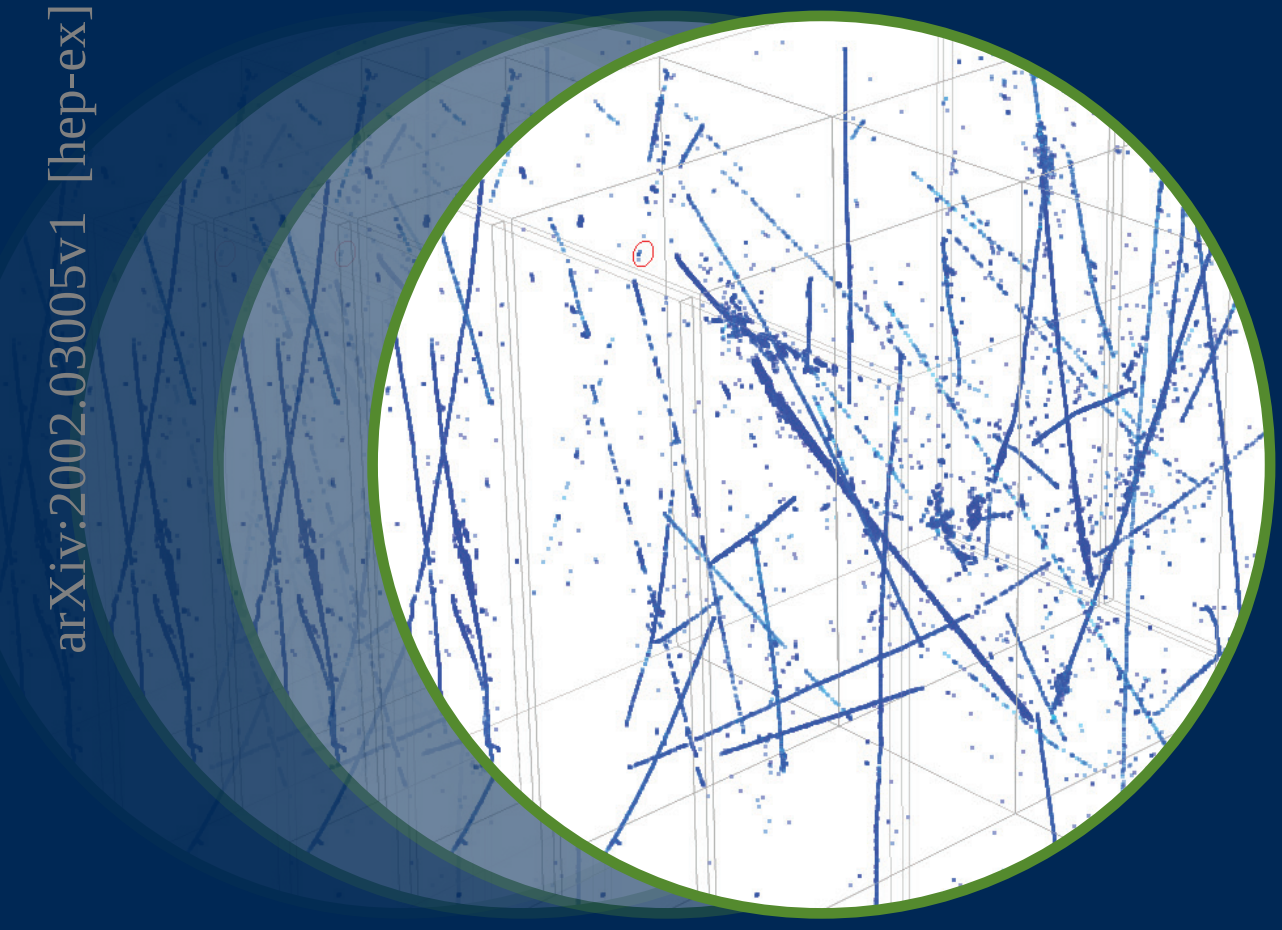

January 2020
The DUNE Collaboration

DEEP UNDERGROUND
NEUTRINO EXPERIMENT

This document was prepared by the DUNE collaboration using the resources of the Fermi National Accelerator Laboratory (Fermilab), a U.S. Department of Energy, Office of Science, HEP User Facility. Fermilab is managed by Fermi Research Alliance, LLC (FRA), acting under Contract No. DE-AC02-07CH11359.

The DUNE collaboration also acknowledges the international, national, and regional funding agencies supporting the institutions who have contributed to completing this Technical Design Report.

Authors

B. Abi,[128] R. Acciarri,[55] Mario A. Acero,[8] G. Adamov,[58] D. Adams,[14] M. Adinolfi,[13] Z. Ahmad,[162] J. Ahmed,[165] J. Ahmed,[165] T. Alion,[152] S. Alonso Monsalve,[17] C. Alt,[48] J. Anderson,[4] C. Andreopoulos,[108] M. P. Andrews,[55] M. Andriamirado,[83] F. Andrianala,[2] S. Andringa,[102] A. Ankowski,[142] J. Anthony,[27] I. M. Antoniu,[72] M. Antonova,[71] S. Antusch,[9] A. Aranda Fernandez,[35] A. Ariga,[10] L. O. Arnold,[38] M. A. Arroyave,[47] J. Asaadi,[156] A. Aurisano,[33] V. Aushev,[100] D. Autiero,[80] F. Azfar,[128] A. Back,[90] H. Back,[129] J. J. Back,[165] C. Backhouse,[160] P. Baesso,[13] L. Bagby,[55] R. Bajou,[1] S. Balasubramanian,[169] P. Baldi,[22] B. Bambah,[69] F. Barao,[102, 104] G. Barenboim,[71] G. J. Barker,[165] W. Barkhouse,[122] C. Barnes,[115] G. Barr,[128] J. Barranco Monarca,[63] N. Barros,[102, 105] J. L. Barrow,[154, 55] A. Bashyal,[127] V. Basque,[113] F. Bay,[121] J. F. Beacom,[126] E. Bechetoille,[80] B. Behera,[37] L. Bellantoni,[55] G. Bellettini,[134] V. Bellini,[73] O. Beltramello,[17] N. Benekos,[17] F. Bento Neves,[103] J. Berger,[135] S. Berkman,[55] P. Bernardini,[143] R. M. Berner,[10] H. Berns,[21] S. Bertolucci,[72] M. Betancourt,[55] M. Bhattacharjee,[85] B. Bhuyan,[85] S. Biagi,[151] J. Bian,[22] M. Biassoni,[75] K. Biery,[55] B. Bilki,[89] M. Bishai,[14] A. Bitadze,[113] A. Blake,[106] B. Blanco Siffert,[54] F. D. M. Blaszczyk,[55] G. C. Blazey,[123] E. Blucher,[31] J. Boissevain,[109] S. Bolognesi,[16] T. Bolton,[97] M. Bonesini,[75] M. Bongrand,[101] F. Bonini,[14] A. Booth,[152] C. Booth,[145] S. Bordoni,[17] A. Borkum,[152] T. Boschi,[46] N. Bostan,[89] P. Bour,[40] S. B. Boyd,[165] D. Boyden,[123] J. Bracinik,[11] D. Braga,[55] D. Brailsford,[106] A. Brandt,[156] J. Bremer,[17] C. Brew,[141] E. Brianne,[113] S. J. Brice,[55] C. Brizzolari,[75] C. Bromberg,[116] G. Brooijmans,[38] J. Brooke,[13] A. Bross,[55] G. Brunetti,[130] N. Buchanan,[37] H. Budd,[139] D. Caiulo,[80] P. Calafiura,[107] J. Calcutt,[116] M. Calin,[15] S. Calvez,[37] E. Calvo,[18] L. Camilleri,[38] A. Caminata,[74] M. Campanelli,[160] D. Caratelli,[55] G. Carini,[14] B. Carlus,[80] P. Carniti,[75] I. Caro Terrazas,[37] H. Carranza,[156] A. Castillo,[144] C. Castromonte,[88] C. Cattadori,[75] F. Cavalier,[101] F. Cavanna,[55] S. Centro,[130] G. Cerati,[55] A. Cervelli,[72] A. Cervera Villanueva,[71] M. Chalifour,[17] E. Chardonnet,[1] A. Chatterjee,[135] S. Chattopadhyay,[162] J. Chaves,[131] H. Chen,[14] M. Chen,[22] Y. Chen,[10] D. Cherdack,[68] C. Chi,[38] S. Childress,[55] A. Chiriacescu,[15] K. Cho,[96] S. Choubey,[65] A. Christensen,[37] D. Christian,[55] G. Christodoulou,[17] E. Church,[129] P. Clarke,[49] T. E. Coan,[149] A. G. Cocco,[77] J. A. B. Coelho,[101] E. Conley,[45] J. M. Conrad,[114] M. Convery,[142] L. Corwin,[146] P. Cotte,[16] L. Cremaldi,[118] L. Cremonesi,[160] J. I. Crespo-Anadón,[38] E. Cristaldo,[6] R. Cross,[106] C. Cuesta,[18] Y. Cui,[24] D. Cussans,[13] M. Dabrowski,[14] H. Da Motta,[29] Q. David,[80] G. S. Davies,[118] S. Davini,[74] J. Dawson,[1] K. De,[156] R. M. De Almeida,[57] P. Debbins,[89] I. De Bonis,[19] M. P. Decowski,[121] A. de Gouvêa,[124] P. C. De Holanda,[28] I. L. De Icaza Astiz,[152] A. Deisting,[84] P. De Jong,[121] A. Delbart,[16] D. Delepine,[63] M. Delgado,[3] A. DellAcqua,[17] P. De Lurgio,[4] D. M. DeMuth,[161] S. Dennis,[108] C. Densham,[141] A. De Roeck,[17] V. De Romeri,[71] J. J. De Vries,[27] R. Dharmapalan,[67] F. Diaz,[136] J. S. Díaz,[87] S. Di Domizio,[74] L. Di Giulio,[17] P. Ding,[55] L. Di Noto,[74] C. Distefano,[151] R. Diurba,[159] M. Diwan,[14] Z. Djurcic,[4] N. Dokania,[150] M. J. Dolinski,[44] L. Domine,[142] D. Douglas,[116] F. Drielsma,[142] D. Duchesneau,[19] K. Duffy,[55] P. Dunne,[84] T. Durkin,[141] H. Duyang,[148] O. Dvornikov,[67] D. A. Dwyer,[107] A. S. Dyshkant,[123] M. Eads,[123] D. Edmunds,[116] J. Eisch,[90] S. Emery,[16] A. Ereditato,[10] C. O. Escobar,[55] L. Escudero Sanchez,[27] J. J. Evans,[113] K. Ewart,[87] A. C. Ezeribe,[145] K. Fahey,[55] A. Falcone,[75] C. Farnese,[130] Y. Farzan,[81] J. Felix,[63] E. Fernandez-Martinez,[112] P. Fernandez Menendez,[71] F. Ferraro,[74] L. Fields,[55] F. Filthaut,[121] R. S. Fitzpatrick,[115] W. Flanagan,[42] B. Fleming,[169] R. Flight,[139] J. Fowler,[45] W. Fox,[87] J. Franc,[40] K. Francis,[123] D. Franco,[169] J. Freeman,[55] J. Freestone,[113] J. Fried,[14] A. Friedland,[142] S. Fuess,[55] I. Furic,[56] A. P. Furmanski,[159] H. Gallagher,[158] A. Gallego-Ros,[18] N. Gallice,[76, 75] V. Galymov,[80] E. Gamberini,[17] T. Gamble,[145] R. Gandhi,[65] R. Gandrajula,[116] S. Gao,[14] D. Garcia-Gamez,[61] M. . Garca-Peris,[71] S. Gardiner,[55] D. Gastler,[12] G. Ge,[38] B. Gelli,[28] A. Gendotti,[48] S. Gent,[147] Z. Ghorbani-Moghaddam,[74] D. Gibin,[130] I. Gil-Botella,[18] C. Girerd,[80] A. K. Giri,[86] O. Gogota,[100] M. Gold,[119] S. Gollapinni,[109] K. Gollwitzer,[55] R. A. Gomes,[51] L. V. Gomez Bermeo,[144] L. S. Gomez Fajardo,[144] F. Gonnella,[11] J. A. Gonzalez-Cuevas,[6] M. C. Goodman,[4] O. Goodwin,[113] S. Goswami,[133] C. Gotti,[75] E. Goudzovski,[11] C. Grace,[107] M. Graham,[142] R. Gran,[117] E. Granados,[63] A. Grant,[43] C. Grant,[12] N. Grant,[165] D. Gratieri,[57] P. Green,[113] S. Green,[27] L. Greenler,[168] J. Greer,[13] D. Gregor Recalde,[6] W. C. Griffith,[152] M. Groh,[87] J. Grudzinski,[4] K. Grzelak,[164] W. Gu,[14] V. Guarino,[4] R. Guenette,[66] A. Guglielmi,[130] B. Guo,[148] K. K. Guthikonda,[64] R. Gutierrez,[3] P. Guzowski,[113] M. M. Guzzo,[28] S. Gwon,[32] A. Habig,[117] H. Hadavand,[156] R. Haenni,[10] A. Hahn,[55] J. Haigh,[165] J. Haiston,[146] T. Hamernik,[55] P. Hamilton,[153] J. Han,[135] K. Harder,[141] D. A. Harris,[171, 55] J. Hartnell,[152] T. Hasegawa,[95] R. Hatcher,[55] E. Hazen,[12] A. Heavey,[55] K. M. Heeger,[169] K. Hennessy,[108] S. Henry,[139] M. A. Hernandez Morquecho,[63] K. Herner,[55] L. Hertel,[22] J. Hewes,[33] A. Higuera,[68] T. Hill,[82] S. J. Hillier,[11] A. Himmel,[55] J. Hoff,[55] C. Hohl,[9] A. Holin,[160] E. Hoppe,[129] G. A. Horton-Smith,[97] M. Hostert,[46] A. Hourlier,[114] B. Howard,[87] R. Howell,[139] J. Huang,[157] J. Huang,[21] J. Hugon,[110] G. Iles,[84] R. Illingworth,[55] A. Ioannisian,[170] R. Itay,[142] A. Izmaylov,[71] E. James,[55] F. Jediny,[40] C. Jess-Valls,[70] X. Ji,[14] S. Jimnez,[18] A. Jipa,[15] C. Johnson,[37] R. Johnson,[33] B. Jones,[156] S. Jones,[160] C. K. Jung,[150]

T. Junk,[55] Y. Jwa,[38] M. Kabirnezhad,[128] A. Kaboth,[141] I. Kadenko,[100] F. Kamiya,[53] G. Karagiorgi,[38] M. Karolak,[16] Y. Karyotakis,[19] S. Kasai,[99] S. P. Kasetti,[110] L. Kashur,[37] N. Kazaryan,[170] E. Kearns,[12] P. Keener,[131] K.J. Kelly,[55] E. Kemp,[28] W. Ketchum,[55] S. H. Kettell,[14] M. Khabibullin,[79] A. Khotjantsev,[79] A. Khvedelidze,[58] B. King,[55] B. Kirby,[14] M. Kirby,[55] J. Klein,[131] K. Koehler,[168] L. W. Koerner,[68] S. Kohn,[20,107] P. P. Koller,[10] M. Kordosky,[167] T. Kosc,[80] U. Kose,[17] V. A. Kostelecký,[87] K. Kothekar,[13] F. Krennrich,[90] I. Kreslo,[10] Y. Kudenko,[79] V. A. Kudryavtsev,[145] S. Kulagin,[79] J. Kumar,[67] R. Kumar,[138] C. Kuruppu,[148] V. Kus,[40] T. Kutter,[110] K. Lande,[131] C. E. Lane,[44] K. Lang,[157] T. Langford,[169] P. Lasorak,[152] D. Last,[131] C. Lastoria,[18] A. Laundrie,[168] I. Lazanu,[15] R. LaZur,[37] T. Le,[158] J. Learned,[67] P. LeBrun,[80] G. Lehmann Miotto,[17] R. Lehnert,[87] M. A. Leigui de Oliveira,[53] M. Leyton,[70] L. Li,[22] S. Li,[14] S. W. Li,[142] T. Li,[49] Y. Li,[14] H. Liao,[97] C. S. Lin,[107] S. Lin,[37] A. Lister,[168] B. R. Littlejohn,[83] S. Lockwitz,[55] T. Loew,[107] M. Lokajicek,[39] I. Lomidze,[58] K. Long,[84] K. Loo,[94] D. Lorca,[10] T. Lord,[165] J. M. LoSecco,[125] W. C. Louis,[109] K. B. Luk,[20,107] X. Luo,[25] N. Lurkin,[11] T. Lux,[70] V. P. Luzio,[53] D. MacFarland,[142] A. A. Machado,[28] P. Machado,[55] C. T. Macias,[87] J. R. Macier,[55] A. Maddalena,[60] P. Madigan,[20,107] S. Magill,[4] K. Mahn,[116] A. Maio,[102,105] J. A. Maloney,[41] G. Mandrioli,[72] J. C. Maneira,[102,105] L. Manenti,[160] S. Manly,[139] A. Mann,[158] K. Manolopoulos,[141] M. Manrique Plata,[87] A. Marchionni,[55] W. Marciano,[14] D. Marfatia,[67] C. Mariani,[163] J. Maricic,[67] F. Marinho,[52] A. D. Marino,[36] M. Marshak,[159] C. Marshall,[107] J. Marshall,[165] J. Marteau,[80] J. Martin-Albo,[71] N. Martinez,[137] D.A. Martinez Caicedo,[146] S. Martynenko,[150] K. Mason,[158] A. Mastbaum,[140] M. Masud,[71] S. Matsuno,[67] J. Matthews,[110] C. Mauger,[131] N. Mauri,[72] K. Mavrokoridis,[108] R. Mazza,[75] A. Mazzacane,[55] E. Mazzucato,[16] E. McCluskey,[55] N. McConkey,[113] K. S. McFarland,[139] C. McGrew,[150] A. McNab,[113] A. Mefodiev,[79] P. Mehta,[93] P. Melas,[7] M. Mellinato,[75] O. Mena,[71] S. Menary,[171] L. Mendes Santos,[28] H. Mendez,[137] A. Menegolli,[78] G. Meng,[130] M. D. Messier,[87] W. Metcalf,[110] M. Mewes,[87] H. Meyer,[166] T. Miao,[55] G. Michna,[147] T. Miedema,[121] J. Migenda,[145] R. Milincic,[67] W. Miller,[159] J. Mills,[158] C. Milne,[82] O. Mineev,[79] O. G. Miranda,[34] S. Miryala,[14] C. S. Mishra,[55] S. R. Mishra,[148] A. Mislivec,[159] D. Mladenov,[17] I. Mocioiu,[132] K. Moffat,[46] N. Moggi,[72] R. Mohanta,[69] T. A. Mohayai,[55] N. Mokhov,[55] J. Molina,[6] L. Molina Bueno,[48] A. Montanari,[72] C. Montanari,[78] D. Montanari,[55] L. M. Montano Zetina,[34] J. Moon,[114] M. Mooney,[37] D. Moreno,[3] B. Morgan,[165] C. Morris,[68] C. Mossey,[55] E. Motuk,[160] C. A. Moura,[53] J. Mousseau,[115] W. Mu,[55] L. Mualem,[26] J. Mueller,[37] M. Muether,[166] S. Mufson,[87] F. Muheim,[49] A. Muir,[43] M. Mulhearn,[21] H. Muramatsu,[159] S. Murphy,[48] J. Musser,[87] J. Nachtman,[89] M. Nalbandyan,[170] R. Nandakumar,[141] D. Naples,[135] S. Narita,[91] N. Nayak,[22] M. Nebot-Guinot,[49] L. Necib,[26] K. Negishi,[91] J. K. Nelson,[167] J. Nesbit,[168] M. Nessi,[17] D. Newbold,[141] M. Newcomer,[131] D. Newhart,[55] R. Nichol,[160] E. Niner,[55] K. Nishimura,[67] A. Norman,[55] R. Northrop,[31] P. Novella,[71] J. Nowak,[106] M. Oberling,[4] A. Olivares Del Campo,[46] A. Olivier,[139] Y. Onel,[89] Y. Onishchuk,[100] J. Ott,[22] L. Pagani,[21] S. Pakvasa,[67] O. Palamara,[55] S. Palestini,[17] J. M. Paley,[55] M. Pallavicini,[74] C. Palomares,[18] E. Pantic,[21] V. Paolone,[135] V. Papadimitriou,[55] R. Papaleo,[151] A. Papanestis,[141] S. Paramesvaran,[13] S. Parke,[55] Z. Parsa,[14] M. Parvu,[15] S. Pascoli,[46] L. Pasqualini,[72] J. Pasternak,[84] J. Pater,[113] C. Patrick,[160] L. Patrizii,[72] R. B. Patterson,[26] S. J. Patton,[107] T. Patzak,[1] A. Paudel,[97] B. Paulos,[168] L. Paulucci,[53] Z. Pavlovic,[55] G. Pawloski,[159] D. Payne,[108] V. Pec,[145] S. J. M. Peeters,[152] Y. Penichot,[16] E. Pennacchio,[80] A. Penzo,[89] O. L. G. Peres,[28] J. Perry,[49] D. Pershey,[45] G. Pessina,[75] G. Petrillo,[142] C. Petta,[73] R. Petti,[148] F. Piastra,[10] L. Pickering,[116] F. Pietropaolo,[17,130] J. Pillow,[165] R. Plunkett,[55] R. Poling,[159] X. Pons,[17] N. Poonthottathil,[90] S. Pordes,[55] M. Potekhin,[14] R. Potenza,[73] B. V. K. S. Potukuchi,[92] J. Pozimski,[84] M. Pozzato,[72] S. Prakash,[28] T. Prakash,[107] S. Prince,[66] D. Pugnere,[80] X. Qian,[14] J. L. Raaf,[55] V. Radeka,[14] J. Rademacker,[13] B. Radics,[48] A. Rafique,[4] E. Raguzin,[14] M. Rai,[165] M. Rajaoalisoa,[33] I. Rakhno,[55] L. Rakotondravohitra,[2] Y. A. Ramachers,[165] R. Rameika,[55] M. A. Ramirez Delgado,[63] B. Ramson,[55] A. Rappoldi,[78] G. Raselli,[78] P. Ratoff,[106] S. Ravat,[17] J.S. Real,[62] B. Rebel,[168,55] D. Redondo,[18] M. Reggiani-Guzzo,[28] T. Rehak,[44] J. Reichenbacher,[146] S. D. Reitzner,[55] A. Renshaw,[68] S. Rescia,[14] F. Resnati,[17] A. Reynolds,[128] G. Riccobene,[151] L. C. J. Rice,[135] K. Rielage,[109] Y. Rigaut,[48] D. Rivera,[131] L. Rochester,[142] M. Roda,[108] P. Rodrigues,[128] M. J. Rodriguez Alonso,[17] J. Rodriguez Rondon,[146] A. J. Roeth,[45] H. Rogers,[37] S. Rosauro-Alcaraz,[112] M. Rossella,[78] J. Rout,[93] S. Roy,[65] A. Rubbia,[48] C. Rubbia,[59] B. Russell,[107] J. Russell,[142] D. Ruterbories,[139] R. Saakyan,[160] S. Sacerdoti,[1] T. Safford,[116] N. Sahu,[86] P. Sala,[76,17] N. Samios,[14] M. C. Sanchez,[90] D. A. Sanders,[118] D. Sankey,[141] S. Santana,[137] M. Santos-Maldonado,[137] N. Saoulidou,[7] P. Sapienza,[151] C. Sarasty,[33] I. Sarcevic,[5] G. Savage,[55] V. Savinov,[135] A. Scaramelli,[78] A. Scarff,[145] A. Scarpelli,[1] T. Schaffer,[117] H. Schellman,[127] P. Schlabach,[55] D. Schmitz,[31] K. Scholberg,[45] A. Schukraft,[55] E. Segreto,[28] J. Sensenig,[131] I. Seong,[22] A. Sergi,[11] D. Sgalaberna,[17] M. H. Shaevitz,[38] S. Shafaq,[93] H. R. Sharma,[92] R. Sharma,[14] T. Shaw,[55] C. Shepherd-Themistocleous,[141] S. Shin,[31] D. Shooltz,[116] R. Shrock,[150] L. Simard,[101] N. Simos,[14] J. Sinclair,[10] G. Sinev,[45] J. Singh,[111] J. Singh,[111] R. Sipos,[17] F. W. Sippach,[38] G. Sirri,[72] A. Sitraka,[146] K. Siyeon,[32]

A. Smith,[45] A. Smith,[27] E. Smith,[87] P. Smith,[87] J. Smolik,[40] M. Smy,[22] P. Snopok,[83] M. Soares Nunes,[28] H. Sobel,[22] M. Soderberg,[153] C. J. Solano Salinas,[88] S. Söldner-Rembold,[113] N. Solomey,[166] V. Solovov,[103] W. E. Sondheim,[109] M. Sorel,[71] J. Soto-Oton,[18] A. Sousa,[33] K. Soustruznik,[30] F. Spagliardi,[128] M. Spanu,[14] J. Spitz,[115] N. J. Spooner,[145] K. Spurgeon,[153] R. Staley,[11] M. Stancari,[55] L. Stanco,[130] H. M. Steiner,[107] J. Stewart,[14] B. Stillwell,[31] J. Stock,[146] F. Stocker,[17] T. Stokes,[110] M. Strait,[159] T. Strauss,[55] S. Striganov,[55] A. Stuart,[35] D. Summers,[118] A. Surdo,[143] V. Susic,[9] L. Suter,[55] C. M. Sutera,[73] R. Svoboda,[21] B. Szczerbinska,[155] A. Szelc,[113] R. Talaga,[4] H. A. Tanaka,[142] B. Tapia Oregui,[157] A. Tapper,[84] S. Tariq,[55] E. Tatar,[82] R. Tayloe,[87] A. M. Teklu,[150] M. Tenti,[72] K. Terao,[142] C. A. Ternes,[71] F. Terranova,[75] G. Testera,[74] A. Thea,[141] J. L. Thompson,[145] C. Thorn,[14] S. C. Timm,[55] J. Todd,[33] A. Tonazzo,[1] J. Torres de Mello Neto,[54] M. Torti,[75] M. Tortola,[71] F. Tortorici,[73] D. Totani,[55] M. Toups,[55] C. Touramanis,[108] J. Trevor,[26] W. H. Trzaska,[94] Y. T. Tsai,[142] Z. Tsamalaidze,[58] K. V. Tsang,[142] N. Tsverava,[58] S. Tufanli,[17] C. Tull,[107] E. Tyley,[145] M. Tzanov,[110] M. A. Uchida,[27] J. Urheim,[87] T. Usher,[142] M. R. Vagins,[98] P. Vahle,[167] G. A. Valdiviesso,[50] Z. Vallari,[26] J. W. F. Valle,[71] S. Vallecorsa,[17] R. Van Berg,[131] R. G. Van de Water,[109] D. Vanegas Forero,[28] F. Varanini,[130] D. Vargas,[70] G. Varner,[67] J. Vasel,[87] G. Vasseur,[16] K. Vaziri,[55] S. Ventura,[130] A. Verdugo,[18] S. Vergani,[27] M. A. Vermeulen,[121] M. Verzocchi,[55] H. Vieira de Souza,[28] C. Vignoli,[60] C. Vilela,[150] B. Viren,[14] T. Vrba,[40] T. Wachala,[120] A. V. Waldron,[84] M. Wallbank,[33] H. Wang,[23] J. Wang,[21] Y. Wang,[23] Y. Wang,[150] K. Warburton,[90] D. Warner,[37] M. Wascko,[84] D. Waters,[160] A. Watson,[11] P. Weatherly,[44] A. Weber,[141,128] M. Weber,[10] H. Wei,[14] A. Weinstein,[90] D. Wenman,[168] M. Wetstein,[90] A. White,[156] L. H. Whitehead,[27] D. Whittington,[153] M. J. Wilking,[150] C. Wilkinson,[10] Z. Williams,[156] F. Wilson,[141] R. J. Wilson,[37] J. Wolcott,[158] T. Wongjirad,[158] K. Wood,[150] L. Wood,[129] E. Worcester,[14] M. Worcester,[14] C. Wret,[139] W. Wu,[55] G. Yang,[150] S. Yang,[33] T. Yang,[55] N. Yershov,[79] K. Yonehara,[55] T. Young,[122] B. Yu,[14] J. Yu,[156] J. Zalesak,[39] L. Zambelli,[19] B. Zamorano,[61] A. Zani,[76] L. Zazueta,[167] G. P. Zeller,[55] J. Zennamo,[55] K. Zeug,[168] C. Zhang,[14] M. Zhao,[14] E. Zhivun,[14] G. Zhu,[126] E. D. Zimmerman,[36] M. Zito,[16] S. Zucchelli,[72] J. Zuklin,[39] V. Zutshi,[123] and R. Zwaska[55]

(The DUNE Collaboration)

[1] *APC - Université de Paris, CNRS/IN2P3, CEA/lrfu, Observatoire de Paris, 10, rue Alice Domon et Léonie Duquet, 75205 Paris Cedex 13, France*
[2] *University of Antananarivo, BP 566, Antananarivo 101, Madagascar*
[3] *Universidad Antonio Nariño, Cra 3 Este No 47A-15, Bogotá, Colombia*
[4] *Argonne National Laboratory, Argonne, IL 60439, USA*
[5] *University of Arizona, 1118 E. Fourth Street Tucson, AZ 85721, USA*
[6] *Universidad Nacional de Asunción, San Lorenzo, Paraguay*
[7] *University of Athens, University Campus, Zografou GR 157 84, Greece*
[8] *Universidad del Atlantico, Carrera 30 Nmero 8- 49 Puerto Colombia - Atlntico, Colombia*
[9] *University of Basel, Klingelbergstrasse 82, CH-4056 Basel, Switzerland*
[10] *University of Bern, Sidlerstrasse 5, CH-3012 Bern, Switzerland*
[11] *University of Birmingham, Edgbaston, Birmingham B15 2TT, United Kingdom*
[12] *Boston University, Boston, MA 02215, USA*
[13] *University of Bristol, H. H. Wills Physics Laboratory, Tyndall Avenue Bristol BS8 1TL, United Kingdom*
[14] *Brookhaven National Laboratory, Upton, NY 11973, USA*
[15] *University of Bucharest, Faculty of Physics, Bucharest, Romania*
[16] *CEA/Saclay, IRFU Institut de Recherche sur les Lois Fondamentales de l'Univers, F-91191 Gif-sur-Yvette CEDEX, France*
[17] *CERN, European Organization for Nuclear Research 1211 Genève 23, Switzerland, CERN*
[18] *CIEMAT, Centro de Investigaciones Energéticas, Medioambientales y Tecnológicas, Av. Complutense, 40, E-28040 Madrid, Spain*
[19] *Laboratoire d'Annecy-le-Vieux de Physique des Particules, CNRS/IN2P3 and Université Savoie Mont Blanc, CNRS/IN2P3 and Université Savoie Mont Blanc, 74941 Annecy-le-Vieux, France*
[20] *University of California Berkeley, Berkeley, CA 94720, USA*
[21] *University of California Davis, Davis, CA 95616, USA*
[22] *University of California Irvine, Irvine, CA 92697, USA*
[23] *University of California Los Angeles, Los Angeles, CA 90095, USA*
[24] *University of California Riverside, 900 University Ave, Riverside CA 92521*
[25] *University of California Santa Barbara, Santa Barbara, California 93106 USA*
[26] *California Institute of Technology, Pasadena, CA 91125, USA*
[27] *University of Cambridge, JJ Thomson Avenue, Cambridge CB3 0HE, United Kingdom*
[28] *Universidade Estadual de Campinas, Campinas - SP, 13083-970, Brazil*
[29] *Centro Brasileiro de Pesquisas Físicas, Rio de Janeiro, RJ 22290-180, Brazil*
[30] *Institute of Particle and Nuclear Physics of the Faculty of Mathematics and Physics of the Charles University in Prague, V Holešovičkách 747/2, 180 00 Praha 8-Libeň, Czech Republic*
[31] *University of Chicago, Chicago, IL 60637, USA*

[32] Chung-Ang University, Dongjak-Gu, Seoul 06974, South Korea
[33] University of Cincinnati, Cincinnati, OH 45221, USA
[34] Centro de Investigacion y de Estudios Avanzados del IPN (Cinvestav), Mexico City
[35] Universidad de Colima, 340 Colonia Villa San Sebastian Colima, Colima, Mexico
[36] University of Colorado Boulder, Boulder, CO 80309, USA
[37] Colorado State University, Fort Collins, CO 80523, USA
[38] Columbia University, New York, NY 10027, USA
[39] Institute of Physics, Czech Academy of Sciences, Na Slovance 2, 182 21 Praha 8, Czech Republic
[40] Czech Technical University in Prague, Břehová 78/7, 115 19 Prague 1, Czech Republic
[41] Dakota State University, Madison, SD 57042, USA
[42] University of Dallas, Irving, TX 75062-4736, USA
[43] Daresbury Laboratory, Daresbury Warrington, Cheshire WA4 4AD, United Kingdom
[44] Drexel University, Philadelphia, PA 19104, USA
[45] Duke University, Durham, NC 27708, USA
[46] Durham University, South Road, Durham DH1 3LE, United Kingdom
[47] Universidad EIA, Via José María Córdoba #km 2 + 200, Envigado, Antioquia
[48] ETH Zurich, Institute for Particle Physics, Zurich, Switzerland
[49] University of Edinburgh, Edinburgh EH8 9YL, United Kingdom
[50] Universidade Federal de Alfenas, Poços de Caldas - MG, 37715-400, Brazil
[51] Universidade Federal de Goias, Goiania, GO 74690-900, Brazil
[52] Universidade Federal de São Carlos, Araras - SP, 13604-900, Brazil
[53] Universidade Federal do ABC, Av. dos Estados 5001, Santo André - SP, 09210-580 Brazil
[54] Universidade Federal do Rio de Janeiro, Rio de Janeiro - RJ, 21941-901, Brazil
[55] Fermi National Accelerator Laboratory, Batavia, IL 60510
[56] University of Florida, PO Box 118440 Gainesville, FL 32611-8440, USA
[57] Fluminense Federal University, Rua Miguel de Frias, 9 Icaraí Niterói - RJ, 24220-900, Brazil
[58] Georgian Technical University, 77 Kostava Str. 0160, Tbilisi, Georgia
[59] Gran Sasso Science Institute, Viale Francesco Crispi 7, L'Aquila, Italy
[60] Laboratori Nazionali del Gran Sasso, I-67010 Assergi, AQ, Italy
[61] University of Granada & CAFPE, Campus Fuentenueva (Edif. Mecenas), 18002 Granada, Spain
[62] University Grenoble Alpes, CNRS, Grenoble INP, LPSC-IN2P3, 38000 Grenoble, France
[63] Universidad de Guanajuato, Gto., C.P. 37000, Mexico
[64] Department of Physics, K L E F, Green Fields, Guntur - 522 502, AP, India
[65] Harish-Chandra Research Institute, Jhunsi, Allahabad 211 019, India
[66] Harvard University, 17 Oxford St. Cambridge, MA 02138, USA
[67] University of Hawaii, Honolulu, HI 96822, USA
[68] University of Houston, Houston, TX 77204, USA
[69] University of Hyderabad, Gachibowli, Hyderabad - 500 046, India
[70] Institut de Fisica d'Altes Energies (IFAE), Campus UAB, Facultat Ciences Nord, 08193 Bellaterra, Barcelona, Spain
[71] Instituto de Fisica Corpuscular, Catedratico Jose Beltran, 2 E-46980 Paterna (Valencia), Spain
[72] Istituto Nazionale di Fisica Nucleare Bologna, 40127 Bologna BO, Italy
[73] Istituto Nazionale di Fisica Nucleare Sezione di Catania, Via Santa Sofia 64, I-95123 Catania, Italy
[74] Università degli studi di Genova, Istituto Nazionale di Fisica Nucleare Genova, 16126 Genova GE, Italy
[75] Istituto Nazionale di Fisica Nucleare Sezione di Milano Bicocca and
University of Milano Bicocca,, Piazza della Scienza, 3 - I-20126 Milano, Italy
[76] Istituto Nazionale di Fisica Nucleare Milano, I-20133 Milano, Italy
[77] Istituto Nazionale di Fisica Nucleare - Sezione di Napoli, Complesso Universitario di Monte S. Angelo, I-80126 Napoli, Italy
[78] Università degli studi di Pavia, Istituto Nazionale di Fisica Nucleare Sezione di Pavia, I-27100 Pavia, Italy
[79] Institute for Nuclear Research of the Russian Academy of Sciences , prospekt 60-letiya Oktyabrya 7a, Moscow 117312, Russia
[80] Institut de Physique des 2 Infinis de Lyon, Rue E. Fermi 4 69622 Villeurbanne, France
[81] Institute for Research in Fundamental Sciences , Farmanieh St. Tehran, 19538-33511, Iran
[82] Idaho State University, Department of Physics, Pocatello, ID 83209, USA
[83] Illinois Institute of Technology, Chicago, IL 60616, USA
[84] Imperial College of Science Technology and Medicine, Blackett
Laboratory Prince Consort Road, London SW7 2BZ, United Kingdom
[85] Indian Institute of Technology Guwahati, Guwahati, 781 039, India
[86] Indian Institute of Technology Hyderabad, Hyderabad, 502285, India
[87] Indiana University, Bloomington, IN 47405, USA
[88] Universidad Nacional de Ingeniería, Av. Tupac Amaru 210, Lima 25, Peru
[89] University of Iowa, Department of Physics and Astronomy 203 Van Allen Hall Iowa City, IA 52242, USA
[90] Iowa State University, Ames, Iowa 50011, USA
[91] Iwate University, Morioka, Iwate 020-8551, Japan
[92] University of Jammu, Physics Department, JAMMU-180006, India
[93] Jawaharlal Nehru University, School of Physical Sciences, New Delhi 110067, India

[94] University of Jyvaskyla, P.O. Box 35, FI-40014, Finland
[95] High Energy Accelerator Research Organization (KEK), Ibaraki, 305-0801, Japan
[96] Korea Institute of Science and Technology Information, Daejeon, 34141, South Korea
[97] Kansas State University, Manhattan, KS 66506, USA
[98] Kavli Institute for the Physics and Mathematics of the Universe , Kashiwa, Chiba 277-8583, Japan
[99] National Institute of Technology, Kure College, Hiroshima, 737-8506, Japan
[100] Kyiv National University, 64, 01601 Kyiv, Ukraine
[101] Laboratoire de l'Accélérateur Linéaire , Bâtiment 200, 91440 Orsay, France
[102] Laboratório de Instrumentação e Física Experimental de Partículas - LIP, Lisboa, Portugal
[103] Laboratório de Instrumentação e Física Experimental de Partículas - LIP, Coimbra, Portugal
[104] Instituto Superior Técnico - IST, Universidade de Lisboa, Portugal
[105] Faculdade de Ciências - FCUL, Universidade de Lisboa, Portugal
[106] Lancaster University, Bailrigg, Lancaster LA1 4YB, United Kingdom
[107] Lawrence Berkeley National Laboratory, Berkeley, CA 94720, USA
[108] University of Liverpool, L69 7ZE, Liverpool, United Kingdom
[109] Los Alamos National Laboratory, Los Alamos, NM 87545, USA
[110] Louisiana State University, Baton Rouge, LA 70803, USA
[111] University of Lucknow, Lucknow 226007, Uttar Pradesh, India
[112] Madrid Autonoma University and IFT UAM/CSIC, Ciudad Universitaria de Cantoblanco 28049 Madrid, Spain
[113] University of Manchester, Oxford Road, Manchester M13 9PL, United Kingdom
[114] Massachusetts Institute of Technology, Cambridge, MA 02139, USA
[115] University of Michigan, Ann Arbor, MI 48109, USA
[116] Michigan State University, East Lansing, MI 48824, USA
[117] University of Minnesota Duluth, Duluth, MN 55812, USA
[118] University of Mississippi, P.O. Box 1848, University, MS 38677 USA
[119] University of New Mexico, 1919 Lomas Blvd. N.E. Albuquerque, NM 87131, USA
[120] H. Niewodniczański Institute of Nuclear Physics, Polish Academy of Sciences, Cracow, Poland
[121] Nikhef National Institute of Subatomic Physics, Science Park, Amsterdam, Netherlands
[122] University of North Dakota, 3501 University Ave Grand Forks, ND 58202-8357, USA
[123] Northern Illinois University, Department of Physics, DeKalb, Illinois 60115, USA
[124] Northwestern University, Evanston, Il 60208, USA
[125] University of Notre Dame, Notre Dame, IN 46556, USA
[126] Ohio State University, 191 W. Woodruff Ave. Columbus, OH 43210, USA
[127] Oregon State University, Corvallis, OR 97331, USA
[128] University of Oxford, Oxford, OX1 3RH, United Kingdom
[129] Pacific Northwest National Laboratory, Richland, WA 99352, USA
[130] Universtà Degli Studi di Padova, Dip. Fisica e Astronomia G. Galilei and INFN Sezione di Padova, I-35131 Padova, Italy
[131] University of Pennsylvania, Philadelphia, PA 19104, USA
[132] Pennsylvania State University, University Park, PA 16802, USA
[133] Physical Research Laboratory, Ahmedabad 380 009, India
[134] Università di Pisa, Theor. Division; Largo B. Pontecorvo 3, Ed. B-C, I-56127 Pisa, Italy
[135] University of Pittsburgh, Pittsburgh, PA 15260, USA
[136] Pontificia Universidad Católica del Perú, Apartado 1761, Lima, Peru
[137] University of Puerto Rico, Mayaguez, 00681, USA
[138] Punjab Agricultural University, Department of Math. Stat. & Physics, Ludhiana 141004, India
[139] University of Rochester, Rochester, NY 14627, USA
[140] Rutgers University, Piscataway, NJ, 08854, USA
[141] STFC Rutherford Appleton Laboratory, OX11 0QX Harwell Campus, Didcot, United Kingdom
[142] SLAC National Acceleratory Laboratory, Menlo Park, CA 94025, USA
[143] Universitá del Salento and Istituto Nazionale Fisica Nucleare, Via Provinciale per Arnesano, 73100 Lecce, Italy
[144] Universidad Sergio Arboleda, Cll 74 -14 -14, 11022 Bogotá, Colombia
[145] University of Sheffield, Department of Physics and Astronomy, Sheffield S3 7RH, United Kingdom
[146] South Dakota School of Mines and Technology, Rapid City, SD 57701, USA
[147] South Dakota State University, Brookings, SD 57007, USA
[148] University of South Carolina, Columbia, SC 29208, USA
[149] Southern Methodist University, Dallas, TX 75275, USA
[150] Stony Brook University, SUNY, Stony Brook, New York 11794, USA
[151] INFN - Laboratori Nazionali del Sud (LNS), Via S. Sofia 62, 95123 Catania, Italy
[152] University of Sussex, Brighton, BN1 9RH, United Kingdom
[153] Syracuse University, Syracuse, NY 13244, USA
[154] University of Tennessee at Knoxville, TN, 37996, USA
[155] Texas A&M University (Corpus Christi), Corpus Christi, TX 78412, USA
[156] University of Texas Arlington, Arlington, TX 76019, USA
[157] University of Texas (Austin), Austin, TX 78712, USA

[158] *Tufts University, Medford, MA 02155, USA*
[159] *University of Minnesota Twin Cities, Minneapolis, MN 55455, USA*
[160] *University College London, London, WC1E 6BT, United Kingdom*
[161] *Valley City State University, Valley City, ND 58072, USA*
[162] *Variable Energy Cyclotron Centre, 1/AF, Bidhannagar Kolkata - 700 064 West Bengal, India*
[163] *Virginia Tech, Blacksburg, VA 24060, USA*
[164] *University of Warsaw, Faculty of Physics ul. Pasteura 5 02-093 Warsaw, Poland*
[165] *University of Warwick, Coventry CV4 7AL, United Kingdom*
[166] *Wichita State University, Physics Division, Wichita, KS 67260, USA*
[167] *William and Mary, Williamsburg, VA 23187, USA*
[168] *University of Wisconsin Madison, Madison, WI 53706, USA*
[169] *Yale University, New Haven, CT 06520, USA*
[170] *Yerevan Institute for Theoretical Physics and Modeling, Halabian Str. 34, Yerevan 0036, Armenia*
[171] *York University, Physics and Astronomy Department, 4700 Keele St. Toronto M3J 1P3, Canada*

Contents

Contents i

List of Figures v

List of Tables x

A Roadmap of the DUNE Technical Design Report 1

1 Introduction and Executive Summary 3
- 1.1 Overview of DUNE and its Science Program . . . 3
  - 1.1.1 Key Goals of the DUNE Science Program . . . 4
  - 1.1.2 Summary of Assumptions and Methods Employed . . . 5
  - 1.1.3 Selected Results from Sensitivity Studies . . . 8
- 1.2 Science Drivers for LBNF/DUNE Design Specifications . . . 13
  - 1.2.1 General LBNF/DUNE Operating Principles . . . 14
  - 1.2.2 Far Detector Performance Requirements . . . 15
- 1.3 Scope and Organization of this Document . . . 23

2 Introduction to LBNF and DUNE 24
- 2.1 The LBNF Facility . . . 24
- 2.2 DUNE: Far Detector Modules . . . 26
  - 2.2.1 Single-phase Technology . . . 28
  - 2.2.2 Dual-phase Technology . . . 29
  - 2.2.3 ProtoDUNEs: Far Detector Prototypes . . . 31
- 2.3 Near Detector Complex . . . 32

3 Scientific Landscape 36
- 3.1 Neutrino Oscillation Physics . . . 36
  - 3.1.1 Oscillation Physics with Three Neutrino Flavors . . . 37
  - 3.1.2 Fermion Flavor Physics: Masses, Mixing Angles and CP-odd Phases . . . 42
  - 3.1.3 Impacts of DUNE for other Experimental Programs . . . 44
  - 3.1.4 Neutrino Masses, CP-violation and Leptogenesis . . . 45
- 3.2 Nucleon Decay and ΔB=2 Physics . . . 46
  - 3.2.1 Experimental Considerations for Nucleon Decay Searches . . . 47
- 3.3 Low-Energy Neutrinos from Supernovae and Other Sources . . . 49
  - 3.3.1 Current Experimental Landscape . . . 50

3.3.2 Projected Landscape in the DUNE Era . . . 50
3.3.3 The Role of DUNE . . . 51
3.3.4 Beyond Core Collapse . . . 51
3.4 Beyond-SM Searches . . . 52
3.4.1 Search for low-mass dark matter . . . 53
3.4.2 Sterile neutrino search . . . 53
3.4.3 Neutrino tridents . . . 56
3.4.4 Heavy neutral leptons . . . 56
3.5 Other Scientific Opportunities . . . 57

4 Tools and Methods 59
4.1 Monte Carlo Simulations . . . 59
4.1.1 Neutrino Flux Modeling . . . 60
4.1.2 Neutrino Interaction Generators . . . 70
4.1.3 Detector Simulation . . . 72
4.1.4 Data Acquisition Simulations and Assumptions . . . 77
4.2 Event Reconstruction in the far detector (FD) . . . 78
4.2.1 TPC Signal Processing . . . 78
4.2.2 Hit and Space-Point Identification . . . 79
4.2.3 Hit Clustering, Pattern Recognition and Particle Reconstruction . . . 84
4.2.4 Calorimetric Energy Reconstruction and Particle Identification . . . 92
4.2.5 Optical Reconstruction . . . 93
4.3 Reconstruction Performance . . . 94
4.3.1 Pandora Performance Assessment . . . 94
4.3.2 Reconstruction Performance in the DUNE FD . . . 95
4.3.3 Reconstruction Performance in ProtoDUNE-SP . . . 101
4.3.4 High-Level Reconstruction . . . 105
4.4 DUNE Calibration Strategy . . . 109
4.4.1 Physics-driven Calibration Requirements . . . 110
4.4.2 Calibration Sources, Systems and External Measurements . . . 111
4.4.3 Calibration Staging Plan . . . 119
4.4.4 ^{39}Ar beta decays . . . 120

5 Standard neutrino oscillation physics program 122
5.1 Overview and Theoretical Context . . . 122
5.2 Expected Event Rate and Oscillation Parameters . . . 127
5.3 Neutrino Beam Flux and Uncertainties . . . 128
5.4 Neutrino Interactions and Uncertainties . . . 132
5.4.1 Interaction Model Summary . . . 132
5.4.2 Interaction Model Uncertainties . . . 133
5.4.3 Listing of Interaction Model Uncertainties . . . 138
5.5 The Near Detector Simulation and Reconstruction . . . 142
5.5.1 The Near Detector Concept . . . 142
5.5.2 Event Simulation and Parameterized Reconstruction . . . 144
5.6 The Far Detector Simulation and Reconstruction . . . 150
5.6.1 Simulation . . . 150
5.6.2 Event Reconstruction and Kinematic Variables . . . 150

5.6.3 Neutrino Event Selection using convolutional visual network (CVN) . . . 152
5.6.4 FD Neutrino Interaction Samples . . . 156
5.7 Detector Model and Uncertainties . . . 156
5.7.1 Energy Scale Uncertainties . . . 157
5.7.2 Acceptance and Reconstruction Efficiency Uncertainties . . . 158
5.8 Sensitivity Methods . . . 159
5.8.1 The Deep Underground Neutrino Experiment (DUNE) Analysis Framework . . . 160
5.8.2 DUNE Sensitivity Studies . . . 161
5.9 Sensitivities . . . 164
5.9.1 CP-Symmetry Violation . . . 165
5.9.2 Mass Hierarchy . . . 168
5.9.3 Precision Oscillation Parameter Measurements . . . 170
5.9.4 Impact of Oscillation Parameter Central Values . . . 173
5.9.5 Impact of Systematic Uncertainties . . . 175
5.9.6 Impact of the Near Detector . . . 178
5.10 Conclusion . . . 189

6 GeV-Scale Non-accelerator Physics Program 191
6.1 Nucleon Decay . . . 191
6.1.1 Experimental Signatures for Nucleon Decay Searches in DUNE . . . 193
6.1.2 Sensitivity to $p \to K^+\overline{\nu}$ Decay . . . 199
6.1.3 Sensitivity to Other Key Nucleon Decay Modes . . . 203
6.1.4 Detector Requirements for Nucleon Decay Searches . . . 204
6.1.5 Nucleon Decay Summary . . . 205
6.2 Neutron-Antineutron Oscillations . . . 205
6.2.1 Sensitivity to Intranuclear Neutron-Antineutron Oscillations in DUNE . . . 206
6.3 Physics with Atmospheric Neutrinos . . . 211
6.3.1 Oscillation Physics with Atmospheric Neutrinos . . . 211
6.3.2 BSM Physics with Atmospheric Neutrinos . . . 213

7 Supernova neutrino bursts and physics with low-energy neutrinos 216
7.1 Supernova neutrino bursts . . . 217
7.1.1 Neutrinos from collapsed stellar cores: basics . . . 217
7.1.2 Stages of the explosion . . . 217
7.2 Low-Energy Events in DUNE . . . 221
7.2.1 Detection Channels and Interaction Rates . . . 221
7.2.2 Event Simulation and Reconstruction . . . 222
7.3 Expected Supernova Burst Signal Properties . . . 225
7.3.1 Directionality: pointing to the supernova . . . 226
7.4 Astrophysics of Core Collapse . . . 230
7.4.1 Supernova Spectral Parameter Fits . . . 231
7.5 Neutrino Physics and Other Particle Physics . . . 233
7.5.1 Neutrino Mass Ordering . . . 234
7.5.2 Lorentz Invariance Violation . . . 237
7.6 Additional Astrophysical Neutrinos . . . 239
7.6.1 Solar Neutrinos . . . 239
7.6.2 Diffuse Supernova Background Neutrinos . . . 240

7.6.3 Other Low-Energy Neutrino Sources . . . 240
7.7 Burst Detection and Alert . . . 241

8 Beyond the Standard Model Physics Program 242
8.1 Executive Summary . . . 242
8.2 Common Tools: Simulation, Systematics, Detector Components . . . 244
8.2.1 Neutrino Beam Simulation . . . 244
8.2.2 Detector Properties . . . 245
8.3 Sterile Neutrino Searches . . . 246
8.3.1 Probing Sterile Neutrino Mixing with DUNE . . . 247
8.3.2 Setup and Methods . . . 248
8.3.3 Results . . . 249
8.4 Non-Unitarity of the Neutrino Mixing Matrix . . . 253
8.4.1 NU constraints from DUNE . . . 254
8.4.2 NU impact on DUNE standard searches . . . 254
8.5 Non-Standard Neutrino Interactions . . . 256
8.5.1 NSI in propagation at DUNE . . . 257
8.5.2 Effects of baseline and matter-density variation on NSI measurements . . . 258
8.6 CPT Symmetry Violation . . . 260
8.6.1 Imposter solutions . . . 264
8.7 Search for Neutrino Tridents at the Near Detector . . . 264
8.7.1 Sensitivity to new physics . . . 266
8.8 Dark Matter Probes . . . 268
8.8.1 Benchmark Dark Matter Models . . . 270
8.8.2 Search for Low-Mass Dark Mater at the Near Detector . . . 271
8.8.3 Inelastic Boosted Dark Matter Search at the DUNE FD . . . 274
8.8.4 Elastic Boosted Dark Matter from the Sun . . . 278
8.8.5 Discussion and Conclusions . . . 281
8.9 Other BSM Physics Opportunities . . . 283
8.9.1 Tau Neutrino Appearance . . . 283
8.9.2 Large Extra-Dimensions . . . 284
8.9.3 Heavy Neutral Leptons . . . 285
8.9.4 Dark Matter Annihilation in the Sun . . . 287
8.10 Conclusions and Outlook . . . 287

Glossary 289

References 299

List of Figures

1.1 Significance of the DUNE determination of CP-violation . . . 10
1.2 Reconstructed dE/dx of protons and muons in ProtoDUNE-SP . . . 12
1.3 Supernova direction determination from $\nu - e$ elastic scattering events . . . 13
1.4 Separation of photons and electrons by dE/dx in the pre-shower region . . . 16
1.5 90% C.L. contours for spectral parameters for a supernova at 5 kpc. . . . 18
1.6 Dependence of reconstructed SNB event energy on timing-based drift correction . . . 22

2.1 LBNF/DUNE project: beam from Illinois to South Dakota . . . 25
2.2 Underground caverns for DUNE in South Dakota . . . 25
2.3 Neutrino beamline and DUNE near detector hall in Illinois . . . 26
2.4 The SP LArTPC operating principle . . . 28
2.5 A 10 kt DUNE far detector SP module . . . 29
2.6 The DP LArTPC operating principle . . . 30
2.7 A 10 kt DUNE far detector DP module . . . 30
2.8 ProtoDUNE cryostats at the CERN Neutrino Platform . . . 31
2.9 Interior views of the ProtoDUNEs . . . 32
2.10 DUNE near detector . . . 33
2.11 DUNE ND Hall with component detectors . . . 35

3.1 Mass Ordering Illustration . . . 39
3.2 Nufit 4.0 global fit . . . 40
3.3 Summary of nucleon decay experimental limits . . . 48
3.4 Results from the MiniBooNE-DM light dark matter search . . . 54
3.5 Exclusion limits for muon neutrino disappearance to sterile species in a 3+1 model . . . 55
3.6 Sensitivities to heavy neutral leptons . . . 57

4.1 Schematic view of a DUNE SP TPC module . . . 60
4.2 Detailed structure of the APA . . . 61
4.3 Visualization of the focusing system as simulated in g4lbnf . . . 61
4.4 Neutrino fluxes at the near detector . . . 63
4.5 Flux uncertainties at the far detector (FD) as a function of neutrino energy . . . 64
4.6 Focusing and hadron production uncertainties on the ν mode ν_μ flux . . . 65
4.7 Correlation of flux uncertainties . . . 66
4.8 Ratio of neutrino-mode muon neutrino fluxes at the near and far detectors . . . 67
4.9 ν energy as function of parent pion energy for off-axis angles . . . 67
4.10 The predicted ND ν_μ energy spectra, on axis and 30 m off axis . . . 68

4.11 On-axis and off-axis flux uncertainties . . . 69
4.12 Comparison of standard and tau-optimized neutrino fluxes . . . 70
4.13 Garfield configuration for simulating the field response functions . . . 74
4.14 Position-dependent (long-range) field response simulated with the Garfield program . . . 75
4.15 Waveform for minimum ionizing particles traveling parallel to the wire plane . . . 76
4.16 ASIC's electronics shaping functions . . . 77
4.17 Measured and deconvolved waveform from an induction U-plane channel of ProtoDUNE-SP 79
4.18 Raw and deconvolved induction U-plane signals from a ProtoDUNE-SP event . . . 80
4.19 An example of reconstructed hits in ProtoDUNE-SP data . . . 81
4.20 Event displays of SpacePointSolver performance . . . 82
4.21 Main stages of the PANDORA pattern recognition chain . . . 87
4.22 Schema of PANDORA consolidated output and reconstruction strategy for surface LArT-PCs . . . 88
4.23 Overview of wire-cell reconstruction paradigm . . . 90
4.24 3D display of interaction in ProtoDUNE-SP . . . 91
4.25 Interaction channels vs true ν energy; simulated events used to assess performance . . . 96
4.26 Reconstruction efficiency of PANDORA pattern recognition for a range of final-state particles at the FD . . . 97
4.27 Completeness and purities for a range of final-state track-like and shower-like particles . 98
4.28 Number of reconstructed particles vs number of true final-state particles, CC and NC DIS events . . . 99
4.29 Displacements between reconstructed and simulated ν interaction vertices . . . 100
4.30 Reconstruction efficiency for triggered test-beam particles as a function of particle momentum . . . 101
4.31 Pandora reconstruction output for 7 GeV MC test beam event . . . 102
4.32 Reconstruction efficiency for test beam particle in MC per momentum and hits . . . 103
4.33 Reconstructed cosmic rays per event for data and MC . . . 104
4.34 Distribution of reconstructed t_0 for cosmic rays . . . 104
4.35 Opening angle between reconstructed and true direction for track- and shower-like particles 105
4.36 Distribution of reconstructed-true length for different track-like particles . . . 106
4.37 Resolution on test beam interaction vertex on ProtoDUNE data and MC events . . . 107
4.38 Stopping muon dE/dx distributions for the ProtoDUNE-SP cosmic data and MC . . . 107
4.39 Proton dE/dx distributions for the ProtoDUNE-SP 1 GeV beam data and MC . . . 108
4.40 Categories of measurements provided by calibration . . . 112
4.41 Sample distortion that may be difficult to detect with cosmic rays . . . 116
4.42 MicroBooNE laser calibration system schematics . . . 117
4.43 Cross sections enabling the PNS concept . . . 117
4.44 Impact of different detector effects on the reconstructed ^{39}Ar β decay energy spectrum . 121

5.1 Appearance probabilities for ν_e and $\bar{\nu}_e$ at 1300 km . . . 125
5.2 ν_e and $\bar{\nu}_e$ appearance spectra . . . 129
5.3 ν_μ and $\bar{\nu}_\mu$ disappearance spectra . . . 129
5.4 Neutrino fluxes at the far detector . . . 131
5.5 ND visualization . . . 144
5.6 ND selected samples . . . 146
5.7 ND acceptance . . . 147
5.8 DUNE-PRISM fluxes . . . 149

5.9 Fractional residuals of reconstructed ν_μ energy in CC events with contained tracks . . . 152
5.10 Fractional residuals of reconstructed ν_μ energy in CC events with exiting tracks 152
5.11 Fractional residuals of reconstructed ν_e energy in CC events 152
5.12 A simulated 2.2 GeV ν_e CC interaction viewed by collection wires in the SP LArTPC . . 153
5.13 The CVN ν_e CC probability and ν_μ CC probability for the FHC beam mode 154
5.14 The ν_e CC selection efficiency for $P(\nu_e\mathrm{CC}) > 0.85$ 155
5.15 The ν_μ CC selection efficiency for $P(\nu_\mu\mathrm{CC}) > 0.5$ 155
5.16 Flux principal components 164
5.17 Significance of the DUNE determination of CP-violation as a function of δ_{CP} 167
5.18 Significance of the DUNE determination of CP-violation as a function of time 168
5.19 Significance of the DUNE determination of CP-violation as a function of exposure . . . 169
5.20 Significance of the DUNE neutrino mass ordering determination, as a function of δ_{CP} . . 170
5.21 Significance of the DUNE neutrino mass ordering determination, as a function of time . 171
5.22 Significance of the DUNE neutrino mass ordering determination as a function of exposure 172
5.23 Significance of the DUNE determination of the neutrino mass ordering: statistical and systematic variations 173
5.24 Resolution for the DUNE measurement of δ_{CP} as a function of δ_{CP} 174
5.25 Resolution of DUNE measurements of δ_{CP} and $\sin^2 2\theta_{13}$, as a function of exposure . . . 175
5.26 Resolution of DUNE measurements of δ_{CP} and $\sin^2 2\theta_{13}$, as a function of exposure . . . 178
5.27 Two-dimensional 90% C.L. region in $\sin^2 2\theta_{13}$ and δ_{CP} 179
5.28 Two-dimensional 90% C.L. region in $\sin^2 \theta_{23}$ and δ_{CP} 180
5.29 Two-dimensional 90% C.L. region in $\sin^2 \theta_{23}$ and δ_{CP} 181
5.30 Sensitivity of determination of the θ_{23} octant as a function of $\sin^2 \theta_{23}$ 182
5.31 Sensitivity to CP violation and neutrino mass ordering, as a function of δ_{CP} 183
5.32 Sensitivity to CP violation and neutrino mass ordering, as a function of δ_{CP} 183
5.33 Sensitivity to CP violation and neutrino mass ordering, as a function of δ_{CP} 184
5.34 Post-fit systematic uncertainties 185
5.35 Post-fit systematic uncertainties 186
5.36 Oscillation sensitivities including example FD-only bias 187
5.37 Shifted proton energy FD spectra 188
5.38 Δm^2_{32}-sin$^2\theta_{23}$ contour for shifted proton energy 189

6.1 Summary of nucleon decay experimental limits and model predictions 192
6.2 Kaon kinetic energy before and after final state interactions 196
6.3 Tracking efficiency of kaons in $p \to K^+\overline{\nu}$ 197
6.4 Particle identification using $PIDA$ for $p \to K^+\overline{\nu}$ 198
6.5 Boosted Decision Tree response for $p \to K^+\overline{\nu}$ 201
6.6 $p \to K^+\overline{\nu}$ signal event display 202
6.7 $p \to K^+\overline{\nu}$ background event displays 203
6.8 Final state interactions in $n - \bar{n}$ 207
6.9 $n - \bar{n}$ Boosted Decision Tree response 208
6.10 Event display for well-classified $n - \bar{n}$ signal event 209
6.11 Event displays for $n - \bar{n}$ background events 210
6.12 Reconstructed L/E Distribution of 'High-Resolution' Atmospheric Neutrinos 212
6.13 Mass Ordering Sensitivity vs. Exposure for Atmospheric Neutrinos 212
6.14 Sensitivity to Lorenz and CPT violation with atmospheric neutrinos 214
6.15 Atmospheric ν and $\bar{\nu}$ fluxes in the non-minimal isotropic Standard Model Extension . . . 215

7.1 Expected core-collapse parameters . . . 219
7.2 Expected fluxess . . . 220
7.3 Cross sections for supernova-relevant interactions in argon . . . 221
7.4 Model of Argon Reaction Low Energy Yields (MARLEY) event . . . 223
7.5 Resolution and efficiency . . . 224
7.6 MARLEY event . . . 225
7.7 Supernova neutrino rates vs distance . . . 227
7.8 elastic scattering (ES) event . . . 228
7.9 ES and CC events . . . 228
7.10 Pointing vs neutrino energy . . . 229
7.11 Pointing for full supernova . . . 229
7.12 Fit to three pinching parameters . . . 232
7.13 Example of distance effect . . . 232
7.14 Event rates with ordering effects at early times . . . 236
7.15 MH1 . . . 237
7.16 DUNE SN sensitivity to Lorentz, charge, parity, and time reversal symmetry (CPT) violation . . . 238
7.17 Solar neutrino efficiency . . . 240

8.1 Regions of L/E probed by DUNE for 3-flavor and 3+1-flavor ν oscillations . . . 248
8.2 Sensitivities to θ_{14} from ν_e CC samples, and to θ_{24} using ν_μ CC and NC samples . . . 250
8.3 Sensitivity to θ_{34} using the NC samples at the ND and FD . . . 251
8.4 Sensitivity to $\theta_{\mu e}$ from (dis)appearance samples and discovery potential at Liquid Scintilator Neutrino Detector (LSND) best fit . . . 252
8.5 Impact of non-unitarity on the CPV discovery potential . . . 255
8.6 Expected frequentist allowed regions at the 1σ, 90% and 2σ confidence level (CL) . . . 256
8.7 Allowed regions for NSI parameters . . . 258
8.8 Projections of the standard oscillation parameters with nonzero NSI . . . 259
8.9 1D DUNE constraints versus current constraints . . . 260
8.10 Sensitivities to the difference of neutrino and antineutrino parameters . . . 263
8.11 Sensitivity to θ_{23} for (anti)neutrinos, and combination under CPT conservation . . . 264
8.12 Example diagrams for ν_μ-induced trident processes in the SM . . . 265
8.13 Signal and background for selecting muonic trident interactions in ND LArTPC . . . 267
8.14 $\nu_\mu N \to \nu_\mu \mu^+ \mu^- N$ cross section at ND and (axial-)vector couplings of ν_μ to muons . . . 268
8.15 Existing constraints and projected sensitivity in the $L_\mu - L_\tau$ parameter space . . . 269
8.16 DM production via meson decays and DM-e$^-$ elastic scattering . . . 272
8.17 90% CL limit for Y as a function of m_χ at the ND . . . 274
8.18 The inelastic BDM signal under consideration. . . . 275
8.19 Experimental sensitivities for m_{χ_n} values in terms of $m_V - \epsilon$ . . . 276
8.20 Model-independent experimental sensitivities of iBDM search . . . 278
8.21 Processes leading to boosted DM signal from the sun . . . 279
8.22 Diagram illustrating each of the three processes contributing to dark matter scattering in argon: elastic (left), baryon resonance (middle), and deep inelastic (right). . . . 280
8.23 Angular distribution of the BDM signal events for a BDM mass of 10 GeV . . . 281
8.24 Expected 5σ discovery reach with one year of DUNE livetime . . . 281
8.25 Comparison of DUNE (10 yr) sensitivity to Super–Kamiokande sensitivity . . . 282
8.26 The 1σ and 3σ expected sensitivity for measuring Δm^2_{31} and $\sin^2\theta_{23}$ . . . 284

8.27 DUNE sensitivity to the LED model 285
8.28 The 90 % CL sensitivity regions for dominant mixings $|U_{\alpha N}|^2$ 286

List of Tables

1.1 ν_e and $\bar{\nu}_e$ appearance rates . . . 9
1.2 ν_μ and $\bar{\nu}_\mu$ disappearance rates . . . 9
1.3 Projected DUNE oscillation physics milestones . . . 11
1.4 High-level DUNE single-phase far detector design specifications . . . 19

2.1 Components of the DUNE ND . . . 34

4.1 Calibration systems and sources of the nominal DUNE FD calibration design . . . 113
4.2 Annual rates for classes of cosmic-ray events useful for calibration . . . 114

5.1 Parameter values and uncertainties from a global fit to neutrino oscillation data . . . 128
5.2 ν_e and $\bar{\nu}_e$ appearance rates . . . 130
5.3 ν_μ and $\bar{\nu}_\mu$ disappearance rates . . . 130
5.4 Neutrino interaction cross-section systematic parameters considered in GENIE . . . 139
5.5 Intra-nuclear hadron transport systematic parameters implemented in GENIE . . . 140
5.6 List of extra interaction model uncertainties in addition to those provided by GENIE . . . 141
5.7 Neutrino interaction cross-section systematic parameters that receive a central-value tune 142
5.8 Summary of biases and resolutions of reconstructed neutrino energy . . . 152
5.9 Energy scale systematics . . . 158
5.10 Oscillation parameter throws . . . 162
5.11 Projected DUNE oscillation physics milestones . . . 166
5.12 Definition of systematic uncertainty parameters . . . 177

6.1 Expected rate of atmospheric neutrino interactions . . . 193
6.2 GENIE nucleon decay topologies . . . 195
6.3 $n - \bar{n}$ annihilation modes . . . 206
6.4 Atmospheric neutrino event rates per year in different analysis categories . . . 211

7.1 Event numbers 40 kt of liquid argon (LAr) at 10 kpc . . . 226
7.2 Supernova mass ordering signatures . . . 235

8.1 Beam power configuration assumed for the LBNF neutrino beam. . . . 245
8.2 ND properties used in the BSM physics analyses. . . . 245
8.3 FD properties used in the BSM physics analyses. . . . 246
8.4 Projected 90% confidence level (CL) upper limits on sterile mixing angles and matrix elements . . . 251
8.5 Expected 90% CL constraints on the non-unitarity parameters α . . . 254

8.6 Oscillation parameters and priors implemented in MCMC. 259
8.7 Oscillation parameters used to simulate (anti)neutrino data. 262
8.8 Expected number of SM ν_μ and $\bar{\nu}_\mu$-induced trident events at ND per ton of Ar per year 266

A Roadmap of the DUNE Technical Design Report

The Deep Underground Neutrino Experiment (DUNE) far detector (FD) technical design report (TDR) describes the proposed physics program, detector designs, and management structures and procedures at the technical design stage.

The TDR is composed of five volumes, as follows:

- Volume I (Introduction to DUNE) provides an overview of all of DUNE for science policy professionals.
- Volume II (DUNE Physics) describes the DUNE physics program.
- Volume III (DUNE Far Detector Technical Coordination) outlines DUNE management structures, methodologies, procedures, requirements, and risks.
- Volume IV (The DUNE Far Detector Single-Phase Technology) and Volume V (The DUNE Far Detector Dual-Phase Technology) describe the two FD liquid argon time-projection chamber (LArTPC) technologies.

The text includes terms that hyperlink to definitions in a volume-specific glossary. These terms appear underlined in some online browsers, if enabled in the browser's settings.

Chapter 1

Introduction and Executive Summary

The Physics volume of the DUNE far detector (FD) Technical Design Report (TDR) presents the science program of DUNE. Within, we describe the array of identified scientific opportunities and key goals. Crucially, we also report our best current understanding of the capability of DUNE to realize these goals, along with the detailed arguments and investigations on which this understanding is based.

In the context of the complete set of DUNE TDR volumes, a central role for this volume is to document the scientific basis underlying the conception and design of the LBNF/DUNE experimental configurations. As a result, it is the description of DUNE's experimental capabilities that constitutes the bulk of the document. Key linkages between requirements for successful execution of the physics program and primary specifications of the experimental configurations are drawn and summarized.

This document also serves a wider purpose as a statement on the scientific potential of DUNE as a central component within a global program of frontier theoretical and experimental particle physics research. Thus, the presentation also aims to serve as a resource for the particle physics community at large.

In this chapter, the scientific goals, the methodologies utilized to obtain sensitivity projections, the corresponding results for selected elements of the scientific program, and the demands placed on the experiment design and performance are presented in summary form. Together with the two chapters that follow, this summary establishes the context for the detailed descriptions specific to each area of research that comprise the remaining chapters.

1.1 Overview of DUNE and its Science Program

The Deep Underground Neutrino Experiment (DUNE) will be a world-class neutrino observatory and nucleon decay detector designed to answer fundamental questions about the nature of elemen-

tary particles and their role in the universe. The international DUNE experiment, hosted by the U.S. Department of Energy's Fermilab, will consist of a far detector to be located about 1.5 km underground at the Sanford Underground Research Facility (SURF) in South Dakota, USA, at a distance of 1300 km from Fermilab, and a near detector to be located at Fermilab in Illinois. The far detector will be a very large, modular liquid argon time-projection chamber (LArTPC) with a total mass of nearly 70 kt (fiducial mass of at least 40 kt). This LAr technology will make it possible to reconstruct neutrino interactions with image-like precision.

The far detector will be exposed to the world's most intense neutrino beam originating at Fermilab. A high-precision near detector, located in a hall 574 m from the neutrino source on the Fermilab site, will be used to characterize the intensity and energy spectrum of this wide-band beam in real time. Over the long term, the near detector will also enable many strategies for mitigating systematic errors, both through direct cancellation of errors common to both near and far detectors, as well as through dedicated studies of exclusive neutrino interaction channels, beam line characteristics, and reconstructed neutrino energy uncertainties, to name a few.

In this section, the goals of the DUNE science program are presented. Assumptions and methods utilized in determining DUNE's capabilities to meet these goals are summarized, with more detail appearing in Chapter 4. Finally, experimental sensitivities for selected physics measurements are shown to illustrate the achieved level of performance demonstrated.

1.1.1 Key Goals of the DUNE Science Program

The LBNF/DUNE strategy has been developed to meet the requirements set by the U.S. Particle Physics Project Prioritization Panel (P5) in 2014. It also takes into account the recommendations of the European Strategy for Particle Physics (ESPP) adopted by the CERN Council in 2013, which classified the long-baseline (LBL) neutrino program as one of the four scientific objectives requiring significant resources, sizable collaborations, and sustained commitment.

As a benchmark, the P5 report [1] set the goal of reaching a sensitivity to charge-parity symmetry violation (CPV) of better than three standard deviations (3σ) over more than 75% of the range of possible values of the unknown CP-violating phase δ_{CP}. Based partly on this goal, it stated that "the minimum requirements to proceed are the identified capability to reach an exposure of 120 kt $\cdot$ MW $\cdot$ year by the 2035 time frame, the far detector situated underground with cavern space for expansion to at least 40 kt LAr fiducial volume, and 1.2 MW beam power upgradeable to multi-megawatt power. The experiment should have the demonstrated capability to search for supernova neutrino bursts (SNBs) and for proton decay, providing a significant improvement in discovery sensitivity over current searches for the proton lifetime." These requirements are discussed below and in the sections that follow.

To summarize, the DUNE experiment will combine the world's most intense neutrino beam, a deep underground site, and massive LAr detectors to enable a broad science program addressing some of the most fundamental questions in particle physics. This program is articulated in brief form below.

The primary science goals of DUNE are to:

- Carry out a comprehensive program of neutrino oscillation measurements using ν_μ and $\bar{\nu}_\mu$ beams from Fermilab. This program includes measurements of the charge parity (CP) phase, determination of the neutrino mass ordering (the sign of $\Delta m^2_{31} \equiv m^2_3 - m^2_1$), measurement of the mixing angle θ_{23} and the determination of the octant in which this angle lies, and sensitive tests of the three-neutrino paradigm. Paramount among these is the search for CPV in neutrino oscillations, potentially offering insight into the origin of the matter-antimatter asymmetry, one of the fundamental questions in particle physics and cosmology.
- Search for proton decay in several decay modes. The observation of proton decay would represent a ground-breaking discovery in physics, satisfying a key requirement of the grand unification of the forces.
- Detect and measure the ν_e flux from a core-collapse supernova within our galaxy, should one occur during the lifetime of the DUNE experiment. Such a measurement would provide a wealth of unique information about the early stages of core-collapse, and could even signal the birth of a black hole.

The intense neutrino beam from LBNF, the massive DUNE LArTPC far detector, and the high-resolution DUNE near detector will also provide a rich ancillary science program, beyond the primary goals of the experiment. The ancillary science program includes:

- Other accelerator-based neutrino flavor transition measurements with sensitivity to beyond the standard model (BSM) physics, such as non-standard interactions (NSIs), Lorentz invariance violation, charge, parity, and time reversal symmetry (CPT) violation, sterile neutrinos, large extra dimensions, heavy neutral leptons, and tests with measurements of tau neutrino appearance;
- Measurements of neutrino oscillation phenomena using atmospheric neutrinos;
- Searches for dark matter utilizing a variety of signatures in both near and far detectors, as well as non-accelerator searches for BSM physics such as neutron-antineutron oscillation.
- A rich neutrino interaction physics program utilizing the DUNE near detector, including a wide-range of measurements of neutrino cross sections and studies of nuclear effects.

Further advancements in the LArTPC technology during the course of the far detector construction may enhance DUNE's capability to observe very low-energy phenomena such as solar neutrinos or even the diffuse supernova neutrino flux.

1.1.2 Summary of Assumptions and Methods Employed

Scientific capabilities are determined assuming DUNE is configured according to the general parameters described above. Further assumptions regarding the neutrino beam and detector systems, and their deployment, are stated here in Sections 1.1.2.1 and 1.1.2.2. More detail is given in later chapters as appropriate.

Determination of experimental sensitivities relies on the modeling of the underlying physics and background processes, as well as the detector response, including calibration and event reconstruction performance and the utilization of data analysis techniques and tools. While a brief discussion of the strategies employed is given below in Sec. 1.1.2.3, a dedicated chapter (4) is devoted to the presentation of this material. Considerations specific to individual elements of the science program are presented in detail in the corresponding chapters.

1.1.2.1 Beam and Detector

This document presents physics sensitivities using the optimized design of the 1.2 MW neutrino beam and corresponding protons on target (POT) per year assumed to be 1.1 $\times 10^{21}$ POT. These numbers assume a combined uptime and efficiency of the Fermilab accelerator complex and the LBNF beamline of 56%.[1] The beam design, simulation and associated uncertainties are described in Sec. 5.3.

For the neutrino oscillation physics program, it is assumed that equal exposures (time-integrated beam power times fiducial mass) are obtained with both horn current polarities, and therefore with the corresponding mix of primarily ν_μ and $\bar{\nu}_\mu$ data samples (see Sec. 5.2).

It is assumed that the DUNE far detector will include some combination of the different 10 kt fiducial volume implementations (single or dual-phase) of the LArTPC concept for which technical designs have been developed. For much of the science program, it is expected that the capabilities of the two proposed far detector module implementations will be comparable. As a result of the current state of reconstruction and analysis software development (see Sec. 1.1.2.3), the physics sensitivity studies reported in this TDR are based on the single-phase LArTPC implementation, documented in full in Volume IV.

It is also assumed that validation of the DUNE far detector designs will come from data and operational experience acquired with the large-scale ProtoDUNE detectors staged at CERN, including single-particle studies of data obtained in test-beam running. Although this program is in early stages, beam data has already been collected with the ProtoDUNE-SP detector. Where possible, preliminary results from initial analyses of these data are presented in this document (see Chapter 4).

The near detector for DUNE has been under active development, and a Conceptual Design Report is in preparation. Correspondingly, the descriptions utilized in this TDR are consistent with this level of development. As the beam-based neutrino oscillation program depends strongly on the capabilities of the near detector systems, a brief summary of these systems and their expected performance is given in Chapter 5.

[1] This projection, from which one year of LBNF beam operations can be expressed as 1.7×10^7 seconds, is based on extensive experience with intense neutrino beams at Fermilab, and in particular the NuMI beam line, which incorporates elements like those in the proposed LBNF beamline design and faces similar operating conditions.

1.1.2.2 Deployment Scenario

Where presented as a function of calendar year, sensitivities are calculated with the following assumed deployment plan, which is based on a technically limited schedule.

- Start of beam run: Two FD module volumes for total fiducial mass of 20 kt, 1.2 MW beam
- After one year: Add one FD module volume for total fiducial mass of 30 kt
- After three years: Add one FD module volume for total fiducial mass of 40 kt
- After six years: Upgrade to 2.4 MW beam

1.1.2.3 Simulation, Reconstruction and Data Analysis Tools

The development of algorithms and software infrastructure needed to carry out physics sensitivity studies has been an active effort within DUNE and the associated scientific community. As demonstrated in Chapter 4, significant progress has been made: event reconstruction codes can be run on fully simulated neutrino interaction events in DUNE far detector modules; the DUNE computing infrastructure allows high-statistics production runs; and end-user interfaces are functioning. Robust end-to-end analyses not possible a year ago have now been done and are being reported in this document.

For some aspects – for example, beamline modeling and GeV-scale neutrino interaction simulations – well-developed and validated (with data) software packages have been available throughout much of DUNE's design phase. For others, corresponding tools did not exist and needed to be either developed from scratch or adapted with substantial modifications from other experimental programs. Concurrent with these development efforts, interim descriptions such as parametric detector response modeling, necessarily simple but based on reasonable extrapolation from experience and dedicated studies, were employed to assess physics capabilities. Even for the case of the better-developed tools – again, neutrino interaction modeling is a good example – significant incremental improvements have been made as data from neutrino experiments and other sources have become available and as theoretical understandings have advanced.

As a result of the rapid pace of development as well as practical considerations including human resource availability, different levels of rigor have been applied in the evaluation of physics capabilities for different elements of the program. The strategy adopted for this TDR has been to hold the primary elements of the program to the highest standard of rigor, involving direct analysis of fully simulated data, utilizing actual event reconstruction codes and analysis tools that could be applied to real data from DUNE far detector modules. For other elements of the program, sensitivities utilize realistic beam and physics simulations, but employ parametric detector response models in place of full reconstruction.

The implementation of this strategy comes with caveats and clarifications that are discussed in the corresponding chapters. Some of these are mentioned here.

- In the case of the long-baseline oscillation physics program, this approach requires a com-

bination of the fully end-to-end analysis of simulated far detector data with the concurrent analysis of simulated data from near detector systems to capture in a realistic way the level of control over systematic errors. Given the current state of development in the DUNE near detector design and corresponding analysis tools, it has been necessary to employ parametric detector response modeling for near detector components, as described in Sec. 5.5.

- In the case of the nucleon decay searches (Sec. 6.1), reconstruction and analysis tools dedicated toward addressing the particular challenges presented are not as well developed as in the case of the beam-based oscillation physics program. Effort is ongoing to improve the performance of these tools.
- The supernova neutrino burst program (Sec. 7.1) relies on reconstruction of event signatures from LArTPC signals generated by low-energy (MeV-scale) particles (electrons and de-excitation gammas). Full simulation and reconstruction is used for some studies, such as for the directionality study described in Sec 7.3.1. For other studies, a modified strategy is employed in order to efficiently explore model space: reconstruction metrics (resolution smearing matrices, for example) are derived from analysis of fully simulated and reconstructed low-energy particles and events in the far detector, and applied to understand mean detector response over a range of signal predictions.
- It should be noted that for scientific program elements where analysis of fully reconstructed simulated data has not yet been performed, the parametric response models used for the analyses presented here have been well characterized with dedicated studies and incorporation of results from other experiments. The demonstration of sensitivities for the long-baseline oscillation physics program (with full reconstruction) that are comparable to those previously obtained based on parametric response provides validation for this approach.

1.1.3 Selected Results from Sensitivity Studies

In this section, selected sensitivity projections from the central elements of the DUNE science program are presented. This selection is intended to convey just the headlines from what is an extensive and diverse program of frontier science.

1.1.3.1 DUNE can discover CPV in the neutrino sector and precisely measure oscillation parameters

The key strength of the DUNE design concept is its ability to robustly measure the oscillation patterns of ν_μ and $\bar{\nu}_\mu$ over a range of energies spanning the first and second oscillation maxima (see, *e.g.*, Fig. 5.1 in Chapter 5). This is accomplished by a coordinated analysis of the reconstructed ν_μ, $\bar{\nu}_\mu$, ν_e, and $\bar{\nu}_e$ energy spectra in near and far detectors, incorporating data collected with forward (neutrino-dominated) and reverse (antineutrino-dominated) horn current polarities.

The statistical power of DUNE relative to the current generation of long-baseline oscillation experiments is a result of many factors including (1) on-axis operations, (2) the LBNF beam power, (3) long baseline and correspondingly high energy oscillation maxima and strong separation of normal and inverted neutrino mass ordering scenarios, (4) detector mass, and (5) event reconstruction and

selection capabilities. Tables 1.1 and 1.2 (reproduced later as Tables 5.2 and 5.3) give the expected event yields for the appearance (ν_e and $\bar{\nu}_e$) and disappearance (ν_μ and $\bar{\nu}_\mu$) channels, respectively, after seven years of operation, assuming $\delta_{\rm CP} = 0$ and NuFIT 4.0 [2, 3] values (given in Table 5.1) for other parameters.

Table 1.1: ν_e and $\bar{\nu}_e$ appearance rates: Integrated rate of selected ν_e charged current (CC)-like events between 0.5 and 8.0 GeV assuming 3.5-year (staged) exposures in the neutrino-beam and antineutrino-beam modes. The signal rates are shown for both normal mass ordering (NO) and inverted mass ordering (IO), and all the background rates assume normal mass ordering. All the rates assume $\delta_{\rm CP} = 0$, and NuFIT 4.0 [2, 3] values for other parameters.

	Expected Events (3.5 years staged per mode)	
	ν mode	$\bar{\nu}$ mode
ν_e Signal NO (IO)	1092 (497)	76 (36)
$\bar{\nu}_e$ Signal NO (IO)	18 (31)	224 (470)
Total Signal NO (IO)	1110 (528)	300 (506)
Beam $\nu_e + \bar{\nu}_e$ CC background	190	117
neutral current (NC) background	81	38
$\nu_\tau + \bar{\nu}_\tau$ CC background	32	20
$\nu_\mu + \bar{\nu}_\mu$ CC background	14	5
Total background	317	180

Table 1.2: ν_μ and $\bar{\nu}_\mu$ disappearance rates: Integrated rate of selected ν_μ CC-like events between 0.5 and 8.0 GeV assuming a 3.5-year (staged) exposure in the neutrino-beam mode and antineutrino-beam mode. The rates are shown for normal mass ordering and $\delta_{\rm CP} = 0$.

	Expected Events (3.5 years)
	ν mode
ν_μ Signal	6200
$\bar{\nu}_\mu$ CC background	389
NC background	200
$\nu_\tau + \bar{\nu}_\tau$ CC background	46
$\nu_e + \bar{\nu}_e$ CC background	8
$\bar{\nu}$ mode	
$\bar{\nu}_\mu$ Signal	2303
ν_μ CC background	1129
NC background	101
$\nu_\tau + \bar{\nu}_\tau$ CC background	27
$\nu_e + \bar{\nu}_e$ CC background	2

Fig. 1.1 (reproduced later as Fig. 5.18) illustrates DUNE's ability to distinguish the value of the CP phase $\delta_{\rm CP}$ from CP-conserving values (0 or π) as a function of time in calendar year. These projections incorporate a sophisticated treatment of systematic error, as described in detail in Chapter 5. Strong evidence ($> 3\sigma$) for CPV is obtained for favorable values (half of the phase space) of $\delta_{\rm CP}$ after five years of running, leading to a $> 5\sigma$ determination after ten years.

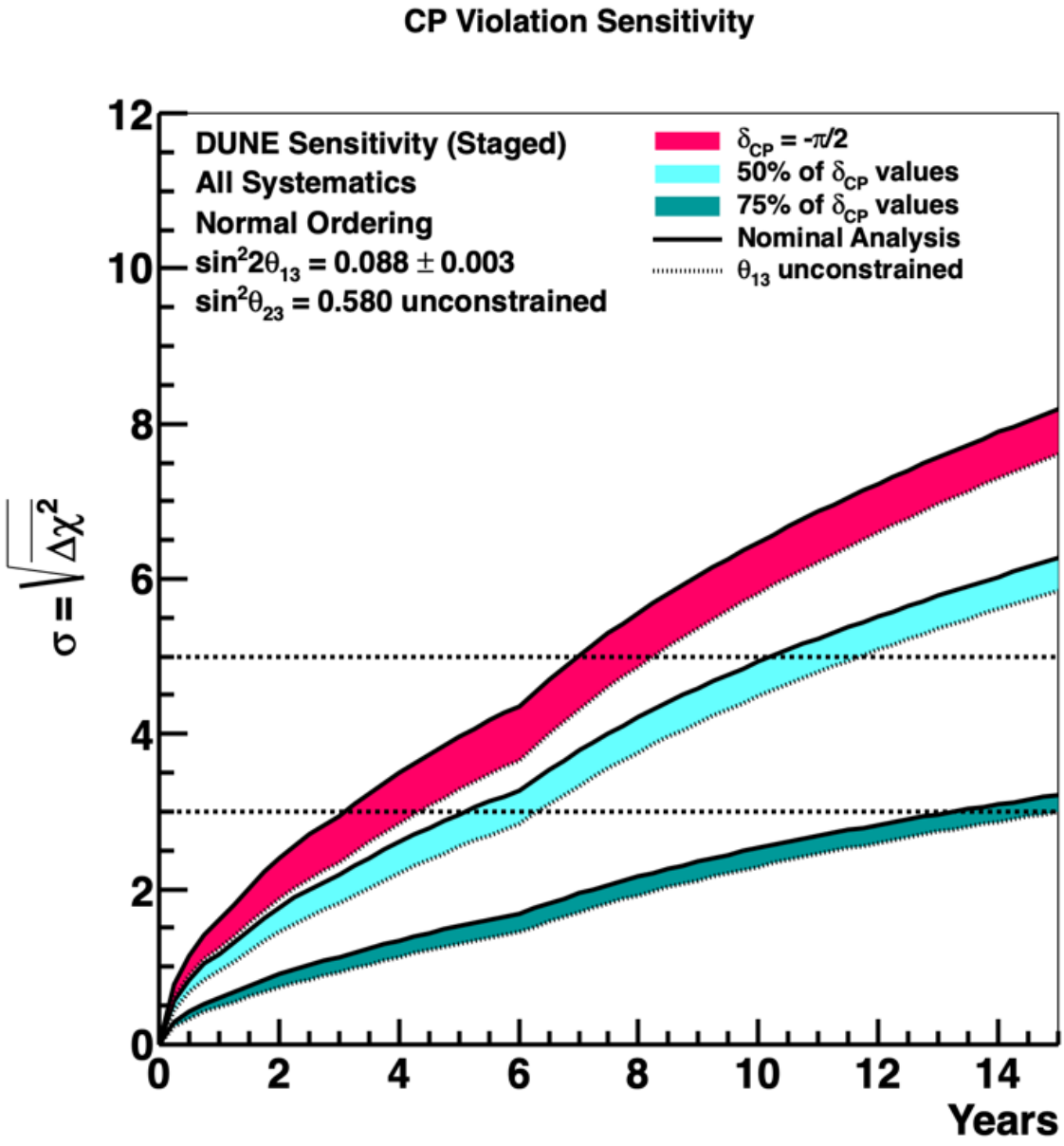

Figure 1.1: Significance of the DUNE determination of CP-violation (i.e.: $\delta_{\rm CP} \neq 0$ or π) for the case when $\delta_{\rm CP} = -\pi/2$, and for 50% and 75% of possible true $\delta_{\rm CP}$ values, as a function of time in calendar years. True normal ordering is assumed. The width of the band shows the impact of applying an external constraint on $\sin^2 2\theta_{13}$.

A summary of representative sensitivity milestones for neutrino mass ordering and CPV discovery, as well as precision on $\delta_{\rm CP}$ and $\sin^2 2\theta_{13}$ is given in Table 1.3. The ultimate level of precision that can be obtained on oscillation parameters highlights the point that DUNE will provide crucial input for flavor physics: Patterns required by particular symmetries underlying fermion masses and mixing angles may appear. The unitarity of the neutrino mixing matrix can be tested directly through comparisons of $\sin^2 2\theta_{13}$ with the value obtained from reactor experiments. In conjunction with $\sin^2 2\theta_{13}$ and other parameters, the precise value of $\delta_{\rm CP}$ can constrain models of leptogenesis that are leading candidates for explanation of the baryon asymmetry of the Universe.

Table 1.3: Exposure in years, assuming true normal ordering and equal running in neutrino and antineutrino mode, required to reach selected physics milestones in the nominal analysis, using the NuFIT 4.0 [2, 3] best-fit values for the oscillation parameters. As discussed in Section 5.9.4, there are significant variations in sensitivity with the value of $\sin^2\theta_{23}$, so the exact values quoted here (using $\sin^2\theta_{23}$ = 0.580) are strongly dependent on that choice. The staging scenario described in Section 1.1.2.2 is assumed. Exposures are rounded to the nearest year.

Physics Milestone	Exposure (staged years)
5σ Mass Ordering ($\delta_{\rm CP} = -\pi/2$)	1
5σ Mass Ordering (100% of $\delta_{\rm CP}$ values)	2
3σ CP Violation ($\delta_{\rm CP} = -\pi/2$)	3
3σ CP Violation (50% of $\delta_{\rm CP}$ values)	5
5σ CP Violation ($\delta_{\rm CP} = -\pi/2$)	7
5σ CP Violation (50% of $\delta_{\rm CP}$ values)	10
3σ CP Violation (75% of $\delta_{\rm CP}$ values)	13
$\delta_{\rm CP}$ Resolution of 10 degrees ($\delta_{\rm CP} = 0$)	8
$\delta_{\rm CP}$ Resolution of 20 degrees ($\delta_{\rm CP} = -\pi/2$)	12
$\sin^2 2\theta_{13}$ Resolution of 0.004	15

1.1.3.2 DUNE can discover proton decay and other baryon-number violating processes

By virtue of its deep underground location and large fiducial mass, as well as its excellent event imaging, particle identification and calorimetric capabilities, the DUNE far detector will be a powerful instrument for discovery of baryon-number violation. As described in Chapter 6, DUNE will be able to observe signatures of decays of protons and neutrons, as well as the phenomenon of neutron-antineutron mixing, at rates below the limits placed by the current generation of experiments.

Many nucleon decay modes are accessible to DUNE. As a benchmark, a particularly compelling discovery channel is the decay of a proton to a positive kaon and a neutrino, $p \rightarrow K^{+}\overline{\nu}$. In this channel, the kaon and its decay products can be imaged, identified, and tested for kinematic consistency with the full decay chain, together with precision sufficient to reject backgrounds due to atmospheric muon and neutrino interactions. Preliminary analysis of single-particle beam and cosmic ray tracks in the ProtoDUNE-SP LArTPC is already demonstrating the particle identification capability of DUNE, as illustrated in Fig. 1.2. The signature of the kaon track and its observable decay particles is sufficiently rich that a credible claim of evidence for proton decay could be made on the basis of just one or two sufficiently well-imaged events, for the case where background sources are expected to contribute much less than one event (see Chapter 6 for a more complete discussion).

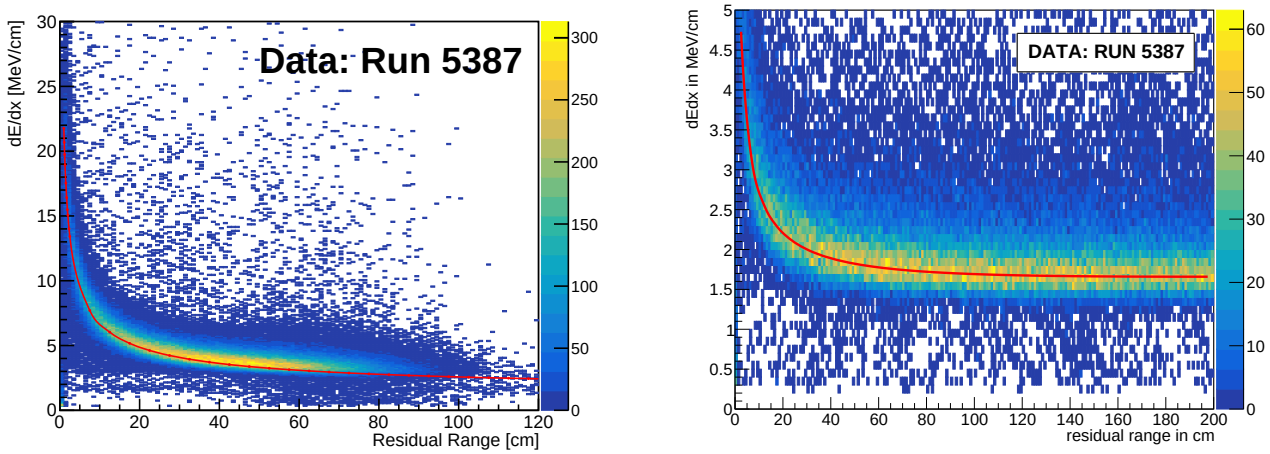

Figure 1.2: Energy loss of protons (left) and muons (right) in 1-GeV running with the ProtoDUNE-SP LArTPC at CERN, as a function of residual range. The protons are beam particles identified from beamline instrumentation; the muons are reconstructed stopping cosmic rays collected concurrently. The red curves represent the mean of the corresponding expected signature. Note the difference in the vertical scale of the two plots. The kaon dE/dx curve will lie between the two curves shown.

Projecting from the current analysis of $p \rightarrow K^{+}\overline{\nu}$ in the DUNE far detector, with a detection efficiency of 30% as described in Chapter 6, the expected 90% CL lower limit on lifetime divided by branching fraction is 1.3×10^{34} years for a 400-kt $\cdot$ year exposure, assuming no candidate events are observed. This is roughly twice the current limit of 5.9×10^{33} years from Super–Kamiokande [4], based on an exposure of 260 kt $\cdot$ year . Thus, should the rate for this decay be at the current Super–Kamiokande limit, five candidate events would be expected in DUNE within ten years of running with four far detector modules. Ongoing work is aimed at improving the efficiency in this and other channels.

1.1.3.3 DUNE can probe galactic supernovae via measurements of neutrino bursts

As has been demonstrated with SN1987a, the observation of neutrinos [5, 6] from a core-collapse supernova can reveal much about these phenomena that is not accessible in its electromagnetic signature. Correspondingly, there is a wide range of predictions from supernova models for even

very basic characteristics of the neutrino bursts. Typical models predict that a supernova explosion in the center of the Milky Way will result in several thousand detectable neutrino interactions in the DUNE far detector occurring over an interval of up to a few tens of seconds. The neutrino energy spectrum peaks around 10 MeV, with appreciable flux up to about 30 MeV.

LAr based detectors are sensitive to the ν_e component of the flux, while water Cherenkov and organic scintillator detectors are most sensitive to the $\bar{\nu}_e$ component. Thus DUNE is uniquely well-positioned to study the neutronization burst, in which ν_e's are produced during the first few tens of milliseconds. More generally, measurements of the (flavor-dependent) neutrino flux and energy spectrum as a function of time over the entirety of the burst can be sensitive to astrophysical properties of the supernova and its progenitor, and distortions relative to nominal expectations can serve as signatures for phenomena such as shock wave and turbulence effects, or even black hole formation.

The sensitivity of the DUNE far detector to these phenomena is discussed in Chapter 7. An illustration of one element of the program is given in Fig. 1.3, which indicates a pointing resolution of better than 5° that can be obtained by analysis of both subdominant highly-directional ν-e elastic scattering events and dominant weakly-directional ν_eCC events within a supernova burst, based on full reconstruction and analysis. The DUNE results can be combined with corresponding measurements in other neutrino detectors to provide supernova localization from neutrinos alone in real time.

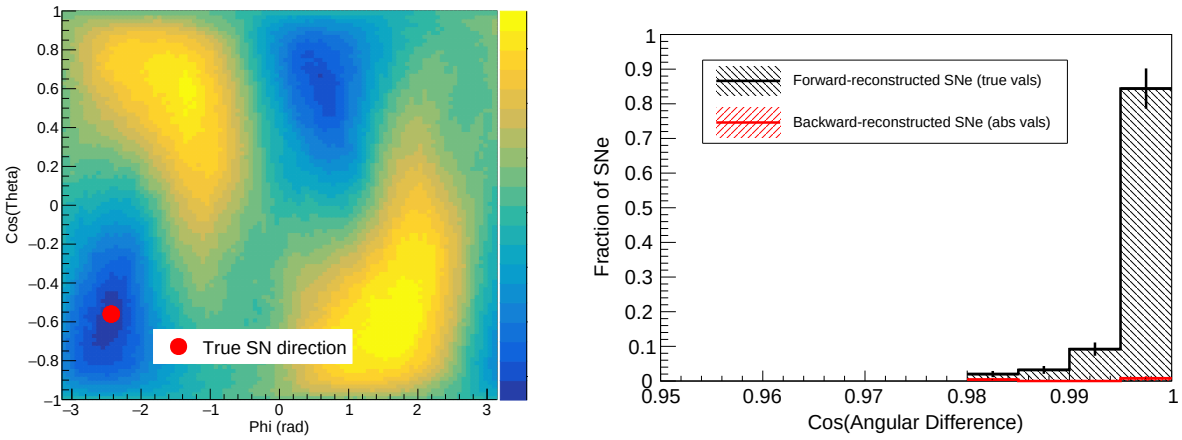

Figure 1.3: Left: Log likelihood values as a function of direction for a supernova sample with 260 ν-e elastic scattering (ES) events. Right: Distribution of angular differences for directions to 10-kpc supernova using a maximum likelihood method.

1.2 Science Drivers for LBNF/DUNE Design Specifications

The scientific case summarized in the sections above is predicated on the suitability of the experimental configuration of LBNF/DUNE. In this section we summarize the ways in which the primary physics goals drive key features of this configuration. Further elaboration of the impacts

of physics goals on specific high-level performance needs of the experimental systems is presented in the corresponding chapters that follow. Translation of performance needs into the corresponding LBNF/DUNE design specifications is addressed within the appropriate TDR volume.

1.2.1 General LBNF/DUNE Operating Principles

Worldwide scientific and technical planning for the ambitious next-generation deep underground long-baseline neutrino oscillation experiment that LBNF/DUNE now represents has been under way for more than a decade. Much development preceded the formation of the DUNE science collaboration in 2015 (see, for example, Refs. [7] and [8]).

Extensive study and discussion within the community have led to the principal elements of the LBNF/DUNE configuration:

- **High-intensity conventional wide-band ν_μ beam**
  The current generation of long-baseline neutrino experiments have benefited from narrow-band beam characteristics associated with off-axis detector deployment. The principal advantage is a low background rate in both ν_e appearance and ν_μ disappearance channels from misidentified neutral current interactions of high energy neutrinos. However, this advantage comes at a cost of flux and spectral information relative to an on-axis detector configuration [7, 9]. The DUNE concept builds on the notion that a highly-performant detector technology with excellent neutrino energy reconstruction and background rejection capabilities can optimize sensitivity and cost with an on-axis exposure to an intense conventional (magnetic horn-focused) beam.
- **Far detector site selection for long baseline**
  The 1300 km baseline offered by locating the DUNE far detector at the Sanford Underground Research Facility in Lead, South Dakota is well-optimized for the neutrino oscillation physics goals of the program [10].
- **Deep underground location for far detector modules**
  Early studies (see, *e.g.*, Ref. [11]) demonstrated that to realize the non-accelerator based elements of the DUNE science program, a deep underground far detector location is required. These studies also indicate that the 4850 Level of Sanford Lab provides sufficient attenuation of cosmic rays in the rock above, conclusions that have been supported by more recent studies (see, *e.g.*, Refs. [12, 13]).
- **LArTPC technology for far detector modules**
  Combining intrinsic scalability with high-performance event imaging, calorimetry and particle identification capabilities, the concept of large liquid argon time-projection chamber (LArTPC) detectors was developed for the broad-based underground science program of DUNE. This design choice integrates well with the other basic design elements described above. For example, the excellent neutrino energy reconstruction capability of LArTPC's is especially important for the long-baseline program with a wide-band neutrino beam. Additionally, the LArTPC technology choice provides valuable complementarity to other existing and planned detectors pursuing many of the same goals. As an example of this complementarity, the sensitivity of DUNE to the ν_e component of supernova neutrino flux, prevalent

in the neutronization phase of the explosion, provides distinct information relative to that provided by water or organic scintillator-based detectors in which $\bar{\nu}_e$ interactions dominate.

The scientific basis for the above foundational experimental design choices has been examined and validated through extensive review, undertaken at all stages of DUNE concept development. Recent experimental and theoretical developments have only strengthened the scientific case for DUNE and its basic configuration. The technical underpinnings for these choices have also been strengthened over time through a worldwide program of R&D and engineering development, as described in a suite of LBNF/DUNE project documents including this technical design report (TDR), as well as in sources describing independent experiments and development activities.

1.2.2 Far Detector Performance Requirements

The number of detector design parameters that have direct or indirect impact on performance is large. These design parameters have been studied over the years by past LArTPC experiments, by DUNE during early detector optimization work, through the successful construction and now operation of ProtoDUNE-SP, and through continuing studies within the DUNE consortia and physics groups.

1.2.2.1 High-level Observables in the Far Detector

DUNE's suite of physics measurements relies on a relatively small number of event observables, through which the physics of interest can be accessed. Foremost are:

- **Particle energies**
  Examples include the total visible energy in a supernova neutrino interaction; the reconstructed energy of a beam neutrino for oscillation measurements; the reconstructed energy of a muon track in a nucleon decay candidate event.
- **Particle identification**
  This comes from spatial patterns and energy depositions. Examples include photon/electron separation in the ν_e appearance analysis; proton/kaon separation in certain nucleon decay channels.
- **Event time**
  This allows for fiducialization in the TPC, drift corrections, and macroscopic timing for beam neutrinos and SNB physics.

1.2.2.2 Physics Case Studies

CP violation search The primary demonstration that the detector design meets the physics needs is the full simulation and analysis being documented in this TDR volume. As described in Sec. 1.1.3, Figure 1.1 presents the time-evolution of the CPV sensitivity obtained in this way.

To break the measurement apart into the three observables above, we start with neutrino energy. The charged lepton and hadronic shower energies are reconstructed separately and then summed. In electron neutrino events, the leptonic energy resolution (spectrum averaged) is 8%, the hadronic energy resolution is 49%, and the neutrino energy resolution is 13%. Note that a significant portion of the energy smearing comes from the physics of neutrino-nucleus scattering and hadronic shower production rather than from detector performance. In the impossible case that the lepton energy could be perfectly reconstructed, the electron neutrino (muon neutrino) energy resolution would only change by approximately 13% $\rightarrow$ 10% (18% $\rightarrow$ 17%). Equivalently, small degradations in detector response have minimal leverage to affect the final neutrino energy resolution.

Particle identification is critical for the oscillation analysis in that it enables neutrino flavor identification. For ν_e appearance in particular, one must positively identify the presence of a high-energy electron while avoiding misclassification of high energy photons as electrons. The LArTPC design meets this challenge by having spatial resolution that is much smaller than the radiation length (0.5 cm $\ll$ 14 cm) to make visible the gaps between an event's reconstructed vertex and any photon conversions, and charge resolution that provides additional dE/dx separation based on pre-EM-shower depositions, as demonstrated in an operating detector by ArgoNeuT [14] and with DUNE simulation in Figure 1.4. The DUNE study [12] also shows alternative detector designs for the single-phase LArTPC implementation. As long as the signal-to-noise ratio is high on the readout wires, minor adjustments to the wire angle and pitch have negligible impact on dE/dx separation power.

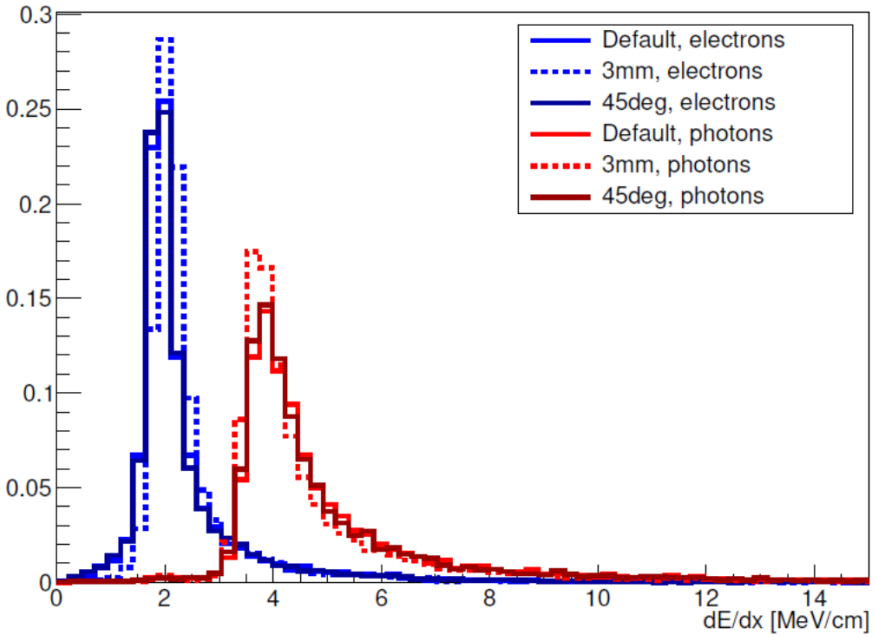

Figure 1.4: Separation of photons and electrons by dE/dx in the pre-shower region. Alternative wire angles and wire pitches are also shown.

In the analysis presented in Chapter 5, and in the preliminary CPV sensitivity in Figure 1.1, neutrino flavor classification is accomplished using a modern convolutional neural network technique that takes directly as input the TPC wire hits in the three detector views.

Event timing requirements for beam events flow from the need to establish the fiducial volume. This is discussed generally in the section on light yield below.

Supernova burst neutrinos. A core-collapse supernova at 10 kiloparsecs will provide ∼1000 neutrino interactions in the FD over the course of ∼10 seconds with typical energies between 5 and 30 MeV. Charged current ν_e events make up the majority of these. Much of the desired astrophysical information comes via the time-dependent energy spectrum of these neutrinos. As shown earlier in Sec. 1.1.3 and later in more detail in Chapter 7, DUNE capabilities are quantified through sensitivities both to generic pinched-thermal spectral parameters and to specific phenomena within the star.

Figure 1.5 shows the precision with which DUNE can measure two of the spectral parameters, ε, related to the binding energy of the neutron star remnant, and $\langle E_{\nu_e} \rangle$, the average energy of the ν_e component, for the time-integrated spectrum. The assumed measured spectrum takes into account some degradation from the neutrino interaction process itself (*e.g.*, energy lost to neutrons), via the Model of Argon Reaction Low Energy Yields (MARLEY) event generator. The colored contours show increasing levels of energy smearing. A 10% resolution is noticeable but insignificant, and the overall precision on the spectral parameters up to 30% resolution does not change dramatically As shown later, the additional smearing introduced by the detector's response falls within the resolution envelope suggested here, and according to detector simulation is closest to the 20% level. In an eventual detailed analysis, the spectral fits will be done in time slices to study the evolution of the supernova, so the minimum contour size in each time slice will be larger due to reduced event counts in each slice.

Given the dominance of ν_e charged current events in the supernova neutrino sample, particle identification is not a requirement for the primary physics measurements. However, additional capability may be possible by identifying separately neutral current and elastic scattering interactions. Studies are on-going, and these possibilities are discussed in Chapter 7.

Timing for SNB events is provided by both the TPC and the photon detector system. Basic timing requirements flow from event vertexing and fiducialization needs. These are discussed generally for DUNE in the light yield section, but here we note a few supernova-specific design considerations. During the first 50 ms of a 10-kpc-distant supernova, the mean interval between successive neutrino interactions is $0.5 - 1.7$ ms depending on the model. The TPC alone provides a time resolution of 0.6 ms (at 500 V/cm), commensurate with the fundamental statistical limitations at this distance. However nearly half of galactic supernova candidates lie closer to Earth than this, so the rate can be tens or (less likely) hundreds of times higher. A resolution of <10 μs, as already provided by the photon detector system, ensures that DUNE's measurement of the neutrino burst time profile is always limited by rate and not detector resolution. The hypothesized oscillations of the neutrino flux due to standing accretion shock instabilities would lead to features with a characteristic time of ∼10 ms, comfortably greater than the time resolution. The possible neutrino trapping notch at the start of the burst has a width of $1 - 2$ ms. Observing the trapping notch could be possible for the closest progenitors.

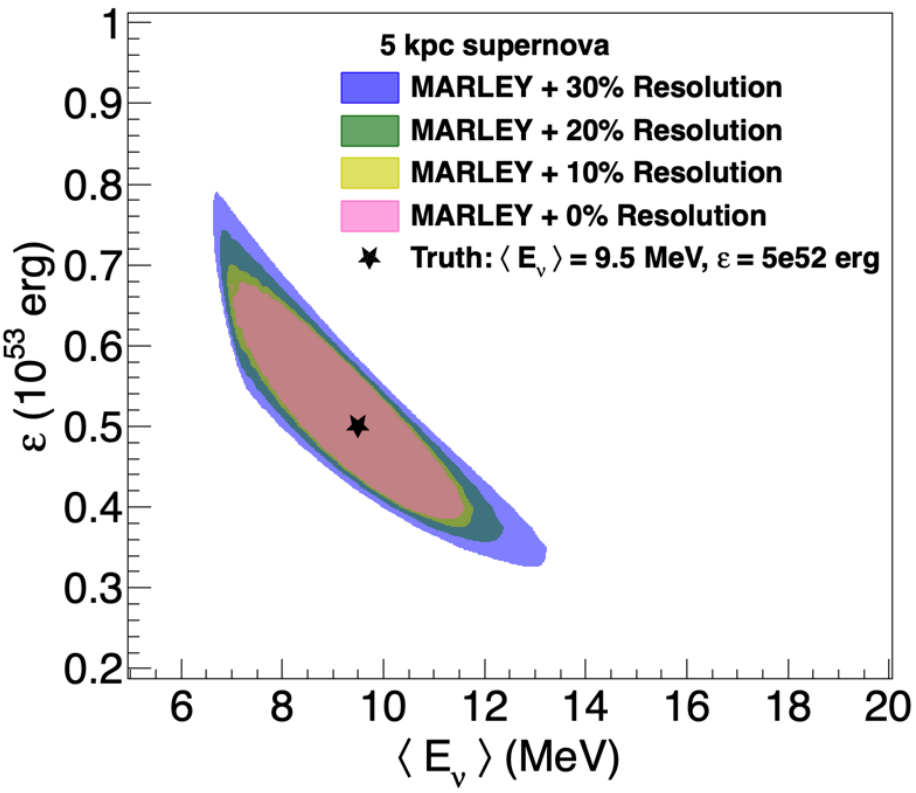

Figure 1.5: 90% C.L. contours for the luminosity and average ν_e energy spectral parameters for a supernova at 5 kpc. The contours are obtained using the time-integrated spectrum. As discussed in the text, the allowed regions change noticeably but not drastically as one moves from no detector smearing (pink) to various realistic resolutions (wider regions).

1.2.2.3 Key High-level Detector Design Specifications

With the discussion above and in later chapters of this document, it is possible to identify several high-level detector design parameters that together characterize the overall function of DUNE single-phase LArTPC modules. These parameters and specified operating points are given in Table 1.4.

Table 1.4: High-level DUNE single-phase far detector design parameters and specifications

Parameter	Specification	Goal
Drift field	$> 250\,\mathrm{V/cm}$	500 V/cm
Electron lifetime	$> 3\,\mathrm{ms}$	10 ms
System noise	< 1000 enc	—
Light yield (at cathode)	$> 0.5\,\mathrm{pe/MeV}$	$> 5\,\mathrm{pe/MeV}$
Time resolution	$< 1\,\mu\mathrm{s}$	100 ns

The column headings in the table are defined as follows:

Specification: This is the intended value for the parameter or, more often, the upper or lower limit for the parameter. Fixed values are given for parameters that are not intrinsically dynamic (*e.g.*, wire pitch). Limits are set by the more stringent driver, either the physics or engineering needs.

Goal: This is an improved value that offers some benefit, and the collaboration aims to achieve this value where it is cost effective to do so. While in some cases the goal offers potential physics benefit directly, more often the goal provides risk mitigation, since improving the performance on one parameter can mean relaxing the requirements on other correlated parameters, thus protecting against unforeseen performance issues.

The first three parameters (drift field, electron lifetime, and TPC system noise) in Table 1.4 enter directly into the ability to discriminate between ionization signals due to physics events and noise. Physics capability degrades if readout noise is not small compared to the ionization signal expected for minimum-ionizing particles located anywhere within the active volume of the detector. The remaining parameters (light yield for events at the cathode, and timing resolution) pertain to the ability of the scintillation photon detection system to enable localization of events within the TPC, needed for the non-accelerator based far detector physics program, both for fiducialization and for corrections to TPC charge attenuation. The general arguments for the specifications listed for each parameter are given below.

Drift field The basic operating principle of the TPC involves the transport of ionization electrons out of the argon volume and to the detection plane. A higher drift field reduces electron transport time and thus electron loss due to impurities; reduces ion-electron recombination (increasing

ionization signal at the expense of reduced scintillation photon yield); increases induction signals due to increased electron velocity; and reduces electron diffusion.

The argon volume in the FD single phase design is divided into four separate drift regions, each with a maximum drift distance of 3.5 m. The design goal of 500 V/cm field implies a voltage across the drift region of approximately 180 kV. At this field, the electron drift velocity is 1.6 mm/μs , implying a maximum drift time $t = 2.2$ ms. This drift time can be compared with the electron lifetime τ set by the argon purity. At $\tau = 3$ ms, signals originating near the cathode will be attenuated to $e^{-t/\tau} = 48\%$ of their original strength. For the minimum field of 250 V/cm, this transmission becomes 23%. Additionally, electron/ion recombination happens more readily at lower field. From 500 V/cm to 250 V/cm, an additional signal loss of 11% (taking 23% to 20%) is introduced due to recombination. The lowered field also reduces the drift velocity and, in proportion, signal pick-up on the induction wires. Moving from 500 V/cm to 250 V/cm drops the induction signal by an additional 34% to an effective transmission for low-field depositions near the cathode (relative to "500 V/cm near the anode") of 14%.

These signal attenuations are acceptable as long as the readout maintains good signal-to-noise (S/N) and charge resolution. High S/N for minimum ionizing particle (MIP) signals has been demonstrated at ProtoDUNE-SP – S/N=30 (collection), 15 (induction) – and the minimum transmissions above would not significantly damage the ability to identify wire hits. The charge resolution on individual wires, while not a driver of overall event resolution, feeds into the dE/dx estimation for short segments of tracks and thus into particle identification. Studies of selection efficiencies at varied signal levels continue, but notably the ν_e selection efficiency exhibits no dependence on drift distance in the default simulation, which is based on a 3 ms electron lifetime. As mentioned below, ProtoDUNE readily achieved higher lifetimes.

Electrons drifting across the full 3.5 m will experience transverse diffusion of 1.7 mm (2.0 mm) at 500 V/cm (250 V/cm). The change in diffusion with field strength is insignificant in comparison to the wire pitch of 5 mm.

The reduced recombination at higher field results in smaller scintillation photon yields. At 500 V/cm, the yield is 60% of that at zero field. Thus any reduction in field strength will improve this detection channel. However, the incremental nature of this improvement and the more critical dependence of successful execution of the science program on the TPC performance together make optimization with respect to scintillation a secondary consideration.

ProtoDUNE-SP is currently operating at 500 V/cm.

Electron lifetime Electronegative impurities (*e.g.*, H_2O, O_2) within the liquid argon must be kept at low levels to prevent the capture of drifting electrons after ionization. Electron lifetime is inversely proportional to the level of these impurities.

The values in Table 1.4 correspond to contamination levels of of 100 ppt O_2-equivalent for 3 ms and 30 ppt for 10 ms. The influence of electron lifetime on physics capabilities has been discussed in the section on drift field above. Indeed, one can largely trade off purity for field. Note that the lower lifetime of 3 ms was assumed versus the goal of 10 ms. ProtoDUNE-SP has achieved

electron lifetimes exceeding 5 ms.

Electronics system noise Noise in the electronics system can limit the ability to identify and correctly associate wire hits and can worsen charge resolution. From engineering considerations, the noise level in the front-end electronics drives the specification. All other pieces of the electronics chain are to be kept well below this level. The specification is given in units of e^- equivalent noise charge (enc).

At current gain settings, 1000 enc corresponds to 6.5 ADC counts. Initial ProtoDUNE analyses are showing 3.5 (4.5) ADC counts on collection (induction) channels. The current FD simulation assumes a noise level similar to ProtoDUNE performance, but higher noise levels are being explored. It is not expected that these relatively small adjustments (factor of $\sim$2) will impact physics analysis in any significant way. Noise assumptions (level and correlations) do influence DAQ design choices.

Light yield and photon-based timing The photon detector system provides an event time based on the scintillation light produced in the liquid argon. In conjunction with the TPC ionization signal, this allows one to determine where the event occurred along the drift direction for event vertexing, fiducialization, and electron attenuation corrections. The specifications here are given for the worst-case event location in the fiducial volume, typically near the cathode and thus far from any photon detector on the anode planes.

A photon-based time resolution of 1 μs corresponds to the time resolution for single TPC wire hits, allowing for useful event matching between the TPC and photon detector systems. Given the drift velocity, 1 μs also corresponds to an effective spatial granularity in the drift direction ($\sim$2 mm) that is similar to the wire pitch. The resulting three-dimensional event vertex provided by combining TPC and photon detector information has essential uses in DUNE physics analyses. A fiducial volume must be defined at the <1% level for the accelerator-based neutrino oscillation measurements and for nearby supernovas, and at less stringent levels for other measurements. Additionally, most cosmogenic and environmental backgrounds for non-accelerator measurements (*e.g.*, neutral particles produced by cosmic rays in the surrounding rock) have tell-tale distributions in the active volume and can thus be mitigated or eliminated through event localization.

The precise event time, and thus event location, also allows a correction for electron attenuation, which otherwise could have a large effect on energy resolutions due to the non-uniformity of response across the drift volume. The minimum TPC performance considered (with $E = 250$ V/cm, $\tau = 3$ ms) would correspond to an energy smearing of 22% due to electron loss. This effect is made negligible at 1 μs time resolution.

This attenuation correction is only possible when photon signals can be successfully associated with a TPC-recorded event. For low energy supernova neutrino events, this association is not 100% efficient. Figure 1.6 shows the smearing on visible energy in the TPC for supernova neutrino events with and without a drift correction based on different photon detector system performance. The difference between no correction and any correction is dramatic. The small differences between different light levels (cast as effective photodetector area in the figure) stem not from improved

spatial resolution but from a higher efficiency at reconstructing and associating light signals with the TPC signals. An effective area of 23 cm^2 corresponds roughly to a light yield of 0.5 p.e./MeV at the cathode, *i.e.* the minimum specification.

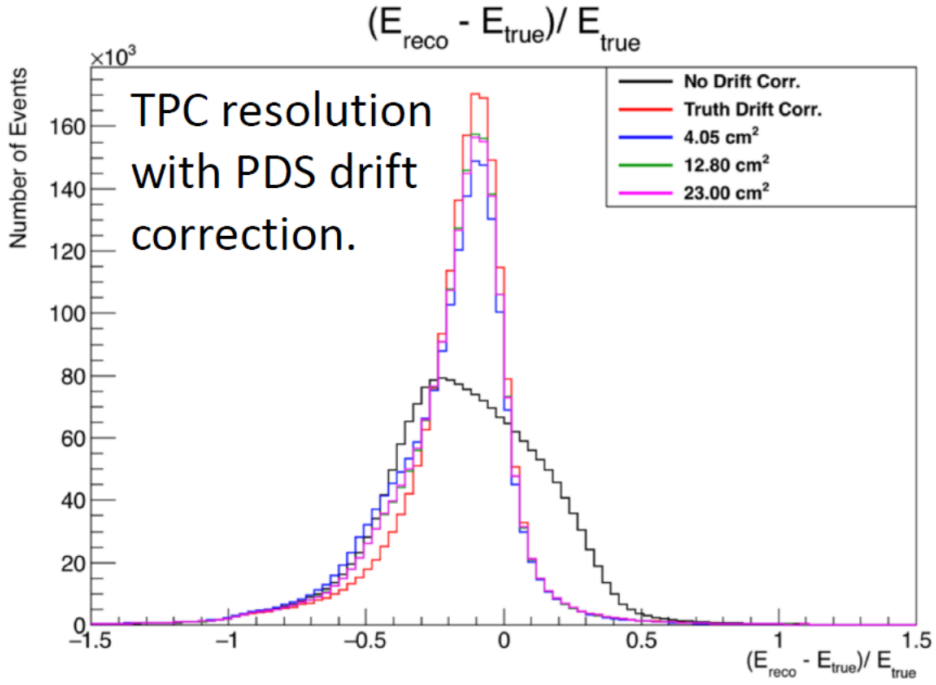

Figure 1.6: Energy residuals for supernova neutrino events without (black) and with (color) a timing-based drift correction to the reconstructed energy. The red histogram assumes the event vertex is known perfectly, and the realistic cases approach that ideal quickly. The 23 cm^2 histogram roughly corresponds to the specification of 0.5 p.e./MeV.

The use of photon signals for direct event calorimetry in supernova neutrino events is under study. Initial tests suggest resolutions around 25% are possible at 0.5 p.e./MeV, which is competitive with the TPC resolution at these energies.

Two light-collection bar designs and one segmented design (ARAPUCA) are operating in ProtoDUNE-SP. Initial performance evaluation is excellent, and a full quantitative assessment, described in Volume IV is in progress.

1.2.2.4 Detector Design Driver Summary

The above discussion provides the basic guidelines for key far detector performance specifications in the context of the single-phase module design. Further elaboration is given in the chapters devoted to science capabilities in this document. Discussion of other significant detector specifications and their impact on physics sensitivity is given in Volumes IV and V. While it is not practical to carry out comprehensive physics sensitivity studies comprehensively, in which every major detector parameter is varied individually or in conjunction with others, such studies have been done for a few significant parameters (such as anode wire pitch for the single-phase LArTPC design). These are reported in the corresponding detector volume.

1.3 Scope and Organization of this Document

The scope and organization of this document follow from both programmatic and practical considerations.

First, while this volume is strongly interconnected with the other TDR volumes, it is written so as to stand on its own to be of best use to the community outside DUNE. To accomplish this, some duplication of material presented in other volumes is unavoidable. At the same time, the full utility of this volume is as just one element within an integrated set of TDR volumes. Thus, explicit and implicit reference to material presented in other volumes is made freely.

Second, while two volumes describe the technical designs for far detector modules based on the single-phase and dual-phase liquid argon TPC technologies, the exact configuration of all four modules is not yet established. As of this writing, it is understood that the first two modules will likely be one of each technology. Practical considerations, including the current state of development of event reconstruction and other software tools, have led the DUNE science collaboration to undertake a rigorous evaluation of capabilities for a DUNE program consisting solely of single-phase far detector modules. Based on the considerable progress already made toward the realization of effective reconstruction software for the dual-phase far detector implementation, current understanding is that its capabilities are at least as well optimized for the key physics goals as those of the single-phase implementation.

Thus it should be understood that the studies and results reported in this document were undertaken with the specification of single-phase detector modules. Where possible, comments on how performance and/or capabilities of dual-phase modules might differ are provided.

Chapter 2

Introduction to LBNF and DUNE

The Deep Underground Neutrino Experiment (DUNE) will be a world-class neutrino observatory and nucleon decay detector designed to answer fundamental questions about elementary particles and their role in the universe. The international DUNE experiment, hosted by the U.S. Department of Energy's Fermi National Accelerator Laboratory (Fermilab), will consist of a far detector (FD) located about 1.5 km underground at the Sanford Underground Research Facility (SURF) in South Dakota, USA, 1300 km from Fermilab, and a near detector (ND) located on site at Fermilab in Illinois. The far detector will be a very large, modular liquid argon time-projection chamber (LArTPC) with a total mass of nearly 70 kt of liquid argon (LAr), at least 40 kt (40 Gg) of which is fiducial. The LAr technology has the unique capability to reconstruct neutrino interactions with image-like precision and unprecedented resolution.

The DUNE detectors will be exposed to the world's most intense neutrino beam originating at Fermilab. A high-precision near detector, 574 m from the neutrino source on the Fermilab site, will be used to characterize the intensity and energy spectrum of this wide-band beam. The ability to compare the energy spectrum of the neutrino beam between the ND and FD is crucial for discovering new phenomena in neutrino oscillations. The Long-Baseline Neutrino Facility (LBNF), also hosted by Fermilab, provides the infrastructure for this complex system of detectors at the Illinois and South Dakota sites. LBNF is responsible for the neutrino beam, the deep-underground site, and the infrastructure for the DUNE detectors.

2.1 The LBNF Facility

The LBNF project is building the facility that will house and provide infrastructure for the first two DUNE FD modules in South Dakota and the ND in Illinois. Figure 2.1 shows a schematic of the facilities at the two sites, and Figure 2.2 shows a diagram of the cavern layout for the FD. The organization and management of LBNF is separate from the DUNE collaboration. LBNF is also hosted by Fermilab and its design and construction are organized as a DOE/Fermilab project incorporating international partners.

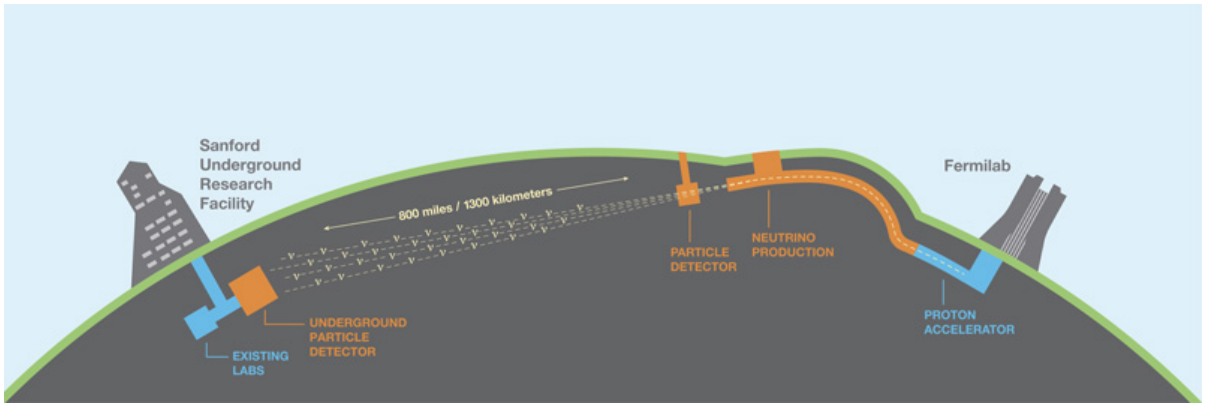

Figure 2.1: LBNF/DUNE project: beam from Illinois to South Dakota.

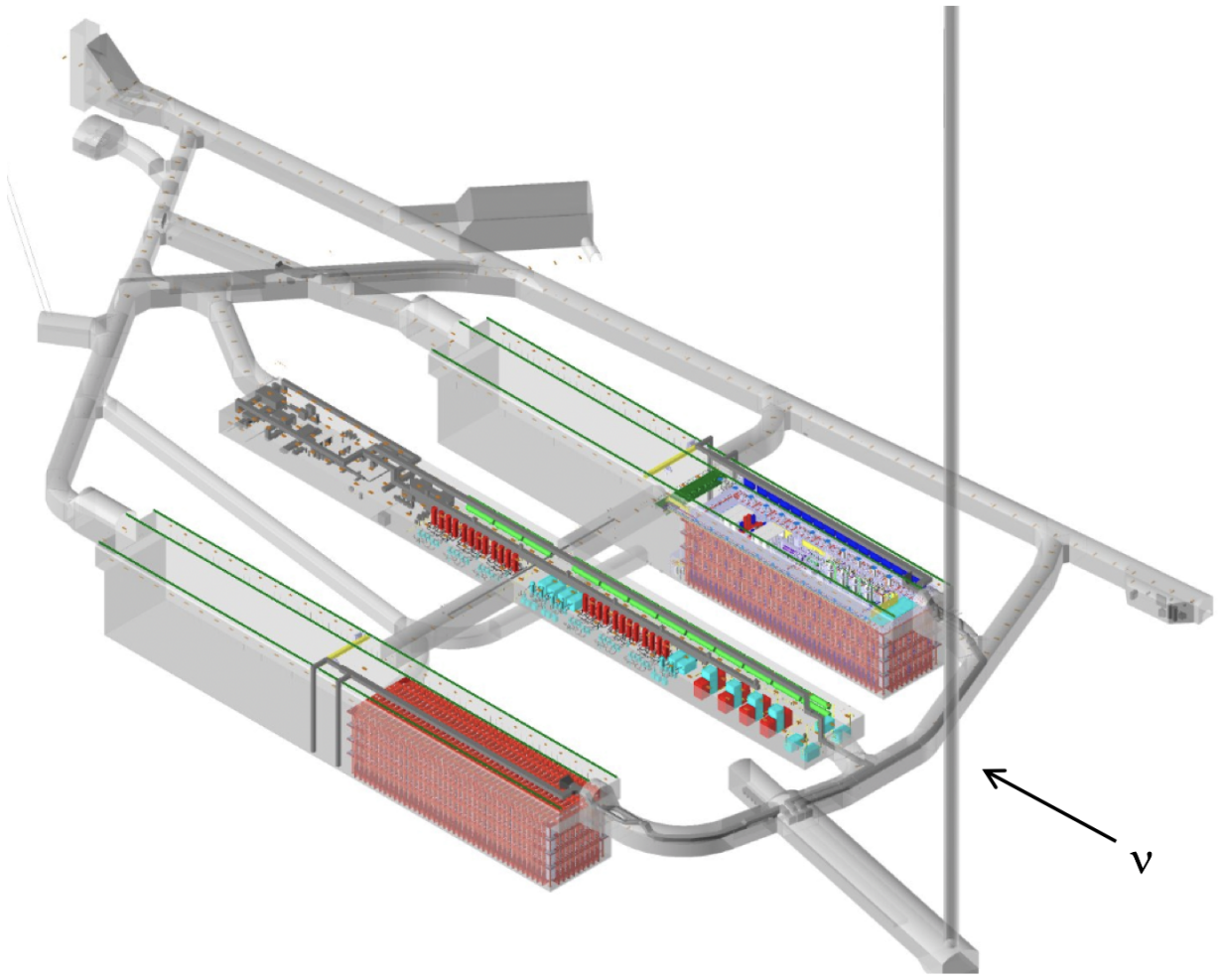

Figure 2.2: Underground caverns for DUNE FD and cryogenics systems at SURF, in South Dakota. The drawing, which looks towards the northeast, shows the first two far detector modules in place.

The LBNF project provides to DUNE

- the technical and conventional facilities for a powerful neutrino beam utilizing the Proton Improvement Plan II (PIP-II) upgrade [15] of the Fermilab accelerator complex. The PIP-II project will deliver between 1.0 MW to 1.2 MW of proton beam power from Fermilab's Main Injector in the energy range 60 GeV to 120 GeV at the start of DUNE operations and provide a platform for extending beam power to DUNE to >2 MW. A further planned upgrade of the accelerator complex will enable it to provide up to 2.4 MW of beam power by 2030.
- the civil construction, or conventional facilities (CF), for the ND systems at Fermilab; (see Figure 2.3);
- the excavation of three underground caverns at SURF to house the DUNE FD. The north and south caverns will each house two cryostats with a minimum 10 kt fiducial mass of liquid argon, while the central utility cavern (CUC) will house cryogenics and data acquisition facilities for all four detector modules;
- surface, shaft, and underground infrastructure to support the outfitting of the caverns with four free-standing, steel-supported cryostats and the required cryogenics systems to enable rapid deployment of the first two 10 kt FD modules. The intention is to install the third and fourth cryostats as rapidly as funding will allow.

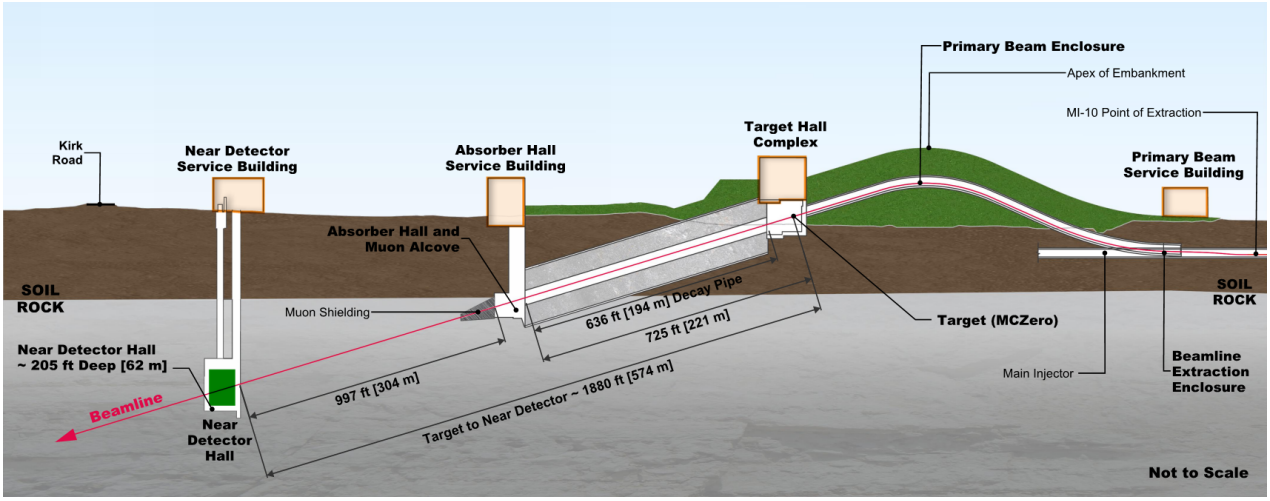

Figure 2.3: Neutrino beamline and DUNE near detector hall at Fermilab in Illinois

2.2 DUNE: Far Detector Modules

The DUNE FD consists of four LArTPC detector modules, each contained in a cryostat that holds 17.5 kt of LAr. Each module, installed approximately 1.5 km underground, has a fiducial mass of at least 10 kt. The LArTPC technology provides excellent tracking and calorimetry performance, making it an ideal choice for the DUNE FD. Each of the LArTPCs fits inside a cryostat of internal dimensions 18.9 m (W) $\times$ 17.8 m (H) $\times$ 65.8 m (L) that contains a total LAr mass of about 17.5 kt. The four identically sized modules provide flexibility for staging construction and for evolution of LArTPC technology.

DUNE is planning for and is prototyping two LArTPC technologies:

- Single-phase (SP): In the SP technology, ionization charges are drifted horizontally in LAr and read out on wires in the liquid. The maximum drift length in the first DUNE SP module is 3.5 m, and the nominal drift field is 500 V/cm, corresponding to a cathode high voltage (HV) of 180 kV. This design requires very low-noise electronics to achieve readout with good signal-to-noise (S/N) because no signal amplification occurs in the liquid. This technology was pioneered by the ICARUS project, and after several decades of worldwide R&D, is now a mature technology. It is the technology used for Fermilab's currently operating MicroBooNE detector, as well as the SBND detector, which is under construction.
- Dual-phase (DP): This technology was pioneered at a large scale by the WA105 DP demonstrator collaboration at European Organization for Nuclear Research (CERN). It is less established than the SP technology but offers a number of potential advantages. Here, ionization charges drift vertically in LAr and are transferred into a layer of gas above the liquid. Devices called large electron multipliers (LEMs) amplify the signal charges in the gas phase. The gain achieved in the gas reduces stringent requirements on the electronics, and increases the possible drift length, which, in turn, requires a correspondingly higher voltage. The nominal drift field is 500 V/cm, as for the SP detector, but in this case corresponds to a cathode HV of 600 kV. The maximum drift length in the DP module is 12.0 m.

In both technologies, the drift volumes are surrounded by a field cage (FC) that defines the volume(s) and ensures uniformity of the E field to 1% within the volume.

LAr is an excellent scintillator at a wavelength of 126.8 nm. This fast scintillation light, once shifted into the visible spectrum, is collected by photon detectors (PDs) in both designs. The PDs provide a time t_0 for every event, indicating when the ionization electrons begin to drift. Comparing the time at which the ionization signal reaches the anode relative to the t_0 allows reconstructing event topology in the drift coordinate; the precision of the measured t_0, therefore, directly corresponds to the precision of the spatial reconstruction in this direction.

Two key factors affect the performance of the DUNE LArTPCs. First, the LAr purity must be high enough to achieve minimum charge attenuation over the longest drift lengths in a given detector module. Thus, the levels of electro-negative contaminants (e.g., oxygen and water) must be maintained at ppt levels. The SP and DP designs have slightly different purity requirements (expressed in minimum electron lifetimes of 3 ms versus 5 ms, respectively) due to the different drift lengths.

Second, the electronic readout of the LArTPC requires very low noise levels to allow the signal from the drifting electrons to be clearly discernible over the baseline of the electronics. This requires using low-noise cryogenic electronics, especially in the case of the SP design.

The plans for the SP and DP time projection chambers (TPCs) are described briefly in the following sections. The DUNE collaboration is committed to deploying both technologies. For planning purposes, we assume that the first detector module will be SP and the second will be DP. Studies are also under way toward a more advanced detector module design that could be realized as the fourth module, for example. The actual sequence of detector module installation will depend on

results from the prototype detectors, described below, and on available resources.

2.2.1 Single-phase Technology

Figure 2.4 shows the general operating principle of the SP LArTPC, as has been previously demonstrated by ICARUS [16], MicroBooNE [17], ArgoNeuT [18], LArIAT [19], and ProtoDUNE [20]. Figure 2.5 shows the configuration of a DUNE SP module. Each of the four drift volumes of LAr is subjected to a strong electric field (E field) of 500 V/cm. Charged particles passing through the TPC ionize the argon, and the ionization electrons drift in the E field to the anode planes.

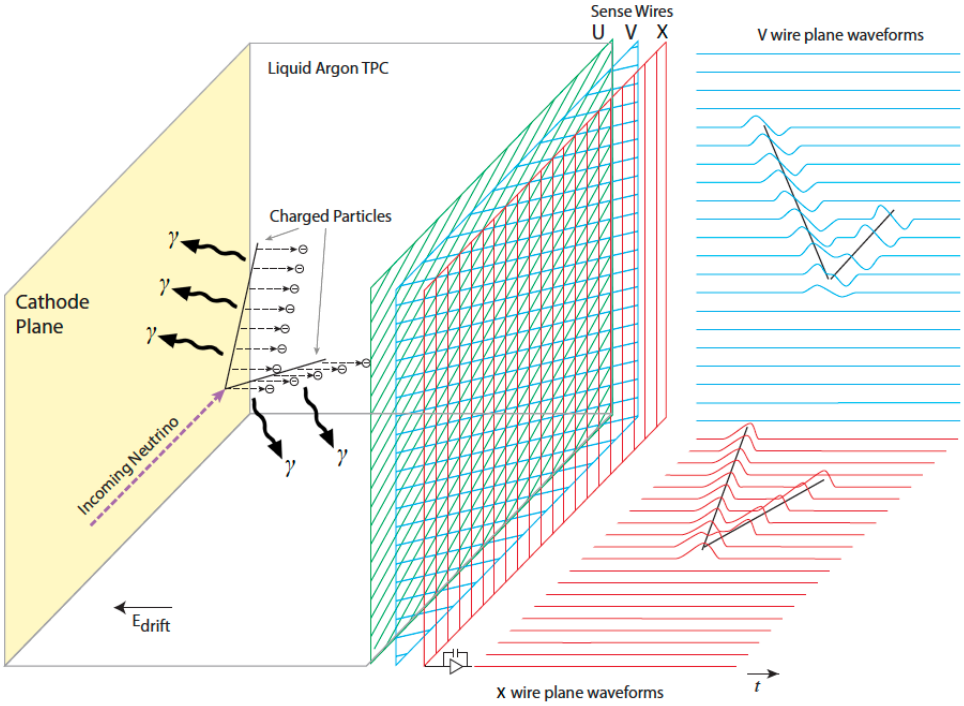

Figure 2.4: The general operating principle of the SP LArTPC.

A SP module is instrumented with three module-length anode planes constructed from 6 m high by 2.3 m wide anode plane assembly (APA)s, stacked two APAs high and 25 wide, for 50 APAs per plane, or 150 total. Each APA is two-sided with three layers of active wires forming a grid on each side of the APA. The relative voltage between the layers is chosen to ensure the transparency to the drifting electrons of the first two layers (U and V). These layers produce bipolar induction signals as the electrons pass through them. The final layer (X) collects the drifting electrons, resulting in a unipolar signal. The pattern of ionization collected on the grid of anode wires provides the reconstruction in the remaining two coordinates perpendicular to the drift direction.

Scintillation photons are detected in novel PD modules, based on a light-trap concept known as ARAPUCA [21, 22, 23] that utilizes dichroic filters, wavelength-shifting plates and silicon photomultiplier (SiPM) read-out. The variant of this technology in the DUNE baseline design (X-ARAPUCA) is described in Volume IV. The PD modules are placed in the inactive space between the innermost wire planes of the APAs, installed through slots in a pre-wound APA frame. There

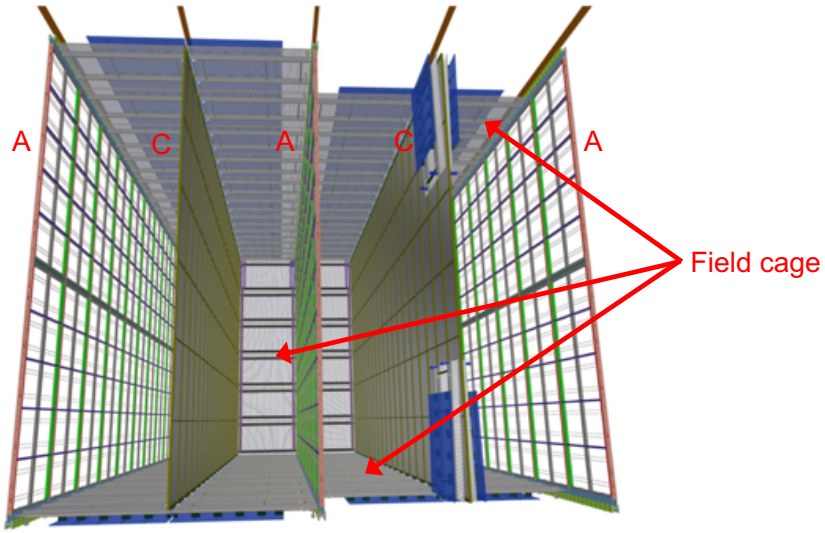

Figure 2.5: Schematic of a 10 kt DUNE FD SP module, showing the alternating anode (A) and cathode (C) planes that divide the LArTPC into four separate drift volumes. The red arrows point to one top and one bottom FC module and to the rear endwall field cage.

are ten PD modules per APA for a total of 1500 per SP module. Of these, 500 are mounted in central APA frames and must collect light from both directions, and 1000 are mounted in frames near the cryostat walls and collect light from only one direction.

2.2.2 Dual-phase Technology

The DP operating principle, illustrated in Figure 2.6, is very similar to that of the SP. Charged particles that traverse the active volume of the LArTPC ionize the medium while also producing scintillation light. The ionization electrons drift along an E field towards a segmented anode where they deposit their charge. Scintillation light is measured in PDs that view the volume from below.

In this design, shown in Figure 2.7, electrons drift upward toward an extraction grid just below the liquid-vapor interface. After reaching the grid, an E field stronger than the 500 V/cm drift field extracts the electrons from the liquid up into the gas phase. Once in the gas, electrons encounter micro-pattern gas detectors, called LEMs, with high-field regions. The LEMs amplify the electrons in avalanches that occur in these high-field regions. The amplified charge is then collected and recorded on a 2D anode consisting of two sets of gold-plated copper strips that provide the x and y coordinates (and thus two views) of an event.

The extraction grid, LEM, and anode are assembled into three-layered sandwiches with precisely defined inter-stage distances and inter-alignment, which are then connected horizontally into 9 m^2 modular detection units. These detection units are called charge-readout planes (CRPs).

The precision tracking and calorimetry offered by the DP technology provides excellent capabilities for identifying interactions of interest while mitigating sources of background. Whereas the SP

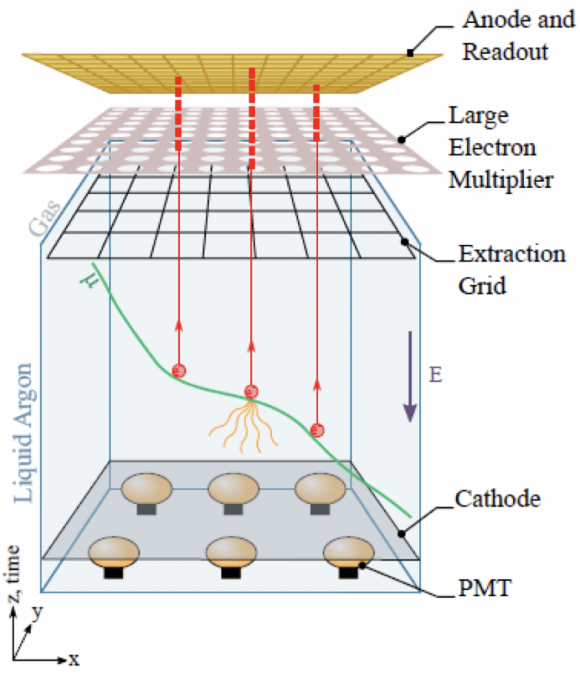

Figure 2.6: The general operating principle of the DP LArTPC.

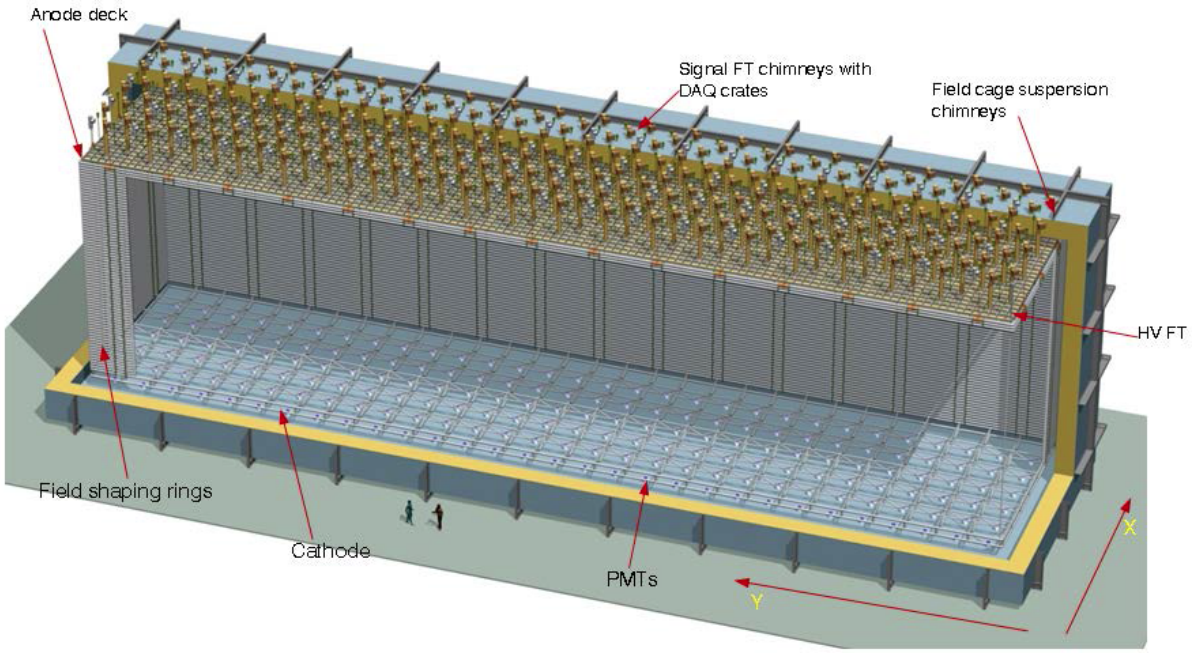

Figure 2.7: Schematic of a 10 kt DUNE FD DP detector module with cathode, photomultiplier tubes (PMTs), FC, and anode plane with signal feedthrough chimneys (SFT chimneys). The drift direction is vertical in the case of a DP module.

design has multiple drift volumes, the DP module design allows a single, fully homogeneous LAr volume with a much longer drift length.

A simple array of PMTs coated with a wavelength-shifting material is located below the cathode. The PMTs record the time and pulse characteristics of the incident light.

2.2.3 ProtoDUNEs: Far Detector Prototypes

The DUNE collaboration has constructed two large prototype detectors (ProtoDUNEs), ProtoDUNE-SP and ProtoDUNE-DP, located at CERN. Each is approximately one-twentieth the size of a DUNE detector module and uses components identical in size to those of the full-scale module. ProtoDUNE-SP has the same 3.5 m maximum drift length as the full SP module. ProtoDUNE-DP has a 6 m maximum drift length, half that planned for the DP module. See the photos in Figures 2.8 and 2.9.

Figure 2.8: ProtoDUNE-SP and ProtoDUNE-DP cryostats in the CERN Neutrino Platform in CERN's North Area. The view is from the downstream end of the hall with respect to the beam lines. At front and center is the top of the ProtoDUNE-SP cryostat. The ProtoDUNE-DP cryostat with its painted red steel support frame visible is located at the rear of the photo on the right side of the hall.

These large-scale prototypes allow us to validate key aspects of the TPC designs, test engineering procedures, and collect valuable calibration data using a hadron test beam.

The construction phase of ProtoDUNE-SP was finished in July 2018, and the detector was filled with LAr in August 2018. The detector collected hadron beam data and cosmic rays during the fall of 2018 and continues to collect cosmic-ray data. The construction of the ProtoDUNE-DP detector was completed in June of 2019, and started operations in September 2019.

Data taken with the ProtoDUNE-SP detector demonstrates its excellent performance and has already provided valuable information on the design, calibration, and simulation of the DUNE

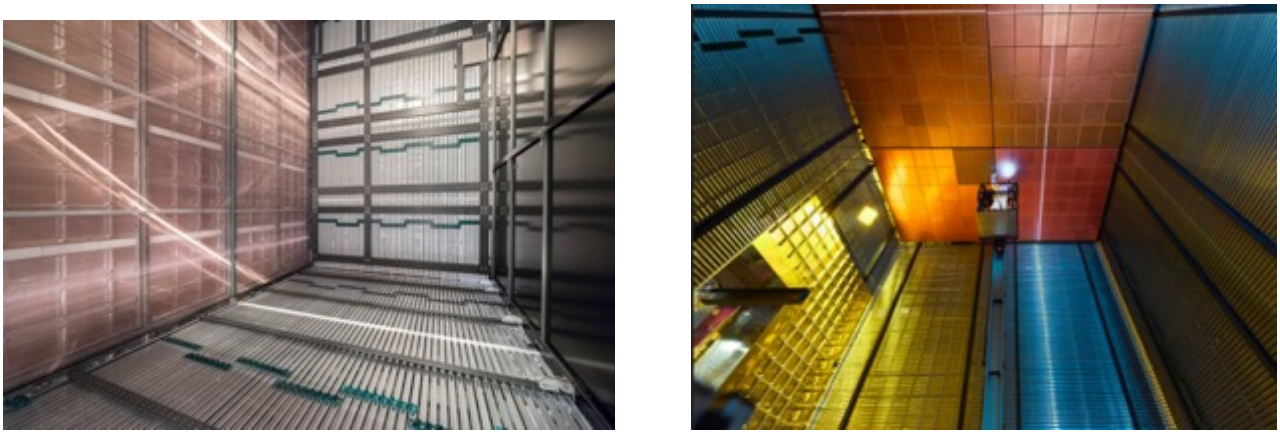

Figure 2.9: Interior views of ProtoDUNE-SP (left) and ProtoDUNE-DP (right). For ProtoDUNE-SP, one of two identical drift volumes is shown.

FD. In all, 99.7% of the 15360 TPC electronics channels are responsive in the LAr. The equivalent noise charge amounts to $\approx 550\ e^-$ on the collection wires and $\approx 650\ e^-$ on the induction wires. An average S/N of 38 for the collection plane is measured using cosmic-ray muons, while for the two induction planes, the S/N is 14 (U) and 17 (V), exceeding the requirement for the DUNE FD. The ProtoDUNE-SP photon detection system has also operated stably, demonstrating the principle of effective collection of scintillation light in a large-volume LArTPC with detectors embedded within the anode plane assemblies.

2.3 Near Detector Complex

The DUNE ND is crucial for the success of the DUNE physics program. It is used to precisely measure the neutrino beam flux and flavor composition. Comparing the measured neutrino energy spectra at the near and far site allows us to disentangle the different energy-dependent effects that modulate the beam spectrum and to reduce the systematic uncertainties to the level required for discovering charge parity (CP) violation. In addition, the ND will measure neutrino-argon interactions with high precision using both gaseous and liquid argon, which will further reduce the systematic uncertainties associated with the modeling of these interactions.

The ND hall will be located 574 m downstream from the target and will include three primary detector components, shown in Figure 2.10 and listed in Table 2.1. Two of them can move off beam axis, providing access to different neutrino energy spectra. The movement off axis, called DUNE Precision Reaction-Independent Spectrum Measurement (DUNE-PRISM), provides a crucial extra degree of freedom for the ND measurement and is an integral part of the DUNE ND concept.

The three detector components – a LArTPC called ArgonCube; a high-pressure gaseous argon TPC (HPgTPC) within a magnet surrounded by an electromagnetic calorimeter (ECAL), together called multi-purpose detector (MPD); and an on-axis beam monitor called System for on-Axis Neutrino Detection (SAND) – serve important individual and overlapping functions in the mission of the ND. The DUNE ND is shown schematically in the DUNE ND hall in Figure 2.11. Table 2.1

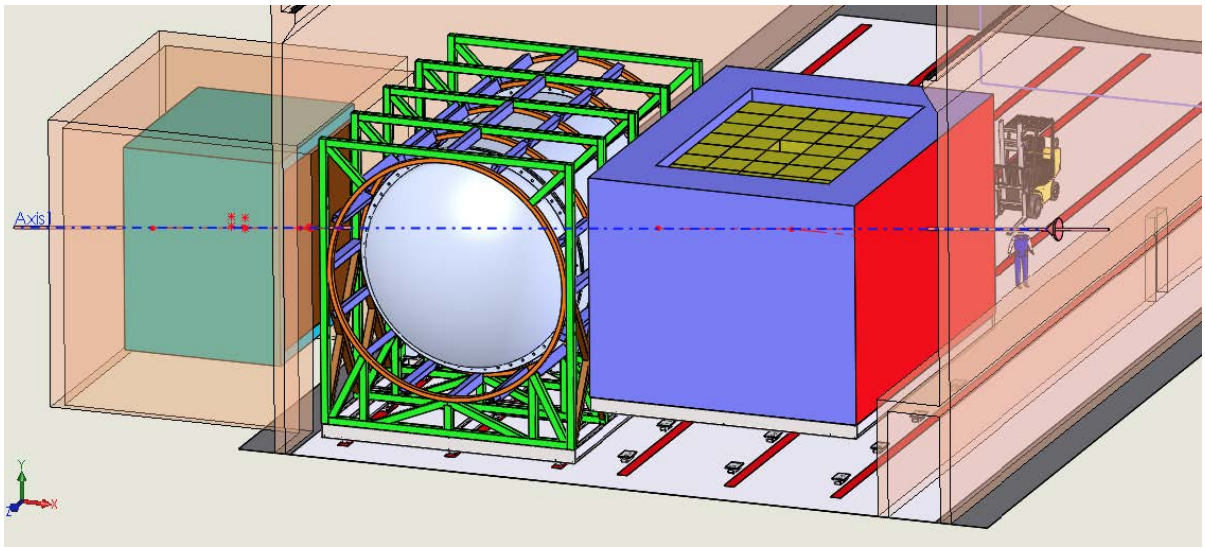

Figure 2.10: DUNE Near Detector. The beam enters from the right and encounters the LArTPC, the MPD, and the SAND on-axis beam monitor.

provides a high-level overview of the three components of the DUNE ND along with the off-axis capability.

The ArgonCube detector contains the same target nucleus and shares some aspects of form and functionality with the FD. The differences are necessitated by the expected high intensity of the neutrino beam at the ND. This similarity in target nucleus and, to some extent, technology, reduces sensitivity to nuclear effects and detector-driven systematic uncertainties in extracting the oscillation signal at the FD. The ArgonCube LArTPC is large enough to provide high statistics ($1 \times 10^8 \nu_\mu$ charged current events/year on axis), and its volume is sufficiently large to provide good hadron containment. The tracking and energy resolution, combined with the mass of the LArTPC, will allow measurement of the flux in the beam using several techniques, including the rare process of ν-e$^-$ scattering.

The LArTPC begins to lose acceptance for muons with a measured momentum higher than $\approx$0.7 GeV/c because the muons will not be contained in the LArTPC volume. Because the muon momentum is a critical component of determining the neutrino energy, a magnetic spectrometer is needed downstream of the LArTPC to measure the charge sign and momentum of the muons. In the DUNE ND concept, this function is accomplished by the MPD, which consists of a HPgTPC surrounded by an ECAL in a 0.5 T magnetic field. The HPgTPC provides a lower density medium with excellent tracking resolution for the muons from the LArTPC.

In addition, neutrinos interacting with the argon in the gas TPC constitute a sample of ν-argon events that can be studied with a very low charged-particle tracking threshold and excellent resolution superior to LAr. The high pressure yields a sample of $2 \times 10^6 \nu_\mu$-CC events/year for these studies. These events will be valuable for studying the charged particle activity near the interaction vertex because this detector can access lower momenta protons than the LAr detector and can better identify charged pions. The lack of secondary interactions in these samples will be helpful for identifying the particles produced in the primary interaction and modeling secondary interactions in denser detectors.

Table 2.1: This table gives a high-level breakdown of the three major detector components and the capability of movement for the DUNE ND along with function and primary physics goals.

Component	Essential Features	Primary function	Select physics aims
LArTPC (ArgonCube)	Mass	Experimental control for the Far Detector	$\nu_\mu(\overline{\nu}_\mu)$ CC
	Target nucleus Ar	Measure unoscillated E_ν spectra	ν-e$^-$ scattering
	Technology FD-like	Flux determination	$\nu_e+\overline{\nu}_e$ CC Interaction model
Multipurpose detector (MPD)	Magnetic field	Experimental control for the LArTPCs	$\nu_\mu(\overline{\nu}_\mu)$ CC
	Target nucleus Ar	Momentum analyze liquid Ar μ	ν_e CC, $\overline{\nu}_e$
	Low density	Measure exclusive final states with low momentum threshold	Interaction model
On-axis beam monitor (SAND)	On-axis	Beam flux monitor	On-axis flux stability
	Mass Magnetic field CH target	Neutrons	Interaction model A dependence ν-e$^-$ scattering
DUNE-PRISM (capability)	LArTPC+MPD move off-axis	Change flux spectrum	Deconvolve xsec*flux Energy response Provide FD-like energy spectrum at ND ID mismodeling

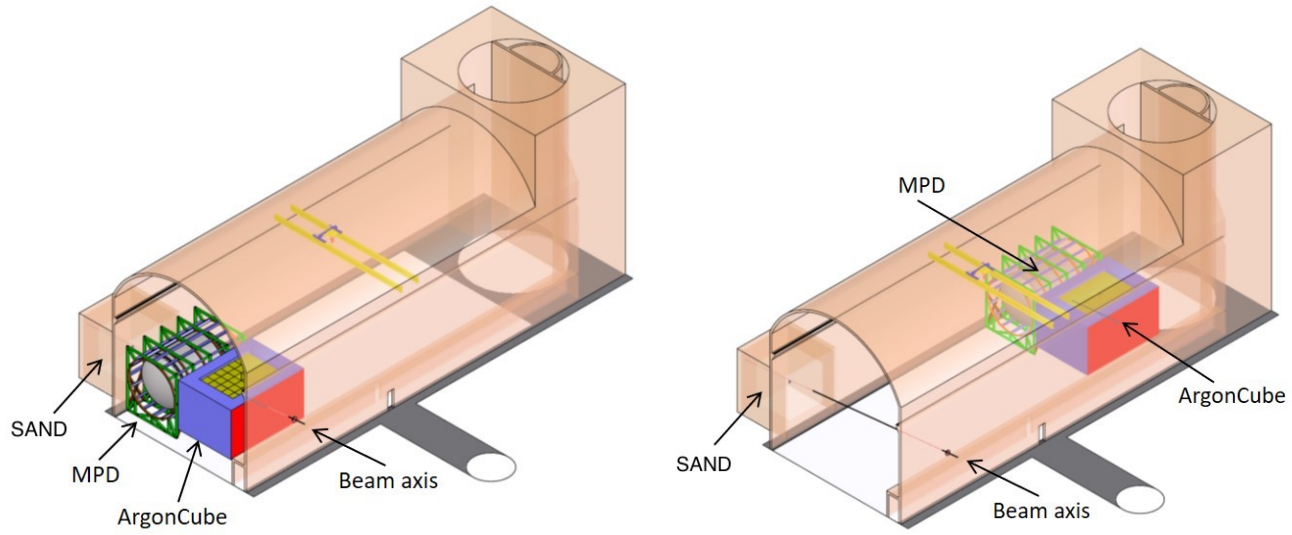

Figure 2.11: DUNE ND hall shown with component detectors all in the on-axis configuration (left) and with the LArTPC and MPD in an off-axis configuration (right). The on-axis monitor SAND is shown in position on the beam axis.

The ECAL adds neutral particle (mainly γ's and neutrons) detection capability otherwise lacking in the MPD. NC-π^0 backgrounds to ν_e CC interactions can be studied, for example. Additionally, neutron production in neutrino-nucleus interactions is poorly understood: the presence of the ECAL opens the possibility of identifying neutrons via time-of-flight.

The LArTPC and MPD can be moved sideways up to 33 m to take data in positions off the beam axis. This capability is referred to as DUNE-PRISM. As the detectors move off-axis, the incident neutrino flux spectrum changes, with the mean energy dropping and the spectrum becoming more monochromatic. Though the neutrino interaction rate drops off-axis, the intensity of the beam and the size of the LArTPC combine to yield ample statistics even in the off-axis positions. The DUNE concept is based on reconstructing the energy-dependent neutrino spectrum and comparing the far and near sites. The ability to modify the energy spectrum at the near site by measuring at the off-axis locations will allow disentangling otherwise degenerate effects due to systematic biases of the energy reconstruction.

The final component of the DUNE ND suite (SAND) is the on-axis beam monitor that remains in fixed position at all times and serves as a dedicated neutrino spectrum monitor. It can also provide an excellent on-axis neutrino flux determination that can be used as an important point of comparison and a systematic crosscheck for the flux as determined by ArgonCube.

Chapter 3

Scientific Landscape

The aim of this chapter is to set the stage for the discussions of DUNE's scientific capabilities that are presented in the chapters that follow. This is implemented as a series of brief descriptions of the theoretical and experimental contexts relevant for key areas of the DUNE physics program.

It is important to state at the outset that a fully comprehensive review is not possible here. Rather, the descriptions presented in this chapter are intended to be illustrative, so as to convey broadly the array of scientific opportunities for which DUNE is designed to realize. Furthermore, the supporting literature is vast, and it is not within the scope or purpose of this chapter to provide an exhaustive list of references. More details, including concrete references to the literature, are provided in subsequent chapters.

3.1 Neutrino Oscillation Physics

The first positive hint for neutrino flavor-change was uncovered in the 1960's with the first measurement of the flux of neutrinos from the sun. The hint compounded in the late 1980's, with high-statistics measurements of the differential flux of muon-type neutrinos produced by the collisions of cosmic rays with the earth's atmosphere. Both hints were ultimately confirmed in the late 1990's and early 2000's by the Super-Kamiokande and SNO experiments. Concurrently, neutrino oscillations were confirmed as the dominant physics behind neutrino flavor change.

Neutrino oscillations imply nonzero neutrino masses and flavor-mixing in the leptonic charged-current interactions. That the neutrino masses are not zero is among the most important discoveries in fundamental particle physics of the twenty-first century. Understanding the mechanism behind nonzero neutrino masses is among the unresolved mysteries that drive particle physics today; they remain one of the few unambiguous facts that point to the existence of new particles and interactions, beyond those that make up the remarkable standard model of particle physics. Learning more about the properties of neutrinos is a very high priority for particle physics, and neutrino oscillations remain, as of today, the only phenomenon capable of observing the neutrino

masses and lepton mixing in action. Precision measurements of neutrino oscillations have the potential to play a leading role in shaping particle physics in the next few decades.

Almost all neutrino data can be understood within the three-flavor paradigm with massive neutrinos, the simplest extension of the standard model capable of reconciling theory with observations. A handful of intriguing results, including those from the LSND, MiniBooNE, and short-baseline reactor experiments, remain unexplained and are currently the subject of intense experimental and theoretical scrutiny. If confirmed as the manifestation of new physics involving neutrinos – e.g., new neutrino states – these will open the door to more neutrino-related questions, many of which can be further explored with DUNE. We will return to those later but assume, conservatively, that the resolutions to these so-called short-baseline anomalies lie outside of neutrino-related particle physics.

3.1.1 Oscillation Physics with Three Neutrino Flavors

The three-flavor paradigm with massive neutrinos consists of introducing distinct, nonzero, masses for at least two neutrinos, while maintaining the remainder of the standard model of particle physics. Hence, neutrinos interact only via the standard model charged-current and neutral-current weak interactions. The neutrino mass eigenstates – defined as ν_1, ν_2, ν_3 with masses, m_1, m_2, m_3, respectively – are distinct from the neutrino charged-current interaction eigenstates, also referred to as the flavor eigenstates – ν_e, ν_μ, ν_τ, labeled according to the respective charged-lepton e, μ, τ to which they couple in the charged-current weak interaction. The flavor eigenstates can be expressed as linear combinations of the mass eigenstates (and vice-versa). The coefficients of the respective linear combinations define a unitary 3×3 mixing matrix, referred to as the neutrino mixing matrix, the leptonic mixing matrix, or the Pontecorvo-Maki-Nakagawa-Sakata (PMNS) matrix, as follows:

$$\begin{pmatrix} \nu_e \\ \nu_\mu \\ \nu_\tau \end{pmatrix} = \begin{pmatrix} U_{e1} & U_{e2} & U_{e3} \\ U_{\mu1} & U_{\mu2} & U_{\mu3} \\ U_{\tau1} & U_{\tau2} & U_{\tau3} \end{pmatrix} \begin{pmatrix} \nu_1 \\ \nu_2 \\ \nu_3 \end{pmatrix}. \tag{3.1}$$

The PMNS matrix is the leptonic-equivalent of the Cabibbo-Kobayashi-Maskawa (CKM) matrix that describes the charged-current interactions of quark mass eigenstates. If the neutrinos are Dirac fermions, taking advantage of the unitary nature of the matrix and the ambiguity in defining the relative phases among the standard model lepton fields, the neutrino mixing matrix, like the CKM matrix, can be unambiguously parameterized with three mixing angles and one complex phase. If, however, the neutrinos are Majorana fermions, there are fewer field-redefinitions available and one ends up with at most two other physical complex phases.[1] Strictly speaking, these so-called Majorana phases can manifest themselves in "neutrino–antineutrino" oscillations [24] and could be observed in neutrino oscillation experiments. These effects, however, are expected to be unobservably small and will be henceforth ignored, along with the Majorana phases. For all practical purposes, neutrino oscillation experiments cannot distinguish Majorana from Dirac neutrinos. Majorana phases are expected to play a significant role in experiments that are sensitive to the Majorana versus Dirac nature of the neutrinos, including searches for neutrinoless double-beta decay.

[1] Majorana phases can also be interpreted as complex phases of the neutrino mass eigenvalues and need not be considered as part of the neutrino mixing matrix.

The PDG-parameterization [25], used throughout this report, makes use of three mixing angles θ_{12}, θ_{13}, and θ_{23}, defined as

$$\sin^2\theta_{12} \equiv \frac{|U_{e2}|^2}{1-|U_{e3}|^2}, \tag{3.2}$$

$$\sin^2\theta_{23} \equiv \frac{|U_{\mu 3}|^2}{1-|U_{e3}|^2}, \tag{3.3}$$

$$\sin^2\theta_{13} \equiv |U_{e3}|^2, \tag{3.4}$$

and one phase $\delta_{\rm CP}$, which in the conventions of [25], is given by

$$\delta_{\rm CP} \equiv -\arg(U_{e3}). \tag{3.5}$$

For values of $\delta_{\rm CP} \neq 0, \pi$, and assuming none of the $U_{\alpha i}$ vanish ($\alpha = e, \mu, \tau,\ i = 1, 2, 3$), the neutrino mixing matrix is complex and CP-invariance is violated in the lepton sector. This, in turn, manifests itself as different oscillation probabilities, in vacuum, for neutrinos and antineutrinos: $P(\nu_\alpha \to \nu_\beta) \neq P(\bar{\nu}_\alpha \to \bar{\nu}_\beta)$, $\alpha, \beta = e, \mu, \tau$, $\alpha \neq \beta$.[2]

Information on the values of the neutrino masses comes from measurements of the neutrino oscillation frequencies, which are proportional to the differences of the squares of the neutrino masses, $\Delta m^2_{ij} \equiv m^2_i - m^2_j$. Since all positive evidence for nonzero neutrino masses comes from measurements of neutrino oscillations, there is no direct information concerning the values of the masses themselves, only the mass-squared differences. As far as neutrino oscillation data are concerned, the hypothesis that the lightest neutrino mass is exactly zero is just as valid as the hypothesis that all neutrino masses are nonzero and almost degenerate. Three neutrino masses allow for two independent mass-squared differences and the existing neutrino data point to two hierarchically different Δm^2, one whose magnitude is of order 10^{-4} eV^2, the other with magnitude of order 10^{-3} eV^2.

With this information, it is possible to unambiguously define the neutrino masses in a convenient way, as follows.[3] The mass-squared difference with the smallest magnitude is defined to be Δm^2_{21}, positive-definite so $m^2_2 > m^2_1$. The third mass eigenvalue is such that $|\Delta m^2_{31}| \sim |\Delta m^2_{32}|$, of order 10^{-3} eV^2 while the sign of $\Delta m^2_{31}, \Delta m^2_{32}$ defines the neutrino mass ordering, or the neutrino mass hierarchy. If $\Delta m^2_{31}, \Delta m^2_{32} > 0$, the neutrino mass ordering is defined to be 'normal' and $m^2_1 < m^2_2 < m^2_3$. If $\Delta m^2_{31}, \Delta m^2_{32} < 0$, the neutrino mass ordering is defined to be 'inverted' and $m^2_3 < m^2_1 < m^2_2$. This definition allows one to change from a normal to an inverted ordering without having to change the relationship between the neutrino mixing matrix and the various experimental results. The distinct neutrino mass orderings are illustrated in Figure 3.1.

[2] For neutrino disappearance, in vacuum, the relation $P(\nu_\alpha \to \nu_\alpha) = P(\bar{\nu}_\alpha \to \bar{\nu}_\alpha)$ is a consequence of the CPT-theorem.

[3] Equivalently, one can use the neutrino mixing matrix to define the neutrino mass eigenstates. ν_1 could be defined as the state associated to the largest $|U_{ei}|^2$ ($i = 1, 2, 3$), ν_2 to the second largest $|U_{ei}|^2$, and ν_3 to the smallest $|U_{ei}|^2$: $|U_{e1}|^2 > |U_{e2}|^2 > |U_{e3}|^2$.

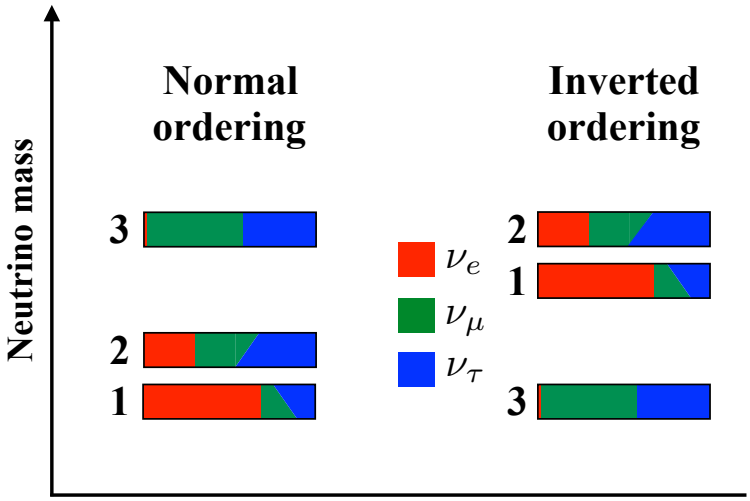

Figure 3.1: Fractional flavor content, $|U_{\alpha i}|^2$ ($\alpha = e, \mu, \tau$) of the three mass eigenstates ν_i, based on the current best-fit values of the mixing angles. $\delta_{\rm CP}$ is varied from 0 (bottom of each colored band) to 180° (top of colored band), for normal and inverted mass ordering on the left and right, respectively. The different colors correspond to the ν_e fraction (red), ν_μ (green) and ν_τ (blue).

3.1.1.1 Synthesis of Experimental Inputs

The world's neutrino data significantly constrain all of the oscillation parameters in the three-flavor paradigm. The results of a recent global fit [2] to all neutrino data, except those associated to the short-baseline anomalies, are depicted in Fig. 3.2. The magnitudes of both mass-squared differences are known at better than 3%, while, at the one sigma level, $\sin^2\theta_{12}$, $\sin^2\theta_{13}$, $\sin^2\theta_{23}$ are known at better than the 5% level. Note, however, that the error bars are rather non-Gaussian, especially for $\sin^2\theta_{23}$. At the three sigma level, according to [2], $\sin^2\theta_{23}$ is constrained to lie between 0.43 and 0.62 so values of $\sin^2\theta_{23} > 0.5$ and $\sin^2\theta_{23} < 0.5$ are allowed.

Critical questions remain open. The neutrino mass ordering is unknown. Current data prefer the normal ordering but the inverted one still provides a decent fit to the data. The octant of θ_{23} (whether $\sin^2\theta_{23} < 0.5$ [$\theta_{23} < \pi/4$] or $\sin^2\theta_{23} > 0.5$ [$\theta_{23} > \pi/4$]) remains unknown. The value of $\delta_{\rm CP}$ is only poorly constrained. While positive values of $\sin\delta_{\rm CP}$ are disfavored, all $\delta_{\rm CP}$ values between π and 2π, including the CP-conserving values $\delta_{\rm CP} = 0, \pi$, are consistent with the world's neutrino data.[4] That the best fit to the world's data favors large charge-parity symmetry violation (CPV) is intriguing, providing further impetus for experimental input to resolve this particular question. It is central to the Deep Underground Neutrino Experiment (DUNE) mission that all of the questions posed here can be addressed by neutrino oscillation experiments.

Other fundamental questions, including the nature of the neutrino – Majorana versus Dirac – and the determination of the values of the neutrino masses – oscillation experiments only measure mass-squared differences – are not accessible to oscillation experiments and must be addressed using different experimental tools.

[4]It should be noted that recent results from the T2K experiment [26] show only marginal consistency with CP-conserving values of $\delta_{\rm CP}$.

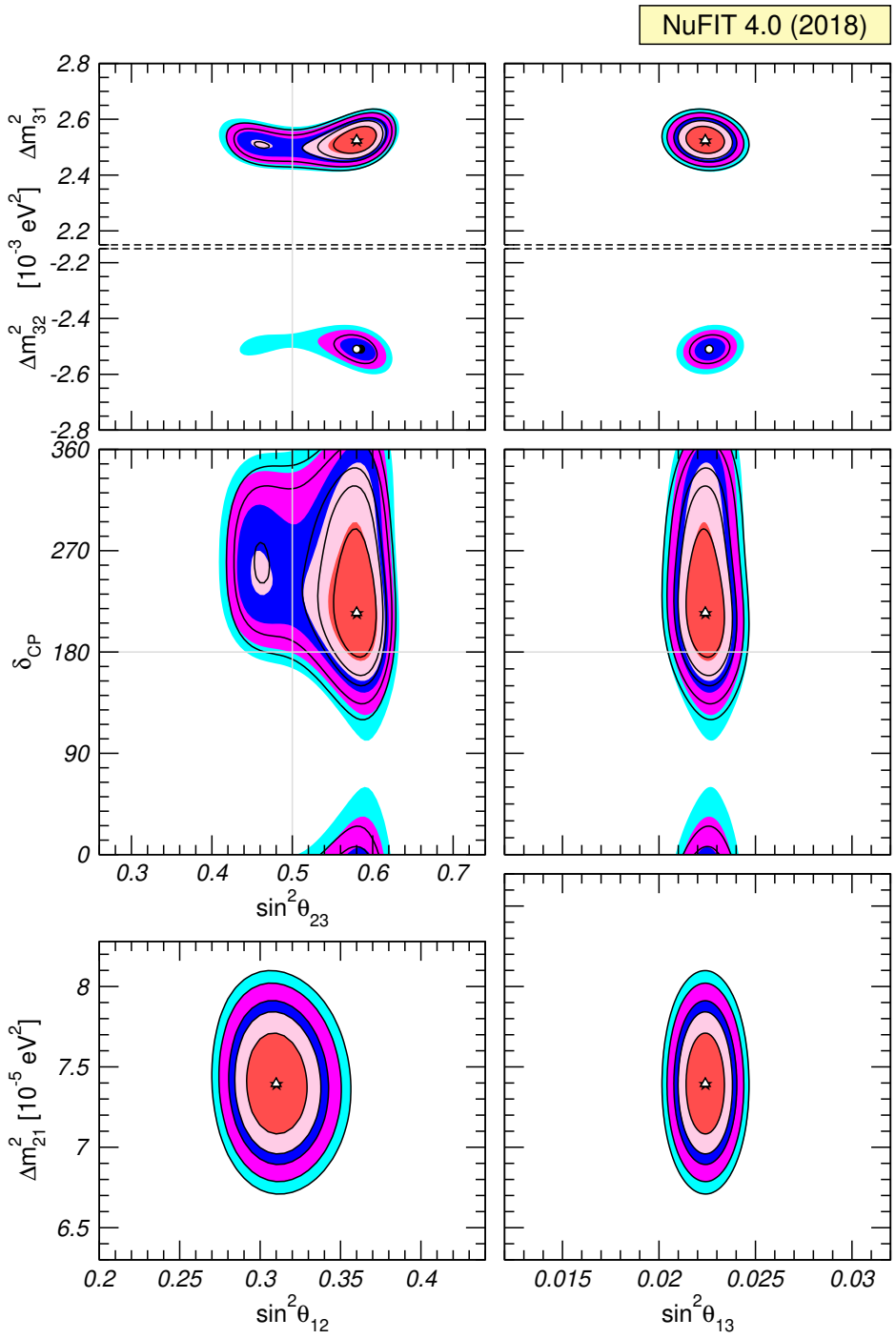

Figure 3.2: Global three-neutrinos-oscillation analysis from [2]. Each panel depicts the two-dimensional projection of the allowed six-dimensional region after marginalization with respect to the undisplayed parameters. The different contours correspond to the two-dimensional allowed regions at 1σ, 90%, 2σ, 99%, 3σ CL (2 dof). Note that the top panel refers to Δm^2_{31} in the case of the normal mass-ordering and Δm^2_{32} in the case of the inverted one. The regions in the lower four panels are defined using $\Delta\chi^2$ relative to minimum value of χ^2 obtained for a fixed choice of the mass ordering, normal ordering on the left-hand-side, inverted ordering on the right-hand-side.

At a more fundamental level, the three-flavor paradigm is yet to be significantly challenged by precision experiments. The overall picture described briefly above, while minimalistic and appealing, may turn out to be incomplete. While we don't know what new neutrino physics, if any, lies beyond the three-flavor paradigm, many possibilities have been identified and are currently the subject of intense phenomenological and theoretical scrutiny. We list a few here; these and a few others are discussed in more detail in this report. There may be more neutrino-like states and hence new oscillation frequencies and mixing parameters. This is true regardless of the solution to the short-baseline anomalies. New neutrino-like states are often a "side-effect" of the physics responsible for nonzero neutrino masses and serve as a natural connection between the standard model and would-be dark sectors that may contain the elusive dark matter particle. Indeed, new neutrino states may, themselves, be a component of the dark matter. Neutrinos may also participate in new, currently, unknown interactions. These can be mediated by new heavy gauge bosons or new, weakly coupled, light particles. The heavier of the known neutrinos may also be much more short-lived than what is expected of the standard model interactions. The neutrino lifetimes are only poorly constrained, and some are best constrained by existing neutrino oscillation data. The quantum interferometric nature of the neutrino oscillation phenomenon also allows searches for new phenomena that manifest themselves as violations of CPT-invariance or violations of the law that governs the time-evolution of quantum states.

Currently, the information that goes into determining the parameters of the three-flavor paradigm comes from a large variety of experiments that make use of different neutrino sources, neutrino flavors, and neutrino energies. Different parameters are determined by different experiments in such a way that there is only limited information on whether the formalism is complete. For example, $\sin^2\theta_{12}$ is best constrained by measurements of the differential flux of solar neutrinos – mostly electron neutrinos with energies between 100 keV and 10 MeV – while Δm^2_{21} is best constrained by the KamLAND experiment – electron antineutrinos from nuclear reactors and baselines around 100 km. While solar experiments are also sensitive to Δm^2_{21} and KamLAND to $\sin^2\theta_{12}$, the respective uncertainties are not relatively competitive. Another example, the mixing parameters $\sin^2\theta_{13}$ is best constrained by reactor experiments with baselines around 1 km. Long-baseline experiments sensitive to $\nu_\mu \to \nu_e$ oscillations – baselines between 100 km and 1000 km, neutrino energies between a few 100 MeV and a few GeV – are also sensitive to $\sin^2\theta_{13}$, but the associated uncertainties cannot compete with those from the reactor experiments. It is, therefore, not possible to compare, in any effective way, the reactor measurement of θ_{13} with the long-baseline measurement of θ_{13} and perform a simple, non-trivial check of the three-flavor paradigm, which predicts those two numbers to be the same.

3.1.1.2 Opportunities for DUNE

The DUNE experiment is well positioned to over-constrain the three-flavor paradigm and reveal what may potentially lie beyond. The high-statistics of DUNE is, for example, capable of extracting $\sin^2\theta_{13}$ via the electron neutrino appearance channel, $\nu_\mu \to \nu_e$, with precision that approaches that of the reactor electron antineutrino disappearance measurements, $\bar{\nu}_e \to \bar{\nu}_e$. If the three-flavor paradigm is incomplete, these two independent values for $\sin^2\theta_{13}$ need not agree. The high-statistics of DUNE also allow one to directly determine whether CP-invariance is violated by comparing how neutrinos and antineutrinos – after matter effects are taken into account – oscillate.

The neutrino energies and the baseline of LBNF-DUNE imply that the oscillation probabilities will be significantly impacted by matter effects. These, in turn, allow DUNE to establish the neutrino mass ordering independent from the results of other neutrino oscillation experiments.[5] The presence of significant matter effects make DUNE sensitive to new neutrino interactions, which can modify neutrinos oscillation probabilities in a way that cannot be constrained by other experiments. The broadband character of the LBNF-DUNE neutrino beam allow one to "see" the oscillations and hence ultimately measure the L/E (L is the baseline and E is the neutrino energy) behavior of the oscillation probabilities in a way that is outside the capabilities of off-axis experimental setups and with better control of systematics than what can be expected of high-statistics measurements of atmospheric neutrinos. Measurements of the oscillation probabilities as a function of L/E performed within the same experimental setup are, for example, sensitive to new oscillation frequencies – and hence new neutrino mass eigenstates – and provide excellent tests of Lorentz-invariance in the neutrino sector.[6] Finally, DUNE energies are high enough that one can start to more seriously explore the dominant $\nu_\mu \to \nu_\tau$ oscillations via the charged-current production and subsequent detection of τ-leptons.

DUNE may also reveal that the three-flavor paradigm provides a complete description of the neutrino oscillation phenomenon. In this case, the impact of DUNE, as far as neutrino oscillation physics is concerned, can be quantified mostly via (i) precision measurements of the neutrino oscillation parameters and (ii) information on CP-invariance in the lepton sector. We comment on those in turn in the section below.

3.1.2 Fermion Flavor Physics: Masses, Mixing Angles and CP-odd Phases

The patterns defined by the fermion masses and mixing parameters have been the subject of intense theoretical activity for the last several decades. The values of masses and mixing parameters, and potential relations among them, may contain invaluable information for physics beyond the standard model and may reveal more fundamental structures and symmetries. The discovery of neutrino masses and lepton mixing provided more and different information that is still being deciphered. Progress depends on how well masses and mixing parameters are known, and one can define, in a mostly model-independent way, useful goals and guidelines.

Grand unified theories posit that quarks and leptons are different manifestations of the same fundamental entities so their masses and mixing parameters are related. While it is very clear that the CKM and PMNS matrices are very different, they may come from the same seed processed in different ways. Different models make different predictions but, in order to compare different possibilities, it is important that lepton mixing parameters be known as precisely as quark mixing parameters. Currently, the precision with which quark mixing parameters are known [25] varies from 0.2% (for V_{us}) to 5% (for V_{ub}). The unitarity-triangle phase γ (or ϕ_3) is known at the 10% level. Future Belle II data are expected to reduce this uncertainty to one or two percent [27].

[5] The current hint for the normal ordering relies on the reactor measurement of $\sin^2\theta_{13}$, the atmospheric neutrino sample from Super-Kamiokande, and the results from the beam experiments T2K and NOνA.

[6] L/E is proportional to the neutrino proper time. Lorentz-invariance dictates that oscillation probabilities, once matter effects are accounted for, only depend on L/E, not on L or E independently. This is true for a large class of phenomena, including allowing for the possibility that the neutrinos decay.

These naively indicate that equal-footing comparisons between quark and lepton mixing require that the mixing angles be determined at the few percent level while $\delta_{\rm CP}$ should be measured at the 10% level or better.

There are other well-motivated scenarios that relate the values of the different lepton mixing parameters in such a way that knowledge of a subset of parameters is enough to determine the entire set. These relations can often be expressed as mathematical constrains of the form:

$$f(\theta_{12}, \theta_{13}, \theta_{23}, \delta_{\rm CP}) = 0 \ , \tag{3.6}$$

where f is some model-dependent function. The ability to test these relations is limited by how well the different mixing parameters – sometimes all of them – are constrained. Optimal power requires all mixing parameters to be known equally well. Right now, θ_{23} is the least well measured mixing parameter other than the CP-odd phase $\delta_{\rm CP}$, which is virtually unconstrained. Improving, very significantly, the uncertainty on both of these is among the neutrino-oscillation goals of DUNE. Note that sometimes these relations among mixing parameters are guided by the physics responsible for nonzero neutrino masses and may include the mass-squared differences (or even the masses themselves).

A concrete example was discussed in Ref. [28] (for many other examples and details, see, for example Ref. [29]). For a large subclass of phenomenological models aimed at explaining the structure of the neutrino mixing matrix, one can derive the following relation (in the limit $\theta_{13} \ll 1$):

$$\sin\theta_{12} - \sin\theta_{13}\tan\theta_{23}\cos\delta_{\rm CP} = A,$$

where A is a parameter that characterizes the model (e.g., $A = 1/\sqrt{2}, 1/\sqrt{3}, 0.22$, etc), i.e., different models make different quantitative predictions for A. While $\sin\theta_{12}$ is rather well constrained experimentally, the uncertainty in $\tan\theta_{23}$ and $\delta_{\rm CP}$ – we currently only suspect that $\cos\delta_{\rm CP} \leq 0$ and, at the three sigma level, $\tan\theta_{23} \sim 1.1 \pm 0.2$ – practically prevents one from testing whether the sum rule is obeyed for most values of A. Indeed, it is challenging to use the sum rule to, for example, predict the value of $\cos\delta_{\rm CP}$ because of the large current error on $\tan\theta_{23}$.

The neutrino mass ordering also contains invaluable clues concerning the pattern of fermion masses and mixing matrices. If the neutrino mass ordering is "normal," the pattern of neutrino masses may mirror that of the charged-fermions: $m_{\rm lightest} \ll m_{\rm middle} \ll m_{\rm largest}$, barring the possibility, which cannot be tested in oscillation experiments, that $m_1 \sim m_2$. If, however, the mass ordering were inverted, we would learn that at least the two heavier neutrinos are almost degenerate in mass. No other matter particles with nonzero masses are quasi-degenerate; quasi-degenerate neutrino masses would inevitably be interpreted as evidence of an internal symmetry that lurks deep inside the neutrino sector and would invite vigorous new research efforts to tease out the nature of this new symmetry.

Even within the three-flavor paradigm, the CP-odd Dirac phase $\delta_{\rm CP}$ is a new source of CP-invariance violation. Indeed, if the neutrinos are Majorana fermions, the standard model accommodates at most five independent CP-odd parameters. Three of these – the majority – "live" in the neutrino sector and one of them can only be probed, at least for the foreseeable future, in neutrino oscillations. If we are to ever understand how and why nature chooses to distinguish matter from antimatter, we will need to explore, in as much detail as possible, CP-violation in the neutrino sector.

3.1.3 Impacts of DUNE for other Experimental Programs

The information on neutrino properties obtained with DUNE data will also serve as invaluable input for other experiments in fundamental physics, including those beyond the realm of neutrino properties. We highlight some of these here.

Long-baseline neutrino oscillation experiments are sensitive to the neutrino mass ordering via matter effects. Information on the mass ordering will also be obtained in atmospheric neutrino experiments and by looking for the Δm^2_{21}–Δm^2_{31} interference in reactor neutrino oscillations in vacuum. Given the importance of this measurement, it is critical to have multiple techniques to corroborate the findings. As DUNE will be able to achieve a 5σ determination of the ordering in a very controlled environment, this input will allow the study of subdominant effects in atmospheric neutrino oscillations, which depend on the Earth matter profile, and in supernova neutrinos.

The predictions for the decay rate of neutrinoless double beta decay critically depend on the neutrino mass ordering, via the effective Majorana mass parameter $m_{\beta\beta}$. If DUNE determines that the neutrino mass ordering is inverted, $m_{\beta\beta}$ is predicted to be bigger than 15 meV, within reach of the next generation of neutrinoless double beta decay experiments. Further conclusions could be obtained depending on future experimental results. For concreteness, let us first assume that the ordering is established to be inverted and consider a few relevant possibilities. (i) If $|m_{\beta\beta}| \geq 15$ meV is measured, one would conclude that neutrinos are Majorana particles and that Majorana neutrino exchange is, most likely, the dominant mechanism behind neutrinoless double-beta decay. In principle, if a very precise measurement of the masses is derived from, for example, cosmic surveys and neutrino oscillation experiments, these data combined with a very accurate determination of $m_{\beta\beta}$ might allow one to search for CP-violating effects due to the Majorana phases. (ii) If, on the other hand, $m_{\beta\beta}$ is experimentally constrained to be smaller than 15 meV, the simplest conclusion would be that neutrinos are Dirac particle unless a cancellation with other sources of lepton-number violation suppresses the decay rate of neutrinoless double beta decay. It would be critical to test this second hypothesis by looking for new particles and interactions which could provide sizable contributions to neutrinoless double beta decay. Second, let us consider the scenario in which DUNE establishes that the ordering is normal, as first hints from current neutrino data seem to indicate. In this case, expectations for $m_{\beta\beta}$ range from the current upper bounds to exactly zero. Information from cosmic surveys on the sum of neutrino masses, combined with data from DUNE, would help evaluate whether $m_{\beta\beta}$ is just around the corner or whether it might be severely suppressed. In the latter case, vigorous research towards multi-ton-scale ultralow-background neutrinoless double beta decay experiments will be required.

Neutrinos have a strong impact on the evolution of the universe as their presence suppresses the growth of cosmological structures such as galaxies and clusters of galaxies at the small scales. This is due to the fact that, being light, they free-streamed from high-density to low-density regions, weakening the effects of the gravitational pull of high-density regions. The effect is greater the larger the neutrino mass. As it is a gravitational effect, it does not depend on the flavor and the relevant parameter is, given current and future expected sensitivities, the sum $\Sigma_i m_i$. If DUNE establishes that the ordering is inverted, this implies that $\Sigma_i m_i \geq 0.1$ eV, while for normal ordering the sum can be as low as 0.06 eV. Future cosmological observations claim to be able to distinguish these two possibilities, under the assumption of the standard cosmological model.

A precise measurement from cosmology would allow an accurate determination of the values of neutrino masses, with implications for neutrinoless double beta decay as discussed above. There is also the possibility that incompatibilities are observed. For instance, if DUNE finds that the ordering is inverted and cosmological observations constrain $\Sigma_i m_i < 0.1$ eV, one would have to conclude that there are new cosmological or particle physics effects which reduce the impact of neutrino masses in the formation of large scale structures or which counter them.

3.1.4 Neutrino Masses, CP-violation and Leptogenesis

The information which can be obtained in neutrino experiments, in particular DUNE, is essential to understand the origin of neutrino masses and possibly of the baryon asymmetry of the universe. The latter can be explained in the context of neutrino mass models, invoking the leptogenesis mechanism [30]. The simplest extension of the Standard Model for neutrino masses requires right-handed (RH) neutrinos, which are singlets with respect to the Standard Model gauge group. They can couple to the Higgs doublet and the leptonic doublet via Yukawa couplings. Dirac masses arise for neutrinos as they do for all the other known fermions. This mechanism, although minimal, requires the promotion of the lepton-number symmetry from an accidental to a fundamental one and does not provide any insight on the smallness of neutrino masses or a rationale for the very different leptonic and quark mixing matrices.

If lepton-number is not imposed as a fundamental symmetry, Majorana masses for the RH neutrinos are also allowed and their magnitudes are unrelated to the scale of electroweak symmetry breaking. Once the Higgs gets a vacuum expectation value, both the Majorana and Dirac mass terms need to be included. If the RH-neutrino Majorana masses are much larger than the Dirac masses, this leads to small Majorana masses for the mostly-active neutrinos (those in the lepton-doublets) that manifest themselves via the Weinberg operator. This is the so-called seesaw mechanism and a strong suppression, without requiring very small Yukawa couplings, can be obtained if the RH neutrino masses are much heavier than the weak scale.

Models for nonzero neutrino masses, including the seesaw models, offer an explanation of the baryon asymmetry of the universe via the leptogenesis mechanism. This problem is one of the most compelling questions in cosmology. The baryon asymmetry of the universe has been measured precisely by Planck [31]

$$Y_B^{\rm CMB} \simeq (8.67 \pm 0.09) \times 10^{-10}\,, \tag{3.7}$$

where Y_B is the baryon to photon ratio at recombination. These results are in good agreement with data on big bang nucleosynthesis. Assuming that the universe initially had the same amount of baryons and antibaryons,[7] the baryon asymmetry can be generated dynamically if the Sakharov conditions [32] are satisfied: lepton or baryon number violation, for instance in presence of RH neutrino Majorana masses, C and CP violation, and out-of-equilibrium dynamics, satisfied by the expansion of the universe.

We restrict the discussion here to high-energy, type-I seesaw models in which RH neutrinos are introduced with very heavy Majorana masses. These models can satisfy all of the Sakharov condi-

[7] A period of inflation in the early universe implies that this assumption is effectively unavoidable.

tions because of the Majorana nature of the RH neutrinos and of the presence of complex Yukawa couplings. The basic picture is the following. In the early universe, RH neutrinos were in thermal equilibrium for large temperatures. Once the temperature dropped below their mass, the bath does not have sufficient energy to keep them in equilibrium and they decouple, decaying into leptons and Higgs bosons. If there is CP violation, the decays of this channel and of the conjugated one can proceed with different rates, controlled by the CP-violating phases in the Yukawa couplings. This asymmetry is partially washed out by inverse processes and the remaining lepton asymmetry is converted into a baryon asymmetry later on by non-perturbative standard model (SM) effects.

The question of whether and how the CP-violation involved in leptogenesis and that observable in DUNE and other long-baseline experiments are related has been debated extensively in the literature. Restricting the discussion to high-energy seesaw models only, for simplicity, the link is provided by the complex Yukawa couplings which control on one side the baryon asymmetry and on the other neutrino masses and consequently the PMNS matrix which diagonalizes them. In general, relationships are rather complex and very indirect because the high-energy theory contains more parameters – including more CP-odd phases – than are measurable at low-energy experiments. In a completely model-independent way, it is not possible to draw a direct link between the two. However, in many models that have a reduced number of parameters, for instance because of flavor symmetries, experimentally accessible CP-odd phases can be directly connected to the baryon asymmetry generated via leptogenesis.

Even without resorting to a restriction of the number of parameters, rather general models present such connection if in the Early universe the thermal bath distinguished between charged lepton flavors in the so-called flavored leptogenesis. It is possible to show that, in these circumstances, the PMNS mixing matrix and specifically the CP-violating phase $\delta_{\rm CP}$ does explicitly contribute to the CP asymmetry, and consequently the baryon asymmetry, and can even generate enough CP-violation to reproduce the observed baryon asymmetry. This is a highly non-trivial statement since its CP-violating effects are suppressed by θ_{13} and hence enough early-universe CP-violation relies crucially on the relatively large observed value of θ_{13}.

The consensus in the community is that one should be able to conclude that, generically, the observation of lepton-number violation (e.g., neutrinoless double beta decay) combined with that of CP-violation in long-baseline neutrino oscillation experiments (or, possibly, neutrinoless double beta decay) constitutes strong circumstantial evidence – albeit not a proof – of the leptogenesis mechanism as the origin of the baryon asymmetry of the universe.

3.2 Nucleon Decay and ΔB=2 Physics

Are protons stable? Few questions within elementary particle physics can be posed as simply and at the same time have implications as immediate. In more general terms, the apparent stability of protons suggests that baryon number is conserved in nature, although no known symmetry requires it to be so. Indeed, baryon number conservation is implicit in the formulation of the SM Lagrangian, and thus observation of baryon-number violating (BNV) processes such as nucleon

decay or neutron-antineutron oscillation would be evidence for physics beyond the SM.[8] On the other hand, continued non-observation of BNV processes will demand an answer to what new symmetry is at play that forbids them.

Especially compelling is that the observation of BNV processes could be the harbinger for grand unified theories (GUTs), in which strong, weak and electromagnetic forces are unified. Numerous GUT models have been proposed, each with distinct features. Yet, BNV processes are expected on general grounds, and it is a feature of many models that nucleon decay channels can proceed at experimentally accessible rates (see, e.g., Refs. [33, 34] and references therein).

The theoretical literature on nucleon decay, and BNV processes in general, is vast, and has been well summarized in recent reviews [33, 34]. It may be sufficient here to simply note that the theoretical motivations for baryon number non-conservation give strong arguments for the discovery potential of experimental searches, and that the existing array of null results from highly sensitive experiments provides hard constraints that models of new physics must abide by. Some additional theoretical context is provided in Chapter 6. The remainder of the discussion in this section focuses on the experimental landscape so as to illustrate the scientific opportunities for DUNE in BNV physics.

3.2.1 Experimental Considerations for Nucleon Decay Searches

The articulation of early GUT ideas led to the development of large-scale detectors located deep underground dedicated toward the search for proton and BNV bound-neutron decay. Illustrating the present context, the limits on a subset of possible nucleon decay modes, from a succession of sensitive experimental searches, are plotted in Fig. 3.3.

Particularly sensitive limits have been obtained with water-based Cherenkov ring imaging detectors, most notably Super–Kamiokande. The strengths of this approach include the cost-effectiveness of utilizing large volumes of water (22.5 kt fiducial mass in the case of Super–Kamiokande) as a source of nucleons and capabilities for particle identification, timing, energy and direction resolution. The technology is scalable to even larger masses, as in the proposed Hyper–Kamiokande [36] experiment, with a 187 kt fiducial mass in its single-tank configuration. The combination of deep underground location with active shielding enables rejection of backgrounds from atmospheric muons. As a result, the dominant backgrounds are due to interactions of atmospheric neutrinos, which are suppressed by event selection on the distinctive kinematic and signal timing features of the various nucleon decay channels.

With published results (see, e.g., Refs. [4, 37, 35]) based on exposures up to 0.32 Mt $\cdot$ year , Super–Kamiokande nucleon decay branching ratio sensitivity continues to increase linearly with exposure for many channels where background estimates are at the one-per-Mt $\cdot$ year level. However, as exposure increases further, the rate of improvement will be diminished as backgrounds enter. Candidate events are starting to appear [35] in channels where the estimated background rate exceeds this level.

[8] Non-perturbative effects that involve tunneling between vacua with differing baryon number do allow for BNV processes within the SM, but at rates many orders of magnitude below directly observable levels (see, e.g., Ref. [33]).

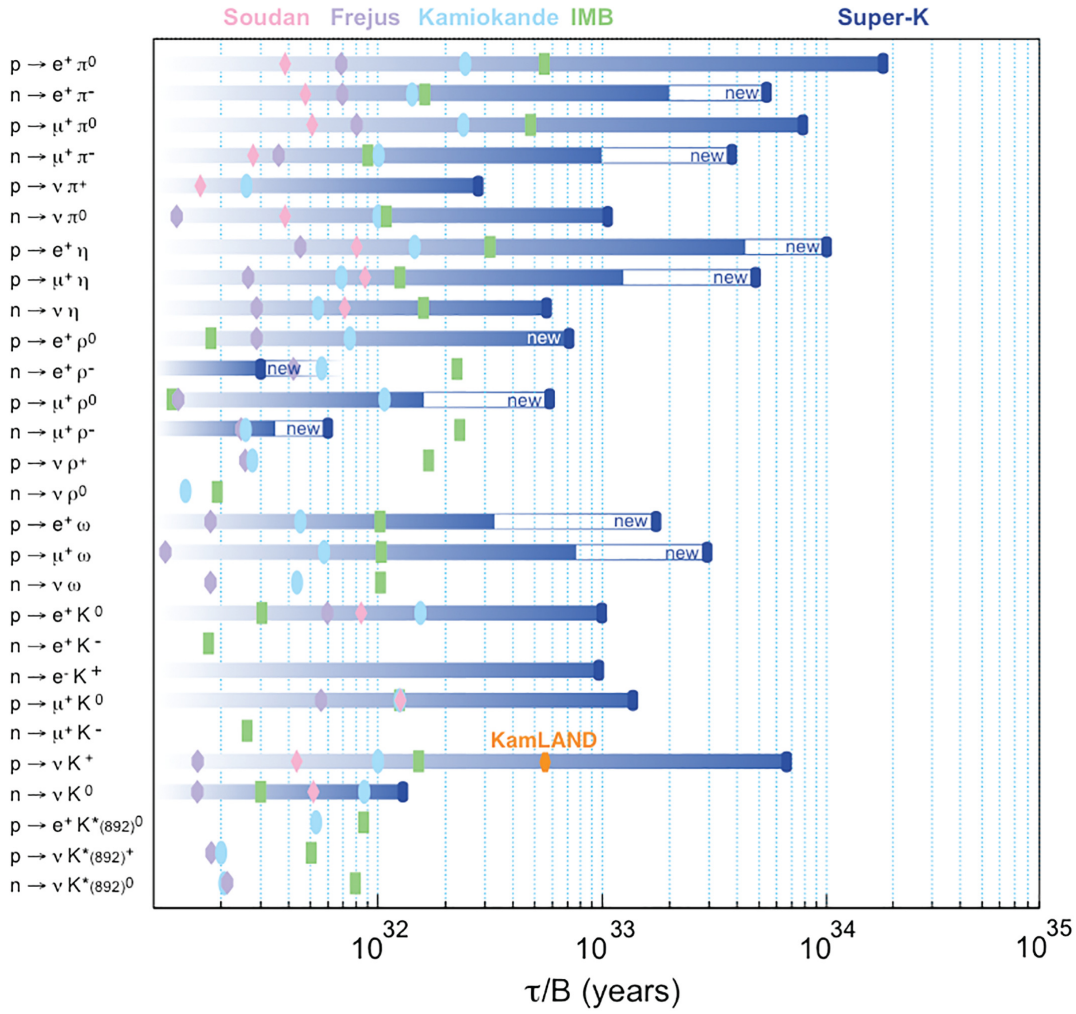

Figure 3.3: Summary of nucleon decay experimental lifetime limits from past and currently running experiments for decays to anti-lepton plus meson final states. Recently reported improvements in limits [35] are highlighted, indicating the ongoing nature of experimental effort in this area. The limits shown are 90% confidence level (CL) lower limits on the partial lifetimes, τ/B, where τ is the total mean life and B is the branching fraction. Updated from [34].

With a fiducial mass of 40 kt, DUNE can capitalize on the potential for discovery of nucleon decay in channels where backgrounds can be reduced below the one-per-Mt · year level thanks to the excellent imaging, calorimetric and particle identification capabilities of the LArTPC for events with 200 to 1000 MeV of deposited energy. In a background-free analysis, sensitivity to channels with partial lifetimes in the range of 10^{33} to a few times 10^{34} years may be achievable, depending on event selection efficiency. The limiting factor for DUNE is likely to be the combined impact of nucleon Fermi motion and final state interactions of decay hadrons as they escape the argon nucleus. Detailed analyses carried out for several prominent nucleon decay channels are described in Chapter 6.

Should nucleon decays occur at rates not far beyond current best limits, as predicted in numerous GUT models, a handful of candidate events could be observed by DUNE in a given decay mode. Even just one or two candidate events may be sufficient on their own to indicate evidence for nucleon decay, or provide confirmation for an excess above background observed in one of the contemporaneous large water or liquid scintillator experiments, e.g., Hyper Kamiokande (HyperK) [36] and JUNO [38, 39] respectively.

3.3 Low-Energy Neutrinos from Supernovae and Other Sources

The burst of neutrinos from the celebrated core-collapse supernova 1987A in the Large Magellanic Cloud, about 50 kpc from Earth, heralded the era of extragalactic neutrino astronomy. The few dozen recorded $\bar{\nu}_e$ events have confirmed the basic physical picture of core collapse and yielded constraints on a wide range of new physics [40, 41]. This sample has nourished physicists and astrophysicists for many years, but has by now been thoroughly picked over. The community anticipates a much more sumptuous feast of data when the next nearby star collapses.

Core-collapse supernovae within a few hundred kiloparsecs of Earth – within our own galaxy and nearby – are quite rare on a human timescale. They are expected once every few decades in the Milky Way (within about 20 kpc), and with a similar rate in Andromeda, about 700 kpc away. However core collapses should be common enough to have a reasonable chance of occurring during the few-decade long lifetime of a typical large-scale neutrino detector. The rarity of these spectacular events makes it all the more critical for the community to be prepared to capture every last bit of information from them.

The information in a supernova neutrino burst available in principle to be gathered by experimentalists is the *flavor, energy and time structure* of several-tens-of-second-long, all-flavor, few-tens-of-MeV neutrino burst [42, 43]. Imprinted on the neutrino spectrum as a function of time is information about the progenitor, the collapse, the explosion, and the remnant, as well as information about neutrino parameters and potentially exotic new physics. Neutrino energies and flavor content of the burst can be measured only imperfectly, due to intrinsic nature of the weak interactions of neutrinos with matter, as well as due to imperfect detection resolution in any real detector. For example, supernova burst energies are below charged-current threshold for ν_μ, ν_τ, $\bar{\nu}_\mu$ and $\bar{\nu}_\tau$ (collectively ν_x), which represent two-thirds of the flux; so these flavors are accessible only via neutral-current interactions, which tend to have low cross sections and indistinct detec-

tor signatures. These issues make a comprehensive unfolding of neutrino flavor, time and energy structure from the observed interactions a challenging problem.

Much has occurred since 1987, both for experimental and theoretical aspects of supernova neutrino detection. There has been huge progress in the modeling of supernova explosions, and there have been many new theoretical insights about neutrino oscillation and exotic collective effects that may occur in the supernova environment. Experimentally, worldwide detection capabilities have increased enormously, such that we now expect several thousands of events from a core collapse at the center of the Galaxy.

3.3.1 Current Experimental Landscape

At the time of this writing, Super-Kamiokande is the leading supernova neutrino detector; it expects ∼8000 events at 10 kpc. As for the 1987A sample, these will be primarily $\bar{\nu}_e$ flavor via inverse beta decay (IBD) on free protons. Super-K will soon be enhanced with the addition of gadolinium, which will aid in IBD tagging. IceCube is another water detector, with a different kind of supernova neutrino sensitivity – it cannot reconstruct individual neutrino events, given that any given interaction in the ice rarely leads to more than one photoelectron detected. However it can measure the overall supernova neutrino "light curve" as a glow of photons over background counts. Scintillator detectors, made of hydrocarbon, also have high IBD rates. There are several kton-scale scintillator detectors online currently: these are KamLAND, LVD, and Borexino. There is one small lead-based detector, HALO. Some surface or near-surface detectors will also usefully record counts even in the presence of significant cosmogenic background: these include NOvA, Daya Bay, and MicroBooNE.

In the world's current supernova neutrino flavor sensitivity portfolio [44, 42], the sensitivity is primarily to electron antineutrino flavor, via IBD. There is only minor sensitivity to the ν_e component of the flux, which carries with it particularly interesting information content of the burst (e.g., neutronization burst neutrinos are created primarily as ν_e). While there is some ν_e sensitivity in other detectors via elastic scattering on electrons and via subdominant channels on nuclei, statistics are relatively small, and it can be difficult to disentangle the flavor content. Neutral-current channels are also of particular interest, given their sensitivity to the entire supernova flux; the only way to access the ν_x component is via NC. NC channels are subdominant in large neutrino detectors, and typically difficult to tag, although scintillator has some sensitivity via NC excitation of ^{12}C as well as elastic scattering on protons. Dark matter detectors have access to the entire supernova flux via NC coherent elastic neutrino-nucleus scattering on nuclei, with statistics at the level of of ∼10 events per ton at 10 kpc.

3.3.2 Projected Landscape in the DUNE Era

The next generation of supernova neutrino detectors, in the era of DUNE, will be dominated by Hyper-Kamiokande, JUNO and DUNE. Hyper-K and JUNO are sensitive primarily to $\bar{\nu}_e$, and will have potentially enormous statistics. The next-generation long-string water detectors, IceCube

and KM3Net, will bring their timing strengths. New tens-of-ton scale noble liquid detectors such as DARWIN will bring new full-flux NC sensitivity. DUNE will bring unique ν_e sensitivity: it will offer a new opportunity to measure the ν_e content of the burst with high statistics and good event reconstruction.

The past decade has also brought rapid evolution of *multi-messenger astronomy*. With the advent of gravitational waves detection, and high-energy extragalactic neutrino detection in IceCube, a broad community of physicists and astronomers are now collaborating to extract maximum information from observation in a huge range of electromagnetic wavelengths, neutrinos, charged particles and gravitational waves. This collaboration resulted in the spectacular multimessenger observation of a kilonova [45]. The next core-collapse supernova will be a similar multimessenger extravaganza. Worldwide neutrino detectors are currently participants in SNEWS, the SuperNova Early Warning System [46], which will be upgraded to have enhanced capabilities over the next few years. Information from DUNE will enhance the SNEWS network's reach.

Neutrino pointing information is vital for prompt multi-messenger capabilities. Only some supernova neutrino detectors have the ability to point back to the source of neutrinos. Imaging water Cherenkov detectors like Super-K can do well at this, via directional reconstruction of neutrino-electron elastic scattering events. However other detectors lack pointing ability, due to intrinsic quasi-isotropy of the neutrino interactions, combined with lack of detector sensitivity to final-state directionality. Like Super-K, DUNE is capable of pointing to the supernova via its good tracking ability.

3.3.3 The Role of DUNE

Supernova neutrino detection is more of a collaborative than a competitive game. The more information gathered by detectors worldwide, the more extensive the knowledge to be gained; the whole is more than the sum of the parts. The flavor sensitivity of DUNE is highly complementary to that of the other detectors, and will bring critical information for reconstruction of the entire burst's flavor and spectral content as a function of time [47].

3.3.4 Beyond Core Collapse

While a core-collapse burst is a known source of a low-energy (<100 MeV) neutrinos, there are other potential interesting sources of neutrinos in this energy range. Nearby thermonuclear or pair instability supernova events may create bursts as well, although they are expected to be fainter in neutrinos than core-collapse supernovae. Mergers of neutron stars and black holes will be low-energy neutrino sources, although the rate of these nearby enough to detect will be small. There are also interesting steady-state sources of low-energy neutrinos – in particular, there may still be useful oscillation and solar physics information to extract via measurement of the solar neutrino flux. DUNE will have the unique capability of measuring solar neutrino energies event by event with the ν_eCC interactions with large statistics, in contrast to other detectors primarily make use of recoil spectra. The technical challenge for solar neutrinos is overcoming radiological

and cosmogenic backgrounds, although preliminary studies are promising. The diffuse supernova neutrino background neutrinos are another target which have a bit higher energy, but which are much more challenging due to very low event rate. There may also be surprises in store for us, both from burst and steady-state signals, enabled by unique DUNE liquid argon tracking technology.

3.4 Beyond-SM Searches

With the advent of a new generation of neutrino experiments which leverage high-intensity neutrino beams for precision measurements, the opportunity arises to explore in depth physics topics Beyond the Standard neutrino-related physics. Given that the realm of BSM physics has been mostly sought at high-energy regimes at colliders, such as the LHC at CERN, the exploration of BSM physics in neutrino experiments will enable complementary measurements at the energy regimes that balance those of the LHC. This, furthermore, is in concert with new ideas for high-intensity beams for fixed target and beam-dump experiments world-wide, e.g., those proposed at CERN [48].

The combination of the high intensity proton beam facilities and massive detectors for precision neutrino oscillation parameter measurements and for CP violation phase measurements will help make BSM physics reachable even in low energy regimes in the accelerator based experiments. Large mass detectors with highly precise tracking and energy measurements, excellent timing resolution, and low energy thresholds will enable the searches for BSM phenomena from cosmogenic origin, as well. Therefore, it can be anticipated that BSM physics topics studied with the next-generation neutrino experiments may have a large impact in the foreseeable future, as the precision of the neutrino oscillation parameter and CPV measurements continues to improve. A recent review of the current landscape of BSM theory in neutrino experiments in two selected areas of the BSM topics – dark matter and neutrino related BSM – has been recently reported in [49].

The DUNE experiment has two important assets that will play a significant role in future searches for BSM physics. The unique combination of the high-intensity LBNF proton beams with a highly-capable precision DUNE Near Detector (ND), and massive liquid argon time-projection chamber (LArTPC) far detector modules at a 1300 km baseline (FD), enables a variety of opportunities for BSM physics, either novel or with unprecedented sensitivity. The planned Near Detector can basically act as a stand alone experiment, to catch long lived particles produced in the proton target beam dump. On the other hand the Far Detector will allow for precision measurements on oscillation parameters, and for measurements cosmogenic and non-accelerator related phenomena, e.g. the detection of dark matter particles in certain scenarios.

In this section we give a few examples of particle searches in New Physics scenarios than can be conducted with the DUNE experiment, for which the sensitivities are discussed in the next chapters of this volume. For those searches for new particles in the ‘beam-dump’ mode, i.e. for searches for long-lived particles that pass through, or decay in, the Near Detector, a few scenarios have been studied in detail, but it will be important in the near future to connect with the Physics Beyond Collider study [48] and compare the potential sensitivity of DUNE for these benchmark scenarios, especially for so called “feebly interacting particle” sensitivity projections as made for potential new beam dump experiments for the next 10-15 years. DUNE is an already planned

facility, which has the potential to cover interesting regions in the coupling/mass phase space for dark photons, dark scalars and axion-like particles, for which the sensitivity has not been studied yet. In addition the precision measurements of the oscillation phenomena will allow also to search for e.g. non-standard interactions, CPT violating effects as discussed before.

3.4.1 Search for low-mass dark matter

Various cosmological and astrophysical observations strongly support the existence of dark matter (DM) representing 27% of the mass-energy of the universe, but its nature and potential non gravitational interactions with regular matter remain undetermined. The lack of evidence for weakly interacting massive particles (WIMP) at direct detection and the LHC experiments has resulted in a reconsideration of the WIMP paradigm. For instance, if dark matter has a mass which is much lighter than the electroweak scale (e.g., below GeV level), it motivates theories for dark matter candidates that interact with ordinary matter through a new vector portal mediator. High flux (neutrino) beam experiments, have been shown to provide coverage of DM+mediator parameter space which cannot be covered by either direct detection or collider experiments. In LBNF, low-mass dark matter may be produced through proton interactions in the target, and can be detected in the ND through neutral current (NC)-like interactions either with electrons or nucleons in the detector material via elastic scattering. Since these experimental signatures are virtually identical to those of neutrinos, neutrinos are a significant background that can be suppressed using timing and kinematics of the final-state electron or nucleons in the ND. Therefore, it is essential for the ND to be able to differentiate arrival time differences of the order a few ns or smaller, which determines the reachable range of the dark matter, and to measure precisely the kinematic parameters of the recoil electrons, such as the scattering angle and the energy. These capabilities will enable DUNE's search for light dark matter to be competitive and complementary to other experiments at mass range below 1-2 GeV.

The capability has recently been demonstrated in a dedicated search by MiniBooNE [50, 51], which placed new limits on the well-motivated vector portal dark matter model [52], as shown in Figure 3.4.

More scenarios for dark matter (DM) detection will become accessible for DUNE, due to its improved sensitivity using LarTPC technology, and the large FD volume, These scenarios include boosted dark matter, produced in models with a multi-particle dark sector. Sensitivities of such scenarios will be examined further in Chapter 8 of this volume.

3.4.2 Sterile neutrino search

Experimental results in tension with the three-neutrino-flavor paradigm, which may be interpreted as mixing between the known active neutrinos and one or more sterile states, have led to a rich and diverse program of searches for oscillations into sterile neutrinos. DUNE will be sensitive over a broad range of values of the sterile neutrino mass splitting by looking for disappearance of charged current (CC) and NC interactions over the long distance separating the near and far detectors, as

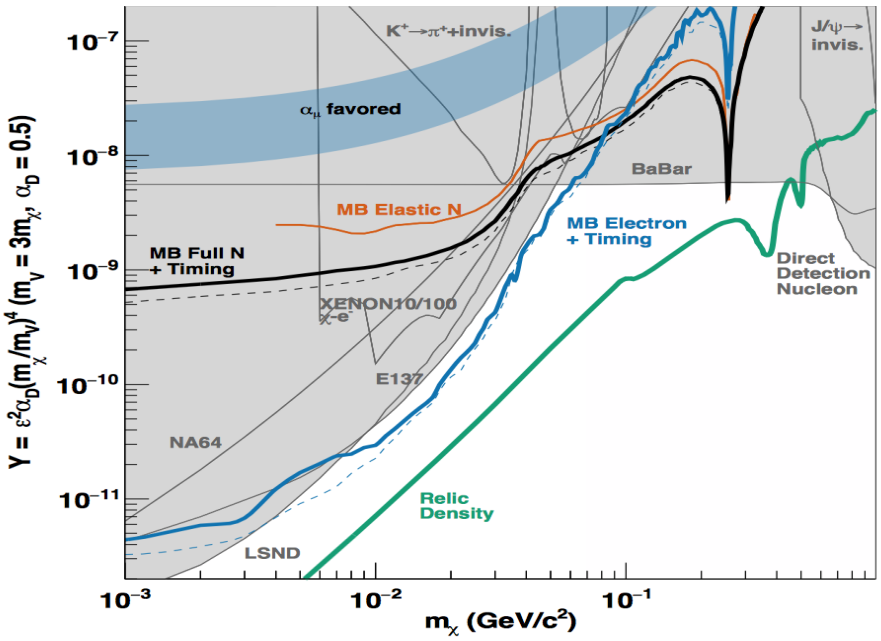

Figure 3.4: Results from the MiniBooNE-DM search for light dark matter from Ref. [50]

well as over the short baseline of the ND.

The present lead in the search for sterile neutrinos, those which couple to standard neutrinos but not to the weak interaction, comes from disappearance experiments such as muon-neutrino accelerators and reactor anti-neutrino experiments, where unitarity is a necessary assumption. All the most precise measurements of the standard oscillation parameters have been made by disappearance experiments as shown in the left panel of Figure 3.5. The Liquid Scintilator Neutrino Detector (LSND) and MiniBooNE anomalies are expected to be elucidated by MicroBooNE due to its unprecedented event reconstruction capabilities. After the recent measurement from MINOS+ and IceCube are combined with unitarity constraints (see e.g. [53]), most of the favored parameter space to explain LSND and MiniBooNE, with a sterile neutrino, is now disfavored as shown in the right panel of Figure 3.5. Addressing the apparent excess of electron events appearing in the muon-neutrino beam at MiniBooNE and LSND is also the main goal for the future SBN program at Fermilab, using for the first time near and far detectors with the same technology for this study. Furthermore in the next years conclusive results will become available from very short baseline reactor experiments, which measure the rate of inverse beta decay as function of length to the reactor core. These aim to see small modulations as function of distance, which could be caused by sterile neutrinos. However given the ensemble of all present data so far, if the anomalies survive it seems to indicate that a (or a few) 'standard' sterile neutrino(s) hypothesis does not fit the data and the explanation may turn out to be much more complex, in which case certainly the capabilities of the DUNE experiment will play an important role in unraveling the exact nature of the new phenomenon.

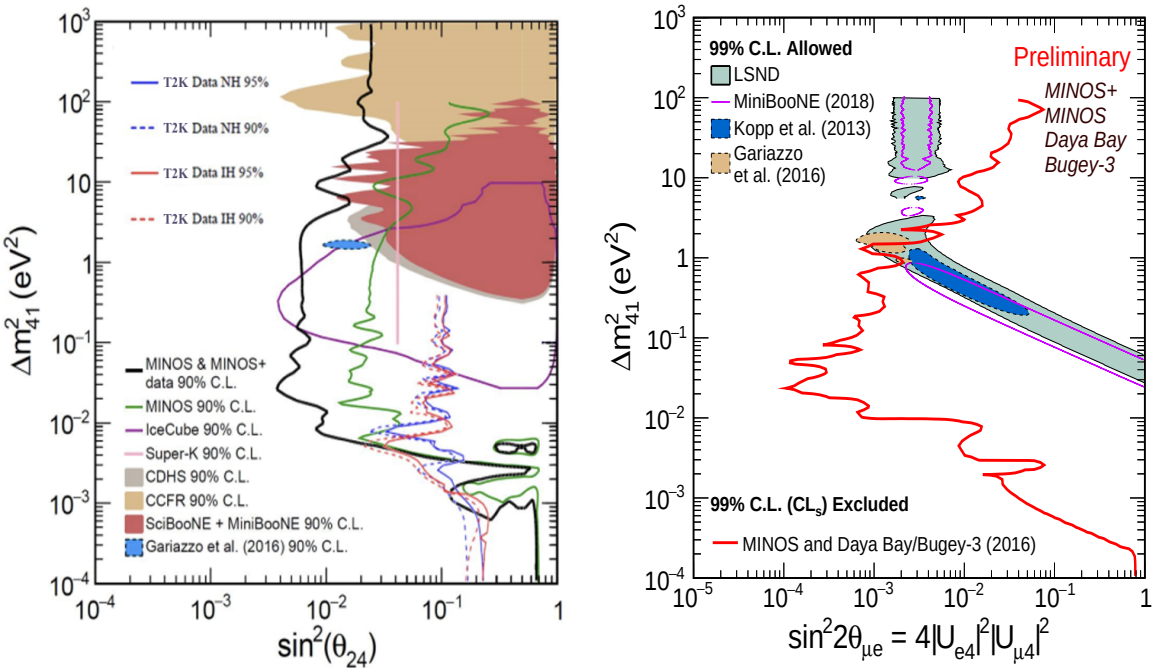

Figure 3.5: Left panel: Comparison of present exclusion limits from various experiments obtained through searches for disappearance of muon neutrinos into sterile species assuming a 3+1 model. The Gariazzo et al. region represents a global fit to neutrino oscillation data [54]. Right panel: The combined results of the disappearance measurements from MINOS+, Daya Bay, and Bugey, compared to the appearance measurements from LSND and MiniBooNE.

3.4.3 Neutrino tridents

Neutrino trident production is a rare weak process in which a neutrino, scattering off the Coulomb field of a heavy nucleus, generates a pair of charged leptons. The typical final state of a neutrino trident interaction contains two leptons of opposite charge. Measurements of muonic neutrino tridents were carried out at the CHARM-II, CCFR, and NuTeV experiments, and yielded results consistent with SM predictions, but those measurements leave ample room for potential searches for New Physics. As an example, a class of models that modify the trident cross section are those that contain an additional neutral gauge boson, Z', that couples to neutrinos and charged leptons. This Z' boson can be introduced by gauging an anomaly-free global symmetry of the SM, with a particular interesting case realized by gauging L_μ–L_τ [55, 56]. Such a Z' is not very tightly constrained and could address [57, 58] the observed discrepancy between the Standard Model prediction and measurements of the anomalous magnetic moment of the muon, $(g–2)_\mu$ The DUNE ND offers an excellent environment to generate a sizable number of trident events, offering very promising prospects to both improve the above measurements, and to look for an excess of events above the SM prediction, which would be an indication of new physics.

Another category of BSM Physics models that can be probed through neutrino trident measurements are dark neutrino sectors. In these scenarios, SM neutrinos mix with heavier SM singlet fermions (dark neutrinos) with their own new interactions. Due to this mixing, neutrinos inherit some of this new interaction and may up-scatter to dark neutrinos. These heavy states in turn decay back to SM fermions, giving rise to trident signatures. These scenarios can explain the smallness of neutrino masses and possibly the MiniBooNE low energy excess of events, discussed above.

3.4.4 Heavy neutral leptons

The DUNE ND can be used to search topologies of rare event interactions and decays that originate from very weakly-interacting long-lived particles, including heavy neutral leptons – right-handed partners of the active neutrinos, vector, scalar, or axion portals to the hidden sector, and light supersymmetric particles. The high intensity of the NuMI source and the capability of production of charm mesons in the beam allow accessing a wide variety of lightweight long-lived, exotic, particles. Competitive sensitivity is expected for the case of searches for decay-in-flight of sub-GeV particles that are also candidates for dark matter, and may provide an explanation for leptogenesis in the case of charge-parity symmetry violation (CPV) indications. DUNE would probe the lighter particles of their hidden sector, which can only decay in SM particles in the form of pairs like e^+e^- , $\mu^+\mu^-$, qq. The parameter space explored by the DUNE ND extends to the cosmologically relevant region that is complementary to the LHC dark-matter searches through missing energy and mono-jets.

A recent study on the present limits and capabilities with future experiments for covering the coupling-mass phase space is shown in Figure 3.6, taken from [48]. These future prospects include proposed experiments, such as SHiP, which would operate over the period of the next 10 to 15 years, hence the same period as for DUNE. While a dedicated analysis of DUNE's sensitivity has

not yet been carried out, the sensitivity from a previous study with the formerly-proposed LBNE Near Detector (shown as a dark-green dashed curve at low values of m_N) may give a representative indication. The FCC curve corresponds to a study aimed much further in the future.

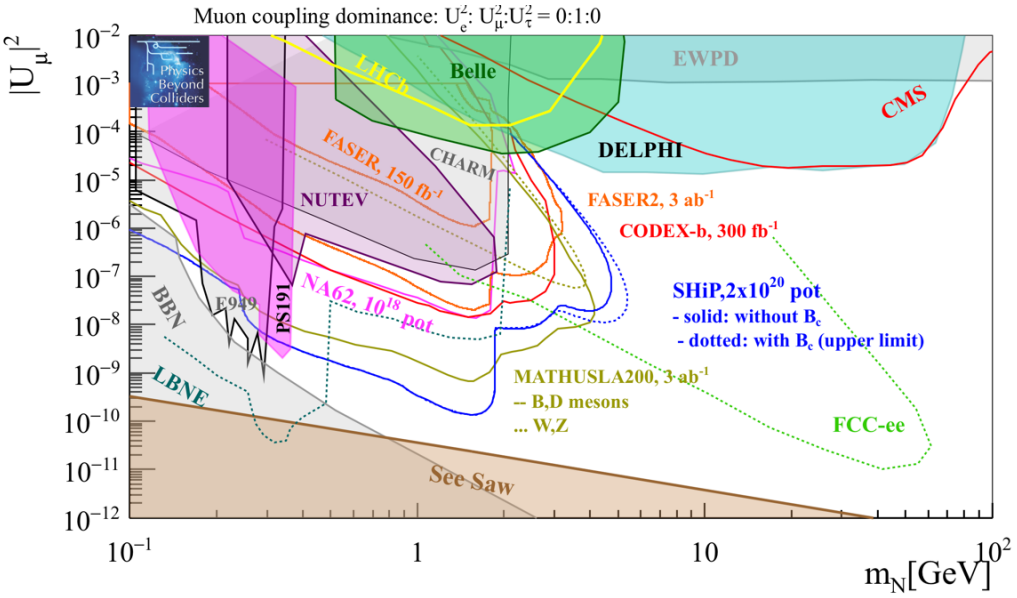

Figure 3.6: Sensitivity to Heavy Neutral Leptons with coupling to the second lepton generation only. Current bounds (filled areas) and 10-15 years prospects for PBC projects (SHiP, MATHUSLA200, CODEX-b and FASER2) (dotted and solid lines). Projections for the formerly-proposed LBNE near detector with 5×10^{21} protons on target (dark green dashed line starting from lower left region of the plot) and FCC-ee with 10^{12} Z^0 decays (light green dashed line at higher m_N values) also shown .

3.5 Other Scientific Opportunities

The high rate of charged-current muon-neutrino argon interactions occurring in the near detector will provide important data samples to understand better neutrino-argon interactions in the relevant energy range for the DUNE far detector. The next chapters will give examples of scenarios where detailed understand of such interactions with precision measurements will have a significant impact on the physics reach for some topics. Effects of final state interactions, event topology and kinematics, neutron production and more can be studied in detail with such large statistics data samples.

The collection of the expected statistics and the determination of the neutrino and antineutrino fluxes to unprecedented precision would solve two main limitations of past neutrino experiments. At the same time, we can then exploit the unique properties of the neutrino probe for the study of fundamental interactions with a broad program of precision SM measurements. These potential measurements have not yet been studied in detail in this technical design report (TDR), as the capabilities depend critically on the final design choice of the near detector, and this is still under discussion.

Neutrinos and anti-neutrinos are effective probes for investigating Electroweak physics. A precise determination of the weak mixing angle ($\sin^2\theta_W$) in neutrino scattering at the DUNE energies is twofold: (a) it provides a direct measurement of neutrino couplings to the Z boson and (b) it probes a different scale of momentum transfer than LEP did by virtue of not being at the Z boson mass peak. The unprecedented large statistics of deep inelastic scattering events will allow for significant measurements of the mixing angle. Other SM measurements include those of nucleon structure functions, the strange content of nucleons, and a precise verification of a number of sum rules. Some of these measurements would need cross section measurements on hydrogen targets. These expected sensitivity of these measurements will be addressed in future studies.

Chapter 4

Tools and Methods

Evaluation of the capabilities of DUNE/LBNF to realize the scientific program envisioned requires a detailed understanding of the experimental signatures of the relevant physical processes, the response of detection elements, and the performance of calibration systems and event reconstruction and other tools that enable analysis of data from the DUNE detectors. It is the aim of this chapter to introduce the network of calibration, simulation, and reconstruction tools that form the basis for the demonstration of science capabilities presented in the chapters that follow. The presentation here covers general components, namely those that are commonly utilized across the science program, although many of these are geared toward application to the long-baseline oscillation physics at the heart of this program. Other tools and methods developed for specific physics applications are described in the corresponding chapters that follow.

Where appropriate, the performance of reconstruction tools and algorithms is quantified. Some of these characterizations form the basis for parameterized-response simulations used by physics sensitivity studies that have not yet advanced to the level of analysis of fully reconstructed simulated data. They also serve as metrics that allow linkages to be drawn between detector configuration specifications and physics sensitivity.

Another critical role for the simulation and reconstruction tools described in this chapter, implicit above, is to enable detailed study of sources of systematic error that can affect physics capability, which can also lead to the development of mitigation strategies. Thus, where possible, assessments of systematic uncertainties in the modeling of LBNF/DUNE conditions and performance are presented.

4.1 Monte Carlo Simulations

Many physics processes are simulated in the DUNE far detector (FD); these include the interactions of beam neutrinos, atmospheric neutrinos, supernova neutrino burst (SNB) neutrinos, proton decays and cosmogenic events. Figure 4.1 shows a portion of the DUNE SP TPC consisting of

anode plane assembly (APA)s and cathode plane assembly (CPA)s.

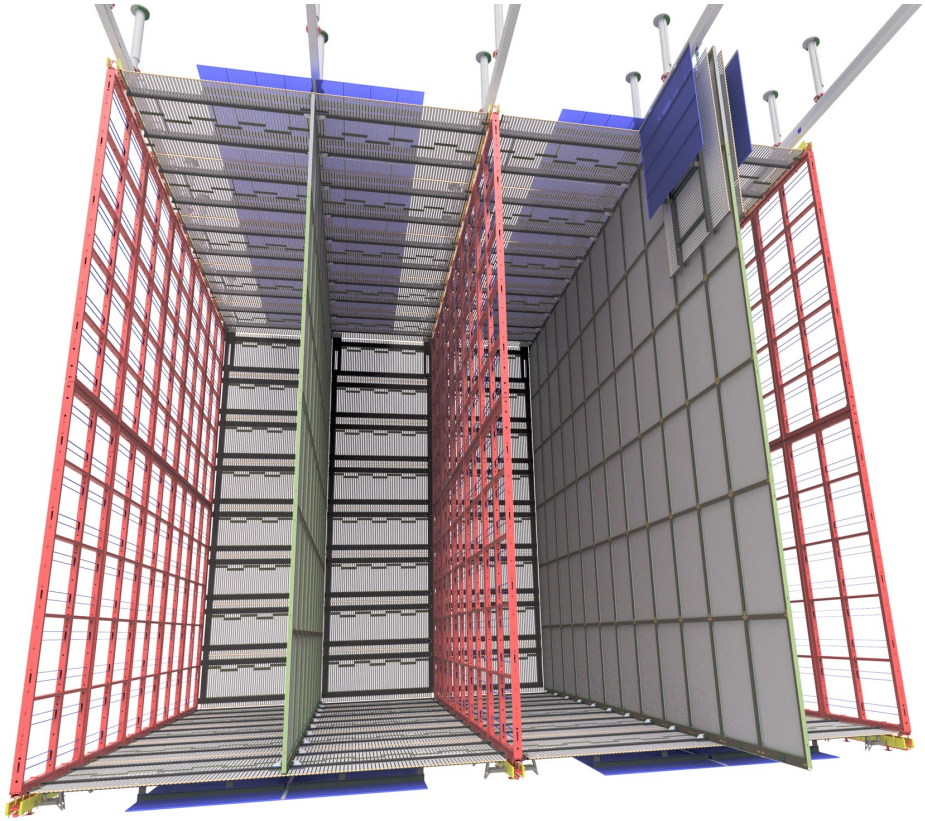

Figure 4.1: A portion of DUNE SP TPC is shown. Four separate drift regions are separated by APAs and CPAs.

To save processing time, all the FD samples except the cosmogenics sample were simulated using a smaller version of the full 10 kt far detector module geometry. This geometry is 13.9 m long, 12 m high and 13.3 m wide, which consists of 12 APAs and 24 CPAs. Figure 4.2 shows the detailed structure of an APA.

For the simulation chain, each sample is simulated in three steps: generation (gen), GEANT4 tracking (g4), TPC signal simulation, and digitization (detsim). The first step is unique for each sample while the second and the third steps are mostly identical for all samples.

4.1.1 Neutrino Flux Modeling

Neutrino fluxes were generated using G4LBNF, a GEANT4-based simulation of the LBNF neutrino beam. The simulation was configured to use a detailed description of the LBNF optimized beam design [59]. That design starts with a 1.2 MW, 120 GeV primary proton beam that impinges on a 2.2 m long, 16 mm diameter cylindrical graphite target. Hadrons produced in the target are focused by three magnetic horns operated with 300 kA currents. The target chase is followed by a 194 m helium-filled decay pipe and a hadron absorber. The focusing horns can be operated in forward or reverse current configurations, creating neutrino and antineutrino beams, respectively.

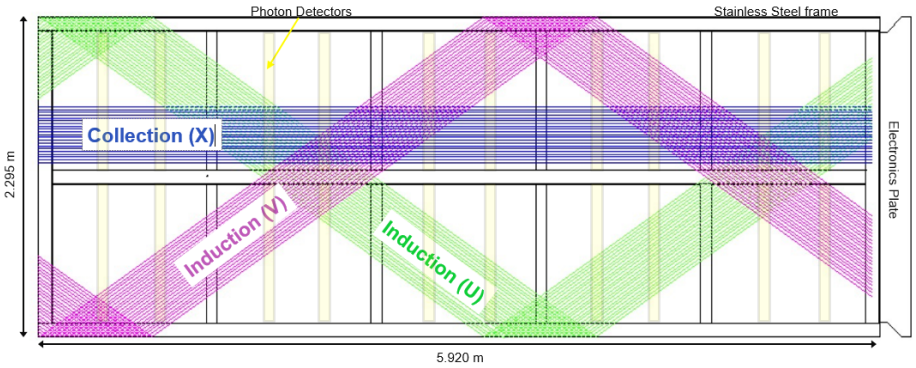

Figure 4.2: The detailed structure of the APA is shown. Each APA consists of four wrapped induction wire planes and two collection wire planes. The photon detector (PD) is sandwiched between the two collection wire planes.

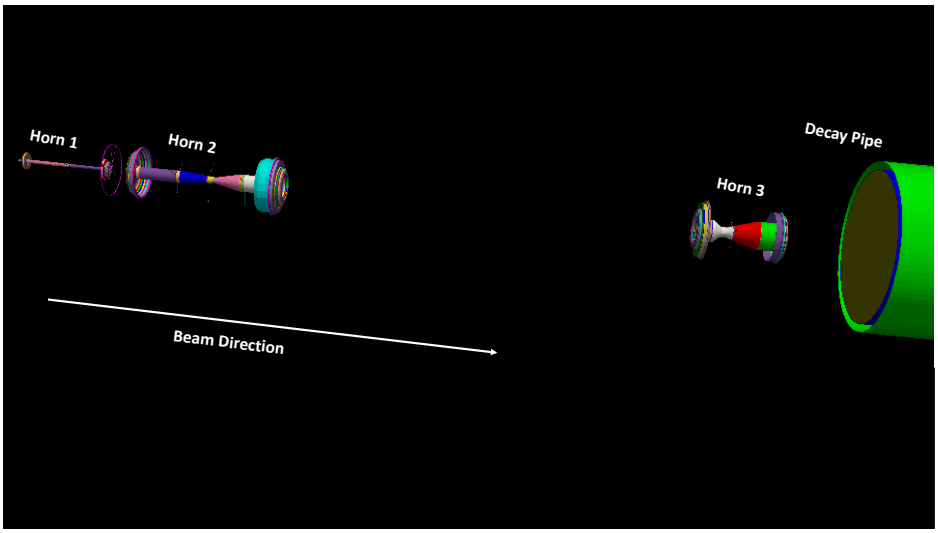

Figure 4.3: Visualization of the focusing system as simulated in g4lbnf.

The optimized LBNF neutrino beam design is the result of several years of effort by LBNF and DUNE to identify a focusing system optimized to DUNE's long-baseline physics goals. The optimization process requires scanning many parameters describing the hadron production target, focusing horns, and the decay pipe. Genetic algorithms have been used successfully in the past to scan the large parameter space to find the optimal beam design [60]. The LBNF beam optimization process began with a genetic algorithm that scanned simulations of many different horn and target geometries to identify those that produced the optimal sensitivity to charge-parity symmetry violation (CPV). The specific metric used was estimated sensitivity to 75% of charge parity (CP) phase space after $300\,\mathrm{kt}\cdot\mathrm{MW}\cdot\mathrm{year}$ of exposure, taking into account the number and neutrino spectra of all neutrino flavors. The resulting beam effectively optimized flux at the first and second oscillation maxima, which also benefits measurements of other oscillation parameters. The output of the genetic algorithm was a simple design including horn conductor and target shapes. This design was transformed into a detailed conceptual design by LBNF engineers, and iterated with DUNE physicists to ensure that engineering changes had minimal impact on physics performance. Relative to the previous NuMI-like design, the optimized design reduces the time to three-sigma coverage of 75% of CP phase space by 42%, which is equivalent to increasing the mass of the far detector by 70%. It also substantially increases sensitivity to the mass hierarchy and improves projected resolution to quantities such as $\sin^2 2\theta_{13}$ and $\sin^2\theta_{23}$ [61].

4.1.1.1 On-axis Neutrino Flux and Uncertainties

The predicted neutrino fluxes for neutrino and antineutrino mode configurations of LBNF are shown in Figure 4.4. In neutrino (antineutrino) mode, the beams are 92% (90.4%) muon neutrinos (antineutrinos), with wrong-sign contamination making up 7% (8.6%) and electron neutrino and antineutrino backgrounds 1% (1%). Although we expect a small nonzero intrinsic tau neutrino flux, this is not simulated by G4LBNF. Nor are neutrinos arising from particle decay at rest.

Uncertainties on the neutrino fluxes arise primarily from uncertainties in hadrons produced off the target and uncertainties in parameters of the beam such as horn currents and horn and target positioning (commonly called "focusing uncertainties"). Uncertainties on the neutrino fluxes arising from both of these categories of sources are shown in Figure 4.5. Hadron production uncertainties are estimated using the Package to Predict the FluX (PPFX) framework developed by the MINERvA collaboration [62, 63], which assigns uncertainties for each hadronic interaction leading to a neutrino in the beam simulation, with uncertainties taken from thin target data (from e.g., the NA49 [64] experiment) where available, and large uncertainties assigned to interactions not covered by data. Focusing uncertainties are assessed by altering beamline parameters in the simulation within their tolerances and observing the resulting change in predicted flux. A breakdown of the hadron production and focusing uncertainties into various components are shown in Figure 4.6 for the neutrino mode muon neutrino flux at the FD.

At most energies, hadron production uncertainties are dominated by the "NucleonA" category, which includes proton and neutron interactions that are not covered by external data. At low energies, uncertainties due to pion reinteractions (denoted "Meson Inc") dominate. The largest source of focusing uncertainty arises from a 1% uncertainty in the horn current, followed by a 2% uncertainty in the number of protons impinging on the target. For all neutrino flavors and all

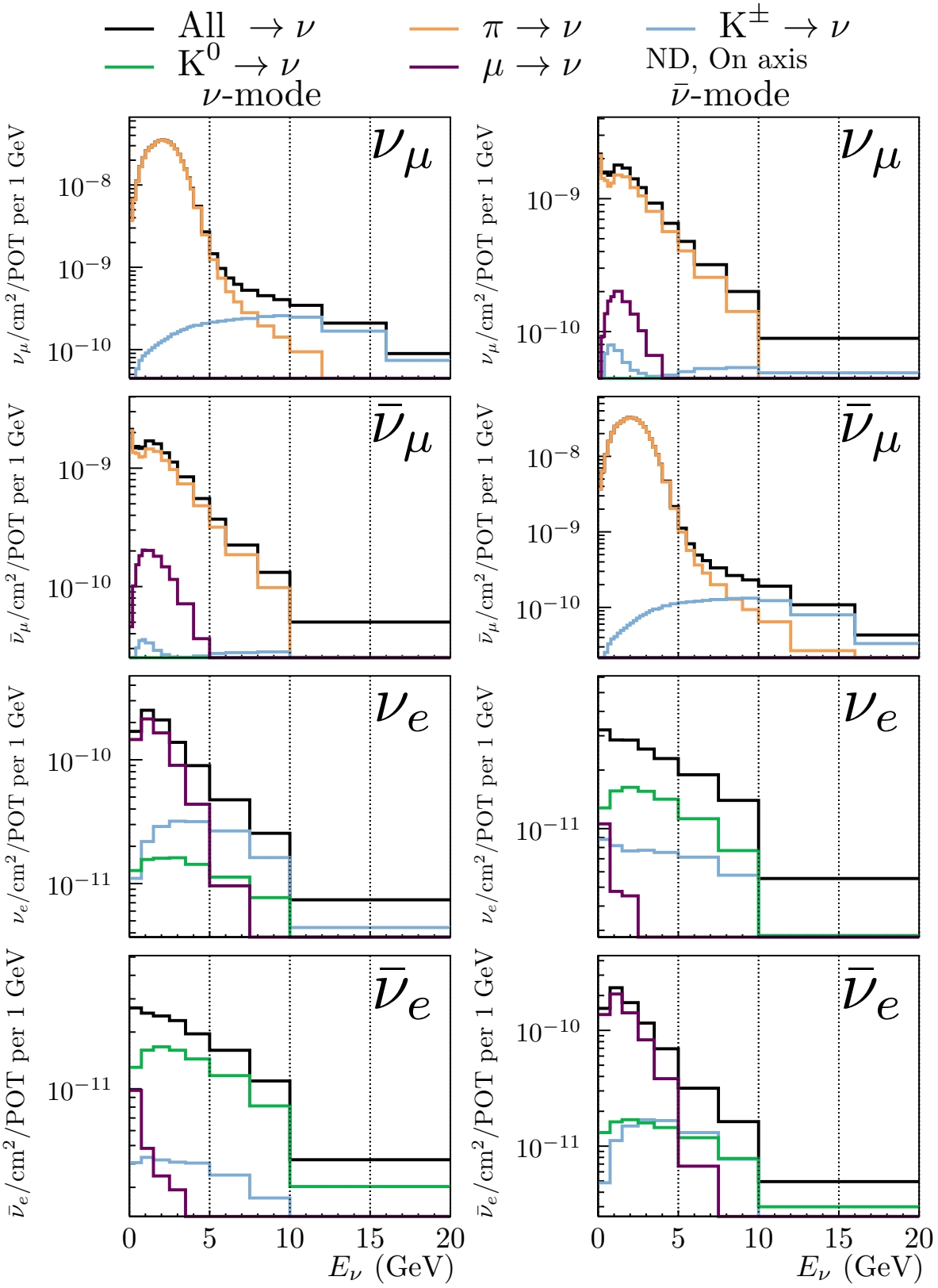

Figure 4.4: Predicted neutrino fluxes at the near detector for neutrino mode (left) and antineutrino mode (right). From top to bottom shown are muon neutrino, muon antineutrino, electron neutrino, and electron antineutrino fluxes.

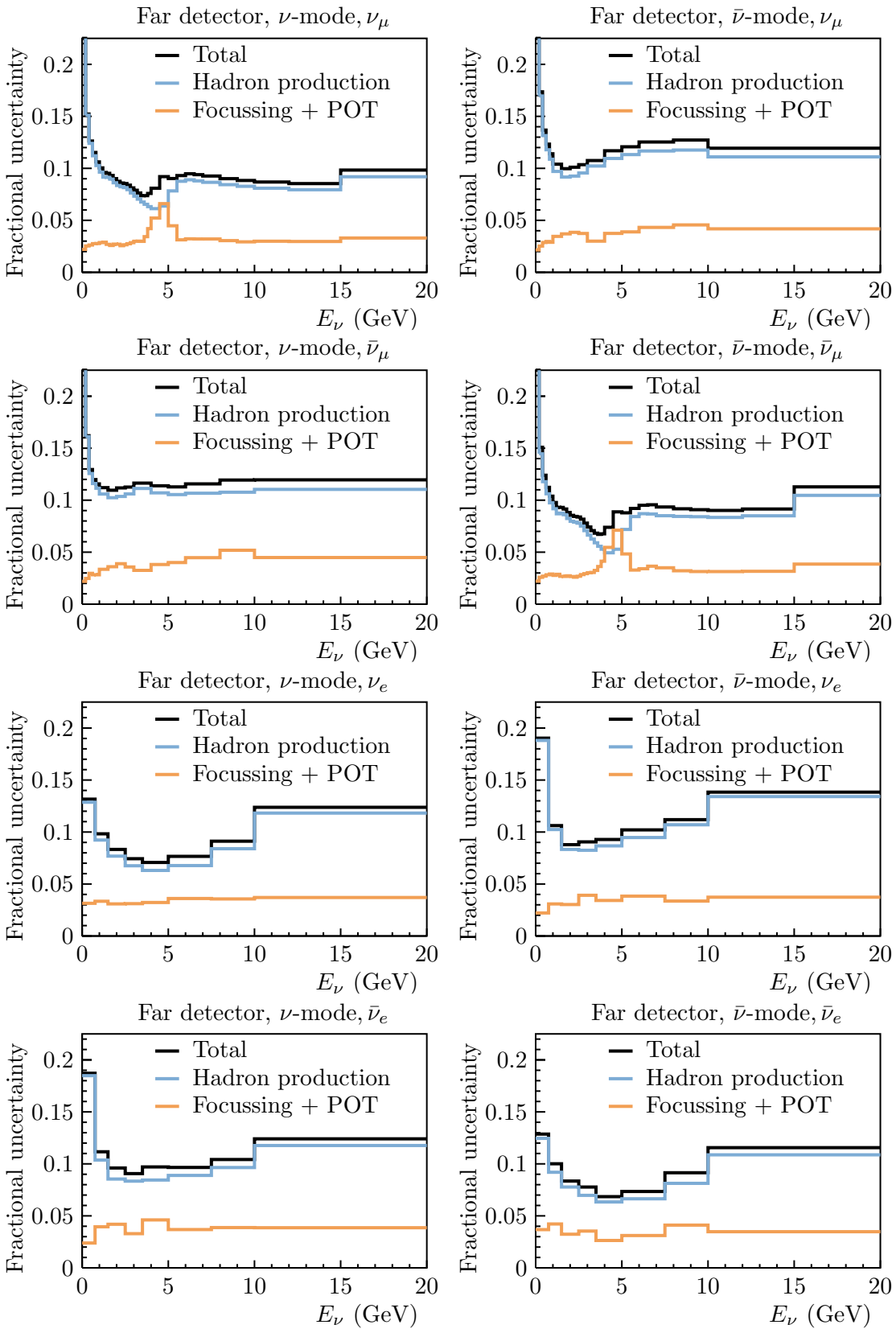

Figure 4.5: Flux uncertainties at the far detector as a function of neutrino energy in neutrino mode (left) and antineutrino mode (right) for, from top to bottom, muon neutrinos, muon antineutrinos, electron neutrinos and electron antineutrinos.

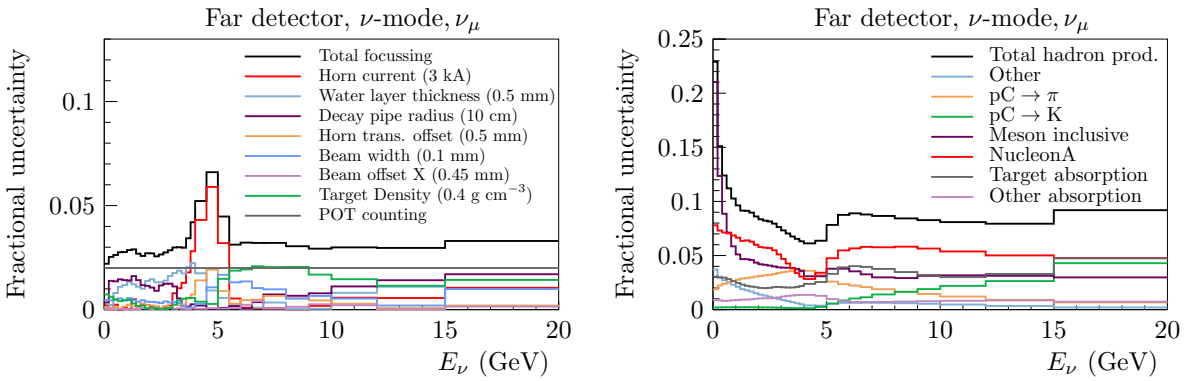

Figure 4.6: Focusing (left) and hadron production (right) uncertainties on the neutrino mode muon neutrino flux at the FD.

neutrino energies, hadron production uncertainties are larger than focusing uncertainties. However, hadron production uncertainties are expected to decrease in the next decade, as more thin target data becomes available. Hadron production measurements taken with a replica target are also being considered and would substantially reduce the uncertainties.

Figure 4.7 shows correlations of the total flux uncertainties. In general, the uncertainties are highly correlated across energy bins. However, the flux in the very high energy, coming predominantly from kaons, tends to be uncorrelated with flux at the peak, arising predominantly from pion decays. Flux uncertainties are also highly correlated between the near and far detectors and between neutrino-mode and antineutrino-mode running. The focusing uncertainties do not affect wrong-sign backgrounds, which reduces correlations between e.g., muon neutrinos and muon antineutrinos in the same running configuration in the energy bins where focusing uncertainties are significant.

The unoscillated fluxes at the near detector (ND) and FD are similar but not identical. Figure 4.8 shows the ratio of the near and far neutrino-mode muon neutrino unoscillated fluxes and the uncertainties on the ratio. The uncertainties are approximately 1% or smaller except at the falling edge of the focusing peak, where they rise to 2%, but are still much smaller than the uncertainty on the absolute fluxes. And unlike the case for absolute fluxes, the uncertainty on the near-to-far flux ratio is dominated by focusing rather than hadron production uncertainties. This ratio and its uncertainty are for the fluxes at the center of the near and far detectors, and do not take into account small variations in flux across the face of the ND.

4.1.1.2 Off-axis Neutrino Flux and Uncertainties

The neutrino flux has a broad angular distribution and extends outward at the ND hall. At an "off-axis" angle relative to the initial beam direction, the subsequent neutrino energy spectrum is narrower and peaked at a lower energy than the on-axis spectrum. The relationship between the parent pion energy and neutrino energy is shown in Figure 4.9. At 575 m, the location of the ND hall, a lateral shift of 1 m corresponds to approximately a 0.1° change in off-axis angle. The DUNE-PRISM concept, in which the near detector LArTPC can be moved to enable off-axis measurements, relies on this feature to help constrain systematic errors for the long-baseline (LBL)

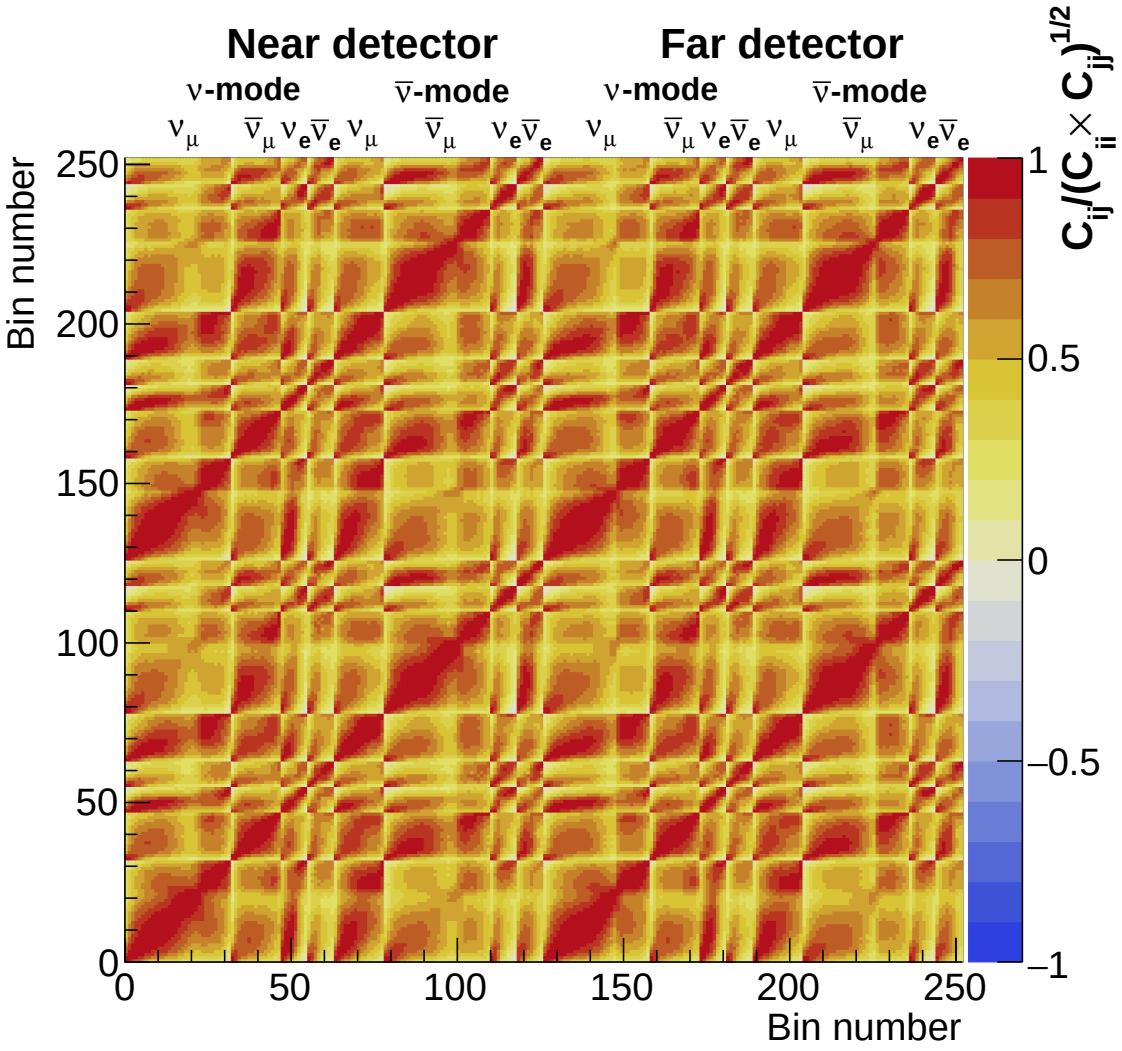

Figure 4.7: Correlation of flux uncertainties. Each block of neutrino flavor corresponds to bins of energy with bin boundaries of [0.0, 0.2, 0.4, 0.6, 0.8, 1.0, 1.2, 1.4, 1.6, 1.8, 2.0, 2.2, 2.4, 2.6, 2.8, 3.0, 3.2, 3.4, 3.6, 3.8, 4.0, 4.5, 5.0, 5.5, 6.0, 6.5, 7.0, 8.0, 9.0, 10.0, 12.0, 15.0, 20.0] GeV for right sign muon neutrinos, [0.0, 0.2, 0.4, 0.6, 0.8, 1.0, 1.5, 2.0, 2.5, 3.0, 4.0, 5.0, 6.0, 8.0, 10.0, 20.0] GeV for wrong sign muon neutrinos, and [0.0, 0.75, 1.5, 2.5, 3.5, 5.0, 7.5, 10.0, 20.0] for electron neutrinos and antineutrinos.

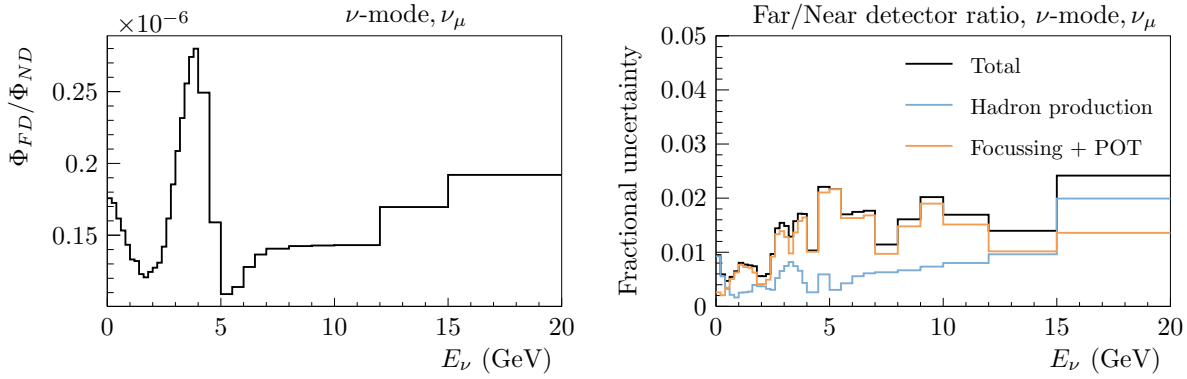

Figure 4.8: Ratio of neutrino-mode muon neutrino fluxes at the near and far detectors (left) and uncertainties on the ratio (right).

oscillation program as described in Section 5.5.2.3.

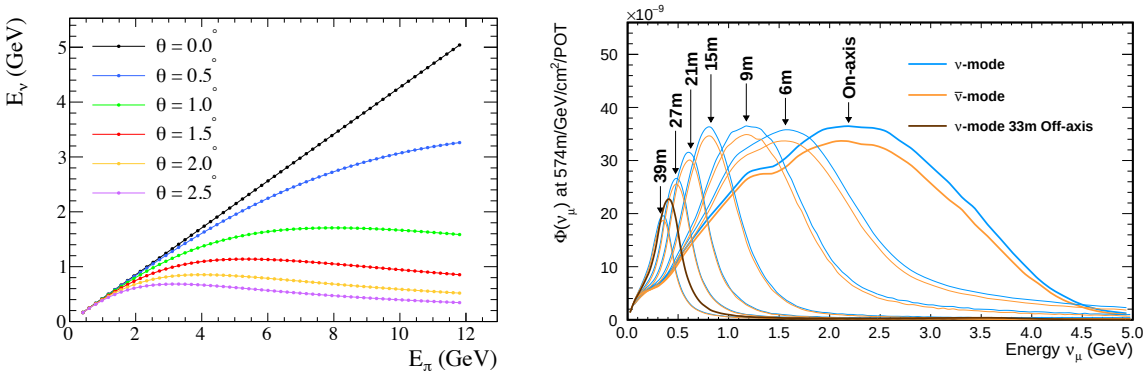

Figure 4.9: (left) The neutrino energy as a function of parent pion energy for different angles away from the pion momentum vector. Figure from Ref. [65]. (right) The DUNE near detector flux predictions over a range of off-axis positions for a near detector at 575 m downstream of the target station.

The intrinsic neutrino flavor content of the beam varies with off-axis angle. Figure 4.10 shows the neutrino-mode and anti-neutrino-mode predictions for the four neutrino flavors at the on-axis position, and a moderately off-axis position. At the 30 m position, a second, smaller energy peak at approximately 4 GeV is due to the charged kaon neutrino parents.

The same sources of systematic uncertainty that affect the on-axis spectra also modify the off-axis spectra. Figure 4.11 shows the on-axis and off-axis hadron production and focusing uncertainties. Generally, the size of the off-axis uncertainties is comparable to the on-axis uncertainties and the uncertainties are highly correlated across off-axis and on-axis positions. While the hadron production uncertainties are similar in size, the focusing uncertainties are smaller for the off-axis flux. The systematic effects have different shapes as a function of neutrino energy at different off-axis locations, making off-axis flux measurements useful to diagnose beamline physics. Measuring on-axis and off-axis flux breaks degeneracy between various systematics and allows better flux constraint.

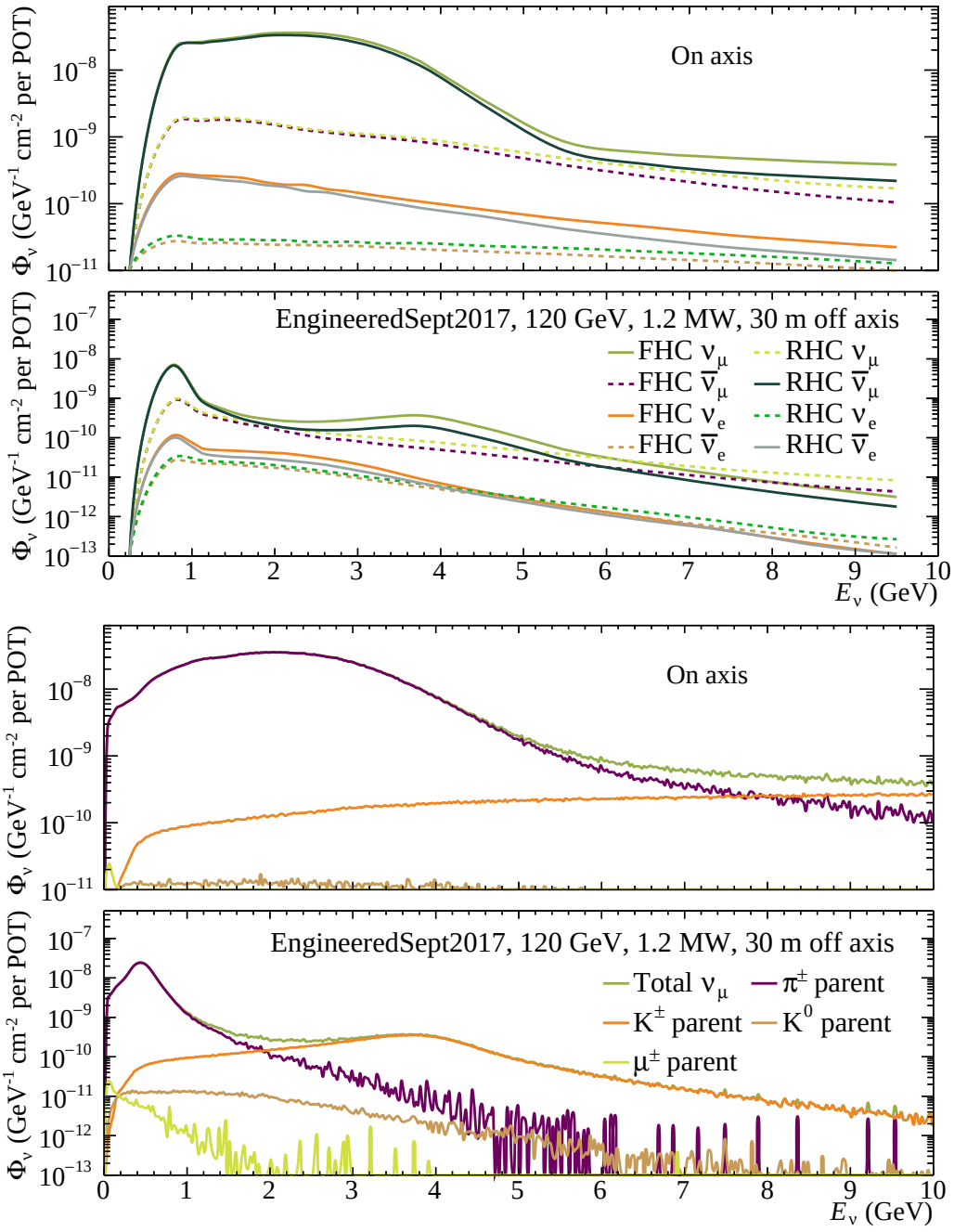

Figure 4.10: The predicted muon neutrino energy spectra at two ND positions, on axis and 30 m off axis. (a) The predicted neutrino flavor-content of the neutrino-mode (FHC) and anti-neutrino-mode (RHC) beam. (b) The neutrino-mode, muon-flavor predicted flux, separated by the particle that decayed to produce the neutrino. The off-axis spectrum displays a double peak structure due to charged kaon parent decay kinematics. The on-axis kaon-peak occurs at higher neutrino energy and will have a significantly broader energy spread. Top: Beam neutrino flavor content, middle: Beam neutrino flavor content; bottom: Beam neutrino decay-parent species

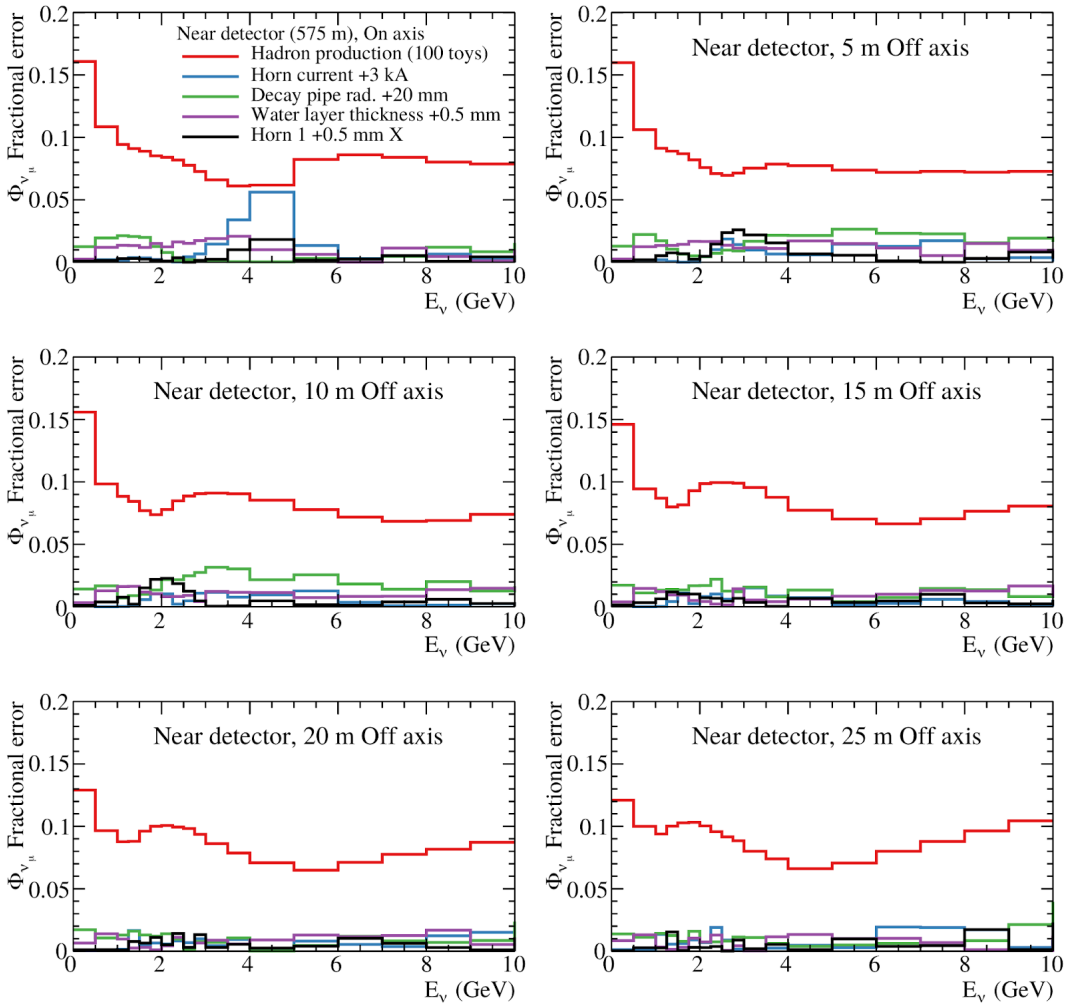

Figure 4.11: The flux uncertainty for the on-axis flux, and several off-axis positions. Shown is the total hadron production uncertainty and several major focusing uncertainties.

4.1.1.3 Alternate Beamline Configurations

Although the LBNF beamline is expected to run for many years in a CP-optimized configuration, it could potentially be modified in the future for other physics goals. For example, it could be altered to produce a higher-energy spectrum to measure tau neutrino appearance. In the standard CP-optimized configuration, we expect about 130 tau neutrino charged current (CC) interactions per year at the FD, before detector efficiency and assuming 1.2 MW beam power. However, replacing the three CP-optimized horns with two NuMI-like parabolic horns can raise this number to approximately 1000 tau neutrinos per year. Figure 4.12 shows the muon neutrino flux for one such configuration. Although the flux in the 0 GeV to 5 GeV region critical to δ_{CP} measurements is much smaller, the flux above 5 GeV, where the tau neutrino interaction cross section becomes significant, is much larger. Many other energy distributions are possible by modifying the position of the targets and horns. Even altering parameters of the CP-optimized horns offers some variablity in energy spectrum, but the parabolic NuMI horns offer more configurability. Because the LBNF horns are not expected to be remotely movable, such reconfigurations of the beamline would require lengthy downtimes to reconfigure target chase shielding and horn modules.

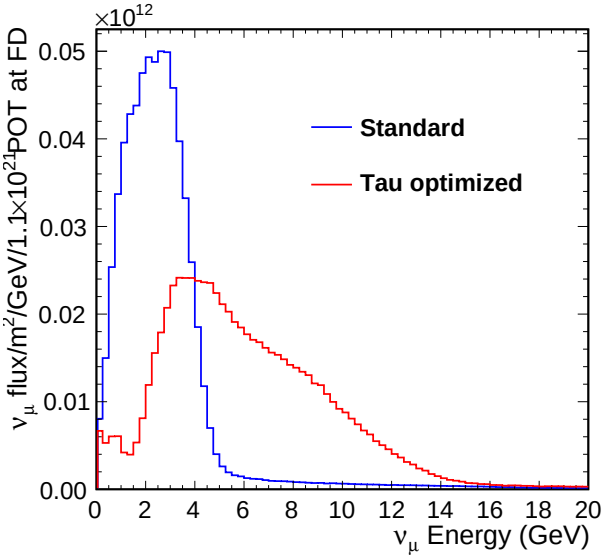

Figure 4.12: Comparison of standard and tau-optimized neutrino fluxes. The tau optimized flux was simulated with a 120 GeV proton beam and two NuMI parabolic horns, with the second horn starting 17.5 m downstream from the start of the first horn, and a 1.5 m long, 10 mm wide carbon fin target starting 2 m from the upstream face of the first horn.

4.1.2 Neutrino Interaction Generators

4.1.2.1 Supernova Neutrinos

The SNB neutrino events were generated using custom code wrapped in a Liquid Argon Software (LArSoft) module. This code simulates CC ν_e-^{40}Ar interactions. For each electron neutrino it calculates probabilities to produce a ^{40}K nucleus in different excited states (using a model from [66]),

randomly selects one, and (with energy levels from [67]) produces several de-excitation γs and an electron carrying the remaining energy. All particles are produced isotropically, and there is no delay between the electron and corresponding de-excitation γs (in this model the ^{40}K nucleus de-excites instantaneously) and they share a vertex, which is simulated with equal probability anywhere in the active volume. The primary neutrino energy distribution used in these samples is the cross-section-weighted energy spectrum obtained from SNOwGLoBES [68] (using the "GKVM" flux [69]). The SNB neutrino generator also allows to simulate a Poisson-distributed random number of neutrino interactions per event. These samples were simulated with, on average, 2 or 20 neutrinos. In addition, one of the samples was generated with 1.01 Bq/kg of ^{39}Ar background.

4.1.2.2 GENIE

The DUNE Monte Carlo (MC) simulation chain is interfaced to the Generates Events for Neutrino Interaction Experiments (GENIE) event generator [70]. This is an open-source product of the GENIE collaboration[1] that provides state-of-the-art modeling of neutrino-nucleus interactions, as well as simulation of several other non-neutrino processes (nucleon decay, neutron-antineutron oscillation, boosted dark matter interactions, hadron and charged lepton scattering off nuclei). The generator product also includes off-the-shelf components (flux drivers and interfaces to outputs of detailed neutrino beamline simulations, detector geometry drivers, and several specialized event generation applications) for the simulation of realistic experimental setups. The GENIE collaboration performs an advanced global analysis of neutrino scattering data, and is leading the development and characterization of comprehensive interaction models. The GENIE comprehensive models and physics tunes which are developed using its proprietary Comparisons and Tuning products, are fully integrated in the GENIE Generator product. Finally, the open-source GENIE Reweight product provides means for propagating modeling uncertainties.

At the time of the technical design report (TDR) writing, the DUNE simulation uses a version in the v2 series of the GENIE generator, which includes empirical comprehensive models, based on home-grown hadronic simulations (AGKY model [71] for neutrino-induced hadronization and INTRANUKE/hA model [72] for hadronic re-interactions) and nuclear neutrino cross sections calculated within the framework of the simple relativistic Fermi gas model [73]. Several processes are simulated within that framework with the most important ones, in terms of the size of the corresponding cross section at a few GeV, being: (1) quasi-elastic scattering, simulated using an implementation of the Llewellyn Smith model [74], (2) multi-nucleon interactions, simulated with an empirical model motivated by the Lightbody model [75] and using a nucleon cluster model for the simulation of the hadronic system, (3) baryon resonance neutrino-production simulated using an implementation of the Rein-Sehgal model [76], and (4) deep-inelastic scattering, simulated using the model of Bodek and Yang [77]. These comprehensive models, as well as the GENIE procedure for tuning the cross section model in the transition region, have been used for several years and are well understood and documented [70]. The actual tune used is the one produced for the analysis of data from the MINOS experiment and, as was already known at that time, it has several caveats as it emphasizes inclusive data and does not address tensions with exclusive data. The future DUNE simulation will be done using the v3 GENIE Generator where improved models and tunes are available.

[1] www.genie-mc.org

Besides simulation of neutrino-nucleus interactions, GENIE provides simulation of several BSM physics channels:

BSM: The implementation of a BSM MC simulation has been motivated by several theory studies [78, 79, 80, 81, 82, 83, 84, 85]. The current implementation focuses on two models presented in [79]. The first has a fermionic dark matter (DM) candidate, a Z' mediator, and velocity independence of the spin-dependent cross section in the non-relativistic limit. The second model has a scalar DM candidate, a Z' mediator, and a u^2 velocity dependence of the spin-dependent cross section in the non-relativistic limit.

Nucleon decay: GENIE simulates several nucleon decay topologies. For the initial nuclear state environment and intranuclear hadron transport, it uses the same modeling as it does for neutrino event simulation. In the nucleon decay simulation, the nucleon binding and momentum distribution is simulated using one of the nuclear models implemented in GENIE (typically a Fermi gas model), and it is decayed to one of many topologies using a phase space decay. The decay products are produced within the nucleus and further re-interactions of hadrons are simulated by the GENIE hadron transport models. The simulated nucleon decay topologies are given in Table 6.2, presented in Sec. 6.1.1.2.

Neutron-antineutron oscillation: GENIE simulates several event topologies that may emerge following the annihilation of the antineutron produced from a bound neutron to antineutron transition. For the initial nuclear state environment and intranuclear hadron transport, the simulation, as in the case of nucleon decay, uses the same modeling as it does for the neutrino event simulation. The simulated reactions are listed in Table 6.3 in Sec. 6.2.1.

4.1.3 Detector Simulation

The detector simulation consists of particle propagation in the liquid argon using GEANT and the TPC and photon detector response simulation. This step is done in the common framework LArSoft and is validated by other liquid argon time-projection chamber (LArTPC) experiments such as ArgoNeuT, MicroBooNE, LArIAT and ProtoDUNE.

4.1.3.1 LArG4

The truth particles generated in the event generator step are passed to a GEANT4 v4_10_1_p03-based detector simulation. In this step, each primary particle from the generator and its decay or interaction daughter particles are tracked when they traverse LAr. The energy deposition is converted to ionization electrons and scintillation photons. Some electrons are recombined with the positive ions [86, 87] while the rest of the electrons are drifted towards the wire planes. The number of electrons is further reduced due to the existence of impurities in the LAr, which is commonly parameterized as the electron lifetime. Unless otherwise specified, an electron lifetime of 3 ms is assumed in the simulations. The longitudinal diffusion smears the arrival time of the electrons at the wires and the transverse diffusion smears the electron location among neighboring wires. More

details regarding the recent measurements of diffusion coefficients can be found in [88, 89].

4.1.3.2 Photon Simulation

When ionization is calculated, the amount of scintillation light is also calculated. The response of the PDs is simulated using a "photon library," a pre-generated table giving the likelihood that photons produced within a voxel in the detector volume will reach any of the PDs. The photon library is generated using Geant4's photon transport simulation, including 66 cm Rayleigh scattering length, 20 m attenuation length, and reflections off of the interior surface detectors. The library also incorporates the response versus location of the PDs, capturing the attenuation between the initial conversion location of the photon and the silicon photomultipliers (SiPMs).

4.1.3.3 TPC Detector Signal Simulation

When ionization electrons drift through the induction wire planes toward the collection wire plane, current is induced on nearby wires. The principle of current induction is described by the Ramo theorem [90, 91]. For an element of ionization charge, the instantaneous induced current i is proportional to the amount of drifted charge q:

$$i = -q \cdot \vec{E}_w \cdot \vec{v}_q. \tag{4.1}$$

The proportionality factor is a product of the weighting field $\vec{E}_w$ at the location of the charge and the charge's drifting velocity $\vec{v}_q$. The weighting field $\vec{E}_w$ depends on the geometry of the electrodes. The charge's drifting velocity $\vec{v}_q$ is a function of the external E field, which also depends on the geometry of the electrodes as well as the applied drifting and bias voltages. The current induced at a given electrode and electron drift path (x) sampled over a period of time (t) is called a "field response function" $R(x, t)$.

The field response functions for a single ionization electron are simulated with Garfield [92]. In the Garfield simulation, a 22 cm (along the E field or drift direction) × 30 cm (perpendicular to the field direction and wire orientation) region is configured. Figure 4.13 shows a part of the region close to the anode wire planes. There are five wire planes with 4.71 mm spacing, referred to as G, U, V, X, and M with operating bias voltages of −665 V, −370 V, 0 V, 820 V, 0 V, respectively. These bias voltages ensure 100% transmission of electrons through the grid plane (G) and the first two induction planes (U and V) and complete collection by the collection plane X with the main drift field at 500 V/cm. In the simulation, each wire plane contains 101 wires with 150 µm diameter separated at ∼4.71 mm wire pitch. The electron drift velocity as a function of electric field is taken from recent measurements [88, 89]. In this simulation, the motion of the positive ions is not included as their drift velocity is about five orders of magnitude slower than that of ionization electrons. In the underground condition, the distortion in E-field caused by the space charge (accumulated positive ions) is expected to be a factor of 100 smaller than that in the surface-operating ProtoDUNE detectors. This leads the maximal position distortion to be less than 3 mm.

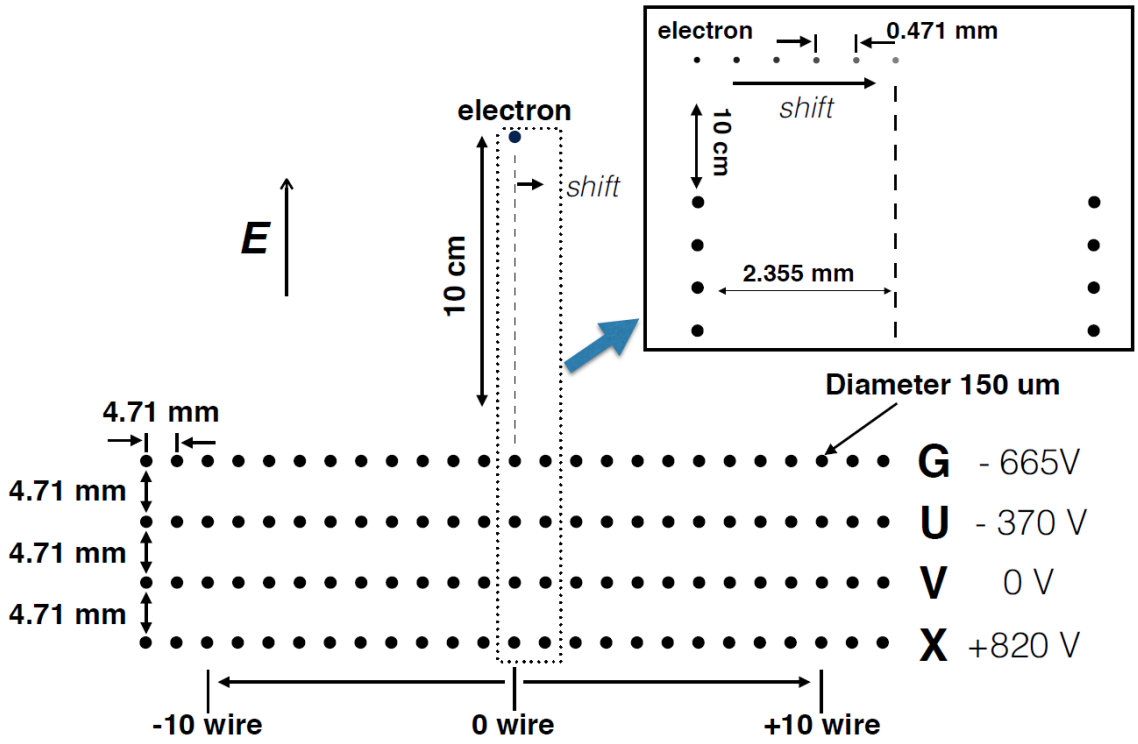

Figure 4.13: Garfield configuration for simulating the field response functions.

Given the above configuration, the field response function can then be calculated in Garfield for each individual wire for an electron starting from any position within the region of simulation. The field response functions for a range ± 10 wires on both sides of the central wire (covering 21 wires in total) are recorded and stored for later application in the TPC detector signal simulation. Figure 4.14 shows the simulated field response.

Following the earlier work in MicroBooNE [93], the TPC detector signal simulation is implemented in the software package Wire-Cell Toolkit [94, 95], which is further interfaced with LArSoft. This simulation procedure has been validated in the MicroBooNE experiment [96]. In the following, we summarize the major features. The TPC signal simulation takes input from the Geant4-simulated energy deposition when particles traverse the detector, and outputs digitized waveforms on the front-end (FE) electronics. A data-driven, analytical simulation of the inherent electronics noise is also performed. Figure 4.15 shows the example waveform for minimum ionizing particles traveling parallel to the wire plane, but perpendicular to the wire orientation.

The signal simulation, i.e., the analog-to-digital converter (ADC) waveform on a given channel,

$$M = (Depo \otimes Drift \otimes Duct + Noise) \otimes Digit, \tag{4.2}$$

is conceptually a convolution of five functions:

Depo represents the initial distribution of the ionization electrons created by energy depositions in space and time as discussed in Section 4.1.3.1.

Drift represents a function that transforms an initial charge cloud to a distribution of electrons arriving at the wires. Physical processes related to drifting, including attenuation due to

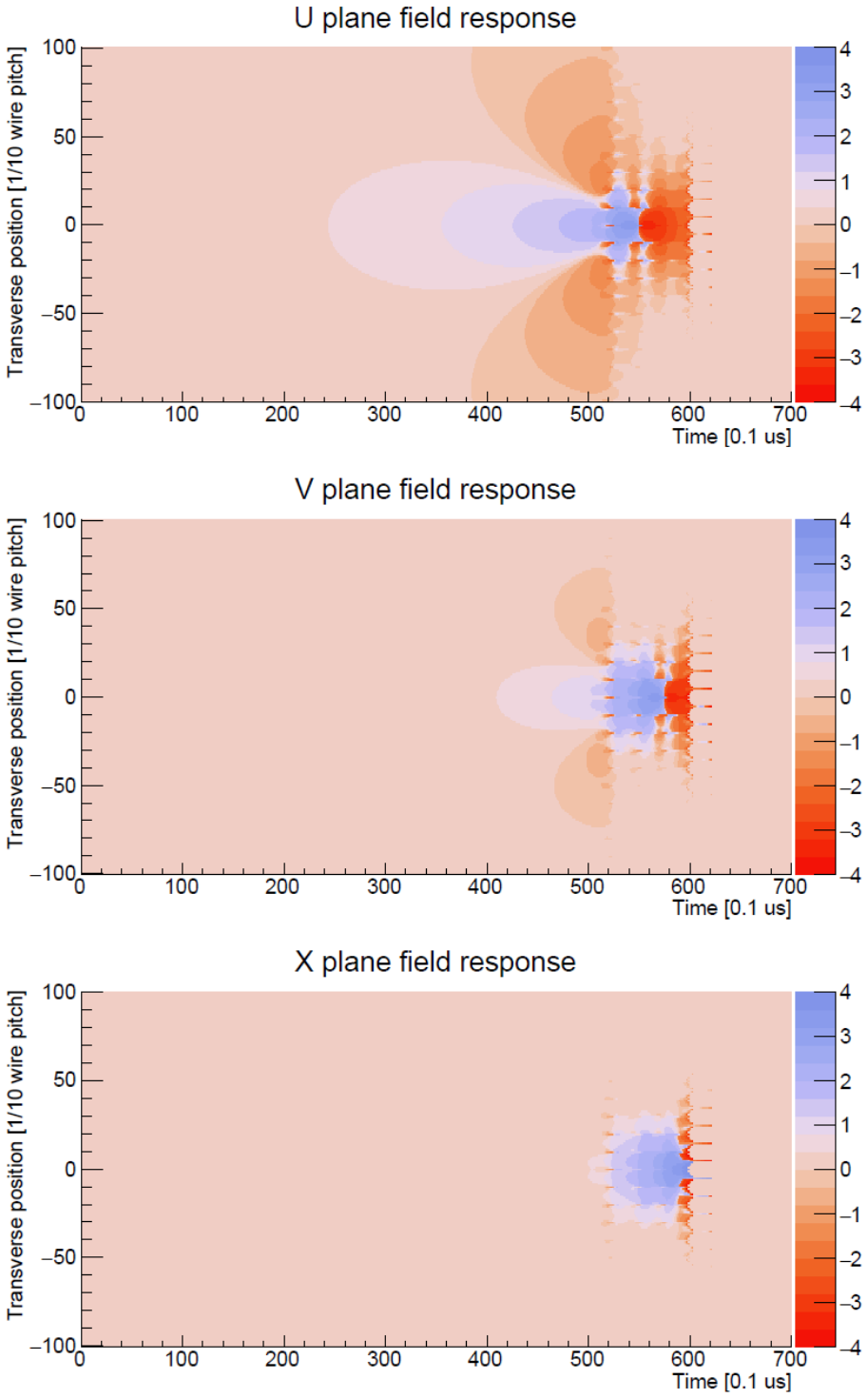

Figure 4.14: Position-dependent (long-range) field response simulated with the Garfield program for two induction and one collection planes. The z-axis scale is logarithmic ($\propto \mathrm{sgn}(i)\log(|i|)$). The wire of interest is assumed to locate at position zero. When a cloud of ionization electrons are drifting through a particular transverse position, the waveform on the wire of interest is shown in z-axis along the x-axis (drift time). Obviously, as the magnitude of transverse positions are large, the induced signal becomes small.

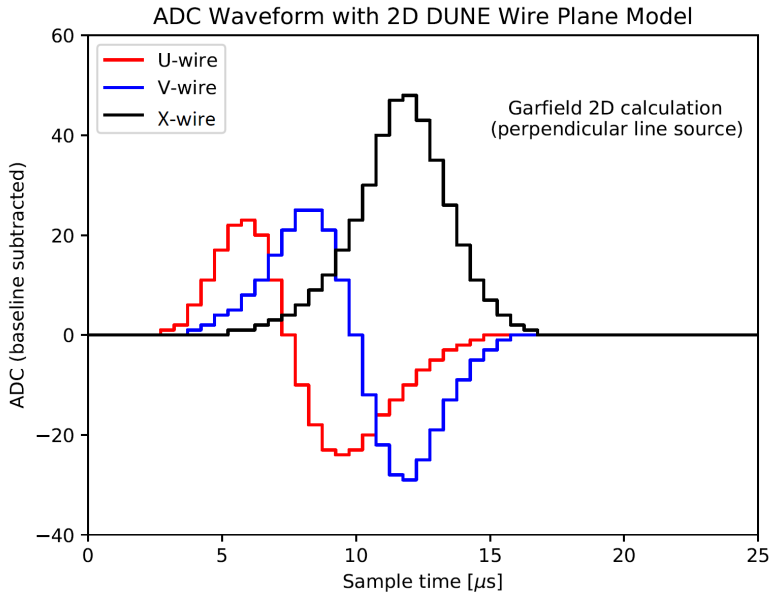

Figure 4.15: Waveform for minimum ionizing particles traveling parallel to the wire plane. For different wire plane, the corresponding track is assumed to travel perpendicular to the wire orientation.

impurities, diffusion and possible distortions to the nominal applied E field, are applied in this function.

Duct is a family of functions, each is a convolution $F \otimes E$ of the field response functions F associated with the sense wire and the element of drifting charge and the electronics response function E corresponding to the shaping and amplification of the FE electronics. More details can be found in Section 4.1.4.

Digit models the digitization electronics according to a given sampling rate, resolution, and dynamic voltage range and baseline offset resulting in an ADC waveform.

Noise simulates the inherent electronics noise by producing a voltage level waveform from a random sampling of a Rayleigh distributed amplitude spectrum and uniformly distributed phase spectrum. The noise spectra used are from measurements with the ProtoDUNE-SP detector after software noise filters, which have excess (non-inherent) noise effects removed.

These functions are defined over broad ranges and with fine-grained resolution. The resolutions are set by the variability (sub millimeter) and extent (several centimeters) of the field response functions and the sampling rate of the digitizer (0.5 µs). Their ranges are set by the size of the detector (several meters) and the length of time over which one exposure is digitized (several milliseconds).

4.1.4 Data Acquisition Simulations and Assumptions

The electrons (∼5300 electrons per mm for MIP signals) on each wire are converted into raw wire signal (ADC vs time) by convolution with the field response and electronics response, which is implemented in the Wire-Cell Toolkit software package [94]. The ASIC electronics response was simulated with the BNL SPICE [97] simulation. For most samples, the ASIC gain was set to 14 mV/fC and the shaping time was set to 2 µs. There are several considerations in choosing the 2 µs shaping time setting (out of 0.5, 1.0, 2.0, 3.0 µs):

- Since the digitization frequency is at 2 MHz, an anti-aliasing filter to ensure the satisfaction of the Nyquist theorem is required. This essentially excludes the 0.5 µs shaping time, which is not enough to ensure complete anti-aliasing.
- A smaller shaping time in principle leads to a slightly better two-peak separation. However, since the drifting time of ionization electrons through one wire plane is about 3 µs, the difference between 1 µs and 2 µs shaping time is limited.
- The electronics noise, as parameterized by the standard deviation of the ADC values on each sample, is slightly lower for the 2 µs and 3 µs shaping-time settings than that of the 1 µs (by about 10% or so).

Te digitization is performed by a 12-bit ADC, which covers a range of about 1.6 V. The number of bits is chosen so that the intrinsic noise introduced by the digitization is negligible. The intrinsic noise level was set to around 2.5 ADC RMS, based on extrapolation from the MicroBooNE experiment [98]. This value was further validated in ProtoDUNE-SP. Figure 4.16 shows the expected electronics shaping functions.

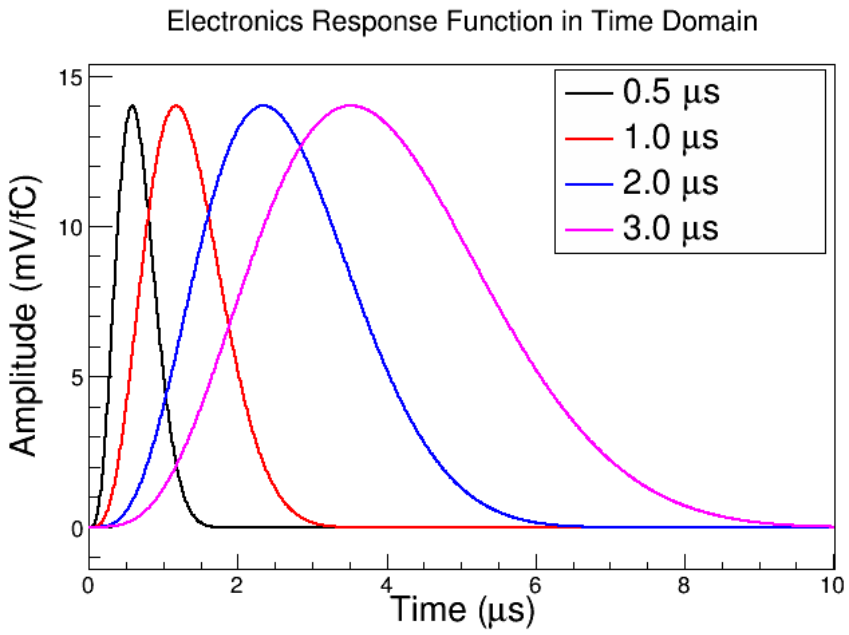

Figure 4.16: The shaping functions of the Front-End ASIC, shown for the four shaping time settings at 14 mV/fC gain.

The PD electronics simulation separately generates waveform for each channel (SiPM) of a PD that

has been hit by photons. Every detected photon appears as a single photoelectron pulse (with the shape taken from [99]) on a randomly selected channel (belonging to the PD in which the photon was registered). Then dark noise (with the rate of 10 Hz) and line noise (Gaussian noise with the RMS of 2.6 ADC counts) are added. Each photon (or a dark-noise pulse) has a probability of appearing as 2 photoelectrons on a waveform (the cross-talk probability is 16.5 %). The final step of the digitization process is recording only fragments of the full simulated waveform that have a signal in them. This is accomplished by passing the waveform through a hit finder described in Sec. 4.2.2.1 and storing parts of the waveform corresponding to the hits found.

4.2 Event Reconstruction in the FD

This section describes various reconstruction algorithms used to reconstruct events in the FD TPC. A successful LArTPC reconstruction needs to deliver reconstructed tracks and showers, particle and event identification, particle momentum and event energy. The reconstruction starts with finding signals on each wire above a threshold and building "hits" out of each pulse. All the LArTPC 3D reconstruction algorithms share the same principle. The x coordinate is determined by the drift time and the y and z coordinates are determined by the intersection of two wires on different planes with coincident hits. There are currently three different reconstruction approaches in the DUNE reconstruction package. The 2D $\rightarrow$3D reconstruction approach starts with clustering together nearby hits on each plane, followed by the use of time information to match 2D clusters between different planes to form 3D tracks and showers. Examples of this approach include TrajCluster and Pandora. The direct 3D approach reconstructs 3D points directly from hits and then proceeds to perform pattern recognition using those 3D points. Examples of this approach include SpacePointSolver and Wire-Cell. The third approach uses a deep-learning technique, known as a convolutional neural network (CNN). There are several tools needed to complete the task of LArTPC reconstruction. These tools include track fitter (Projection Matching Algorithm (PMA) or KalmanFilter), calorimetry, particle ID (PID) and track momentum reconstruction using range for contained tracks or multiple Coulomb scattering for exiting tracks. In addition to the TPC reconstruction, the PD reconstruction provides trigger and t_0 information for non-beam physics.

4.2.1 TPC Signal Processing

The raw data are in the format of ADC counts as a function of TPC ticks (0.5 µs on each channel. The signal has a unipolar shape for a collection wire and a bipolar shape for an induction wire. The first step in the reconstruction is to reconstruct the distribution of ionization electrons arriving at the anode plane. This is achieved by passing the raw data through a deconvolution algorithm. In real detectors, excess noise may exist and require removal through a dedicated noise filter [98].

The deconvolution technique was introduced to LArTPC signal processing in the context ArgoNeuT data analysis [100]. The goal of the deconvolution is to "remove" the impact of field and electronics responses from the measured signal along the time dimension in order to reconstruct the number of ionized electrons. This technique has the advantages of being robust and fast, and is an

essential step in the overall drifted-charge profiling process. This 1D deconvolution procedure was improved to a 2D deconvolution procedure by the MicroBooNE collaboration [93, 96], which further took into account the long-range induction effects in the spatial dimension. Two-dimensional software filters (channel and time) are implemented to suppress high-frequency noise after the deconvolution procedure. For induction plane signals, regions of interest (ROIs) are selected to minimize the impact of electronics noise. More details of this algorithm can be found in [93].

This procedure, implemented in the Wire-Cell toolkit software package [94], has been used in the TPC signal processing in ProtoDUNE-SP. Figure 4.17 shows an example induction U-plane waveform before and after the signal processing procedure. The bipolar shape is converted into a unipolar shape after the 2D deconvolution. Figure 4.18 shows the full 2D image of induction U-plane signal from a ProtoDUNE-SP event [101]. The measured signal (left) has a bipolar shape with red (blue) color representing positive (negative) signals. The deconvolved signal after the 2D deconvolution procedure (right) represents the reconstructed distribution of ionization electrons arriving at the anode wire plane. The deconvolved signal becomes unipolar, and the long-range induction effect embedded in the field response is largely removed.

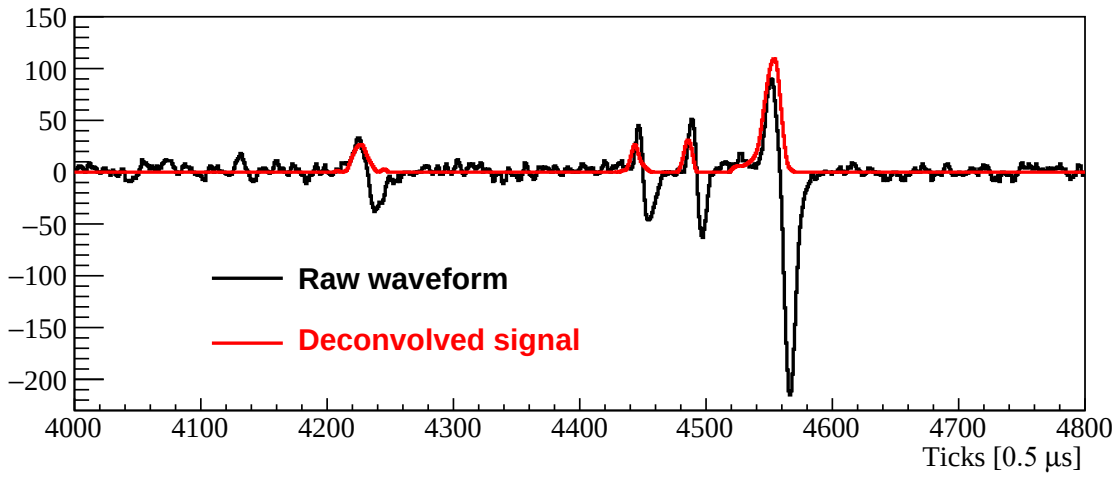

Figure 4.17: An example of measured (black) and deconvolved waveform from an induction U-plane channel of ProtoDUNE-SP before and after the signal processing procedure. For the measured waveform, the unit is ADC. For the deconvolved waveform, the unit is number of electrons after scaling down by a factor of 125. Bipolar signal shapes are converted into unipolar signal shapes after 2D deconvolution.

4.2.2 Hit and Space-Point Identification

4.2.2.1 Gaussian Hit Finder

The reconstruction algorithms currently employed by LArSoft are based on finding hits on the deconvolved waveforms for each plane. A key assumption is that the process of deconvolution will primarily result in Gaussian-shaped charge deposits on the waveforms and this drives the design of the Gaussian hit finder module. Generally, the module loops over the input deconvolved waveforms

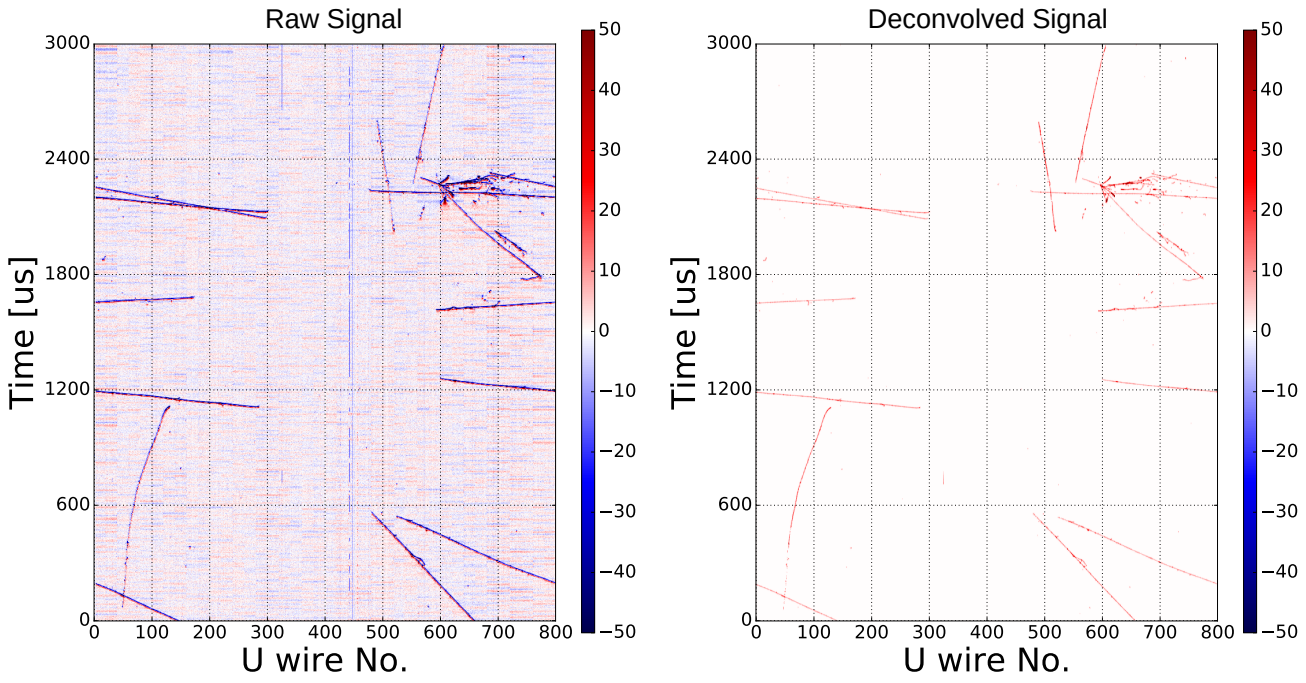

Figure 4.18: Comparison of raw (left) and deconvolved induction U-plane signals (right) before and after the signal processing procedure from a ProtoDUNE-SP event. The bipolar shape with red (blue) color representing positive (negative) signals is converted to the unipolar shape after the 2D deconvolution.

and handles each in three main steps: first it searches the waveforms for candidate pulses, it then fits these candidates to a Gaussian shape and, finally, it places the resulting hit in the output hit collection. Not all charge deposits will be strictly Gaussian shaped, for example a track can emit a delta ray and it can take several wire spacings before the two charge depositions are completely separated. Alternatively, a track can have a trajectory at large angles to the sense wire plane creating a charge deposition over a large number of waveform ticks. The candidate peak-finding stage of the hit finder attempts to resolve the individual hits in both of these cases, still under an assumption that the shape of each individual charge deposition is Gaussian. If this results in candidate peak trains that are "too long" then special handling breaks these into a number of evenly-spaced hits and bypasses the hit-fitting stage.

Figure 4.19 displays the results of the Gaussian hit finder for the case of two or three hits only barely separated in ProtoDUNE-SP data. In this figure the deconvolved waveform is shown in blue, the red line represents the fit of the candidate peak to two or three Gaussian shapes, the crosses represent the centers of the fit peaks, the pulse heights above the waveform baseline and their fit widths.

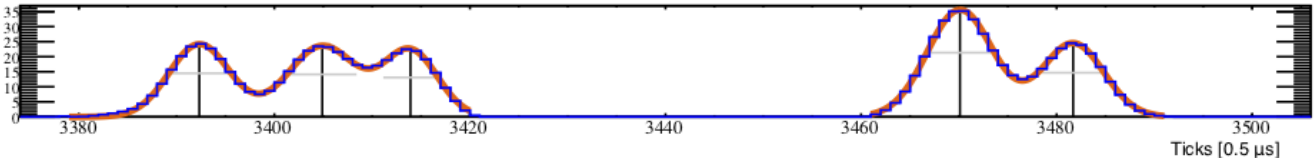

Figure 4.19: An example of reconstructed hits in ProtoDUNE-SP data. The deconvolved waveform is shown in blue, the red line represents the fit of the candidate peak to two or three Gaussian shapes, the crosses represent the centers of the fit peaks, the pulse heights above the waveform baseline and their fit widths.

4.2.2.2 Space Point Solver

The SpacePointSolver algorithm aims to transform the three 2D views provided by the wire planes into a single collection of 3D "space points."

First, triplets of wires are found with hits that are coincident in time within a small window (corresponding to 2 mm in the drift direction) and where the crossing positions of the wires are consistent within 3.55 mm. In some cases a collection wire hit may have only a single candidate pair of induction hits and the space point can be formed immediately. Often though, there are multiple candidate triplets, for example when two tracks are overlapped as seen in one view.

SpacePointSolver resolves these ambiguities by distributing the charge from each collection wire hit between the candidate space points so as to minimize the deviations between the expected and observed charges of the induction wire hits

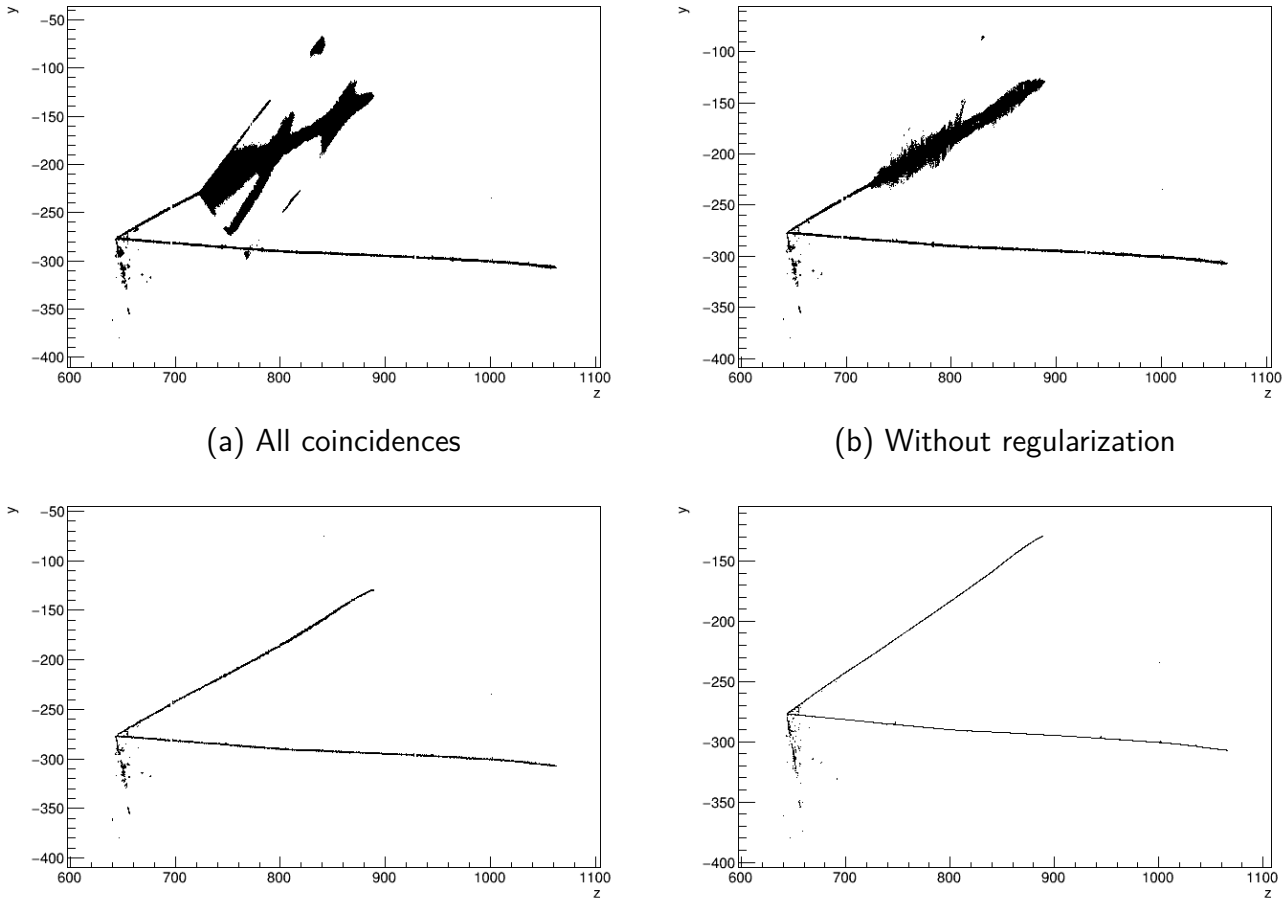

(a) All coincidences

(b) Without regularization

(c) With regularization

(d) True charge distribution

Figure 4.20: Performance of SpacePointSolver on a simulated FD neutrino interaction. The first panel shows the position of all triplet coincidences in the zy view (looking from the side of the detector), displaying multiple ambiguous regions. The second and third panels show the solution with and without regularization, the regularization disfavoring various erroneous scattered hits. The final panel shows the true charge distribution, demonstrating the fidelity of the regularized reconstruction.

$$\chi^2 = \sum_{i}^{\text{wires}} \left(q_i - \sum_{j}^{\text{points}} T_{ij} p_j \right)^2 \tag{4.3}$$

where q_i is the charge observed in the i^{th} induction hit, p_j is the solved charge at space point j, and $T_{ij} \in \{0, 1\}$ encodes whether space point j is coincident in space and time with wire hit i.

The minimization is subject to the condition that each predicted charge $p_j \geq 0$, and that the total predicted charge for each collection wire hit exactly matches observations:

$$\sum_{j}^{\text{points}} U_{jk} p_j = Q_k \tag{4.4}$$

where Q_k is the charge observed on the k^{th} collection wire, and U_{jk} encodes the coincides of space point charges with the collection wires.

The problem as formulated is convex and can thus be solved exactly in a deterministic fashion. A single extra term can be added to the expression while retaining this property:

$$\chi^2 \to \chi^2 - \sum_{ij}^{\text{points}} V_{ij} p_i p_j. \tag{4.5}$$

By setting V_{ij} larger for neighboring points this term acts as a regularization such that solutions with a denser collection of space points are preferred. The V function is chosen empirically to have an exponential fall-off with constant 2 cm.

Figure 4.20 shows the performance of this algorithm on a sample FD MC event, demonstrating good performance at eliminating spurious coincidences, and the importance of the regularization term.

SpacePointSolver was developed with the intention of acting as the first stage of a fully 3D reconstruction for FD neutrinos, but it has been successfully put to use in a more restricted role to solve the disambiguation problem in ProtoDUNE. The full problem is solved, but for this application the information retained is restricted to the drift volume to which the corresponding space points for each induction hit are assigned. This technique correctly resolves more than 99% of hits while requiring less CPU time than the standard disambiguation algorithm.

The outcome of the SpacePointSolver reconstruction, which associates a 3D point with three hits on three wire planes, is used in the process of disambiguation for ProtoDUNE and has been tested and used as well for FD. This process of disambiguation determines which wire segment corresponds to the energy deposited by the particle in the TPC, since the induction wires are wrapped in the FD TPC design in order to save cost on electronics and minimize dead regions between APAs,

which as a consequence produces that multiple induction wire segments will be read out by the same electronic channel.

4.2.3 Hit Clustering, Pattern Recognition and Particle Reconstruction

There are different approaches for hit clustering, pattern recognition and particle reconstruction that are being explored in the context of DUNE FD interactions. The main ones are described in this section.

4.2.3.1 Line Cluster

The intent of the Line Cluster algorithm is to construct 2D line-like clusters using local information. The algorithm was originally known as Cluster Crawler. The "Crawler" name is derived from the similarity of this technique to "gliders" in 2D cellular automata. The concept is to construct a short line-like "seed" cluster of proximate hits in an area of low hit density where hit proximity is a good indication that the hits are indeed associated with each other. Additional nearby hits are attached to the leading edge of the cluster if they are similar to the hits already attached to it. The conditions are that the impact parameter between a prospective hit and the cluster projection is similar to those previously added and the hit charge is similar as well. These conditions are moderated to include high charge hits that are produced by large dE/dx fluctuations and the rapid increase in dE/dx at the end of stopping tracks while rejecting large charge hits from δ-rays. Seed clusters are formed at one end of the hit collection so that crawling in only one direction is sufficient. LineCluster uses disambiguated hits as input and produces a new set of refined hits. More details on the Line Cluster algorithm can be found in [102].

4.2.3.2 TrajCluster

TrajCluster reconstructs 2D trajectories in each plane. It incorporates elements of pattern recognition and Kalman Filter fitting. The concept is to construct a short "seed" trajectory of nearby hits. Additional nearby hits are attached to the leading edge of the trajectory if they are similar to the hits already attached to it. The similarity requirements use the impact parameter between the projected trajectory position and the prospective hit, the hit width and the hit charge. This process continues until a stopping condition is met such as lack of hits, an abnormally high or low charge environment, or encountering a 2D vertex or a Bragg peak.

2D vertices are found between trajectories in each plane. The set of 2D vertices is matched between planes to create 3D vertices. A search is made of the "incomplete" 3D vertices, those that are only matched in two planes, to identify trajectories in the third plane that were poorly reconstructed.

Two recent additions to TrajCluster are matching trajectories in 3D and tagging of shower-like trajectories. More details on the TrajCluster algorithm can be found in [103].

4.2.3.3 Pandora

The Pandora software development kit [104] was created to address the problem of identifying energy deposits from individual particles in fine-granularity detectors, using a multi-algorithm approach to solving pattern-recognition problems. Complex and varied topologies in particle interactions, especially with the level of detail provided by LArTPCs, are unlikely to be solved successfully by a single clustering algorithm. Instead, the Pandora approach is to break the pattern recognition into a large number of decoupled algorithms, where each algorithm addresses a specific task or targets a particular topology. The overall event is then built up carefully using a chain of many tens of algorithms. The Pandora multi-algorithm approach has already been applied to LArTPC detectors, and has been successfully used in different analyses for the automated reconstruction of cosmic-ray muons and neutrino interactions in the MicroBooNE experiment [105] as well as test beam interactions in the ProtoDUNE-SP detector (see Section 4.3.3).

The input to the Pandora pattern recognition is a list of reconstructed and disambiguated 2D hits, alongside detector information (such as dimensions, unresponsive or dead material regions). The specified chain of pattern-recognition algorithms is applied to these input hits (once translated into native Pandora 2D hits). The results of the pattern recognition are persisted in the art/LArSoft framework, with the major output being a list of reconstructed 3D particles (termed particle flow particles (PFParticles)). A PFParticle corresponds to a distinct track or shower in the event, and has associated objects such as collections of 2D hits for each view (Clusters), 3D positions (SpacePoints) and a reconstructed Vertex position that defines its interaction point or first energy deposit. Navigation along PFParticle hierarchies is achieved using the PFParticle interface, which connects parent and daughter PFParticles, providing a particle flow description of the interaction. The identity of each particle is currently not reconstructed by Pandora, but PFParticles are instead characterized as track-like or shower-like based on their topological features.

The main stages of the Pandora pattern recognition chain are outlined below, and are illustrated in Figure 4.21. Note that both the individual pattern recognition algorithms and the overall reconstruction strategy are under continual development and will evolve over time, with a current emphasis on the inclusion of machine-learning approaches to drive decisions in some key algorithms. The current chain of pattern-recognition algorithms has largely been tuned for neutrino interactions from the Fermilab Booster Neutrino Beam; however, the algorithms are designed to be generic and easily reusable, and they are in the process of being adapted for neutrino interactions in the energy regime of DUNE. A more detailed description of the algorithms can be found in [105].

1. **Input hits:** The input list of reconstructed and disambiguated 2D hits are translated into native Pandora 2D hits and separated into the different views and into "drift volumes", defined as the regions of the detector with a common drift readout.

2. **2D track-like clusters:** The first phase of the Pandora pattern recognition is track-oriented 2D clustering, creating "proto-clusters" that represent continuous, unambiguous lines of 2D hits. This early clustering phase is careful to ensure that the proto-clusters have high purity (i.e., represent energy deposits from exactly one true particle) even if this means they are initially of low completeness (i.e., only contain a small fraction of the total hits within a single true particle). A series of cluster-merging and cluster-splitting algorithms then examine the

2D proto-clusters and try to extend them, making decisions based on topological information, aiming to improve completeness without compromising purity.

3. **3D vertex reconstruction:** The neutrino interaction vertex is an important feature point. Once identified, any 2D clusters can be split at the projected vertex position, reducing chances of merging particles in any view. Cluster-merging operations also take proximity to the vertex into account, in order to protect primary particles emerging from the vertex region, and ensure good reconstruction performance for interactions with many final-state particles. Pairs of 2D clusters from different views are first used to produce lists of possible 3D vertex positions. These candidate vertices are examined and scored, and the best vertex is selected. Pandora has developed different algorithms for the selection of the neutrino vertex, including the use of machine-learning approaches in MicroBooNE. Similar approaches can be harnessed in the future for interactions in the FD, where a score-based approach is currently used.

4. **3D track reconstruction:** The aim of the 3D track reconstruction is to identify the combinations of 2D clusters (from the different views) that represent the same true, track-like particle. These 2D clusters are formally associated by the construction of a 3D track particle. During this process, 3D information can also be used to improve the quality of the 2D clustering. A Pandora algorithm considers all possible combinations of 2D clusters, one from each view, and builds (what is loosely termed) a rank-three tensor to store a comprehensive set of cluster-consistency information. This tensor can be queried to identify and understand any cluster-matching ambiguities. 3D track particles are first built for any unambiguous combinations of 2D clusters. Cases of cluster-matching ambiguities are then addressed, with iterative corrections to the 2D clustering being made to resolve the ambiguities and so enable 3D particle creation.

5. **2D and 3D shower reconstruction:** A series of topological metrics (additional use of some calorimetric information would be desirable in the future) are used to characterize each 2D cluster as track-like or shower-like. This information is analyzed to identify the longest shower-like clusters, which form the "seeds" or "spines" for 2D and 3D shower reconstruction. A recursive algorithm is used to add shower branches onto each top-level shower seed, then branches onto branches, etc. The 2D showers are then matched between views to form 3D showers, reusing ideas from the 3D track-matching procedure.

6. **2D and 3D particle refinement and event building:** Following the 3D track and shower reconstruction, a series of algorithms is used to improve the completeness of the reconstructed particles by merging together any nearby particles that are just fragments of the same true particle. Both 2D and 3D approaches are used, where a typical approach uses combinations of 2D clusters (from different views) to identify features in 3D, or projects 3D features into each of the 2D views. This is a powerful demonstration of the Pandora rotational coordinate transformation system, which allows seamless use of 2D and 3D information to drive pattern-recognition decisions. Finally, 3D space points are created for each 2D input hit, and the 3D particle trajectories are used to organize the reconstructed particles into a hierarchy. Final-state particles can be navigated via parent-daughter links, thus reconstructing their subsequent interactions or decays. For neutrino interactions, a top-level reconstructed neutrino particle is created; it represents the primary particle in the hierarchy linking together

the daughter final-state particles and provides the information about the neutrino interaction vertex.

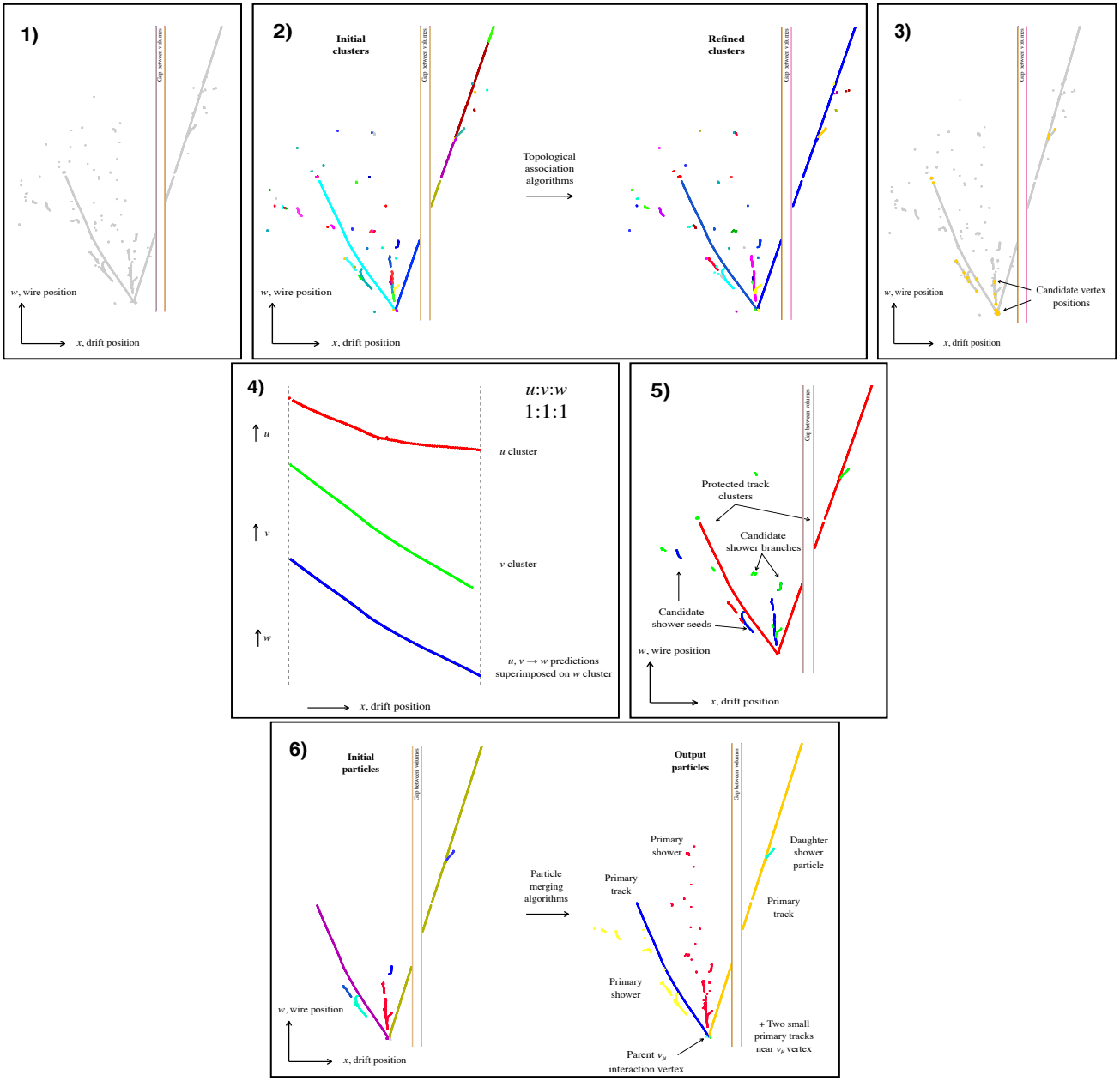

Figure 4.21: Illustration of the main stages of the Pandora pattern recognition chain: (1) Input Hits; (2) 2D track-like cluster creation and association; (3) 3D vertex reconstruction; (4) 3D track reconstruction; (5) Track/Shower separation; (6) 2D and 3D particle refinement and event building.

The algorithms forming the stages described above can be used in different ways, thanks to the multi-algorithm approach. Currently, two Pandora reconstruction paths (*Pandora Cosmic* and *Pandora Neutrino*) have been created, using chains of tens of algorithms each (note that over 130 algorithms and tools are used in total). Although many algorithms are shared between the two paths, the overall algorithm selection results in different key features:

1. Pandora Cosmic: Strongly track-oriented, optimized for the reconstruction of cosmic-ray

muons and their daughter (shower-like) delta rays.

2. Pandora Neutrino: Optimized for the reconstruction of neutrino or test beam particle interactions, carefully building the event using the reconstructed interaction vertex (protecting particles emerging from it) and including a careful treatment of tracks versus showers.

These two chains of algorithms are harnessed together to provide a consolidated output in the case of surface detectors exposed to cosmic rays, such as MicroBooNE and ProtoDUNE-SP (without significant cosmic-ray background, only the Pandora Neutrino algorithm chain is necessary for the FD). The overall reconstruction strategy in such detectors is illustrated in Figure 4.22. It starts by running the Pandora Cosmic reconstruction on the entire collection of input hits, then identifies "clear" cosmic rays. This identification uses a geometrical approach to tag through-going cosmic rays and examines the consistency of the cosmic rays with the t_0 appropriate to the neutrino beam spill. Clear cosmic rays are output at this stage. For the remaining ambiguous hits, however, additional stages are required. A *slicing* process is applied to the remaining hits, dividing them into smaller regions (slices) that represent separate, distinct interactions. Each slice is reconstructed using both the Pandora Neutrino and Pandora Cosmic reconstruction chains and the results are compared directly to identify whether the slice corresponds to a cosmic ray or a neutrino interaction (in the case of MicroBooNE) or test beam interaction (in the case of ProtoDUNE-SP). The consolidated event output is formed of three classes of reconstructed particles: (1) clear cosmic rays, (2) cosmic rays that are spatially and temporally consistent with being a neutrino interaction in the detector (remaining cosmic-rays) and (3) candidate neutrino or test beam interactions.

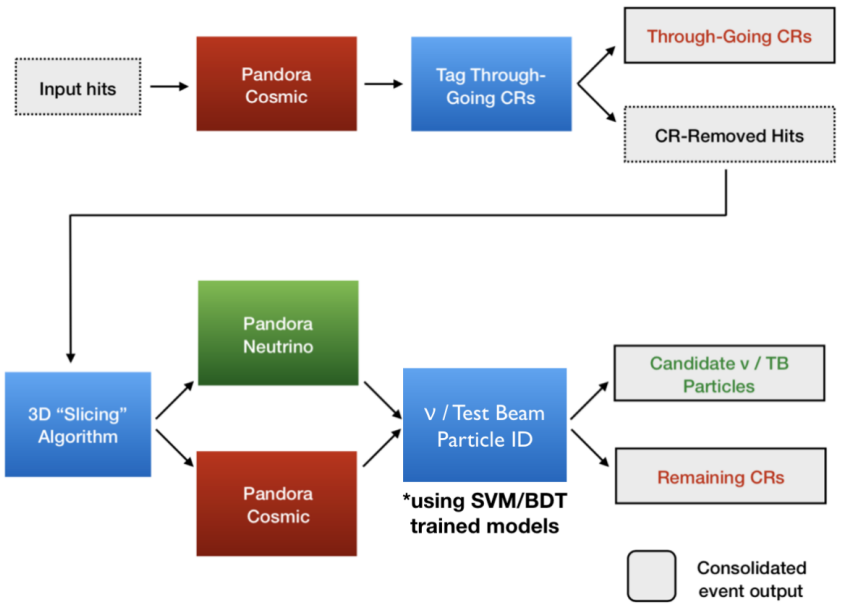

Figure 4.22: Schema of the Pandora consolidated output and overall reconstruction strategy for surface LArTPCs such as MicroBooNE and ProtoDUNE-SP. See text for more details.

Of particular importance in this overall reconstruction strategy is the neutrino (MicroBooNE) or test beam particle (ProtoDUNE-SP) identification tool. This tool is responsible for deciding whether to output the cosmic ray or neutrino (or test beam) reconstruction outcomes for a given

slice. For ProtoDUNE-SP, this decision is based on the output from adaptive boosted decision trees (BDTs), trained to distinguish between cosmic-ray and test beam particles, which has proved to be highly efficient across the momentum range of ProtoDUNE-SP data (see Section 4.3.3).

The performance obtained with the current algorithms are shown in Section 4.3, both for the FD and ProtoDUNE-SP. As previously mentioned, both the individual pattern recognition algorithms and the overall reconstruction strategy are under continual development. Many algorithms still require explicit tuning for the DUNE energy ranges, and new algorithms, designed specifically for DUNE, will be added to the multi-algorithm pattern recognition. The performance presented in this document therefore represents a current snapshot and is expected to improve with future dedicated work.

4.2.3.4 Projection Matching Algorithm

PMA was primarily developed as a technique of 3D reconstruction of individual particle trajectories (trajectory fit) Ref [106]. PMA was designed to address a challenging issue of transformation from a set of independently reconstructed 2D projections of objects into a 3D representation. Reconstructed 3D objects are also providing basic physics quantities like particle directions and dE/dx evolution along the trajectories. PMA uses as its input the output from 2D pattern recognition: clusters of hits. For the purposes of the DUNE reconstruction chain the Line Cluster algorithm (Section 4.2.3.1) is used as input to PMA, however the use of hit clusters prepared with other algorithms may be configured as well. As a result of 2D pattern recognition, particles may be broken into several clusters of 2D projections, fractions of particles may be missing in individual projections, and clusters obtained from complementary projections may not cover corresponding sections of trajectories. Such behavior is expected since ambiguous configurations of trajectories can be resolved only if the information from multiple 2D projections is used. Searching for the best matching combinations of clusters from all 2D projections was introduced to the PMA implementation in the LArSoft framework. The algorithm also attempts to correct hit-to-cluster assignments using properties of 3D reconstructed objects. In this sense PMA is also a pattern-recognition algorithm. The underlying idea of PMA is to build and optimize objects in 3D space (formed as polygonal lines with the number of segments iteratively increased) by minimizing the cost function calculated simultaneously in all available 2D projections. Several features were developed in LArSoft's PMA implementation to address detector-specific issues like stitching the particle fragments found in different TPCs or performing disambiguation at the 3D reconstruction stage. Since algorithms existing within or interfaced to the LArSoft framework (see Section 4.2.3.3) can provide pattern reconstruction results that include the particle hierarchy description, the mode for applying PMA to calculate trajectory fits alone was developed. In this mode the collections of clusters forming particles are taken from the "upstream" algorithm and hit-to-cluster associations remain unchanged.

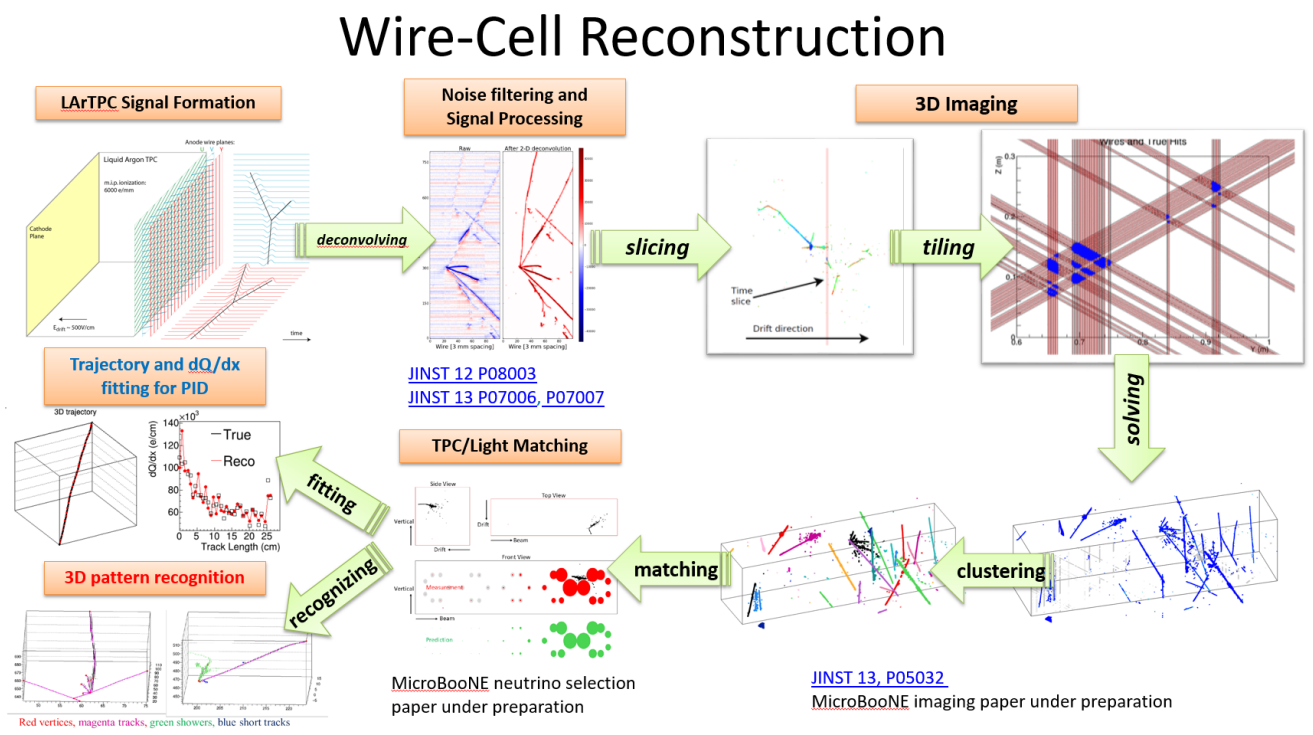

Figure 4.23: Overview of the Wire-Cell reconstruction paradigm, taken from [107]. See text for more details.

4.2.3.5 Wire Cell

Wire-Cell is a new reconstruction package under development. The current status of this reconstruction paradigm is shown in Figure 4.23. The simulation of the induction signal in a LArTPC and the overall signal processing process, which are general to all reconstruction methods, are described in Sections 4.1.3.3 and 4.2.1, respectively. The subsequent reconstruction in Wire-Cell adopts a different approach from the aforementioned algorithms. Instead of directly performing pattern recognition on each of the 2D views (drift time versus wire number), 3D imaging of events is obtained with time, geometry, and charge information. This step is independent from the event topologies, and the usage of the charge information takes advantage of a unique feature of the projection views, as each of the wire plane detects the same amount of the ionization electrons under transparency condition. The strong requirement of the time, geometry, and charge information provides a natural way to suppress electronic noise while combining with successful signal processing maintains high hit efficiency. Details of this step is described in [108]. The subsequent reconstruction involves the object clustering and TPC and light matching, which has been crucial for selecting neutrino interactions in the MicroBooNE experiment [109]. The current focus of the Wire-Cell algorithm development is on the trajectory and dQ/dx fitting, which aims at enabling precision particle identification in a LArTPC. Development of 3D pattern recognition also needs to be revisited before reaching a complete reconstruction chain.

The Wire-Cell team also created an advanced web-based 3D event display, "Bee" [110], to aid the reconstruction development and provide interactive visualizations to end users. Bee, together with 2D Magnify event display tools, have played important roles in the development of various

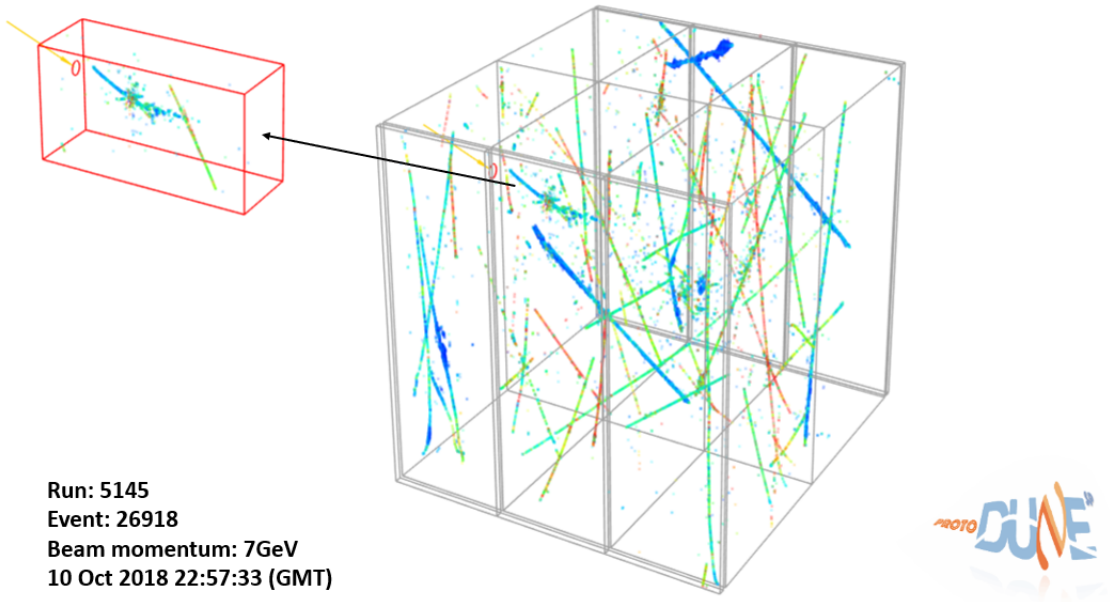

Figure 4.24: This 3D display shows the full size of the ProtoDUNE-SP detector (gray box) and the direction of the particle beam (yellow arrow). Particles from other sources (such as cosmic rays) can be seen throughout the white box, while the red box highlights the region of interest: in this case, an interaction resulting from the 7 GeV beam particle through the detector. The 3D points are obtained using the Space Point Solver reconstruction algorithm. This event can be accessed through interactive web-based event display Bee at `https://www.phy.bnl.gov/twister/bee/set/protodune-gallery/event/0/`.

reconstruction algorithms, including signal processing, 3D event imaging, object clustering, TPC and light matching, and trajectory and dQ/dx fitting. The Bee event display was also used during the ProtoDUNE data-taking period to stream real-time reconstructed events to the users. Figure 4.24 shows an example of a data event from the ProtoDUNE-SP detector [111]. The full video of this event can be found in [112].

4.2.3.6 Deep Learning

Deep learning methods are used in two main areas of the DUNE event reconstruction. Both of these algorithms are based on CNNs. In recent years CNNs have become the method of choice for many image recognition tasks in commerce and industry, and lately have been applied to high energy physics. The CNNs contain a series of filters that are applied to the input detector data images in order to extract the features required to classify the images.

4.2.3.7 CNN for track and shower separation

The hit-level CNN aims to classify each reconstructed hit as either track-like or shower-like by looking at the local region surrounding the hit in (charge, time) coordinates. The CNN is trained using a large number of simulated images with the known true origin of the energy deposits. Once trained, the CNN provides the track-like or shower-like classification for each hit object in the event. This algorithm is applied to each readout view in each TPC separately.

4.2.3.8 CNN for event selection

The algorithm used for the classification of neutrino interaction types is called the convolutional visual network (CVN) and is based on a CNN. The primary goal of the CVN is to provide a probability for each neutrino interaction to be CC ν_μ, CC ν_e, CC ν_τ or neutral current (NC). The CVN takes three 500×500 pixel images of the neutrino interactions as input, one from each view. The images contain the charge and the peak time of the reconstructed hits and does not use any information beyond the hit reconstruction. The CVN is discussed in more detail in Chapter 5.

4.2.4 Calorimetric Energy Reconstruction and Particle Identification

As charged particles traverse a LAr volume, they deposit energy through ionization and scintillation. It is important to measure the energy deposition, as it provides information on particle energy and species. The algorithm for reconstructing the ionization energy in LArSoft is optimized for line-like tracks and is being extended to more complicated event topology such as showers. The algorithm takes all the hits associated with a reconstructed track and for each hit, it converts the hit area or amplitude, in ADC counts, to the charge Q_{det}, in units of fC, on the wire using an

ADC-to-fC conversion factor that was determined by muons or test stand measurements. To account for the charge loss along the drift due to impurities, a first correction is applied to $Q_{\rm det}$ to get the free charge after recombination $Q_{\rm free} = Q_{det}/e^{-t/\tau_e}$, where t is the electron drift time for the hit and τ_e is the electron lifetime measured by the muons or purity monitors. The charge $Q_{\rm free}$ is divided by the track pitch dx, which is defined as wire spacing divided by the cosine of the angle between the track direction and the direction normal to the wire direction in the wire plane, to get the $dQ_{\rm free}/dx$ for the hit. Finally, to account for charge loss due to recombination, also known as "charge quenching," a second correction is applied to convert $dQ_{\rm free}/dx$ to dE/dx based on the modified Box's model [86] or the Birks's model [87]. The total energy deposition from the track is obtained by summing the dE/dx from each hit: $\sum_{i}^{\text{all hits}} (dE/dx)_i \cdot dx_i$.

If the incident particle stops in the LArTPC active volume, the energy loss dE/dx as a function of the residual range (R), the path length to the endpoint of the track, is used as a powerful method for particle identification. There are two methods in LArSoft to determine particle species using calorimetric information. The first method calculates four χ^2 values for each track by comparing measured dE/dx versus R to hypotheses for the proton, charged kaon, charged pion and muon, and identifies the track as the particle that gives the smallest χ^2 value. The second method calculates the quantity $PIDA = \langle A_i \rangle = \langle (dE/dx)_i R_i^{0.42} \rangle$ [86], which is defined to be the average of $A_i = (dE/dx)_i R_i^{0.42}$ over all track points where the residual range R_i is less than 30 cm. The particle species can be determined by making a selection on the $PIDA$ value.

4.2.5 Optical Reconstruction

4.2.5.1 Optical Hit Finder

The first step of the DUNE optical reconstruction is reading individual waveforms from the simulated PD electronics and finding optical hits – regions of the waveforms containing pulses. The optical hit contains the optical channel (SiPM) that the hit was found on, time corresponding to the hit, its width, area, amplitude, and number of photoelectrons.

The current DUNE optical-hit-finder algorithm then searches for regions of the waveform exceeding a certain threshold (13 ADC counts), checking whether that region is wider than 10 optical time ticks[2], and, if it is, calculating the aforementioned optical-hit parameters for the region (including parts of the waveform around it that have ADC values greater than 1) and recording it as an optical hit. The number of photoelectrons is calculated by dividing the full area of the hit by the area of a single-photoelectron pulse. The pedestal is assumed to be constant and is specified in the hit finder as 1500 ADC counts (always correct for the MC).

[2]The current simulation assumes a 150 MHz digitizer like that used in ProtoDUNE, though the final far detector electronics will use an 80 MHz digitizer.

4.2.5.2 Optical Flash Finder

After optical hits are reconstructed, they are grouped into higher-level objects called optical flashes. The optical flash contains the time and time width of the flash, its approximate y and z coordinates (and spatial widths along those axes), its location and size in the wire planes, the distribution of photoelectrons across all PDs, and the total number of photoelectrons in the flash, among other parameters.

The flash-finding algorithm searches for an increase in PD activity (the number of photoelectrons) in time using information from optical hits on all photon detectors. When a collection of hits with the total number of photoelectrons greater than or equal to 2 is found, the algorithm begins creating an optical flash. It starts with the largest hit and adds hits from the found hit collection that lie closer than half the combined widths of the flash under construction a nd the hit being added to it. The flash is stored after no more hits can be added to it and if it has more than two photoelectrons.

The algorithm also estimates spatial parameters of the optical flash by calculating the number-of-photoelectron-weighted mean and root mean square of locations of the optical hits (defined as centers of PDs where those hits were detected) contained in the flash.

4.3 Reconstruction Performance

An automated reconstruction of the neutrino interaction events in DUNE, often complex topologies with multiple final state particles, is a significant challenge. The current chain of Pandora pattern recognition algorithms has been tuned for neutrino interactions from the Fermilab Booster Neutrino Beam, and is in the process of being adapted for the wide range of energies of the DUNE FD. Despite this, and thanks to the reusability of Pandora algorithms for different single phase LArTPC detectors, good performance is already achieved with this first-pass pattern recognition, and output from Pandora is used in the computation of the energy reconstruction in the oscillation analysis. Significant improvements are expected in the upcoming years with a more dedicated tune of the current algorithms, and the development of new ones, as needed.

The current reconstruction performance, evaluated using metrics introduced in 4.3.1, is presented for simulated neutrino interactions in a SP 10 kt FD module in 4.3.2, and for simulated and real data test beam events in ProtoDUNE-SP in 4.3.3. These results outline the baseline performance on which improvements will continue to be made in the next years. In addition, examples of current high-level reconstruction performance are presented in 4.3.4.

4.3.1 Pandora Performance Assessment

The performance of the Pandora pattern recognition is assessed by matching reconstructed PFParticles to the simulated Monte Carlo Particle (MCParticle)s. These matches are used to evaluate

the efficiency with which MCParticles are reconstructed as PFParticles, and to calculate the completeness and purity of each reconstructed PFParticle.

The following procedure is used to match reconstructed PFParticles with simulated MCParticles:

- *Selection of MCParticles:* The full hierarchy of true particles is extracted from the simulated neutrino interaction. A list of "target" particles is then compiled by navigating through this hierarchy and selecting the final-state "visible" particles producing a minimum number of reconstructed hits (allowed to be: $e^{\pm}$, $\mu^{\pm}$, γ, $\pi^{\pm}$, $\kappa^{\pm}$, p)[3]. Any downstream daughter particles are folded in these target particles.
- *Matching of reconstructed 2D hits to MCParticles:* Each reconstructed 2D hit is matched to the target MCParticle responsible for depositing the most energy within the region of space covered by the hit. The collection of 2D hits matched to each target MCParticle is known as its "true hits".
- *Matching of MCParticles to reconstructed PFParticles:* The reconstructed PFParticles are matched to target MCParticles by analyzing their shared 2D hits. A PFParticle and MCParticle will be matched if the MCParticle contributes the most hits to the PFParticle, and if the PFParticle contains the largest collection of hits from the MCParticle. The matching procedure is iterative, such that once each set of matched particles has been identified, these PFParticles and MCParticles are removed from consideration when making the next set of matches.

Using the output of this matching scheme, the following performance metrics can be calculated:

- *Efficiency:* Fraction of MCParticles with a matched PFParticle,
- *Completeness:* The fraction of 2D hits in a MCParticle that are shared with its matched reconstructed PFParticle, and
- *Purity:* The fraction of 2D hits in a PFParticle that are shared with its matched MCParticle.

4.3.2 Reconstruction Performance in the DUNE FD

The performance of the Pandora pattern recognition has been evaluated using a sample of accelerator neutrino and antineutrino interactions simulated using the reference DUNE neutrino energy spectrum and the 10 kt detector module geometry. The breakdown of the different interaction channels as a function of the true neutrino energy in the samples used is presented in Fig. 4.25, for the events in the neutrino mode in which at least one "target" reconstructable MCParticle is created and therefore evaluated. The following plots show that a good efficiency has already been achieved, and indicate particular regions and channels in which improvements can be made.

[3] A minimum number of 15 reconstructed hits, with at least two views with 5 or more hits, is required in the definition of "target" MCParticle. This corresponds to true momentum thresholds of approximately 60 MeV for muons and 250 MeV for protons in the MicroBooNE simulation [105]. Note that this selection is purely for performance assessment purposes, and that particles with fewer hits might still be created by Pandora.

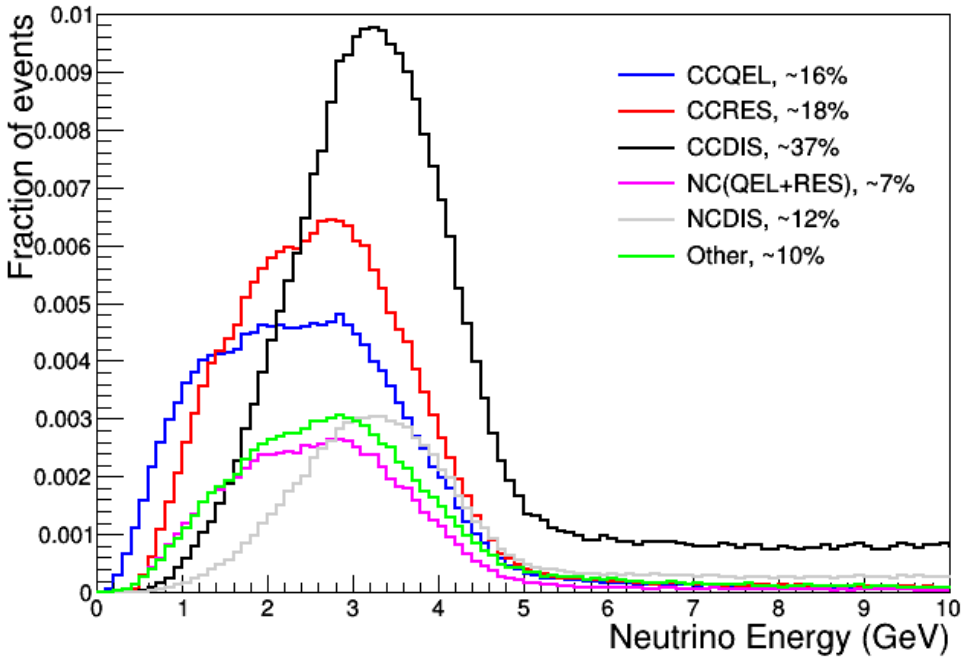

Figure 4.25: Breakdown of the different interaction channels as a function of the true neutrino energy in the samples used in the assessment of reconstruction performance, for the simulated events in the neutrino mode in which at least one "target" reconstructable MCParticle particle is created and therefore evaluated. Percentages indicate the fraction of each channel in the total number of events.

Figure 4.26 shows the reconstruction efficiency as a function of the number of total true 2D hits and as a function of the true momentum for a range of final-state particles. The typical reconstruction efficiencies obtained for track-like MCParticles ($\mu^{\pm}$, $\pi^{\pm}$, p) rise from 65 % to 85 % for simulated particles depositing 100 hits to 85 % to 100 % for particles with 1000 hits. It should be emphasized that inefficiencies almost always result from accidental merging of multiple nearby true particles, rather than an inability to cluster hits from a true particle. The reconstruction efficiency for shower-like MCParticles (e^{-},γ) is a bit lower than the equivalent for track-like particles at lower number of hits, but comparable with >100 hits.

Figure 4.27 shows distributions of completenesses and purities for a range of final-state particles. In the case of final-state track-like particles, good completeness and purity are achieved, indicating that the track-based pattern recognition algorithms currently provide a high-quality reconstruction. It can be seen that final-state shower-like particles are typically reconstructed with high purity, but somewhat lower completeness, indicating that, although the shower reconstruction is fairly good already, there is room for addition of new algorithms specifically targeting an increase in shower completeness at DUNE.

For deep inelastic interactions, in which tens of final-state particles may be produced, a breakdown such as in Figures 4.26 and 4.27 is less representative and informative (however, no significant impact has been observed when adding DIS events in the calculation of such quantities). Instead, Figure 4.28 presents an assessment of the reconstruction of such events by comparing the number of reconstructed particles as a function of the number of true final-state particles in the event for NC

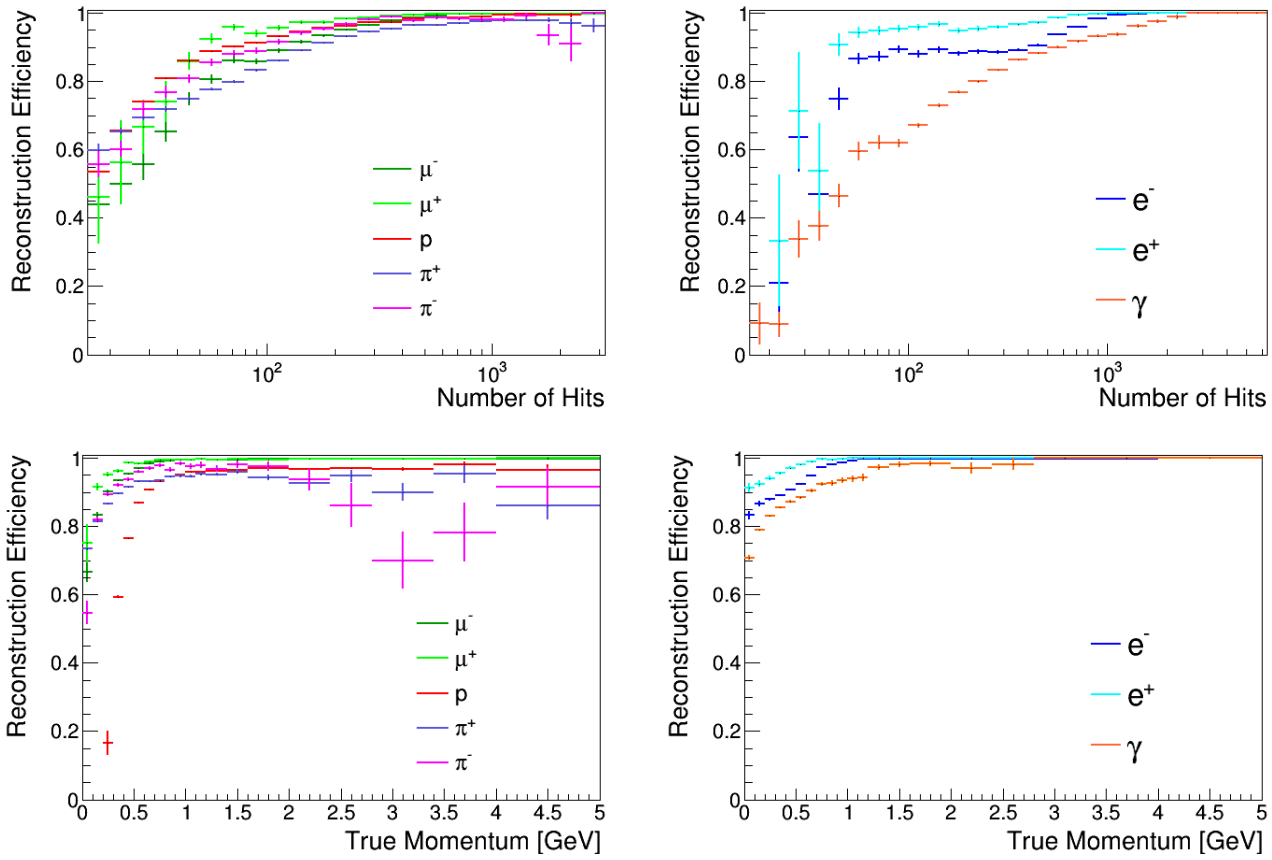

Figure 4.26: The reconstruction efficiency of the Pandora pattern recognition obtained for a range of final-state particles produced in all types of accelerator neutrino interactions except deep inelastic ones at DUNE FD. The efficiency is plotted as a function of the total number of 2D hits associated with the final-state MCParticles (summed across all views) on the top row, and as a function of the true momentum of the particle on the bottom row. Plots are shown for track-like particles (left) and shower-like particles (right) of each type leading in the event.

(left) and CC (middle) deep inelastic interactions. These distributions are more populated in the diagonal, as they should be for perfect 1:1 reconstruction, indicating a good level of reconstruction of such events up to >5 final-state particles. In addition, the number of reconstructed particles matching the leading lepton in CC deep inelastic interactions is also presented (right), which shows a consistently predominant single match for the leading lepton.

Figure 4.29 shows distributions of the displacements Δx, Δy, Δz and $\Delta R^2 = (\Delta x)^2+(\Delta y)^2+(\Delta z)^2$ between the reconstructed and simulated neutrino interaction positions for all types of accelerator neutrino events. It can be seen that, for the vast majority of events, the reconstructed neutrino interaction vertex lies within 2 cm of the MC truth in x, y and z. While the Δx and Δy distributions are both symmetrical and sharply peaked around the origin, a small forward bias can be seen in the Δz distribution. The reason for this bias comes from the fact that the neutrino interaction will be boosted in the forward z direction, so vertex candidates are more likely created at $\Delta z > 0$ than $\Delta z < 0$.

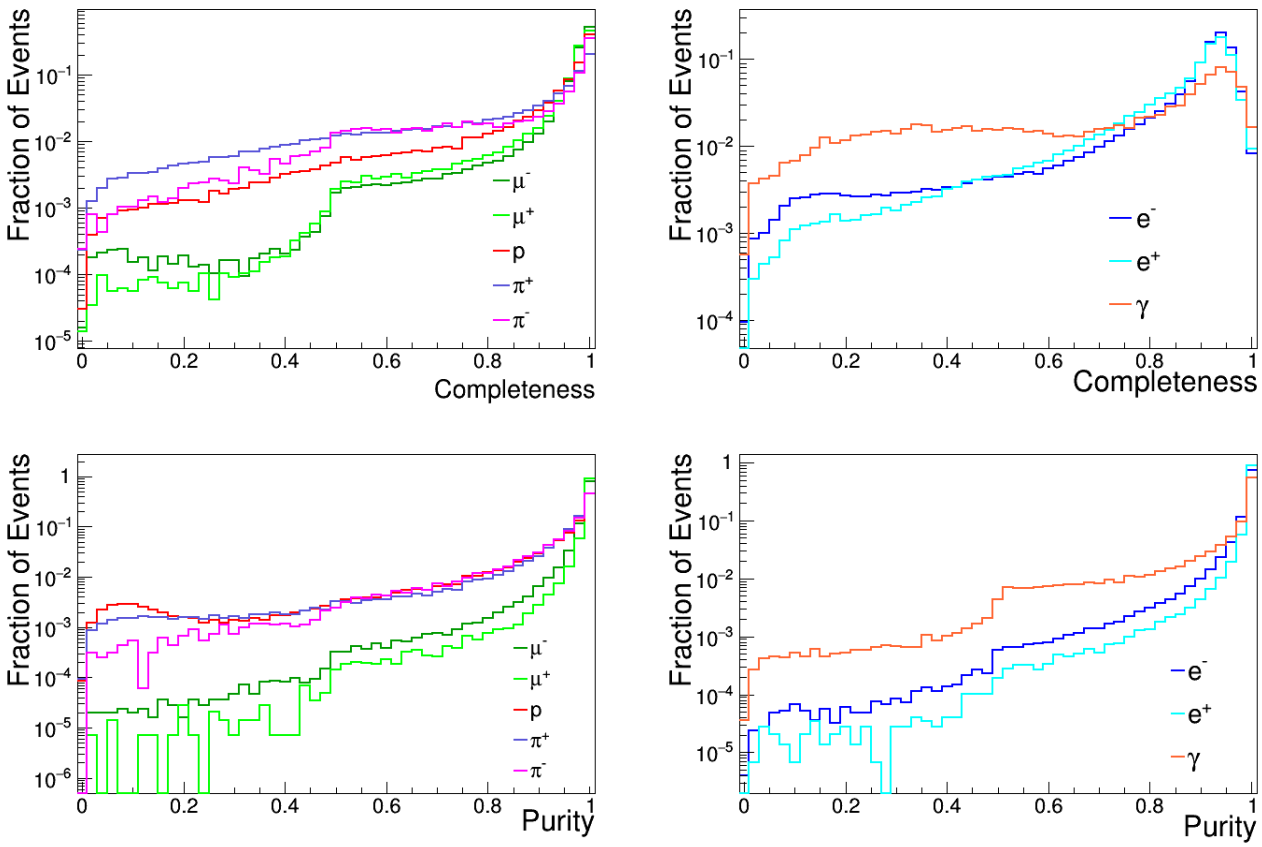

Figure 4.27: Distributions of completenesses (top) and purities (bottom) for a range of final-state particles divided into track-like (left) and shower-like (right), produced in all types of accelerator neutrino interactions except deep inelastic ones at DUNE FD.

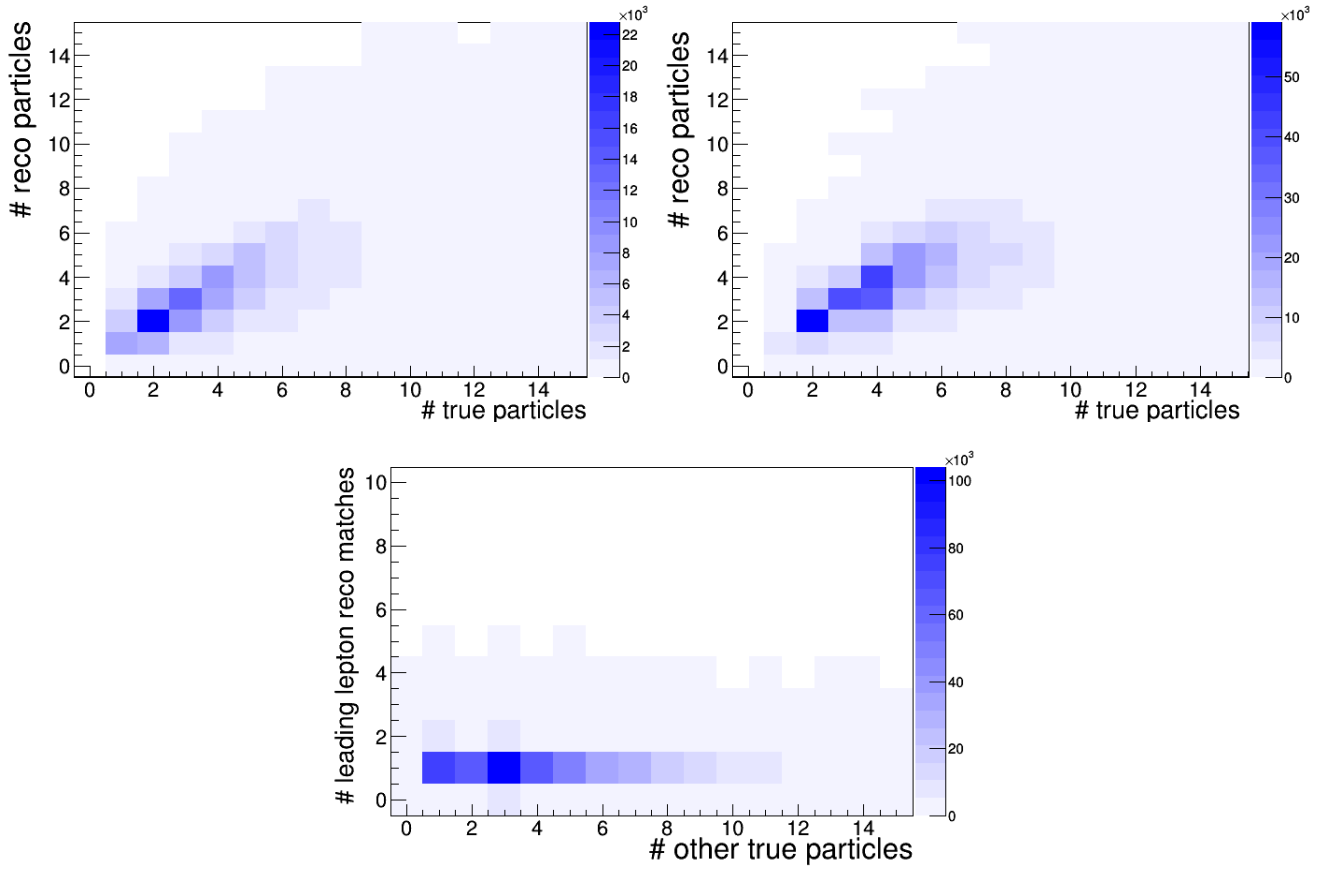

Figure 4.28: Distributions of number of reconstructed particles as a function of number of true final-state particles in deep inelastic events for neutral-current (left) and charged-current (right) interactions. In addition, the number of reconstructed particles matching the leading lepton in charged-current deep inelastic interactions is also presented (bottom).

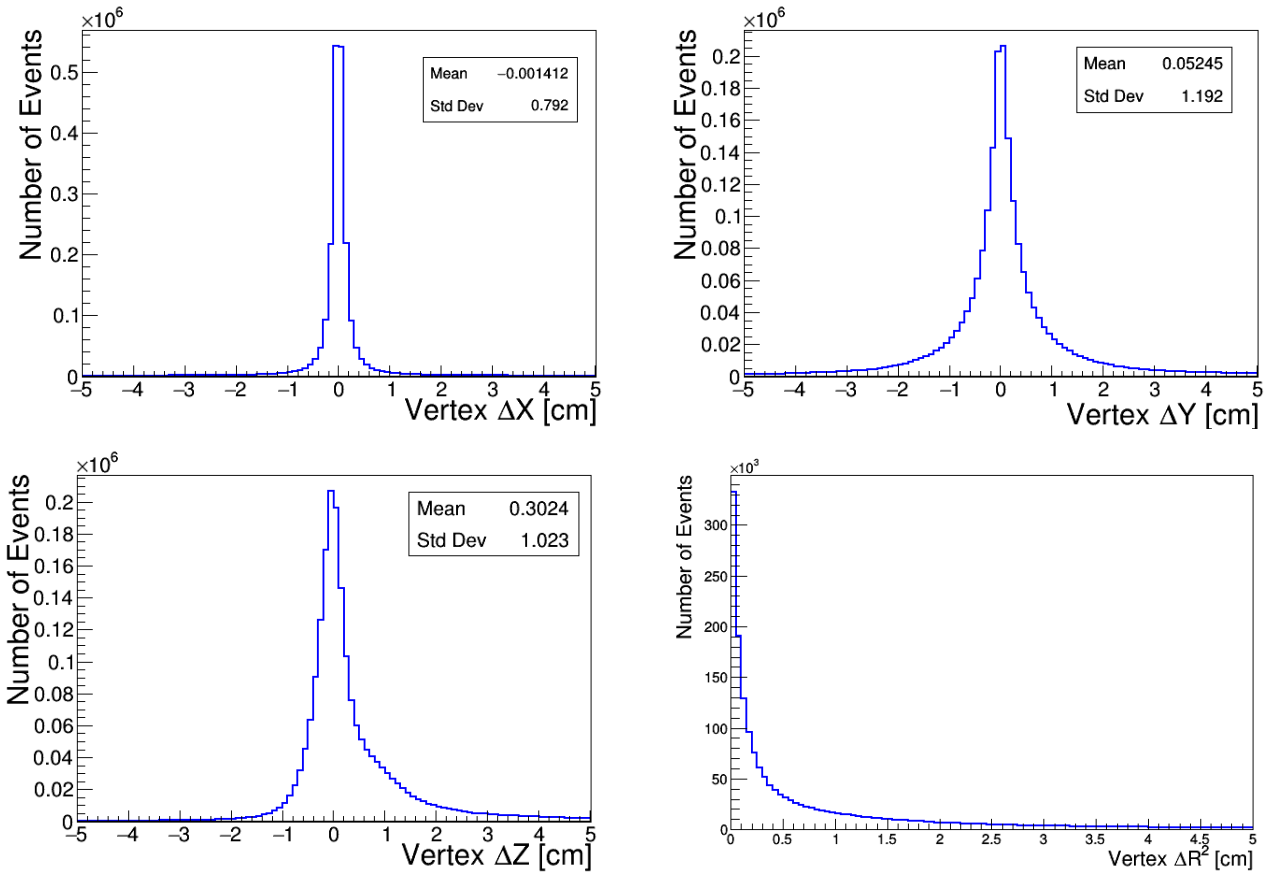

Figure 4.29: The displacements between the reconstructed and simulated neutrino interaction vertices. The distributions are plotted for x (top left), y (top right), z (bottom left) and R^2 (bottom right) and include all types of accelerator neutrino interaction (also deep inelastic events).

4.3.3 Reconstruction Performance in ProtoDUNE-SP

Further examination of the performance of the Pandora pattern recognition is provided through studies of the test-beam data taken by ProtoDUNE-SP. Figure 4.30 shows the reconstruction efficiency for triggered test-beam particles as a function of the momentum recorded by the trigger. The reconstruction efficiency metric folds in many effects, including reconstruction, removal of cosmic-ray background and identification of the reconstructed particle as originating from the test beam. An example of the Pandora reconstruction output for ProtoDUNE MC simulations is shown in Figure 4.31. For high-momenta test-beam particle interactions, a close agreement between the reconstruction efficiency for MC simulations and data is observed in Figure 4.30. At high-momenta, the effect of beam-halo particles in the simulation appears to be overestimated, which results in the marginally lower reconstruction efficiency observed in simulation when comparison to data. For low-momenta test-beam particle interactions, the reconstruction efficiency for data is significantly lower than that see in MC simulations. This is due to particles interacting between the trigger and the LArTPC before reaching its active volume in data.

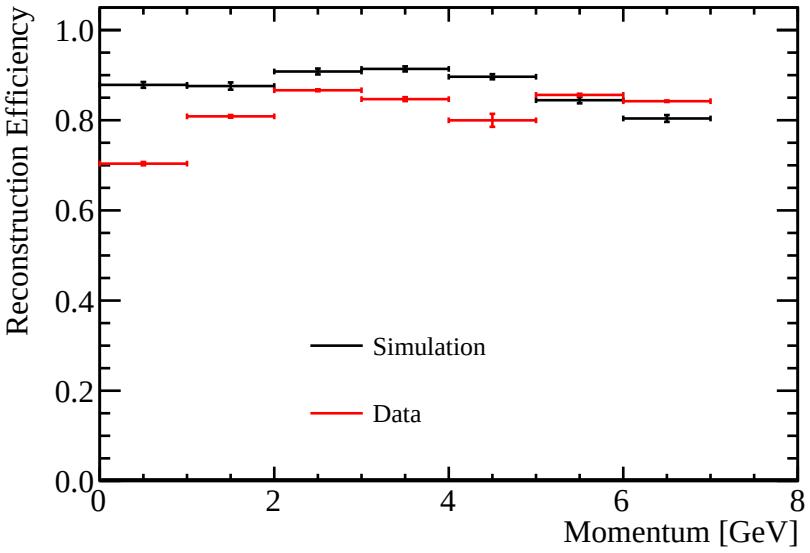

Figure 4.30: The efficiency of reconstruction for the triggered test-beam particle as a function of particle momentum in data (red) and simulation (black).

The effect of cosmic-ray backgrounds and the test beam particle halo on the reconstructed test beam particle efficiency is illustrated in Figure 4.32, where the efficiency is shown as a function of the momentum of the triggered particle (4.32a) and the number of hits produced by the triggered particle (4.32b). These figures indicate that the primary loss mechanisms in the test beam particle reconstruction, accounting for $\approx 70\%$ of all inefficiencies, are due to irreducible cosmic-ray and beam halo backgrounds.

Alongside the test beam particle reconstruction metrics, the Pandora cosmic ray reconstruction has been studied using ProtoDUNE-SP data.

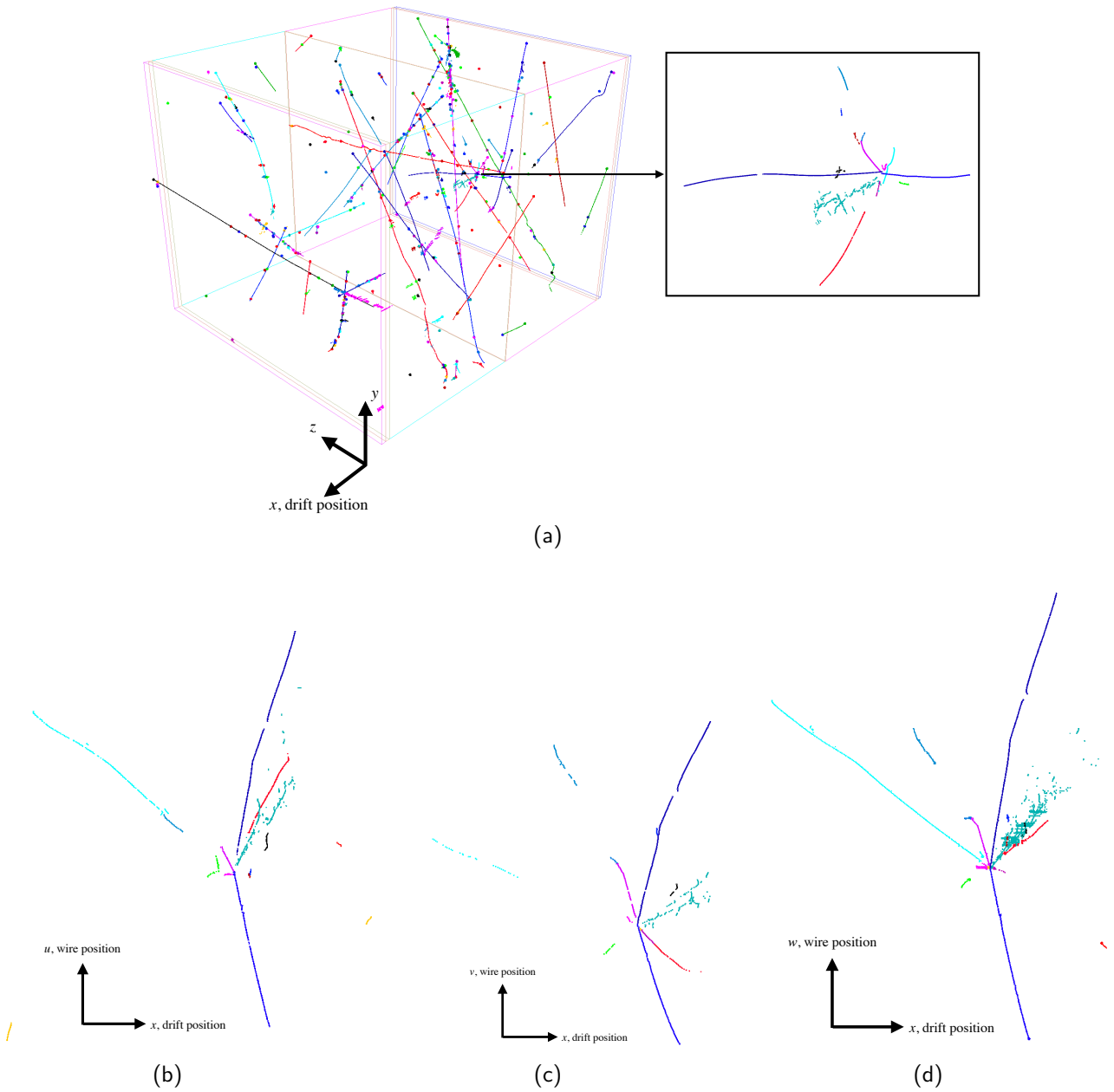

Figure 4.31: An example of the Pandora reconstruction output for a 7 GeV Monte Carlo test beam event. Figure (a) shows the 3D reconstruction output for this event where the correctly reconstructed and tagged triggered test beam particle has been highlighted. Figures (b), (c) and (d) show the 2D hits for the reconstructed test beam particle where each colored cluster of hits represents a different particle in the reconstructed particle hierarchy.

Figure 4.33a shows the number of distinct, i.e. that contain at least 100 hits, reconstructed cosmic rays per event. Both data and MC have a similar average number of cosmic rays per event; 53.17 ± 0.02 for data and 54.34 ± 0.06 for simulation. However, the MC distribution has a larger tail suggesting differences between the cosmic-ray profile in data and that used in simulation. Figure 4.33b shows the number of matched reconstructed cosmic rays per event as a function of the number of "target" reconstructable (as explained in Section 4.3.1) distinct cosmic rays per event for MC simulation, illustrating that the Pandora cosmic ray reconstruction is highly efficient.

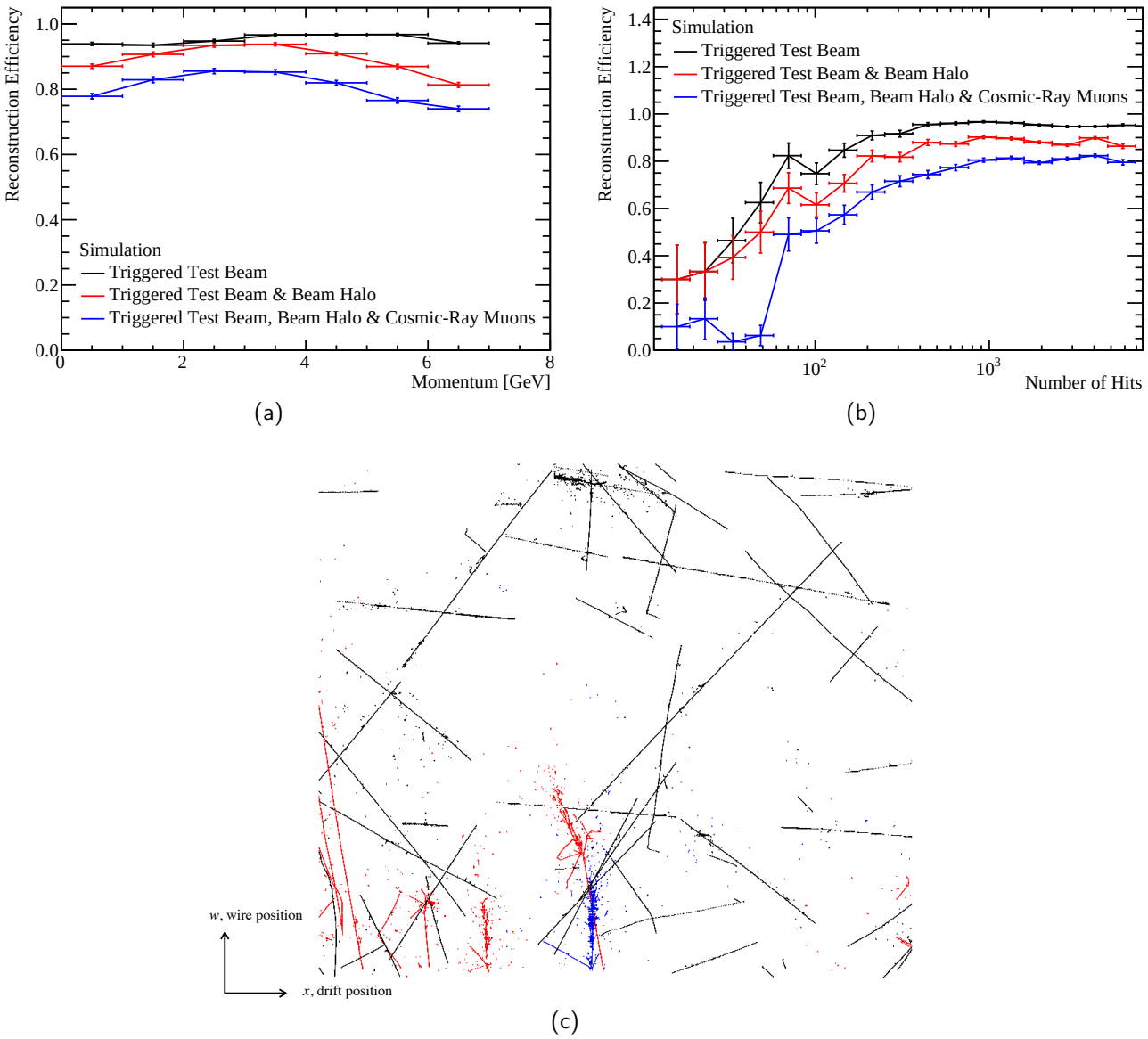

Figure 4.32: The efficiency of reconstruction for the triggered test beam particle in Monte-Carlo as a function of (a) the triggered beam momenta and (b) the number of hits made by the triggered particle. The three curves show the reconstruction efficiency of the triggered test beam particle in isolation (black), with beam particle halo overlaid (red) and with both beam particle halo and cosmic-ray backgrounds overlaid (blue). Figure (c) shows the W plane view for a Monte-Carlo event where the triggered beam particle is shown in blue, the beam halo in red and the cosmic-ray backgrounds in black.

The Pandora reconstruction is also able to tag the true time that a cosmic ray passes through the detector, t_0, should it cross a drift volume boundary, either CPA or APA. This allows us to compare the t_0 distribution for tagged cosmic rays in data and MC, shown in Figure 4.34a. There is excellent agreement between data and MC in this instance. The peak in the data distribution at ≈ 75 ns appears due to channels affected by a known issue with the cold electronics that is now mitigated in the latest reconstruction.

Figure 4.34b shows the resolution on the reconstructed t_0 for MC, which indicates that the Pandora t_0 tagging is precise to the order of microseconds. The shift in the mean of the distribution when applying the space charge effects is due to the effect of bowing of the tracks when space charge is applied. Furthermore, the broadening of the distribution when applying the fluid flow model, in comparison to space charge, is due to the fact that the bowing effect is no longer correlated between tracks in the asymmetric fluid flow model. The size of the space charge effect is computed from simulations and efforts are ongoing to produce a data-driven space charge simulation.

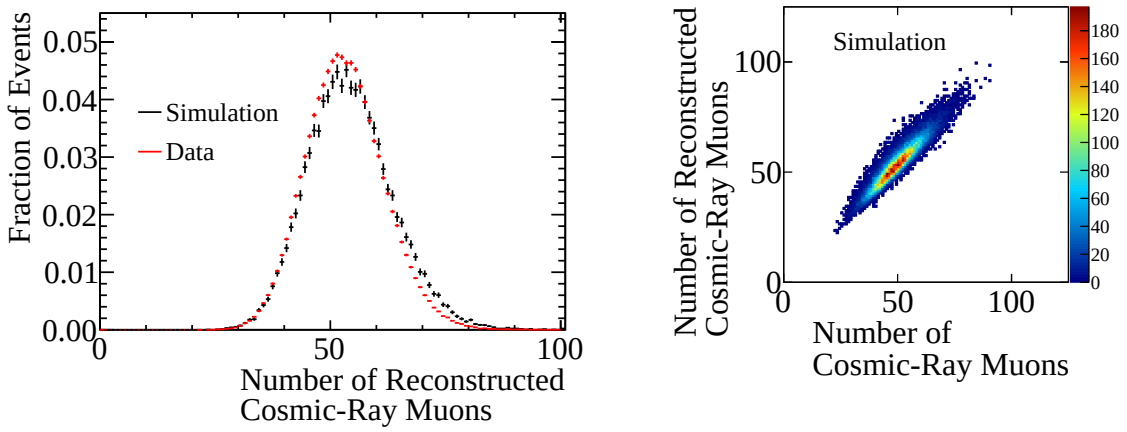

(a) (b)

Figure 4.33: The number of distinct, i.e., containing at least 100 hits, reconstructed cosmic rays per event is shown in figure (a) for data and MC. Figure (b) shows the number of matched reconstructed cosmic rays per event as a function of the true number of reconstructable distinct cosmic rays passing through the detector per event for MC.

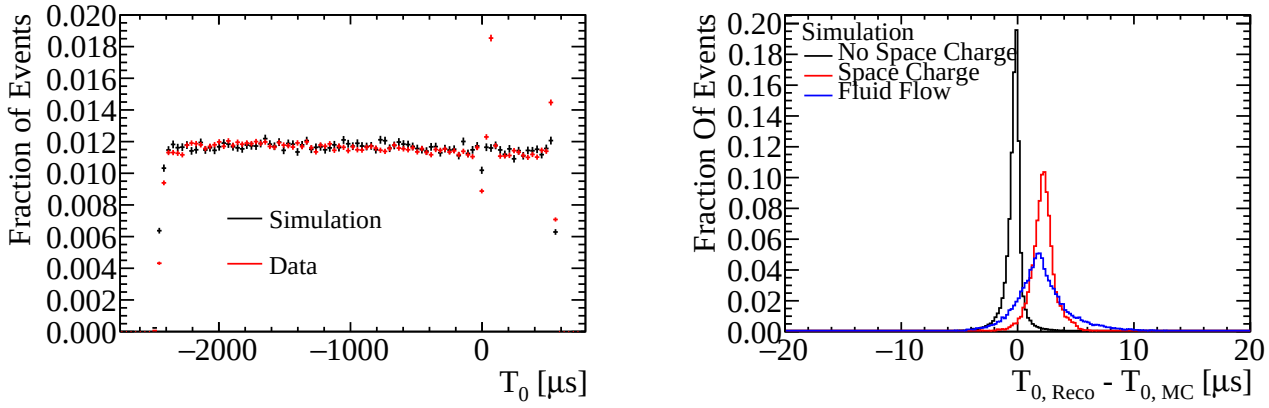

(a) (b)

Figure 4.34: (a) The distribution of the reconstructed t_0 for cosmic rays crossing the CPA in both data and MC. (b) the resolution on the reconstructed t_0 in MC with different space charge effects applied; No space charge (black), space charge (red) and fluid flow (blue).

4.3.4 High-Level Reconstruction

This section presents a series of studies to illustrate the results of current efforts on high-level reconstruction, analyzing different reconstructed quantities for tracks and showers. After the pattern recognition stage provided by Pandora, further fits to the reconstructed 3D particles can be made in order to characterize their properties. For the moment, the results presented here use only the output provided by Pandora, which includes a first pass of high-level reconstruction to build these objects. For tracks, Pandora sliding linear fits are used to calculate the trajectory of the particle, whereas for showers a principal component analysis (principal component analysis (PCA)) is used to estimate directions and opening angles.

The opening angle between the reconstructed and the true 3D direction of tracks and showers is presented in Fig. 4.35 in simulated FD neutrino events[4]. The reconstructed direction of tracks is obtained as the initial momentum of the track, after a Pandora sliding linear fit is performed to its reconstructed 3D points. For showers, the reconstructed direction corresponds to the primary eigenvector result of the PCA fit to its reconstructed 3D points. In both cases, the opening angle is very small, indicating a good agreement between the reconstructed and true direction of the particles. The few cases in which an opening angle of π is obtained are explained by a good reconstruction of the particle (hit clustering) but the particle vertex placed at its wrong end.

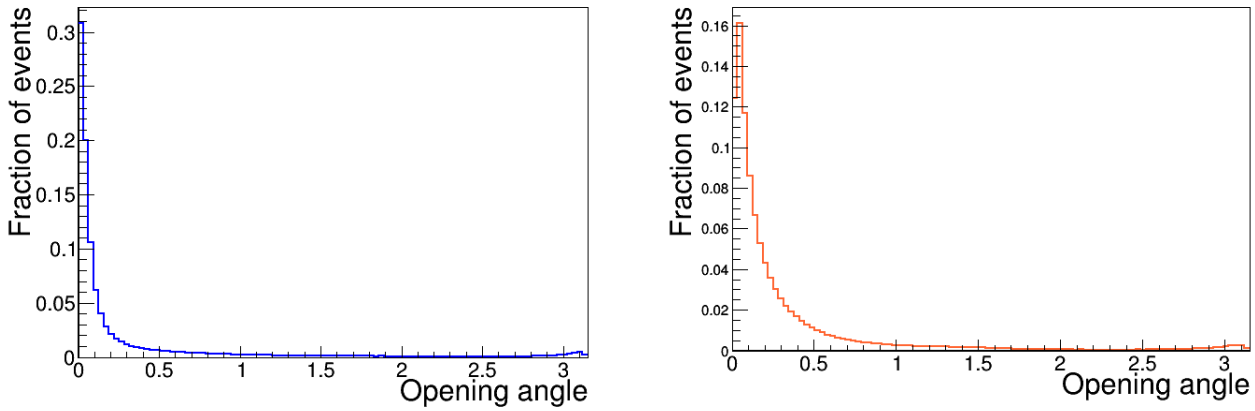

Figure 4.35: Distribution of opening angle (in radians) between reconstructed and true direction for track-like (left) and shower-like (right) particles in simulated FD neutrino events.

For track-like particles, another quantity that can be explored in the high-level reconstruction is the length. Figure 4.36a shows the difference between reconstructed and true particle length (ΔL), computed as the 3D distance between start and end positions, for simulated track-like particles of various types in the FD. The difference in length ΔL clearly depends on the particle type: for example, ∼90% (∼83%) of muons have a ΔL smaller than 10 cm (5cm), whereas for protons (pions) the fraction within 5 cm is ∼78% (∼54%). ΔL depends on the true length of the particle, as shown in Fig. 4.36b, which presents the mean and sigma (as marker and error bar respectively) of the

[4]The distributions in Figs. 4.35 and 4.36 include only good reco-true matches, requiring a minimum of 10% completeness and 50% purity for the match. In addition, Fig. 4.36 is made using only contained tracks, by requiring that both true start and end point are within the fiducial volume.

ΔL distribution in different ranges of true length for different particle types[5]. In general, small values of ΔL can be understood in terms of the efficiency of 3D points creation, and resolution of the vertex reconstruction. Particles presenting kinks due to scattering, such as pions and to a lesser extent protons, have the additional risk of merging parent and daughter particles when the scattering angle is small, increasing the value of ΔL. Short pions are in particular subject to this effect, in addition to merges with other close or overlapping particles in complex topologies, which might translate into larger values of ΔL.

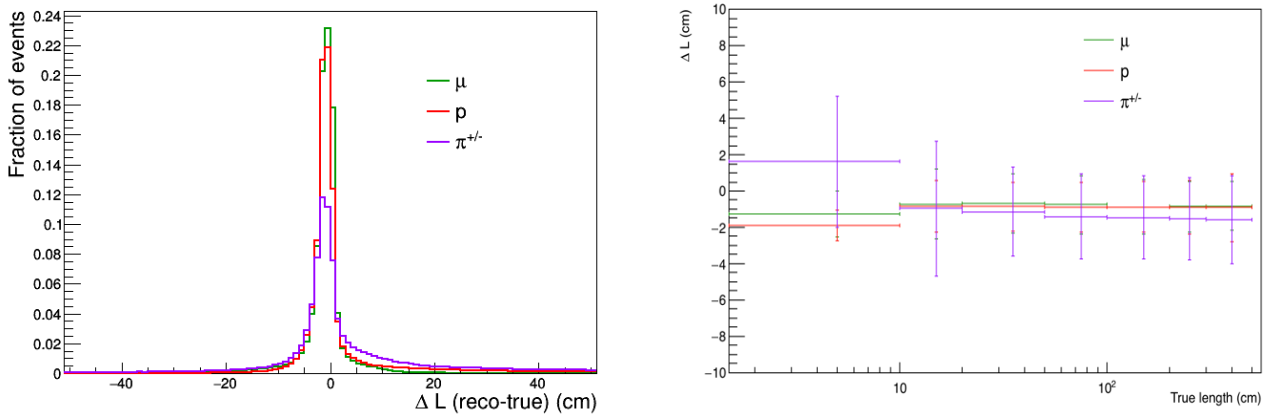

(a) (b)

Figure 4.36: Distribution of reconstructed - true length (3D distance between start and end positions) for different track-like particles (a), and mean and sigma (as marker and error bar respectively) of the ΔL distribution in different ranges of true length(b),

A number of these variables can be also explored in experimental data taken by the ProtoDUNE-SP detector. For example, figure 4.37 presents a measurement of the test beam particle interaction vertex by comparing the end point of the primary test beam particle track and the fitted interaction vertex for ProtoDUNE-SP data and MC events.

Cosmic-ray muons in the ProtoDUNE-SP detector are also used to calibrate the detector nonuniformity and determine the absolute energy scale. Cathode crossing cosmic-ray muons with t_0 information are used to correct for the attenuation effect caused by impurities in the LAr. Stopping cosmic-ray muons are used to determine the calorimetry constants that convert the calibrated ADC counts to the number of electrons so that the dE/dx versus residual range distributions match the expectation, as shown in Figures 4.38a and 4.38b for ProtoDUNE-SP data and MC simulation with space charge effects after calibration. The data dE/dx distribution has better resolution because the purity in data is better than in the simulation.

The same attenuation correction and calorimetry constants are applied to the beam proton data and MC and the resulting dE/dx distributions are shown in Figure 4.39. The data and MC dE/dx distributions agree well. Discrepancy with expectation is observed in the large residual range region, which corresponds to the beam entering point on the TPC front face where space

[5]A Gaussian fit is performed to the ΔL distributions in each range of true length, except the first one (true length $<$ 10cm) which presents a larger tail and its behavior is better represented by a Landau distribution, of which the most probable value is given instead

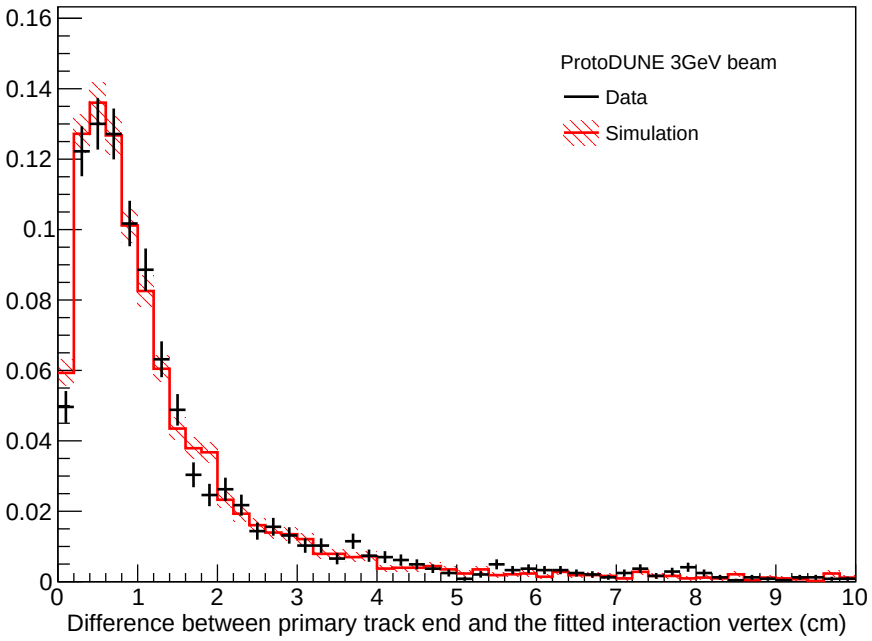

Figure 4.37: Resolution on the test beam particle interaction vertex on ProtoDUNE data and MC events, calculated comparing the end point of the primary test beam particle track and the fitted interaction vertex.

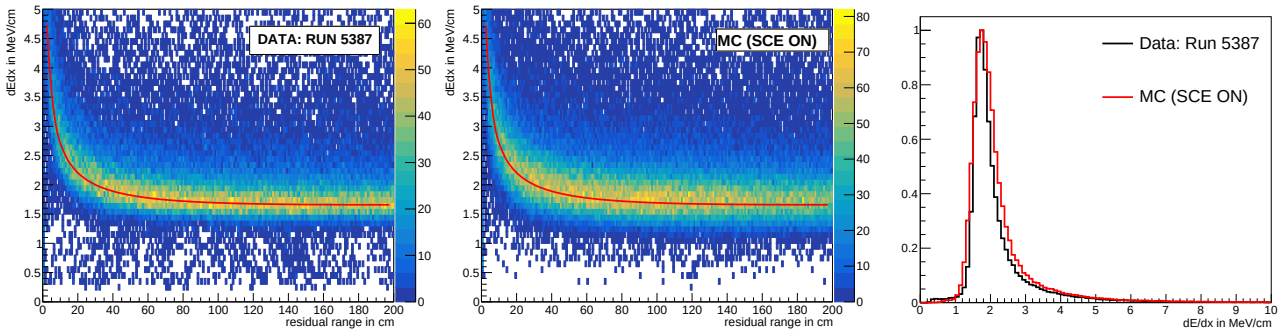

(a) (b) (c)

Figure 4.38: Stopping muon dE/dx distributions for the ProtoDUNE-SP cosmic data and MC. The red curves in (a) and (b) are the expected most probable value of dE/dx versus residual range.

charge effects are large. Good progress is being made on the space charge effects calibration, which will lead to more accurate dE/dx measurements.

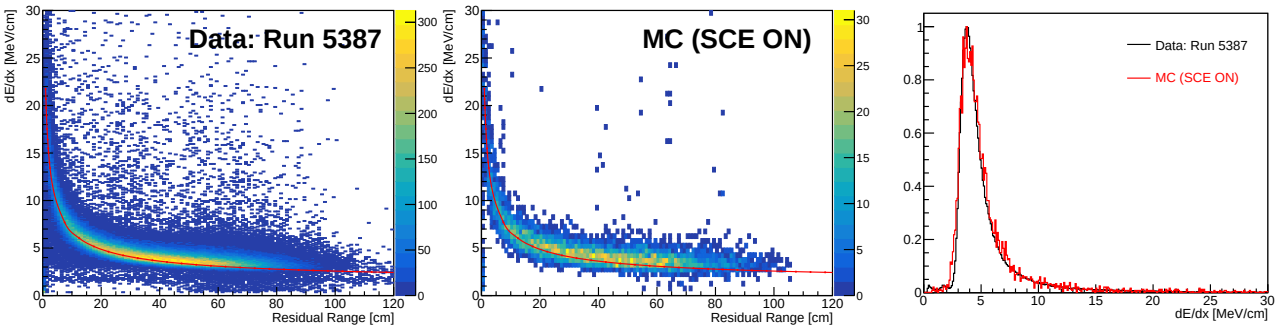

(a) (b) (c)

Figure 4.39: Proton dE/dx distributions for the ProtoDUNE-SP 1 GeV beam data and MC. The red curves in (a) and (b) are the expected most probable value of dE/dx vs residual range.

4.4 DUNE Calibration Strategy

The DUNE FD presents a unique challenge for calibration in many ways. It differs from existing LBL neutrino detectors and existing LArTPCs because of its size – the largest LArTPC ever constructed – but also because of its deep underground location. The DUNE ND, which we expect to include a LArTPC, will also differ from previous experiments (e.g., MINOS and NOvA). In particular, while the ND will be highly capable, pile-up and readout will be different, and this may complicate extrapolation of all relevant detector characteristics.

As for any LArTPC, full exploitation of DUNE's capability for precision tracking and calorimetry requires a detailed understanding of the detector response. The inherently highly convolved detector response model and the strong correlations that exist between various calibration quantities make this challenging. For example, the determination of energy associated with an event of interest will depend on the simulation model, associated calibration parameters, non-trivial correlations between the parameters, and spatial and temporal dependence of those parameters caused by the non-static nature of the FD. Changes can be abrupt (e.g., noise, a broken resistor in the field cage (FC)), or ongoing (e.g., exchange of fluid through volume, ion accumulation).

Convincing physics measurements will require a demonstration that the overall detector response is well understood. The systematic uncertainties for the LBL and low-energy (SNB) program will determine the required precision on dedicated calibration systems. The calibration program must provide measurements at the few-percent-or-better level stably across an enormous volume and over a long period of time, and provide sufficient redundancy.

This section describes the current calibration strategy for DUNE that uses existing sources of particles, external measurements, and dedicated external calibration hardware systems. Existing calibration sources for DUNE include beam or atmospheric neutrino-induced samples, cosmic rays, argon isotopes, and instrumentation devices such as LAr purity and temperature monitors. Dedicated calibration hardware systems currently include laser and pulsed neutron system (PNS). The responsibility of these hardware systems and assessment of alternative calibration system designs fall under the joint single-phase (SP) and dual-phase (DP) calibration consortium. External measurements by ProtoDUNE and SBN will validate techniques, tools and the design of systems applicable to the DUNE calibration program; ProtoDUNE will also perform essential measurements of charged particle interactions in liquid argon (LAr).

Under current assumptions, the calibration strategy described in this document is applicable to both SP modules and DP modules. Section 4.4.1 briefly describes the physics-driven calibration requirements. The nominal Deep Underground Neutrino Experiment (DUNE) FD calibration design is described in Section 4.4.2. Finally, Section 4.4.3 describes a staging plan for calibration from after the TDR through to the operation of the experiment including design validation at ProtoDUNE.

4.4.1 Physics-driven Calibration Requirements

To perform adequate calibrations the physics processes that lead to the formation of the signals required for DUNE's broad physics program, expected (and unexpected) detector effects must be carefully understood, as they ultimately affect the detector's energy, position and particle identification response. Other categories of effects, such as the neutrino interaction model or reconstruction pathologies, can impact measurements of physical quantities. These other effects are beyond the scope of the FD calibration effort and would only lead to a higher overall error budget.

4.4.1.1 LBL physics

Calibration information needs to provide an approximately 1-2% understanding of normalization and position resolution within the detector to support DUNE LBL physics. A bias on the lepton energy has a significant impact on the sensitivity to CPV. A 3% bias in the hadronic state (excluding neutrons) is important, as the inelasticity distribution for neutrinos and antineutrinos is quite different. Different fractions of their energies go into the hadronic state. Finally, while studies largely consider a single, absolute energy scale, DUNE will need to monitor and correct relative spatial differences across the enormous DUNE FD volume; this is also true for time-dependent changes [113].

A number of in situ calibration sources will be required to address these broad range of requirements. Michel electrons, neutral pions and radioactive sources (both intrinsic and external) are needed for calibrating detector response to electromagnetic activity in the tens-to-hundreds of MeV energy range. Stopping protons and muons from cosmic rays or beam interactions form an important calibration source for calorimetric reconstruction and particle identification. ProtoDUNE, as a dedicated test beam experiment, provides important measurements to characterize and validate particle identification strategies in a 1 kt-scale detector and is an essential input to the overall program. Dedicated calibration systems, like lasers, will be useful to provide in situ full-volume measurements of E field distortions. Measuring the strength and uniformity of the E field is a key aspect of calibration, as estimates of calorimetric response and PID depend on the E field through recombination. The stringent physics requirements on energy scale and fiducial volume also put similarly stringent requirements on detector physics quantities such as E field, drift velocity, electron lifetime, and the time dependencies of these quantities; this is discussed in more detail in the dedicated laser system discussion under Section 4.4.2.4.

4.4.1.2 SNB and low-energy neutrino physics

A combination of 6 MeV (direct neutron capture response), 9 MeV (peak visible γ-energy of interest to SNB and ^8B/hep solar neutrinos), 15 MeV (upper visible energy of ^8B/hep solar neutrinos) and $\sim$30 MeV (decay electrons) is needed to map the low energy response. Supernova signal events present specific reconstruction and calibration challenges, and observable energy is shared between different charge clusters and types of energy depositions. In particular, the supernova sig-

nal will have a low-energy electron, gamma and neutron capture component, and each needs to be characterized. As discussed further in Section 7, primary requirements for this physics include (1) calibration of absolute energy scale and energy resolution, which is important for resolving spectral features of SNB events; (2) calibration of time and light yield response of optical photon detectors; (3) absolute timing of events; (4) measurement of trigger efficiency at low energies; and (5) understanding of detector response to radiological backgrounds. Further details on the necessary energy scale, energy resolution and trigger efficiency targets needed can be in Ref [114]. Potential calibration sources in this energy range include Michel electrons from muon decays (successfully utilized by ICARUS and MicroBooNE [115]), which have a well known spectrum up to $\sim 50\,\text{MeV}$. Photons from neutral pion decay (from atmospheric and beam induced π^0) will provide an overall energy scale between 50 MeV and 100 MeV, in addition to cosmic ray muon energy loss. However, the limited statistical power of those samples (see Table 4.2) mean that it is not possible for these samples to provide the energy scale or resolution at the spatial and temporal granularity needed. The pulsed neutron system can provides a source of direct neutron capture across the entire DUNE volume, providing a timing and energy calibration. The proposed radioactive source system provides an in situ source of the electrons and de-excitation γ rays, which are directly relevant for physics signals from SNB or ^8B solar neutrinos. These two systems (discussed in more detail in Section 4.4.2.4) can provide calibrations of photon, electron, and neutron response for energies below 10 MeV, where photons and electrons may have very different characteristics in LAr.

4.4.1.3 Nucleon decay and other exotic physics

The calibration needs for nucleon decay and other exotic physics are comparable to those for the LBL program, as listed in Section 4.4.1.1. Signal channels for light DM and sterile neutrino searches will be NC interactions that are background to the LBL physics program. Based on the widths of dE/dx-based metrics of PID, qualitatively, we need to calibrate dE/dx across all drift and track orientations at the few-percent level, similar to the LBL effort.

4.4.2 Calibration Sources, Systems and External Measurements

Calibration sources and systems provide measurements of the detector response model parameters, or provide tests of the response model itself. Calibration measurements can also provide corrections to data, data-driven efficiencies, systematics and particle responses. Figure 4.40 shows the broad range of categories of measurements that calibrations can provide, and lists important calibration parameters for DUNE's detector response model applicable to both SP or DP. Due to the significant interdependencies of many parameters (e.g., recombination, E field, and LAr purity), a calibration strategy will either need to measure parameters iteratively, or find sources that break these correlations.

Table 4.1 provides a list of the calibration sources and dedicated calibration systems, along with their primary usage, that will comprise the current nominal DUNE FD calibration design. The next sections provide more details on each of them. ProtoDUNE and previous measurements provide independent tests of the response model, indicating that the choice of parameterization

and values correctly reproduces real detector data. Not all of the ex situ measurements can be directly extrapolated to DUNE, however, due to other detector effects and conditions – only those considered to be universal (e.g., argon ionization energy).

Each of the many existing calibration sources comes with its own challenges. For example, while electrons from muon decay (Michel electrons) are very useful for studying the detector response to low-energy electrons (50 MeV), these low-energy electrons present reconstruction challenges due to the loss of charge from radiative photons, as demonstrated in MicroBooNE [115]. Michel electrons are therefore considered an important, independent, and necessary test of the TPC energy response model, but they will not provide a measurement of a particular response parameter.

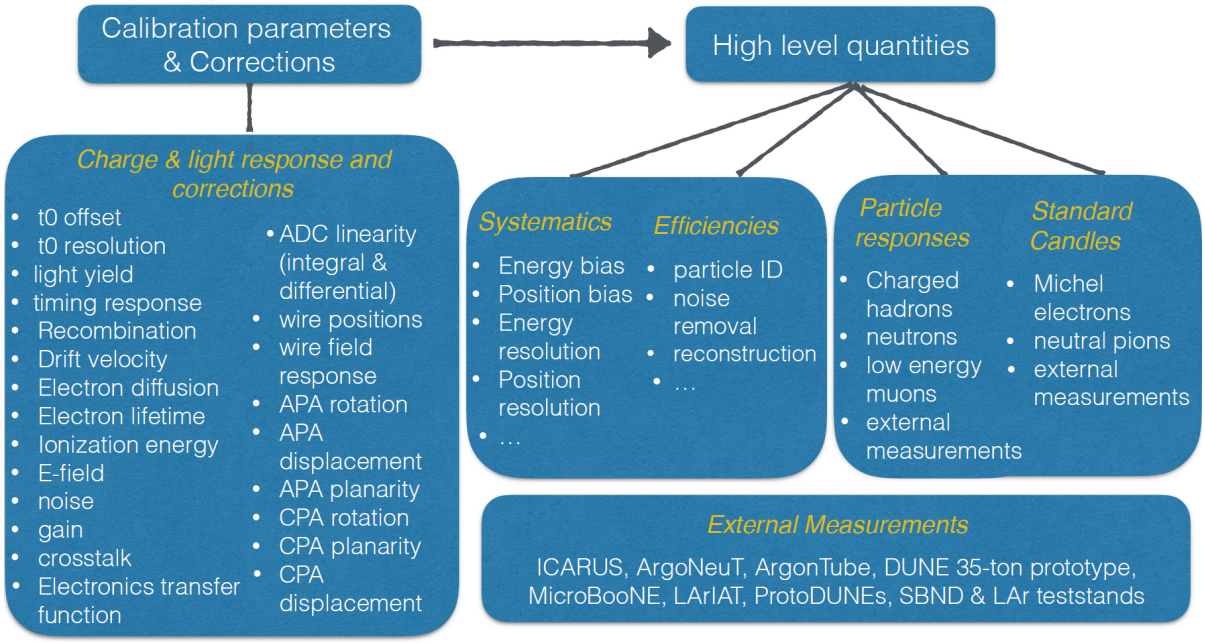

Figure 4.40: Categories of measurements provided by calibration.

4.4.2.1 Existing sources

Cosmic rays and neutrino-induced interactions provide commonly used "standard candles," e.g., electrons from muon decays, and photons from neutral pions, which have characteristic energy spectra. Cosmic ray muons are also used to determine detector element locations (alignment), timing offsets or drift velocity, electron lifetime, and channel-by-channel response, and to help constrain E field distortions. Table 4.2 summarizes the rates for cosmic ray events. Certain measurements (e.g., channel-to-channel gain uniformity and cathode panel alignment) are estimated to take several months of data. Table 6.4 gives the atmospheric ν interaction rates, which are comparable to beam-induced events – neither occurs at sufficient rates to provide meaningful spatial or temporal calibration; they will likely provide supplemental measurements only. (The beam will not yet be operational for calibration of the first detector module during early data taking.) Instead, we can use the reconstructed energy spectrum of ^{39}Ar beta decays to make a precise measurement of electron lifetime with spatial and temporal variations. This can also provide

Table 4.1: Primary calibration systems and sources that comprise the nominal DUNE FD calibration design along with their primary usage.

System	Primary Usage
Existing Sources	**Broad range of measurements**
μ, predominantly from cosmic ray	Position (partial), angle (partial), electron lifetime, wire response, dE/dx calibration etc.
Decay electrons, π^0 from beam, cosmic, atm ν	Test of electromagnetic response model
^{39}Ar beta decays	electron lifetime (x,y,z,t), diffusion, wire response
External Measurements	**Tests of detector model, techniques and systems**
ArgoNeuT [86], ICARUS [87, 116, 117], MicroBooNE	Model parameters (e.g., recombination, diffusion)
DUNE 35 ton prototype [118]	Alignment and *t0* techniques
ArgonTUBE [119], MicroBooNE [120], SBND, ICARUS [121], ProtoDUNE [20]	Test of systems (e.g., Laser)
ArgoNeuT [122], MicroBooNE [123, 124, 125, 115, 126, 86], ICARUS [127, 128, 129], ProtoDUNE	Test of calibration techniques and detector model (e.g., electron lifetime, Michel electrons, ^{39}Ar beta decays)
ProtoDUNE, LArIAT [19], CAPTAIN [130]	Test of particle response models and fluid flow models
LArTPC test stands [131, 132, 133, 88]	Light and LAr properties; signal processing techniques
Monitoring Systems	**Operation, Commissioning and Monitoring**
Purity monitors	Electron lifetime
Photon detection monitoring System	photon detection system (PD system) response
Thermometers	Temperature, velocity; test of fluid flow model
Charge injection	Electronics response
Dedicated Calibration Systems	**Targeted (near) independent, precision calibration**
Direct ionization via laser	Position, angle, electric field (x,y,z,t)
Photoelectric ejection via laser	Position, electric field (partial)
Neutron injection	Test of SNB signal, neutron capture model
Proposed Radioactive source deployment	Test of SNB signal model

other necessary calibrations, such as measurements of wire-to-wire response variations and diffusion measurements using the signal shapes associated with the beta decays. The ^{39}Ar beta decay rate in commercially-provided argon is about $1\,\mathrm{Bq}\cdot\mathrm{kg}^{-1}$, so $O(50\mathrm{k})$ ^{39}Ar beta decays are expected in a single 5 ms event readout in an entire 10 kt detector module. The ^{39}Ar beta decay cutoff energy is 565 keV, which is close to the energy deposited on a single wire by a minimum ionizing particle (MIP). However, several factors can impact the observed charge spectrum from ^{39}Ar beta decays, such as electronics noise, electron lifetime and recombination fluctuations; more details can be found in the Appendix 4.4.4. MicroBooNE [134] and ProtoDUNE are actively pursuing this technique, thus providing valuable inputs for DUNE.

Table 4.2: Annual rates for classes of cosmic-ray events described in this section assuming 100% reconstruction efficiency. Energy, angle, and fiducial requirements have been applied. Rates and geometrical features apply to the single-phase far detector design.

Sample	Annual Rate	Detector Unit
Inclusive	1.3×10^6	Per 10 kt module
Vertical-Gap crossing	3300	Per gap
Horizontal-Gap crossing	3600	Per gap
APA-piercing	2200	Per APA
APA-CPA piercing	1800	Per active APA side
APA-CPA piercing, CPA opposite to APA	360	Per active APA side
Collection-plane wire hits	3300	Per wire
Stopping Muons	28600	Per 10 kt module
π^0 Production	1300	10 kt module

4.4.2.2 Monitors

Chapter 8 of The DUNE Far Detector Single-Phase Technology and The DUNE Far Detector Dual-Phase Technology discuss several instrumentation and detector monitoring devices in detail. These devices, including liquid argon temperature monitors, LAr purity monitors, gaseous argon analyzers, cryogenic (cold) and inspection (warm) cameras, and liquid level monitors, will provide valuable information for early calibrations and for tracking the space-time dependence of the detector modules. The computational fluid dynamics (CFD) simulations play a key role for calibrations initially in the design of the cryogenics recirculation system, and later for physics studies when the cryogenics instrumentation data can be used to validate the simulations. Chapters 4 and 5 of the detector module volumes discuss other instrumentation devices essential for calibration, such as drift high voltage (HV) current monitors and external charge injection systems.

4.4.2.3 External measurements

DUNE will use external measurements from past experimental runs (e.g., ArgoNeuT, the DUNE 35 ton prototype, ICARUS, and LArIAT), from ongoing and future experiments (e.g., MicroBooNE,

ProtoDUNE, and SBND), and from small scale LArTPC test stands. External measurements provide a test bed for dedicated calibration hardware systems and techniques for the FD. In particular, ProtoDUNE will provide validation of the fluid flow model using cryogenic instrumentation data. Early calibration for physics in DUNE will utilize LAr physical properties from ProtoDUNE or SBN for tuning detector response models in simulation. Table 4.1 provides references for specific external measurements. The usability of ^{39}Ar has been demonstrated with MicroBooNE data [134]. Use of ^{39}Ar and other radiological sources and, in particular, the data acquisition (DAQ) readout challenges associated with their use, will be tested on the ProtoDUNE detectors. Dedicated systems for DUNE, including the laser system, have been used by previous experiments (ARGONTUBE [135, 136], CAPTAIN, and MicroBooNE experiments) and at SBND in the future, and will provide more information on use of the system and optimization of the design. The small-scale LAr test stand planned at Brookhaven National Lab, USA, will provide important information on simulation and calibration of field response for DUNE.

External measurements of particle response (e.g. pion interactions in LAr) are also important inputs to the detector model. These include dedicated measurements made with ProtoDUNE, LArIAT, and CAPTAIN [130]; the DUNE ND, with both a LAr and low density gas detector, will also make measurements which characterize the relevant cross sections and outgoing final state particles.

4.4.2.4 Dedicated Calibration Hardware Systems

This section briefly describes the physics motivation and measurement goals for the calibration hardware systems and the designs currently envisioned. The calibration chapters in The DUNE Far Detector Single-Phase Technology and The DUNE Far Detector Dual-Phase Technology of the TDR provide further details on the design and development plan for these systems. We plan to deploy prototype designs of these systems in the phase 2 of ProtoDUNE to demonstrate proof-of-principle.

Laser systems

The primary purpose of a laser system is to provide an independent, fine-grained estimate of the E field in space or time, which is a critical parameter for physics signals as it ultimately impacts the spatial resolution and energy response of the detector. External measurements, e.g., MicroBooNE's, use both a laser system and cosmic rays to estimate the E field, however the expected cosmic rate at the deep underground installation of the FD will not provide sufficient spatial or temporal granularity to study local distortions.

E field distortions can arise from multiple sources. Current simulation studies indicate that positive ion accumulation and drift (space charge) due to ionization sources such as cosmic rays or ^{39}Ar are small in the FD; however, the fluid flow pattern in the FD is not yet sufficiently understood to exclude the possibility of stable eddies that may amplify the effect for both SP and DP modules. The DP module risks significant further amplification due to accumulation in the liquid of ions created by the electron multiplication process in the gas phase. Detector imperfections can also cause localized E field distortions. Examples include FC resistor failures, non-uniform resistivity

in the voltage dividers, CPA misalignment, CPA structural deformations, and APA and CPA offsets and deviations from flatness. Individual E field distortions may add in quadrature with other effects, and can reach 4-5% under certain conditions, which corresponds to a 1-2% impact on charge, and a $\sim$ 2 cm impact on position (and fiducial volume). Both charge and position distortions affect energy scale. Understanding all these effects requires an in situ calibration of the E field with a precision of about 1% with a coverage of at least 75% of the detector volume.

The laser calibration system offers secondary uses, e.g., alignment (especially modes that are weakly constrained by cosmic rays, see Figure 4.41), stability monitoring, and diagnosing detector failures in systems such as HV.

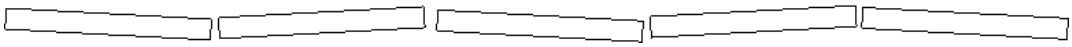

Figure 4.41: An example of a distortion that may be difficult to detect with cosmic rays. The APA frames are shown as rotated rectangles, as viewed from the top.

Two systems are under consideration to extract the E field map: photoelectrons from the LArTPC cathode and direct ionization of the LAr, both driven by a 266 nm laser. The reference design from MicroBooNE [137] and SBND uses direct ionization laser light with multiple laser paths. This can provide field map information in (x, y, z, t); a photoelectron laser only provides an integrated measurement of the E field along the drift direction. The ionization-based system can characterize the E field with fewer dependencies compared to other systems. If two laser tracks enter the same spatial voxel in a detector module, the relative position of the tracks provides an estimate of the local 3D E field. The deviation from straightness of single "laser tracks" can also be used to constrain local E fields. Comparison of the known laser track path against the path reconstructed from cosmic or beam data, assuming uniform E field, can also be used to estimate local E field distortions. A schematic of the ionization laser setup and a laser track from MicroBooNE is shown in Figure 4.42.

A photoelectron-based calibration system was used in the T2K gaseous (predominantly Ar), TPCs [139]. Thin metal surfaces placed at surveyed positions on the cathode provided point-like and line sources of photoelectrons when illuminated by a laser. The T2K photoelectron system provided measurements of adjacent electronics modules' relative timing response, drift velocity with a few ns resolution over their 870 mm drift distance, electronics gain, transverse diffusion, and an integrated measurement of the E field along the drift direction. DUNE would use the system similarly to diagnose electronics or TPC response issues on demand, and to provide an integral field measurement across drift as well as measure relative distortions of y, z positions with time, x and/or drift velocity. MicroBooNE has also observed ejection of photoelectrons from the cathode using the direct ionization laser system.

Pulsed neutron source

An external neutron generator system would provide a triggered, well defined energy deposition from neutron capture in ^{40}Ar detectable throughout the detector module volume. Neutron capture is a critical component of signal processes for SNB and LBL physics; this system would enable direct testing of the detector response spatially and temporally for the low-energy program. This is important to measure energy scale, energy resolution and detection threshold spatially and temporally across the enormous DUNE volume.

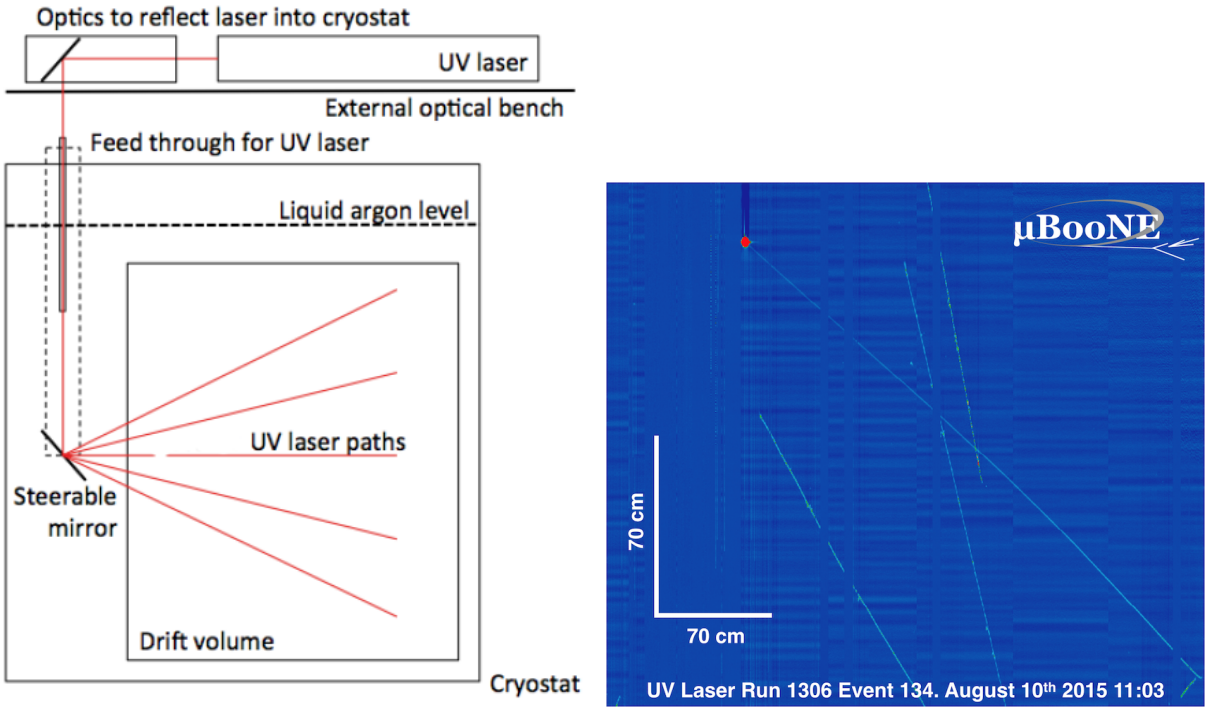

Figure 4.42: Left: Schematics of the ionization laser system in MicroBooNE [138]. Right: A UV laser event in the MicroBooNE detector [137]. The laser track can be identified by the endpoint on the cathode (larger charge visible at the top of the image) and the absence of charge fluctuations along the track. The charge released at the cathode comes from photoelectric effect. Other tracks seen in the display are from cosmic muons.

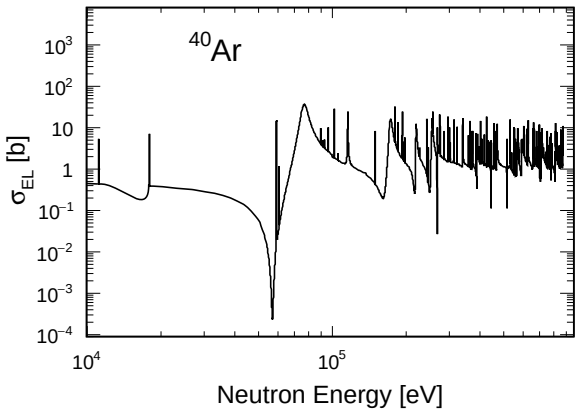

Figure 4.43: Illustration of interference anti-resonance dip in the cross section of ^{40}Ar. Elastic scattering cross section data is obtained from ENDF VIII.0

A triggered pulse of neutrons can be generated outside the TPC and injected into the LAr, where it spreads through the entire volume to produce a mono-energetic cascade of photons via the ^{40}Ar(n,γ)^{41}Ar capture process. The uniform population of neutrons throughout the detector module volume exploits a remarkable property of argon – the near transparency to neutrons of energy near 57 keV. This is due to a deep minimum in the cross section caused by the destructive interference between two high-level states of the ^{40}Ar nucleus (see Fig. 4.43). This cross section "anti-resonance" is approximately 10 keV wide, and 57 keV neutrons consequently have a scattering length of 859 m; the scattering length averaged over the isotopic abundance in natural Ar is approximately 30 m. For neutrons moderated to this energy the DUNE LArTPC is essentially transparent. The 57 keV neutrons that do scatter quickly leave the anti-resonance and thermalize, at which time they capture. Each neutron capture releases exactly the binding energy difference between ^{40}Ar and ^{41}Ar, about 6.1 MeV, in the form of gamma rays. The neutron capture cross-section and the γ spectrum have been measured and characterized. Recently, the ACED Collaboration performed a neutron capture experiment using the Detector for Advanced Neutron Capture Experiments at DANCE (ACED) at the Los Alamos Neutron Science Center (LANSCE). The result of neutron capture cross-section was published [140] and will be used to prepare a database for the neutron capture studies. The data analysis of the energy spectrum of correlated gamma cascades from neutron captures is underway.

DUNE plans to place a fixed, shielded deuterium-deuterium (DD) neutron generator above a penetration in the hydrogenous insulation of the detector module cryostat. Between the generator and the cryostat, layers of water or plastic and intermediate fillers would provide sufficient degradation of the neutron energy.

Additional Systems

There are additional systems under consideration for DUNE calibration. Radioactive source deployment provides an in situ source of low energy electrons and de-excitation gamma rays at a known location and with a known activity, which are directly relevant for detection of SNB or ^{8}B solar neutrinos. As shown in Section 7, the electron and photon response in the TPC is quite different (electrons leave worm-like tracks, photons leave 'blips'). The PNS source will provide a 6.1 MeV multi-photon signal; radioactive sources can provide a single photon signal to measure detection threshold and demonstrate sufficient uncertainty on energy resolution at the peak of the SNB photon signal. The radioactive source system is under study, and feasibility and safety of deployment would be established with a dedicated run using a prototype system in ProtoDUNE.

The utility of internal source injection (e.g., ^{222}Rn or ^{220}Rn injection) for mapping electron lifetime and fluid flow in the time projection chamber (TPC), used in dark matter experiments, will also be considered in the future. The major challenge for this system is if the coverage of the PD system is sufficient, and whether or not it will be able to identify a signal and trigger over the massive amount of ^{39}Ar present. Recognizing that the presence of radioactive impurities can also impact such a system, the newly formed DUNE FD Background Task Force will address this concern. This system would not require any cryostat penetrations or affect major DAQ requirements.

4.4.3 Calibration Staging Plan

The calibration strategy for DUNE will need to address the evolving operational and physics needs at every stage of the experiment in a timely manner using the primary sources and systems listed in Table 4.1. Here we describe the validation plan for calibration systems at ProtoDUNE and a staging plan to deploy calibration systems during different phases of the experiment: commissioning, early data taking, and stable operations.

This TDR presents the baseline calibration systems and strategy. Post-TDR, once the calibration strategy is set, the calibration consortium will need to develop the necessary designs for calibration hardware along with tools and methods to be used with various calibration sources. To allow for flexibility in this process, the physical interfaces for calibration such as flanges or ports on the cryostat will be designed to accommodate the calibration hardware. As described in the calibration SP detector volume, the calibration task force has provided the necessary feedthrough penetration design for the SP module and will soon finalize the design for the DP module. As DUNE physics turns on at different rates and times, a calibration strategy at each stage for physics and data taking is required. The strategy described in this section assumes that all systems are commissioned and deployed according to the nominal DUNE run plan.

Design Validation: A second run of ProtoDUNE will be used to validate the designs of dedicated calibration systems, including the laser, PNS, and possibly the proposed radioactive source. In addition, ProtoDUNE data (and the SBN program) will provide data analysis techniques, tools, and detector model simulation improvements in advance of DUNE operation.

Commissioning: When a detector module is filled, data from various instrumentation devices validate the argon fluid flow model and purification system. Once filled and at the desired high voltage, the detector module immediately becomes live for SNB and proton decay signals (beam and atmospheric neutrino physics will require a few years of data accumulation) at which point it is critical that early calibration track the space-time dependence of the detector. Noise data and pulser data (taken with signal calibration pulses injected into the electronics) are needed to understand the TPC electronics response. Essential systems at this stage include temperature monitors, purity monitors, HV monitors, robust FE charge injection system for cold electronics, and a PD system monitoring system. In addition, as the ^{39}Ar data is available immediately, DUNE must be ready (in terms of reconstruction tools and methods) to utilize ^{39}Ar decays for understanding both low-energy response and space-time uniformity. Dedicated calibration systems as listed in Table 4.1 are deployed and commissioned at this stage. Commissioning data from these systems must verify the expected configuration for each system and identify any needed adjustments to tune for data taking.

Early data taking: Since DUNE will not yet have all in situ measurements of LAr physical properties at this stage, early calibration of the detector will use LAr measurements from ProtoDUNE or SBN, and E fields from calculations tuned to measured HV values. This early data will most likely need to be recalibrated at a later stage with dedicated calibration runs when in situ measurements are available and as data taking progresses. The early physics will also require analysis of cosmic ray muon data to develop methods and tools for muon reconstruction from MeV to TeV and a well validated cosmic ray event generator with data. Dedicated early calibration runs using calibration

hardware systems will develop and tune calibration tools to beam data taking and correct for any space-time irregularities observed in the TPC. Given the expected low rate of cosmic ray events at the underground location (see Section 4.4.2), calibration with cosmic rays is not possible over short time scales and will proceed from coarse-grained to fine-grained over the course of years, as statistics accumulate. The experiment will rely on calibration hardware systems, such as a laser system, for calibrations that require an independent probe with reduced or removed interdependencies, fine-grained measurements (both in space and time), and detector stability monitoring on the time scales required by physics. Some measurements are simply not possible with cosmic rays (e.g., APA flatness, global alignment of all APAs).

Stable operations: Once the detector is running stably, dedicated calibration runs, ideally before, during and after each run period, will ensure that detector conditions have not significantly changed. As statistics accumulate, DUNE can use standard-candle data samples (e.g., Michel electrons and neutral pions) from cosmic rays and beam-induced and atmospheric neutrinos to validate and improve the detector response models needed for precision physics. As DUNE becomes systematics-limited, dedicated precision-calibration campaigns using the calibration hardware systems will become crucial for meeting the stringent physics requirements on energy scale reconstruction and detector resolution. For example, understanding electromagnetic (EM) response in the FD will require both cosmic rays and external systems. The very high energy muons from cosmic rays at that depth that initiate EM showers (which would be rare at ProtoDUNE or SBND), will provide information to study EM response at high energies. External systems such as the pulsed neutron source system or the proposed radioactive source system will provide low energy EM response at the precision required for low energy supernovae physics. Dedicated measurements of charged hadron interactions, initially in ProtoDUNE and later with DUNE ND will also be important in this phase.

4.4.4 ^{39}Ar beta decays

Assuming the ^{39}Ar beta decays are uniformly distributed in the drift direction, one is able to precisely determine the expected reconstructed energy spectrum provided a given set of well measured detector response parameters. This can be done independently of using timing information (e.g. from prompt scintillation light).

A number of factors can impact accurately measuring the end point energy, including noise, wire response, electron lifetime, recombination (and electric field), cosmogenic activity, and other radiological backgrounds. Many of the detector effects may be determined in-situ. For instance, measuring the electronics response can be done in situ with pulser data (charge injection on the front-end ASICs); measuring the wire field response can be done with cosmic tracks and other dedicated measurements ex-situ. There are also plans to measure recombination parameters ex-situ (e.g. ProtoDUNE, MicroBooNE). Figure 4.44 illustrates the different possible reconstructed ^{39}Ar beta decay electron energy spectra one might see in the SP DUNE far detector after correcting for all other detector effects except for electron lifetime. Also shown in Figure 4.44 is the impact of varying the recombination model. The impact on the reconstructed energy spectrum is very different for the two detector effects, allowing for simultaneous determination of both quantities.

This method is one foreseeable way to obtain a fine-grained (spatially and temporally) electron lifetime measurement in the DUNE FD. It can also provide other necessary calibrations, such as measurements of wire-to-wire response variations and diffusion measurements, and could serve as an online monitor of E field distortions in the detector by looking at the relative number of decays near the edges of the detector.

One important consideration is whether or not the DUNE DAQ can provide the necessary rate and type of data to successfully carry out this calibration at the desired frequency and level of spatial precision. Knowing that the ^{39}Ar beta decay rate is about 1 Bq/kg in natural (atmospheric) argon, one finds that $O(50\text{k})$ ^{39}Ar beta decays are expected in a single 5 ms event readout in an entire 10 kt module. From studies at MicroBooNE, $O(250\text{k})$ will be needed for percent-level calibration of electron lifetime which means that for DUNE one would only need roughly five readout events in order to make a single measurement. However, to allow for the electron lifetime to spatially vary throughout the entire 10 kt module, it may be necessary to collect much more data in order to obtain a precise electron lifetime measurement throughout the detector. Studies of data rates and alternative methods for recording special ^{39}Ar calibration data are currently in progress.

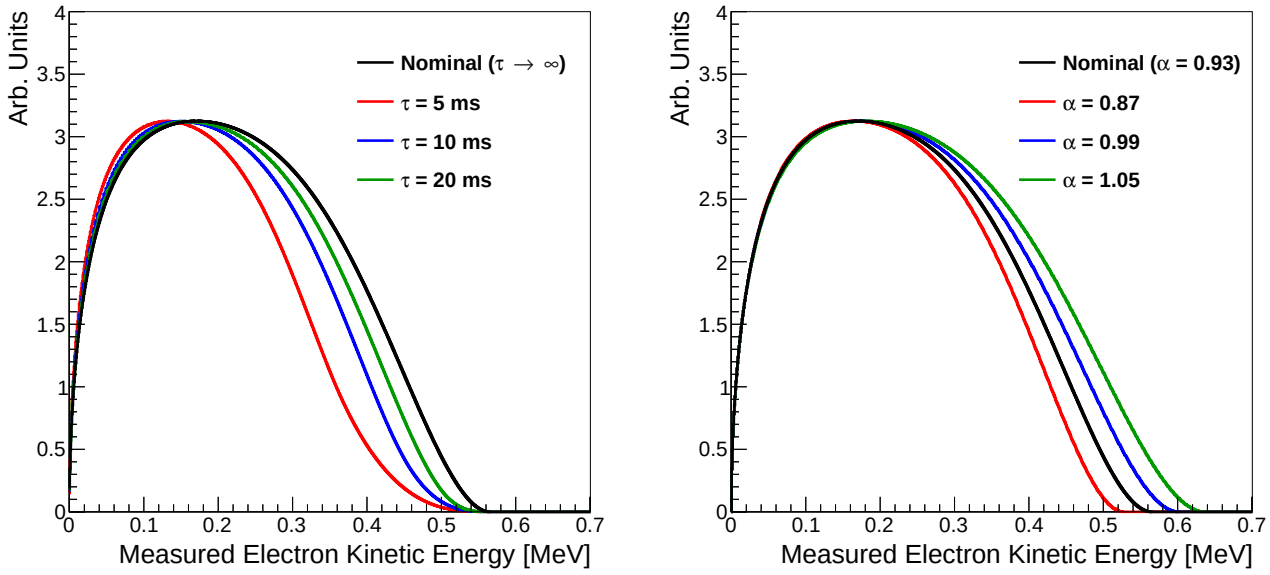

Figure 4.44: Illustration of the impact of different detector effects on the reconstructed ^{39}Ar beta decay electron energy spectrum for decays observed in the SP DUNE far detector. On the left are examples of the reconstructed energy spectrum for various different electron lifetimes, as well as the nominal ^{39}Ar beta decay spectrum (corresponding to an infinite electron lifetime). On the right are examples of the reconstructed energy spectrum when the true recombination model is different from the one assumed in energy reconstruction (varying the α parameter of the modified Box model, $\mathcal{R} = \ln(\alpha+\xi)/\xi$, where $\xi = \beta\frac{dE}{dx}/\rho E_{\text{drift}}$ and with fixed $\beta = 0.212$) and the electron lifetime is infinite. All curves have been normalized to have the same maximal value.

Chapter 5

Standard neutrino oscillation physics program

5.1 Overview and Theoretical Context

The standard model (SM) of particle physics presents a remarkably accurate description of the elementary particles and their interactions. However, its limitations pose deeper questions about Nature. With the discovery of the Higgs boson at the European Organization for Nuclear Research (CERN), the Standard Model would be "complete" except for the discovery of neutrino mixing, which indicates neutrinos have a very small but nonzero mass. In the SM, the simple Higgs mechanism is responsible for both quark and charged lepton masses, quark mixing and charge-parity symmetry violation (CPV). However, the small size of neutrino masses and their relatively large mixing bears little resemblance to quark masses and mixing, suggesting that different physics – and possibly different mass scales – in the two sectors may be present, thus motivating precision study of mixing and CPV in the lepton sector of the SM.

The Deep Underground Neutrino Experiment (DUNE) plans to pursue a detailed study of neutrino mixing, resolve the neutrino mass ordering, and search for CPV in the lepton sector by studying the oscillation patterns of high-intensity ν_μ and $\bar{\nu}_\mu$ beams measured over a long baseline. Neutrino oscillation arises from mixing between the flavor (ν_e, ν_μ, ν_τ) and mass (ν_1, ν_2, ν_3) eigenstates of neutrinos. In direct correspondence with mixing in the quark sector, the transformation between basis states is expressed in the form of a complex unitary matrix, known as the Pontecorvo-Maki-Nakagawa-Sakata (PMNS) matrix:

$$\begin{pmatrix} \nu_e \\ \nu_\mu \\ \nu_\tau \end{pmatrix} = \underbrace{\begin{pmatrix} U_{e1} & U_{e2} & U_{e3} \\ U_{\mu 1} & U_{\mu 2} & U_{\mu 3} \\ U_{\tau 1} & U_{\tau 2} & U_{\tau 3} \end{pmatrix}}_{U_{\mathrm{PMNS}}} \begin{pmatrix} \nu_1 \\ \nu_2 \\ \nu_3 \end{pmatrix}. \tag{5.1}$$

The PMNS matrix in full generality depends on just three mixing angles and a charge parity (CP)-violating phase[1]. The mixing angles and phase are designated as (θ_{12}, θ_{23}, θ_{13}) and δ_{CP}.

[1] In the case of Majorana neutrinos, there are two additional CP phases, but they are unobservable in the oscillation

This matrix can be expressed as the product of three two-flavor mixing matrices as follows [141], where $c_{\alpha\beta} = \cos\theta_{\alpha\beta}$ and $s_{\alpha\beta} = \sin\theta_{\alpha\beta}$:

$$U_{\mathrm{PMNS}} = \underbrace{\begin{pmatrix} 1 & 0 & 0 \\ 0 & c_{23} & s_{23} \\ 0 & -s_{23} & c_{23} \end{pmatrix}}_{\mathrm{I}} \underbrace{\begin{pmatrix} c_{13} & 0 & e^{-i\delta_{\mathrm{CP}}} s_{13} \\ 0 & 1 & 0 \\ -e^{i\delta_{\mathrm{CP}}} s_{13} & 0 & c_{13} \end{pmatrix}}_{\mathrm{II}} \underbrace{\begin{pmatrix} c_{12} & s_{12} & 0 \\ -s_{12} & c_{12} & 0 \\ 0 & 0 & 1 \end{pmatrix}}_{\mathrm{III}}. \tag{5.2}$$

The parameters of the PMNS matrix determine the probability amplitudes of the neutrino oscillation phenomena that arise from mixing. The frequency of neutrino oscillation depends on the difference in the squares of the neutrino masses, $\Delta m^2_{ij} \equiv m^2_i - m^2_j$; a set of three neutrino mass states implies two independent mass-squared differences (the "solar" mass splitting, Δm^2_{21}, and the "atmospheric" mass splitting, Δm^2_{31}), where $\Delta m^2_{31} = \Delta m^2_{32} + \Delta m^2_{21}$. The use of numbers to label the neutrino mass states is arbitrary; by convention, the numbering is defined such that the solar mass splitting is positive, in accordance to the ordering determined from solar matter effects. This leaves two possibilities for the ordering of the mass states, known as the *neutrino mass ordering* or *neutrino mass hierarchy*. An ordering of $m_1 < m_2 < m_3$ is known as the *normal ordering* since it matches the mass ordering of the charged leptons in the SM, whereas an ordering of $m_3 < m_1 < m_2$ is referred to as the *inverted ordering*.

The entire complement of neutrino experiments to date has measured five of the mixing parameters [2, 142, 143]: the three angles θ_{12}, θ_{23}, and θ_{13}, and the two mass differences Δm^2_{21} and Δm^2_{31}. The neutrino mass ordering (i.e., the sign of Δm^2_{31}) is unknown. The values of θ_{12} and θ_{23} are large, while θ_{13} is smaller. The value of δ_{CP} is not well known, though neutrino oscillation data are beginning to provide some information on its value. The absolute values of the entries of the PMNS matrix, which contains information on the strength of flavor-changing weak decays in the lepton sector, can be expressed in approximate form as

$$|U_{\mathrm{PMNS}}| \sim \begin{pmatrix} 0.8 & 0.5 & 0.1 \\ 0.5 & 0.6 & 0.7 \\ 0.3 & 0.6 & 0.7 \end{pmatrix}, \tag{5.3}$$

using values for the mixing angles given in Table 5.1. While the three-flavor-mixing scenario for neutrinos is now well established, the mixing parameters are not known to the same precision as are those in the corresponding quark sector, and several important quantities, including the value of δ_{CP} and the sign of the large mass splitting, are still undetermined.

The oscillation probability of $\nu_\mu \to \nu_e$ through matter in a constant density approximation is, to

processes.

first order [144]:

$$
\begin{aligned}
P(\nu_\mu \to \nu_e) \;\simeq\; & \sin^2\theta_{23}\sin^2 2\theta_{13}\frac{\sin^2(\Delta_{31}-aL)}{(\Delta_{31}-aL)^2}\Delta_{31}^2 \\
& + \sin 2\theta_{23}\sin 2\theta_{13}\sin 2\theta_{12}\frac{\sin(\Delta_{31}-aL)}{(\Delta_{31}-aL)}\Delta_{31}\frac{\sin(aL)}{(aL)}\Delta_{21}\cos(\Delta_{31}+\delta_{\rm CP}) \\
& + \cos^2\theta_{23}\sin^2 2\theta_{12}\frac{\sin^2(aL)}{(aL)^2}\Delta_{21}^2,
\end{aligned}
\tag{5.4}
$$

where $\Delta_{ij} = \Delta m^2_{ij} L/4E_\nu$, $a = G_F N_e/\sqrt{2}$, G_F is the Fermi constant, N_e is the number density of electrons in the Earth, L is the baseline in km, and E_ν is the neutrino energy in GeV. In the equation above, both $\delta_{\rm CP}$ and a switch signs in going from the $\nu_\mu \to \nu_e$ to the $\bar{\nu}_\mu \to \bar{\nu}_e$ channel; i.e., a neutrino-antineutrino asymmetry is introduced both by CPV ($\delta_{\rm CP}$) and the matter effect (a). The origin of the matter effect asymmetry is simply the presence of electrons and absence of positrons in the Earth. In the few-GeV energy range, the asymmetry from the matter effect increases with baseline as the neutrinos pass through more matter; therefore an experiment with a longer baseline will be more sensitive to the neutrino mass ordering. For baselines longer than ∼1200 km, the degeneracy between the asymmetries from matter and CPV effects can be resolved [10]. DUNE, with a baseline of 1300 km, will be able to unambiguously determine the neutrino mass ordering *and* measure the value of $\delta_{\rm CP}$ [145].

The electron neutrino appearance probability, $P(\nu_\mu \to \nu_e)$, is shown in Figure 5.1 at a baseline of 1300 km as a function of neutrino energy for several values of $\delta_{\rm CP}$. As this figure illustrates, the value of $\delta_{\rm CP}$ affects both the amplitude and phase of the oscillation. The difference in probability amplitude for different values of $\delta_{\rm CP}$ is larger at higher oscillation nodes, which correspond to energies less than 1.5 GeV. Therefore, a broadband experiment, capable of measuring not only the rate of ν_e appearance but of mapping out the spectrum of observed oscillations down to energies of at least 500 MeV, is desirable.

In the particular expression of the PMNS matrix shown in Equation 5.2, the middle factor labeled "II" describes the mixing between the ν_1 and ν_3 mass states, and depends on the CP-violating phase $\delta_{\rm CP}$. The variation in the $\nu_\mu \to \nu_e$ oscillation probability with the value of $\delta_{\rm CP}$ indicates that it is experimentally possible to measure the value of $\delta_{\rm CP}$ at a fixed baseline using only the observed shape of the $\nu_\mu \to \nu_e$ *or* the $\bar{\nu}_\mu \to \bar{\nu}_e$ appearance signal measured over an energy range that encompasses at least one full oscillation interval. A measurement of the value of $\delta_{\rm CP} \neq 0$ or π, assuming that neutrino mixing follows the three-flavor model, would imply CPV. In the approximation for the electron neutrino appearance probability given in Equation 5.5, expanding the middle term results in the presence of CP-odd terms (dependent on $\sin\delta_{\rm CP}$) that have opposite signs in $\nu_\mu \to \nu_e$ and $\bar{\nu}_\mu \to \bar{\nu}_e$ oscillations. For $\delta_{\rm CP} \neq 0$ or π, these terms introduce an asymmetry in neutrino versus antineutrino oscillations. Regardless of the measured value obtained for $\delta_{\rm CP}$, the explicit observation of the asymmetry in $\nu_\mu \to \nu_e$ and $\bar{\nu}_\mu \to \bar{\nu}_e$ oscillations is sought to directly demonstrate the leptonic CPV effect. Furthermore, for long-baseline experiments such as DUNE where the neutrino beam propagates through the Earth's mantle, the leptonic CPV effects must be disentangled from the matter effects.

The 1300 km baseline establishes one of DUNE's key strengths: sensitivity to the matter effect. This effect leads to a large asymmetry in the $\nu_\mu \to \nu_e$ versus $\bar{\nu}_\mu \to \bar{\nu}_e$ oscillation probabilities, the

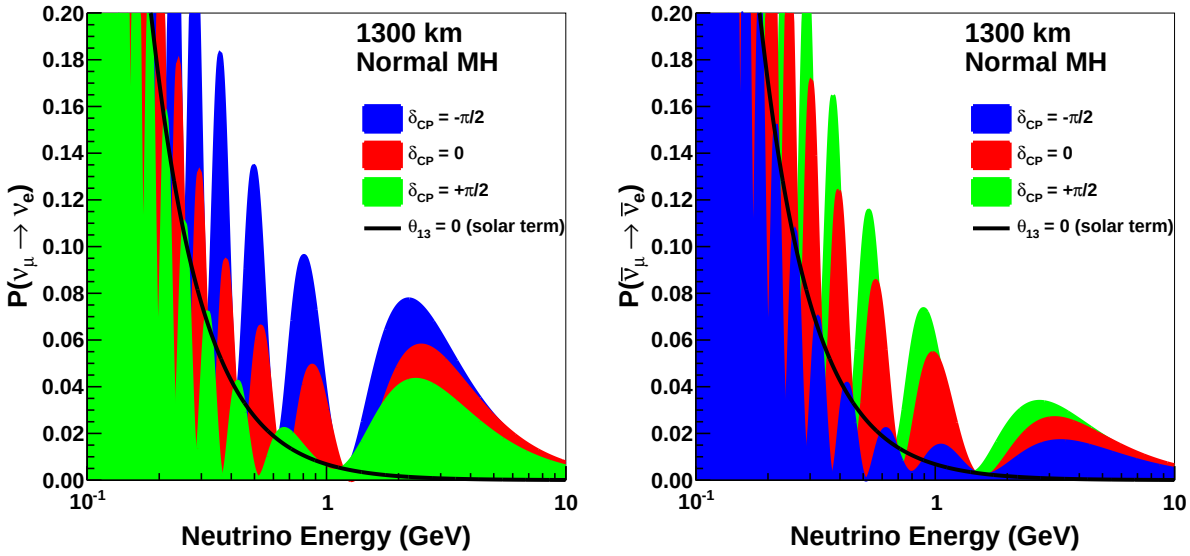

Figure 5.1: The appearance probability at a baseline of 1300 km, as a function of neutrino energy, for $\delta_{\rm CP} = -\pi/2$ (blue), 0 (red), and $\pi/2$ (green), for neutrinos (left) and antineutrinos (right), for normal ordering. The black line indicates the oscillation probability if θ_{13} were equal to zero. Note that DUNE will be built at a baseline of 1300 km

sign of which depends on the neutrino mass ordering. At 1300 km this asymmetry is approximately $\pm 40\%$ in the region of the peak flux; this is larger than the maximal possible CP-violating asymmetry associated with $\delta_{\rm CP}$, meaning that both the mass hierarchy (MH) and $\delta_{\rm CP}$ can be determined unambiguously with high confidence within the same experiment using the beam neutrinos. Concurrent analysis of the corresponding atmospheric-neutrino samples may provide an independent measurement of the neutrino mass ordering.

The rich oscillation structure that can be observed by DUNE will enable precision measurement in a single experiment of all the mixing parameters governing ν_1-ν_3 and ν_2-ν_3 mixing. Higher-precision measurements of the known oscillation parameters improves sensitivity to physics beyond the three-flavor oscillation model, particularly when compared to independent measurements by other experiments, including reactor measurements of θ_{13} and measurements with atmospheric neutrinos. DUNE will seek not only to demonstrate explicit CPV by observing a difference in the neutrino and antineutrino oscillation probabilities, but also to precisely measure the value of $\delta_{\rm CP}$.

The mixing angle θ_{13} has been measured accurately in reactor experiments. While the constraint on θ_{13} from the reactor experiments will be important in the early stages of DUNE, DUNE itself will eventually be able to measure θ_{13} independently with a similar precision to reactor experiments. Whereas the reactor experiments measure θ_{13} using $\bar{\nu}_e$ disappearance, DUNE will measure it through ν_e and $\bar{\nu}_e$ appearance, thus providing an independent constraint on the three-flavor mixing matrix.

Current world measurements of $\sin^2\theta_{23}$ leave an ambiguity as to whether the value of θ_{23} is in the lower octant (less than 45°), the upper octant (greater than 45°), or exactly 45°. The value of $\sin^2\theta_{23}$ from NuFIT 4.0 [2, 3] is in the upper octant, but the distribution of the χ^2 has another

local minimum in the lower octant. A *maximal* mixing value of $\sin^2\theta_{23} = 0.5$ is therefore still allowed by the data and the octant is still largely undetermined. A value of θ_{23} exactly equal to 45° would indicate that ν_μ and ν_τ have equal contributions from ν_3, which could be evidence for a previously unknown symmetry. It is therefore important to experimentally determine the value of $\sin^2\theta_{23}$ with sufficient precision to determine the octant of θ_{23}.

The magnitude of the CP-violating terms in the oscillation depends most directly on the size of the Jarlskog invariant [146], a function that was introduced to provide a measure of CP violation independent of the mixing-matrix parameterization. In terms of the parameterization presented in Equation 5.2, the Jarlskog invariant is:

$$J_{CP}^{\mathrm{PMNS}} \equiv \frac{1}{8}\sin 2\theta_{12}\sin 2\theta_{13}\sin 2\theta_{23}\cos\theta_{13}\sin\delta_{\mathrm{CP}}. \tag{5.5}$$

The relatively large values of the mixing angles in the lepton sector imply that leptonic CPV effects may be quite large, though this depends on the value of δ_{CP}, which is currently unknown. Given the current best-fit values of the mixing angles [2, 3] and assuming normal ordering,

$$J_{CP}^{\mathrm{PMNS}} \approx 0.03\sin\delta_{\mathrm{CP}}. \tag{5.6}$$

This is in sharp contrast to the very small mixing in the quark sector, which leads to a very small value of the corresponding quark-sector Jarlskog invariant [25],

$$J_{CP}^{\mathrm{CKM}} \approx 3\times 10^{-5}, \tag{5.7}$$

despite the large value of $\delta_{CP}^{\mathrm{CKM}} \approx 70^\circ$.

A comparison among the values of the parameters in the neutrino and quark sectors suggest that mixing in the two sectors may be qualitatively different. Illustrating this difference, the value of the entries of the Cabibbo-Kobayashi-Maskawa matrix (CKM matrix) quark-mixing matrix (analogous to the PMNS matrix for neutrinos, and thus indicative of the strength of flavor-changing weak decays in the quark sector) can be expressed in approximate form as

$$|V_{\mathrm{CKM}}| \sim \begin{pmatrix} 1 & 0.2 & 0.004 \\ 0.2 & 1 & 0.04 \\ 0.008 & 0.04 & 1 \end{pmatrix}, \tag{5.8}$$

for comparison to the entries of the PMNS matrix given in Equation 5.3. As discussed in [147], the question of why the quark mixing angles are smaller than the lepton mixing angles is an important part of the flavor pattern question. Data on the patterns of neutrino mixing are already contributing to the quest to understand whether there is a relationship between quarks and leptons and their seemingly arbitrary generation structure.

DUNE is designed to make significant contributions to completion of the standard three-flavor mixing picture. Scientific goals are definitive determination of the neutrino mass ordering, definitive observation of CP violation for more than 50% of possible true δ_{CP} values, and precise measurement of oscillation parameters, particularly δ_{CP}, $\sin^2 2\theta_{13}$, and the octant of $\sin^2\theta_{23}$. There is great value in obtaining this set of measurements in a single experiment using a broadband beam, so that the oscillation pattern may be clearly observed and a detailed test of the three-flavor neutrino model may be performed.

5.2 Expected Event Rate and Oscillation Parameters

The signal for ν_e ($\bar{\nu}_e$) appearance is an excess of charged current (CC) ν_e and $\bar{\nu}_e$ interactions over the expected background in the far detector. The background to ν_e appearance is composed of: (1) CC interactions of ν_e and $\bar{\nu}_e$ intrinsic to the beam; (2) misidentified neutral current (NC) interactions; (3) misidentified ν_μ and $\bar{\nu}_\mu$ CC interactions; and (4) ν_τ and $\bar{\nu}_\tau$ CC interactions in which the τs decay leptonically into electrons/positrons. NC and ν_τ backgrounds emanate from interactions of higher-energy neutrinos that feed down to lower reconstructed neutrino energies due to missing energy in unreconstructed final-state neutrinos. The selected NC and CC ν_μ generally include an asymmetric decay of a relatively high energy π^0 coupled with a prompt photon conversion.

A full simulation chain that includes the beam flux, the Generates Events for Neutrino Interaction Experiments (GENIE) neutrino interaction generator [70], and Geant4-based detector models has been implemented. Section 5.3 describes the beam design, simulated flux, and associated uncertainties. Event rates are based on a 1.2 MW neutrino beam and corresponding protons-on-target per year assumed to be 1.1 $\times 10^{21}$ POT. These numbers assume a combined uptime and efficiency of the Fermi National Accelerator Laboratory (Fermilab) accelerator complex and the Long-Baseline Neutrino Facility (LBNF) beamline of 56%. An upgrade to 2.4 MW is assumed after six years of data collection. The neutrino interaction model has been generated using GENIE 2.12 and the choices of models and tunes as well as associated uncertainties are described in detail in Section 5.4. The performance parameters for the near and far detectors are described in detail in Sections 5.5 and 5.6. Near Detector Monte Carlo has been generated using Geant4 and a parameterized reconstruction based on true energy deposits in the active detector volumes has been used as described in Section 5.5. Far detector Monte Carlo has been generated using LArSoft and the reconstruction and event selection in the Far Detector has been fully implemented, as described in Section 5.6. Uncertainties associated with detector effects in the near and far detectors are described in Section 5.7. The methods used in calculating the DUNE sensitivity results are described in Section 5.8 and these results based on the full framework are shown in Section 5.9.

The neutrino oscillation parameters and the uncertainty on those parameters are taken from the NuFIT 4.0 [2, 3] global fit to neutrino data; the values are given in Table 5.1. (See also [142] and [143] for other recent global fits.) The sensitivities in this chapter are shown assuming normal ordering; this is an arbitrary choice for simplicity of presentation.

Event rates are presented as a function of calendar years and are calculated with the following assumed deployment plan, which is based on a technically limited schedule.

- Start of beam run: Two far detector (FD) module volumes for total fiducial mass of 20 kt, 1.2 MW beam
- After one year: Add one FD module volume for total fiducial mass of 30 kt
- After three years: Add one FD module volume for total fiducial mass of 40 kt
- After six years: Upgrade to 2.4 MW beam

Figures 5.2 and 5.3 show the expected rate of selected events for ν_e appearance and ν_μ disappear-

Parameter	Central Value	Relative Uncertainty
θ_{12}	0.5903	2.3%
θ_{23} (NO)	0.866	4.1%
θ_{23} (IO)	0.869	4.0%
θ_{13} (NO)	0.150	1.5%
θ_{13} (IO)	0.151	1.5%
Δm^2_{21}	7.39×10^{-5} eV^2	2.8%
Δm^2_{32} (NO)	2.451×10^{-3} eV^2	1.3%
Δm^2_{32} (IO)	-2.512×10^{-3} eV^2	1.3%

Table 5.1: Central value and relative uncertainty of neutrino oscillation parameters from a global fit [2, 3] to neutrino oscillation data. Because the probability distributions are somewhat non-Gaussian (particularly for θ_{23}), the relative uncertainty is computed using 1/6 of the 3σ allowed range from the fit, rather than the 1σ range. For θ_{23}, θ_{13}, and Δm^2_{31}, the best-fit values and uncertainties depend on whether normal mass ordering (NO) or inverted mass ordering (IO) is assumed.

ance, respectively, including expected flux, cross section, and oscillation probabilities, as a function of reconstructed neutrino energy at a baseline of 1300 km. The spectra are shown for a 3.5 year (staged) exposure each for neutrino and antineutrino beam mode, for a total run time of seven years. Tables 5.2 and 5.3 give the integrated rate for the ν_e appearance and ν_μ disappearance spectra, respectively.

5.3 Neutrino Beam Flux and Uncertainties

The neutrino fluxes are described in detail in Section 4.1.1. They were generated using G4LBNF, a GEANT4-based simulation of the LBNF neutrino beam. The simulation is configured to use a detailed description of the LBNF optimized beam design [59], which includes horns and target designed to maximize sensitivity to CPV given the physical constraints on the beamline design.

Neutrino fluxes for neutrino and antineutrino mode configurations of LBNF are shown in Figure 5.4. Uncertainties on the neutrino fluxes arise primarily from uncertainties in hadrons produced off the target and uncertainties in the design parameters of the beamline, such as horn currents and horn and target positioning (commonly called "focusing uncertainties"). Given current measurements of hadron production and LBNF estimates of alignment tolerances, flux uncertainties are approximately 8% at the first oscillation maximum and 12% at the second. These uncertainties are highly correlated across energy bins and neutrino flavors

Future hadron production measurements are expected to improve the quality of and the resulting constraints on these flux uncertainty estimates. Approximately 40% of the interactions that produce neutrinos in the LBNF beam simulation have no data constraints whatsoever. Large uncertainties are assumed for these interactions. The largest unconstrained sources of uncertainty are proton quasielastic interactions and meson incident interactions. The proposed EMPHATIC experiment [148] at Fermilab will be able to constrain quasielastics and low energy interactions

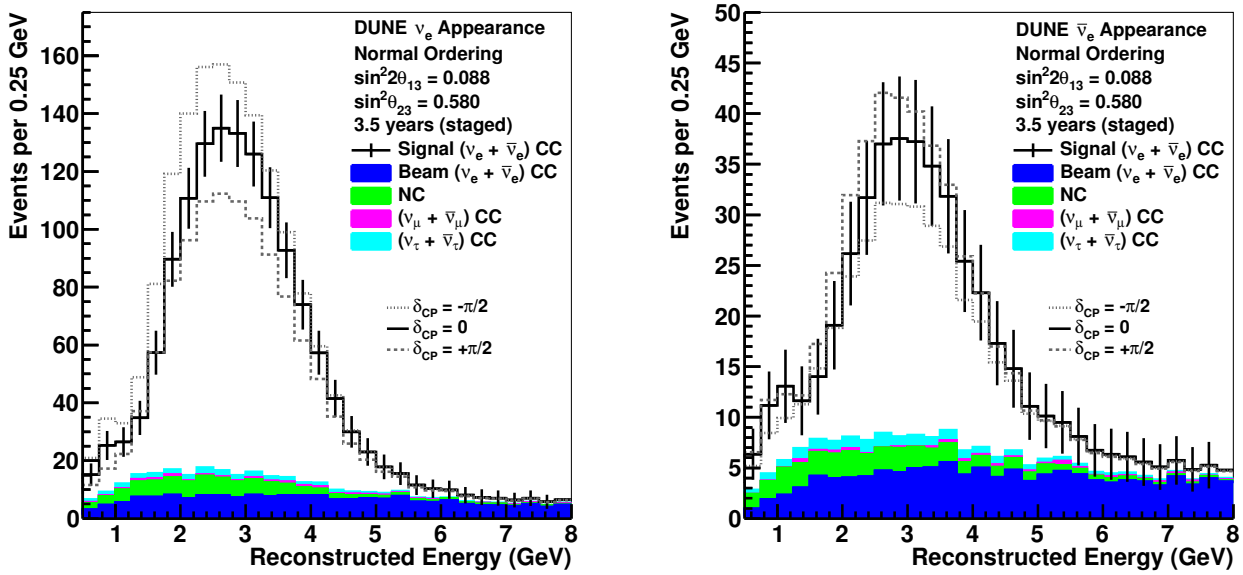

Figure 5.2: ν_e and $\bar{\nu}_e$ appearance spectra: Reconstructed energy distribution of selected ν_e CC-like events assuming 3.5 years (staged) running in the neutrino-beam mode (left) and antineutrino-beam mode (right), for a total of seven years (staged) exposure. The plots assume normal mass ordering and include curves for $\delta_{\rm CP} = -\pi/2, 0$, and $\pi/2$.

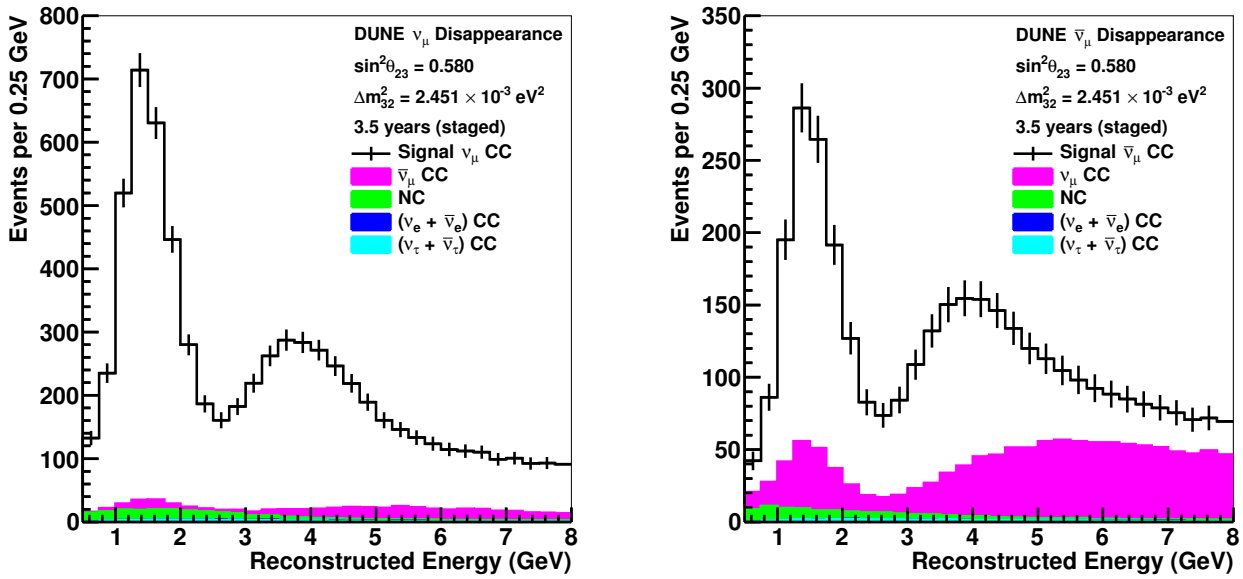

Figure 5.3: ν_μ and $\bar{\nu}_\mu$ disappearance spectra: Reconstructed energy distribution of selected ν_μ CC-like events assuming 3.5 years (staged) running in the neutrino-beam mode (left) and antineutrino-beam mode (right), for a total of seven years (staged) exposure. The plots assume normal mass ordering.

Table 5.2: ν_e and $\bar{\nu}_e$ appearance rates: Integrated rate of selected ν_e CC-like events between 0.5 and 8.0 GeV assuming a 3.5-year (staged) exposure in the neutrino-beam mode and antineutrino-beam mode. The signal rates are shown for both normal mass ordering (NO) and inverted mass ordering (IO), and all the background rates assume normal mass ordering. All the rates assume $\delta_{\rm CP} = 0$.

	Expected Events (3.5 years staged)
ν mode	
ν_e Signal NO (IO)	1092 (497)
$\bar{\nu}_e$ Signal NO (IO)	18 (31)
Total Signal NO (IO)	1110 (528)
Beam $\nu_e + \bar{\nu}_e$ CC background	190
NC background	81
$\nu_\tau + \bar{\nu}_\tau$ CC background	32
$\nu_\mu + \bar{\nu}_\mu$ CC background	14
Total background	317
$\bar{\nu}$ mode	
ν_e Signal NO (IO)	76 (36)
$\bar{\nu}_e$ Signal NO (IO)	224 (470)
Total Signal NO (IO)	300 (506)
Beam $\nu_e + \bar{\nu}_e$ CC background	117
NC background	38
$\nu_\tau + \bar{\nu}_\tau$ CC background	20
$\nu_\mu + \bar{\nu}_\mu$ CC background	5
Total background	180

Table 5.3: ν_μ and $\bar{\nu}_\mu$ disappearance rates: Integrated rate of selected ν_μ CC-like events between 0.5 and 8.0 GeV assuming a 3.5-year (staged) exposure in the neutrino-beam mode and antineutrino-beam mode. The rates are shown for normal mass ordering and $\delta_{\rm CP} = 0$.

	Expected Events (3.5 years staged)
ν mode	
ν_μ Signal	6200
$\bar{\nu}_\mu$ CC background	389
NC background	200
$\nu_\tau + \bar{\nu}_\tau$ CC background	46
$\nu_e + \bar{\nu}_e$ CC background	8
$\bar{\nu}$ mode	
$\bar{\nu}_\mu$ Signal	2303
ν_μ CC background	1129
NC background	101
$\nu_\tau + \bar{\nu}_\tau$ CC background	27
$\nu_e + \bar{\nu}_e$ CC background	2

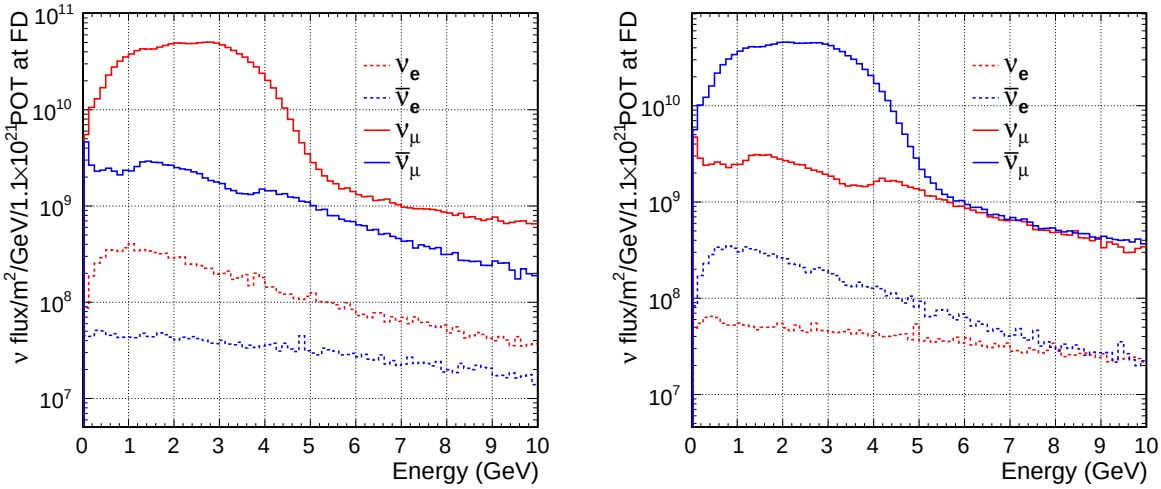

Figure 5.4: Neutrino fluxes at the FD for neutrino mode (left) and antineutrino mode (right).

that dominate the lowest neutrino energy bins. The NA61 experiment at CERN has taken data that will constrain many higher energy interactions, including pion reinteractions. It also plans to measure hadrons produced off of a replica LBNF target, which would provide tight constraints on all interactions occurring in the target. A similar program at NA61 has reduced flux uncertainties for T2K from 10% to 5% [149], and NOvA is currently analyzing NA61 replica target data [150]. Another proposed experiment, the LBNF spectrometer, would measure hadrons after both production and focusing in the horns, effectively constraining nearly all hadron production uncertainties, and could also enable measurement of the impact on focused hadrons of shifted alignment parameters (which is currently taken from simulations). The neutrino flux uncertainties, as well as their bin-to-bin and flavor-to-flavor correlations, are very sensitive to correlations in hadron production measurements. None of the currently available measurements have provided correlations, so the uncertainty estimates make basic assumptions that statistical uncertainties are not correlated between bins but systematic uncertainties are completely correlated. New hadron production measurements that cover phase space similar to past measurements but that provide bin-to-bin correlations would also improve the quality of the estimated neutrino flux uncertainties at DUNE.

The unoscillated fluxes at the near detector (ND) and FD are similar, but not identical (since the ND sees a line source, while the FD sees a point source. The relationship is well understood, and flux uncertainties mostly cancel for the ratio of fluxes between the two detectors. Uncertainties on the ratio are around 1% or smaller except at the falling edge of the focusing peak, where they rise to 2%. The far to near flux ratio and uncertainties on this ratio are shown in Fig. 4.8.

The peak energy of neutrino flux falls off and the width of the peak narrows as the distance from the beams central axis increases. The flux at these "off-axis" positions can be understood through the relationship between the parent pion energy and neutrino energy, as shown in Figure 4.9. For an off-axis angle relative to the initial beam direction, the subsequent neutrino energy spectra is narrower and peaked at a lower energy than the on-axis spectra. At 575 m, the location of the ND hall, a lateral shift of 1 m corresponds to approximately a 0.1° change in off-axis angle.

The same sources of systematic uncertainty which affect the on-axis spectra also modify the off-axis spectra. Generally, the size of the off-axis uncertainties is comparable to the on-axis uncertainties and the uncertainties are highly correlated across off-axis and on-axis positions. The impact of focusing and alignment uncertainties varies depending on off-axis angle. Therefore, off-axis flux measurements are useful to diagnose beamline aberrations, and to further constrain flux uncertainties.

5.4 Neutrino Interactions and Uncertainties

5.4.1 Interaction Model Summary

The goal of parameterizing the neutrino interaction model uncertainties is to provide a framework for considering how these uncertainties affect the oscillation analysis at the FD, and for considering how constraints at the ND can limit those uncertainties.

The model developed for this purpose generally factorizes the neutrino interaction on nuclei into an incoherent sum of hard scattering neutrino interactions with the single nucleons in the nucleus. The effect of the nucleus is implemented as initial and final state interaction effects, with some (albeit few) nucleus-dependent hard scattering calculations. Schematically, we express this concept as Scattering Process = Initial State $\otimes$ Nucleon Interaction $\otimes$ Final State Propagation.

The initial state effects relate to the description of the momentum and position distributions of the nucleons in the nucleus, kinematic modifications to the final state (such as separation energy, or sometimes described as a binding energy), and Coulomb effects. The concept of binding energy reflects the idea that the struck nucleon may be off the mass-shell inside the nucleus. Final state interactions refer to the propagation and interaction of hadrons produced in the nucleon interaction through the nucleus. The final-state interactions (FSI) alter both the momentum and energy of the recoiling particles produced in the final state, and may also alter their identity and multiplicity in the case of inelastic reinteractions (e.g., in a nucleus a hadron may be absorbed, rescattered, or create a secondary hadron). The FSI model implemented in the GENIE, NuWro, and neutrino interaction generator (NEUT) neutrino interaction generators is a semi-classical cascade model. In particular, GENIE's hA model is a single step scaled model, based on hadron-nucleus and hadron-nucleon scattering data and theoretical corrections.

Generators vary in their attempts to accurately model the largely undetected final state "spectator" nuclear system. The nuclear system can carry away significant undetected momentum—hundreds of MeV is not unusual—in the form of one or more heavy, non-relativistic particles. These particles typically carry off very little kinetic energy; however they can absorb on the order of tens of MeV of energy from the initial state from breakup or excitation of the target nucleus. This energy and momentum will typically be invisible to the detector.

The factorization outlined above is not present in all parts of the model. Most modern generators include "2p2h" (two particle, two hole) interactions that model meson exchange processes and

scattering on highly correlated pairs of nucleons in the nucleus. These interactions are often implemented as another process that incorporates both hard scattering and initial state effects in processes that create multiple final state nucleons, with a different prescription for different nuclei. Neutrino scattering on atomic electrons and the coherent production of pions (which scatters off the entire nucleus) also do not follow this factorization.

The interaction model and its variations are implemented in the GENIE generator. The fixed version of GENIE used for this report, v2.12.10[2], will not contain all of the possible cross section variations which need to be modeled. Therefore, the variations in the cross sections to be considered are implemented as some combination of: GENIE weighting parameters (sometimes referred to as "GENIE knobs"), *ad hoc* weights of events that are designed to parameterize uncertainties or cross section corrections currently not implemented within GENIE, and discrete alternative model comparisons, achieved through alternative generators, alternative GENIE configurations, or custom weightings. For the studies presented in this chapter we have identified classes of uncertainties that are intended to span a representative range of alternative models such as those found in other generators.

In this work, two example alternative models are used directly to evaluate additional uncertainties in the case where the assumptions about the near detector are relaxed. These studies are described in Section 5.9.6. The first is based on the NuWro generator and the second is designed to produce the same on-axis visible energy distributions as the nominal model, but with a different relationship between true neutrino energy and visible energy.

5.4.2 Interaction Model Uncertainties

The interaction uncertainties are divided into seven roughly exclusive groups: (1) initial state uncertainties, (2) hard scattering uncertainties and nuclear modifications to the quasielastic process, (3) uncertainties in multinucleon (2p2h) hard scattering processes, (4) hard scattering uncertainties in pion production processes, (5) uncertainties governing other, higher W and neutral current processes, (6) final state interaction uncertainties, (7) neutrino flavor dependent uncertainties. Uncertainties are intended to reflect current theoretical freedom, deficiencies in implementation, and/or current experimental knowledge. There are constraints on nuclear effects because of measurements on lighter targets, however for the argon nuclear target some additional sources of uncertainty are identified. We also discuss cases where the parameterization is limited or simplified.

5.4.2.1 Initial State Uncertainties

The default nuclear model in GENIE is a modified global Fermi gas model of the nucleons in the nucleus. There are significant deficiencies that are known in global Fermi gas models. These include a lack of consistent incorporation of the tails that result from correlations among nucleons,

[2]At the time of the development of this model for interactions and their uncertainties, initial pieces of GENIE 3 had just recently been released (October 2018) and reweighting and documentation followed after this. The timing made it impractical to use GENIE 3 for this work.

the lack of correlation between location within the nucleus and momentum of the nucleon, and an incorrect relationship between momentum and energy of the off-shell, bound nucleon within the nucleus. GENIE modifies the nucleon momentum distribution empirically to account for short-range correlation effects, which populates tails above the Fermi cutoff, but the other deficiencies persist. Alternative initial state models, such as spectral functions [151, 152], the mean field model of GiBUU [153], or continuum random phase approximation (CRPA) calculations [154] may provide better descriptions of the nuclear initial state [155].

5.4.2.2 Quasielastic uncertainties

The primary uncertainties considered in quasielastic interactions are the axial form factor of the nucleon and nuclear screening—from the so-called random phase approximation (RPA) calculations—of low momentum transfer reactions.

The axial form factor uncertainty has been historically described with a single parameter uncertainty with the dipole form by varying M_A, and we will continue this for these studies. Unfortunately, this framework overconstrains the form factor at high Q^2, and an alternative parameterization based on the z-expansion has been proposed as a replacement [156]. However, this parameterization is multi-dimensional and poses problems for the analysis framework of this study which factorizes all N-dimensional variations out into $N \times 1$-dimensional analysis bin response functions. For some multi-dimensional parameterizations, this simplification is an adequate approximation, e.g., the BeRPA described below.

One part of the Nieves et al.[157, 158] description of the 0π interaction on nuclei includes RPA, used to sum the $W^{\pm}$ self-energy terms. In practice, this modifies the 1p1h/Quasi-Elastic cross-section in a non-trivial way. The calculations from Nieves et al. have associated uncertainties presented in [**?**], which were evaluated as a function of Q^2 [159]. In 2018, MINERvA and NOvA parameterized the central value and uncertainty in (q_0, q_3) using RPA uncertainties as parameterized in [160], whereas T2K used central values and uncertainties in Q^2 only. Here we use T2K's 2017/8 parameterization of the RPA effect [161] due to its simplicity. The shape of the correction and error is parameterized with a Bernstein polynomial up to $Q^2 = 1.2$ GeV^2 which switches to a decaying exponential. The BeRPA (Bernstein RPA) function has three parameters controlling the polynomial (A, B, C), where the parameters control the behavior at increasing Q^2 and a fourth parameter E controls the high Q^2 tail.

The axial form factor parameterization we use is known to be inadequate. However, the convolution of BeRPA uncertainties with the limited axial form factor uncertainties do provide more freedom as a function of Q^2, and the two effects likely provide adequate freedom for the Q^2 shape in quasielastic events.

5.4.2.3 $2p2h$ uncertainties

We start with the Nieves et al. or "Valencia" model [157, 158] for multinucleon ($2p2h$) contributions to the cross section. However, MINERvA has shown directly [162], and NOvA indirectly, that this description is missing observed strength on carbon. As a primary approach to the model, we add that missing strength to a number of possible reactions. We then add uncertainties for energy dependence of this missing strength and uncertainties in scaling the $2p2h$ prediction from carbon to argon.

The extra strength from the "MINERvA tune" to $2p2h$ is applied in (q_0, q_3) space (where q_0 is energy transfer from the leptonic system, and q_3 is the magnitude of the three momentum transfer) to fit reconstructed MINERvA CC-inclusive data [162] in E_{avail}[3] and q_3. Reasonable fits to MINERvA's data are found by attributing the missing strength to any of $2p2h$ from np initial state pairs, $2p2h$ from nn initial state pairs, or $1p1h$ or quasielastic processes. The default tune uses an enhancement of the np and nn initial strengths in the ratio predicted by the Nieves model, and alternative systematic variation tunes ("MnvTune" 1-3) attribute the missing strength to the individual hypotheses above. Implementation of the "MnvTune" is based on weighting in true (q_0, q_3). The weighting requires GENIE's Llewelyn-Smith $1p1h$ and Valencia $2p2h$ are used as the base model. To ensure consistency in using these different tunes as freedom in the model, a single systematic parameter is introduced that varies smoothly between applying the $1p1h$ tune at one extreme value to applying the nn tune at the other extreme via the default tune which is used as the central value. The np tune is neglected in this prescription as being the most redundant, in terms of missing energy content of the final state, of the four discrete hypotheses.

The rates for $1p1h$ and $2p2h$ processes could be different on argon and carbon targets. There is little neutrino scattering data to inform this, but there are measurements of short-ranged correlated pairs from electron scattering on different nuclei [163]. These measurements directly constrain $2p2h$ from short range correlations, although the link to dynamical sources like meson exchange current processes (MEC) is less direct. Interpolation of that data in A (Nucleon number) suggests that scaling from carbon relative to the naive $\propto A$ prediction for $2p2h$ processes would give an additional factor of 1.33 ± 0.13 for np pairs, and 0.9 ± 0.4 for pp pairs. GENIE's prediction for the ratio of $2p2h$ cross-sections in Ar^{40}/C^{12} for neutrinos varies slowly with neutrino energy in the DUNE energy range: from 3.76 at 1 GeV to 3.64 at 5 GeV. The ratio for antineutrino cross sections is consistent with 3.20 at all DUNE energies. Since the ratio of A for Ar^{40}/C^{12} is 3.33, this is consistent with the ranges suggested above by the measured pp and np pair scaling. A dedicated study by the SuSA group using their own theoretical model for the relevant MEC process also concludes that the transverse nuclear response (which drives the $\nu - A$ MEC cross section) ratio between Ca^{40} (the isoscalar nucleus with the same A as Ar^{40}) and C^{12} is 3.72 [164]. We vary GENIE's Valencia model based prediction, including the MINERvA tune, for $2p2h$ by $\sim 20\%$ to be consistent with the correlated pair scaling values above. This is done independently for neutrino and antineutrino scattering.

The MINERvA tune may be E_ν dependent. MINERvA separated its data into an $E_\nu < 6$ GeV and an $E_\nu > 6$ GeV piece, and sees no dependence with a precision of better than 10% [162]. The mean

[3] E_{avail} is calorimetrically visible energy in the detector, roughly speaking total recoil hadronic energy, less the masses of $\pi^\pm$ and the kinetic energies of neutrons

energy of the $E_\nu < 6$ GeV piece is roughly $\langle E_\nu \rangle \approx 3$ GeV. In general, an exclusive cross-section will have an energy dependence $\propto \frac{A}{E_\nu^2} + \frac{B}{E_\nu} + C$ [165]; therefore, unknown energy dependence may be parameterize by an *ad hoc* factor of the form $1/\left(1 + \frac{A^{'}}{E_\nu^2} + \frac{B^{'}}{E_\nu}\right)$. The MINERvA constraints suggest $A^{'} < 0.9$ GeV^2 and $B^{'} < 0.3$ GeV. The variations for neutrinos and antineutrinos could be different since this is an effective modification. Ideally this energy dependent factor would only affect the MINERvA tune, but practically, because of analysis framework limitations already discussed, this is not possible. As a result, this energy dependent factor is applied to all true $2p2h$ events.

5.4.2.4 Single pion production uncertainties

GENIE uses the Rein-Sehgal model for pion production. Tunes to D_2 data have been performed, both by the GENIE collaboration itself and in subsequent re-evaluations [166]; we use the latter tune as our base model. For simplicity of implementation, the 'v2.8.2 (no norm.)' results are used here.

MINERvA single pion production data [167, 168, 169] indicates disagreement at low Q^2 which may correspond to an incomplete nuclear model for single pion production in the generators. A similar effect was observed at MINOS [170] and NOvA implements a similar correction in analyses [171]. A fit to MINERvA data [172] measured a suppression parameterized by

$$R(Q^2 < x_3) = \frac{R_2(Q^2 - x_1)(Q^2 - x_3)}{(x_2 - x_1)(x_2 - x_3)} + \frac{(Q^2 - x_1)(Q^2 - x_2)}{(x_3 - x_1)(x_3 - x_2)} \tag{5.9}$$

$$W(Q^2) = 1 - (1 - R_1)(1 - R(Q^2))^2 \tag{5.10}$$

where R_1 defines the magnitude of the correction function at the intercept, $x_1 = 0.0$. x_2 is chosen to be $Q^2 = 0.35$ GeV^2 so that R_2 describes the curvature at the center point of the correction. The fit found $R_1 \approx 0.3$ and $R_2 \approx 0.6$. The correction is applied to events with a resonance decay inside the nucleus giving rise to a pion, based on GENIE event information.

An improved Rein-Sehgal-like resonance model has recently been developed [173] which includes a non-resonant background in both $I = \frac{1}{2}$ and $I = \frac{3}{2}$ channels and interference between resonant-resonant and resonant-non-resonant states. It also improves on the Rein-Sehgal model in describing the outgoing pion and nucleon kinematics using all its resonances. A template weighting in (W, Q^2, E_ν) is implemented to cover the differences between the two models as a systematic uncertainty. The weighting also suppresses GENIE non-resonant pion production events (deep inelastic scattering events with $W < 1.7$ GeV) as the new model already includes the non-resonant contribution coherently. The weighting is only applied to true muon-neutrino charged-current resonant pion production interactions.

Coherent inelastic pion production measurements on carbon are in reasonable agreement with the GENIE implementation of the Berger-Sehgal model [174]. The process has not been measured at

high statistics in argon. While coherent interactions provide a very interesting sample for oscillation analyses, they are a very small component of the event rate and selections will depend on the near detector configuration. Therefore we do not provide any evaluation of a systematic uncertainty for this extrapolation or any disagreements between the Berger-Sehgal model and carbon data.

5.4.2.5 Other hard scattering uncertainties

NOvA oscillation analyses [171] have found the need for excursions beyond the default GENIE uncertainties to describe their single pion to deep inelastic scattering (DIS) transition region data. Following suit, we drop GENIE's default "Rv[n,p][1,2]pi" knobs and instead implement separate, uncorrelated uncertainties for all perturbations of 1, 2, and ≥ 3 pion final states, CC/NC, neutrinos/anti-neutrinos, and interactions on protons/neutrons, with the exception of CC neutrino 1-pion production, where interactions on protons and neutrons are merged, following [166]. This leads to 23 distinct uncertainty channels ([3 pion states] x [n,p] x [nu/anti-nu] x [CC/NC] - 1), all with a value of 50% for $W \leq 3$ GeV. For each channel, the uncertainty drops linearly above $W = 3$ GeV until it reaches a flat value of 5% at $W = 5$ GeV, where external measurements better constrain this process.

5.4.2.6 Final state interaction uncertainties

GENIE includes a large number of final state uncertainties to its hA final state cascade model which are summarized in Table 5.5. These uncertainties have been validated in neutrino interactions primarily on light targets such as carbon, but there is very little data available on argon targets. The lack of tests against argon targets is difficult to address directly because there are many possible FSI processes that could be varied.

5.4.2.7 Neutrino flavor dependent uncertainties

The cross sections include terms proportional to lepton mass, which are significant contributors at low energies where quasielastic processes dominate. Some of the form factors in these terms have significant uncertainties in the nuclear environment. Ref. [175] ascribes the largest possible effect to the presence of poorly constrained second-class current vector form factors in the nuclear environment, and proposes a variation in the cross section ratio of σ_μ/σ_e of $\pm 0.01/\mathrm{Max}(0.2\ \mathrm{GeV}, E_\nu)$ for neutrinos and $\mp 0.018/\mathrm{Max}(0.2\ \mathrm{GeV}, E_\nu)$ for anti-neutrinos. Note the anticorrelation of the effect in neutrinos and antineutrinos.

In addition, radiative Coulomb effects may also contribute, which for T2K is of order ± 5 MeV shifts in reconstructed lepton momentum. Like the second class current effect in the cross section, it flips sign between neutrinos and antineutrinos and is significant only at low energies. This effect is not implemented herein.

Finally, some electron neutrino interactions occur at four momentum transfers where a correspond-

ing muon neutrino interaction is kinematically forbidden, therefore the nuclear response has not been constrained by muon neutrino cross section measurements. This region at lower neutrino energies has a significant overlap with the Bodek-Ritchie tail of the Fermi gas model. There are significant uncertainties in this region, both from the form of the tail itself, and from the lack of knowledge about the effect of RPA and $2p2h$ in this region. The allowed phase space in the presence of nonzero lepton mass is $E_\nu - \sqrt{(E_\nu - q_0)^2 - m_l^2} \leq q_3 \leq E_\nu + \sqrt{(E_\nu - q_0)^2 - m_l^2}$. Here, a 100% variation is allowed in the phase space present for ν_e but absent for ν_μ.

A similar prescription cannot applied for differences between interactions of ν_μ and ν_τ because the τ mass scale is of the same order of magnitude as the neutrino energies, and is thus a leading effect. No specific uncertainties were developed for ν_τ interactions as there is little theoretical guidance.

5.4.3 Listing of Interaction Model Uncertainties

The complete set of interaction model uncertainties includes GENIE implemented uncertainties (Tables 5.4, and 5.5), and new uncertainties developed for this effort (Table 5.6) which represent uncertainties beyond those implemented in the GENIE generator.

Table 5.6 separates the interaction model parameters into three categories based on their treatment in the analysis:

- Category 1: On-axis near detector data is expected to constrain these parameters; the uncertainty is implemented in the same way in near and far detectors. All GENIE uncertainties (original or modified) are all treated as Category 1.
- Category 2: These uncertainties are implemented in the same way in near and far detectors, but on-axis data alone is not sufficient to constrain these parameters. We use two subcategories. The first category (2A) corresponds to interaction effects which may be difficult to disentangle from detector effects. A good example of this is the E_b parameter, which may be degenerate with the energy scale of the near detector. This may be constrained with electron scattering and dedicated studies carefully selected samples of near detector data, but would be difficult to constrain with inclusive near detector samples. The second category (2B) corresponds to parameters that can be constrained by off-axis samples, described in Section 5.5.
- Category 3: These uncertainties are implemented only in the far detector. Examples are ν_e and $\overline{\nu}_e$ rates which are small and difficult to precisely isolated from background at the near detector. Therefore, near detector data is not expected to constrain such parameters.

Finally, there are a number of tunes applied to the default model, to represent known deficiencies in GENIE's description of neutrino data, and these are listed in Table 5.7.

x_P	Description of P	P_{CV}	$\delta P/P$
	Quasielastic		
$x_{M_A}^{CCQE}$	Axial mass for CCQE		$^{+0.25}_{-0.15}$ GeV
x_{VecFF}^{CCQE}	Choice of CCQE vector form factors (BBA05 $\leftrightarrow$ Dipole)		N/A
x_{kF}^{CCQE}	Fermi surface momentum for Pauli blocking		$\pm$30%
	Low W		
$x_{M_A}^{CCRES}$	Axial mass for CC resonance	0.94	$\pm$0.05 GeV
$x_{M_V}^{CCRES}$	Vector mass for CC resonance		$\pm$10%
$x_{\eta\ BR}^{\Delta Decay}$	Branching ratio for $\Delta \to \eta$ decay		$\pm$50%
$x_{\gamma\ BR}^{\Delta Decay}$	Branching ratio for $\Delta \to \gamma$ decay		$\pm$50%
$x_{\theta_\pi^{\Delta Decay}}$	θ_π distribution in decaying Δ rest frame (isotropic $\to$ RS)		N/A
	High W		
$x_{A_{HT}^{BY}}^{DIS}$	A_{HT} higher-twist param in BY model scaling variable ξ_w		$\pm$25%
$x_{B_{HT}^{BY}}^{DIS}$	B_{HT} higher-twist param in BY model scaling variable ξ_w		$\pm$25%
$x_{C_{V1u}^{BY}}^{DIS}$	C_{V1u} valence GRV98 PDF correction param in BY model		$\pm$30%
$x_{C_{V2u}^{BY}}^{DIS}$	C_{V2u} valence GRV98 PDF correction param in BY model		$\pm$40%
	Other neutral current		
$x_{M_A}^{NCEL}$	Axial mass for NC elastic		$\pm$25%
x_{η}^{NCEL}	Strange axial form factor η for NC elastic		$\pm$30%
$x_{M_A}^{NCRES}$	Axial mass for NC resonance		$\pm$10%
$x_{M_V}^{NCRES}$	Vector mass for NC resonance		$\pm$5%
	Misc.		
x_{FZ}	Vary effective formation zone length		$\pm$50%

Table 5.4: Neutrino interaction cross-section systematic parameters considered in GENIE. GENIE default central values and uncertainties are used for all parameters except $x_{M_A}^{CCRES}$. Missing GENIE parameters were omitted where uncertainties developed for this analysis significantly overlap with the supplied GENIE freedom, the response calculation was too slow, or the variations were deemed unphysical.

x_P	Description of P	$\delta P/P$
x^N_{cex}	Nucleon charge exchange probability	$\pm$50%
x^N_{el}	Nucleon elastic reaction probability	$\pm$30%
x^N_{inel}	Nucleon inelastic reaction probability	$\pm$40%
x^N_{abs}	Nucleon absorption probability	$\pm$20%
x^N_{π}	Nucleon π-production probability	$\pm$20%
x^{π}_{cex}	π charge exchange probability	$\pm$50%
x^{π}_{el}	π elastic reaction probability	$\pm$10%
x^{π}_{inel}	π inelastic reaction probability	$\pm$40%
x^{π}_{abs}	π absorption probability	$\pm$20%
x^{π}_{π}	π π-production probability	$\pm$20%

Table 5.5: The intra-nuclear hadron transport systematic parameters implemented in GENIE with associated uncertainties considered in this work. Note that the 'mean free path' parameters are omitted for both N-N and π-N interactions as they produced unphysical variations in observable analysis variables. Table adapted from Ref [176].

Uncertainty	Mode	Description	Category
BeRPA	1p1h/QE	RPA/nuclear model suppression	1
MnvTune1	2p2h	Strength into (nn)pp only	1
MnvTuneCV	2p2h	Strength into 2p2h	1
MnvTune2	1p1h/QE	Strength into 1p1h	1
ArC2p2h	2p2h Ar/C scaling	Electron scattering SRC pairs	1
E_{2p2h}	2p2h	2p2h Energy dependence	2B
Low Q^2 1π	RES	Low Q^2 (empirical) suppression	1
MK model	ν_μ CC-RES	alternative strength in W	1
CC Non-resonant $\nu \to \ell + 1\pi$	ν DIS	Norm. for $\nu + n/p \to \ell + 1\pi$ (*c.f.[166]*)	1
Other Non-resonant π	$N\pi$ DIS	Per-topology norm. for $1 < W < 5$ GeV.	1
E_{avail}/q_0	all	Extreme FSI-like variations	2B
Modified proton energy	all	20% change to proton E	2B
$\nu_\mu \to \nu_e$	$\nu_e/\overline{\nu}_e$	100% uncertainty in ν_e unique phase space	3
$\nu_e/\overline{\nu}_e$ norm	ν_e,$\overline{\nu}_e$	Ref. [175]	3

Table 5.6: List of extra interaction model uncertainties in addition to those provided by GENIE.

x_P	Description of P	P_{CV}
	Quasielastic	
BeRPA	Random Phase Approximation tune	$A : 0.59$
	A controls low Q^2, B controls low-mid Q^2	$B : 1.05$
	D controls mid Q^2, E controls high Q^2 fall-off	$D : 1.13$
	U controls transition from polynomial to exponential	$E : 0.88$
		$U : 1.20$
	2p2h	
MINERvA 2p2h tune	$q0, q3$ dependent correction to 2p2h events	
	Low W single pion production	
$x_{M_A}^{CCRES}$	Axial mass for CC resonance in GENIE	0.94
Non-res CC1π norm.	Normalization of CC1π non-resonant interaction	0.43

Table 5.7: Neutrino interaction cross-section systematic parameters that receive a central-value tune

5.5 The Near Detector Simulation and Reconstruction

Oscillation parameters are determined by comparing observed charged-current event spectra at the FD to predictions that are, *a priori*, subject to uncertainties on the neutrino flux and cross sections at the level of tens of percent as described in the preceding sections. To achieve the required few percent precision of DUNE, it is necessary to constrain these uncertainties with a highly capable ND suite. The ND is described in more detail in Volume I, Introduction to DUNE.

The broad ND concept is described briefly in Section 5.5.1, along with an outline of the ND's role in the oscillation analysis. The parameterized reconstruction and event selection is described in Section 5.5.2. ND and FD uncertainties, including those due to energy estimation and selection efficiencies, are discussed in Section 5.7.

5.5.1 The Near Detector Concept

The DUNE ND system consists of a liquid argon time-projection chamber (LArTPC) functionally coupled to a magnetized multi-purpose detector (MPD), and a System for on-Axis Neutrino Detection (SAND). The ND hall is located at Fermilab 574 m from the neutrino beam source and 60 m underground. The long dimension of the hall is oriented at 90 degrees with respect to the beam axis to facilitate measurements at both on-axis and off-axis locations with a movable detector system.

The LArTPC is modular, with fully-3D pixelated readout and optical segmentation. These features greatly reduce reconstruction ambiguities that hamper monolithic, projective-readout time projection chambers (TPCs), and enable the ND to function in the high-intensity environment of the DUNE ND site. Each module is itself a liquid argon (LAr) TPC with two anode planes and a central cathode. The active dimensions of each module are $1 \times 3 \times 1$ m ($x \times y \times z$), where the z direction is 6° upward from the neutrino beam, and the y direction points upward. Charge drifts in the $\pm x$ direction, with a maximum drift distance of 50 cm for ionization electrons produced in the center of a module. The module design is described in detail in Ref. [177]. The full LAr detector consists of an array of modules in a single cryostat. The minimum active size for full containment of hadronic showers is $3 \times 4 \times 5$ m. High-angle muons can also be contained by extending the width to 7 m. For this analysis, 35 modules are arranged in an array 5 modules deep in the z direction and 7 modules across in x so that the total active dimensions are $7 \times 3 \times 5$ m. The total active LAr volume is 105 m^3, corresponding to a mass of 147 tons.

The anode planes are tiled with readout pads, such that the yz coordinate is given by the pad location and the x coordinate is given by the drift time, and the three-dimensional position of an energy deposit is uniquely determined. A dedicated, low-power readout ASIC is being developed, which will enable single-pad readout without analog multiplexing [178]. The module walls orthogonal to the anode and cathode are lined with a photon detector that is sensitive to scintillation light produced inside the module, called ArCLight [179]. The detector is optically segmented, and tiled so that the vertical position of the optical flash can be determined with ∼30 cm resolution. It is therefore possible to isolate flashes to a volume of roughly 0.3 m^3, and associate them to a specific neutrino interaction even in the presence of pile-up. The neutrino interaction time, t_0, is determined from the prompt component of the scintillation light.

The MPD consists of a high-pressure gaseous argon time-projection chamber (GArTPC) in a cylindrical pressure vessel at 10 bar, surrounded by a granular, high-performance electromagnetic calorimeter. The MPD sits immediately downstream of the LAr cryostat so that the beam center crosses the exact center of both the LAr and gaseous argon active volumes. The pressure vessel is 5 m in diameter and 5 m long. The TPC is divided into two drift regions by a central cathode, and filled with a 90/10 Ar/CH_4 gas mixture, such that 97% of neutrino interactions will occur on the Ar target. The gas TPC is described in detail in Ref. [180].

The electromagnetic calorimeter is composed of a series of absorber layers followed by arrays of scintillator read out by SiPMs mounted directly onto boards. The inner-most layers will be tiled, giving 3D position information for each hit, and sufficient granularity to enable reconstruction of the angle of incoming photons. The electromagnetic calorimeter (ECAL) design is described in Ref. [181]. The entire MPD sits inside a magnetic field with a strength of at least 0.4 T. A superconducting magnet is preferred, to reduce the total amount of mass near the detectors.

The optimization of the detector design is still underway at the time of preparing this document, and the eventual parameters may be somewhat different from what is simulated. For the oscillation analysis presented herein, only the LAr event sample is explicitly used. The ECAL, pressure vessel, and magnet design have a small impact on the acceptance of muons originating in the LAr. The ECAL is assumed to be 30 layers of alternating planes of 5mm CH and 2mm Cu. The pressure vessel is assumed to be 3 cm thick titanium. The magnet is a solenoid with an inner radius of 320 cm, with a yoke cut out of the upstream barrel to minimize the passive material between the

two TPC detectors. The on-axis neutrino beam monitor SAND is not functionally coupled to the LAr detector and thus is not included in these simulations. Small changes in these parameters are not expected to significantly impact the acceptance. A profile view visualization of the ND as implemented in this analysis is shown in Figure 5.5.

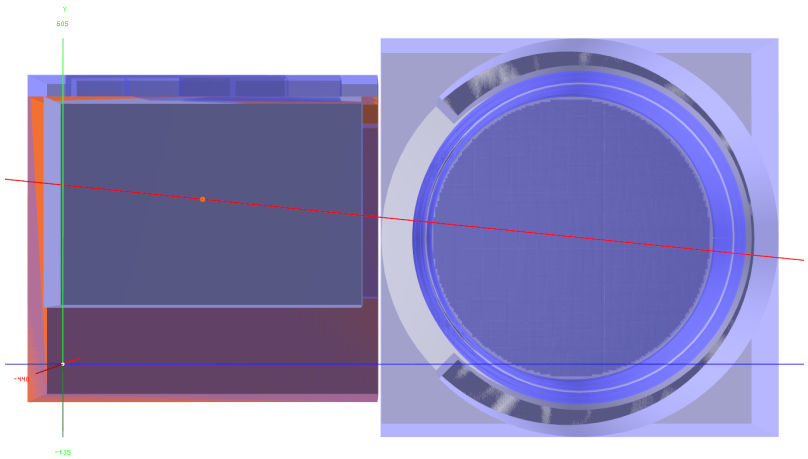

Figure 5.5: The near detector shown from the side. The neutrinos are incident from the left along the axis shown, which intersects the center of the LAr and GAr detectors.

The oscillation analysis includes samples of ν_μ and $\bar{\nu}_\mu$ charged-current interactions originating in the LAr. The samples are binned in 2D as a function of neutrino energy and inelasticity, $y = 1 - E_\mu/E_\nu$, where E_μ and E_ν are the muon and neutrino energies, respectively.

5.5.2 Event Simulation and Parameterized Reconstruction

Neutrino interactions are simulated in the active volumes of the LAr and high-pressure gas (HPG) TPCs. The neutrino flux prediction is described in Section 5.3. Interactions are simulated with the GENIE event generator using the model configuration described in Section 5.4. The propagation of neutrino interaction products through the detector volumes is simulated using a Geant4-based model. Pattern recognition and reconstruction software has not yet been developed for the ND. Instead, we perform a parameterized reconstruction based on true energy deposits in active detector volumes as simulated by Geant4.

5.5.2.1 Liquid Argon charged-current interactions

Liquid argon events are required to originate in a fiducial volume that excludes 50 cm from the sides and upstream edge, and 150 cm from the downstream edge of the active region, for a total of $6 \times 2 \times 3$ m^2. A hadronic veto region is defined as the outer 30 cm of the active volume on all sides. Events with more than 30 MeV total energy deposit in the veto region are excluded from analysis, as this energy near the detector edge suggests leakage, resulting in poor energy reconstruction. Even with the containment requirement, events with large shower fluctuations to neutral particles can still be very poorly reconstructed. Neutrons, in particular, are largely unreconstructed energy.

Electrons are reconstructed calorimetrically in the liquid argon. The radiation length is 14 cm in LAr, so for fiducial interactions and forward-going electrons there are between 10 and 30 radiation lengths between the vertex and the edge of the TPC. As there is no magnetic field in the LAr TPC region, electrons and positrons cannot be distinguished and the selected ν_e sample contains both neutrino- and antineutrino-induced events.

Muons with kinetic energy greater than ∼1 GeV typically exit the LAr. An energetic forward-going muon will pass through the ECAL and into the gaseous TPC, where its momentum and charge are reconstructed by curvature. For these events, it is possible to differentiate between μ^+ and μ^- event by event. Muons that stop in the LAr or ECAL are reconstructed by range. Exiting muons that do not match to the HPG TPC are not reconstructed, and events with these tracks are rejected from analysis. These are predominantly muon CC, where the muon momentum cannot be determined. Forward exiting muons will enter the magnetized MPD, where their momenta and charge sign are reconstructed by curvature. The asymmetric transverse dimensions of the LAr volume make it possible to reconstruct wide-angle muons with some efficiency. High-angle tracks are typically lost when the $\nu - \mu$ plane is nearly parallel to the y axis, but are often contained when it is nearly parallel to the x axis.

The charge of stopping muons in the LAr volume cannot be determined. However, the wrong-sign flux is predominantly concentrated in the high-energy tail, where leptons are likelier to be forward and energetic. In FHC mode, the wrong-sign background in the focusing peak is negligibly small, and μ^- is assumed for all stopping muon tracks. In RHC mode, the wrong-sign background is larger in the peak region. Furthermore, high-angle leptons are generally at higher inelasticity, y, which enhances the wrong-sign contamination in the contained muon subsample. To mitigate this, a Michel electron is required. The wrong-sign μ^- captures on Ar with 75% probability, effectively suppressing the relative μ^- component by a factor of four.

Events are classified as either ν_μ CC, $\bar{\nu}_\mu$ CC, ν_e+$\bar{\nu}_e$ CC, or NC. True muons and charged pions are evaluated as potential muon candidates. The track length is determined by following the true particle trajectory until it hard scatters or ranges out. The particle is classified as a muon if its track length is at least 1 m, and the mean energy deposit per centimeter of track length is less than 3 MeV. The mean energy cut rejects tracks with detectable hadronic interactions. The minimum length requirement imposes an effective threshold on true muons of about 200 MeV kinetic energy, but greatly suppresses potential NC backgrounds with short, non-interacting charged pions.

True electrons are reconstructed with an ad-hoc efficiency that is zero below 300 MeV, and rises linearly to unity between 300 and 700 MeV. Neutral-current backgrounds arise from photon and π^0 production. Photons are misreconstructed as electrons when the energy deposit per centimeter in the first few cm after conversion is less than 4 MeV. This is typically for Compton scatters, and can also occur due to a random downward fluctuation in the e^+e^- dE/dx. The conversion distance must also be small so that no visible gap can be identified. We consider a photon gap to be clear when the conversion distance is greater than 2 cm, which corresponds to at least four pad widths. For π^0 events, the second photon must also be either less than 50 MeV, or have an opening angle to the first photon less than 10 mrad. Electrons are generally contained in the LAr and are reconstructed calorimetrically. It is possible for CC ν_μ events to be reconstructed as CC ν_e when the muon is too soft and a π^0 fakes the electron.

LAr events are classified as ν_μ CC, $\bar{\nu}_\mu$ CC, $\nu_e + \bar{\nu}_e$ CC, or NC. Charged-current events are required to have exactly one reconstructed lepton of the appropriate flavor. The muon-flavor samples are separated by reconstructed charge, but the electron-flavor sample is combined because the charge cannot be determined. The neutral-current sample includes all events with zero reconstructed leptons. Spectra for selected ν_μ CC events in FHC are shown in Figure 5.6 as a function of both neutrino energy and inelasticity.

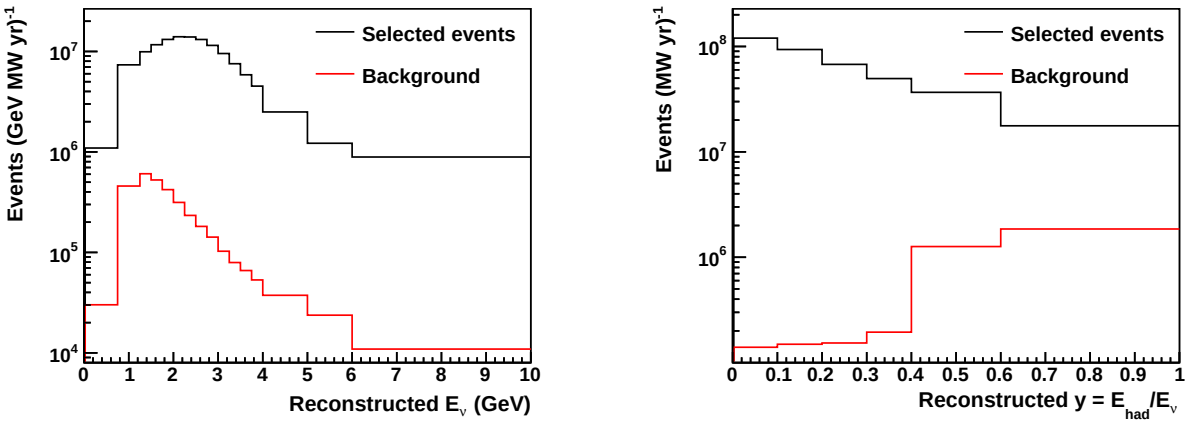

Figure 5.6: Reconstructed neutrino energy and y for events classified as ν_μ CC in FHC mode. Background events are predominantly neutral currents and are shown in red.

Hadronic energy is estimated by summing visible energy deposits in the active LAr volume. Events are rejected when energy is observed in the outer 30 cm of the detector, which is evidence of poor hadronic containment. Events with more than 30 MeV of visible hadronic energy in the veto region are also excluded. This leads to an acceptance that decreases with hadronic energy, as shown in the right panel of Figure 5.7.

Events are classified as either ν_μ CC, $\bar{\nu}_\mu$ CC, ν_e+$\bar{\nu}_e$ CC, or NC based on the presence of charged leptons. Backgrounds to ν_μ CC arise from NC $\pi^\pm$ production where the pion leaves a long track and does not shower. Muons below about 400 MeV kinetic energy have a significant background from charged pions, so these CC events are excluded from the selected sample. Backgrounds to ν_e CC arise from photons that convert very near the interaction vertex. The largest contribution is from π^0 production with highly asymmetric decay.

5.5.2.2 Neutrino-electron elastic scattering

In addition to the CC event selections, neutrino-electron elastic scattering is also selected. Measurements of neutrino-nucleus scattering are sensitive to the product of the flux and cross section, both of which are uncertain. This can lead to a degeneracy between flux and cross section nuisance parameters in the oscillation fit, and results in significant anti-correlations, even when the uncertainty on the diagonal component is small. One way to break this degeneracy is by including a sample for which the a priori cross section uncertainties are very small.

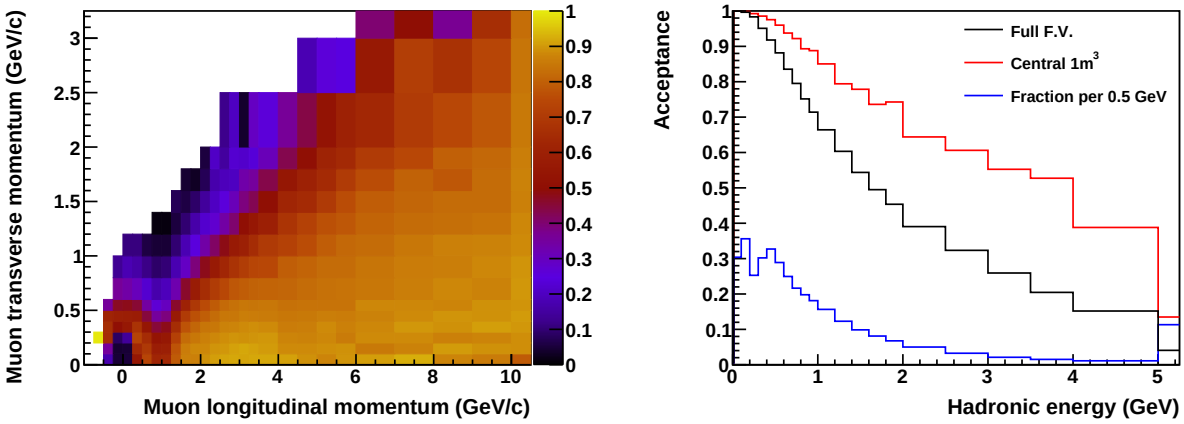

Figure 5.7: Left: Detector acceptance for ν_μ CC events as a function of muon transverse and longitudinal momentum. Right: Acceptance as a function of hadronic energy; the black line is for the full fiducial volume while the red line is for a $1 \times 1 \times 1$ m^3 volume in the center, and the blue curve is the expected distribution of hadronic energy given the DUNE flux.

Neutrino-electron scattering is a pure-electroweak process with calculable cross section. It is therefore possible to directly constrain the flux by measuring the event rate of $\nu + e \to \nu + e$ and dividing by the known cross section. The final state consists of a single electron, subject to the kinematic limit

$$1 - \cos\theta = \frac{m_e(1-y)}{E_e}, \tag{5.11}$$

where θ is the angle between the electron and incoming neutrino, E_e and m_e are the electron mass and total energy, respectively, and $y = T_e/E_\nu$ is the fraction of the neutrino energy transferred to the electron. For DUNE energies, $E_e \gg m_e$, and the angle θ is very small, such that $E_e\theta^2 < 2m_e$.

The overall flux normalization can be determined by counting $\nu e \to \nu e$ events. Events can be identified by searching for a single electromagnetic shower with no other visible particles. Backgrounds from ν_e charged-current scattering can be rejected by looking for large energy deposits near the interaction vertex, which are evidence of nuclear breakup. Photon-induced showers from neutral-current π^0 events can be distinguished from electrons by the energy profile at the start of the track. The dominant background is expected to be ν_e charged-current scattering at very low Q^2, where final-state hadrons are below threshold, and $E_e\theta^2$ happens to be small. The background rate can be constrained with a control sample at higher $E_e\theta^2$, but the shape extrapolation to $E_e\theta^2 \to 0$ is uncertain at the 10-20% level.

For the DUNE flux, approximately 100 events per year per ton of fiducial mass are expected with electron energy above 0.5 GeV. For a LAr TPC mass of 25 tons, this corresponds to 2500 events per year, or 12500 events in the full 5-year FHC run, assuming the ND stays on axis. Given the very forward signal, it may be possible to expand the fiducial volume to enhance the rate. The statistical uncertainty on the flux normalization from this technique is expected to be $\sim$1%.

To evaluate the impact of neutrino-electron scattering, a dedicated high-statistics signal-only sample is generated. Due to the simple nature of the signal, it is possible to estimate backgrounds without a full detector simulation. A single electromagnetic shower (electron, positron or photon) is required. To reject π^0 events with clearly-identifiable second photons, no additional showers over 50 MeV are allowed.

Charged-current ν_e interactions can be rejected when there is evidence of nuclear breakup in the form of final-state charged hadrons. A conservative cut of 40 MeV total charged hadron kinetic energy is applied. For a single proton, this corresponds to $\sim$ 1 cm of track length, which will leave energy on two or three readout pads and be easily identified. Finally, a cut requiring low $E_e\theta_e^2$ isolates the $\nu + e$ signal. Alternatively, templates in (E_e, θ_e) can be formed, and the unique shape of the signal can be used in a fit to extract the flux normalization.

5.5.2.3 Off-axis ND measurements

Neutrino energy reconstruction is one of the biggest challenges in a precision long-baseline oscillation experiment like DUNE. Even with a highly capable FD, a fraction of the final-state hadronic energy is typically not observed. For example, neutrons may travel meters without interacting, and can exit the detector with significant kinetic energy. This missing energy is typically corrected with a neutrino interaction generator, which is used to relate the true neutrino energy to the observed energy. These models have many tens of uncertain parameters, which can be constrained by ND measurements. However, there may be many different parameter combinations that adequately describe the ND data. These degenerate solutions can extrapolate differently to the FD, where the flux is significantly different due to oscillations. This can lead to biases in the fitted oscillation parameters, including δ_{CP}, despite an apparently good quality of fit.

While these biases can be partially mitigated by an on-axis ND capable of making numerous exclusive measurements, the energy dependence of the interaction cross section and the bias in reconstructed neutrino energy cannot be measured in a single beam. To gain sensitivity to these, the LArTPC and MPD combination is movable, and the ND hall is oriented to facilitate both on-axis measurements and measurements at positions up to 33 m off axis. The flux spectrum varies as a function of off-axis angle, peaking lower in energy as the angle is increased, from $\sim$2.5 GeV in the on-axis position down to $\sim$0.5 GeV at 33 m off axis. As uncertainties in the flux prediction are strongly correlated across off-axis angles, off-axis measurements of reconstructed neutrino energy constrain cross section uncertainties and provide further handles on possible degeneracies in the fit.

By taking linear combinations of such measurements, it is also possible to reproduce the predicted FD oscillated flux for some set of oscillation parameters, and directly compare visible energy between ND and FD over essentially the same "oscillated" flux, and with greatly reduced model dependence. Figure 5.8 shows the result of such a linear combination, overlaid with the FD flux. The oscillated flux is well reproduced between $\sim$0.5 GeV and $\sim$3.5 GeV. The lower E_ν bound is determined by the range of accessible off-axis angles; to cover down to 0.5 GeV, measurements out to 33 m off axis are required. The off-axis technique cannot reproduce the high-energy flux tail seen in the FD spectrum. This is because the off-axis spectra all provide lower peak energies; it is

not possible to produce a peak energy higher than that of the FD because the FD is on axis.

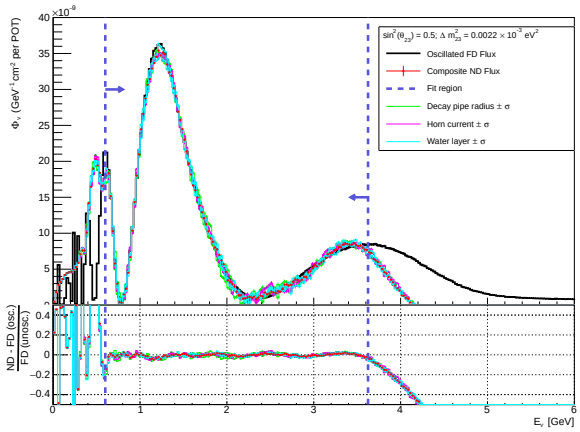

Figure 5.8: The predicted FD flux (black), and a prediction made up of linear combinations of ND fluxes (green).

A potential run plan is to take on-axis data approximately 50% of the time, with the other 50% split among enough off-axis positions so that the fiducial volumes of adjacent "stops" overlap, giving a continuous range of angles. Event selection at an off-axis location of the LAr detector is identical to the on-axis case. The selection efficiency varies as a function of muon energy due to containment and matching to the downstream magnetized tracker, and as a function of hadronic energy due to containment. As muon and hadronic energy are correlated to neutrino energy, the efficiency varies with off-axis position. The efficiency also varies as a function of vertex position; interactions occurring near the edges of the detector are more likely to fail containment requirements. These effects are corrected with simulation; as they are largely geometric, the uncertainties that arise from the corrections are small compared to the uncertainties on neutrino cross sections and energy reconstruction.

5.5.2.4 Gaseous argon charged-current interactions

With over 30 million charged-current events per year, the LArTPC event sample can be analyzed in many different exclusive channels and provide powerful constraints. However, its relatively high density makes certain hadronic topologies challenging to reconstruct. The gaseous TPC complements the LAr detector by providing low reconstruction thresholds, excellent pion/proton separation, and charge-sign reconstruction. In particular, measurements of proton and charged pion multiplicities as a function of neutrino energy constrain cross section uncertainties not accessible to the LAr alone.

In addition, the gas TPC provides a useful check on the reconstruction efficiency of the LAr selection. Due to the combining of contained muons with gas TPC-matched events, there are kinematic regions where the acceptance of the LArTPC is uncertain. Also, without a magnetic field, the wrong sign contamination cannot be directly measured, especially at high angle and low energy. The gas TPC, however, has uniform acceptance over the full 4π, as well as charge measurement capability except when the muon is nearly parallel to the magnetic field lines.

Unlike the LArTPC, where the hadronic energy is determined by a calorimetric sum of energy deposits, the gas TPC hadronic energy is reconstructed particle-by-particle, including pion masses. For this analysis, samples of ν_μ CC events are selected in slices of charged pion multiplicity, and fit as a function of reconstructed neutrino energy. The threshold for charged pion selection is 5 MeV, and π^+ can be reliably separated from protons up to momenta of 1.3 GeV/c.

5.6 The Far Detector Simulation and Reconstruction

The calculation of DUNE sensitivities to oscillation parameter measurements requires predictions for the number of events to be observed in the FD fiducial volume, the reconstructed neutrino energy for each of these events, and the probability that they will be correctly identified as signal for each analysis samples. To build these analysis samples a Geant4 simulation of the FD has been developed. The output of that simulation has been used to build neutrino energy estimators, and an event selection discriminant that can separate ν_e CC, ν_μ CC, and NC events. Each of these components is described in detail in this section. The uncertainties associated with each step in the simulation and reconstruction chain, including the FD simulation, reconstructed energy estimators, and selection efficiencies are discussed in Section 5.7.

5.6.1 Simulation

The neutrino samples were simulated using a smaller version of the full 10 kt far detector module geometry. This geometry is 13.9 m long, 12.0 m high and 13.3 m wide, which consists of 12 anode plane assemblies (APAs) and 24 cathode plane assemblies (CPAs). The reference flux was used (Section 5.3) and samples were produced with both the forward-horn-current (neutrino enhanced) and inverted-horn-current (antineutrino enhanced) beam configurations. Three samples were generated. The first sample keeps the original neutrino flavor composition of the neutrino beam. The second sample converts all the muon neutrinos to electron neutrinos. The third sample converts all the muon neutrinos to tau neutrinos. Oscillation probabilities are used to weight CC events to build oscillated FD predictions from the three event samples. GENIE 2.12.10 was used to model the neutrino-argon interactions in the volume of cryostat. The produced final-state (after FSI) particles were propagated in the detector through Geant4. The ionization electrons and scintillation light were digitized to produce signals in the wire planes and photon detectors (PDs). More details on the simulation can be found in Section 4.1.3.

5.6.2 Event Reconstruction and Kinematic Variables

The first step in the reconstruction is to convert the raw signal from each wire to a standard (e.g., Gaussian) shape. This is achieved by passing the raw data through a calibrated deconvolution algorithm to remove the impact of the LArTPC E field and the electronic response from the measured signal. The resulting wire waveform possesses calibrated charge information.

The hit-finding algorithm scans the processed wire waveform looking for local minima. If a minimum is found, the algorithm follows the waveform after this point until it finds a local maximum. If the maximum is above a specified threshold, the program scans to the next local minimum and identifies this region as a hit. Hits are fit with a Gaussian function whose features identify the correct position (time coordinate), width, height, and area (deposited charge) of the hit. A single Gaussian function is used to describe hits produced by isolated single particles. In regions where there are overlapping particles (e.g., around the neutrino interaction vertex) single Gaussian fits may fail, and fits to multiple Gaussian functions may be used. The reconstructed hits are used by reconstruction and event selection pattern recognition algorithms. In particular the convolutional visual network (CVN) event selection algorithm is described later in this section.

The reconstruction algorithms (Pandora and Projection Matching Algorithm (PMA)) define clusters as hits that may be grouped together due to proximity in time and space to one another. Clusters from different wire planes are matched to form high-level objects such as tracks and showers. These high level objects are used as inputs to the neutrino energy reconstruction algorithm. More details on the reconstruction can be found in section 4.2.

The energy of the incoming neutrino in CC events is estimated by adding the reconstructed lepton and hadronic energies. If the event is selected as ν_μ CC, the neutrino energy is estimated as the sum of the energy of the longest reconstructed track and the hadronic energy. The energy of the longest reconstructed track is estimated from its range if the track is contained in the detector, and this is calibrated using simulated ν_μ CC events with true muon energies from 0.2-1.7 GeV. If the longest track exits the detector, its energy is estimated from multi-Coulomb scattering, and corrected using simulated events with true muon energies from 0.5-3 GeV. The hadronic energy is estimated from the charge of reconstructed hits that are not in the longest track, and corrections are applied to each hit charge for recombination and the electron lifetime. An additional correction is then made to the hadronic energy to account for missing energy due to neutral particles and final-state interactions, and this is done using simulated events with true hadronic energies from 0.1-1.6 GeV. The same hadronic shower energy calibration is used for both ν and $\bar{\nu}$ based on a sample of ν and $\bar{\nu}$ events.

If the event is selected as ν_e CC, the energy of the neutrino is estimated as the sum of the energy of the reconstructed shower with the highest energy and the hadronic energy. The former is estimated from the charges of the reconstructed hits in the shower, and the latter from the hits not in the shower; the recombination and electron lifetime corrections are applied to the charge of each hit. Subsequently the shower energy is corrected using simulated events with true electron energies from 0.5-3 GeV, and the missing energy correction is applied to the hadronic energy.

The fractional residuals of reconstructed neutrino energy are shown for ν_μ CC events with contained tracks in figure 5.9, for ν_μ CC events with exiting tracks in figure 5.10 and for ν_e CC events in figure 5.11. The biases and resolutions of reconstructed neutrino energy are summarized in Table 5.8.

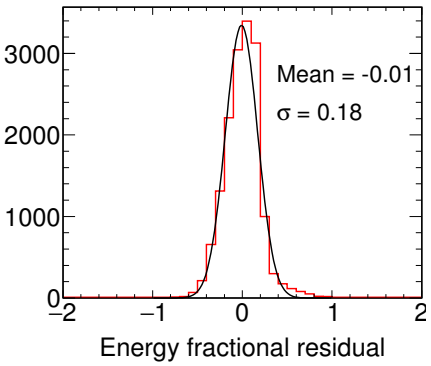

Figure 5.9: Fractional residuals of reconstructed ν_μ energy in ν_μ CC events with contained tracks

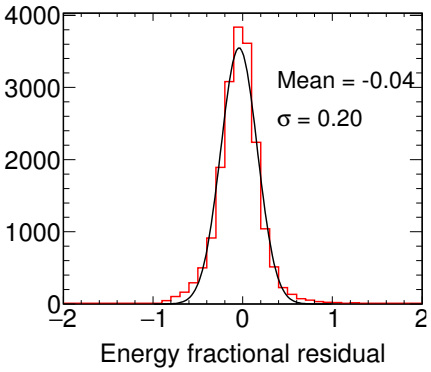

Figure 5.10: Fractional residuals of reconstructed ν_μ energy in ν_μ CC events with exiting tracks

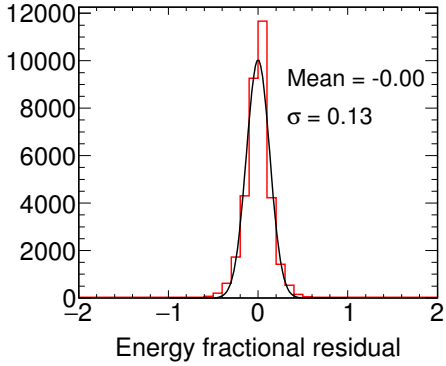

Figure 5.11: Fractional residuals of reconstructed ν_e energy in ν_e CC events

Event selection	Bias (%)	Resolution (%)
ν_μ CC with contained track	-1	18
ν_μ CC with exiting track	-4	20
ν_e CC	0	13

Table 5.8: Summary of biases and resolutions of reconstructed neutrino energy

5.6.3 Neutrino Event Selection using CVN

The DUNE CVN classifies neutrino interactions in the DUNE FD through image recognition techniques. In general terms it is a convolutional neural network (CNN). Similar techniques have been demonstrated to outperform traditional methods in many aspects of high energy physics [182].

The primary goal of the CVN is to efficiently and accurately produce event selections of the following interactions: ν_μ CC and ν_e CC in the FHC beam mode, and $\bar{\nu}_\mu$ CC and $\bar{\nu}_e$ CC in the RHC beam mode. Future goals will include studies of exclusive neutrino interaction final states since separating the event selections by interaction type can improve the sensitivity as interaction types have different energy resolutions and systematic uncertainties. Detailed descriptions of the CVN architecture can be found in [183].

An important feature for the DUNE CVN is the fine-grained detail of a LArTPC encoded in the input images to be propagated further into the CVN. This detail is more than what would be possible using a traditional CNN, such as the GoogLeNet-inspired network (also called Inception v1) [184] used by NOvA [183]. To accomplish this, the CVN design is based on the SE-ResNet architecture, which consists of a standard ResNet (residual neural network) architecture [185] along with Squeeze-and-Excitation blocks [186]. Residual neural networks allow the n^{th} layer access to the output of both the $(n-1)^{th}$ layer and the $(n-k)^{th}$ layer via a residual connection, where k is

a positive integer (≥ 2).

In order to build the training input to the DUNE CVN three images of the neutrino interactions are produced, one for each of the three readout views, using the reconstructed hits on the individual wire planes. The images are not dependent on any further downstream reconstruction algorithms. The images contain 500 $\times$ 500 pixels, each in the (wire, time) parameter space, where the wire is the wire channel number and the time is the peak time of the reconstructed hit. The value of each pixel represents the integrated charge of the reconstructed hit. An example simulated 2.2 GeV ν_e CC interaction is shown in all three views in Figure 5.12 demonstrating the fine-grained detail available from the LArTPC technology.

Figure 5.12: A simulated 2.2 GeV ν_e CC interaction shown in the collection view of the DUNE LArTPCs. The horizontal axis shows the wire number of the readout plane and the vertical axis shows time. The greyscale shows the charge of the energy deposits on the wires. The interaction looks similar in the other two views.

The CVN is trained using approximately three million neutrino interactions from the Monte Carlo (MC) simulation. An independent sample is used to generate the physics measurement sensitivities. The training sample is chosen to ensure similar numbers of training examples from the different neutrino flavors. Validation is performed to ensure that similar classification performance is obtained for the training and test samples, i.e., the CVN is not overtrained.

For the analysis presented here, we have used the primary output of the CVN, namely the neutrino flavor which returns probabilities that each interaction is one of the following classes: ν_μ CC, ν_e CC, ν_τ CC and NC.

5.6.3.1 Neutrino Flavor Identification Efficiency

The primary goal of the CVN algorithm is to accurately identify ν_e CC interactions and ν_μ CC interactions to allow for the selection of the samples required for the neutrino oscillation analysis. The ν_e CC probability distribution, $P(\nu_e \text{ CC})$, and the ν_μ CC probability distribution, $P(\nu_\mu \text{ CC})$, are shown on the left and right of Figure 5.13, respectively. Excellent separation between the signal

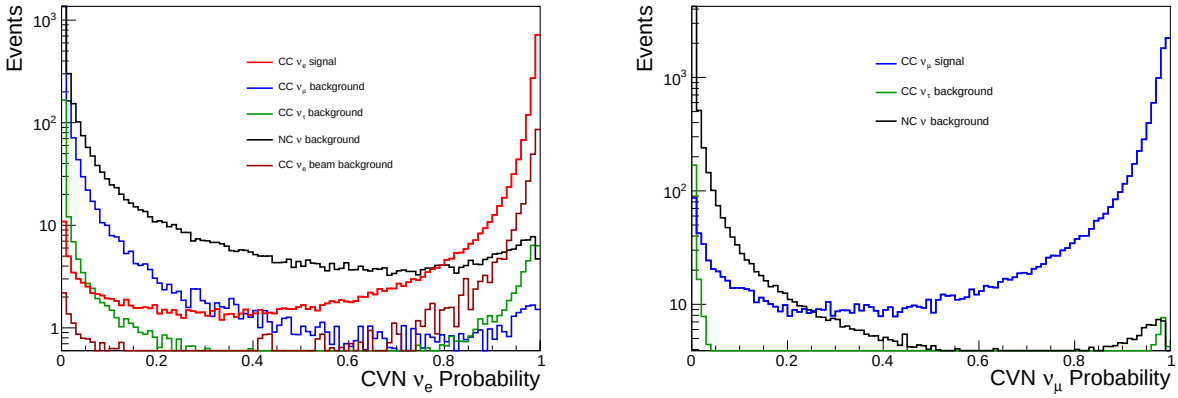

Figure 5.13: The CVN ν_e CC probability (left) and ν_μ CC probability (right) for the FHC beam mode shown with a log scale.

and background interactions is seen in both cases.

The ν_e CC event selection uses events where $P(\nu_e \text{ CC}) > 0.85$ for an interaction to be considered a candidate event of this type. Similarly, interactions are selected as ν_μ CC candidates if $P(\nu_\mu \text{ CC}) > 0.5$. Note that since all of the flavor classification probabilities must sum to one, the interactions selected in the two event selections are completely independent. The same selection criteria are used for both FHC and RHC beam modes. The values used in the selection criteria were optimized to produce the best δ_{CP} sensitivity.

Figure 5.14 shows the efficiency as a function of reconstructed energy (under the electron neutrino hypothesis) for the ν_e event selection. The efficiency in both the FHC and RHC beam modes exceeds 90% in the neutrino flux peak. Figure 5.15 shows the corresponding excellent selection efficiency for the ν_μ event selection.

5.6.3.2 Neutrino Flavor Identification Robustness

A common concern on the applications of Deep Learning in high energy physics is the potential for differences in performance between data and simulation. Work is in progress to evaluate the DUNE CVN using data from a large DUNE prototype, ProtoDUNE-SP [20]. While the data-based validation is underway a thorough investigation of the selection efficiency as a function of various event kinematics was carried out. The results of the investigation is that the CVN selection does not suffer from model dependence at a level that would undermine the conclusions of the oscillation analysis studies. All efficiency curves are consistent with a few key observations.

The ability of the CVN to identify neutrino flavor is dependent on its ability to resolve and identify the charged lepton. Backgrounds are induced by mis-identification of charged pions for ν_μ disappearance, and photons for ν_e appearance samples. Efficiency for these backgrounds tracks directly with the momentum and isolation of the energy depositions from the pions and photons. Efficiency was also observed to drop as a function of track/shower angle when energy depositions

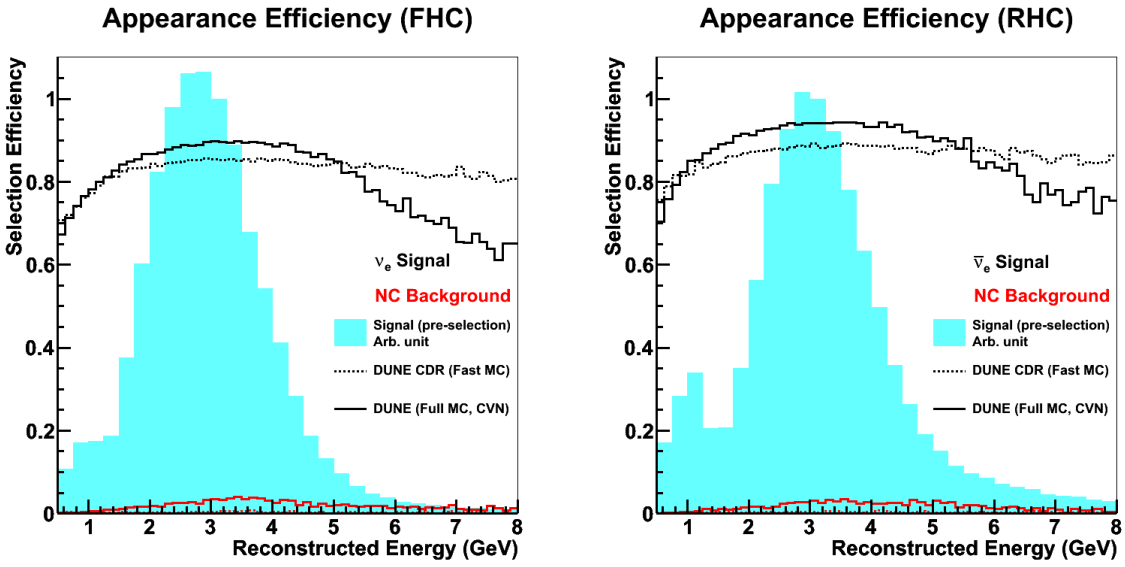

Figure 5.14: The ν_e CC selection efficiency for FHC-mode (left) and RHC-mode (right) simulation with the criterion $P(\nu_e \text{ CC}) > 0.85$. The solid (dashed) lines show results from the CVN (conceptual design report (CDR)) for signal ν_e CC and $\bar{\nu}_e$ CC events in black and NC background interaction in red. The blue region shows the oscillated flux (A.U.) to illustrate the most important regions of the energy distribution.

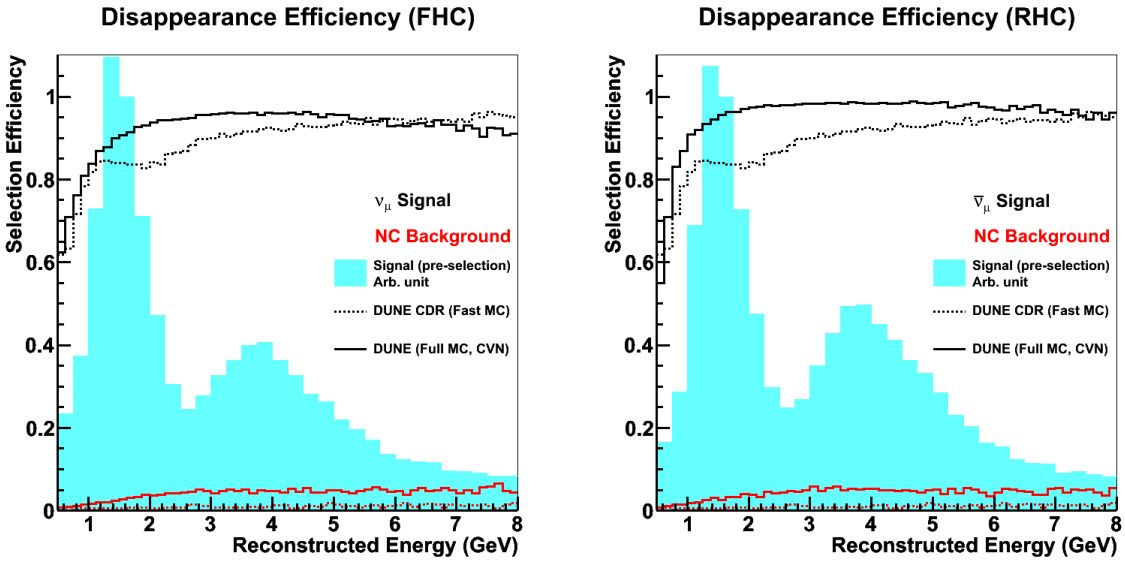

Figure 5.15: The ν_μ CC selection efficiency for FHC-mode (left) and RHC-mode (right) simulation with the criterion $P(\nu_\mu \text{ CC}) > 0.5$. The solid (dashed) lines show results from the CVN (CDR) for signal ν_μ CC and $\bar{\nu}_\mu$ CC events in black and NC background interaction in red. The blue region shows the oscillated flux (A.U.) to illustrate the most important regions of the energy distribution.

aligned with wire planes. The shapes of the efficiency functions in lepton momentum, lepton angle, and hadronic energy fraction (inelasticity) were all observed to be consistent with results from previous studies, including hand scans of LArTPC simulations. It is still conceivable that the efficacy is increased, especially at low charged lepton momentum, by the CVN identifying fine details of model dependent event kinematics. However, these effects are small enough to be covered by the assigned uncertainties.

Experience in ensuring robustness of deep learning image recognition techniques already exists within the community; similar techniques will be applied to future DUNE analyses. For example, the NOvA experiment uses a technique that takes clear ν_μ CC interactions identified in data and simulation and removes all of the reconstructed hits associated with the reconstructed muon track. The reconstructed muon is replaced by a simulated electron with the same kinematic variables [187, 188]. This procedure was originally developed by MINOS [189], and allows a large sample of data-like electron neutrino interactions to be studied and excellent agreement was seen between the performance of the event selection for data and simulation. This approach will prove critical once DUNE begins data taking to ensure the performance of the CVN is the same for data and simulation.

5.6.4 FD Neutrino Interaction Samples

A complete neutrino interaction event simulation has been implemented, including realistic neutrino energy reconstruction and event selection algorithms which yields an appropriately accurate representation of the FD samples to be used in the long-baseline oscillation analysis. The samples used in the sensitivity studies presented in this document require event by event simulations that effectively produce the convolution of the neutrino flux model, neutrino-argon scattering models, and models of the detector response. This last step must include estimates of energy smearing and bias, as well as the impact of a realistic event selection on signal acceptance and background rejection rates. This section has outlined the methods used to implement these algorithms. The final product is the selected FD event samples shown as a function of reconstructed neutrino energy in Section 5.2. Figure 5.2 shows the $\nu_\mu \to \nu_e$ and $\bar{\nu}_\mu \to \bar{\nu}_e$ appearance spectra and Figure 5.3 shows the $\nu_\mu \to \nu_\mu$ and $\bar{\nu}_\mu \to \bar{\nu}_\mu$ disappearance spectra. Tables 5.2 and 5.3 provide the signal and background event rates for the appearance and disappearance analyses, respectively. Based on these predictions we observe the largest background to the ν_e CC appearance signal to be the intrinsic beam ν_e interactions. There is also a contribution from misidentified neutral current interactions as well as small contributions from misidentified ν_μ and ν_τ interactions. The ν_μ disappearance signal has negligible background, though there is a significant "wrong-sign" ν_μ component in the $\bar{\nu_\mu}$ sample.

5.7 Detector Model and Uncertainties

Detector effects impact the event selection efficiency as well as the reconstruction of quantities used in the oscillation fit, such as neutrino energy. The main sources of detector systematic uncertainties

are limitations of calibration and modeling of particles in the detector. While neutrino interaction uncertainties can also affect reconstruction, this section is focused on effects that arise from the detectors.

The near LArTPC detector uses a similar technology as the far detector, namely they are both LArTPCs. However, important differences lead to uncertainties that do not fully correlate between the two detectors. First, the readout technology is different, as the near LArTPC uses pixels as well as a different, modular photon detector. Therefore, the charge response to particle types (e.g., muons and protons) will be different between near and far due to differences in electronics readout, noise, and local effects like alignment. Second, the high-intensity environment of the ND complicates associating detached energy deposits to events, a problem which does not exist in the FD. Third, the calibration programs will be different. For example, the ND has a high-statistics calibration sample of through-going, momentum-analyzed muons from neutrino interactions in the upstream rock, which does not exist for the FD. Finally, the reconstruction efficiency will be inherently different due to the relatively small size of the ND. Containment of charged hadrons will be significantly worse at the ND, especially for events with energetic hadronic showers or with vertices near the edges of the fiducial volume. Detector systematic uncertainties in the GArTPC at the near site will be entirely uncorrelated to the FD.

5.7.1 Energy Scale Uncertainties

An uncertainty on the overall energy scale is included in the analysis presented here, as well as particle response uncertainties that are separate and uncorrelated between four species: muons, charged hadrons, neutrons, and electromagnetic showers. In the ND, muons reconstructed by range in LAr and by curvature in MPD are treated separately. The energy scale and particle response uncertainties are allowed to vary with energy; each term is described by three free parameters:

$$E'_{rec} = E_{rec} \times (p_0 + p_1\sqrt{E_{rec}} + \frac{p_2}{\sqrt{E_{rec}}}) \tag{5.12}$$

where E_{rec} is the nominal reconstructed energy, E'_{rec} is the shifted energy, and p_0, p_1, and p_2 are free fit parameters that are allowed to vary within *a priori* constraints. The energy scale and resolution parameters are conservatively treated as uncorrelated between the ND and FD. With a better understanding of the relationship between ND and FD calibration and reconstruction techniques, it may be possible to correlate some portion of the energy response. The full list of energy scale uncertainties is given as Table 5.9. Uncertainties on energy resolutions are also included and are taken to be 2% for muons, charged hadrons, and EM showers and 40% for neutrons.

The scale of these uncertainties is derived from recent experiments, including calorimetric based approaches (NOvA, MINERvA) and LArTPCs (LArIAT, MicroBooNE, ArgoNeuT). On NOvA [190], the muon (proton) energy scale achieved is $< 1\%$ (5%). Uncertainties associated to the pion and proton re-interactions in the detector medium are expected to be controlled from ProtoDUNE and LArIAT data, as well as the combined analysis of low density (gaseous) and high density (LAr)

Table 5.9: Uncertainties applied to the energy response of various particles. p_0, p_1, and p_2 correspond to the constant, square root, and inverse square root terms in the energy response parameterization given in Equation 5.12. All are treated as uncorrelated between the ND and FD.

Particle	p_0	p_1	p_2
all (except muons)	2%	1%	2%
μ (range)	2%	2%	2%
μ (curvature)	1%	1%	1%
p, $\pi^{\pm}$	5%	5%	5%
e, γ, π^0	2.5%	2.5%	2.5%
n	20%	30%	30%

NDs. Uncertainties in the E field also contribute to the energy scale uncertainty, and calibration is needed (with cosmics at ND, laser system at FD) to constrain the overall energy scale. The recombination model will continue to be validated by the suite of LAr experiments and is not expected to be an issue for nominal field provided minimal E field distortions. Uncertainties in the electronics response are controlled with dedicated charge injection system and validated with intrinsic sources, Michel electrons and ^{39}Ar.

The response of the detector to neutrons is a source of active study and will couple strongly to detector technology. The validation of neutron interactions in LAr will continue to be characterized by dedicated measurements (e.g., CAPTAIN [191, 130]) and the LAr program (e.g., ArgoNeuT [192]). However, the association of the identification of a neutron scatter or capture to the neutron's true energy has not been demonstrated, and significant reconstruction issues exist, so a large uncertainty (20%) is assigned comparable to the observations made by MINERvA [193] assuming they are attributed entirely to the detector model. Selection of photon candidates from π^0 is also a significant reconstruction challenge, but a recent measurement from MicroBooNE indicates this is possible and the π^0 invariant mass has an uncertainty of 5%, although with some bias [194].

5.7.2 Acceptance and Reconstruction Efficiency Uncertainties

The ND and FD have different acceptance to CC events due to the very different detector sizes. The FD is sufficiently large that acceptance is not expected to vary significantly as a function of event kinematics. However, the ND selection requires that hadronic showers be well contained in LAr to ensure a good energy resolution, resulting in a loss of acceptance for events with energetic hadronic showers. The ND also has regions of muon phase space with lower acceptance due to tracks exiting the side of the TPC but failing to match to the MPD.

Uncertainties are evaluated on the muon and hadron acceptance of the ND. The detector acceptance for muons and hadrons is shown in Figure 5.7. Inefficiency at very low lepton energy is due to events being misreconstructed as neutral current, which can also be seen in Figure 5.7. For high energy, forward muons, the inefficiency is only due to events near the edge of the fiducial volume where the muon happens to miss the MPD. At high transverse momentum, muons begin to exit the side of the LAr active volume, except when they happen to go along the 7 m axis. The acceptance is sensitive to the modeling of muons in the detector. An uncertainty is estimated based on the change in the acceptance as a function of muon kinematics. This uncertainty can be constrained with the MPD by comparing the muon spectrum in CC interactions between the liquid and gaseous argon targets. The acceptance in the MPD is expected to be nearly 4π due to the excellent tracking and lack of scattering in the detector. Since the target nucleus is the same, and the two detectors are exposed to the same flux, the ratio between the two detectors is dominated by the LAr acceptance. Given the rate in the MPD, the expected constraint is at the level of $\sim$0.5% in the peak and $\sim$3% in the tail.

Inefficiency at high hadronic energy is due to the veto on more than 30 MeV deposited in the outer 30 cm collar of the active volume. Rejected events are typically poorly reconstructed due to low containment, and the acceptance is expected to decrease at high hadronic energy. Similar to the muon reconstruction, this acceptance is sensitive to detector modeling, and an uncertainty is evaluated based on the change in the acceptance as a function of true hadronic energy. This is more difficult to constrain with the MPD because of the uncertain mapping between true and visible hadronic energy in the LAr.

5.8 Sensitivity Methods

Sensitivities to the neutrino mass ordering, CP violation, and θ_{23} octant, as well as expected resolution for neutrino oscillation parameter measurements, are obtained by simultaneously fitting the $\nu_\mu \to \nu_\mu$, $\bar{\nu}_\mu \to \bar{\nu}_\mu$, $\nu_\mu \to \nu_e$, and $\bar{\nu}_\mu \to \bar{\nu}_e$ far detector spectra along with selected samples from the near detector. It is assumed that 50% of the total exposure is in neutrino beam mode and 50% in antineutrino beam mode. A 50%/50% ratio of neutrino to antineutrino data has been shown to produce a nearly optimal $\delta_{\rm CP}$ and mass ordering sensitivity, and small deviations from this (e.g., 40%/60%, 60%/40%) produce negligible changes in these sensitivities.

In the sensitivity calculations, neutrino oscillation parameters governing long-baseline neutrino oscillation are allowed to vary. In all sensitivities presented here (unless otherwise noted) $\sin^2 2\theta_{13}$ is constrained by a Gaussian prior with 1σ width as given by the relative uncertainty shown in Table 5.1, while $\sin^2\theta_{23}$, Δm^2_{32}, and $\delta_{\rm CP}$ are allowed to vary freely. The oscillation parameters θ_{12} and Δm^2_{12} are allowed to vary constrained by the uncertainty in Table 5.1. The matter density of the earth is allowed to vary constrained by a 2% uncertainty on its nominal value. Systematic uncertainty constraints from the near detector are included either by explicit inclusion of ND samples within the fit or by applying constraints expected from the ND data to FD-only fits.

The experimental sensitivity is quantified using a test statistic, $\Delta\chi^2$, which is calculated by comparing the predicted spectra for alternate hypotheses. The details of the sensitivity calculations

are described in Section 5.8.2. A "typical experiment" is defined as one with the most probable data given a set of input parameters, i.e., in which no statistical fluctuations have been applied. In this case, the predicted spectra and the true spectra are identical; for the example of CPV, $\chi^2_{\delta^{true}_{\rm CP}}$ is identically zero and the $\Delta\chi^2_{CP}$ value for a typical experiment is given by $\chi^2_{\delta^{test}_{\rm CP}}$. The interpretation of $\sqrt{\Delta\chi^2}$ has been discussed in [195, 196]; it may be interpreted as approximately equivalent to significance in σ for $\Delta\chi^2 > 1$.

DUNE sensitivity has been studied using several different fitting frameworks. General Long-Baseline Experiment Simulator (GLoBES) [197, 198] -based fits have been used extensively in the past, in particular for sensitivity studies presented in the DUNE CDR; details are available in [199, 200, 201]. GLoBES is now used primarily for studies in support of algorithm development and optimization. VALOR[202] has also been used for internal studies. The sensitivities presented in this document are calculated using the CAFAna analysis framework described below.

5.8.1 The DUNE Analysis Framework

To demonstrate the sensitivity reach of DUNE, we have adopted the analysis framework known as CAFAna [203]. This framework was developed for the NOvA experiment and has been used for ν_μ-disappearance, ν_e-appearance, and joint fits, plus sterile neutrino searches and cross-section analyses. Unless otherwise noted, sensitivity results presented in this document are performed within CAFAna.

In the sensitivity studies, the compatibility of a particular oscillation hypothesis with the data is evaluated using the likelihood appropriate for Poisson-distributed data [25]:

$$\chi^2 = -2\log\mathcal{L} = 2\sum_i^{N_{\rm bins}}\left[M_i - D_i + D_i\ln\left(\frac{D_i}{M_i}\right)\right] \tag{5.13}$$

where M_i is the MC expectation in bin i and D_i is the observed count. Most often the bins here represent reconstructed neutrino energy, but other observables, such as reconstructed kinematic variables or event classification likelihoods may also be used. Multiple samples with different selections can be fit simultaneously, as can multi-dimensional distributions of reconstructed variables.

Event records representing the reconstructed properties of neutrino interactions and, in the case of MC, the true neutrino properties are processed to fill the required histograms. Oscillated FD predictions are created by populating 2D histograms, with the second axis being the true neutrino energy, for each oscillation channel ($\nu_\alpha \to \nu_\beta$). These are then reweighted as a function of the true energy axis according to an exact calculation of the oscillation weight at the bin center and summed to yield the total oscillated prediction:

$$M_i = \sum_\alpha^{e,\mu}\sum_\beta^{e,\mu,\tau}\sum_j P_{\alpha\beta}(E_j)M_{ij}^{\alpha\beta} \tag{5.14}$$

where $P_{\alpha\beta}(E)$ is the probability for a neutrino created in flavor state α to be found in flavor state β at the FD. $M_{ij}^{\alpha\beta}$ represents the number of selected events in bin i of the reconstructed variable with true energy E_j, taken from a simulation where neutrinos of flavor α from the beam have been replaced by equivalent neutrinos in flavor β. Oscillation parameters that are not displayed in a given figure are profiled over using MINUIT [204]. That is, their values are set to those that produce the best match with the simulated data at each point in displayed parameter space.

Systematic uncertainties are included to account for the expected uncertainties in the beam flux, neutrino interaction, and detector response models used in the simulation at the time of the analysis. The neutrino interaction systematic uncertainties expand upon the existing GENIE systematic uncertainties to include recently exposed data/MC differences that are not expected to be resolved by the time DUNE starts running. The impact of systematic uncertainties is included by adding additional nuisance parameters into the fit. Each of these parameters can have arbitrary effects on the MC prediction, and can affect the various samples and channels within each sample in different ways. These parameters are profiled over in the production of the result. The range of these parameters is controlled by the use of Gaussian penalty terms to reflect our prior knowledge of reasonable variations.

For each systematic parameter under consideration, the matrices $M_{ij}^{\alpha\beta}$ are evaluated for a range of values of the parameter, by default $\pm 1, 2, 3\sigma$. The predicted spectrum at any combination of systematic parameters can then be found by interpolation. Cubic interpolation is used, which guarantees continuous and twice-differentiable results, advantageous for gradient-based fitters such as MINUIT.

For many systematic variations, a weight can simply be applied to each event record as it is filled into the appropriate histograms. For others, the event record itself is modified, and for a few systematic uncertainties it is necessary to use an entirely separate sample that has been simulated with some alteration made to the simulation parameters.

5.8.2 DUNE Sensitivity Studies

DUNE sensitivity studies are performed using the CAFAna framework, which works as described in the previous section. Sensitivity calculations for CPV, neutrino mass ordering, and octant are performed, in addition to studies of oscillation parameter resolution in one and two dimensions. The experimental sensitivity and resolution functions are quantified using a test statistic, $\Delta\chi^2$, which is calculated by comparing the predicted spectra for alternate hypotheses. These quantities are defined for neutrino mass ordering, θ_{23} octant, and CPV sensitivity as follows:

$$\Delta\chi^2_{\text{ordering}} = \chi^2_{\text{opposite}} - \chi^2_{\text{true}} \quad (5.15)$$

$$\Delta\chi^2_{\text{octant}} = \chi^2_{\text{opposite}} - \chi^2_{\text{either}} \quad (5.16)$$

$$\Delta\chi^2_{\text{CPV}} = \text{Min}[\Delta\chi^2_{CP}(\delta^{\text{test}}_{\text{CP}} = 0), \Delta\chi^2_{CP}(\delta^{\text{test}}_{\text{CP}} = \pi)], \quad (5.17)$$

where $\Delta\chi^2_{CP} = \chi^2_{\delta^{test}_{\rm CP}} - \chi^2_{\delta^{true}_{\rm CP}}$, and χ^2 is defined in Equation 5.14. Where appropriate, a scan is performed over all possible values of $\delta^{true}_{\rm CP}$, and the neutrino mass ordering and the θ_{23} octant are also assumed to be unknown and are free parameters. The lowest value of $\Delta\chi^2$ is obtained by finding the combination of fit parameters that best describe the simulated data. The size of $\Delta\chi^2$ is a measure of how well those data can exclude this alternate hypothesis given the uncertainty in the model.

The expected resolution for oscillation parameters is determined from the spread in best-fit values obtained from an ensemble of data sets that vary both statistically and systematically. For each data set, the true value of each nuisance parameter is chosen randomly from a distribution determined by the a priori uncertainty on the parameter. For some studies, oscillation parameters are also randomly chosen as described in Table 5.10. Poisson fluctuations are then applied to all analysis bins, based on the mean event count for each bin after the systematic adjustments have been applied. For each simulated data set in the ensemble, the test statistic is minimized, and the best-fit value of all parameters is determined. When calculating $\Delta\chi^2$ values from Equation 5.15, both of the individual χ^2 values used are calculated with the same data set. The one-sigma resolution is defined as the width of the interval around the true value containing 68% of simulated data sets. An alternative method of determining parameter resolutions, namely by identifying the range of parameters satisfying $\Delta\chi^2 < 1$, is also used for some studies.

Table 5.10: Treatment of the oscillation parameters for the simulated data set studies. The width of the θ_{13} range is determined from the NuFIT 4.0 result.

Parameter	Prior	Range
$\sin^2\theta_{23}$	Uniform	[0.4; 0.6]
$\lvert\Delta m^2_{32}\rvert$ ($\times 10^{-3}$ eV^2)	Uniform	|[2.3;2.7]|
$\delta_{\rm CP}$ (π)	Uniform	[-1;1]
θ_{13}	Gaussian	NuFIT 4.0

The DUNE oscillation sensitivities presented here include four FD CC samples binned as a function of reconstructed neutrino energy: $\nu_\mu \rightarrow \nu_\mu$, $\overline{\nu_\mu} \rightarrow \overline{\nu_\mu}$, $\nu_\mu \rightarrow \nu_e$, and $\overline{\nu_\mu} \rightarrow \overline{\nu_e}$. Systematic parameters are constrained by unoscillated ND ν_μ and $\bar{\nu}_\mu$ CC samples selected from the LAr TPC and binned in two dimensions as a function of reconstructed neutrino energy (E_ν) and reconstructed Bjorken y (i.e. inelasticity).

For some systematic uncertainties, such as uncertainties on the neutrino flux (Section 5.4), the natural treatment leads to a large number of parameters that have strongly-correlated effects on the predicted spectrum. In this case, principal component analysis (PCA) is used to create a greatly reduced set of systematic parameters which cover the vast majority of the allowed variation, and remove degenerate parameters. The flux PCA is described in Section 5.8.2.2.

Information from the ND, which is used to constrain systematic uncertainties, is included via additional χ^2 contributions (Equation 5.14) without oscillations. Specific ND samples such as

neutrino-electron elastic scattering and off-axis samples may be included separately. External constraints, for example from solar neutrino experiments, can be included as an arbitrary term in the χ^2 depending on the oscillation parameters. In practice, a quadratic term, corresponding to a Gaussian likelihood, is used.

5.8.2.1 Covariance matrix for ND uncertainties

Far detector energy scale and resolution uncertainties are treated as nuisance parameters in the oscillation fits. These parameters are allowed to vary, and in practice become very weakly constrained in Asimov fits due to the limited statistics of the FD. Detector uncertainties in the ND, in contrast, are included by adding a covariance matrix to the χ^2 calculation. This choice protects against overconstraining that could occur given the limitations of the parameterized ND reconstruction described in Section 5.5.2 taken together with the high statistical power at the ND. This covariance matrix is constructed with a many-universes technique. In each universe, all ND energy scale, resolution, and acceptance parameters are simultaneously thrown according to their respective uncertainties. The resulting spectra, in the same binning as is used in the oscillation sensitivity analysis, are compared with the nominal prediction to determine the bin-to-bin covariance.

5.8.2.2 Implementation of flux uncertainties

Uncertainties on the flux prediction are described by a covariance matrix, where each bin corresponds to an energy range of a particular beam mode, neutrino species, and detector location. The covariance matrix includes all beam focusing uncertainties evaluated by reproducing the simulation many times, each with simultaneous random variations in the underlying hadron production model. Each random model variation is referred to as a universe. The matrix used is 208×208 bins, despite having only $\sim$30 input uncertainties (and thus $\sim$30 significant eigenvalues). To evaluate the impact of these uncertainties on the long-baseline oscillation sensitivity, it is possible to include each focusing parameter, and each hadron production universe, as separate nuisance parameters. It is also possible to treat each bin of the prediction as a separate nuisance parameter, and include the covariance matrix in the log-likelihood calculation. However, both of these options are computationally expensive, and would include many nuisance parameters with essentially no impact on any distributions.

Instead, a principal component analysis is used, primarily to improve the computational performance of the analysis by reducing the number of parameters while still capturing the same physical effects. The covariance matrix is diagonalized, and each principal component is treated as an uncorrelated nuisance parameter. The 208 principal components are ordered by the magnitude of their corresponding eigenvalues, and only the first $\sim$30 are large enough that they need to be included. By the 10th principal component, the eigenvalue is 1% of the 0th eigenvalue. Since the time required to perform a fit scales $\sim$linearly with the number of nuisance parameters, including only 30 principal components reduces the computing time by an order of magnitude.

This is purely a mathematical transformation; the same effects are described by the PCA as by

a full analysis, including correlations between energy bins. As expected, the largest uncertainties correspond to the largest principal components. This can be seen in Figure 5.16. The largest principal component matches the hadron production uncertainty on nucleon-nucleus interactions in a phase space region not covered by data (N+A unconstrained). Components 3 and 7 correspond to the data-constrained uncertainty on proton interactions in the target producing pions and kaons, respectively. Components 5 and 11 correspond to two of the largest focusing uncertainties, the density of the target and the horn current, respectively. Other components not shown either do not fit a single uncertain parameter and may represent two or more degenerate systematics or ones that produce anticorrelations in neighboring energy bins.

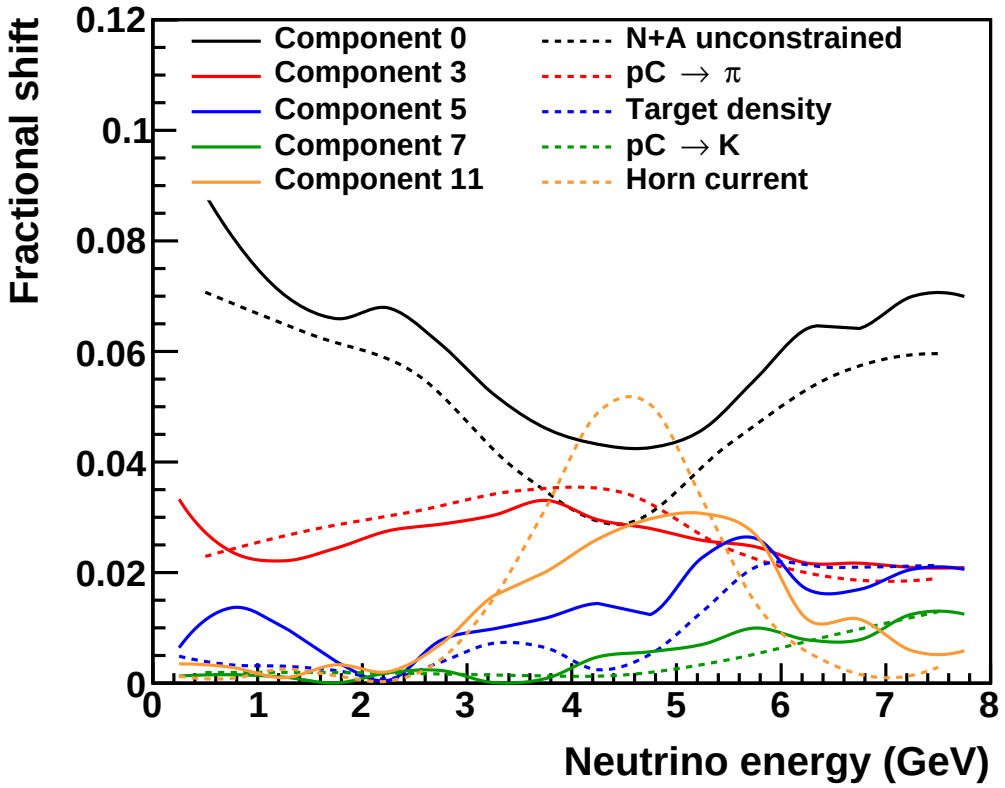

Figure 5.16: Select flux principal components are compared to specific underlying uncertainties from the hadron production and beam focusing models. See text.

5.9 Sensitivities

Using the analysis framework described in the preceding sections, the simulated data samples for the far and near detectors are input to fits for CP violation sensitivity, mass ordering sensitivity, parameter measurement resolutions, and octant sensitivity. The results of these fits are presented in the following sections. Unless otherwise noted, all results include samples from both the near

and far detectors and all systematic uncertainties are applied. Nominal exposures of seven, ten, and fifteen years are considered, where the staging plan described in Section 5.2, including a beam upgrade to 2.4 MW after six years, has been assumed. Results are shown as a function of the true values of oscillation parameters and/or as a function of exposure in staged years and/or kt-MW-years. In all cases, equal running in neutrino and antineutrino mode is assumed; no attempt is made to anticipate a realistic schedule of switching between neutrino and antineutrino mode. For the sake of simplicity, only true normal ordering is shown.

Possible variations of sensitivity are presented in several ways. For results at the nominal exposures, the sensitivity is calculated by performing fits in which the systematic parameters, oscillation parameters, and event rates are chosen at random, constrained in some cases by pre-fit uncertainties, as described in Section 5.8.2. A fit is performed for each of these simulated data sets or "throws;" the nominal result is the median of these fit results and the uncertainty band is calculated to be the interval containing 68% of the fit results. For these results, the uncertainty band is drawn as as transparent filled area. In other cases, ranges of possible sensitivity results are explored by considering different true values of oscillation parameters or different analysis assumptions, such as removal of external constraints or variation in systematic uncertainties assumptions. For these results, a solid band indicates the range of possible results; this band is not intended to be interpreted as an uncertainty.

The exposures required to reach selected sensitivity milestones for the nominal analysis are summarized in Table 5.11. CP violation sensitivity is discussed in Section 5.9.1, neutrino mass ordering sensitivity is discussed in Section 5.9.2, and precision measurements of oscillation parameters are discussed in Section 5.9.3. The impact of the true values of oscillation parameters, systematic uncertainties, and near detector measurements are explored in Sections 5.9.4, 5.9.5, and 5.9.6, respectively.

5.9.1 CP-Symmetry Violation

Figure 5.17 shows the significance with which CP violation ($\delta_{\rm CP} \neq 0$ or π) can be observed as a function of the true value of $\delta_{\rm CP}$ for exposures corresponding to seven and ten years of data, with equal running in neutrino and antineutrino mode, using the staging scenario described in Section 5.2. This sensitivity has a characteristic double peak structure because the significance of a CPV measurement necessarily drops to zero where there is no CPV: at the CP-conserving values of $-\pi$, 0, and π. The width of the transparent band represents 68% of fits when random throws are used to simulate statistical variations and select true values of the oscillation and systematic uncertainty parameters, constrained by pre-fit uncertainties. The solid curve is the median sensitivity. As illustrated in Section 5.9.4, variation in the true value of $\sin^2\theta_{23}$ is responsible for a significant portion of this variation.

Figure 5.18 shows the significance with which CP violation can be determined for 75% and 50% of $\delta_{\rm CP}$ values, and when $\delta_{\rm CP} = -\pi/2$, as a function of exposure in years, using the staging scenario described in Section 5.2. It is not possible for any experiment to provide 100% coverage in $\delta_{\rm CP}$ for a CPV measurement because CPV effects vanish at certain values of $\delta_{\rm CP}$. The changes in trajectory of the curves in the first three years results from the staging of far detector module installation;

Physics Milestone	Exposure (staged years, $\sin^2\theta_{23} = 0.580$)
5σ Mass Ordering $\delta_{\rm CP} = \text{-}\pi/2$	1
5σ Mass Ordering 100% of $\delta_{\rm CP}$ values	2
3σ CP Violation $\delta_{\rm CP} = \text{-}\pi/2$	3
3σ CP Violation 50% of $\delta_{\rm CP}$ values	5
5σ CP Violation $\delta_{\rm CP} = \text{-}\pi/2$	7
5σ CP Violation 50% of $\delta_{\rm CP}$ values	10
3σ CP Violation 75% of $\delta_{\rm CP}$ values	13
$\delta_{\rm CP}$ Resolution of 10 degrees $\delta_{\rm CP} = 0$	8
$\delta_{\rm CP}$ Resolution of 20 degrees $\delta_{\rm CP} = \text{-}\pi/2$	12
$\sin^2 2\theta_{13}$ Resolution of 0.004	15

Table 5.11: Exposure in years, assuming true normal ordering and equal running in neutrino and antineutrino mode, required to reach selected physics milestones in the nominal analysis, using the NuFIT 4.0 best-fit values for the oscillation parameters. As discussed in Section 5.9.4, there are significant variations in sensitivity with the value of $\sin^2\theta_{23}$, so the exact values quoted here are strongly dependent on that choice. The staging scenario described in Section 5.2 is assumed. Exposures are rounded to the nearest year. For reference, 30, 100, 200, 336, 624, and 1104 kt · MW · year correspond to 1.2, 3.1, 5.2, 7, 10, and 15 staged years, respectively.

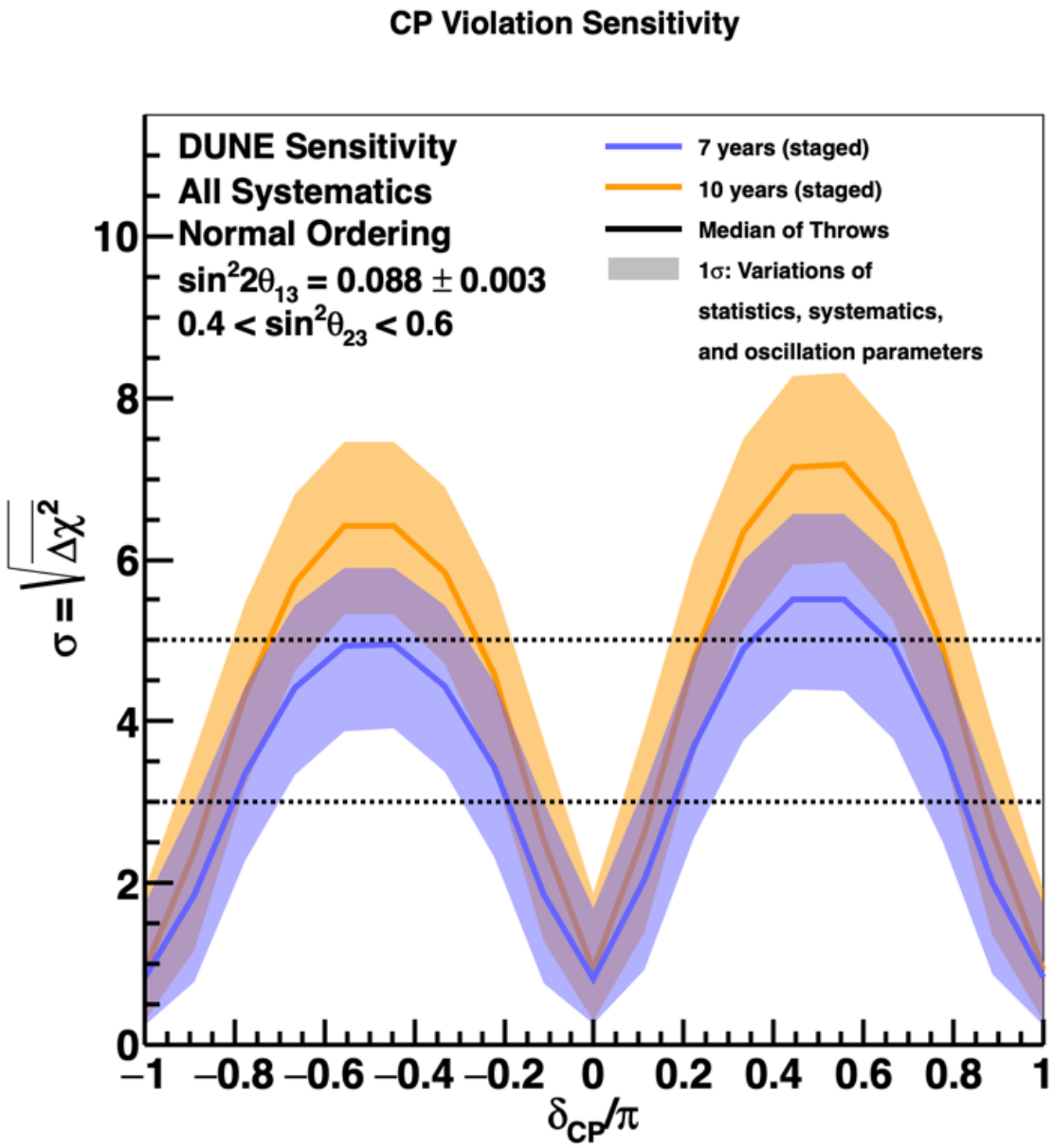

Figure 5.17: Significance of the DUNE determination of CP-violation (i.e.: $\delta_{\rm CP} \neq 0$ or π) as a function of the true value of $\delta_{\rm CP}$, for seven (blue) and ten (orange) years of exposure. True normal ordering is assumed. The width of the transparent bands cover 68% of fits in which random throws are used to simulate statistical variations and select true values of the oscillation and systematic uncertainty parameters, constrained by pre-fit uncertainties. The solid lines show the median sensitivity.

the change at 6 years is due to the upgrade from 1.2- to 2.4-MW beam power. The width of the bands show the impact of applying an external constraint on $\sin^2 2\theta_{13}$. As seen in Table 5.11, CP violation can be observed with 5σ significance after about 7 years if $\delta_{\rm CP} = -\pi/2$ and after about 10 years for 50% of $\delta_{\rm CP}$ values. CP violation can be observed with 3σ significance for 75% of $\delta_{\rm CP}$ values after about 13 years of running. Figure 5.19 shows the same CP violation sensitivity as a function of exposure in kt-MW-years. In the left plot, the width of the bands shows the impact of applying an external constraint on $\sin^2 2\theta_{13}$, while in the right plot, the width of the bands is the result of varying the true value of $\sin^2 \theta_{23}$ within the NuFIT 4.0 90% C.L. allowed region.

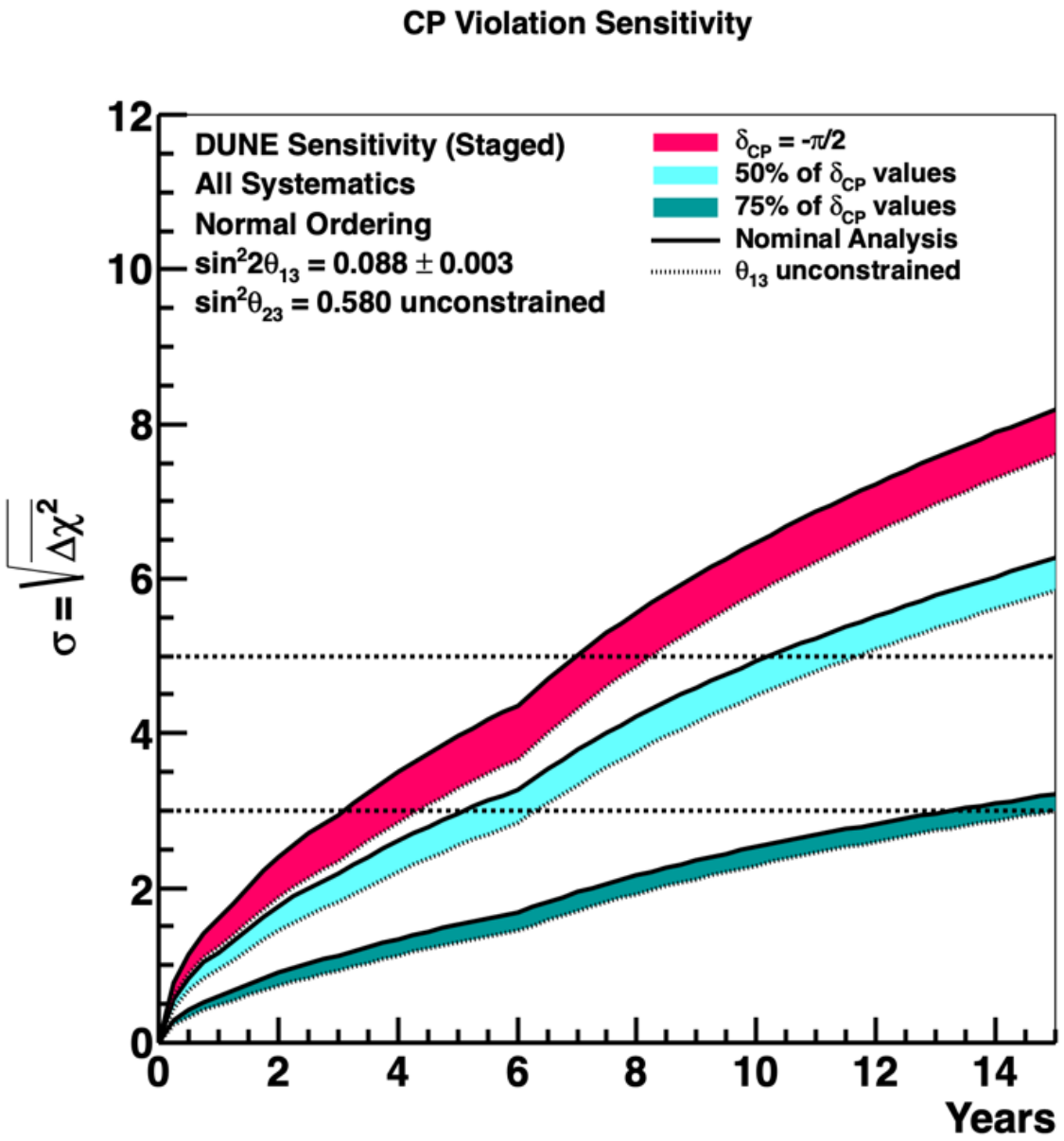

Figure 5.18: Significance of the DUNE determination of CP-violation (i.e.: $\delta_{\rm CP} \neq 0$ or π) for the case when $\delta_{\rm CP} = -\pi/2$, and for 50% and 75% of possible true $\delta_{\rm CP}$ values, as a function of time in calendar years. True normal ordering is assumed. The width of the band shows the impact of applying an external constraint on $\sin^2 2\theta_{13}$.

5.9.2 Mass Hierarchy

Figure 5.20 shows the significance with which the neutrino mass ordering can be determined as a function of the true value of $\delta_{\rm CP}$, using the same exposures and staging assumptions described in the previous section. The characteristic shape results from near degeneracy between matter and CP-violating effects that occurs near $\delta_{\rm CP} = \pi/2$ for true normal ordering. As in the CP violation sensitivity, the solid curve represents the median sensitivity, the width of the transparent band represents 68% of fits when random throws are used to simulate statistical variations and

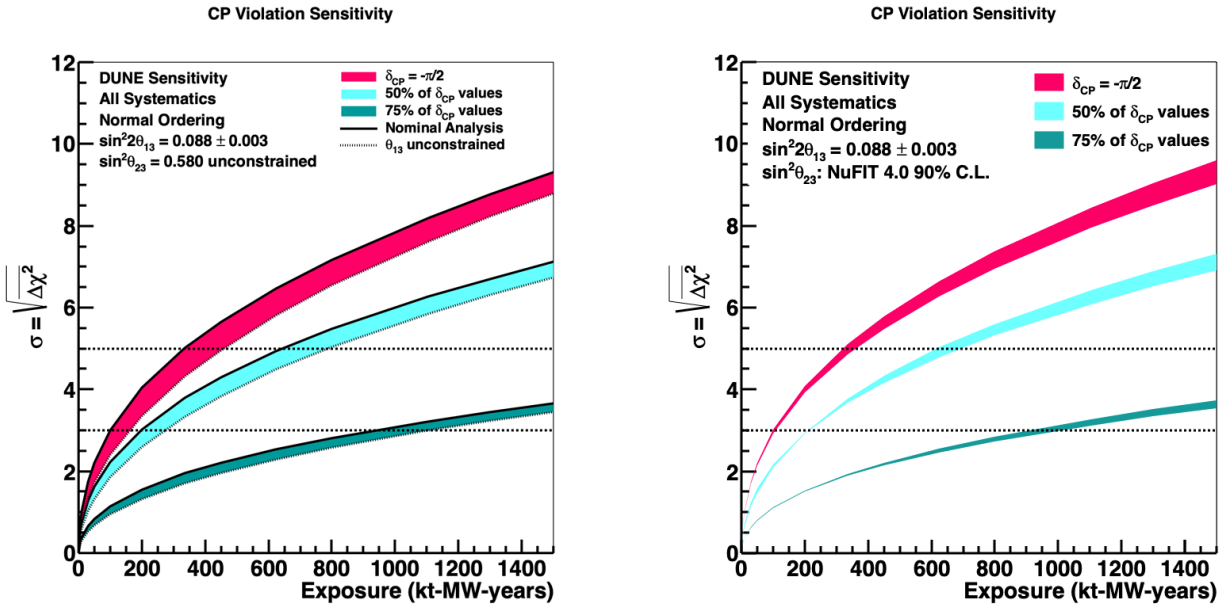

Figure 5.19: Significance of the DUNE determination of CP-violation (i.e.: $\delta_{\rm CP} \neq 0$ or π) for the case when $\delta_{\rm CP} = -\pi/2$, and for 50% and 75% of possible true $\delta_{\rm CP}$ values, as a function of exposure in kt-MW-years. True normal ordering is assumed. Left: The width of the band shows the impact of applying an external constraint on $\sin^2 2\theta_{13}$. Right: The width of the band shows the impact of varying the true value of $\sin^2\theta_{23}$ within the NuFIT 4.0 90% C.L. region. For reference, 30, 100, 200, 336, 624, and 1104 kt · MW · year correspond to 1.2, 3.1, 5.2, 7, 10, and 15 staged years, respectively.

select true values of the oscillation and systematic uncertainty parameters, constrained by pre-fit uncertainties, and variation in the true value of $\sin^2\theta_{23}$ is responsible for a significant portion of this variation.

Figure 5.21 shows the significance with which the neutrino mass ordering can be determined for 100% of $\delta_{\rm CP}$ values, and when $\delta_{\rm CP} = -\pi/2$, as a function of exposure in years. The width of the bands show the impact of applying an external constraint on $\sin^2 2\theta_{13}$. Figure 5.22 shows the same sensitivity as a function of exposure in kt-MW-years. As DUNE will be able to establish the neutrino mass ordering at the 5-σ level for 100% of $\delta_{\rm CP}$ values after between two and three years, these plots extend only to seven years and 500 kt-MW-years, respectively.

Studies have indicated that special attention must be paid to the statistical interpretation of neutrino mass ordering sensitivities [195, 196] because the $\Delta\chi^2$ metric does not follow the expected chi-squared function for one degree of freedom, so the interpretation of the sensitivity given by the Asimov data set is less straightforward. The error band on the mass ordering sensitivity shown in Figure 5.20 includes this effect using the technique of statistical throws described in Section 5.8.2. The effect of statistical fluctuation and systematic uncertainties in the neutrino mass ordering sensitivity for values of $\sin^2\theta_{23}$ in the range 0.56 to 0.60 is explored using random throws to determine the 1- and 2-σ ranges of possible sensitivity. The resulting range of sensitivities is shown in Figure 5.23, for 10 years of exposure.

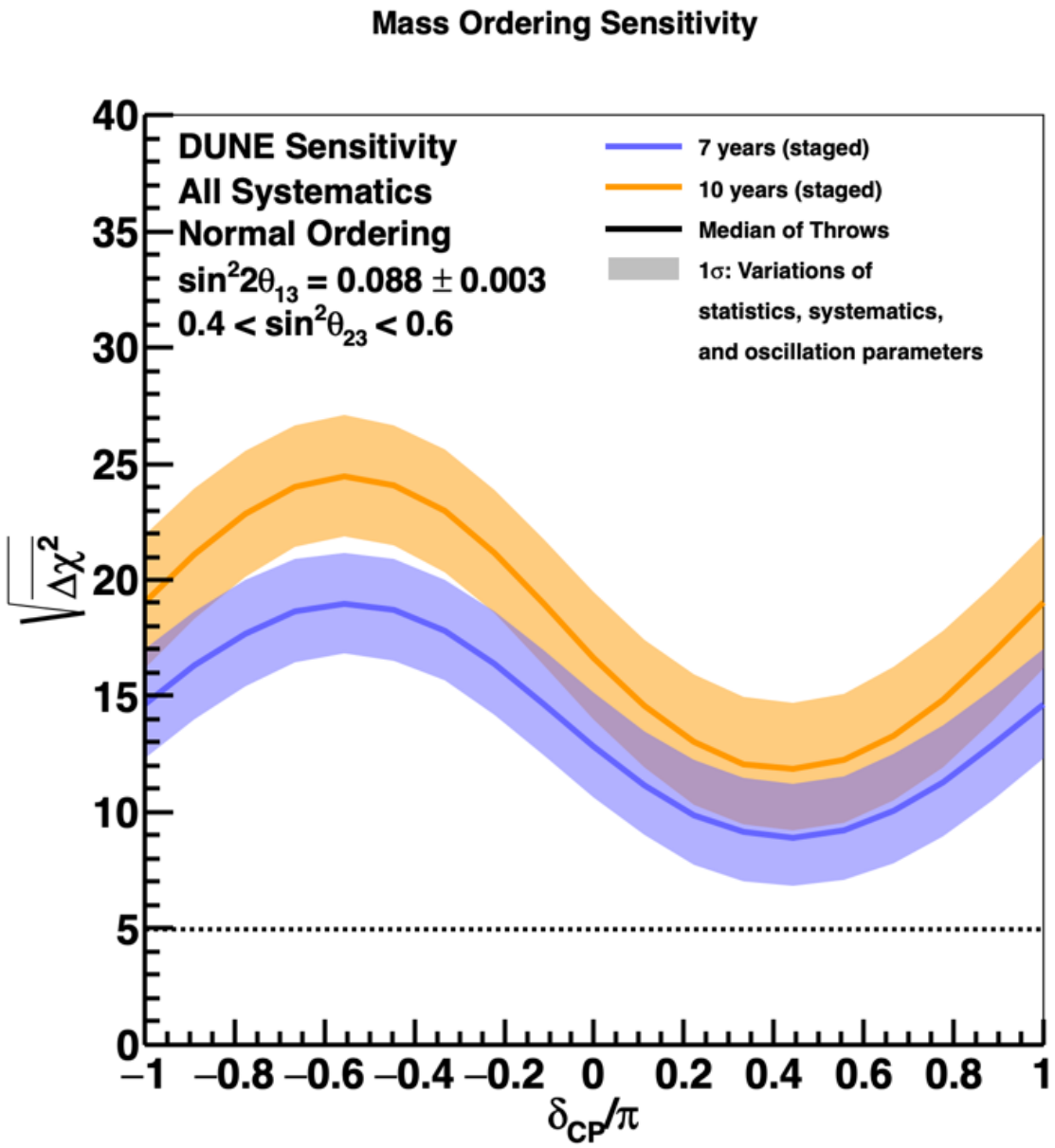

Figure 5.20: Significance of the DUNE determination of the neutrino mass ordering, as a function of the true value of $\delta_{\rm CP}$, for seven (blue) and ten (orange) years of exposure. True normal ordering is assumed. The width of the transparent bands cover 68% of fits in which random throws are used to simulate statistical variations and select true values of the oscillation and systematic uncertainty parameters, constrained by pre-fit uncertainties. The solid lines show the median sensitivity.

5.9.3 Precision Oscillation Parameter Measurements

In addition to the discovery potential for neutrino mass hierarchy and CPV, DUNE will improve the precision on key parameters that govern neutrino oscillations, including: $\delta_{\rm CP}$, $\sin^2 2\theta_{13}$, Δm^2_{31}, $\sin^2\theta_{23}$ and the octant of θ_{23}.

Figure 5.24 shows the resolution, in degrees, of DUNE's measurement of $\delta_{\rm CP}$, as a function of the

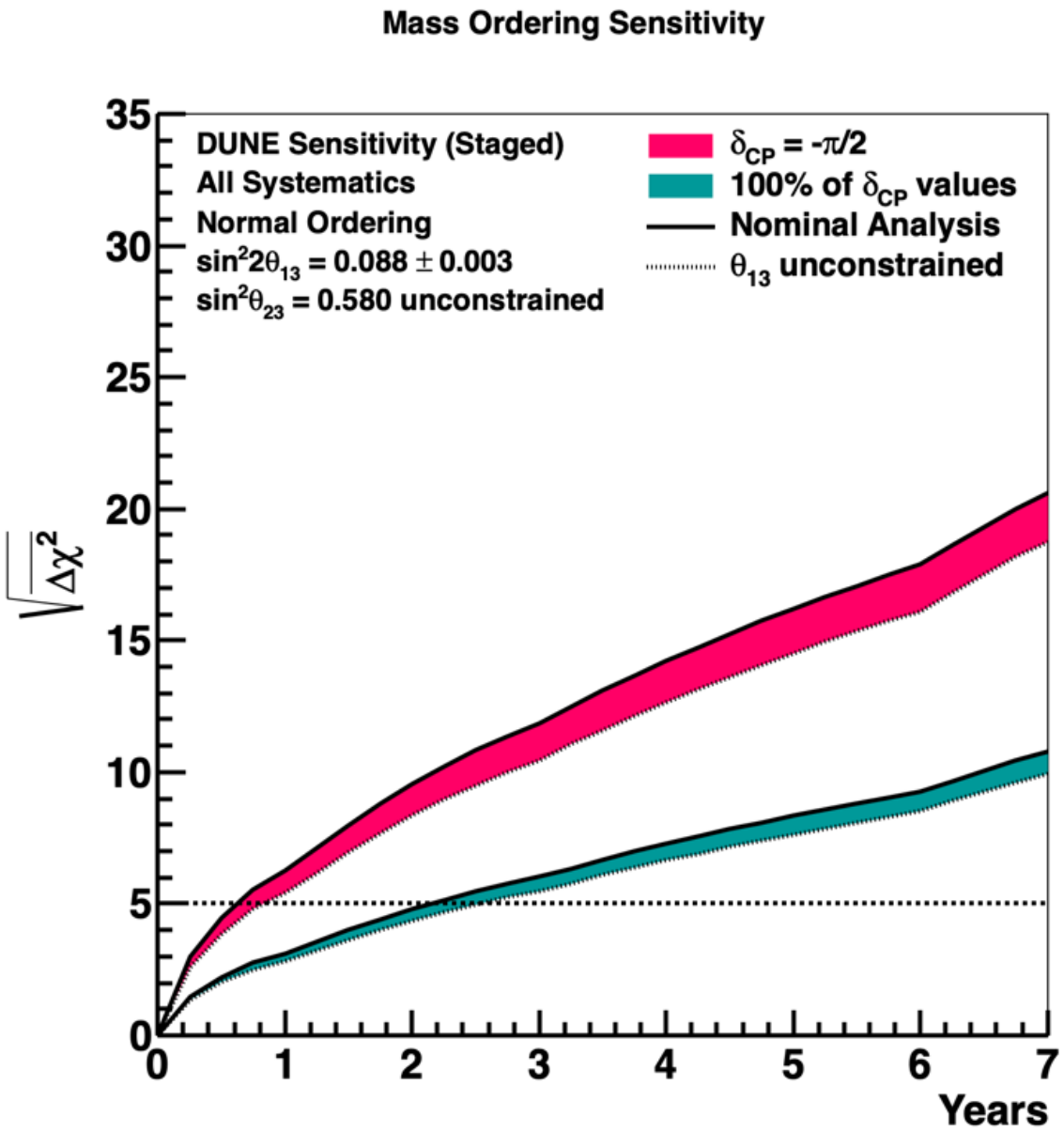

Figure 5.21: Significance of the DUNE determination of the neutrino mass ordering for the case when $\delta_{\rm CP} = -\pi/2$, and for 100% of possible true $\delta_{\rm CP}$ values, as a function of time in calendar years. True normal ordering is assumed. The width of the band shows the impact of applying an external constraint on $\sin^2 2\theta_{13}$.

true value of $\delta_{\rm CP}$. The resolution of this measurement is significantly better near CP-conserving values of $\delta_{\rm CP}$, compared to maximally CP-violating values. For fifteen years of exposure, resolutions between five and fifteen degrees are possible, depending on the true value of $\delta_{\rm CP}$. A smoothing algorithm has been applied to interpolate between values of $\delta_{\rm CP}$ at which the full analysis has been performed.

Figures 5.25 and 5.26 show the resolution of DUNE's measurements of $\delta_{\rm CP}$ and $\sin^2 2\theta_{13}$ and of $\sin^2 2\theta_{23}$ and Δm^2_{32}, respectively, as a function of exposure in kt-MW-years. As seen in Figure 5.24, the $\delta_{\rm CP}$ resolution varies significantly with the true value of $\delta_{\rm CP}$, but for favorable values, resolutions

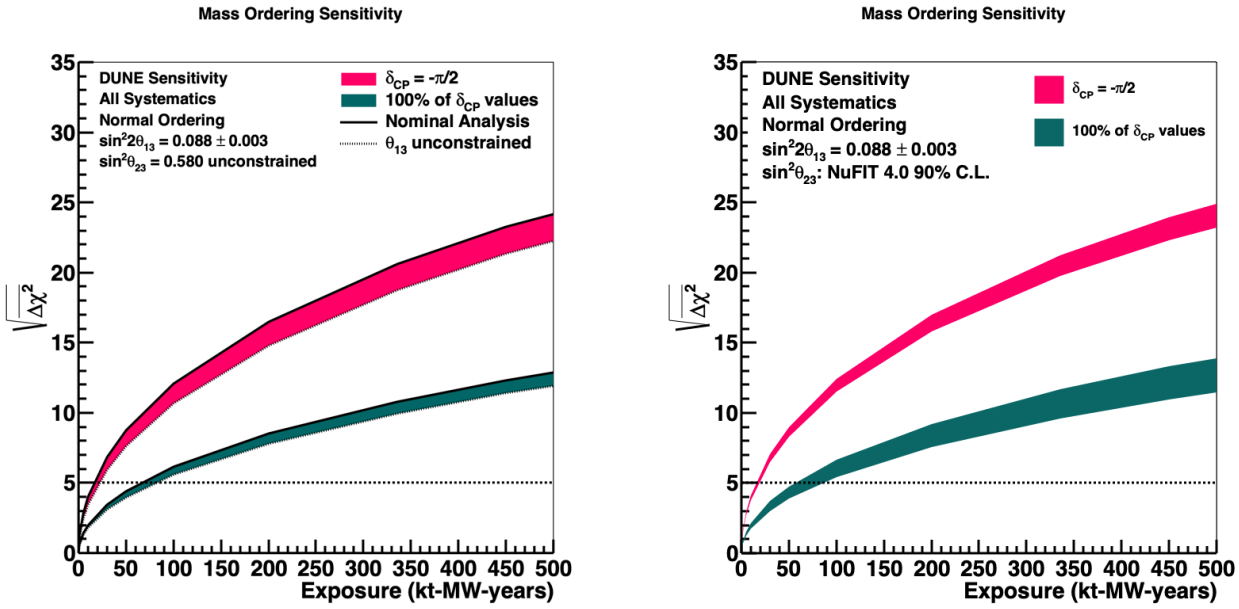

Figure 5.22: Significance of the DUNE determination of the neutrino mass ordering for the case when $\delta_{\rm CP} = -\pi/2$, and for 100% of possible true $\delta_{\rm CP}$ values, as a function of exposure in kt-MW-years. True normal ordering is assumed. Left: The width of the band shows the impact of applying an external constraint on $\sin^2 2\theta_{13}$. Right: The width of the band shows the impact of varying the true value of $\sin^2\theta_{23}$ within the NuFIT 4.0 90% C.L. region. For reference, 30, 100, 200, and 336 kt · MW · year correspond to 1.2, 3.1, 5.2, and 7 staged years, respectively.

near five degrees are possible for large exposure. The DUNE measurement of $\sin^2 2\theta_{13}$ approaches the precision of reactor experiments for high exposure, allowing a comparison between the two results, which is of interest as a test of the unitarity of the PMNS matrix.

One of the primary physics goals for DUNE is the simultaneous measurement of all oscillation parameters governing long-baseline neutrino oscillation, without a need for external constraints. Figure 5.27 shows the 90% C.L. allowed regions for $\sin^2 2\theta_{13}$ and $\delta_{\rm CP}$ for 7, 10, and 15 years of running, when no external constraints are applied, compared to the current measurements from world data. Note that a degenerate lobe at higher values of $\sin^2 2\theta_{13}$ is present in the 7-year exposure, but is resolved for higher exposures. Figure 5.28 shows the two-dimensional allowed regions for $\sin^2\theta_{23}$ and $\delta_{\rm CP}$. Figure 5.29 explores the resolution sensitivity that is expected for values of $\sin^2\theta_{23}$ different from the NuFIT 4.0 central value. It is interesting to note that the lower exposure, opposite octant solutions for $\sin^2\theta_{23}$ are allowed at 90% C.L. in the absence of an external constraint on $\sin^2 2\theta_{13}$; however, at the 10 year exposure, this degeneracy is resolved by DUNE data without external constraint.

The measurement of $\nu_\mu \to \nu_\mu$ oscillations is sensitive to $\sin^2 2\theta_{23}$, whereas the measurement of $\nu_\mu \to \nu_e$ oscillations is sensitive to $\sin^2\theta_{23}$. A combination of both ν_e appearance and ν_μ disappearance measurements can probe both maximal mixing and the θ_{23} octant. Figure 5.30 shows the sensitivity to determining the octant as a function of the true value of $\sin^2\theta_{23}$.

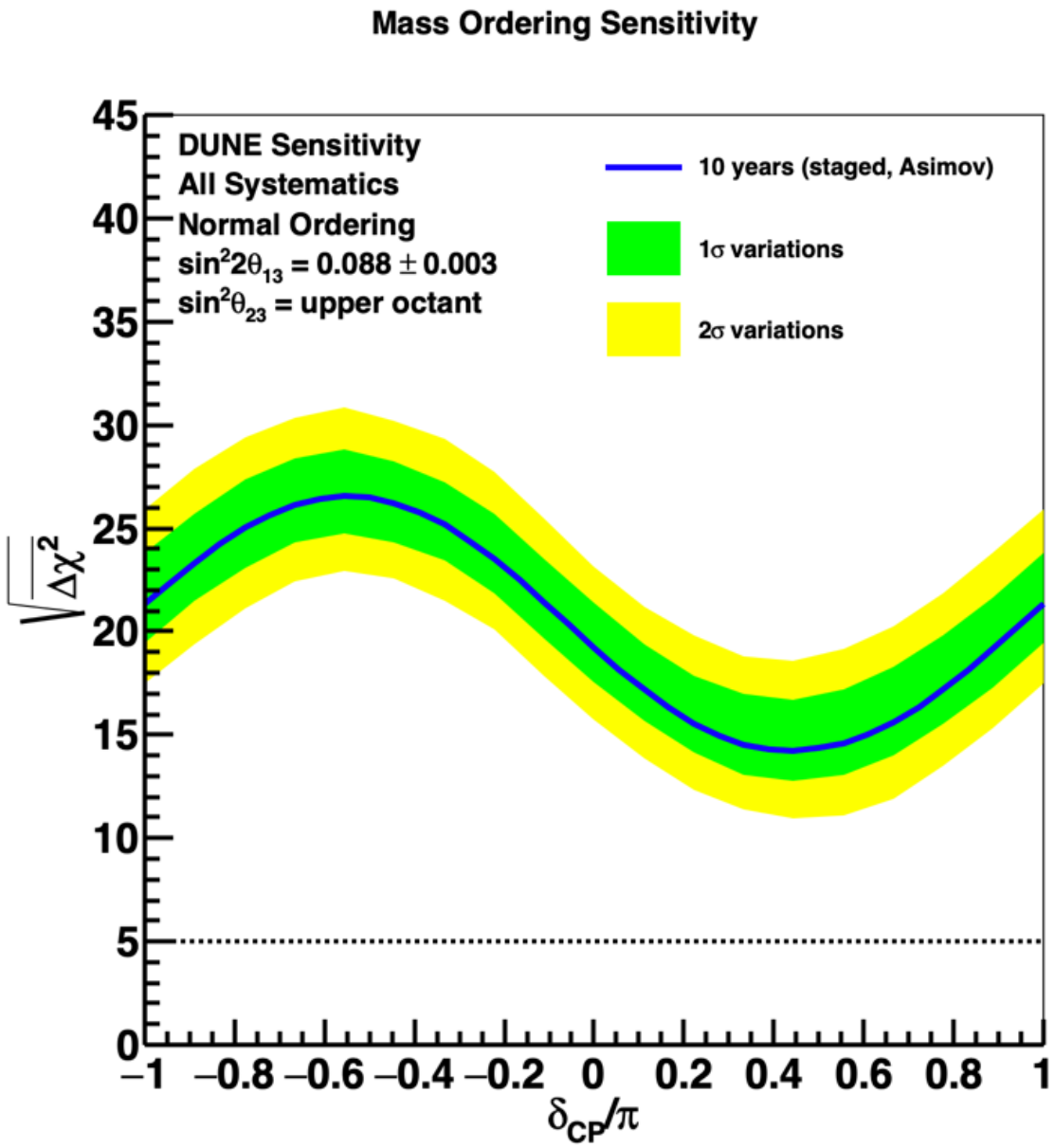

Figure 5.23: Significance of the DUNE determination of the neutrino mass ordering, as a function of the true value of $\delta_{\rm CP}$, for ten years of exposure. True normal ordering is assumed. The width of the bands are 1- and 2-σ statistical and systematic variations. The blue curve shows sensitivity for the Asimov set.

5.9.4 Impact of Oscillation Parameter Central Values

The sensitivity results presented in the preceding sections assume that the true values of the parameters governing long-baseline neutrino oscillation are the central values of the NuFIT 4.0 global fit, given in Table 5.1. In this section, variations in DUNE sensitivity with other possible true values of the oscillation parameters are explored. Figures 5.31, 5.32, and 5.33 show DUNE sensitivity to CP violation and neutrino mass ordering when the true values of θ_{23}, θ_{13}, and Δm^2_{32}, respectively, vary within the 3σ range allowed by NuFIT 4.0. The largest effect is the variation in

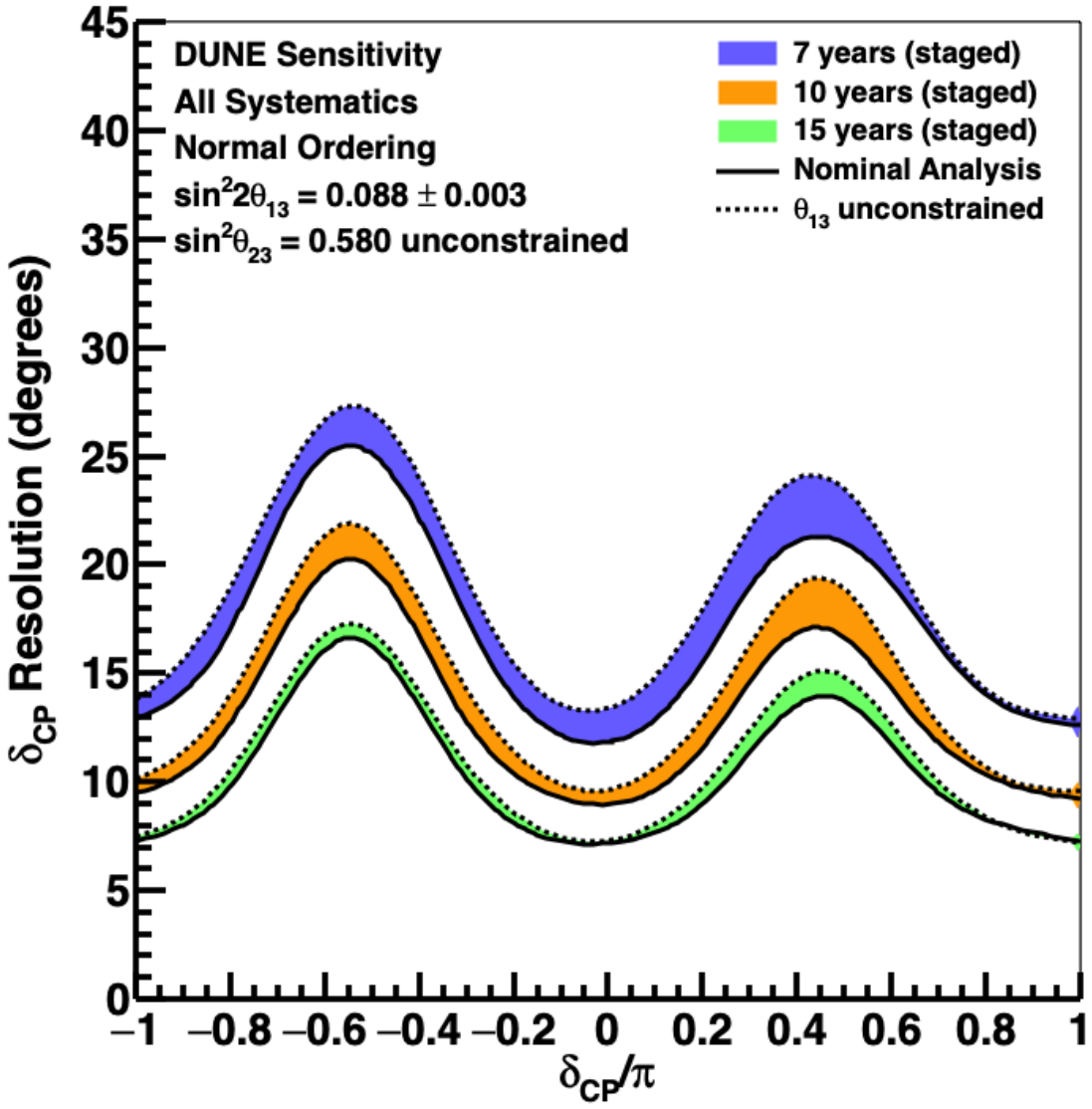

Figure 5.24: Resolution in degrees for the DUNE measurement of $\delta_{\rm CP}$, as a function of the true value of $\delta_{\rm CP}$, for seven (blue), ten (orange), and fifteen (green) years of exposure. True normal ordering is assumed. The width of the band shows the impact of applying an external constraint on $\sin^2 2\theta_{13}$.

sensitivity with the true value of θ_{23}, where degeneracy with $\delta_{\rm CP}$ and matter effects are significant. Values of θ_{23} in the lower octant lead to the best sensitivity to CP violation and the worst sensitivity to neutrino mass ordering, while the reverse is true for the upper octant. DUNE sensitivity for the case of maximal mixing is also shown. The true values of θ_{13} and Δm^2_{32} are highly constrained by global data and, within these constraints, do not have a dramatic impact on DUNE sensitivity.

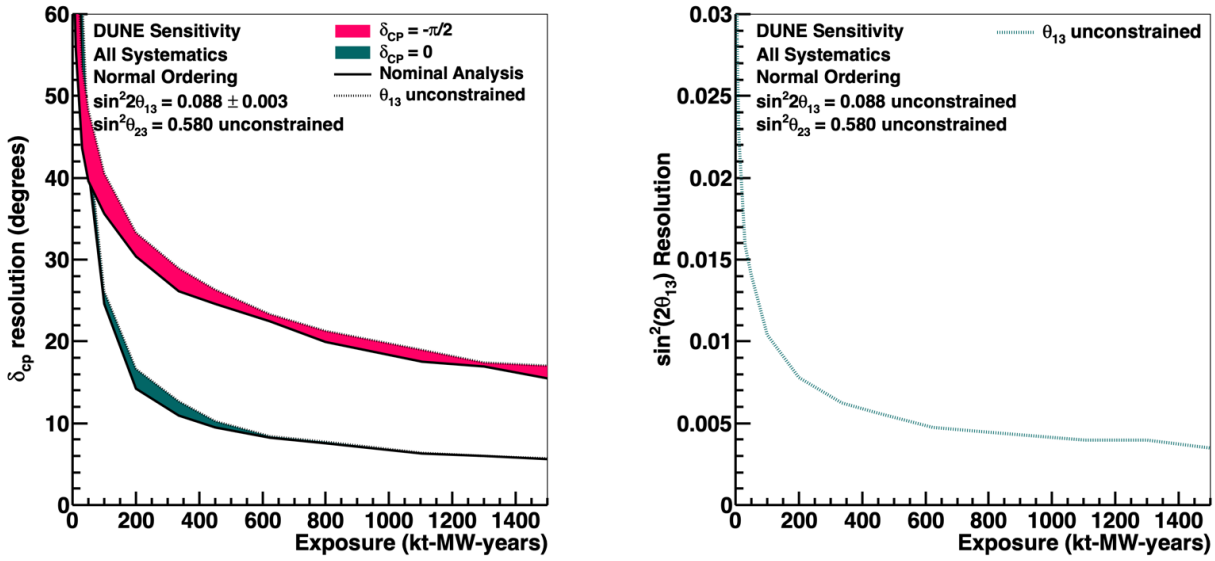

Figure 5.25: Resolution of DUNE measurements of δ_{CP} (left) and $\sin^2 2\theta_{13}$ (right), as a function of exposure in kt-MW-years. As seen in Figure 5.24, the δ_{CP} resolution has a significant dependence on the true value of δ_{CP}, so curves for $\delta_{\mathrm{CP}} = -\pi/2$ (red) and $\delta_{\mathrm{CP}} = 0$ (green) are shown. The width of the band shows the impact of applying an external constraint on $\sin^2 2\theta_{13}$. For the $\sin^2 2\theta_{13}$ resolution, an external constraint does not make sense, so only the unconstrained curve is shown. For reference, 30, 100, 200, 336, 624, and 1104 kt · MW · year correspond to 1.2, 3.1, 5.2, 7, 10, and 15 staged years, respectively.

5.9.5 Impact of Systematic Uncertainties

Implementation of systematic uncertainties in the nominal fits are described in Sections 5.3, 5.4, and 5.7. All considered systematic parameters are summarized in Table 5.12. In the nominal fits, many systematic uncertainties are constrained by DUNE data, as described in the following section.

Brief Name	Description of Uncertainty
Flux:	
flux[N]	Nth component of flux PCA
Interaction Model:	
MaCCQE	Axial mass for CCQE
VecFFCCQEshape	Choice of CCQE vector form factors
MaCCRES	Axial mass for CC resonance
MvCCRES	Vector mass for CC resonance

Theta Delta2Npi	θ_π distribution in decaying Δ rest frame
AhtBY	A_{HT} higher-twist param in BY model scaling variable ϵ_ω
BhtBY	B_{HT} higher-twist param in BY model scaling variable ϵ_ω
CV1uBY	C_{V1u} valence GRV98 PDF correction param in BY model
CV2uBY	C_{V2u} valence GRV98 PDF correction param in BY model
MaNCEL	Axial mass for NC elastic
MaNCRES	Axial mass for NC resonance
MvNCRES	Vector mass for NC resonance
FrCEx N	Nucleon charge exchange probability
FrElas N	Nucleon elastic reaction probability
FrInel N	Nucleon inelastic reaction probability
FrAbs N	Nucleon absorption probability
FrPiProd N	Nucleon π-production probability
FrCEx pi	π charge exchange probability
FrElas pi	π elastic reaction probability
FrInel pi	π inelastic reaction probability
FrAbs pi	π absorption probability
FrPiProd pi	π π-production probability
BeRPA A	Random Phase Approximation tune: controls low Q^2
BeRPA B	Random Phase Approximation tune: controls low-mid Q^2
BeRPA D	Random Phase Approximation tune: controls mid Q^2
Mnv2p2hGaussEnhancement	Extra strength into 2p2h
C12ToAr40 2p2hScaling nu	neutrino 2p2h Ar/C scaling
C12ToAr40 2p2hScaling nubar	antineutrino 2p2h Ar/C scaling
E2p2h [A,B] [nu,nubar]	2p2h energy dependence
SPPLowQ2Suppression	Low Q^2 (empirical) suppression
MKSPP ReWeight	MK model - alternative strength in W

NR nu np CC 1Pi	Norm for $\nu + n/p \to l + 1\pi$
NR [nu,nubar] [p,n] [CC,NC] [1,2,3]Pi	non-resonant pion production topology norms
nuenumu xsec ratio	ν_e/ν_μ uncertainty in ν_e unique phase space
nuenuebar xsec ratio	Modification of ν_e/ν_μ and $\bar{\nu}_e/\bar{\nu}_\mu$ xsec
Detector Effects:	
FVNueFD	FD ν_e fiducial volume
FVNueFD	FD ν_μ fiducial volume
FDRecoNueSyst	FD ν_e selection
FDRecoNumuSyst	FD ν_μ selection
ChargedHadResFD	FD charged hadron resolution
EMResFD	FD electromagnetic shower resolution
MuonResFD	FD muon resolution
EMUncorrFD	FD electromagnetic shower energy scale
EScaleNFD	FD neutron visible energy scale
EScaleMuLArFD	FD muon energy scale
EScaleFD	FD overall energy scale

Table 5.12: Definition of systematic uncertainty parameters. The brief names are used in Figures 5.34 and 5.35.

5.9.5.1 Systematic Uncertainty Constraints

Prefit uncertainties on flux and cross section parameters are at the level of ∼10%. These uncertainties become constrained in the fit, especially by the ND. Figure 5.34 shows the level of constraint on each systematic parameter after the fit. The larger band shows the constraint that arises from the far detector alone, while the inner band shows the (much stronger) constraint from the near detector. Figure 5.35 compares the parameter constraints for two different exposures. The wider band shows the ND+FD constraint expected after 7 years, and the narrower band shows the constraint after 15 years. The effect of increasing the exposure is very small because the ND is already systematically limited in the ν_μ CC channel after 7 years. The impact of adding the near detector is significant; flux and cross section parameters are very weakly constrained by the far detector

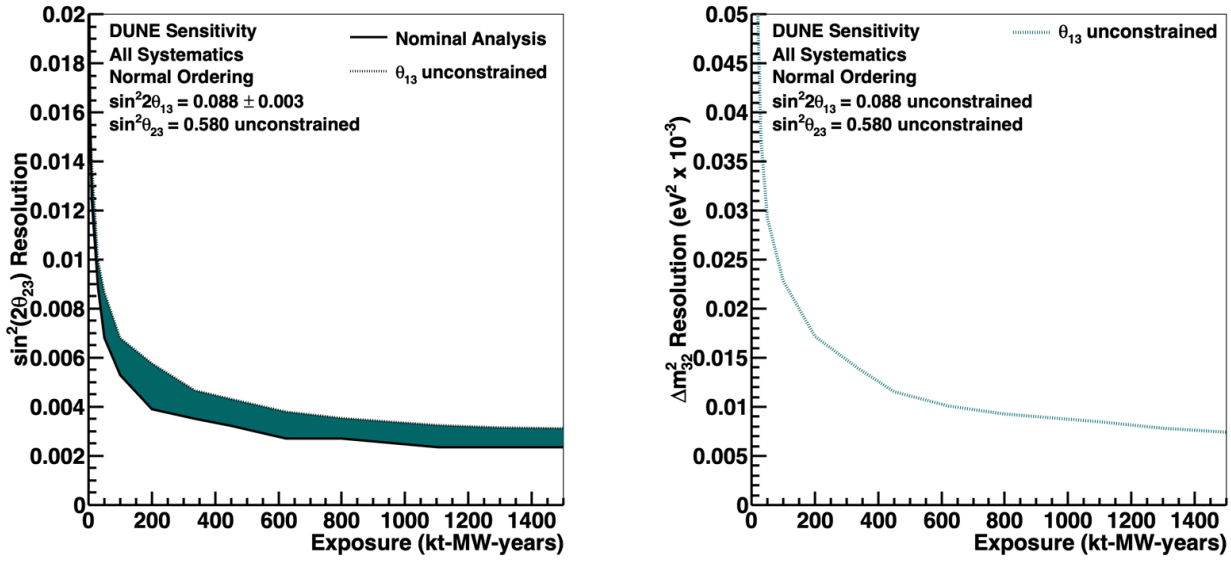

Figure 5.26: Resolution of DUNE measurements of $\sin^2 2\theta_{23}$ (left) and Δm^2_{32} (right), as a function of exposure in kt-MW-years. The width of the band for the $\sin^2 2\theta_{23}$ resolution shows the impact of applying an external constraint on $\sin^2 2\theta_{13}$. For the Δm^2_{32} resolution, an external constraint does not have a significant impact, so only the unconstrained curve is shown. For reference, 30, 100, 200, 336, 624, and 1104 kt · MW · year correspond to 1.2, 3.1, 5.2, 7, 10, and 15 staged years, respectively.

alone. Parameters are implemented in such a way that there are no prefit correlations, but the constraints from the near detector cause parameters to become correlated, which is not shown in the figure.

Some uncertainties are not reduced by the ND. For example, the energy scale parameters are treated as uncorrelated between detectors, so naturally the ND does not constrain them. Several important cross section uncertainties are not constrained by the near detector. In particular, an uncertainty on the ratio of ν_μ to ν_e cross sections is totally unconstrained. The most significant flux terms are constrained at the level of 20% of their *a priori* values. Less significant principal components have little impact on the observed distributions at either detector, and receive weaker constraints. Most cross section parameters that affect CC interactions are well constrained.

5.9.6 Impact of the Near Detector

The oscillation sensitivity analysis presented in the previous section is intended to demonstrate the full potential of DUNE, with constraints from the full suite of near detectors described in Volume I, Introduction to DUNE, Chapter 5, including the LAr TPC, MPD, SAND, and off-axis measurements. In addition to the ν_μ and $\bar{\nu}_\mu$ CC spectra used explicitly in this analysis, the LAr TPC is also expected to measure numerous exclusive final-state CC channels, including $1\pi^\pm$, $1\pi^0$, and multi-pion production. Measurements will be made as a function of other kinematic quantities in addition to reconstructed E_ν and y, such as four-momentum transfer to the nucleus,

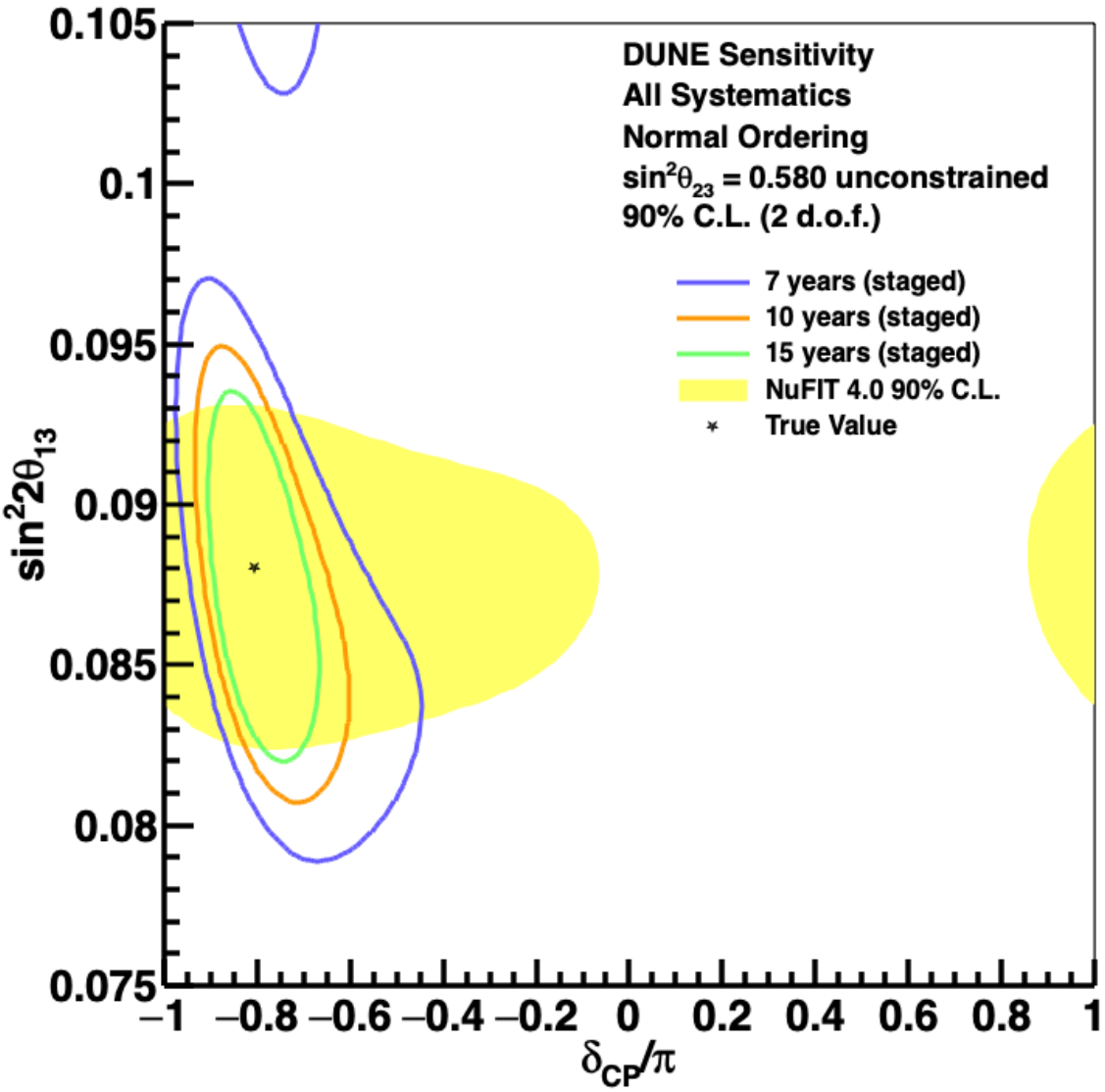

Figure 5.27: Two-dimensional 90% C.L. region in $\sin^2 2\theta_{13}$ and $\delta_{\rm CP}$, for 7, 10, and 15 years of exposure, with equal running in neutrino and antineutrino mode. The 90% C. L. region for the NuFIT 4.0 global fit is shown in yellow for comparison. The true values of the oscillation parameters are assumed to be the central values of the NuFIT 4.0 global fit and the oscillation parameters governing long-baseline oscillation are unconstrained.

lepton angle, or final-state meson kinematics. The LAr TPC will also measure the sum of ν_e and $\bar{\nu}_e$ CC scattering, and NC events. Direct flux measurements will be possible with neutrino-electron elastic scattering, and the low-ν technique.

In addition to the many on-axis LAr samples, a complementary set of neutrino-argon measurements is expected from the HPG TPC. This detector will be sensitive to charged tracks at kinetic energies of just a few MeV, enabling the study of nuclear effects in unprecedented detail. It will also sign-select all charged particles, with nearly perfect pion-proton separation from dE/dx out to over 1

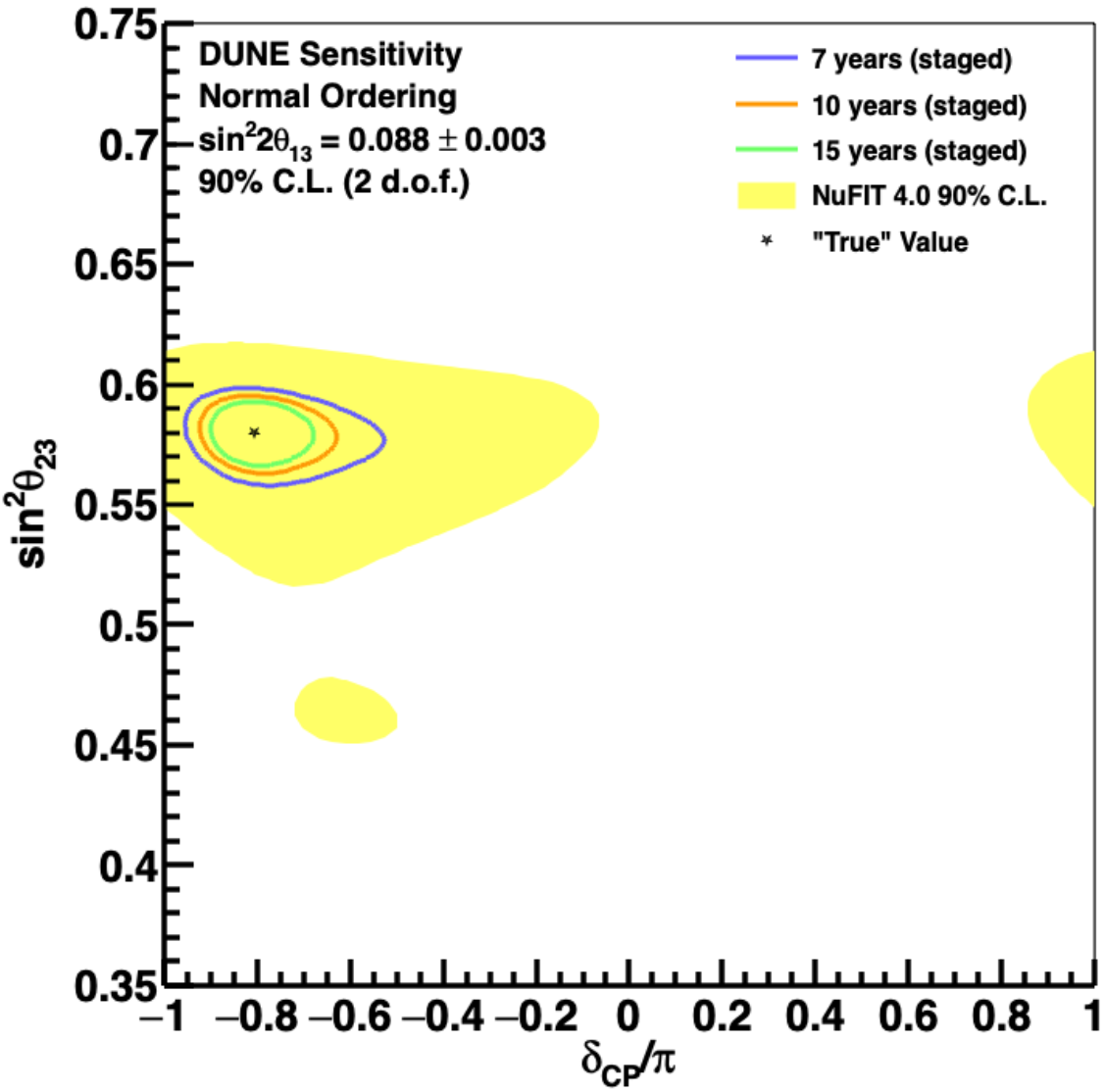

Figure 5.28: Two-dimensional 90% C.L. region in $\sin^2\theta_{23}$ and $\delta_{\rm CP}$, for 7, 10, and 15 years of exposure, with equal running in neutrino and antineutrino mode. The 90% C. L. region for the NuFIT 4.0 global fit is shown in yellow for comparison. The true values of the oscillation parameters are assumed to be the central values of the NuFIT 4.0 global fit and $\sin^2 2\theta_{13}$ is constrained by NuFIT 4.0

GeV/c momentum, so that high-purity measurements of CC1π^+ and CC1π^- are possible. It may be possible to directly measure neutron energy spectra from time of flight using the HPG TPC coupled to a high-performance ECAL. The SAND on-axis beam monitor will measure neutrino-carbon scattering and neutron production while ensuring excellent beam stability.

The LAr and MPD will also move off-axis to measure neutrino-argon interactions in many different fluxes. This will provide a direct constraint on the relationship between neutrino energy and visible energy in LAr. By taking linear combinations of spectra at many off-axis positions, it is possible to reproduce the expected FD energy spectrum for a given set of oscillation parameters and directly

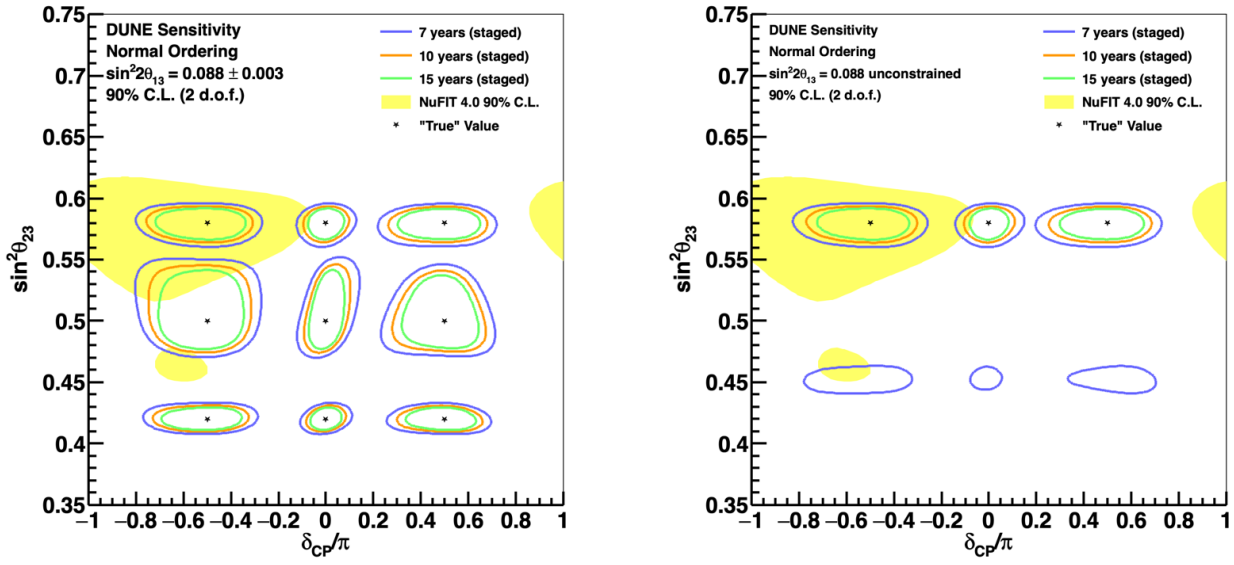

Figure 5.29: Two-dimensional 90% C.L. region in $\sin^2\theta_{23}$ and δ_{CP}, for 7, 10, and 15 years of exposure, with equal running in neutrino and antineutrino mode. The 90% C.L. region for the NuFIT 4.0 global fit is shown in yellow for comparison. Several possible true values of the oscillation parameters, denoted by stars, are considered, and $\sin^2 2\theta_{13}$ is constrained (left) or unconstrained (right) by NuFIT 4.0. In the plot on the right, only one value for $\sin^2\theta_{23}$ is shown; without the constraint on $\sin^2 2\theta_{13}$, degenerate regions are allowed for lower exposures.

measure visible energy.

All of these capabilities of the ND benefit the DUNE physics program. However, due to the timing of the ND process, design details of the ND are not available at the time of preparing this document, and it is not practical to include all of these samples and demonstrate their impact on oscillation sensitivity directly. Instead, we assume a model that implicitly includes these constraints, with further direct demonstration planned for the ND technical design report (TDR).

The neutrino interaction model uncertainties shown in Section 5.4 represent our current knowledge of neutrino interactions, motivated by measurements wherever possible. The DUNE ND is able to constrain these uncertain parameters, as demonstrated in the previous section. However, due to the complexity of modeling neutrino-argon interactions, and the dearth of neutrino-argon measurements in the energy range relevant for DUNE, this is a necessary but insufficient condition for the ND program. There are possible variations to the interaction model that cannot be readily estimated, simply because we have yet to observe the inadequacy of the model. While these "unknown unknowns" are impossible to predict, guarding against them is critically important to the success of the DUNE physics program. For this reason, the ND is designed under the assumption that it must not only constrain some finite list of model parameters, but also be sensitive to general modeling deficiencies.

The sensitivity analysis presented in the previous section assumes the success of the ND program. Because of this assumption, in order to estimate the expected sensitivity without a ND, it is

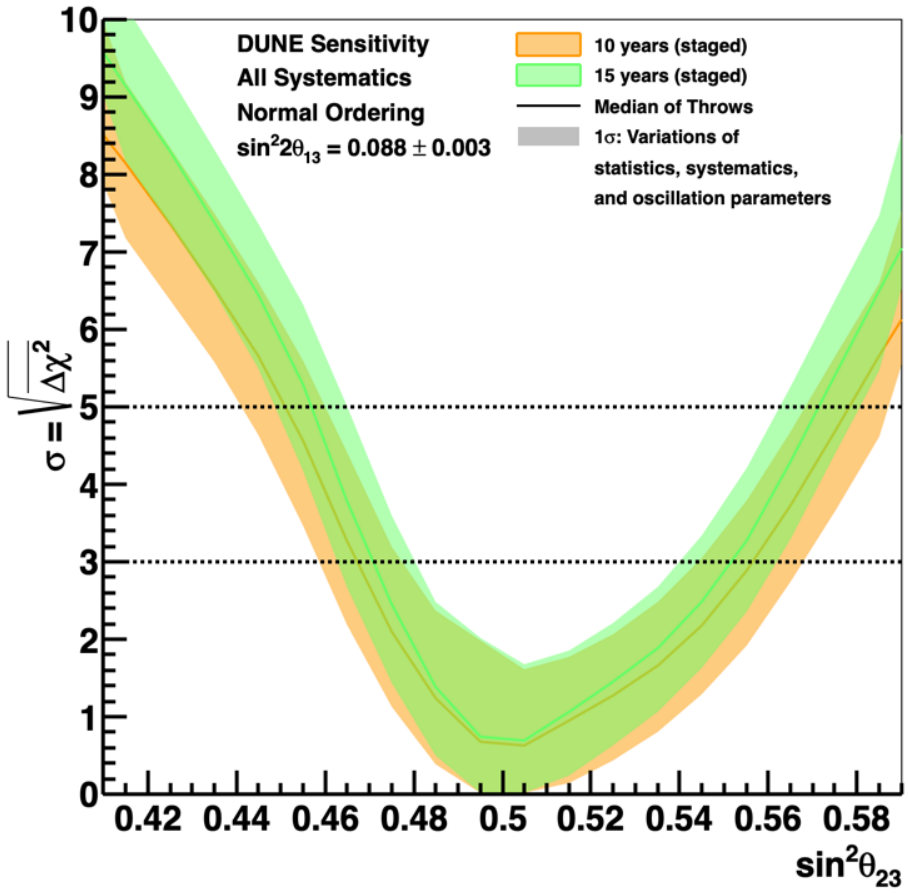

Figure 5.30: Sensitivity to determination of the θ_{23} octant as a function of the true value of $\sin^2\theta_{23}$, for ten (orange) and fifteen (green) years of exposure. True normal ordering is assumed. The width of the transparent bands cover 68% of fits in which random throws are used to simulate statistical variations and select true values of the oscillation and systematic uncertainty parameters, constrained by pre-fit uncertainties. The solid lines show the median sensitivity.

not sufficient to simply remove the on-axis LAr ND sample that is explicitly included in the analysis. We must also account for other potential biases from the interaction model, the "unknown unknowns." In this section, we consider two simple examples of bias, and evaluate the potential impact on oscillation parameter measurements in a scenario where the ND capacity is reduced. In Section 5.9.6.1, we consider the case where there is no near detector, and show a "mock data" sample that results in a high-quality FD-only fit with a significant bias in the measured value of δ_{CP}. This bias would be undetectable with a FD-only fit, but easily detected at the ND. In Section 5.9.6.2, we consider an alternative mock data set that gives a high-quality fit to the FD as well as the on-axis ND spectra, but has significant biases that are easily detected with off-axis ND data. These bias tests are not meant as exact estimates of the reduction in sensitivity that would be expected without a ND or with only on-axis ND, but they do serve as examples of the kind of bias that is possible. By estimating an additional uncertainty on oscillation parameters to cover the observed bias, it is possible to produce a sensitivity estimate; however, as it is based on one single possible bias, *it should be considered a lower bound on the potential reduction in sensitivity.*

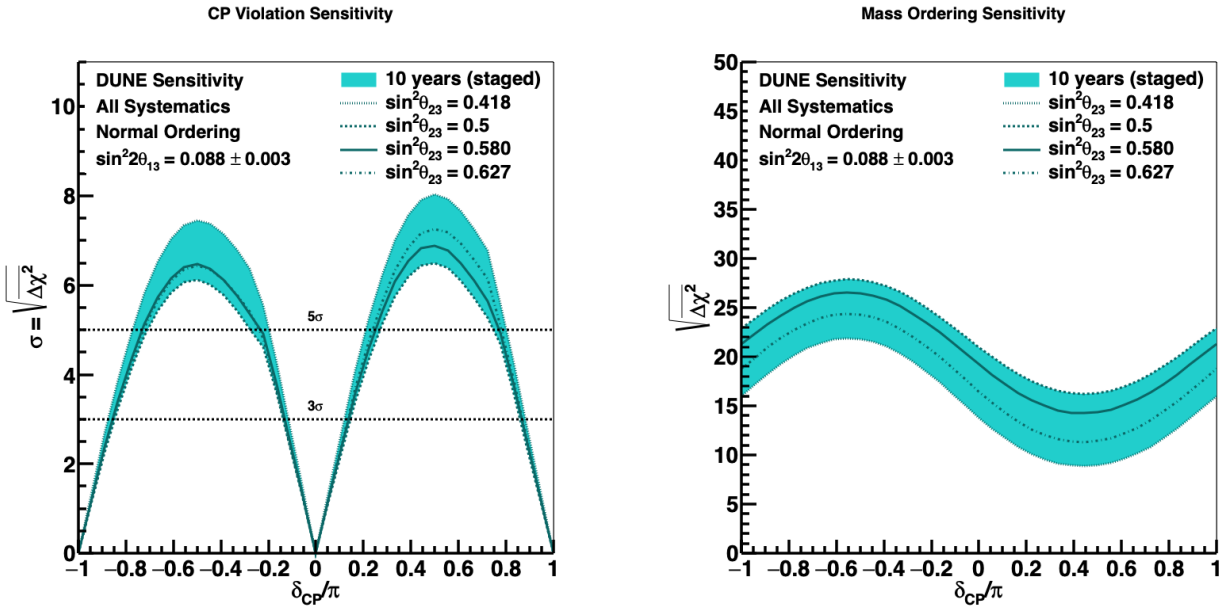

Figure 5.31: Sensitivity to CP violation (left) and neutrino mass ordering (right), as a function of the true value of $\delta_{\rm CP}$, for 10 years of exposure, with equal running in neutrino and antineutrino mode. Curves are shown for true values of θ_{23} corresponding to the 3σ range of values allowed by NuFIT 4.0, as well as the NuFIT 4.0 central value and maximal mixing. The nominal sensitivity analysis is performed.

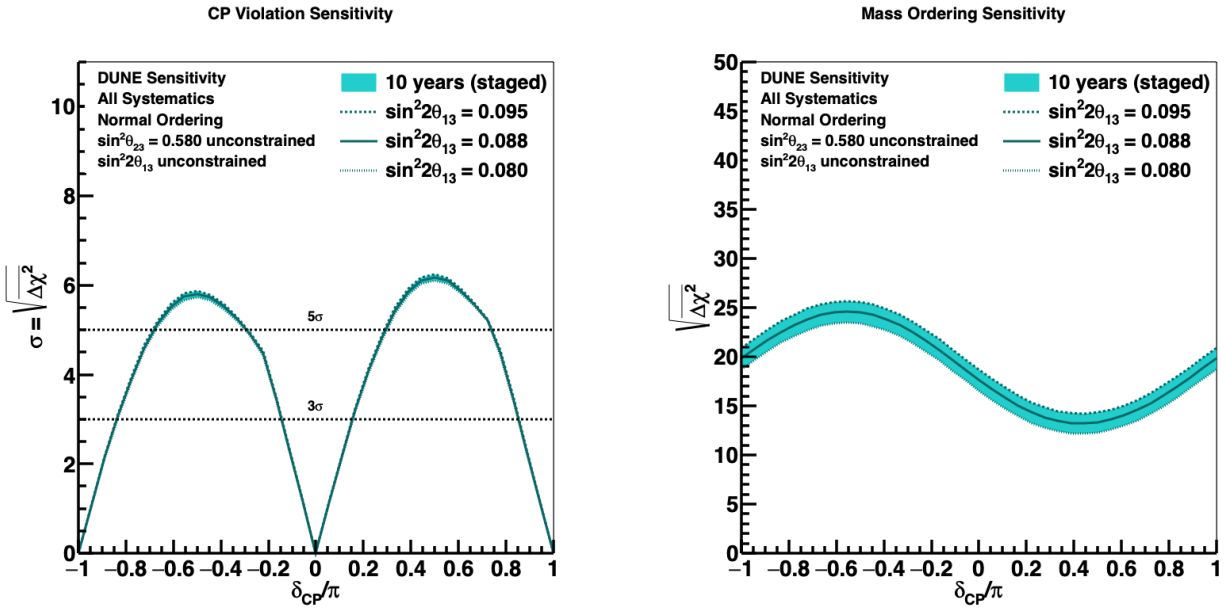

Figure 5.32: Sensitivity to CP violation (left) and neutrino mass ordering (right), as a function of the true value of $\delta_{\rm CP}$, for 10 years of exposure, with equal running in neutrino and antineutrino mode. Curves are shown for true values of θ_{13} corresponding to the 3σ range of values allowed by NuFIT 4.0, as well as the NuFIT 4.0 central value. The nominal sensitivity analysis is performed, with the exception that θ_{13} is not constrained at the NuFit4.0 central value in the fit.

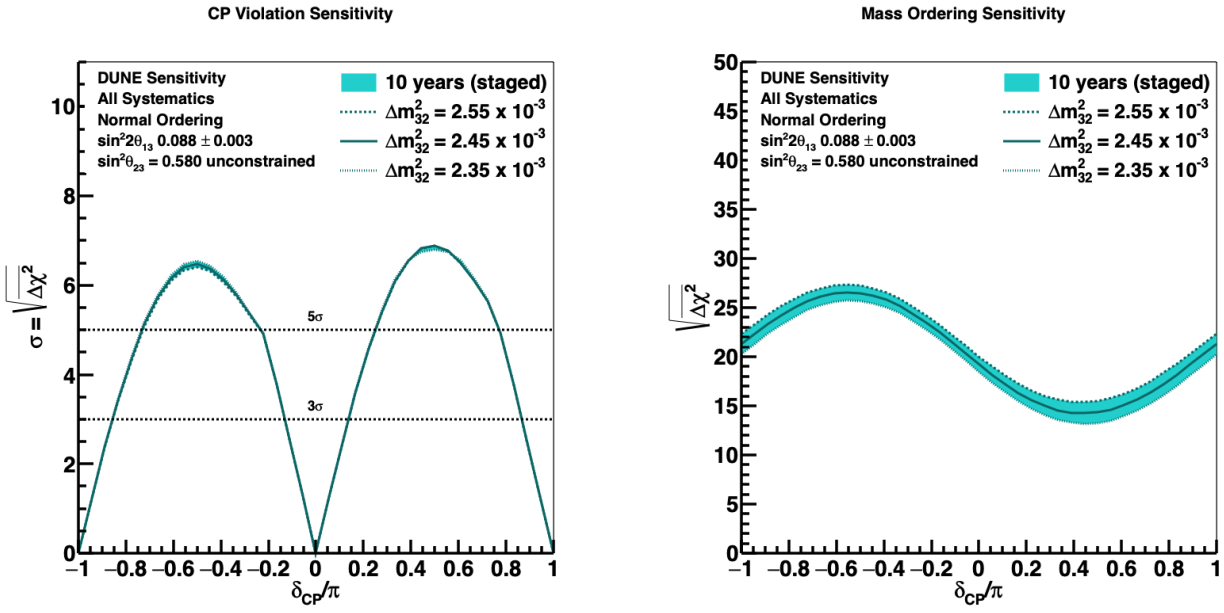

Figure 5.33: Sensitivity to CP violation (left) and neutrino mass ordering (right), as a function of the true value of δ_{CP}, for 10 years of exposure, with equal running in neutrino and antineutrino mode. Curves are shown for true values of Δm^2_{32} corresponding to the 3σ range of values allowed by NuFIT 4.0, as well as the NuFIT 4.0 central value. The nominal sensitivity analysis is performed.

5.9.6.1 Bias study: FD-only fit to NuWro

An alternative Monte Carlo sample is produced by reweighting the GENIE simulated events to NuWro. The objective of the reweighting is to reproduce the NuWro event spectra as a function of reconstructed neutrino energy, but without re-running the reconstruction. Simple reweighting schemes typically determine weights by taking the ratio between two generators in some limited kinematic space of true quantities. A common shortcoming of such techniques is that the reconstructed energy depends on many true quantities, and perhaps in a complicated way. Defining weights in a limited space effectively projects away any differences in other variables. To overcome this limitation, 18 true quantities that impact the reconstructed neutrino energy are identified: neutrino energy, lepton energy, lepton angle, Q^2, W, x, y, as well as the number and total kinetic energy carried by protons, neutrons, π^+, π^-, π^0, and the number of electromagnetic particles. A boosted decision tree (BDT) is trained on vectors of these 18 quantities in GENIE and NuWro. The BDT minimizes a logistic loss function between GENIE and NuWro in the 18-dimensional space, producing a set of weights. When these weights are applied to GENIE events, the resulting event spectra match the NuWro spectra in all 18 quantities.

The resulting selected samples of FD ν_μ and ν_e CC events in FHC and RHC beam modes are fit using the nominal GENIE-based model and its uncertainties as described in Sections 5.4 and 5.7. The fit quality in the FD-only scenario is high, with χ^2 per degree of freedom smaller than unity for all oscillation parameters. Systematic nuisance parameters are pulled from their best fit values by more than $\sim 0.6\sigma$.

The best-fit value of δ_{CP} is determined for the full range of possible true δ_{CP} values between $-\pi$ and

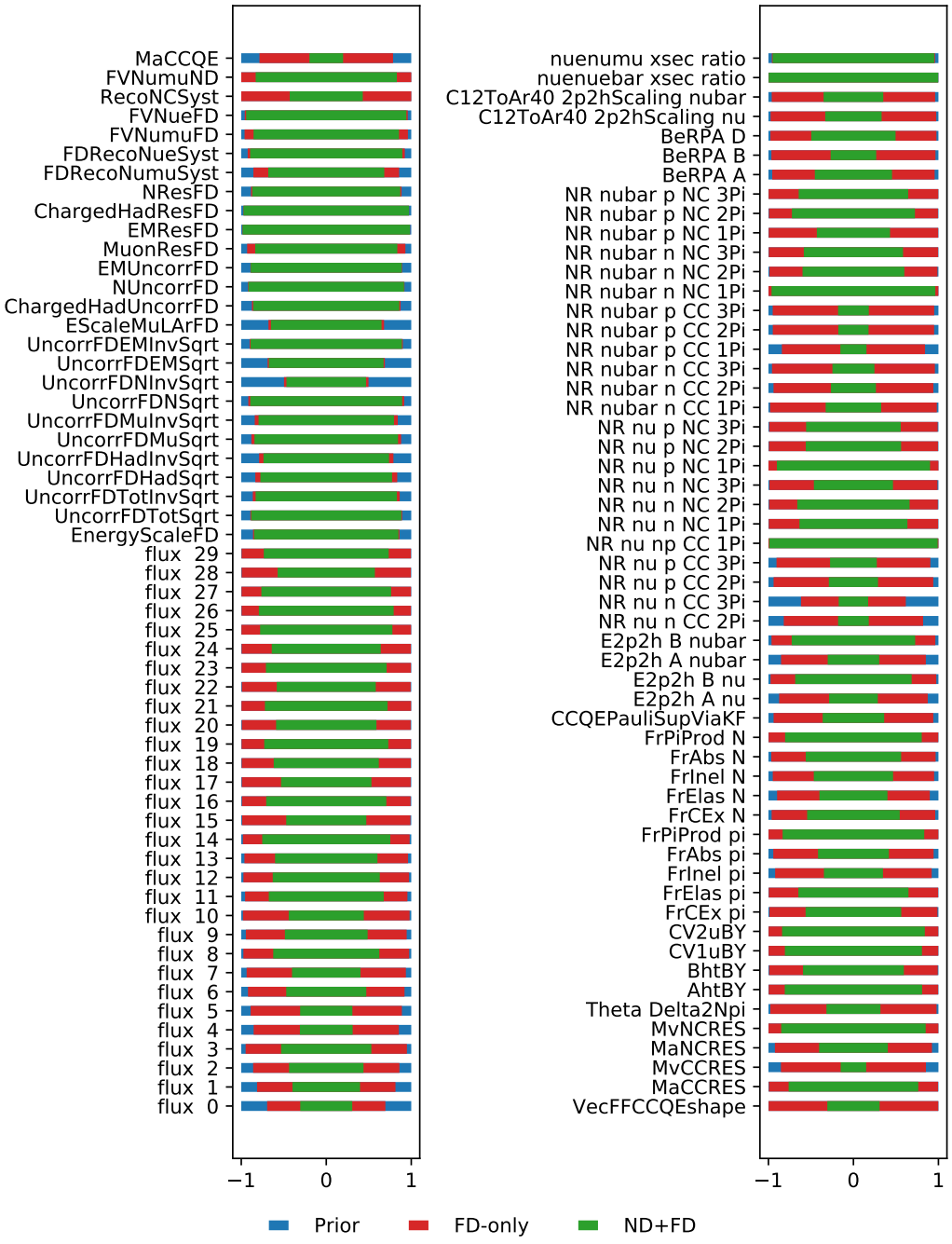

Figure 5.34: The ratio of post-fit to pre-fit uncertainties for various systematic parameters for a 15-year staged exposure. The red band shows the constraint from the FD only in 15 years, while the green shows the ND+FD constraints. Systematic parameter names are defined in Table 5.12.

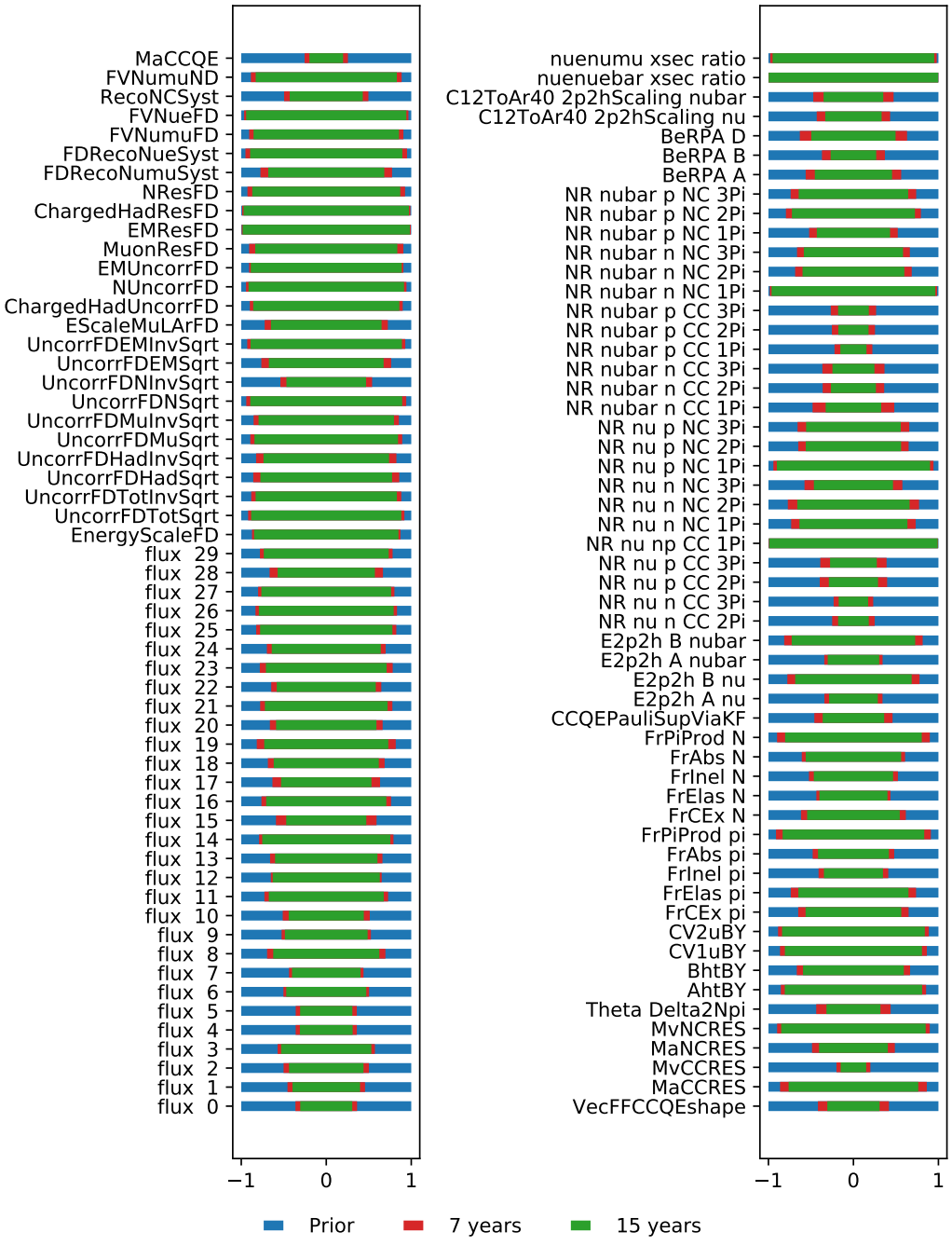

Figure 5.35: The ratio of post-fit to pre-fit uncertainties for various systematic parameters for a ND+FD constraint after 7 and 15 years. The difference in parameter constraints due to increasing the exposure is very small. Systematic parameter names are defined in Table 5.12.

$+\pi$. The difference between the best-fit and true values of δ_{CP} is found to be less than 14 degrees for 68% of the true values. To estimate the impact of such a bias on CP-violation sensitivity, an uncertainty equal to 14 degrees is added to the δ_{CP} resolution in quadrature. For a 10-year staged DUNE FD exposure, the resulting resolution is shown in the left panel of Figure 5.36 compared to the nominal sensitivity with the ND included. In the ND+FD (nominal) fit the bias is excluded, because in the ND the bias is easily detected and not attributable to oscillations. To estimate the sensitivity to nonzero CP violation as shown in the right panel of Figure 5.36, the nominal FD-only curve is reduced by the fractional increase in the δ_{CP} resolution at each point. The latter step is necessary because the uncertainty on δ_{CP} is not Gaussian.

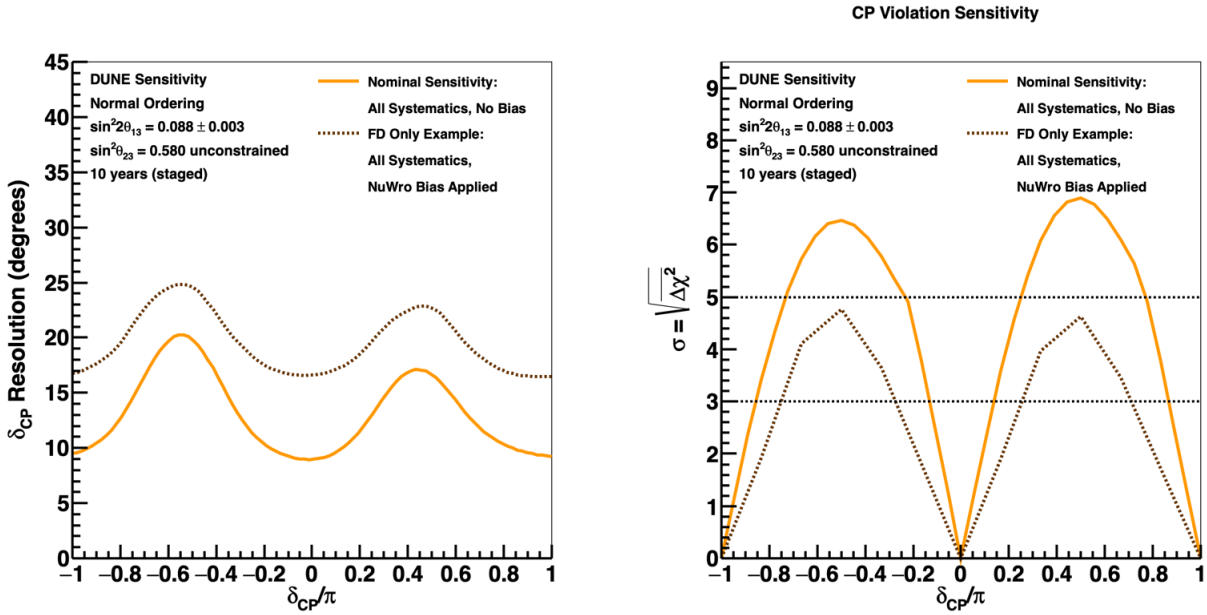

Figure 5.36: The CP violation sensitivity for a FD-only scenario with an additional uncertainty added to cover the observed bias from one example variation. The δ_{CP} resolution (left) and CP violation sensitivity (right) are compared to the results from the nominal ND+FD analysis.

As seen in Figure 5.36, the reduction in experimental sensitivity that would result from treating this example bias as a systematic uncertainty, which would be required in the absence of near detector data, is dramatic. Many other reasonable variations of the neutrino interaction model are allowed by world data and would also have to be considered as potential sources of uncertainty without near detector data to observe and resolve model incompatibility.

5.9.6.2 Bias study: shifted visible energy

As another example, we consider a possible deficiency of the GENIE model, specifically the case where the energy of final-state protons is reduced by 20%, with the energy going to neutrons instead. As neutrons are generally not observed, this will modify the relationship between neutrino energy and visible energy at the ND and FD. At the same time, the cross section model is altered so that the distribution of proton kinetic energy is unchanged. This alternate model is perfectly consistent with all available data; there is no reason to prefer our nominal GENIE model to this one.

By construction, this alternate model will not affect the fit at the on-axis near detector, as the cross section shift exactly cancels the loss in hadronic visible energy due to changing protons for neutrons. Nuisance parameters that affect the near detector spectra, namely flux and cross section uncertainties, are not pulled and remain at their nominal values with the same post-fit uncertainties observed in the Asimov sensitivity. At the far detector, however, the different neutrino energy spectrum leads to an observed shift in reconstructed energy with respect to the nominal prediction, visible in Figure 5.37.

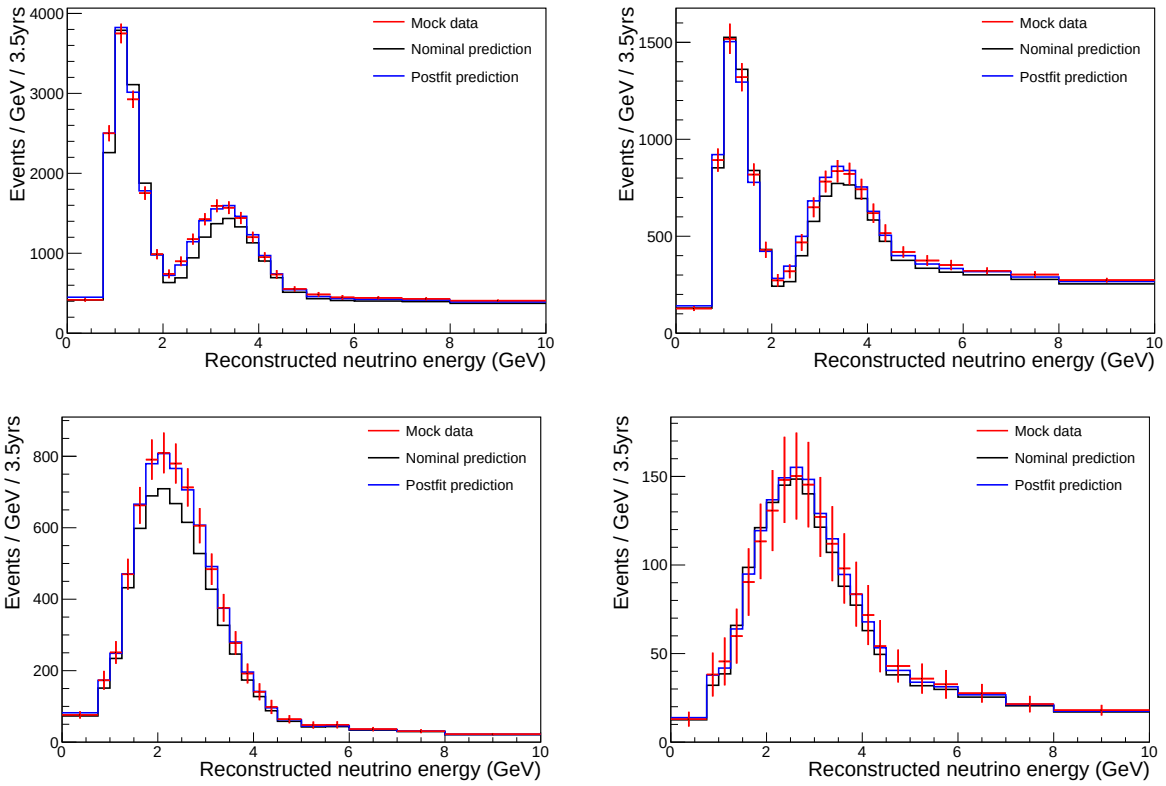

Figure 5.37: Predicted distributions of reconstructed neutrino energy for selected ν_μ (top) and ν_e (bottom) events, in FHC (left) and RHC (right) beam modes in 7 years. The black curve shows the nominal GENIE prediction, while the red points are the mock data, where 20% of proton energy is shifted to neutrons. The blue curve is the post-fit result, where systematic and oscillation parameters are shifted to match the mock data. The ND spectra match the pre-fit prediction by construction and are not shown.

Measured oscillation parameters returned by this fit are biased with respect to their true values. In particular, the best-fit values of Δm^2_{32} and $\sin^2\theta_{23}$ are significantly incorrect, as shown in Figure 5.38. Other parameters, including δ_{CP}, happen not to be pulled significantly from their true values by this particular model variation.

While the nominal model gives a good fit to the mock data in the on-axis ND, reconstructed spectra from off-axis ND data give a poor fit. This occurs because the cancellation between the cross section shift and the final-state proton-to-neutron ratio is dependent on the true neutrino energy spectrum. Off-axis data access different neutrino energy spectra, where the relationship is broken. By combining data at many off-axis positions, it is possible to produce a data-driven

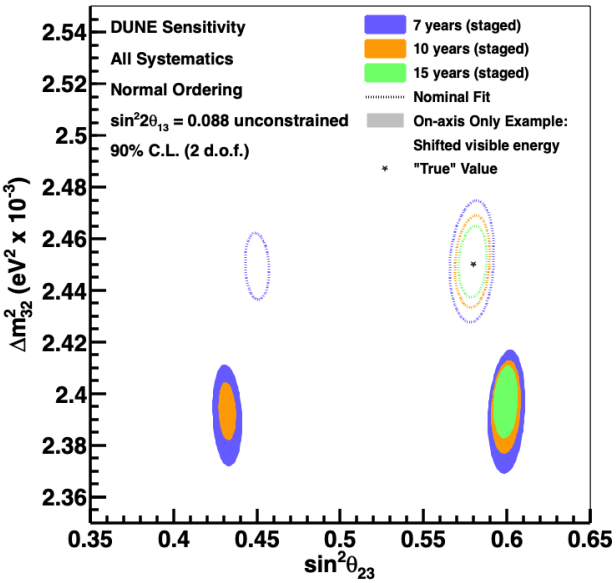

Figure 5.38: Results of a fit to mock data where 20% of proton energy is shifted to neutrons. The true values of Δm^2_{32} and $\sin^2\theta_{23}$ are given by the star, while the allowed 90% C.L. regions are drawn around the best-fit point, for 7, 10, and 15 years of exposure. The solid region shows the result for a fit using the mock data, while the dashed curve shows the result for a fit using nominal simulation, for comparison.

prediction of the expected FD flux for a given set of oscillation parameters, and directly compare this to the observation. Such a technique is not possible with solely on-axis ND data. This example demonstrates the importance of a capable ND, including the capability for off-axis measurements, to constrain not only the uncertain parameters of the interaction model, but also the physics in the model itself.

5.10 Conclusion

The studies presented in this chapter are based on full, end-to-end simulation, reconstruction, and event selection of FD Monte Carlo and parameterized analysis of ND Monte Carlo. Detailed uncertainties from flux, the neutrino interaction model, and detector effects have been included in the analysis. Sensitivity results are obtained using a sophisticated, custom fitting framework. These studies demonstrate that DUNE will be able to achieve its primary physics goals of measuring $\delta_{\rm CP}$ to high precision, unequivocally determining the neutrino mass ordering, and making precise measurements of the oscillation parameters governing long-baseline neutrino oscillation. It has also been demonstrated that accomplishing these goals relies upon accumulated statistics from a well-calibrated, full-scale FD, operation of a 1.2-MW beam upgraded to 2.4 MW, and detailed analysis of data from a highly capable ND.

DUNE will be able to establish the neutrino mass ordering at the 5σ level for 100% of $\delta_{\rm CP}$ values

after between two and three years. CP violation can be observed with 5σ significance after about 7 years if $\delta_{\rm CP} = -\pi/2$ and after about 10 years for 50% of $\delta_{\rm CP}$ values. CP violation can be observed with 3σ significance for 75% of $\delta_{\rm CP}$ values after about 13 years of running. For 15 years of exposure, $\delta_{\rm CP}$ resolution between five and fifteen degrees are possible, depending on the true value of $\delta_{\rm CP}$. The DUNE measurement of $\sin^2 2\theta_{13}$ approaches the precision of reactor experiments for high exposure, allowing measurements that do not rely on an external $\sin^2 2\theta_{13}$ constraint and facilitating a comparison between the DUNE and reactor $\sin^2 2\theta_{13}$ results, which is of interest as a potential signature for beyond the standard model physics. DUNE will have significant sensitivity to the θ_{23} octant for values of $\sin^2 \theta_{23}$ less than about 0.47 and greater than about 0.55.

These measurements will make significant contributions to completion of the standard three-flavor mixing picture and guide theory in understanding if there are new symmetries in the neutrino sector or whether there is a relationship between the generational structure of quarks and leptons. Observation of CP violation in neutrinos would be an important step in understanding the origin of the baryon asymmetry of the universe. Precise measurements made in the context of the three-flavor paradigm may also yield inconsistencies that point us to physics beyond the standard three-flavor model.

Chapter 6

GeV-Scale Non-accelerator Physics Program

6.1 Nucleon Decay

Unifying three of the fundamental forces in the universe, the strong, electromagnetic, and weak interactions, is a shared goal for the current world-wide program in particle physics. Grand unified theories (GUTs), extending the standard model of particle physics to include a unified gauge symmetry at very high energies (more than 1×10^{15} GeV), predict a number of observable effects at low energies, such as nucleon decay [205, 206, 207, 208, 209, 33]. Since the early 1980s, supersymmetric GUT models were preferred for a number of reasons, including gauge-coupling unification, natural embedding in superstring theories, and their ability to solve the fine-tuning problem of the standard model (SM). Supersymmetric GUT models generically predict that the dominant proton decay mode is $p \to K^+\overline{\nu}$, in contrast to non-supersymmetric GUT models, which typically predict the dominant decay mode to be $p \to e^+\pi^0$. Although the LHC has not found evidence for supersymmetry (SUSY) at the electroweak scale as was expected if SUSY were to solve the gauge hierarchy problem in the SM, the appeal of a GUT still remains. In particular, gauge-coupling unification can still be achieved in non-supersymmetric GUT models by the introduction of one or more intermediate scales (see, for example, [210]). Several experiments have sought signatures of nucleon decay, with the best limits for most decay modes set by the Super–Kamiokande experiment [4, 37, 35], which features the largest sensitive mass and exposure to date.

Although no evidence for proton decay has been found, lifetime limits from the current generation of experiments already constrain many GUT models, as shown in Figure 6.1 (updated from [34]). In some cases, these limits have eliminated models and approach the upper bounds of what other models will allow. This situation points naturally toward continuing the search with new, highly capable underground detectors, especially those with improved sensitivity to specific proton decay modes favored by GUT models. Given Super–Kamiokande's long exposure time (more than 30 years), extending the lifetime limits will require detectors with long exposure times coupled with larger sensitive mass or improved detection efficiency and background rejection.

The excellent imaging, as well as calorimetric and particle identification capabilities, of the liquid

argon time-projection chamber (LArTPC) technology implemented for the Deep Underground Neutrino Experiment (DUNE) far detector (FD) will exploit a number of complementary signatures for a broad range of nucleon decay channels. Should nucleon decay rates lie just beyond current limits, observation of even one or two candidate events with negligible background could constitute compelling evidence.

In the DUNE era, possibly two other large detectors, Hyper–Kamiokande [36] and JUNO [38] will be conducting nucleon decay searches. Should a signal be observed in any single experiment, confirmation from experiments using different detector technologies, and therefore different backgrounds, would be very powerful.

As mentioned above, the GUT models present two benchmark decay modes, $p \to e^+\pi^0$ and $p \to K^+\overline{\nu}$. The decay $p \to e^+\pi^0$ arises from gauge boson mediation and is often predicted to have the higher branching fraction of the two key modes. In this mode, the total mass of the proton is converted into the electromagnetic shower energy of the positron and two photons from π^0 decay with a net momentum vector near zero. The second key mode is $p \to K^+\overline{\nu}$. This mode is dominant in most supersymmetric GUT models, many of which also favor other modes involving kaons in the final state [207]. Although significant attention will focus on these benchmark modes, the nucleon decay program at DUNE will be a broad effort, covering many possible decay channels.

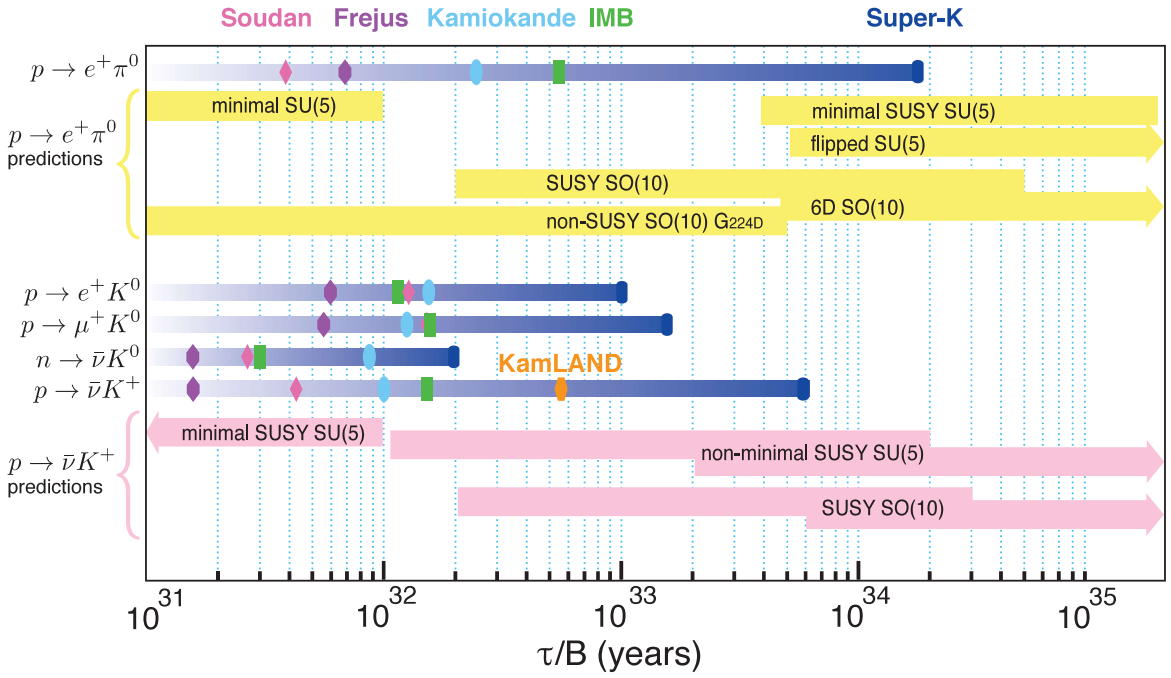

Figure 6.1: Summary of nucleon decay experimental lifetime limits from past or currently running experiments for several modes and a set of model predictions for the lifetimes in the two benchmark modes. The limits shown are 90% confidence level (CL) lower limits on the partial lifetimes, τ/B, where τ is the total mean life and B is the branching fraction. Updated from [34].

6.1.1 Experimental Signatures for Nucleon Decay Searches in DUNE

The DUNE FD, with the largest active volume of liquid argon (LAr), will be highly sensitive to several possible nucleon decay modes, in many cases complementing the capabilities of large water detectors. In particular, LArTPC technology offers the opportunity to observe the entire decay chain for nucleon decays into charged kaons; in $p \to K^+\overline{\nu}$, the kaon is typically below Cherenkov threshold in a water Cherenkov detector, but can be identified by its distinctive dE/dx signature as well as by its decay in a LArTPC. Therefore, this mode can be tagged in a LArTPC if a single kaon within a proper energy/momentum range can be reconstructed with its point of origin lying within the fiducial volume followed by a known decay mode of the kaon. Background events initiated by cosmic-ray muons can be controlled by requiring no activity close to the edges of the time projection chambers (TPCs) and by stringent single kaon identification within the energy range of interest [12, 13]. Atmospheric neutrinos make up the dominant background.

Because of the already stringent limits set by Super–Kamiokande on $p \to e^+\pi^0$ and the unique ability to track and identify kaons in a LArTPC, the initial nucleon decay studies in DUNE have focused on nucleon decay modes featuring kaons. Studies of $p \to e^+\pi^0$ have begun (see Section 6.1.3) but are less advanced than the kaon studies. The remainder of this section describes the background assumptions, signal simulation, particle tracking and identification, and event classification with a focus on nucleon decay involving kaons.

6.1.1.1 Background Simulation

The main background for nucleon decay searches is in the interactions of atmospheric neutrinos. In this analysis, the Bartol model of atmospheric neutrino flux [211] is used. Neutrino interactions in argon are simulated with the Generates Events for Neutrino Interaction Experiments (GENIE) event generator [70]. To estimate the event rate, we integrate the product of the neutrino flux and interaction cross section. Table 6.1 shows the event rate for different neutrino species for an exposure of $10\,\mathrm{kt}\cdot\mathrm{year}$, where oscillation effects are not included.

Table 6.1: Expected rate of atmospheric neutrino interactions in ^{40}Ar for a $10\,\mathrm{kt}\cdot\mathrm{year}$ exposure (not including oscillations).

10 kt · year	CC	NC	Total
ν_μ	1038	398	1436
$\bar{\nu}_\mu$	280	169	449
ν_e	597	206	83
$\bar{\nu}_e$	126	72	198
Total	2014	845	2886

Thus, to suppress atmospheric neutrino background to the level of one event per Mt · year , which would yield 0.4 events after ten years of operation with a 40 kt fiducial volume, the necessary background rejection is $1 - (1/288600) = 1 - 3 \times 10^{-6} = 0.999997$, where background rejection is defined as the fraction of background that is not selected.

6.1.1.2 Nucleon Decay Simulation

The simulation of nucleon decay events is performed using GENIE v.2.12.10. A total of 68 single-nucleon exclusive decay channels listed in the 2016 update of the PDG [25] is available in GENIE (see Table 6.2). The list includes two-, three-, and five-body decays. If a bound nucleon decays, the remaining nucleus can be in an excited state and will typically de-excite by emitting nuclear fission fragments, nucleons, and photons. At present, de-excitation photon emission is simulated only for oxygen [176]. However, the ArgoNeuT collaboration [192] has reported measurements of argon de-excitation photons in LArTPC detectors, where energy depositions and positions of these depositions have been compared to those from simulations of neutrino-argon interactions using the FLUKA Monte Carlo generator.

6.1.1.3 Kaon Final State Interactions

The propagation of the decay products in the nucleus is simulated using an intranuclear cascade Monte Carlo (MC). Charged kaons can undergo various scattering processes in the nucleus: elastic scattering, charge exchange, absorption (only K^-; K^+ absorption is forbidden), and K^+ production via strong processes such as $\pi^+ n \to K^+\Lambda$. In this analysis, the $hA2015$ model in GENIE is used as the default model for these final-state interactions (FSI). $hA2015$ is an empirical, data-driven method that does not model the cascade of hadronic interactions step by step, but instead uses one effective interaction where hadron+nucleus data is used to determine the final state. For kaons, $K^+ + C$ data [212, 213] is used when available. $hA2015$ only considers kaon-nucleon elastic scattering inside the nucleus. Charge exchange is not included, nor is K^+ production in pion reactions, and therefore a K^+ is never added or removed from the final state in this model.

Other FSI models include the full cascade, but there is not enough data to favor one model over the other. As an example of the limitations of the current data on kaon FSI, a recent measurement of kaon production in neutrino interactions shows only a weak preference for including FSI as opposed to a model with no FSI [214]. In this case, the kaon FSI have a relatively subtle effect on the differential cross section, and the available statistics are not sufficient to conclusively prefer one model over another. For nucleon decay into kaons, the FSI have a much larger impact, and the differences between models are less significant than the overall effect. Kaon FSI introduce an important uncertainty that is included in this analysis.

FSI can significantly modify the observable distributions in the detector. For example, Figure 6.2 shows the kinetic energy of a kaon from $p \to K^+\overline{\nu}$ before and after FSI. Because of FSI the kaon spectrum becomes softer on average. Of the kaons, 31.5% undergo elastic scattering resulting in events with very low kinetic energy; 25% of kaons have a kinetic energy of ≤ 50 MeV. When the

ID	Decay channel(s)	ID	Decay channel(s)	ID	Decay channel(s)
Antilepton + Meson		Antilepton + Mesons		Antilepton + Photon(s)	
1	$p \to e^+\pi^0$, $n \to e^+\pi^-$	23	$p \to e^+\pi^+\pi^-$	42	$p \to e^+\gamma$
2	$p \to \mu^+\pi^0$, $n \to \mu^+\pi^-$	24	$p \to e^+\pi^0\pi^0$	43	$p \to \mu^+\gamma$
3	$p \to \bar{\nu}\pi^+$, $n \to \bar{\nu}\pi^0$	25	$n \to e^+\pi^-\pi^0$	44	$n \to \bar{\nu}\gamma$
4	$p \to e^+\eta$	26	$p \to \mu^+\pi^+\pi^-$	45	$p \to e^+\gamma\gamma$
5	$p \to \mu^+\eta$	27	$p \to \mu^+\pi^0\pi^0$	46	$n \to \bar{\nu}\gamma\gamma$
6	$n \to \bar{\nu}\eta$	28	$n \to \mu^+\pi^-\pi^0$	Three or more leptons	
7	$p \to e^+\rho^0$, $n \to e^+\rho^-$	29	$n \to e^+\pi^- K^0$	49	$p \to e^+e^+e^-$
8	$p \to \mu^+\rho^0$, $n \to \mu^+\rho^-$	Lepton + Meson		50	$p \to e^+\mu^+\mu^-$
9	$p \to \bar{\nu}\rho^+$, $n \to \bar{\nu}\rho^0$	30	$n \to e^-\pi^+$	51	$p \to e^+\bar{\nu}\nu$
10	$p \to e^+\omega$	31	$n \to \mu^-\pi^+$	52	$n \to e^+e^-\bar{\nu}$
11	$p \to \mu^+\omega$	32	$n \to e^-\rho^+$	53	$n \to \mu^+e^-\bar{\nu}$
12	$n \to \bar{\nu}\omega$	33	$n \to \mu^-\rho^+$	54	$n \to \mu^+\mu^-\bar{\nu}$
13	$p \to e^+K^0$, $n \to e^+K^-$	34	$n \to e^- K^+$	55	$n \to \mu^+e^+e^-$
14	$p \to e^+K_S^0$	35	$n \to \mu^- K^+$	56	$n \to \mu^+\mu^+\mu^-$
15	$p \to e^+K_L^0$	Lepton + Mesons		57	$p \to \mu^+\bar{\nu}\nu$
16	$p \to \mu^+K^0$, $n \to \mu^+ + K^-$	36	$p \to e^-\pi^+\pi^+$	58	$p \to e^-\mu^+\mu^+$
17	$p \to \mu^+K_S^0$	37	$n \to e^-\pi^+\pi^0$	59	$n \to \bar{\nu}\bar{\nu}\nu$
18	$p \to \mu^+K_L^0$	38	$p \to \mu^-\pi^+\pi^+$	60	$n \to \bar{\nu}\bar{\nu}\bar{\nu}\nu\nu$
19	$p \to \bar{\nu}K^+$, $n \to \bar{\nu}K^0$	39	$n \to \mu^-\pi^+\pi^0$		
20	$n \to \bar{\nu}K_S^0$	40	$p \to e^-\pi^+K^+$		
21	$p \to e^+K^{\star 0}$	41	$p \to \mu^-\pi^+K^+$		
22	$p \to \bar{\nu}K^{\star +}$, $n \to \bar{\nu}K^{\star 0}$				

Table 6.2: Decay topologies considered in GENIE nucleon decay simulation.

kaon undergoes elastic scattering, a nucleon can be knocked out of the nucleus. Of decays via this channel, 26.7% have one neutron coming from FSI, 15.3% have at least one proton, and 10.3% have two protons coming from FSI. These secondary nucleons are detrimental to reconstructing and selecting K^+.

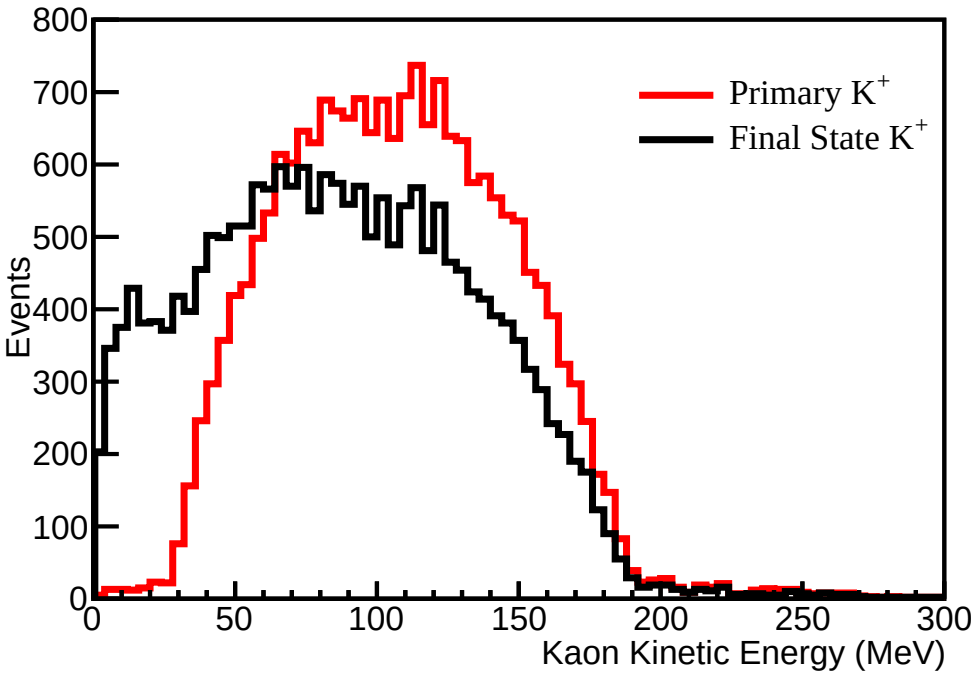

Figure 6.2: Kinetic energy of kaons in simulated proton decay events, $p \to K^+\overline{\nu}$. The kinetic energy distribution is shown before and after final state interactions in the argon nucleus.

The kaon FSI in Super–Kamiokande's simulation of $p \to K^+\overline{\nu}$ in oxygen seem to have a smaller effect on the outgoing kaon momentum distribution [4] than is seen here with the GENIE simulation on argon. Some differences are expected due to the different nuclei, but differences in the FSI models are under investigation.

6.1.1.4 Tracking and Particle Identification

The DUNE reconstruction algorithms are described in Chapter 4. This analysis uses 3D track and vertex reconstruction provided by Projection Matching Algorithm (PMA).

Track reconstruction efficiency for a charged particle $x^\pm$ is defined as

$$\epsilon_{x^\pm} = \frac{x^\pm \text{ particles with a reconstructed track}}{\text{events with } x^\pm \text{ particle}}. \tag{6.1}$$

The denominator includes events in which an $x^\pm$ particle was created and has deposited energy within any of the TPCs. The numerator includes events in which an $x^\pm$ particle was created and has deposited energy within any of the TPCs, and a reconstructed track can be associated to the

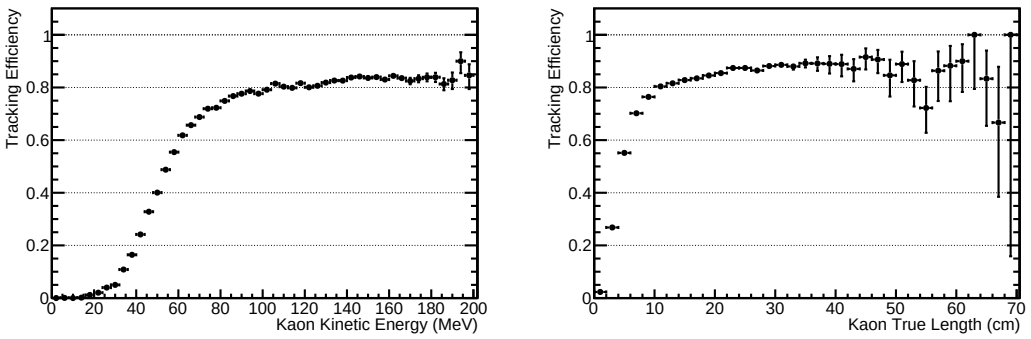

Figure 6.3: Tracking efficiency for kaons in simulated proton decay events, $p \to K^+\overline{\nu}$, as a function of kaon kinetic energy (left) and true path length (right).

$x^{\pm}$ particle based on the number of hits generated by that particle along the track. This efficiency can be calculated as a function of true kinetic energy and true track length.

Figure 6.3 shows the tracking efficiency for K^+ from proton decay via $p \to K^+\overline{\nu}$ as a function of true kinetic energy and true path length. The overall tracking efficiency for kaons is 58.0%, meaning that 58.0% of all the simulated kaons are associated with a reconstructed track in the detector. From Figure 6.3, the tracking threshold is approximately $\sim 40\,\text{MeV}$ of kinetic energy, which translates to $\sim 4.0\,\text{cm}$ in true path length. The biggest loss in tracking efficiency is due to kaons with $< 40\,\text{MeV}$ of kinetic energy due to scattering inside the nucleus as described in Section 6.1.1.3. The efficiency levels off to approximately 80% above 80 MeV of kinetic energy. This inefficiency even at high kinetic energy is due mostly to kaons that decay in flight./footnoteNo attempt has been made at this point to recover such events. Both kaon scattering in the LAr and charge exchange are included in the simulation but are relatively small effects (4.6% of kaons scatter in the LAr and 1.2% of kaons experience charge exchange). The tracking efficiency for muons from the decay of the K^+ in $p \to K^+\overline{\nu}$ is 90%.

Charged particles lose energy through ionization and scintillation when traversing the LAr. This energy loss provides valuable information on particle energy and species. To identify a given particle, the hits associated with a reconstructed track are used. If the charged particle stops in the LArTPC active volume, a combination of dE/dx and the reconstructed residual range (R, the path length to the end point of the track) is used to define a parameter for particle ID (PID). The parameter, $PIDA$, is defined as [86]

$$PIDA = \left\langle \left(\frac{dE}{dx} \right)_i R_i^{0.42} \right\rangle, \tag{6.2}$$

where the median is taken over all track points i for which the residual range R_i is less than 30 cm.

Figure 6.4 shows the $PIDA$ performance for kaons (from proton decay), muons (from kaon decay), and protons produced by atmospheric neutrino interactions. The tail with lower values in each distribution is due to cases where the decay/stopping point was missed by the track reconstruction. The tail with higher values is caused when a second particle overlaps at the decay/stopping point causing higher values of dE/dx and resulting in higher values of $PIDA$. In addition, ionization fluctuations smear out these distributions.

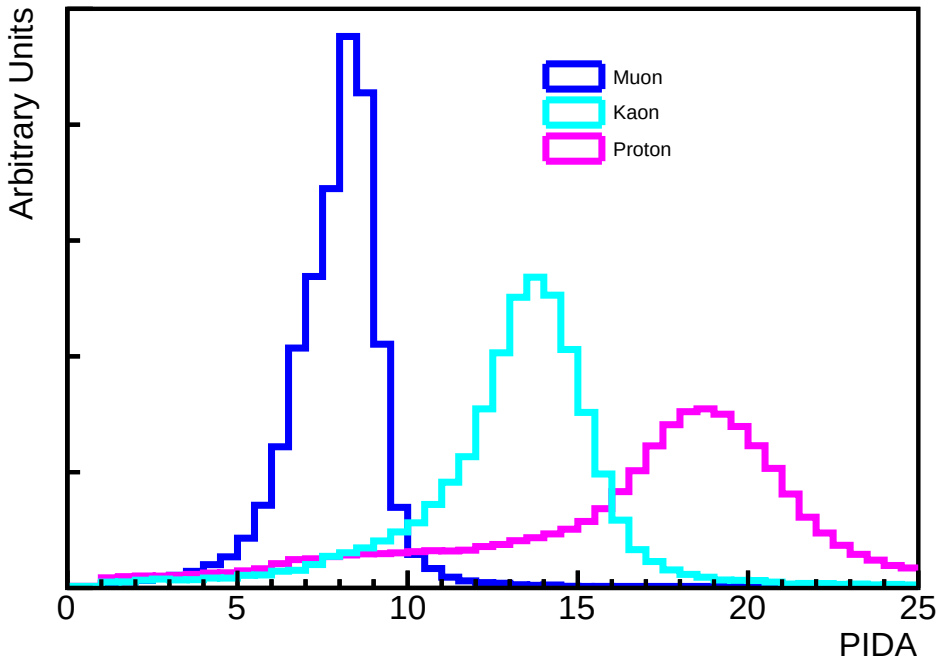

Figure 6.4: Particle identification using $PIDA$ for muons and kaons in simulated proton decay events, $p \to K^+\overline{\nu}$, and protons in simulated atmospheric neutrino background events. The curves are normalized by area.

A complication for PID via dE/dx results when ambiguity occurs in reconstructing track direction, which is even more problematic because additional energy deposition may occur at the originating point in events where FSI is significant. The dominant background to $p \to K^+\overline{\nu}$ in DUNE is atmospheric neutrino charged current (CC) quasi-elastic (QE) scattering, $\nu_\mu n \to \mu^- p$. When the muon happens to have very close to the 237 MeV/c momentum expected from a K^+ decay at rest and does not capture, it is indistinguishable from the muon resulting from $p \to K^+\overline{\nu}$ followed by $K^+ \to \mu^+\nu_\mu$. When the proton is also mis-reconstructed as a kaon, this background mimics the signal process.

The most important difference between signal and this background source is the direction of the hadron track. For an atmospheric neutrino, the proton and muon originate from the same neutrino interaction point, and the characteristic Bragg rise occurs at the end of the proton track farthest from the muon-proton vertex. For signal, the kaon-muon vertex location is where the K^+ stops and decays at rest, so its ionization energy deposit is highest near the kaon-muon vertex. To take advantage of this difference, a log-likelihood ratio discriminator is used to distinguish signal from background. Templates are formed by taking the reconstructed and calibrated energy deposit as a function of the number of wires from both the start and end of the K^+ candidate hadron track. Two log-likelihood ratios are computed separately for each track. The first begins at the hadron-muon shared vertex and moves along the hadron track (the "backward" direction). The second begins at the other end of the track, farthest from the hadron-muon shared vertex, moves along the hadron track the other way (the "forward" direction). For signal events, this effectively looks for the absence of a Bragg rise at the K^+ start, and the presence of one at the end, and vice versa for background. At each point, the probability density for signal and background, P^{sig} and P^{bkg},

are determined from the templates. Forward and backward log-likelihood ratios are computed as

$$\mathcal{L}_{fwd(bkwd)} = \sum_i \log \frac{P_i^{sig}}{P_i^{bkg}}, \tag{6.3}$$

where the summation is over the wires of the track, in either the forward or backward direction. Using either the forward or backward log-likelihood ratio alone gives some discrimination between signal and background, but using the sum gives better discrimination. While the probability densities are computed based on the same samples, defining one end of the track instead of the other as the vertex provides more information. The discriminator is the sum of the forward and backward log-likelihood ratios:

$$\mathcal{L} = \mathcal{L}_{fwd} + \mathcal{L}_{bkwd}. \tag{6.4}$$

Applying this discriminator to tracks with at least ten wires gives a signal efficiency of roughly 0.4 with a background rejection of 0.99.

6.1.1.5 Event Classification

Multivariate classification methods based on machine learning techniques have become a fundamental part of most analyses in high-energy physics. To develop an event selection to search for nucleon decay, a boosted decision tree (BDT) classifier is used. The software package Toolkit for Multivariate Data Analysis with ROOT (TMVA4) [215] was used with AdaBoost as the boosted algorithm. In the analyses presented here, the BDT is trained on a sample of MC events (50,000 events for signal and background) that is statistically independent from the sample of MC events used in the analysis (approximately 100,000 events for signal and 600,000 events for background.) This technique is used for the nucleon decay and neutron-antineutron analyses presented below.

As an independent method of identifying nucleon decay events, image classification using a convolutional neural network (CNN) can be performed using 2D images of DUNE MC events. The image classification provides a single score value as a metric of whether any given event is consistent with a proton decay, and this score can be used as a powerful discriminant for event identification. In the analyses presented here, the CNN technique alone does not discriminate between signal and background as well as a BDT. For that reason, the CNN score is used as one of the input variables in the BDT in each analysis.

6.1.2 Sensitivity to $p \to K^+\overline{\nu}$ Decay

Monte Carlo studies of the $p \to K^+\overline{\nu}$ signal and corresponding atmospheric neutrino backgrounds have been carried out with the DUNE multipurpose full event simulation and reconstruction software. As indicated in Section 6.1.1.4, they reveal that one of the main challenges in identifying proton decay candidates is suppressing backgrounds arising from the mis-reconstruction of protons as positive kaons. This happens when a CC neutrino interaction produces a muon and a recoiling proton, and the primary vertex for neutrino interaction is mislabeled as a secondary vertex where

the kaon decays. Complicating the ability to reject pathological events of this type is the presence of FSI, which can shift the spectrum of kaons toward low energies, with possible concurrent emission of nucleons, which together weaken the otherwise distinct energy and dE/dx signature of the kaon.

The branching fraction for leptonic decay of charged kaons, $K \to \mu\nu_\mu$, is approximately 64%. The remaining decay modes are semileptonic or hadronic and include charged and neutral pions. The leptonic decay offers a distinguishable topology with a heavy ionizing particle followed by a minimum ionizing particle. In addition, given the kinematics of a proton decay event, 92% of kaons decay at rest. Using two-body kinematics, the momentum of the muon is approximately $237\,\mathrm{MeV}/c$. The reconstructed momentum of the muon offers a powerful discriminating variable to separate signal from background events. This analysis includes all modes of kaon decay, but the selection strategy so far has focused on kaon decay to muons.

The proton decay signal and atmospheric neutrino background events are processed using the same reconstruction chain and subject to the same selection criteria. There are two pre-selection cuts to remove obvious background. One cut requires at least two tracks, which aims to select events with a kaon plus a kaon decay product (usually a muon). The other cut requires that the longest track be less than 100 cm; this removes backgrounds from high energy neutrino interactions. After these cuts, 50% of the signal and 17.5% of the background remain in the sample. The signal inefficiency at this stage of selection is due mainly to the kaon tracking efficiency.

A CNN was developed to classify signal and background events that gives 99.9% background rejection at 6% signal efficiency. Better discriminating power is achieved using a BDT with 14 input variables, including the CNN score as one variable. The other variables in the BDT include numbers of reconstructed objects (tracks, showers, vertices), variables related to visible energy deposition, PID variables ($PIDA$, Equation 6.2, and $\mathcal{L}$, Equation 6.4), reconstructed track length, and reconstructed momentum.

Figure 6.5 shows the distribution of the BDT output for signal and background.

Figure 6.6 shows a signal event with high BDT response value (0.605), meaning a well-classified event. The event display shows the reconstructed kaon track in green, the reconstructed muon track from the kaon decay in maroon, and the reconstructed shower from the Michel electron coming from the muon decay in red. Figure 6.7 shows event displays for atmospheric neutrino interactions. The left figure (BDT response value of 0.394) shows the interaction of an atmospheric electron neutrino, $\nu_e + n \to e^- + p + \pi^0$. This event is clearly distinguishable from the signal. However, the right figure (BDT response value 0.587) shows a CCQE interaction of an atmospheric muon neutrino, $\nu_\mu + n \to \mu^- + p$, which is more likely to be mis-classified as a signal interaction. These types of interactions present a challenge if the proton track is misidentified as kaon. A tight cut on BDT response can remove most of these events, but this significantly reduces signal efficiency.

Optimal lifetime sensitivity is achieved by combining the pre-selection cuts with a BDT cut that gives a signal efficiency of 0.15 and a background rejection of 0.999997, which corresponds to approximately one background event per $\mathrm{Mt} \cdot \mathrm{year}$.

The limiting factor in the sensitivity is the kaon tracking efficiency. With the current reconstruc-

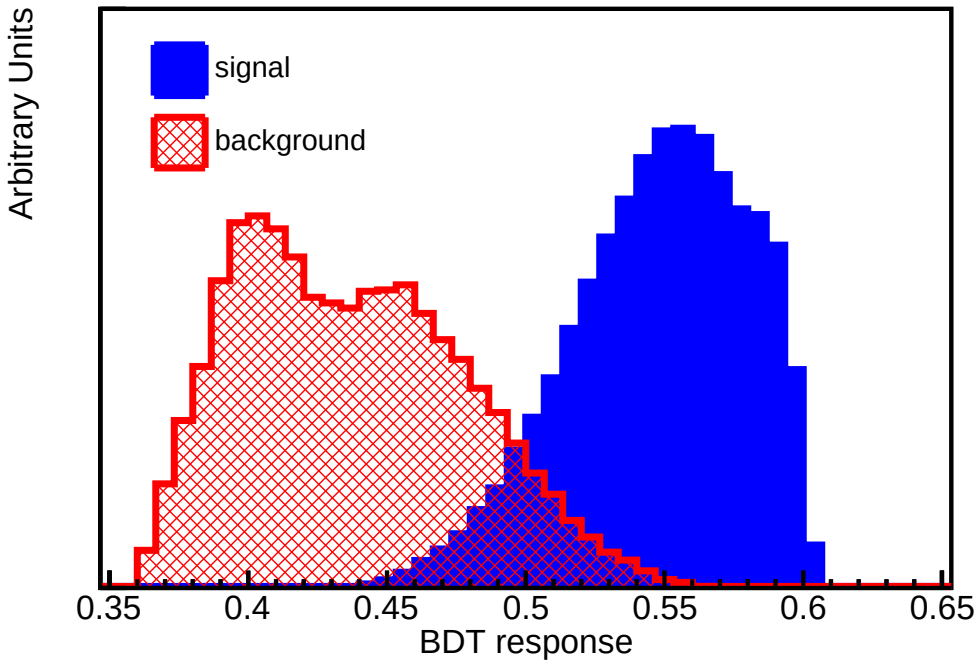

Figure 6.5: Boosted Decision Tree response for $p \to K^+\overline{\nu}$ for signal (blue) and background (red).

tion, the overall kaon tracking efficiency is 58%. The reconstruction is not yet optimized, and the kaon tracking efficiency should increase with improvements in the reconstruction algorithms. To understand the potential improvement, a visual scan of simulated decays of kaons into muons was performed. For this sample of events, with kaon momentum in the 150 MeV/c to 450 MeV/c range, scanners achieved greater than 90% efficiency at recognizing the $K^+ \to \mu^+ \to e^+$ decay chain. The inefficiency came mostly from short kaon tracks (momentum below 180 MeV/c) and kaons that decay in flight. Note that the lowest momentum kaons (<150 MeV/c) were not included in the study; the path length for kaons in this range would also be too short to track. Based on this study, the kaon tracking efficiency could be improved to a maximum value of approximately 80% with optimized reconstruction algorithms, where the remaining inefficiency comes from low-energy kaons and kaons that charge exchange, scatter, or decay in flight. Combining this tracking performance improvement with some improvement in the K/p separation performance for short tracks, the overall signal selection efficiency improves from 15% to approximately 30%.

The analysis presented above is inclusive of all possible modes of kaon decay; however, the current version of the BDT preferentially selects kaon decay to muons, which has a branching fraction of roughly 64%. The second most prominent kaon decay is $K^+ \to \pi^+\pi^0$, which has a branching fraction of 21%. Preliminary studies that focus on reconstructing a $\pi^+\pi^0$ pair with the appropriate kinematics indicate that the signal efficiency for kaons that decay via the $K^+ \to \pi^+\pi^0$ mode is approximately the same as the signal efficiency for kaons that decay via the $K^+ \to \mu^+\nu_\mu$ mode. This assumption is included in our sensitivity estimates below.

The dominant systematic uncertainty in the signal is expected to be due to the kaon FSI. To account for this uncertainty, kaon-nucleon elastic scattering ($K^+p(n) \to K^+p(n)$) is re-weighted by ±50% in the simulation. The absolute uncertainty on the efficiency with this re-weighting is 2%,

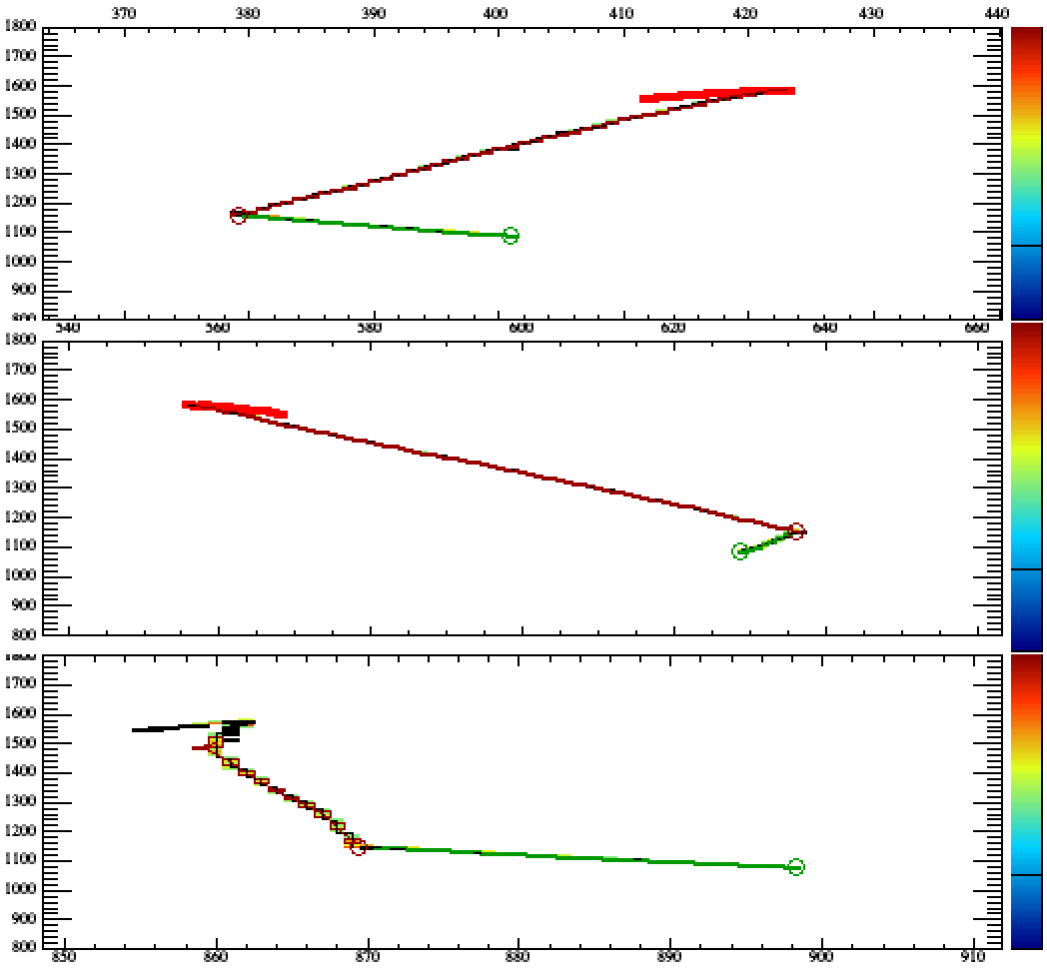

Figure 6.6: Event display for a well-classified $p \to K^+\overline{\nu}$ signal event. The vertical axis is time ticks (each time tick corresponds to 500 ns), and the horizontal axis is wire number. The bottom view is induction plane one, middle is induction plane two and top is the collection plane. The color represents the charge deposited in each hit.

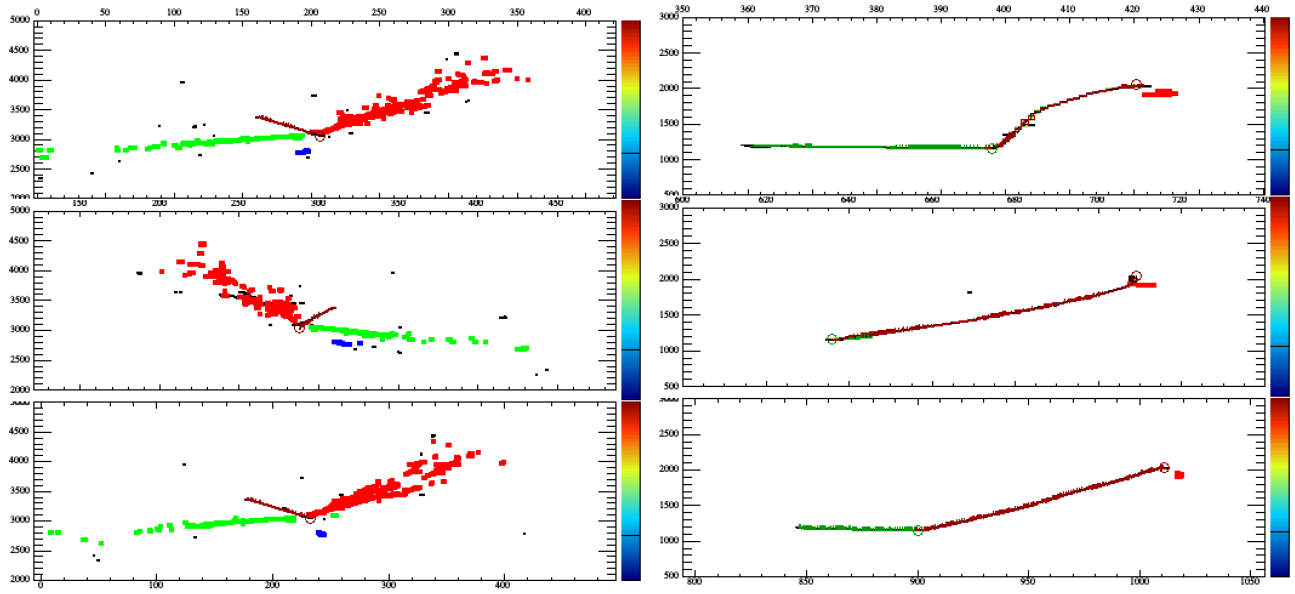

Figure 6.7: Event displays for $p \to K^+\overline{\nu}$ backgrounds. The vertical axis is time ticks (each time tick corresponds to 500 ns), and the horizontal axis is wire number. The bottom view is induction plane one, middle is induction plane two and top is the collection plane. The color represents the charge deposited in each hit. The left shows an atmospheric neutrino interaction unlikely to be classified as signal. The right shows an atmospheric neutrino interaction which could make it into the selected sample without a tight cut.

which is taken as the systematic uncertainty on the signal efficiency. The dominant uncertainty in the background is due to the absolute normalization of the atmospheric neutrino rate. The Bartol group has carried out a detailed study of the systematic uncertainties, where the absolute neutrino fluxes have uncertainties of approximately 15% [216]. The remaining uncertainties are due to the cross section models for neutrino interactions. The uncertainty on the CC0π cross section in the energy range relevant for these backgrounds is roughly 10% [217]. Based on these two effects, a conservative 20% systematic uncertainty in the background is estimated.

With a 30% signal efficiency and an expected background of one event per Mt $\cdot$ year , a 90% CL lower limit on the proton lifetime in the $p \to K^+\overline{\nu}$ channel of 1.3×10^{34} years can be set, assuming no signal is observed over ten years of running with a total of 40 kt of fiducial mass. This calculation assumes constant signal efficiency and background rejection over time and for each of the FD modules. Additional running improves the sensitivity proportionately if the experiment remains background-free.

6.1.3 Sensitivity to Other Key Nucleon Decay Modes

Another potential mode for a baryon number violation search is the decay of the neutron into a charged lepton plus meson, i.e. $n \to e^-K^+$. In this mode, $\Delta B = -\Delta L$, where B is baryon number and L is lepton number. The current best limit on this mode is 3.2×10^{31} years from the FREJUS collaboration [218]. The reconstruction software for this analysis is the same as for the

$p \to K^+\overline{\nu}$ analysis; the analysis again uses a BDT that includes image classification score as an input. To calculate the lifetime sensitivity for this decay mode the same systematic uncertainties and procedure is used. The selection efficiency for this channel including the expected tracking improvements is 0.47 with a background rejection of 0.99995, which corresponds to 15 background events per Mt · year . The lifetime sensitivity for a $400\,\text{kt} \cdot \text{year}$ exposure is 1.1×10^{34} years. The DUNE FD technology can improve the lifetime limit for this particular channel by more than two orders of magnitude from the current world's best limit.

The sensitivity to the $p \to e^+\pi^0$ mode has also been calculated. For this analysis, reconstruction was not applied, and true quantities were used as inputs to a BDT to isolate events that contain a positron and two photons from the π^0 decay. Energy smearing simulated the effects of reconstruction. Applying the same selection to the atmospheric neutrino background and calculating the limit yields a sensitivity for an exposure of $400\,\text{kt} \cdot \text{year}$ in the range of 8.7×10^{33} years to 1.1×10^{34} years depending on the level of energy smearing (in the range 5-30%). This initial study indicates that with a longer exposure of $800\,\text{kt} \cdot \text{year}$ DUNE could achieve a sensitivity comparable to Super–Kamiokande's current limit of 1.6×10^{34} years [37].

6.1.4 Detector Requirements for Nucleon Decay Searches

As is the case for the entire FD non-accelerator based physics program of DUNE, nucleon decay searches require efficient triggering and event localization capabilities. The nucleon decay search program also relies on both the event imaging and particle identification (via dE/dx) capabilities of the LArTPC technology.

Event localization within the FD along the ionization drift direction is required in order to reject cosmic ray backgrounds via fiducial volume cuts. This can be achieved by requiring an event time (t_0) signal for nucleon decay candidates so that TPC anode signal times can be used to determine the drift time. Within DUNE, the t_0 is provided by the photon detection system (PD system), which must have high detection efficiency throughout the FD active volume for a scintillation photon signal corresponding to $> 200\,\text{MeV}$ of deposited energy.

For nucleon decays into charged kaons, the possibility of using the time difference between the kaon scintillation signal and the scintillation signal from the muon from the kaon decay has been investigated. In the Super–Kamiokande analysis of $p \to K^+\overline{\nu}$, the corresponding timing difference (between the de-excitation photons from the oxygen nucleus and the muon from kaon decay) was found to be an effective way to reduce backgrounds [4]. Studies indicate that measuring time differences on the scale of the kaon lifetime (12 ns) is difficult in DUNE, independent of photon detector acceptance and timing resolution, due to both the scintillation process in argon – consisting of fast (ns-scale) and slow (µs-scale) components – and Rayleigh scattering over long distances.

Given the $\sim 1\,\text{GeV}$ energy release, the requirements for tracking and calorimetry performance are similar to those for the beam-based neutrino oscillation program described in Chapter 5. Especially important are the event imaging function and the dE/dx measurement capability for particle identification. With a well-functioning LArTPC, nucleon decay search capabilities are ultimately

limited by physics, namely complexities arising from final state interactions (such as nucleon emission) as well as ionization fluctuations for example, rather than by detector performance per se. This is the case provided that readout noise is small compared to the ionization signal expected for minimum-ionizing particles located anywhere within the active volume of the detector (see Sec. 1.2).

6.1.5 Nucleon Decay Summary

In summary, projecting from our current analysis of the sensitivity to proton decay via $p \to K^+\overline{\nu}$ in DUNE with full simulation and reconstruction, we find that the sensitivity after a $400\,\mathrm{kt}\cdot\mathrm{year}$ exposure is roughly twice the current limit from Super–Kamiokande based on an exposure of $260\,\mathrm{kt}\cdot\mathrm{year}$ [4]. An analysis of the sensitivity to neutron decay via $n \to e^- K^+$ has also been completed; DUNE could improve the lifetime limits in this mode by more than two orders of magnitude from the current world's best limit. Future studies of nucleon decay into kaons will focus on potential improvements in track reconstruction, improved methods of particle and event identification, and understanding kaon FSI models. Analysis of other modes of nucleon decay into kaons is underway, as well as the first investigations of the $p \to e^+\pi^0$ with full simulation and reconstruction.

6.2 Neutron-Antineutron Oscillations

Neutron-antineutron ($n-\bar{n}$) oscillation is a baryon number violating process that has never been observed but is predicted by a number of BSM theories [219]. Discovering baryon number violation via observation of this process would have implications about the source of matter-antimatter symmetry in our universe given Sakharov's conditions for such asymmetry to arise [32]. In particular, the neutron-antineutron oscillation ($n-\bar{n}$) process violates baryon number by two units and, therefore, could also have further implications for the smallness of neutrino masses [219]. Since the $n-\bar{n}$ transition operator is a six-quark operator, of Maxwellian dimension 9, with a coefficient function of dimension $(\mathrm{mass})^{-5}$, while the proton decay operator is a four-fermion operator, of dimension 6, with a coefficient function of dimension $(\mathrm{mass})^{-2}$, one might naively assume that $n-\bar{n}$ oscillations would always be suppressed relative to proton decay as a manifestation of baryon number violation. However, this is not necessarily the case; indeed, there are models [220] in which proton decay is very strongly suppressed down to an unobservably small level, while $n-\bar{n}$ oscillations occur at a level comparable to present limits. This shows the value of a search for $n-\bar{n}$ transitions at DUNE. The $n-\bar{n}$ process is one of many possible baryon number violating processes that can be investigated in DUNE. Searches for this process using both free neutrons and nucleus-bound neutron states have continued since the 1980s. The current best 90% CL limits on the (free) neutron oscillation lifetime are $8.6\times10^7\,\mathrm{s}$ from free $n-\bar{n}$ searches and $2.7\times10^8\,\mathrm{s}$ from nucleus-bound $n-\bar{n}$ searches [221, 222].

Neutron-antineutron oscillations can be detected via the subsequent antineutron annihilation with a neutron or a proton. Table 6.3 shows the branching ratios for the antineutron annihilation

Table 6.3: Effective branching ratios for antineutron annihilation in ^{40}Ar, as implemented in GENIE.

$\bar{n}+p$		$\bar{n}+n$	
Channel	Branching ratio	Channel	Branching ratio
$\pi^+\pi^0$	1.2%	$\pi^+\pi^-$	2.0%
$\pi^+2\pi^0$	9.5%	$2\pi^0$	1.5%
$\pi^+3\pi^0$	11.9%	$\pi^+\pi^-\pi^0$	6.5%
$2\pi^+\pi^-\pi^0$	26.2%	$\pi^+\pi^-2\pi^0$	11.0%
$2\pi^+\pi^-2\pi^0$	42.8%	$\pi^+\pi^-3\pi^0$	28.0%
$2\pi^+\pi^-2\omega$	0.003%	$2\pi^+2\pi^-$	7.1%
$3\pi^+2\pi^-\pi^0$	8.4%	$2\pi^+2\pi^-\pi^0$	24.0%
		$\pi^+\pi^-\omega$	10.0%
		$2\pi^+2\pi^-2\pi^0$	10.0%

modes applicable to intranuclear searches. This annihilation event will have a distinct signature of a vertex with several emitted light hadrons, with total energy of twice the nucleon mass and zero net momentum. Reconstructing these hadrons correctly and measuring their energies is key to identifying the signal event. The main background for these $n-\bar{n}$ annihilation events is caused by atmospheric neutrinos. Most common among mis-classified events are neutral current (NC) deep inelastic scattering (DIS) events without a lepton in the final state. As with nucleon decay, nuclear effects and FSI make the picture more complicated.

6.2.1 Sensitivity to Intranuclear Neutron-Antineutron Oscillations in DUNE

The simulation of neutron-antineutron oscillation was developed [223] and implemented in GENIE. This analysis uses GENIE v.2.12.10. Implementing this process in GENIE used GENIE's existing modeling of Fermi momentum and binding energy for both the oscillating neutron and the nucleon with which the resulting antineutron annihilates. Once a neutron has oscillated to an antineutron in a nucleus, the antineutron has a 18/39 chance of annihilating with a proton in argon, and a 21/39 chance of annihilating with a neutron. The energies and momenta of the annihilation products are assigned randomly but consistently with four-momentum conservation. The products of the annihilation process follow the branching fractions (shown in Table 6.3) measured in low-energy

antiproton annihilation on hydrogen. Since the annihilation products are produced inside the nucleus, GENIE further models re-interactions of those products as they propagate in the nucleus (until they escape the nucleus). The FSI are simulated using the $hA2015$ model in GENIE as described in Section 6.1.1.3.

Figure 6.8 shows the momentum distributions for charged and neutral pions before FSI and after FSI. These distributions show the FSI makes both charged and neutral pions less energetic. The effect of FSI on pion multiplicity is also rather significant; 0.9% of the events have no charged pions before FSI, whereas after FSI 11.1% of the events have no charged pions. In the case of the neutral pion, 11.0% of the events have no neutral pions before FSI, whereas after FSI, 23.4% of the events have no neutral pions. The decrease in pion multiplicity is primarily due to pion absorption in the nucleus. Another effect of FSI is nucleon knockout from pion elastic scattering. Of the events, 94% have at least one proton from FSI and 95% of the events have at least one neutron from FSI. Although the kinetic energy for these nucleons peak at a few tens of MeV, the kinetic energy can be as large as hundreds of MeV. In summary, the effects of FSI in $n-\bar{n}$ become relevant because they modify the kinematics and topology of the event. For instance, even though the decay modes of Table 6.3 do not include nucleons in their decay products, nucleons appear with high probability after FSI.

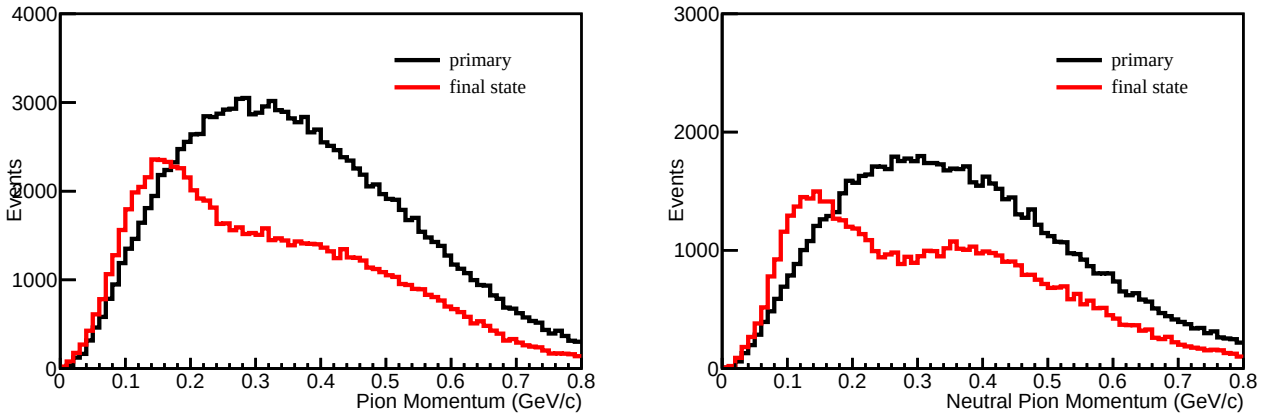

Figure 6.8: Momentum of an individual charged pion before and after final state interactions (left): momentum of an individual neutral pion before and after final state interactions (right).

The main background process in search of bound $n-\bar{n}$ oscillation in DUNE is assumed to be atmospheric neutrino interactions in the detector. This is simulated in GENIE as described in Section 6.1.1.1.

As with the $p \to K^+\overline{\nu}$ analysis, two distinct methods of reconstruction and event selection have been applied in this search. One involves traditional reconstruction methods (3D track and vertex reconstruction by PMA); the other involves image classification of 2D images of reconstructed hits (CNN). The two methods, combined in the form of a multivariate analysis, uses the image classification score with other physical observables extracted from traditional reconstruction. A BDT classifier is used. Ten variables are used in the BDT event selection, including number of reconstructed tracks and showers; variables related to visible energy deposition; $PIDA$ and dE/dx; reconstructed momentum; and CNN score. Figure 6.9 shows the distribution of the BDT output for signal and background.

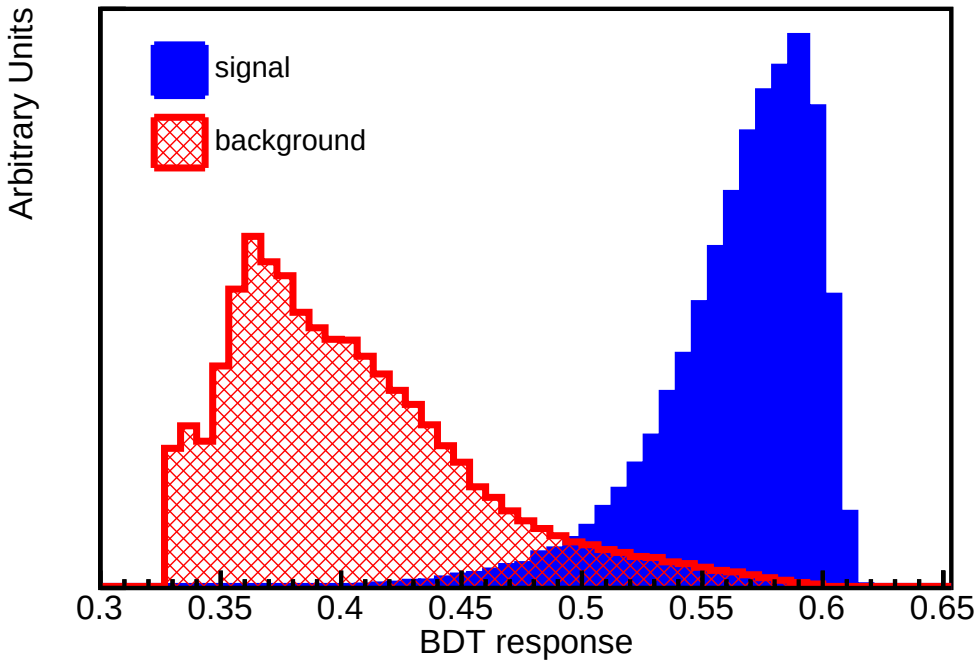

Figure 6.9: Boosted Decision Tree response for $n-\bar{n}$ oscillation for signal (blue) and background (red).

Figure 6.10 shows an $n-\bar{n}$ event with high BDT response value (0.592). Showers from neutral pions are shown in red, blue, yellow, and green. The reconstructed charged pion tracks are shown as dark green and maroon lines. The topology of this event is consistent with charged pion and neutral pion production.

The left side plot in Figure 6.11 shows a NC atmospheric neutrino interaction $\nu_e + n \rightarrow \nu_e + p + p$ with a low BDT response value (0.388). This type of interaction is easily distinguished from the signal. The two protons from the NC interaction are reconstructed as tracks, and no shower activity is present. However, the right side plot in Figure 6.11 displays a CC atmospheric neutrino interaction $\nu_e + n \rightarrow e^- + p + \pi + p$ with a high BDT response value (0.598). This background event mimics the signal topology by having multi-particle production and an electromagnetic shower. Further improvements in shower reconstruction, especially dE/dx, should help in classifying these types of background events in the future because the electron shower dE/dx differs from the dE/dx of a shower induced by a gamma-ray.

The sensitivity to the $n-\bar{n}$ oscillation lifetime can be calculated for a given exposure, the efficiency of selecting signal events, and the background rate along their uncertainties. The lifetime sensitivity is obtained at 90% CL for the bound neutron. Then, the lifetime sensitivity for a free neutron is acquired using the conversion from nucleus bounded neutron to free neutron $n-\bar{n}$ oscillation [224]. The uncertainties on the signal efficiency and background rejection are conservatively estimated to be 25%. A detailed evaluation of the uncertainties is in progress.

The free $n-\bar{n}$ oscillation lifetime, $\tau_{n-\bar{n}}$, and bounded $n-\bar{n}$ oscillation lifetime, $T_{n-\bar{n}}$, are related

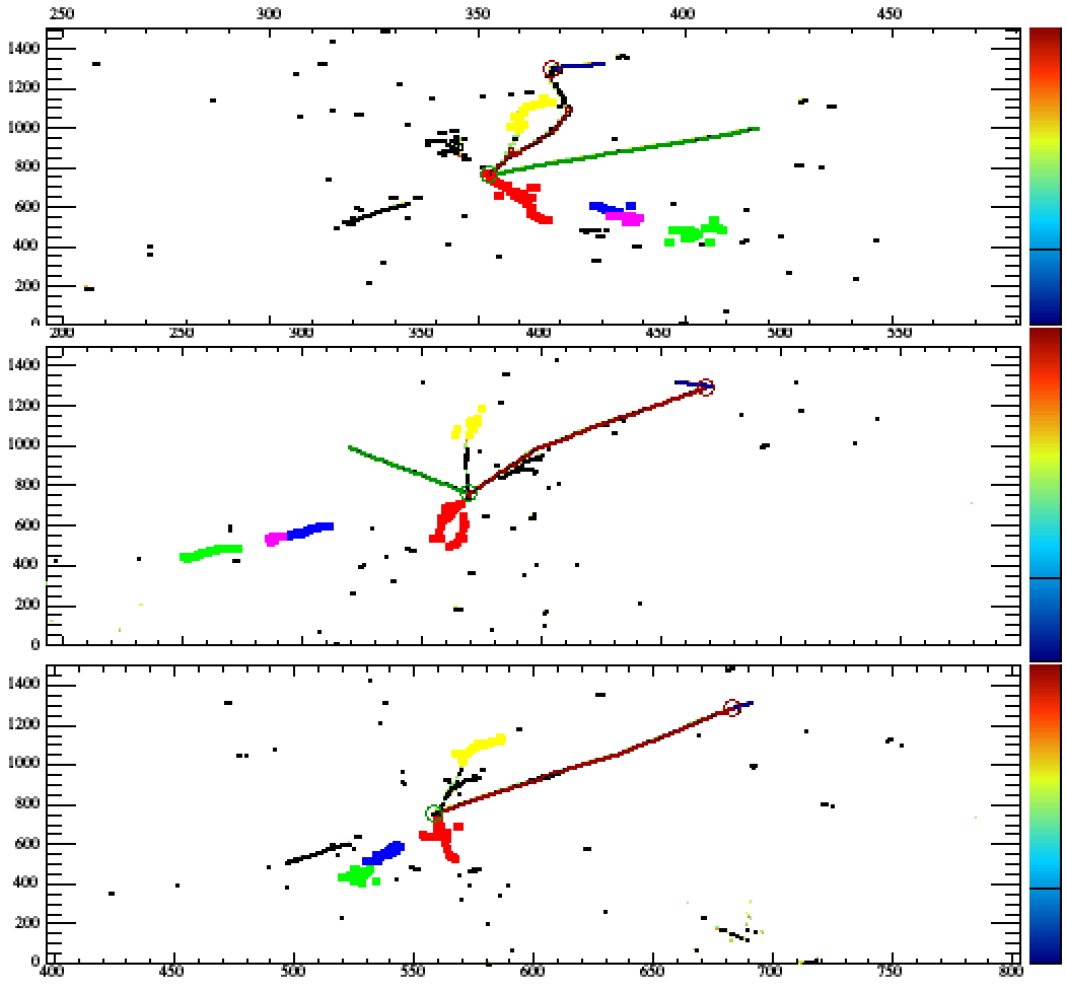

Figure 6.10: Event display for a well-classified $n - \bar{n}$ signal event. The vertical axis is time ticks (each time tick corresponds to 500 ns), and the horizontal axis is wire number. The bottom view is induction plane one, middle is induction plane two, and the top is the collection plane. The color represents the charge deposited in each hit.

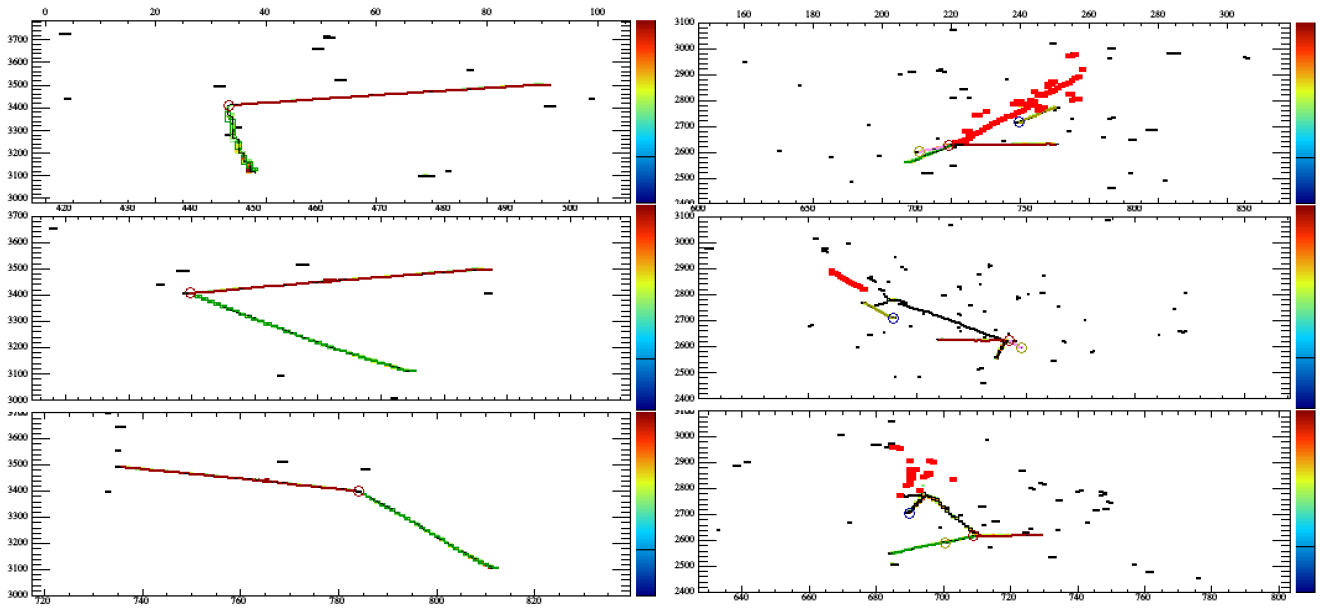

Figure 6.11: Event displays for $n - \bar{n}$ backgrounds. The vertical axis is time ticks (each time tick corresponds to 500 ns), and the horizontal axis is wire number. The bottom view is induction plane one, middle is induction plane two, and the top is the collection plane. The color represents the charge deposited in each hit. The left plot shows an atmospheric neutrino interaction unlikely to be classified as signal. The right plot shows an atmospheric neutrino interaction which could make it into the selected sample.

to each other through the suppression factor R as

$$\tau^2_{n-\bar{n}} = \frac{T_{n-\bar{n}}}{R} \ . \tag{6.5}$$

The suppression factor R varies for different nuclei. This suppression factor was calculated for ^{16}O and ^{56}Fe [224]. The R for ^{56}Fe, $0.666 \times 10^{23}\,\mathrm{s}^{-1}$, is used in this analysis for ^{40}Ar nuclei.

The best bound neutron lifetime limit is achieved using a signal efficiency of 8.0% at the background rejection probability of 99.98%. The 90% CL limit of a bound neutron lifetime is 6.45×10^{32} years for a $400\,\mathrm{kt} \cdot \mathrm{year}$ exposure. The corresponding limit for the oscillation time of free neutrons is calculated to be 5.53×10^8 s. This is approximately an improvement by a factor of two from the current best limit, which comes from Super–Kamiokande [222]. Planned improvements to this analysis include improved CNN performance and better estimates of systematic uncertainties. As with nucleon decay, searches for $n - \bar{n}$ oscillations performed by DUNE and those performed by Super–Kamiokande or Hyper–Kamiokande are highly complementary. Should a signal be observed in any one experiment, confirmation from another experiment with a different detector technology and backgrounds would be very powerful.

6.3 Physics with Atmospheric Neutrinos

Atmospheric neutrinos are a unique tool for studying neutrino oscillations: the oscillated flux contains all flavors of neutrinos and antineutrinos, is very sensitive to matter effects and to both Δm^2 parameters, and covers a wide range of L/E. In principle, all oscillation parameters could be measured, with high complementarity to measurements performed with a neutrino beam. In addition, atmospheric neutrinos are available all the time, in particular before the beam becomes operational. The DUNE FD, with its large mass and the overburden to protect it from atmospheric muon background, is an ideal tool for these studies. Given the strong overlap in event topology and energy scale with beam neutrino interactions, most requirements will necessarily be met by the FD design. Additional requirements include a self-trigger because atmospheric neutrino events are asynchronous with accelerator timing and a more stringent demand on neutrino direction reconstruction.

6.3.1 Oscillation Physics with Atmospheric Neutrinos

Sensitivity to oscillation parameters with atmospheric neutrinos in DUNE has been evaluated. The fluxes of each neutrino species were computed at the FD location after oscillation. Interactions in the LAr medium were simulated with the GENIE event generator. Detection thresholds and energy resolutions based on full simulations were applied to the outgoing particles to take detector effects into account. Events were classified as fully contained or partly contained by placing the vertex at a random position inside the detector and tracking the lepton until it reaches the edge of the detector. Partly contained events are those where a final state muon exits the detector. The number of events expected for each flavor and category is summarized in Table 6.4.

Table 6.4: Atmospheric neutrino event rates per year in 40 kt of fiducial mass including oscillations in different analysis categories

Sample	Event rate per year
fully contained electron-like	1600
fully contained muon-like	2400
partly contained muon-like	790

Figure 6.12 shows the expected L/E distribution for high-resolution, muon-like events from a $400\,\mathrm{kt}\cdot\mathrm{year}$ exposure. The data provide excellent resolution of the first two oscillation nodes, even with the expected statistical uncertainty. In performing oscillation fits, the data in each flavor/containment category are binned in energy and zenith angle.

When neutrinos travel through the Earth, the Mikheyev-Smirnov-Wolfenstein effect (MSW) resonance influences electron neutrinos in the few-GeV energy range. More precisely, the resonance occurs for ν_e in the case of normal ordering and for $\bar{\nu}_e$ in the case of inverted ordering.

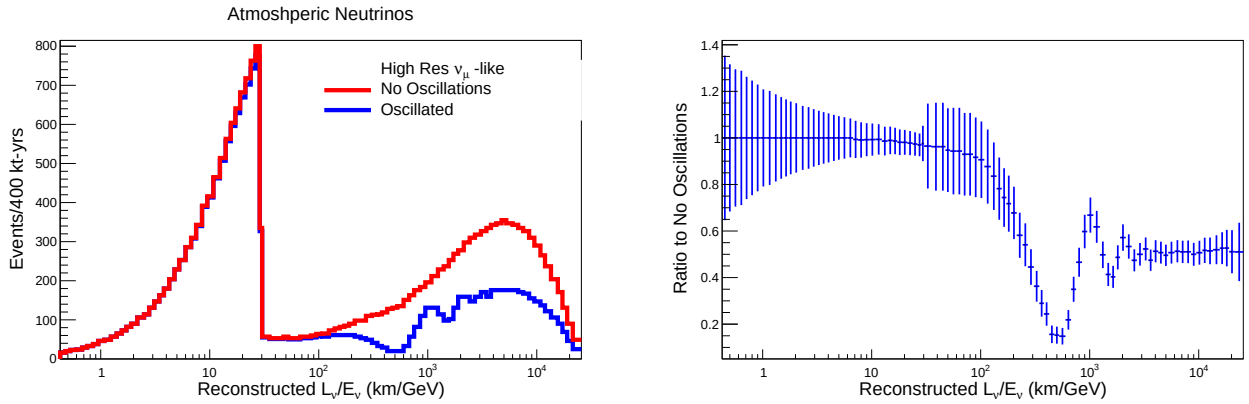

Figure 6.12: Reconstructed L/E Distribution of 'High-Resolution' μ-like atmospheric neutrino events in a 400 kt · year exposure with and without oscillations (left), and the ratio of the two (right), with the error bars indicating the size of the statistical uncertainty.

The mass ordering sensitivity can be greatly enhanced if neutrino and antineutrino events can be separated. The DUNE FD will not be magnetized, but its high-resolution imaging offers possibilities for tagging features of events that provide statistical discrimination between neutrinos and antineutrinos. For the sensitivity calculations, two such tags were included: a proton tag and a decay electron tag.

Figure 6.13 shows the mass ordering sensitivity as a function of the fiducial exposure. Over this range of fiducial exposures, the sensitivity essentially follows the square root of the exposure, indicating that the measurement is not systematics-limited. Unlike beam measurements, the sensitivity to the mass ordering with atmospheric neutrinos is nearly independent of the charge parity (CP) violating phase. The sensitivity comes from both electron neutrino appearance as well as muon neutrino disappearance and depends strongly on the true value of $\sin^2\theta_{23}$, as shown in Figure 6.13. For comparison, the sensitivity for Hyper–Kamiokande atmospheric neutrinos with a 1900 kt · year exposure is also shown.

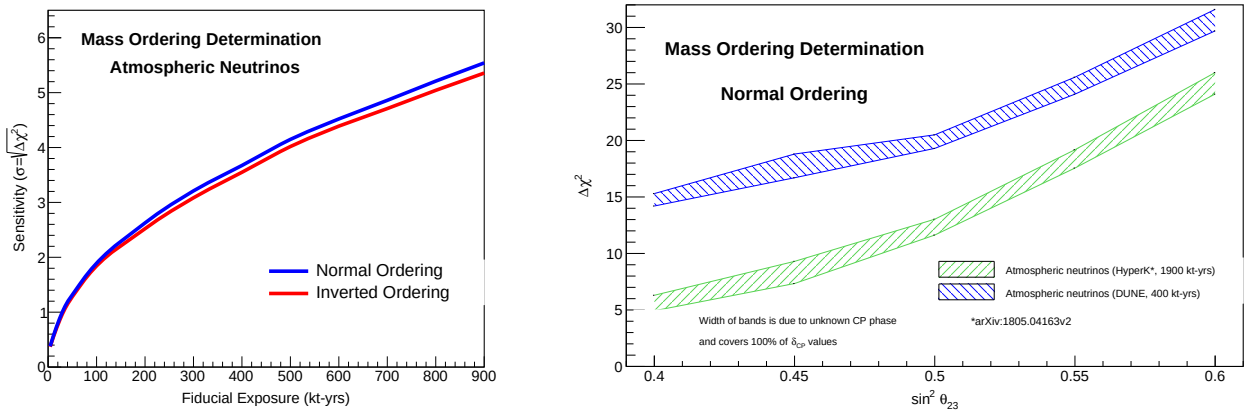

Figure 6.13: Sensitivity to mass ordering using atmospheric neutrinos as a function of fiducial exposure in DUNE (left) and as a function of the true value of $\sin^2\theta_{23}$ (right). For comparison, Hyper–Kamiokande sensitivities are also shown [36].

In the two-flavor approximation, neutrino oscillation probabilities depend on $\sin^2\theta$, which is invariant when changing θ to $\pi/2 - \theta$. In this case, the octant degeneracy remains for θ_{23} in the leading order terms of the full three-flavor oscillation probability, making it impossible to determine whether $\theta_{23} < \pi/4$ or $\theta_{23} > \pi/4$. Accessing full three-flavor oscillation with atmospheric neutrinos should help solve the ambiguity.

These analyses will provide an approach complementary to the beam neutrino approach. For instance, atmospheric neutrinos should resolve degeneracies present in beam analyses because the mass ordering sensitivity is essentially independent of $\delta_{\rm CP}$. Atmospheric neutrino data will be acquired even in the absence of the beam and will provide a useful sample for developing reconstruction software, analysis methodologies, and calibrations. Atmospheric neutrinos provide a window into a range of new physics scenarios, and may allow DUNE to place limits on Lorentz and charge, parity, and time reversal symmetry (CPT) violation (see Section 6.3.2), non-standard interactions [225], mass-varying neutrinos [226], and sterile neutrinos [227]. Recent studies have also indicated that sub-GeV atmospheric neutrinos could be used to exclude some values of $\delta_{\rm CP}$ independently from the beam neutrino measurements [228].

6.3.2 BSM Physics with Atmospheric Neutrinos

Studying DUNE atmospheric neutrinos is a promising approach to search for BSM effects such as Lorentz and CPT violation, which has been hypothesized to emerge from an underlying Planck-scale theory like strings [229, 230]. The comprehensive realistic effective field theory for Lorentz and CPT violation, the standard-model extension (SME) [231, 232, 233, 234], is a powerful and calculable framework for analyzing experimental data. All SME coefficients for Lorentz and CPT violation governing the propagation and oscillation of neutrinos have been enumerated [235, 236], and many experimental measurements of SME coefficients have been performed to date [237]. Nonetheless, much of the available SME coefficient space in the neutrino sector remains unexplored.

Experimental signals predicted by the SME include corrections to standard neutrino-neutrino and antineutrino-antineutrino mixing probabilities, oscillations between neutrinos and antineutrinos, and modifications of oscillation-free propagation, all of which incorporate unconventional dependencies on the magnitudes and directions of momenta and spin. For DUNE atmospheric neutrinos, the long available baselines, the comparatively high energies accessible, and the broad range of momentum directions offer advantages that can make possible great improvements in sensitivities to certain types of Lorentz and CPT violation [235, 236, 238, 239, 240, 241, 242]. To date, experimental searches for Lorentz and CPT violation with atmospheric neutrinos have been published by the IceCube and Super–Kamiokande collaborations [243, 244, 245]. Similar studies are possible with DUNE, and many SME coefficients can be measured that remain unconstrained to date.

An example of the potential reach of studies with DUNE atmospheric neutrinos is shown in Figure 6.14, which displays estimated sensitivities from DUNE atmospheric neutrinos to a subset of coefficients controlling isotropic (rotation-invariant) violations in the Sun-centered frame [246]. The sensitivities are estimated by requiring that the Lorentz/CPT-violating effects are comparable in size to those from conventional neutrino oscillations. The eventual DUNE constraints will be determined by the ultimate precision of the experiment (which is set in part by the exposure).

The gray bars in Figure 6.14 show existing limits. These conservative sensitivity estimates show that DUNE can achieve first measurements (red) on some coefficients and improved measurements (green) on others.

To illustrate an SME modification of oscillation probabilities, consider a measurement of the atmospheric neutrino and antineutrino flux as a function of energy. For definiteness, we adopt atmospheric neutrino fluxes [247], evaluated using the NRLMSISE-00 global atmospheric model [248], that result from a production event at an altitude of 20 km. Assuming conventional oscillations with standard mass-matrix values from the PDG [25], the fluxes at the FD are shown in Figure 6.15. The sum of the ν_e and $\bar{\nu}_e$ fluxes is shown as a function of energy as a red dashed line, while the sum of the ν_μ and $\bar{\nu}_\mu$ fluxes is shown as a blue dashed line. Adding an isotropic non-minimal coefficient for Lorentz violation of magnitude $\mathring{c}^{(6)}_{e\mu} = 1 \times 10^{-28}\,\mathrm{GeV}^{-1}$ changes the fluxes from the dashed lines to the solid ones. This coefficient is many times smaller than the current experimental limit. Nonetheless, the flux spectrum is predicted to change significantly at energies over approximately 100 GeV.

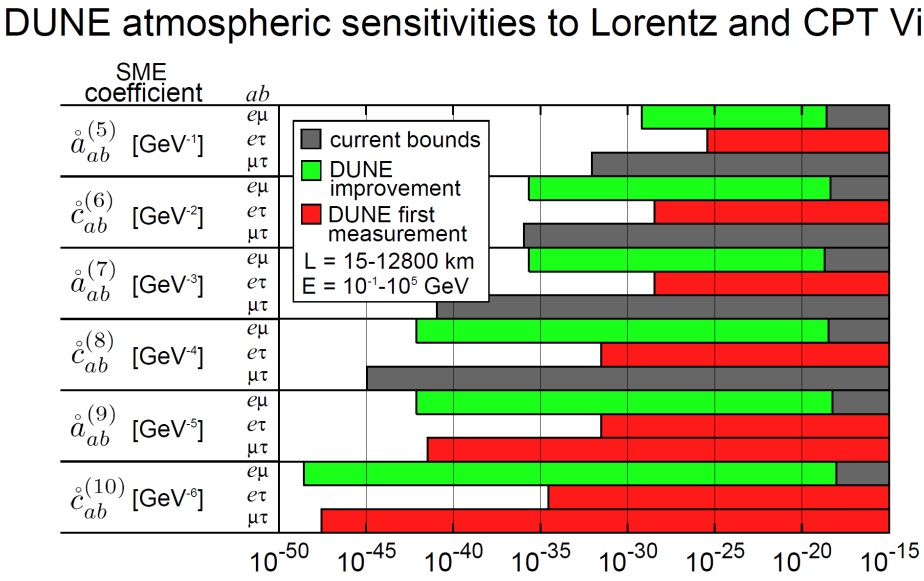

Figure 6.14: Estimated sensitivity to Lorenz and CPT violation with atmospheric neutrinos in the non-minimal isotropic Standard Model Extension. The sensitivities are estimated by requiring that the Lorentz/CPT-violating effects are comparable in size to those from conventional neutrino oscillations.

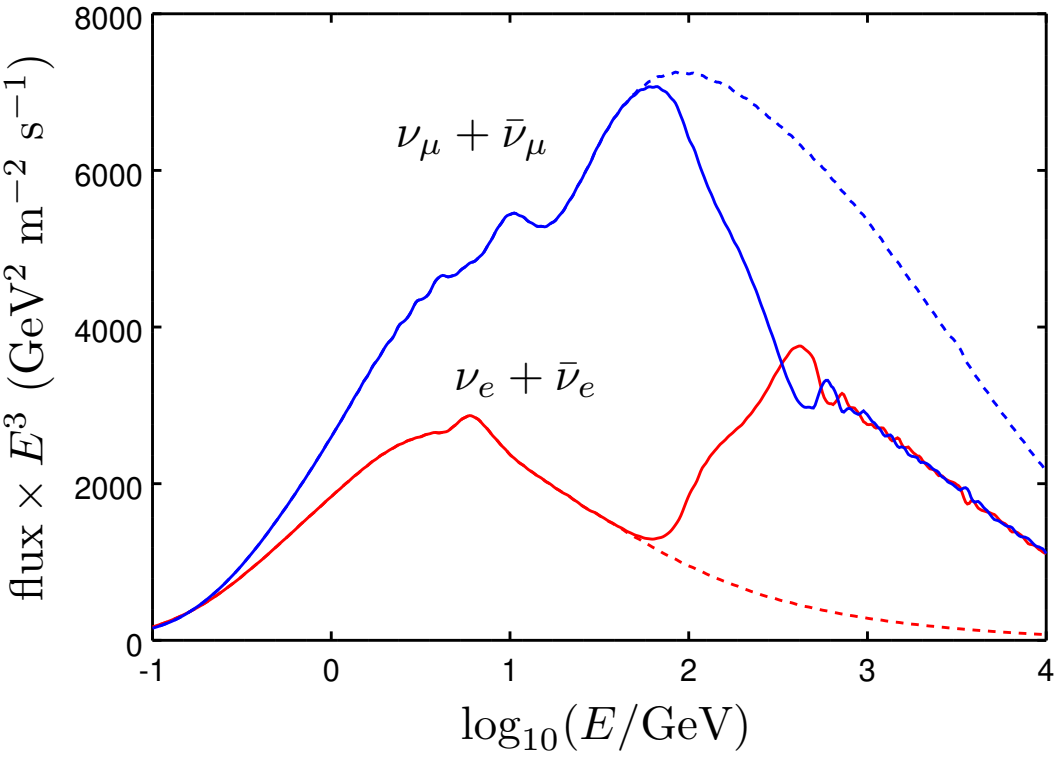

Figure 6.15: Atmospheric fluxes of neutrinos and antineutrinos as a function of energy for conventional oscillations (dashed line) and in the non-minimal isotropic Standard Model Extension (solid line).

Chapter 7

Supernova neutrino bursts and physics with low-energy neutrinos

The DUNE experiment will be sensitive to neutrinos from around 5 MeV to a few tens of MeV. Charged-current interactions of neutrinos in this range create short electron tracks in liquid argon, potentially accompanied by gamma ray and other secondary particle signatures. This regime is of particular interest for detection of the burst of neutrinos from a galactic core-collapse supernova (the primary focus of this section). The sensitivity of DUNE is primarily to *electron flavor* supernova neutrinos, and this capability is unique among existing and proposed supernova neutrino detectors for the next decades. Neutrinos and antineutrinos from other astrophysical sources are also potentially detectable. The low-energy event regime has particular reconstruction, background and triggering challenges.

In this section we will describe studies done in the DUNE supernova neutrino burst and low energy (SNB/LE) physics working group so far towards understanding of DUNE's sensitivity to low-energy neutrinos, with an emphasis on supernova burst signals. In Sec. 7.1, we describe basic supernova neutrino physics. In Sec. 7.2 we describe the general properties of low-energy events in DUNE including interaction channels, the tools we have developed so far, and backgrounds. The tools include a neutrino event generator specifically for this energy regime, and the SuperNova Observatories with GLoBES (SNOwGLoBES) fast event-rate calculation tool. Some of the subsequent studies are done using a full simulation and reconstruction, whereas others make use of SNOwGLoBES. Section 7.3 describes the expected supernova signal: event rates, and pointing properties. Section 7.4 describes astrophysics of the collapse, explosion and remnant that we will learn from the burst. Section 7.5 describes neutrino physics that can be extracted from a supernova neutrino burst (SNB) observation. Section 7.6 mentions some other possible astrophysical neutrinos, including solar and diffuse supernova background neutrinos. Section 7.7 summarizes the detector requirements.

7.1 Supernova neutrino bursts

7.1.1 Neutrinos from collapsed stellar cores: basics

A core-collapse supernova[1] occurs when a massive star reaches the end of its life. As a result of nuclear burning throughout the star's life, the central region of such a star gains an "onion" structure, with an iron core at the center surrounded by concentric shells of lighter elements (silicon, oxygen, neon, magnesium, carbon, etc). At temperatures of $T \sim 10^{10}$ K and densities of $\rho \sim 10^{10}$ g/cm^3, the Fe core continuously loses energy by neutrino emission (through pair annihilation and plasmon decay). Since iron cannot be further burned, the lost energy cannot be replenished throughout the volume and the core continues to contract and heat up, while also growing in mass thanks to the shell burning. Eventually, the critical mass of about $1.4M_\odot$ of Fe is reached, at which point a stable configuration is no longer possible. As electrons are absorbed by the protons and some iron is disintegrated by thermal photons, the pressure support is suddenly removed and the core collapses essentially in free fall, reaching speeds of about a quarter of the speed of light.[2]

The collapse of the central region is suddenly halted after $\sim 10^{-2}$ seconds, as the density reaches nuclear (and up to supra-nuclear) values. The central core bounces and a shock wave is formed. The extreme physical conditions of this core, in particular the densities of order $10^{12} - 10^{14}$ g/cm^3, create a medium that is opaque even for neutrinos. As a consequence, the core initially has a trapped lepton number. The gravitational energy of the collapse at this stage is stored mostly in the degenerate Fermi sea of electrons ($E_F \sim 200$ MeV) and electron neutrinos, which are in equilibrium with the former. The temperature of this core is not more than 30 MeV, which means the core is relatively *cold*.

At the next stage, the trapped energy and lepton number both escape from the core, carried by the least interacting particles, which in the Standard Model are neutrinos. Neutrinos and antineutrinos of all flavors are emitted in a time span of a few seconds (their diffusion time). The resulting central object then settles to a neutron star, or a black hole. A tremendous amount of energy, some 10^{53} ergs, is released in 10^{58} neutrinos with energies ~ 10 MeV. A fraction of this energy is absorbed by beta reactions behind the shock wave that blasts away the rest of the star, creating a spectacular explosion. Yet, from the energetics point of view, this visible explosion is but a tiny perturbation. Over 99% of all gravitational binding energy of the $1.4M_\odot$ collapsed core – some 10% of its rest mass – is emitted in neutrinos.

7.1.2 Stages of the explosion

Electron antineutrinos from the celebrated SN1987A core collapse [5, 6] in the Large Magellanic Cloud outside the Milky Way were reported in water Cherenkov and scintillator detectors. This

[1] "Supernova" always refers to a "core-collapse supernova" in this chapter.

[2] Other collapse mechanisms are possible: an "electron-capture" supernova does not reach the final burning phase before highly degenerate electrons break apart nuclei and trigger a collapse.

observation provided qualitative validation of the basic physical picture outlined above and provided powerful constraints on numerous models of new physics. At the same time, the statistics were sparse and a great many questions remain. A high-statistics observation of a nearby supernova neutrino burst will be possible with the current generation of detectors. Such an observation will shed light on the nature of the astrophysical event, as well as on the nature of neutrinos themselves. Sensitivity to the *different flavor components* of the flux is highly desirable.

The core-collapse neutrino signal starts with a short, sharp *neutronization* (or *break-out*) burst primarily composed of ν_e. These neutrinos are messengers of the shock front breaking through the neutrinosphere (the surface of neutrino trapping): when this happens, iron is disintegrated, the neutrino scattering cross section drops and the lepton number trapped just below the original neutrinosphere is suddenly released. This quick and intense burst is followed by an *"accretion" phase* lasting some hundreds of milliseconds, depending on the progenitor star mass, as matter falls onto the collapsed core and the shock is stalled at the distance of perhaps $\sim$ 200 km. The gravitational binding energy of the accreting material is powering the neutrino luminosity during this stage. The later *"cooling" phase* over $\sim$10 seconds represents the main part of the signal, over which the proto-neutron star sheds its trapped energy.

The flavor content and spectra of the neutrinos emitted from the neutrinosphere change throughout these phases, and the supernova's evolution can be followed with the neutrino signal. Some fairly generic features of these emitted neutrino fluxes are illustrated in Figures 7.1, 7.2.

The physics of neutrino decoupling and spectra formation is far from trivial, owing to the energy dependence of the cross sections and the roles played by both charged- and neutral-current reactions. Detailed transport calculations using methods such as Monte Carlo (MC) or Boltzmann solvers have been employed. It has been observed that spectra coming out of such simulations can typically be parameterized at a given moment in time by the following ansatz (e.g., [250, 251]):

$$\phi(E_\nu) = \mathcal{N} \left(\frac{E_\nu}{\langle E_\nu \rangle} \right)^\alpha \exp \left[- (\alpha + 1) \frac{E_\nu}{\langle E_\nu \rangle} \right] , \tag{7.1}$$

where E_ν is the neutrino energy, $\langle E_\nu \rangle$ is the mean neutrino energy, α is a "pinching parameter", and $\mathcal{N}$ is a normalization constant. Large α corresponds to a more "pinched" spectrum (suppressed high-energy tail). This parameterization is referred to as a "pinched-thermal" form. The different ν_e, $\overline{\nu}_e$ and ν_x, $x = \mu, \tau$ flavors are expected to have different average energy and α parameters and to evolve differently in time.

The initial spectra get further processed (permuted) by flavor oscillations and understanding these oscillations is very important for extracting physics from the detected signal.

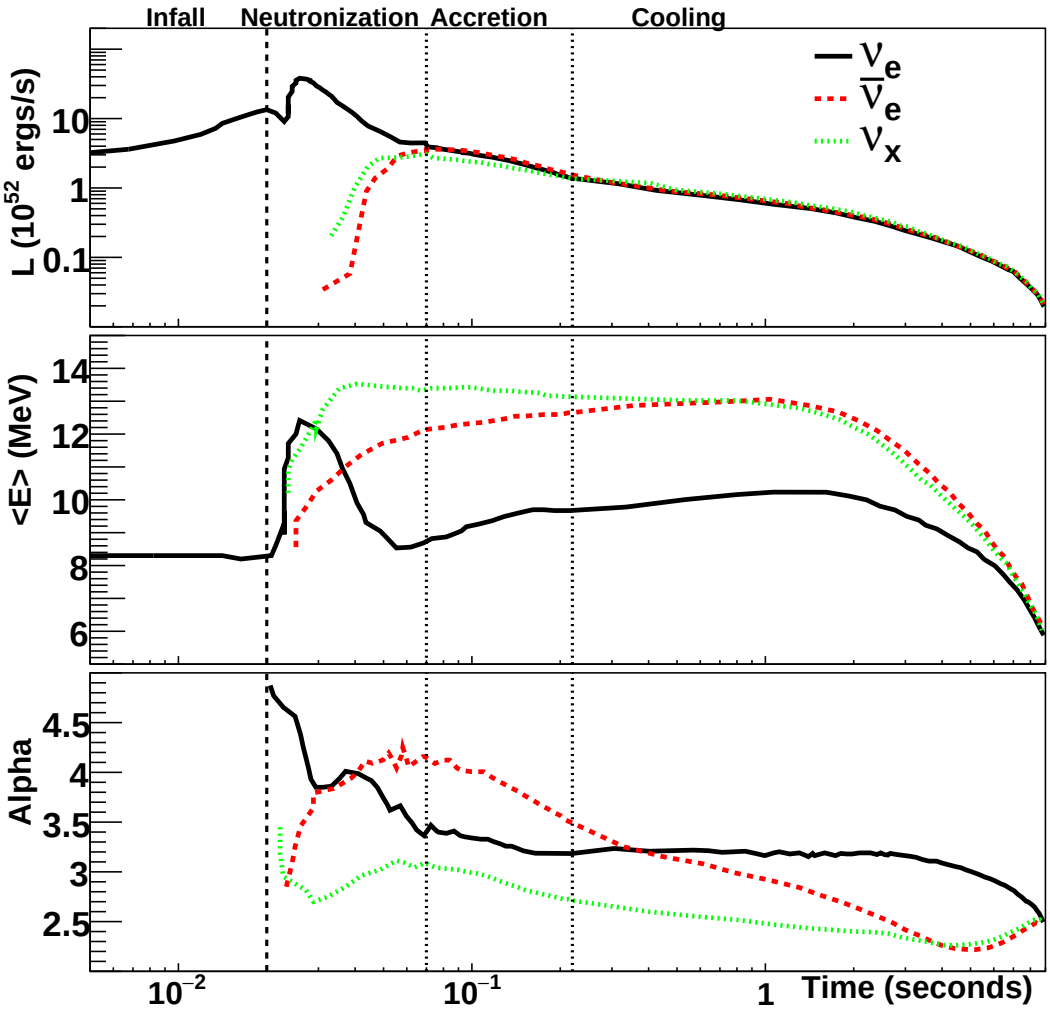

Figure 7.1: Expected time-dependent signal for a specific flux model for an electron-capture supernova [249] at 10 kpc. No oscillations are assumed. The top plot shows the luminosity as a function of time, the second plot shows average neutrino energy, and the third plot shows the α (pinching) parameter. The vertical dashed line at 0.02 seconds indicates the time of core bounce, and the vertical lines indicate different eras in the supernova evolution. The leftmost time interval indicates the infall period. The next interval, from core bounce to 50 ms, is the neutronization burst era, in which the flux is composed primarily of ν_e. The next period, from 50 to 200 ms, is the accretion period. The final era, from 0.2 to 9 seconds, is the proto-neutron-star cooling period. The general features are qualitatively similar for most core-collapse supernovae.

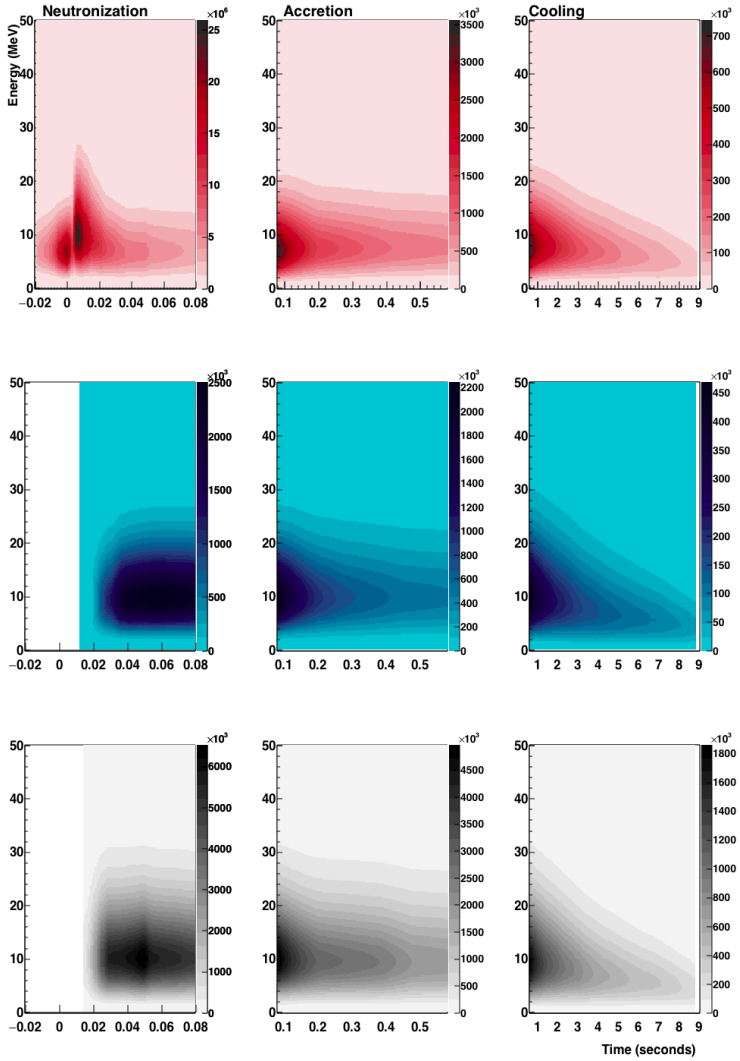

Figure 7.2: Example of time-dependent spectra for the electron-capture supernova model [249] parameterized in Figure 7.1, on three different timescales. The z-axis units are neutrinos per cm^2 per millisecond per 0.2 MeV. Top: ν_e. Center: $\bar{\nu}_e$. Bottom: ν_x. Oscillations are not included here; note they can have dramatic effects on the spectra.

7.2 Low-Energy Events in DUNE

7.2.1 Detection Channels and Interaction Rates

Liquid argon should have a particular sensitivity to the ν_e component of a supernova neutrino burst, via the dominant interaction, charged-current absorption of ν_e on ^{40}Ar,

$$\nu_e + ^{40}\mathrm{Ar} \rightarrow e^- + ^{40}\mathrm{K}^*, \tag{7.2}$$

for which the observable is the e^- plus deexcitation products from the excited K^* final state. Additional channels include a $\bar{\nu}_e$ CC interaction and elastic scattering on electrons. Cross sections for the most relevant interactions are shown in Figure 7.3. It is worth noting that none of the neutrino-^{40}Ar cross sections in this energy range have been experimentally measured; theoretical calculations may have large uncertainties.

Another process of interest for supernova detection in liquid argon (LAr) detectors, not yet fully studied, is neutral-current scattering on Ar nuclei by any type of neutrino: $\nu_x + \mathrm{Ar} \rightarrow \nu_x + \mathrm{Ar}^*$, for which the signature is given by the cascade of deexcitation γs from the final state Ar nucleus. A dominant 9.8-MeV Ar* decay line has been recently identified as a spin-flip M1 transition [252]. At this energy the probability of e^+e^- pair production is relatively high, offering a potentially interesting neutral-current tag. Other transitions are under investigation.

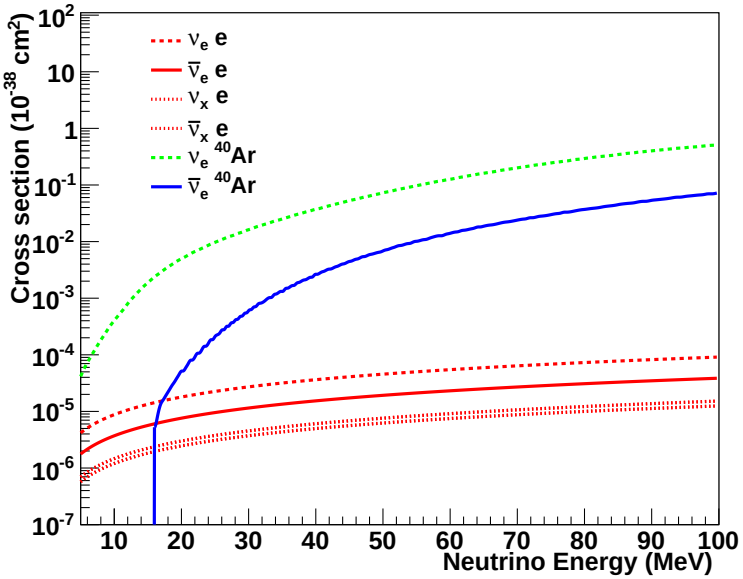

Figure 7.3: Cross sections for supernova-relevant interactions in argon [68, 253].

The predicted event rate from a supernova burst may be calculated by folding expected neutrino differential energy spectra with cross sections for the relevant channels, and with detector response; we do this using SNOwGLoBES [68] (see Sec. 7.2.2.3.)

7.2.2 Event Simulation and Reconstruction

Supernova neutrino events, due to their low energies, will manifest themselves primarily as spatially small events, perhaps up to a few tens of cm scale, with stub-like tracks from electrons (or positrons from the rarer $\bar{\nu}_e$ interactions). Events from ν_e charged-current interactions, $\nu_e + {}^{40}\mathrm{Ar} \rightarrow e^- + {}^{40}\mathrm{K}^*$, are likely to be accompanied by de-excitation products– gamma rays and/or ejected nucleons. Gamma-rays are in principle observable via energy deposition from Compton scattering, which will show up as small charge blips in the time projection chamber (TPC). Ejected nucleons may result in loss of observed energy for the event. Elastic scattering on electrons will result in single scattered electrons, and single gamma rays may result from neutral current (NC) excitations of the argon nucleus. Each event category has, in principle, a distinctive signature.

The canonical reconstruction task is to identify the interaction channel, the neutrino flavor for charged current (CC) events, and to determine the 4-momentum of the incoming neutrino; this overall task is the same for low-energy events as for high-energy ones. The challenge is to reconstruct the properties of the lepton (if present), and to the extent possible, to tag the interaction channel by the pattern of final-state particles.

While some physics studies in the SNB/LE group use a fast event-rate calculation tool called SNOwGLoBES, most activity is towards development of realistic and comprehensive simulation and reconstruction tools, from neutrino interaction event generators through full event reconstruction, in both single and dual-phase detectors, with Liquid Argon Software (LArSoft).

7.2.2.1 MARLEY

Model of Argon Reaction Low Energy Yields (MARLEY) [254] simulates tens-of-MeV neutrino-nucleus interactions in liquid argon. Currently, MARLEY can only simulate charged-current ν_e scattering on ^{40}Ar, but other reaction channels will be added in the future.

MARLEY weights the incident neutrino spectrum, selects an initial excited state of the residual $^{40}\mathrm{K}^*$ nucleus, and samples an outgoing electron direction using the allowed approximation for the ν_e CC differential cross section.[3] MARLEY computes this cross section using a table of Fermi and Gamow-Teller nuclear matrix elements. Their values are taken from experimental measurements at low excitation energies and a quasiparticle random phase approximation (QRPA) calculation at high excitation energies. As the code develops, a more sophisticated treatment of this cross section will be included.

[3] That is, the zero momentum transfer and zero nucleon velocity limit of the tree-level ν_e CC differential cross section, which may be written as

$$\frac{d\sigma}{d\cos\theta} = \frac{G_F^2 |V_{ud}|^2}{2\pi} |\mathbf{p}_e| \, E_e \, F(Z_f, \beta_e) \left[(1 + \beta_e \cos\theta) B(F) + \left(\frac{3 - \beta_e \cos\theta}{3} \right) B(GT) \right].$$

In this expression, θ is the angle between the incident neutrino and the outgoing electron, G_F is the Fermi constant, V_{ud} is the quark mixing matrix element, $F(Z_f, \beta_e)$ is the Fermi function, and $|\mathbf{p}_e|$, E_e, and β_e are the outgoing electron's three momentum, total energy, and velocity, respectively. $B(F)$ and $B(GT)$ are the Fermi and Gamow-Teller matrix elements.

After simulating the initial two-body $^{40}\mathrm{Ar}(\nu_e, e^-)^{40}\mathrm{K}^*$ reaction for an event, MARLEY also handles the subsequent nuclear de-excitation. For bound nuclear states, the de-excitation γ-rays are sampled using tables of experimental branching ratios. These tables are supplemented with theoretical estimates when experimental data are unavailable. For particle-unbound nuclear states, MARLEY simulates the competition between γ-ray and nuclear fragment[4] emission using the Hauser-Feshbach statistical model. Figure 7.4 shows an example visualization of a simulated MARLEY event.

Although many refinements remain to be made, MARLEY's treatment of high-lying Gamow-Teller strength and nuclear de-excitations represents a significant improvement over existing tools for simulating supernova ν_e CC events. MARLEY has been now been fully incorporated into the LArSoft code base.

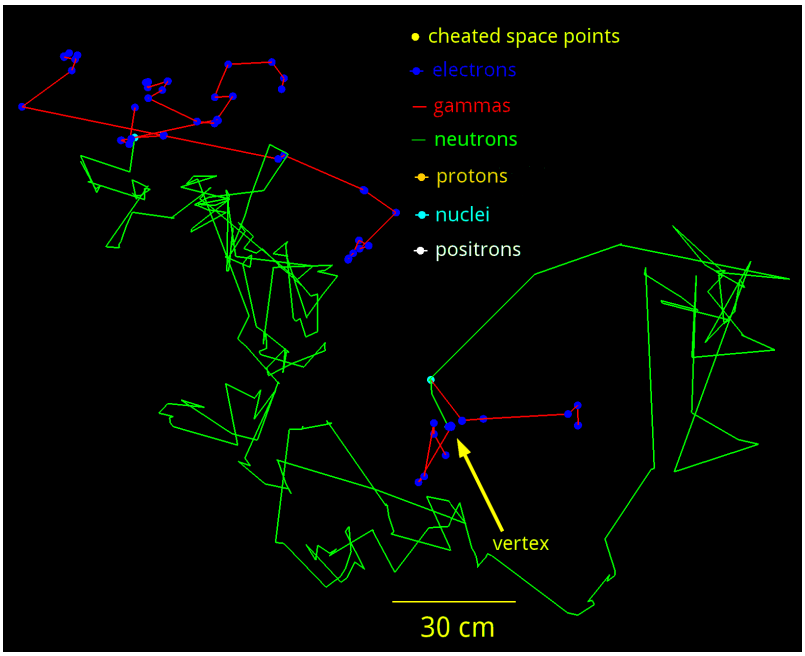

Figure 7.4: Visualization of an example MARLEY-simulated ν_eCC event, showing the trajectories and energy deposition points of the interaction products.

7.2.2.2 Low-energy Event Reconstruction Performance

The standard DUNE reconstruction tools in LArSoft provide energy and track reconstruction for low energy events. Photons may also be used for calorimetry. Figure 7.5 shows summarized resolution and efficiency for MARLEY events.

[4] Nucleons and light nuclei up to ^{4}He are considered.

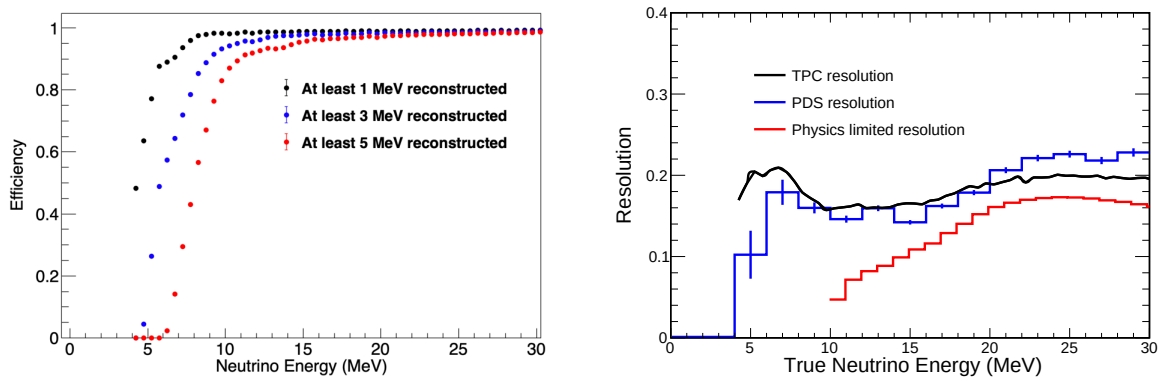

Figure 7.5: Left: reconstruction efficiency as a function of neutrino energy for MARLEY events, for different minimum required reconstructed energy. Right: fractional energy resolution as a function of neutrino energy for TPC tracks (black) and photon detector calorimetry (blue). The red "physics-limited resolution" assumes all energy deposited by final-state particles is reconstructed; the finite resolution represents loss of energy from escaping particles.

7.2.2.3 SNOwGLoBES

Most supernova neutrino studies done for DUNE so far, including of the plots included in the conceptual design report (CDR) [199], have employed SNOwGLoBES[68], a fast event-rate computation tool. This uses General Long-Baseline Experiment Simulator (GLoBES) front-end software [197] to convolve fluxes with cross-sections and detector parameters. The output is in the form of interaction rates for each channel as a function of neutrino energy, and "smeared" rates as a function of detected energy for each channel (i.e., the spectrum that actually would be observed in a detector). The smearing (transfer) matrices incorporate both interaction product spectra for a given neutrino energy, and detector response. Figure 7.6 shows such a transfer matrix created using MARLEY, by determining the distribution of observed charge, and a full simulation of the detector response (including the generation, transport, and detection of ionization signals and the electronics) as a function of neutrino energy in 0.5-MeV neutrino energy steps. Time dependence in SNOwGLoBES can be straightforwardly handled by providing multiple files with fluxes divided into different time bins. [5]

While SNOwGLoBES is, and will continue to be, a fast, useful tool, it has limitations with respect to a full simulation. One loses correlated event-by-event angular and energy information, for example; some studies, such as the directionality study in Section 7.3.1 require such complete event-by-event information. Nevertheless, transfer matrices generated with the best available simulations can be used to compute observed event rates and energy distributions and draw useful conclusions.

[5] Note that SNOwGLoBES is *not* a Monte Carlo code— it calculates mean event rates using a transfer matrix to convert neutrino spectra to observed spectra. This will produce equivalent results to reweighting Monte Carlo.

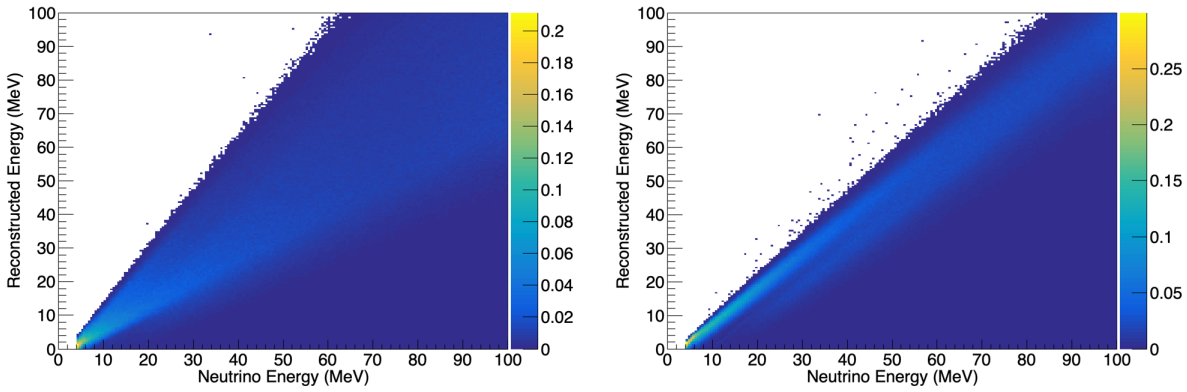

Figure 7.6: Smearing matrix for SNOwGLoBES created with monochromatic MARLEY samples run though LArSoft, describing detected charge distribution as a function of neutrino energy. The effects of interaction product distributions and detector smearing are both incorporated in this matrix. The right hand plot incorporates an assumed correction for charge attenuation due to electron drift, based on Monte Carlo truth position of the interaction. The drift correction improves resolution.

7.2.2.4 Backgrounds

Understanding of cosmogenic and radiological backgrounds is also important for understanding of how well we can reconstruct low energy events, and for setting detector requirements. Small single-hit blips from ^{39}Ar or other impurities may fake de-excitation gammas. While preliminary studies show that backgrounds will have a minor effect on reconstruction of triggered supernova burst events, their effects on a data acquisition (DAQ) and triggering system that satisfies supernova burst triggering requirements requires separate consideration. These issues are addressed in the DAQ and backgrounds sections of this TDR.

7.3 Expected Supernova Burst Signal Properties

Table 7.1 shows rates calculated for the dominant interactions in argon for the "Livermore" model [255] (out of date, but included for comparison with literature), and the "GKVM" model [256]; for the former, no oscillations are assumed in the supernova or Earth; the latter assumes collective effects in the supernova. In general, there is a rather wide variation— up to an order of magnitude — in event rate for different models, due to different numerical treatment (e.g., neutrino transport, dimensionality), physics input (nuclear equation of state, nuclear correlation and impact on neutrino opacities, neutrino-nucleus interactions) and oscillation effects. In addition, there is intrinsic variation in the nature of the progenitor and collapse mechanism. Neutrino emission from the supernova may furthermore have an emitted lepton-flavor asymmetry [257], so that observed rates may be dependent on the supernova direction.

Clearly, the ν_e flavor dominates. Although water and scintillator detectors will record ν_e events [258, 259], liquid argon is the only future prospect for a large, clean supernova ν_e sample [44].

Table 7.1: Event counts for different supernova models in 40 kt of liquid argon for a core collapse at 10 kpc, for ν_e and $\bar{\nu}_e$ charged-current channels and elastic scattering (ES) on electrons. Event rates will simply scale by active detector mass and inverse square of supernova distance. No oscillations are assumed; we note that oscillations (both standard and "collective") will potentially have a large, model-dependent effect, discussed in Sec. 7.5.1.

Channel	Events "Livermore" model	Events "GKVM" model
$\nu_e + {}^{40}\mathrm{Ar} \rightarrow e^- + {}^{40}\mathrm{K}^*$	2720	3350
$\overline{\nu}_e + {}^{40}\mathrm{Ar} \rightarrow e^+ + {}^{40}\mathrm{Cl}^*$	230	160
$\nu_x + e^- \rightarrow \nu_x + e^-$	350	260
Total	3300	3770

The number of signal events scales with mass and inverse square of distance as shown in Figure 7.7. For a collapse in the Andromeda galaxy, 780 kpc away, a 40-kton detector would observe a few events.

7.3.1 Directionality: pointing to the supernova

It will be valuable to use DUNE's tracking ability to reconstruct the direction of the incoming neutrinos to the extent possible. Reconstruction of direction to a supernova (or other astrophysical event) will be of obvious use to astronomers for prompt detection of the early turn-on of the light. Furthermore, some core collapse events may not yield bright electromagnetic fireworks, in which case directional information may help in location of a dim supernova or even a "disappeared" progenitor [260]. Directional information can be used for correlation with gravitational wave observations, which also have some directionality. Pointing resolution for low-energy events will also be helpful for selecting signal from background for solar neutrinos or other sources with known angular distribution. The directional information could also potentially be used in a high-level trigger.

The pointing resolution incorporates the intrinsic angular spread of the interaction products of the neutrino interaction, as well as resolution for detector reconstruction. A large fraction of the events expected from the supernova will not point well; in particular, the expected angular distribution of the ν_e CC absorption events which will make up the bulk of the signal events are expected to have relatively weak, but usable, anisotropy, with intrinsic physics-related (not detector-related) head-tail ambiguity. Fermi transitions to the final state are described by a $\propto (1 + \cos\theta)$ angular distribution and Gamow-Teller transitions are described by a $\propto (1 - \frac{1}{3}\cos\theta)$ angular distribution; these are modeled in MARLEY. In contrast, the elastic scattering component of the signal should point more sharply. Directionality depends also on event energy. See Figure 7.9.

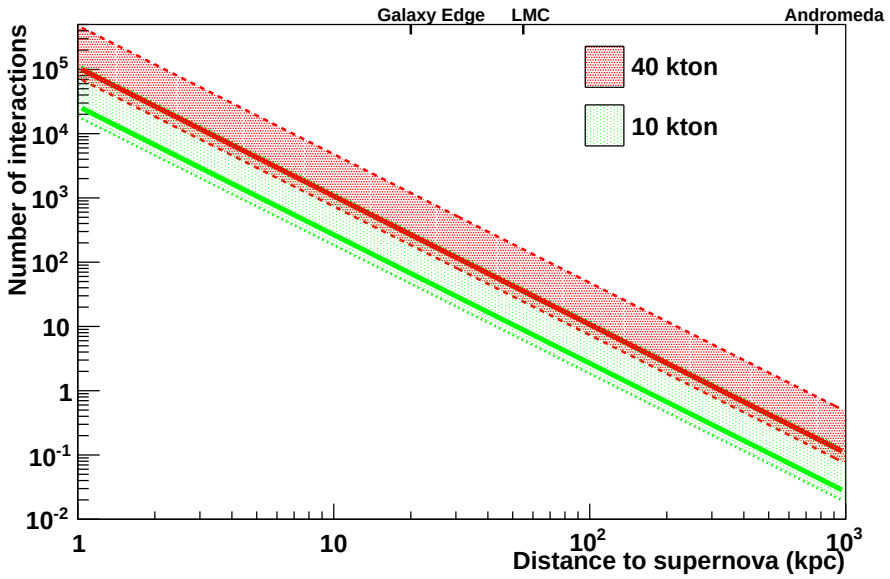

Figure 7.7: Estimated numbers of supernova neutrino interactions in DUNE as a function of distance to the supernova, for different detector masses (ν_e events dominate). The red dashed lines represent expected events for a 40-kton detector and the green dotted lines represent expected events for a 10-kton detector. The lines limit a fairly wide range of possibilities for "Garching-parameterized" supernova flux spectra (Equation 7.1) with luminosity 0.5×10^{52} ergs over ten seconds. The optimistic upper line of a pair gives the number of events for average ν_e energy of $\langle E_{\nu_e} \rangle = 12$ MeV, and "pinching" parameter $\alpha = 2$; the pessimistic lower line of a pair gives the number of events for $\langle E_{\nu_e} \rangle = 8$ MeV and $\alpha = 6$. (Note that the luminosity, average energy and pinching parameters will vary over the time frame of the burst, and these estimates assume a constant spectrum in time. Oscillations will also affect the spectra and event rates.) The solid lines represent the integrated number of events for the specific time-dependent neutrino flux model in [249] (see Figures 7.1 and 7.2; this model has relatively cool spectra and low event rates). Core collapses are expected to occur a few times per century, at a most-likely distance of around 10 to 15 kpc.

We describe here a study of the ability of DUNE to point to a supernova using the TPC tracks. This study makes use of full simulation and reconstruction tools. We have studied single electrons, neutrino-electron elastic scattering events, and the full expected supernova signal, looking at both elastic scattering events and ν_eCC events. Future studies will incorporate additional interaction channels, as well as backgrounds.

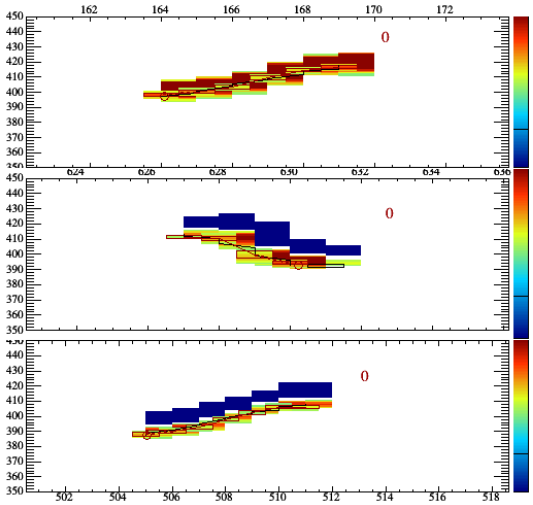

Figure 7.8: Example event display for a single simulated 10.25 MeV electron, with track reconstruction, in time vs wire, with color representing charge. The top panel shows the collection plane and the bottom panels show induction planes. The boxes represent reconstructed hits.

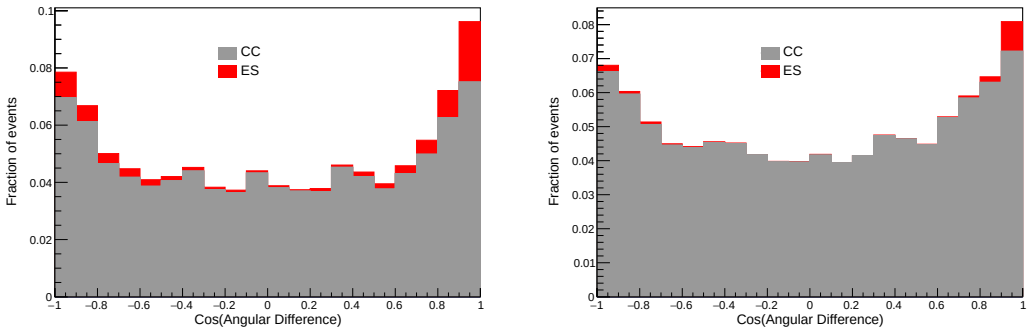

Figure 7.9: Example distribution of reconstructed directions of ES and CC supernova neutrino events in a 12-14 MeV reconstructed energy bin (left) and a 24-26 MeV reconstructed energy bin (right).

The pointing resolution of the reconstructed electron direction with respect to the true neutrino direction, defined as the angle at which 68% of angular differences are closer to truth, is plotted in Figure 7.10 on the right. The absolute values of cosines of the angular differences are used, which does not capture the head-tail directional ambiguity of the electron track. This pointing resolution is a result of both the neutrino-electron angle spread, electron scattering and the error in reconstruction. The left plot shows the pointing resolution for electrons only, and the effect of a head-tail disambiguation using bremsstrahlung directionality ("daughter flipping"). Work is continuing to improve the directional disambiguation algorithm, including use of increased multiple scattering towards the end of a track.

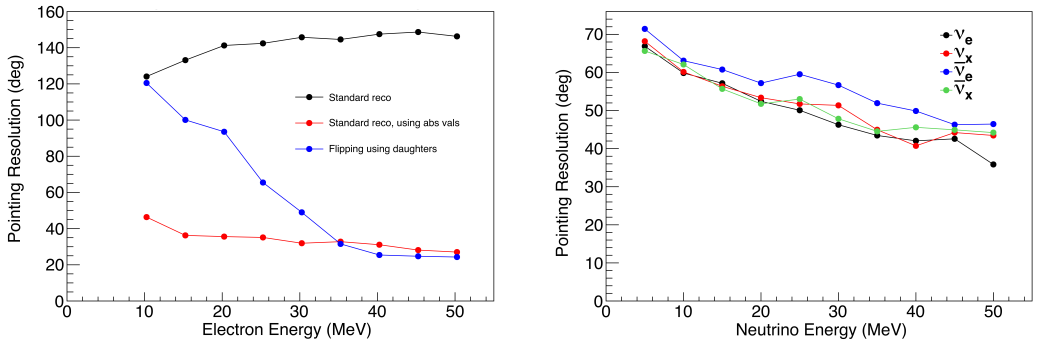

Figure 7.10: Left: Pointing resolution for electron tracks, showing effect of direction ambiguity, which can be partially resolved using bremsstrahlung directionality. The black line shows the angle at which 68% of angular differences are closer to truth, given the entire distribution including events misreconstructed $\sim$180° away from the true direction. The red line shows the same when the absolute value of the cosine of the angle with respect to the true direction is used, effectively disambiguating head-tail using truth. The blue line uses a "daughter flipping" algorithm which preferentially selects the track's forward direction using the relative positions with respect to the track of Compton-scatter blips from bremsstrahlung gamma daughters. Right: Pointing resolution of elastic scattering events versus neutrino energy for each neutrino flavor.

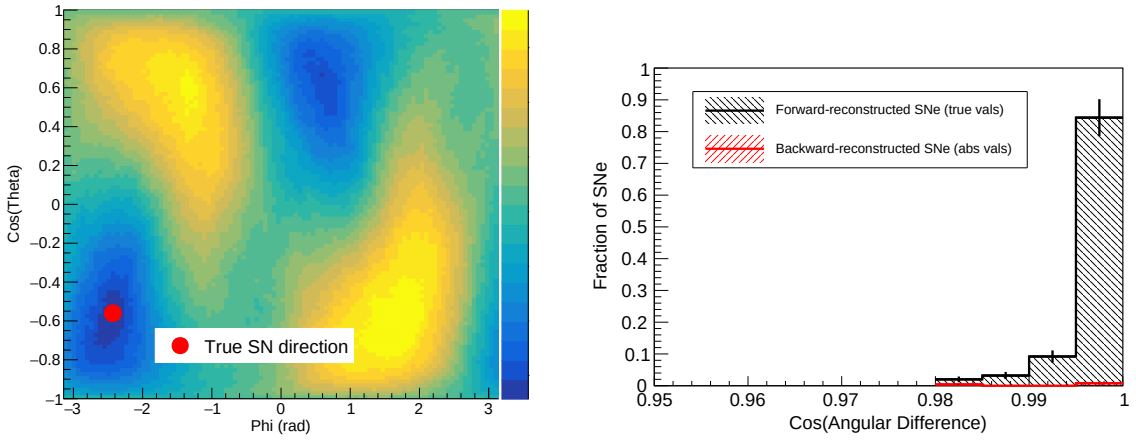

Figure 7.11: Left: Negative log likelihood values as a function of direction for a 10-kpc supernova sample. The sample used to compute the likelihood includes also the dominant ν_eCC interactions. Right: Distribution of angular differences for directions to a 10-kpc supernovae using a maximum likelihood method. The supernovae incorrectly reconstructed in the backwards direction, shown in red, have the distribution of absolute value of $\cos\theta$ plotted for display purposes.

If the direction can be disambiguated for >50% of the individual elastic scatters, the overall direction to the supernova can be disambiguated with sufficient statistics. Since the angular distribution depends on event energy, we can also make use of measured electron energy to improve the pointing from an ensemble of events. We employ a maximum likelihood algorithm to estimate the overall pointing resolution to a supernova, given a mean of 260 neutrino-electron elastic scatters and 3350 ν_eCC at ∼10 kpc . Using 16 energy bins in the likelihood, the results are shown in Figure 7.11. Overall resolution is about 4.5 degrees.

The result shown in the figure includes both ES and ν_eCC interactions in the likelihood, without radiological backgrounds or noise. The addition of ν_eCC events improves the pointing resolution, even without ES vs ν_eCC channel tagging. We will likely be able to improve the pointing further by making use of channel-tagging algorithms.

7.4 Astrophysics of Core Collapse

A number of astrophysical phenomena associated with supernovae are expected to be observable in the supernova neutrino signal, providing a remarkable window into the event. In particular, the supernova explosion mechanism, which in the current paradigm involves energy deposition via neutrinos, is still not well understood, and the neutrinos themselves will bring the insight needed to confirm or refute the paradigm.

There are many other examples of astrophysical observables.

- The initial burst, primarily composed of ν_e and called the "neutronization" or "breakout" burst, represents only a small component of the total signal. However, oscillation effects can manifest themselves in an observable manner in this burst, and flavor transformations can be modified by the "halo" of neutrinos generated in the supernova envelope by scattering [261].
- The formation of a black hole would cause a sharp signal cutoff (e.g., [262, 263]).
- Shock wave effects (e.g., [264]) would cause a time-dependent change in flavor and spectral composition as the shock wave propagates.
- The standing accretion shock instability (SASI) [265, 266], a "sloshing" mode predicted by three-dimensional neutrino-hydrodynamics simulations of supernova cores, would give an oscillatory flavor-dependent modulation of the flux.
- Turbulence effects [267, 268] would also cause flavor-dependent spectral modification as a function of time.

Observation of a supernova neutrino burst in coincidence with gravitational waves (which would also be prompt, and could indeed provide a time reference for a a time-of-flight analysis) would be especially interesting [269, 270, 271, 272].

The supernova neutrino burst is prompt with respect to the electromagnetic signal and therefore can be exploited to provide an early warning to astronomers [273, 274]. Additionally, a liquid argon signal [275] is expected to provide some pointing information, primarily from elastic scattering

on electrons. We note that not every core collapse will produce an observable supernova, and observation of a neutrino burst in the absence of an electromagnetic event would be very interesting.

Even non-observation of a burst, or non-observation of a ν_e component of a burst in the presence of supernovae (or other astrophysical events) observed in electromagnetic or gravitational wave channels, would still provide valuable information about the nature of the sources. Further, a long-timescale, sensitive search yielding no bursts will also provide limits on the rate of core-collapse supernovae.

We note that the better one can understand the astrophysical nature of core-collapse supernovae, the easier it will be to extract information about particle physics. DUNE's capability to characterize the ν_e component of the signal is unique and critical.

7.4.1 Supernova Spectral Parameter Fits

We have investigated how well it will be possible to fit to the supernova spectral parameters, to determine, for example, the ϵ parameter related to the total binding energy release of the supernova. We use SNOwGLoBES to model signals described by the pinched-thermal form.

We have developed a forward fitting algorithm requiring a SNOwGLoBES binned energy spectrum for a supernova at a given distance and a "true" set of pinched-thermal parameters $(\alpha^0, \langle E_\nu \rangle^0, \varepsilon^0)$. As an example, we define the true parameter values as $(\alpha^0, \langle E_\nu \rangle^0, \varepsilon^0) = (2.5, 9.5, 5 \times 10^{52})$, with $\langle E_\nu \rangle^0$ in MeV and ε in ergs, assumed integrated over a ten-second burst. We focus on the electron neutrino flux. The algorithm uses this spectrum as a "test spectrum" to compare against a grid of energy spectra generated with many different combinations of $(\alpha, \langle E_\nu \rangle, \varepsilon)$. To quantify these comparisons, the algorithm employs χ^2 minimization technique to find the best-fit spectrum.

A test spectrum input into the forward fitting algorithm produces a set of χ^2 values for every element in a grid. While the smallest χ^2 value determines the best fit to the test spectrum, there exists other grid elements that reasonably fit the test spectrum according to their χ^2 values. The collection of these grid elements help determine the parameter measurement uncertainty, and we represent this using "sensitivity regions" in 2D spectral parameter space. We can use three sets of 2D parameter spaces: $(\langle E_\nu \rangle, \alpha)$, $(\langle E_\nu \rangle, \varepsilon)$, and (α, ε).

One "point" in 2D parameter space encompasses several grid elements, e.g., the $(\langle E_\nu \rangle, \alpha)$ space contains different ε values for a given values of $\langle E_\nu \rangle$ and α. To determine the χ^2 value, we profile over ε to select the grid element with the smallest χ^2. We determine the sensitivity regions by placing a cut of $\chi^2 = 4.61$ corresponding to a 90% coverage probability for three free parameters. Figure 7.12 shows an example of a resulting fit, with the approximate parameters for some specific models superimposed. Figure 7.13 shows the statistical effect of supernova distance.

We have used this method to study the effect of detector parameters, and required *knowledge* of detector parameters, on ability to extract the flux parameters. While the size of the sensitivity regions is highly dependent on statistics (and hence distance), we find biases in the best-fit physics parameters if assumed understanding of detector parameters such as energy resolution, energy

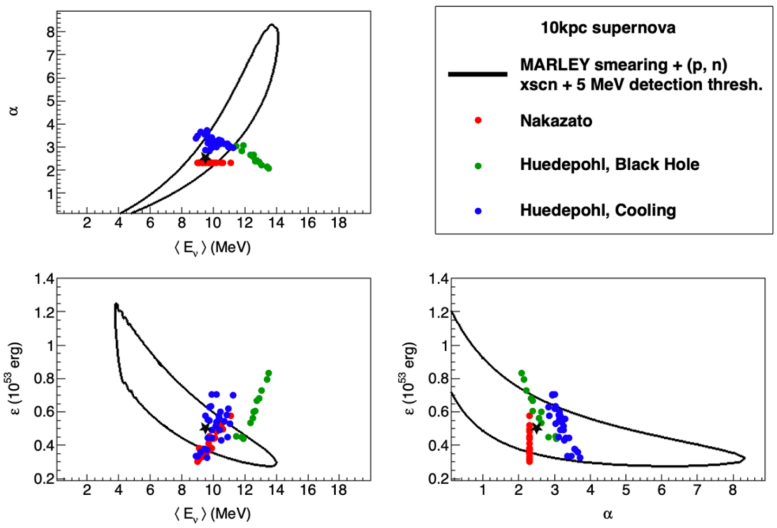

Figure 7.12: Sensitivity regions for the three pinched-thermal parameters (90% C.L.). SNOwGLoBES assumed a cross section model from MARLEY, realistic detector smearing and a step efficiency function with a 5 MeV detected energy threshold, for a supernova at 10 kpc. Superimposed are parameters corresponding to the time-integrated flux for three different sets of models: Nakazato [276], Huedepohl black hole formation models, and Huedepohl cooling models [277]. For the Nakazato parameters (for which there is no explicit pinching, corresponding to $\alpha = 2.3$), the parameters are taken directly from the reference; for the Huedepohl models, they are fit to a time-integrated flux.

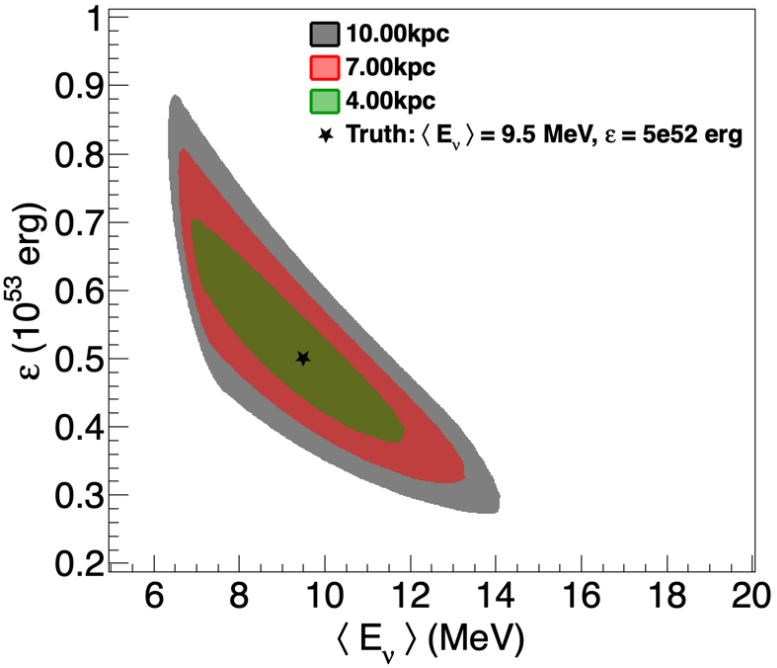

Figure 7.13: Sensitivity regions generated in $(\langle E_\nu \rangle, \varepsilon)$ space for three different supernova distances (90% C.L.). SNOwGLoBES used a smearing matrix with 15% Gaussian resolution, a cross section model from MARLEY, and a step efficiency function with a 5 MeV detected energy threshold.

threshold, and energy scale does not match the truth. We have also studied the effect of imperfect knowledge of the ν_e cross section on argon. The results of these studies are extensive and documented in [114].

7.5 Neutrino Physics and Other Particle Physics

A core-collapse supernova is essentially a gravity-powered neutrino bomb: the energy of the collapse is initially stored in the Fermi seas of electrons and neutrinos and then gradually leaked out by neutrino diffusion. The key property of neutrinos that makes them play such a dominant role in the supernova dynamics is the feebleness of their interactions. It then follows that should there be new light (< 100 MeV) particles with even weaker interactions, they could alter the energy transport process and the resulting evolution of the nascent proto-neutron star. Moreover, additional interactions or properties of neutrinos could also be manifested in this way.

Thus, a core-collapse supernova can therefore be thought of as an extremely hermetic system, which can be used to search for numerous types of new physics (e.g., [40, 278]). The list includes various Goldstone bosons (e.g., Majorons), neutrino magnetic moments, new gauge bosons ("dark photons"), "unparticles", and extra-dimensional gauge bosons. The existing data from SN1987A already provides significant constraints on these scenarios, by confirming the basic energy balance of the explosion. At the same time, more precision is highly desirable and should be provided with the next galactic supernova.

Such energy-loss-based analysis will make use of two types of information. First, the total energy of the emitted neutrinos should be compared with the expected release in the gravitational collapse. Note that measurements of all flavors, including ν_e, are needed for the best estimate of the energy release. Second, the rate of cooling of the protoneutron state should be measured and compared with what is expected from diffusion of the standard neutrinos.

Because DUNE is mostly sensitive to ν_e, complementary data from water Cherenkov detector and scintillator for the measurement of $\bar{\nu}_e$ and a careful analysis of the oscillation pattern (see below) will enable inference of the fluxes of μ and τ flavors. As for measuring the energy loss rate, it will require sufficient statistics at late times.

The flavor oscillation physics and its signatures are a major part of the physics program. Compared to the well-understood case of solar neutrinos, in a supernova, neutrino flavor transformations are much more involved. For supernovae, there are both neutrinos and antineutrinos, and two mass splittings—"solar" and "atmospheric" to worry about. While flavor transitions can be reasonably well understood during early periods of the neutrino emission as standard Mikheyev-Smirnov-Wolfenstein effect (MSW) transitions in the varying density profile of the overlying material, during later periods the physics of the transformations is significantly richer. For example, several seconds after the onset of the explosion, the flavor conversion probability is affected by the expanding shock front and the turbulent region behind it. The conversion process in such a stochastic profile is qualitatively different from the adiabatic MSW effect in the smooth, fixed density profile of the Sun.

Even more complexity is brought about by the coherent scattering of neutrinos off each other. This neutrino "self-refraction" results in highly nontrivial flavor transformations close to the neutrinosphere, typically within a few hundred kilometers from the center, where the density of streaming neutrinos is very high. Since the evolving flavor composition of the neutrino flux feeds back into the oscillation Hamiltonian, the problem is *nonlinear*. Furthermore, as the interactions couple neutrinos and antineutrinos of different flavors and energies, the oscillations are characterized by *collective* modes. This leads to very rich physics that has been the subject of intense interest over the last decade and a voluminous literature exists exploring these collective phenomena, e.g., [279, 280, 281, 282, 283, 284, 285, 286, 287, 288]. This is an active theoretical field and the effects are not yet fully understood. A supernova burst is the only opportunity to study neutrino-neutrino interactions experimentally.

One may wonder whether all this complexity will impede the extraction of useful information from the future signal. In fact, the opposite is true: the new effects can *imprint* information about the inner workings of the explosion on the signal. The oscillations can modulate the characteristics of the signal (both event rates and spectra as a function of time). Moreover, the oscillations can imprint *non-thermal* features on the energy spectra, potentially making it possible to disentangle the effects of flavor transformations and the physics of neutrino spectra formation. This in turn should help us learn about the development of the explosion during the crucial first 10 seconds. It is important to note that the features depend on the unknown mass ordering, and so can potentially tell us what the ordering is.

In the following, we examine quantitatively two examples of particle physics that can be accessed: neutrino mass ordering and Lorentz invariance violation.

7.5.1 Neutrino Mass Ordering

As described above, flavor transitions in the supernova can be fairly complex, and the rich phenomenology is at this time still under active investigation. The neutrino mass ordering affects the specific flavor composition in multiple ways during the different eras of neutrino emission. References [42, 289] survey in some detail the multiple signatures of mass ordering that will imprint themselves on the flux. Table 7.2 summarized several of them. For many of these, the ν_e component of the signal will be critical to measure. Some signatures of mass ordering are more robust than others, in the sense that the assumptions are less subject to theoretical uncertainties. One of the more robust of these is the early-time signal, including the *neutronization burst*. At early times, the matter potential is dominant over the neutrino-neutrino potential, which means that standard MSW effects are in play. In this case, for the normal ordering (NO), the neutronization burst, which is emitted as nearly pure ν_e, is strongly suppressed, whereas for the inverted ordering (IO), the neutronization burst is only partly suppressed. Figure 7.14 gives an example for a specific model, but which shows typical features. The same MSW-dominated transitions also affect the subsequent rise of the signal over a fraction of a second; here the time profile will depend on the turn-on of the non-ν_e flavors.

Of course, if the mass ordering is already known, we can turn it around and use the terrestrial determination to better disentangle the other particle physics and astrophysics knowledge from

Table 7.2: Table taken from [289] qualitatively summarizing different neutrino mass ordering signatures that will manifest themselves in the supernova neutrino time, energy and flavor structure of the burst.

Signature	Normal	Inverted	Robustness	Observability
Neutronization	Very suppressed	Suppressed	Excellent	Good, need ν_e
Early time profile	Low then high	Flatter	Good, possibly some self-interaction	Good
Shock wave	Time-dependent	Time-dependent	Fair, entangled with self-interaction effects	May be statistics limited
Collective effects	Various time- and energy-dependent signatures		Unknown, but multiple signatures	Want all flavors
Earth matter	Wiggles in $\bar{\nu}_e$	Wiggles in ν_e	Excellent	Difficult, need energy resolution, Earth shadowing
Type Ia	Lower flux	Higher flux	Moderate	Need large detectors, very close SN

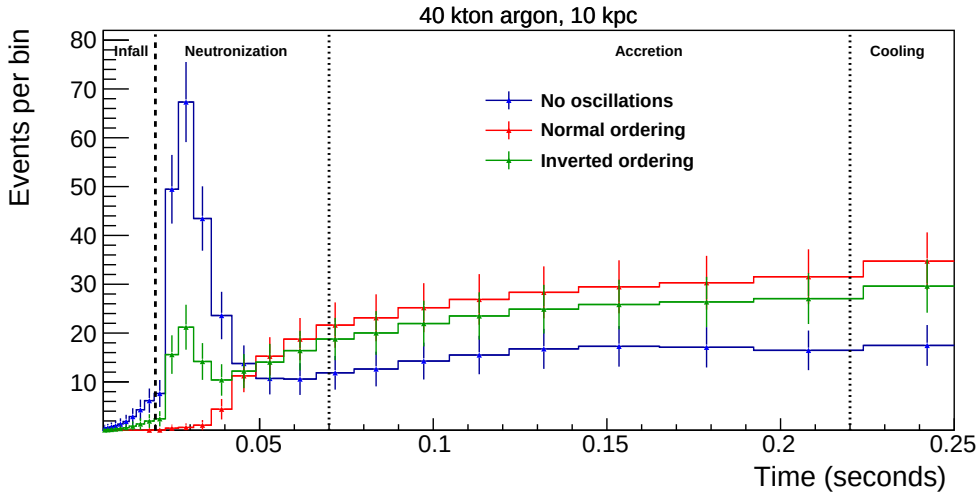

Figure 7.14: Expected event rates as a function of time for the electron-capture model in [249] for 40 kt of argon during early stages of the event – the neutronization burst and early accretion phases, for which self-induced effects are unlikely to be important. Shown is the event rate for the unrealistic case of no flavor transitions (blue), the event rate including the effect of matter transitions for the normal (red) and inverted (green) orderings. Error bars are statistical, in unequal time bins.

the observed signal.

Figure 7.15 shows the results of a simple quantitative study based in counting observed events in DUNE in the first 50 milliseconds of the burst. We expect this early neutronization-burst period to be dominated by adiabatic MSW transitions driven by the "H-resonance" for $\Delta m^2_{3\ell}$, for which the following neutrino-energy-independent relations apply:

$$F_{\nu_e} = F^0_{\nu_x} \quad \text{(NO)} \ , \tag{7.3}$$

$$F_{\nu_e} = \sin^2\theta_{12} F^0_{\nu_e} + \cos^2\theta_{12} F^0_{\nu_x} \quad \text{(IO)} \tag{7.4}$$

and

$$F_{\bar{\nu}_e} = \cos^2\theta_{12} F^0_{\bar{\nu}_e} + \sin^2\theta_{12} F^0_{\bar{\nu}_x} \quad \text{(NO)} \ , \tag{7.5}$$

$$F_{\bar{\nu}_e} = F^0_{\bar{\nu}_x} \quad \text{(IO)} \tag{7.6}$$

where F's are the fluxes corresponding to the respective flavors, and the ^{o} subscript represents flux before transition.

Figure 7.15 shows that for this model, the event count will be well separated under the two different assumptions, out to the edge of the Galaxy. The right hand plot shows also the effect of uncertainty on the distance to the supernova, in the scenario of evaluating the mass ordering based on absolute neutronization-burst counts. Note that while the neutronization burst is thought to be a "standard candle" [42], there will likely be some model dependence, and early-time-window event count by itself is not likely a sufficiently robust discriminant. There will, however, be additional information from other time eras of the burst signal. Further studies for a range of additional models and making use of the full burst time information are underway.

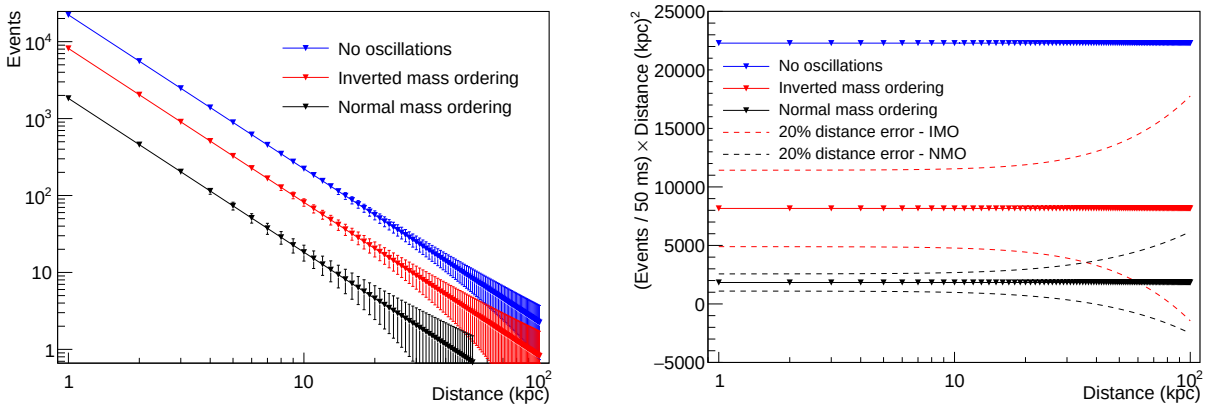

Figure 7.15: Event counts in the first 50 milliseconds for the model in [249], under assumptions of no oscillations, normal ordering and inverted ordering, assuming adiabatic MSW transitions. The left plot shows the event number as a function of distance with statistical errors. The right plot shows the event number scaled by square of distance, under the assumption of a 20% uncertainty on distance.

7.5.2 Lorentz Invariance Violation

As another example of a probe of new physics with supernova neutrinos or antineutrinos, a class of tests of Lorentz and charge, parity, and time reversal symmetry (CPT) violation involves comparing the propagation of neutrinos with other species of neutrinos of the same flavor but different energies [235, 238, 236, 240]. These amount to time-of-flight or dispersion studies. Time-of-flight and dispersion effects lack the interferometric resolving power available to neutrino oscillations, but they provide instead sensitivity to Lorentz- and CPT-violating effects that leave unaffected neutrino oscillations and so cannot be measured using atmospheric or long-baseline neutrinos. The corresponding standard-model extension (SME) coefficients controlling these effects are called oscillation-free coefficients [236].

Supernova neutrinos are of particular interest in this context because of the long baseline, which implies sensitivities many orders of magnitude better than available from time-of-flight measurements in beams. Observations of the supernova SN1987A yield constraints on the difference between the speed of light and the speed of antineutrinos, which translates into constraints on isotropic and anisotropic coefficients in both the minimal and nonminimal sectors of the SME. Knowledge of the spread of arrival times constrains the maximum speed difference between SN1987A antineutrinos of different energies in the approximate range 10–40 MeV, which restricts the possible antineutrino dispersion and yields further constraints on SME coefficients [236].

Analyses of this type would be possible with DUNE if supernova neutrinos are observed. Key features to maximize sensitivity would include absolute timing information to compare with photon spectral observations (and perhaps ultimately with gravitational-wave data [290]) along with relative timing information for different components of the neutrino energy spectrum. Significant improvements over existing limits are possible.

Figure 7.16 displays DUNE supernova sensitivities to these relevant oscillation-free coefficients for Lorentz and CPT violation. The estimated sensitivities are obtained using the general expression

(125) in [236] for the neutrino velocity in oscillation-free models and its application (132) to dispersion studies. The figure assumes a supernova comparable to SN1987A and at the same location on the sky. Enhancements of the displayed sensitivities from angular factors can occur for different sky locations. Studies of supernova neutrinos using DUNE can measure many coefficients (green) at levels improving over existing limits (gray).

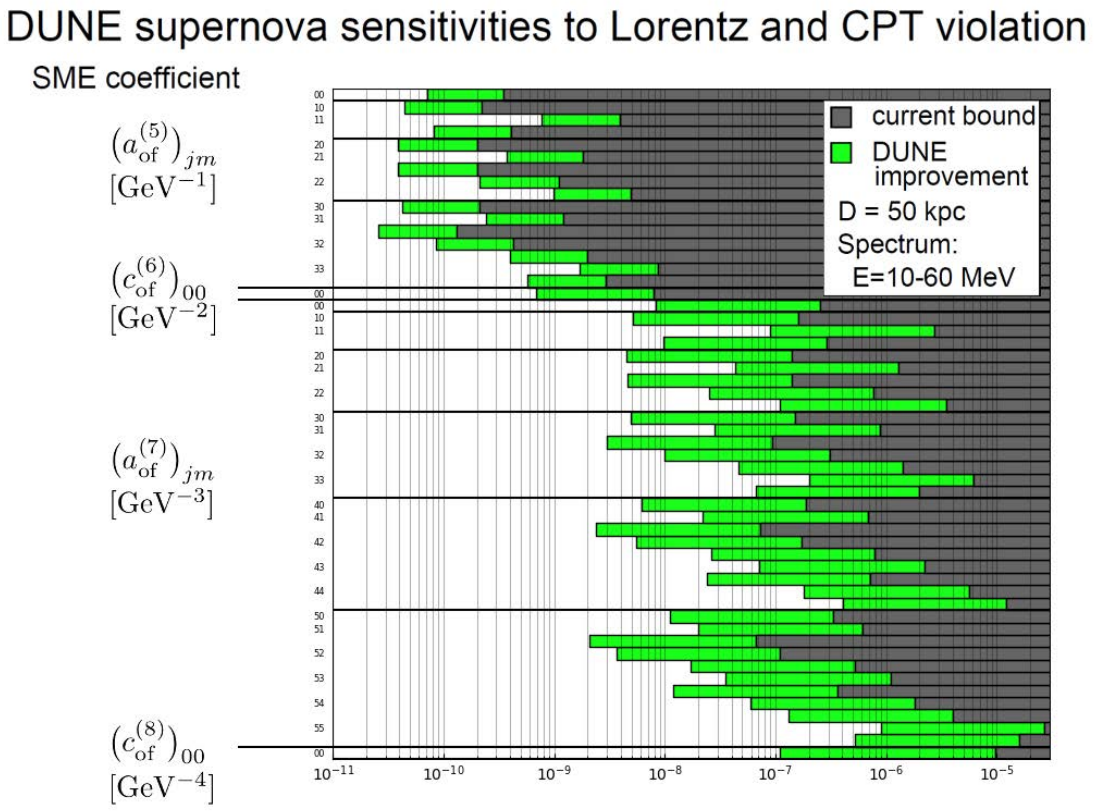

Figure 7.16: DUNE supernova sensitivities to oscillation-free coefficients for Lorentz and CPT violation. Studies of DUNE supernova neutrinos can measure many coefficients (green) at levels improving over existing limits (grey). These Lorentz- and CPT- violating effects leave oscillations unchanged and so are challenging to detect in atmospheric or long-baseline measurements [291].

Finally, via detection of time-of-flight delayed ν_e from the neutronization burst, DUNE will be able to probe neutrino mass bounds of $\mathcal{O}(1)$ eV for a 10-kpc supernova [292] (although likely not competitive near-future terrestrial kinematic limits). If eV-scale sterile neutrinos exist, they will likely have an impact on astrophysical and oscillation aspects of the signal (e.g., [293, 294, 295]), as well as time-of-flight observables.

7.6 Additional Astrophysical Neutrinos

7.6.1 Solar Neutrinos

Intriguing questions in solar neutrino physics remain, even after data from the Super-Kamiokande and Sudbury Neutrino Observatory (SNO) [296, 297] experiments explained the long-standing mystery of missing solar neutrinos [298] as due to flavor transformations. Some unknowns, such as the fraction of energy production via the carbon nitrogen oxygen (CNO) cycle in the Sun, flux variation due to helio-seismological modes that reach the solar core, or long-term stability of the solar core temperature, are astrophysical in nature. Others directly impact particle physics. Can the MSW model explain the amount of flavor transformation as a function of energy, or are non-standard neutrino interactions required? Do solar neutrinos and reactor antineutrinos oscillate with the same parameters? There is a modest tension between the Δm^2_{21} values indicated by current global solar neutrino measurements and the KamLAND reactor measurement [299], and further solar neutrino measurements could help to resolve this. Interesting observables are the day/night effect, and potentially the hep flux at higher energies.

Detection of solar and other low-energy neutrinos is challenging in a liquid argon time-projection chamber (LArTPC) because of relatively high intrinsic detection energy thresholds for the charged-current interaction on argon (>5 MeV). However, compared with other technologies, a LArTPC offers a large cross section and unique potential channel-tagging signatures from deexcitation photons. Furthermore, observed energy from the final state ν_eCC interaction follows neutrino energy more closely on an event-by-event basis (see Figure 7.6) with respect to the recoil spectrum from the ES channel that has been used for most solar neutrino observations so far. This feature of DUNE enables more precise spectral measurements. The solar neutrino event rate in a 40 kt LArTPC is ∼100 per day. Reference [299] explores the solar neutrino potential of DUNE, with somewhat optimistic energy resolution assumptions.

Detailed simulation studies making use of both TPC and photon information are underway, and preliminary event selection criteria for solar neutrinos are under development. Figure 7.17 shows an example of event selection efficiency as a function of neutrino energy. These preliminary cuts require three nearby TPC hits, an associated optical photon flash, and nearby TPC activity associated with deexcitation gammas. For these cuts, background in 10 kt is reduced to less than 0.1 Hz.

Backgrounds for triggering and reconstruction are the most serious issue. Cosmogenic backgrounds are likely tractable, but radiological backgrounds are more troublesome. In particular, neutron capture on argon is troublesome, and a relatively rare (and poorly known) alpha-capture channel on argon may contribute to the background in the solar neutrino energy regime. It is plausible that with sophisticated event selection, and possibly with additional shielding, a high-statistics solar neutrino sample may be selected.

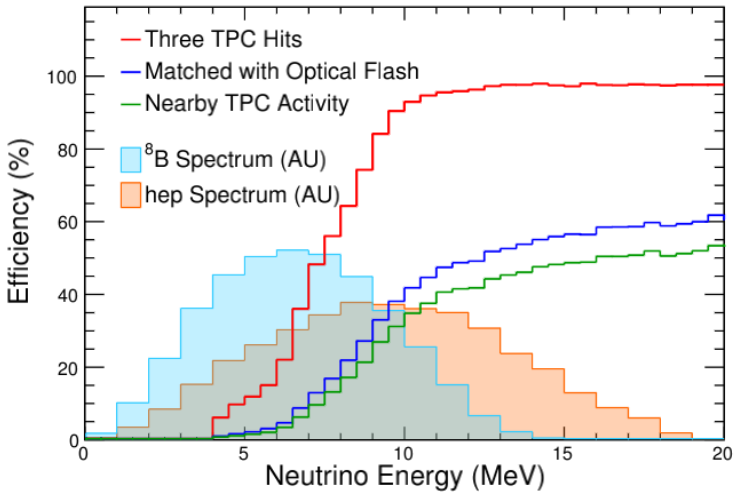

Figure 7.17: Efficiency for selection of neutrinos as a function of neutrino energy, for preliminary event selection cuts. Normalized spectra for solar neutrino signals are superimposed.

7.6.2 Diffuse Supernova Background Neutrinos

Galactic supernovae are relatively rare, occurring somewhere between once and four times a century. In the universe at large, however, thousands of neutrino-producing explosions occur every hour. The resulting neutrinos — in fact most of the neutrinos emitted by all the supernovae since the onset of stellar formation — suffuse the universe. Known as the diffuse supernova neutrino background (DSNB), their energies are in the few-to-30 MeV range. DSNB have not yet been observed, but an observation would greatly enhance our understanding of supernova-neutrino emission and the overall core-collapse rate [300, 301, 302].

A liquid argon detector such as DUNE's far detector is sensitive to the ν_e component of the diffuse relic supernova neutrino flux, whereas water Cherenkov and scintillator detectors are sensitive to the antineutrino component.

Background is a serious issue for DSNB detection. The solar *hep* neutrinos, which have an endpoint at 18.8 MeV, will determine the lower bound of the DSNB. The upper bound is determined by the atmospheric ν_e flux and is around 40 MeV. Although the LArTPC provides a unique sensitivity to the electron-neutrino component of the DSNB flux [303], event rates are very low. The expected number of relic supernova neutrinos, N_{DSNB}, that could be observed is 1-2 per MeV per 20 years in 10 kt [302] within the 19-31 MeV window. For this low signal rate, even rare radiological cosmogenic backgrounds will be challenging, and are under study.

7.6.3 Other Low-Energy Neutrino Sources

We note some other potential sources of signals in the tens-of-MeV range which may be observable in DUNE. A small flux is expected from Type I (thermonuclear) supernovae [304, 305], with

potential detectability by DUNE within a few kpc. Other signals include neutrinos from accretion disks [306] and black-hole/neutron star mergers [307]. These will create spectra not unlike those from core-collapse events, and with potentially large fluxes. However they are expected to be considerably rarer than core-collapse supernovae within an observable distance range. There may also be signatures of dark-matter weakly-interacting massive particle (WIMP) annihilations in the low-energy signal range [308, 309].

7.7 Burst Detection and Alert

For supernova burst physics, the detector must be able to detect and reconstruct as well as possible events in the range 5–100 MeV. As for proton decay and atmospheric neutrinos, no beam trigger will be available; therefore there must be special triggering and DAQ requirements that take into account the short, intense nature of the burst, and the need for prompt propagation of information in a worldwide context. The trigger requirement is for 90% trigger efficiency for a supernova burst at 100 kpc.

Events are expected within a time window of approximately 30 seconds, but possibly over an interval as long as a few hundred seconds; a large fraction of the events are expected within approximately the 1-2 seconds of the burst. The data acquisition buffers must be sufficiently large and the data acquisition system sufficiently robust to allow full capture of neutrino event information for a supernova as close as 0.1 kpc. At 10 kpc, one expects thousands of events within approximately 10 seconds, but a supernova at a distance of less than 1 kpc would result in $10^5 - 10^7$ events over 10 seconds.

The far detector must have high uptime to allow the capture of low-probability astrophysical events that could occur at any time with no external trigger. Supernova events are expected to occur a few times per century within the Milky Way galaxy. For any 10-year period, the probability of a supernova could be 20 to 30%. Capturing such an event at the same time as many of the other detectors around the Earth is very important.

The DUNE detector systems must be configured to provide information to other observatories on possible astrophysical events (such as a galactic supernova) in a short enough time to allow global coordination. This interval should be less than 30 minutes, and preferably on a few-minute timescale. To obtain maximum scientific value out of a singular astronomical event, it is very important to inform all other observatories (including optical ones) immediately via SNEWS [273, 274], so that they can begin observation of the evolution of the event. Pointing information should also be made available as promptly as possible.

Volume IV, The DUNE Far Detector Single-Phase Technology, Chapter 7 describes the DUNE triggering and DAQ configurations designed to meet these challenges for the SP module, and similarly for the DP module.

Chapter 8

Beyond the Standard Model Physics Program

8.1 Executive Summary

The unique combination of the high-intensity LBNF neutrino beam with DUNE's near detector (ND) and massive LArTPC far detector (FD) modules at a 1300 km baseline enables a variety of probes of beyond the standard model BSM physics, either novel or with unprecedented sensitivity. This section describes a selection of such topics, and briefly summarizes how DUNE can make leading contributions in this arena.

Search for active-sterile neutrino mixing: Experimental results in tension with the three-neutrino-flavor paradigm, which may be interpreted as mixing between the known active neutrinos and one or more sterile states, have led to a rich and diverse program of searches for oscillations into sterile neutrinos [310, 311]. DUNE is sensitive over a broad range of potential sterile neutrino mass splittings by looking for disappearance of charged current (CC) and neutral current (NC) interactions over the long distance separating the ND and FD, as well as over the short baseline of the ND . With a longer baseline, a more intense beam, and a high-resolution large-mass FD, compared to previous experiments, DUNE provides a unique opportunity to improve significantly on the sensitivities of the existing probes, and greatly enhance the ability to map the extended parameter space if a sterile neutrino is discovered.

Searches for non-unitarity of the Pontecorvo-Maki-Nakagawa-Sakata (PMNS) matrix: A generic characteristic of most models explaining the neutrino mass pattern is the presence of heavy neutrino states, additional to the three light states of the standard model (SM) of particle physics [312, 313, 314, 315]. This implies a deviation from unitarity of the 3×3 PMNS matrix that can become particularly sizable the lower the mass of the extra states are. For values of the unitarity deviations of order 10^{-2}, this would decrease the expected reach of DUNE to the standard parameters, although stronger bounds existing from charged leptons would be able to restore its expected performance.

Searches for nonstandard interaction (NSI): NSI affecting neutrino propagation through the Earth, can significantly modify the data to be collected by DUNE as long as the new physics parameters are large enough [316]. Leveraging its very long baseline and wide-band beam, DUNE is uniquely sensitive to these probes. If the DUNE data are consistent with standard oscillations for three massive neutrinos, interaction effects of order 0.1 G_F can be ruled out at DUNE. We note that DUNE will improve current constraints on $\epsilon_{\tau e}$ and $\epsilon_{\mu e}$, the magnitude of the NSI relative to standard weak interactions, by a factor of 2 to 5.

Searches for violation of Lorentz or charge, parity, and time reversal symmetry (CPT) Symmetry: CPT symmetry, the combination of charge conjugation, parity and time reversal, is a cornerstone of our model-building strategy and therefore the repercussions of its potential violation will severely threaten the SM of particle physics [317, 318, 235, 240, 236, 319]. DUNE can improve the present limits on Lorentz and CPT violation by several orders of magnitude, contributing as a very important experiment to test these fundamental assumptions underlying quantum field theory.

Searches for neutrino trident production: The intriguing possibility that neutrinos may be charged under new gauge symmetries beyond the SM $SU(3)_c \times SU(2)_L \times U(1)_Y$, and interact with the corresponding new gauge bosons can be tested with unprecedented precision by DUNE through ND measurements of neutrino-induced di-lepton production in the Coulomb field of a heavy nucleus, also known as neutrino trident interactions [320, 321, 322, 323, 324, 325, 326]. Although this process is extremely rare (SM rates are suppressed by a factor of $10^{-5} - 10^{-7}$ with respect to CC interactions), the CHARM-II collaboration and the CCFR collaboration both reported detection of several trident events (~ 40 events at CCFR) and quoted cross-sections in good agreement with the SM predictions. With a predicted annual rate of over 100 dimuon neutrino trident interactions at the ND, DUNE will be able to measure deviations from the SM rates and test the presence of new gauge symmetries [327, 328, 329].

Search for light-mass dark matter (LDM): Various cosmological and astrophysical observations strongly support the existence of dark matter (DM) representing $\approx$27% of the mass-energy of the universe, but its nature and potential non-gravitational interactions with regular matter remain undetermined [31]. The lack of evidence for weakly-interacting massive particles (WIMPs) at direct detection and the LHC experiments has resulted in a reconsideration of the WIMP paradigm. For instance, if DM has a mass that is much lighter than the electroweak scale (e.g., below GeV level), it motivates theories for DM candidates that interact with ordinary matter through a new "vector portal" mediator. High-flux neutrino beam experiments, such as DUNE, have been shown to provide coverage of DM+mediator parameter space that cannot be covered by either direct detection or collider experiments [330, 331, 332, 199]. DM particles can be detected in the ND through neutral-current-like interactions either with electrons or nucleons in the detector material. The neutrino-induced backgrounds can be suppressed using timing and the kinematics of the scattered electron. These enable DUNE's search for LDM to be competitive and complementary to other experiments.

Search for boosted dark matter (BDM): Using its large FD, DUNE will be able to search for BDM [78, 333]. A representative model is composed of heavy and light DM components and the lighter one can be produced from the annihilation of the heavier one in, e.g., the nearby sun or galactic centers. Due to the large mass difference between the two DM components, the lighter one is produced relativistically. The incoming energy of the lighter DM component can be high

enough above the expected energy thresholds of DUNE in a wide range of parameter space. A first attempt at observing the inelastic BDM signal with ProtoDUNE prior to running DUNE is proposed in Ref. [334]. Further, a significant BDM flux can arise from DM annihilation in the core of the sun [335, 79, 80, 336]. DM particles can be captured by the sun through their scattering with the nuclei in the sun, mostly hydrogen and helium. This makes the core of the sun a region with concentrated DM distribution. Through various processes, this DM can then be emitted as BDM and its flux probed on Earth by DUNE.

Section 8.9 details several other compelling BSM Physics scenarios DUNE will be sensitive to.

8.2 Common Tools: Simulation, Systematics, Detector Components

DUNE will be the future leading-edge neutrino experiment. The DUNE detector-beam configuration provides an excellent opportunity to study the physics beyond standard neutrino oscillations. It utilizes a megaWatt class proton accelerator (with beam power of up to 2.4 MW), a massive (40 kt) liquid argon time-projection chamber (LArTPC) FD, and a high-resolution near detector. The neutrino beam, ND and FD configurations used for the BSM searches are discussed in the following sections.

8.2.1 Neutrino Beam Simulation

The DUNE experiment will use an optimized neutrino beam designed to provide maximum sensitivity to leptonic charge parity (CP) violation. The optimized beam includes a three-horn system with a longer target embedded within the first horn and a decay pipe with 194 m length and 4 m diameter. In this design, a genetic algorithm is used to determine values for 20 beamline parameters describing the primary proton momentum and the target dimensions, along with the horn shapes, horn positions, and horn current values that maximize DUNE's sensitivity to charge-parity symmetry violation (CPV). The optimized neutrino beam is further described in [337]. We discuss the ND and FD flux used for the BSM searches below.

The neutrino flux for the ND is generated at a distance of 574 m downstream of the start of horn 1. Fluxes have been generated for both neutrino mode and antineutrino mode. The detailed beam configuration used for the ND analysis is given in Table 8.1.

Unless otherwise noted, the neutrino fluxes used in the BSM physics analysis are the same as those used in the long-baseline three-flavor analysis, introduced in Section 5.6. These fluxes were produced using G4LBNF, a Geant4-based simulation. The fluxes are weighted at the FD, located 1297 km downstream of the start of horn 1. The flux files contain NC and CC spectra, which are obtained by multiplying the flux by inclusive cross sections supplied by Generates Events for Neutrino Interaction Experiments (GENIE) version 2.8.4. Note that these histograms have variable bin widths, so discontinuities in the number of events per bin are expected.

The beam power configuration used for both ND and FD is given in Table 8.1.

Table 8.1: Beam power configuration assumed for the LBNF neutrino beam.

Energy (GeV)	Beam Power (MW)	Uptime Fraction	POT/year
120	1.2	0.56	1.1×10^{21}

8.2.2 Detector Properties

The ND configuration is not yet finalized, so we have adopted an overall structure for the liquid argon time-projection chamber (LArTPC) component of the detector and its fiducial volume. The ND will be located at a distance of 574 m from the target. The ND dimensions and properties used for the BSM searches are given below. The ND concept consists of a modular LArTPC and a magnetized high-pressure gas argon TPC. In the BSM physics analysis, the LArTPC is assumed to be 7 m wide, 3 m high, and 5 m long. The fiducial volume is assumed to include the detector volume up to 50 cm of each face of the detector. The ND properties are given in Table 8.2. The signal and background efficiencies for different physics models are different. Detailed signal and background efficiencies for each physics topic are discussed along with each analysis.

Table 8.2: ND properties used in the BSM physics analyses.

ND Properties	Values
Dimensions	7 m wide, 3 m high, and 5 m long
Dimensions of fiducial volume	6 m wide, 2 m high, and 4 m long
Total mass	147 ton
Fiducial mass	67.2 ton
Distance from target	574 m

The DUNE FD will consist of four 10 kt LArTPC modules located at Sanford Underground Research Facility (SURF), either single-phase (SP) or dual-phase (DP) with integrated photon detection systems (PD systems). The effective active mass of the detector used for the analysis is 40 kt. The FD dimensions and General Long-Baseline Experiment Simulator (GLoBES) configurations are given below. The geometry description markup language (GDML) files for the two FD workspace geometries described here, with and without the anode plane assembly (APA) sense wires, are the same used in the long-baseline three-flavor analysis, as described in Section 5.6. The single-particle detector responses used for the analyses are listed in Table 8.3.

Table 8.3: FD properties used in the BSM physics analyses.

Particle Type	Threshold	Energy Resolution	Angular Resolution
$\mu^{\pm}$	30 MeV	Contained track: track length	1^o
$e^{\pm}$	30 MeV	2%	1^o
$\pi^{\pm}$	100 MeV	30%	5^o

8.2.2.1 GLoBES Configuration for the FD analysis

The GLoBES configuration files reproduce the FD simulation used in the long-baseline three-flavor analysis, introduced in Section 5.6. The flux normalization factor is included using a GLoBES Abstract Experiment Definition Language (AEDL) file to ensure that all variables have the proper units; its value is $@norm = 1.017718 \times 10^{17}$. Cross-section files describing NC and CC interactions with argon, generated using GENIE 2.8.4, are included in the configuration. The true-to-reconstructed smearing matrices and the selection efficiency as a function of energy for various signal and background modes are included within GLoBES. The GLoBES configuration provided in the ancillary files corresponds to $300\,\mathrm{kt} \cdot \mathrm{MW} \cdot \mathrm{year}$ of exposure, with 3.5 years each of running in neutrino and antineutrino mode. A 40 kt fiducial mass is assumed for the FD, exposed to a 120 GeV, 1.2 MW beam.The ν_e and $\bar{\nu}_e$ signal modes have independent normalization uncertainties of 2% each, while ν_μ and $\bar{\nu}_\mu$ signal modes have independent normalization uncertainties of 5%. The background normalization uncertainties range from 5% to 20% and include correlations among various sources of background; the correlations among the background normalization parameters are given in the AEDL file of Ref. [200]. The FD response for the different particles used are the same as used in Section 5.6.

8.3 Sterile Neutrino Searches

Experimental results in tension with the three-neutrino-flavor paradigm [338, 339, 340, 341, 310, 311], which may be interpreted as mixing between the known active neutrinos and one or more *sterile* states, have led to a rich and diverse program of searches for oscillations into sterile neutrinos. Having a longer baseline, a more intense beam, and a high-resolution large-mass FD, compared to previous experiments, DUNE provides a unique opportunity to improve significantly on the sensitivities of existing probes, and to enhance the ability to map the extended parameter space if a sterile neutrino is discovered. Conversely, the presence of light sterile neutrino mixing would impact the interpretation of the DUNE physics results [342], so studying sterile neutrinos within DUNE is essential.

8.3.1 Probing Sterile Neutrino Mixing with DUNE

Long-baseline experiments like DUNE can look for sterile neutrino oscillations by measuring disappearance of the beam neutrino flux between the ND and FD. This results from the quadratic suppression of the sterile mixing angle measured in appearance experiments, $\theta_{\mu e}$, with respect to its disappearance counterparts, $\theta_{\mu\mu} \approx \theta_{24}$ for long-baseline (LBL) experiments, and $\theta_{ee} \approx \theta_{14}$ for reactor experiments. These disappearance effects have not yet been observed and are in tension with appearance results [310, 311] when global fits of all available data are carried out. The exposure of DUNE's high-resolution FD to the high-intensity LBNF beam will also allow direct probes of nonstandard electron (anti)neutrino appearance.

DUNE will look for active-to-sterile neutrino mixing using the reconstructed energy spectra of both NC and CC neutrino interactions in the FD, and their comparison to the extrapolated predictions from the ND measurement. Since NC cross sections and interaction topologies are the same for all three active neutrino flavors, the NC spectrum is insensitive to standard neutrino mixing. However, should there be oscillations into a fourth light neutrino, an energy-dependent depletion of the neutrino flux would be observed at the FD, as the sterile neutrino would not interact in the detector volume. Furthermore, if sterile neutrino mixing is driven by a large mass-square difference $\Delta m^2_{41} \sim 1\,\mathrm{eV}^2$, the CC spectrum will be distorted at energies higher than the energy corresponding to the standard oscillation maximum. Therefore, CC disappearance is also a powerful probe of sterile neutrino mixing at long baselines.

At long baselines, the NC disappearance probability to first order in small mixing angles is given by:

$$\begin{aligned} 1 - P(\nu_\mu \to \nu_s) \approx 1 &- \cos^4\theta_{14}\cos^2\theta_{34}\sin^2 2\theta_{24}\sin^2\Delta_{41} \\ &- \sin^2\theta_{34}\sin^2 2\theta_{23}\sin^2\Delta_{31} \\ &+ \frac{1}{2}\sin\delta_{24}\sin\theta_{24}\sin 2\theta_{23}\sin\Delta_{31}, \end{aligned} \tag{8.1}$$

where $\Delta_{ji} = \frac{\Delta m^2_{ji} L}{4E}$. The relevant oscillation probability for ν_μ CC disappearance is the ν_μ survival probability, similarly approximated by:

$$\begin{aligned} P(\nu_\mu \to \nu_\mu) \approx 1 &- \sin^2 2\theta_{23}\sin^2\Delta_{31} \\ &+ 2\sin^2 2\theta_{23}\sin^2\theta_{24}\sin^2\Delta_{31} \\ &- \sin^2 2\theta_{24}\sin^2\Delta_{41}. \end{aligned} \tag{8.2}$$

Finally, the disappearance of $\overset{(-)}{\nu}_e$ CC is described by:

$$\begin{aligned} P(\overset{(-)}{\nu}_e \to \overset{(-)}{\nu}_e) \approx 1 &- \sin^2 2\theta_{13}\sin^2\Delta_{31} \\ &- \sin^2 2\theta_{14}\sin^2\Delta_{41}. \end{aligned} \tag{8.3}$$

Figure 8.1 shows how the standard three-flavor oscillation probability is distorted at neutrino energies above the standard oscillation peak when oscillations into sterile neutrinos are included.

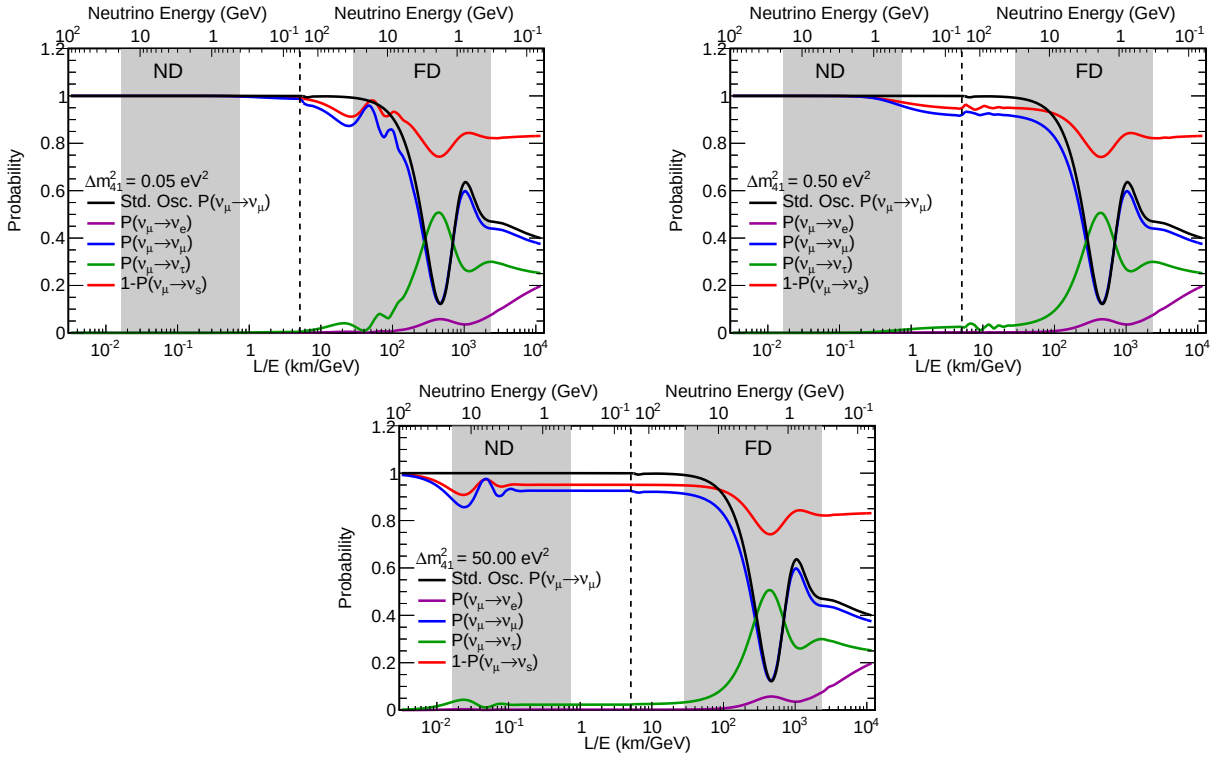

Figure 8.1: Regions of L/E probed by the DUNE detector compared to 3-flavor and 3+1-flavor neutrino disappearance and appearance probabilities. The gray-shaded areas show the range of true neutrino energies probed by the ND and FD. The top axis shows true neutrino energy, increasing from right to left. The top-left plot shows the probabilities assuming mixing with one sterile neutrino with $\Delta m^2_{41} = 0.05$ eV^2, corresponding to the slow oscillations regime. The top-right plot assumes mixing with one sterile neutrino with $\Delta m^2_{41} = 0.5$ eV^2, corresponding to the intermediate oscillations regime. The bottom plot includes mixing with one sterile neutrino with $\Delta m^2_{41} = 50$ eV^2, corresponding to the rapid oscillations regime. As an example, the slow sterile oscillations cause visible distortions in the three-flavor ν_μ survival probability (blue curve) for neutrino energies ~ 10 GeV, well above the three-flavor oscillation minimum.

8.3.2 Setup and Methods

The simulation of the DUNE experimental setup was performed with the GLoBES software [197, 198] using the same flux and equivalent detector definitions used by the three-neutrino flavor analysis presented in Section 5.6. Specifically, the neutrino flux used assumes 120 GeV protons incident on the LBNF target, with 1.1×10^{21} protons on target (POT) collected per year. A total exposure of 300 kton.MW.year is used in assessing DUNE's physics reach in probing the relevant sterile neutrino mixing parameter space.

The sterile neutrino effects have been implemented in GLoBES via the existing plug-in for sterile neutrinos and NSI [343]. As described above, the ND will play a very important role in the sensitivity to sterile neutrinos both directly, for rapid oscillations with $\Delta m^2_{41} > 1$ eV^2 where the sterile oscillation matches the ND baseline, and indirectly, at smaller values of Δm^2_{41} where the ND is crucial to reduce the systematics affecting the FD to increase its sensitivity. To include these ND

effects in these studies, the latest GLoBES DUNE technical design report (TDR) configuration files describing the detectors were modified by adding a ND with correlated systematic errors with the FD. As a first approximation, the ND is assumed to be an identical scaled-down version of the TDR FD where the same efficiencies, backgrounds and energy reconstruction as presented in Section 5.6 have been assumed, with detector properties the same as described in Section 8.2.2. The systematic uncertainties originally defined in the GLoBES DUNE conceptual design report (CDR) configuration already took into account the effect of the ND constraint. Thus, since we are now explicitly simulating the ND, larger uncertainties have been adopted but partially correlated between the different channels in the ND and FD, so that their impact is reduced by the combination of both data sets. The full list of systematic uncertainties considered and their values is summarized in a technical note [344].

Finally, for oscillations observed at the ND, the uncertainty on the production point of the neutrinos can play an important role. We have included an additional 20% energy smearing, which produces a similar effect given the L/E dependence of oscillations. We implemented this smearing in the ND through multiplication of the migration matrices provided with the GLoBES files by an additional matrix with the 20% energy smearing obtained by integrating the Gaussian

$$R^c(E, E') \equiv \frac{1}{\sigma(E)\sqrt{2\pi}} e^{-\frac{(E-E')^2}{2\sigma(E)}}, \tag{8.4}$$

with $\sigma(E) = 0.2E$ in reconstructed energy E'.

8.3.3 Results

By default, GLoBES treats all systematic uncertainties included in the fit as normalization shifts. However, depending on the value of Δm^2_{41}, sterile mixing will induce shape distortions in the measured energy spectrum beyond simple normalization shifts. As a consequence, shape uncertainties are very relevant for sterile neutrino searches, particularly in regions of parameter space where the ND, with virtually infinite statistics, has a dominant contribution. The correct inclusion of systematic uncertainties affecting the shape of the energy spectrum in the two-detector fit GLoBES framework used for this analysis posed technical and computational challenges beyond the scope of the study. Therefore, for each limit plot, we present two limits bracketing the expected DUNE sensitivity limit, namely: the black limit line, a best-case scenario, where only normalization shifts are considered in a ND+FD fit, where the ND statistics and shape have the strongest impact; and the grey limit line, corresponding to a worst-case scenario where only the FD is considered in the fit, together with a rate constraint from the ND.

Studying the sensitivity to θ_{14}, the dominant channels are those regarding ν_e disappearance. Therefore, only the ν_e CC sample is analyzed and the channels for NC and ν_μ CC disappearance are not taken into account, as they do not influence greatly the sensitivity and they slow down the simulations. The sensitivity at the 90% confidence level (CL), taking into account the systematics mentioned above, is shown in Figure 8.2, along with a comparison to current constraints.

For the θ_{24} mixing angle, we analyze the ν_μ CC disappearance and the NC samples, which are the main contributors to the sensitivity. The results are shown in Figure 8.2, along with comparisons

with present constraints.

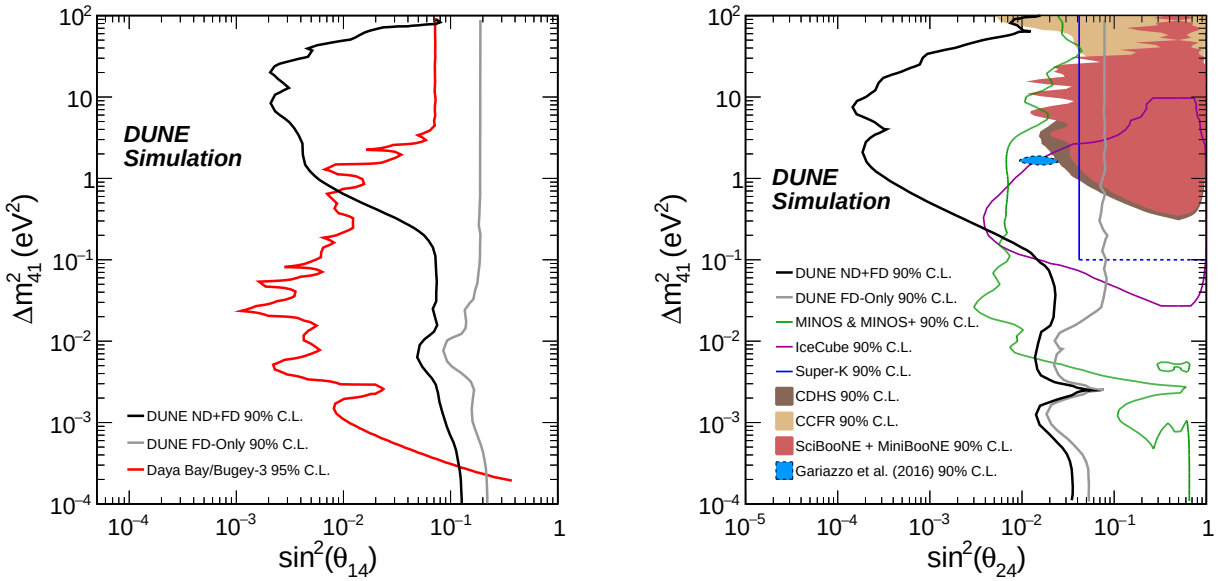

Figure 8.2: The left-hand plot shows the DUNE sensitivities to θ_{14} from the ν_e CC samples at the ND and FD, along with a comparison with the combined reactor result from Daya Bay and Bugey-3. The right-hand plot displays sensitivities to θ_{24} using the ν_μ CC and NC samples at both detectors, along with a comparison with previous and existing experiments. In both cases, regions to the right of the contours are excluded.

In the case of the θ_{34} mixing angle, we look for disappearance in the NC sample, the only contributor to this sensitivity. The results are shown in Figure 8.3. Further, a comparison with previous experiments sensitive to ν_μ, ν_τ mixing with large mass-squared splitting is possible by considering an effective mixing angle $\theta_{\mu\tau}$, such that $\sin^2 2\theta_{\mu\tau} \equiv 4|U_{\tau 4}|^2|U_{\mu 4}|^2 = \cos^4\theta_{14}\sin^2 2\theta_{24}\sin^2\theta_{34}$, and assuming conservatively that $\cos^4\theta_{14} = 1$, and $\sin^2 2\theta_{24} = 1$. This comparison with previous experiments is also shown in Figure 8.3. The sensitivity to θ_{34} is largely independent of Δm^2_{41}, since the term with $\sin^2\theta_{34}$ in the expression describing $P(\nu_\mu \to \nu_s)$ Eq. 8.1, depends solely on the Δm^2_{31} mass splitting.

Another quantitative comparison of our results for θ_{24} and θ_{34} with existing constraints can be made for projected upper limits on the sterile mixing angles assuming no evidence for sterile oscillations is found, and picking the value of $\Delta m^2_{41} = 0.5$ eV^2 corresponding to the simpler counting experiment regime. For the $3+1$ model, upper limits of $\theta_{24} < 1.8°(15.1°)$ and $\theta_{34} < 15.0°(25.5°)$ are obtained at the 90% CL from the presented best(worst)-case scenario DUNE sensitivities. If expressed in terms of the relevant matrix elements

$$\begin{aligned} |U_{\mu 4}|^2 &= \cos^2\theta_{14}\sin^2\theta_{24} \\ |U_{\tau 4}|^2 &= \cos^2\theta_{14}\cos^2\theta_{24}\sin^2\theta_{34}, \end{aligned} \tag{8.5}$$

these limits become $|U_{\mu 4}|^2 < 0.001(0.068)$ and $|U_{\tau 4}|^2 < 0.067(0.186)$ at the 90% CL, where we conservatively assume $\cos^2\theta_{14} = 1$ in both cases, and additionally $\cos^2\theta_{24} = 1$ in the second case.

Finally, sensitivity to the $\theta_{\mu e}$ effective mixing angle, defined above as $\sin^2 2\theta_{\mu e} \equiv 4|U_{e4}|^2|U_{\mu 4}|^2 = \sin^2 2\theta_{14}\sin^2\theta_{24}$, is shown in Figure 8.4, which also displays a comparison with the allowed re-

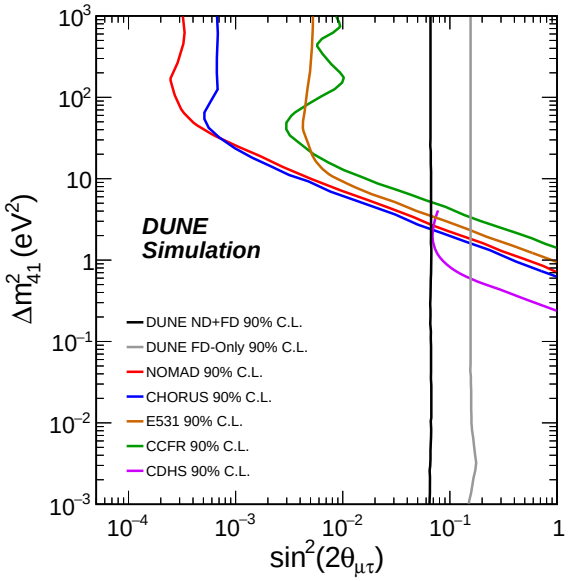

Figure 8.3: DUNE sensitivity to θ_{34} using the NC samples at the ND and FD compared to previous and existing experiments. Regions to the right of the contour are excluded.

Table 8.4: The projected DUNE 90% CL upper limits on sterile mixing angles and matrix elements compared to the equivalent 90% CL upper limits from NOvA [345], MINOS/MINOS+ [346], Super–Kamiokande [347], IceCube [348], and IceCube-DeepCore [349]. The limits are shown for $\Delta m^2_{41} = 0.5$ eV^2 for all experiments, except for IceCube-DeepCore, where the results are reported for $\Delta m^2_{41} = 1.0$ eV^2.

	θ_{24}	θ_{34}	$\lvert U_{\mu 4}\rvert^2$	$\lvert U_{\tau 4}\rvert^2$
DUNE Best-Case	$1.8°$	$15.0°$	0.001	0.067
DUNE Worst-Case	$15.1°$	$25.5°$	0.068	0.186
NOvA	$20.8°$	$31.2°$	0.126	0.268
MINOS/MINOS+	$4.4°$	$23.6°$	0.006	0.16
Super–Kamiokande	$11.7°$	$25.1°$	0.041	0.18
IceCube	$4.1°$	-	0.005	-
IceCube-DeepCore	$19.4°$	$22.8°$	0.11	0.15

gions from Liquid Scintilator Neutrino Detector (LSND) and MiniBooNE, as well as with present constraints and projected constraints from the Fermilab Short-Baseline Neutrino (SBN) program.

Further, to illustrate that DUNE would not be limited to constraining active-sterile neutrino mixing, we have produced a discovery potential plot, for a scenario with one sterile neutrino governed by the LSND best-fit parameters: $\left(\Delta m^2_{14} = 1.2\ \mathrm{eV}^2;\ \sin^2 2\theta_{\mu e} = 0.003\right)$ [338]. A small 90% CL allowed region, shown in Figure 8.4, is obtained, which can be compared with the LSND allowed region in the same figure.

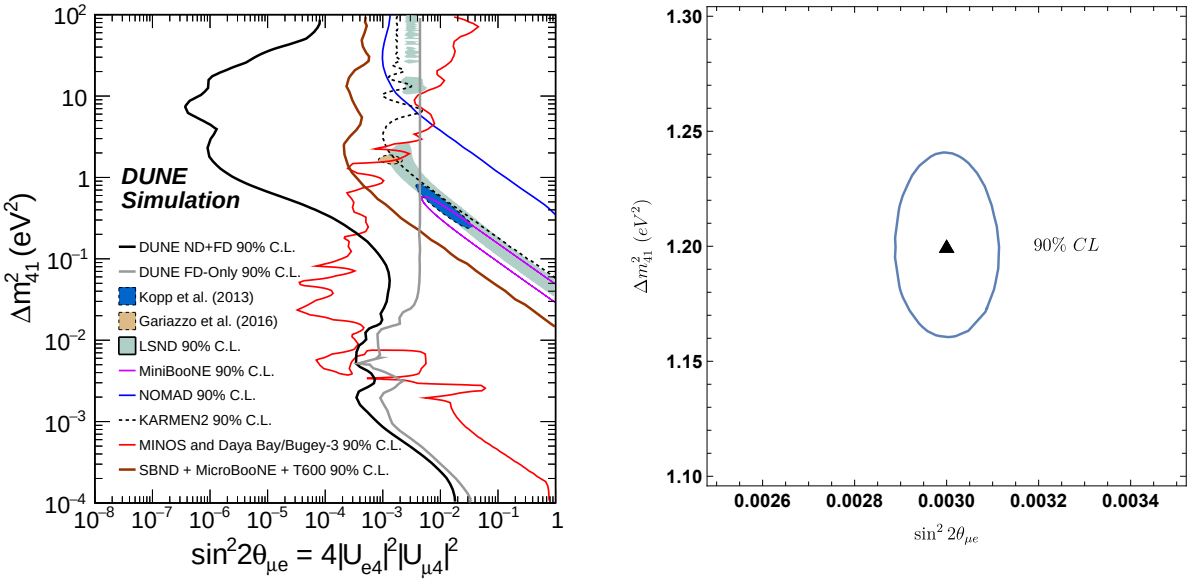

Figure 8.4: DUNE sensitivities to $\theta_{\mu e}$ from the appearance and disappearance samples at the ND and FD is shown on the left-hand plot, along with a comparison with previous existing experiments and the sensitivity from the future SBN program. Regions to the right of the DUNE contours are excluded. The right-hand plot displays the discovery potential assuming $\theta_{\mu e}$ and Δm^2_{41} set at the best-fit point determined by LSND [338] for the best-case scenario referenced in the text.

The physics reach plots shown above illustrate the excellent potential of DUNE to discover or constrain mixing with sterile neutrinos. Notably, in the case of sterile-mediated ν_μ to ν_e transitions, DUNE can place very competitive constraints on its own, without requiring a combination with reactor experiments.

These studies show compelling motivation for DUNE to deploy a highly-capable ND given its high potential for discovery or constraining of new physics, including mixing with sterile neutrino species. These capabilities can be further improved by a high-precision muon monitor system for the LBNF beam, which would provide an independent constraint on the neutrino flux through measurements of the associated muon flux, not susceptible to mixing with sterile neutrinos.

8.4 Non-Unitarity of the Neutrino Mixing Matrix

A generic characteristic of most models explaining the neutrino mass pattern is the presence of heavy neutrino states, beyond the three light states of the SM of particle physics [312, 313, 314, 315]. This implies a deviation from unitarity of the 3×3 PMNS matrix, which can be particularly sizable as the mass of the extra states becomes lower [350, 141, 351, 352, 353, 354]. For values of non-unitarity parameter deviations of order 10^{-2}, this would decrease the expected reach of DUNE to the standard parameters, although stronger bounds existing from charged leptons would be able to restore its expected performance [355, 356].

A generic characteristic of most models explaining the neutrino mass pattern is the presence of heavy neutrino states, additional to the three light states of the SM of particle physics [357, 358, 359]. These types of models will imply that the 3×3 PMNS matrix is not unitary due to the mixing with the additional states. Besides the type-I seesaw mechanism [315, 314, 313, 141], different low-scale seesaw models include right-handed neutrinos that are relatively not-so-heavy [351] and perhaps detectable at collider experiments.

These additional heavy leptons would mix with the light neutrino states and, as a result, the complete unitary mixing matrix would be a squared $n \times n$ matrix, with n the total number of neutrino states. As a result, the usual 3×3 PMNS matrix, which we dub N to stress its non-standard nature, will be non-unitary. One possible general way to parameterize these unitarity deviations in N is through a triangular matrix [360][1]

$$N = \begin{pmatrix} 1-\alpha_{ee} & 0 & 0 \\ \alpha_{\mu e} & 1-\alpha_{\mu\mu} & 0 \\ \alpha_{\tau e} & \alpha_{\tau\mu} & 1-\alpha_{\tau\tau} \end{pmatrix} U\,, \tag{8.6}$$

with U a unitary matrix that tends to the usual PMNS matrix when the non-unitary parameters $\alpha_{ij} \to 0$[2] . The triangular matrix in this equation accounts for the non-unitarity of the 3×3 matrix for any number of extra neutrino species. This pasteurization has been shown to be particularly well-suited for oscillation searches [360, 355] since, compared to other alternatives, it minimizes the departures of its unitary component U from the mixing angles that are directly measured in neutrino oscillation experiments when unitarity is assumed.

The phenomenological implications of a non-unitary leptonic mixing matrix have been extensively studied in flavor and electroweak precision observables as well as in the neutrino oscillation phenomenon [363, 141, 364, 365, 366, 367, 368, 369, 370, 371, 372, 373, 374, 375, 376, 377, 378, 379, 360, 53, 380, 381, 356]. For recent global fits to all flavor and electroweak precision data summarizing present bounds on non-unitarity see Refs. [377, 382].

[1] For a similar parameterization corresponding to a $(3+1)$ and a $(3+3)$-dimensional mixing matrix, see Refs. [361, 362]

[2] The original parameterization in Ref. [360] uses α_{ii} instead of $\alpha_{\beta\gamma}$. The equivalence between the two notations is as follows: $\alpha_{ii} = 1 - \alpha_{\beta\beta}$ and $\alpha_{ij} = \alpha_{\beta\gamma}$.

Table 8.5: Expected 90% CL constraints on the non-unitarity parameters α from DUNE.

Parameter	Constraint
α_{ee}	0.3
$\alpha_{\mu\mu}$	0.2
$\alpha_{\tau\tau}$	0.8
$\alpha_{\mu e}$	0.04
$\alpha_{\tau e}$	0.7
$\alpha_{\tau\mu}$	0.2

8.4.1 NU constraints from DUNE

Recent studies have shown that DUNE can constrain the non-unitarity parameters [355, 356]. The summary of the 90% CL bounds on the different α_{ij} elements profiled over all other parameters is given in Table 8.5. These bounds are comparable with other constraints from present oscillation experiments, although they are not competitive with those obtained from flavor and electroweak precision data. For this analysis, and those presented below, we have used the GLoBES software [197, 198] with the DUNE CDR configuration presented in Ref. [200], and assuming a data exposure of 300 kton.MW.year. The standard (unitary) oscillation parameters have also been treated as in [200]. The unitarity deviations have been included both by an independent code (used to obtain the results shown in Ref. [356]) and via the MonteCUBES [383] plug-in to cross validate our results.

8.4.2 NU impact on DUNE standard searches

Conversely, the presence of non-unitarity may affect the determination of the Dirac CP-violating phase δ_{CP} in long-baseline experiments [380, 382, 356]. Indeed, when allowing for unitarity deviations, the expected CP discovery potential for DUNE could be significantly reduced. However, the situation is alleviated when a combined analysis with the constraints on non-unitarity from other experiments is considered. This is illustrated in Figure 8.5. In the left panel, the discovery potential for CPV is computed when the non-unitarity parameters introduced in Eq. (8.6) are allowed in the fit. While for the Asimov data all $\alpha_{ij} = 0$, the non-unitary parameters are allowed to vary in the fit with 1σ priors of 10^{-1}, 10^{-2} and 10^{-3} for the dotted green, dashed blue and solid black lines respectively. For the dot-dashed red line no prior information on the non-unitarity parameters has been assumed. As can be observed, without additional priors on the non-unitarity parameters, the capabilities of DUNE to discover CPV from δ_{CP} would be seriously compromised [356]. However, with priors of order 10^{-2} matching the present constraints from other neutrino oscillation experiments [356, 355], the standard sensitivity is almost recovered. If the more stringent priors of

order 10^{-3} stemming from flavor and electroweak precision observables are added [377, 382], the standard sensitivity is obtained.

The right panel of Figure 8.5 concentrates on the impact of the phase of the element $\alpha_{\mu e}$ in the discovery potential of CPV from δ_{CP}, since this element has a very important impact in the ν_e appearance channel. In this plot the modulus of α_{ee}, $\alpha_{\mu\mu}$ and $\alpha_{\mu e}$ have been fixed to 10^{-1}, 10^{-2}, 10^{-3} and 0 for the dot-dashed red, dotted green, dashed blue and solid black lines respectively. All other non-unitarity parameters have been set to zero and the phase of $\alpha_{\mu e}$ has been allowed to vary both in the fit and in the Asimov data, showing the most conservative curve obtained. As for the right panel, it can be seen that a strong deterioration of the CP discovery potential could be induced by the phase of $\alpha_{\mu e}$ (see Ref. [356]). However, for unitarity deviations of order 10^{-2}, as required by present neutrino oscillation data constraints, the effect is not too significant in the range of δ_{CP} for which a 3σ exclusion of CP conservation would be possible and it becomes negligible if the stronger 10^{-3} constraints from flavor and electroweak precision data are taken into account.

Similarly, the presence of non-unitarity worsens degeneracies involving θ_{23}, making the determination of the octant or even its maximality challenging. This situation is shown in Figure 8.6 where an input value of $\theta_{23} = 42.3°$ was assumed. As can be seen, the fit in presence of non-unitarity (solid lines) introduces degeneracies for the wrong octant and even for maximal mixing [355]. However, these degeneracies are solved upon the inclusion of present priors on the non-unitarity parameters from other oscillation data (dashed lines) and a clean determination of the standard oscillation parameters following DUNE expectations is again recovered.

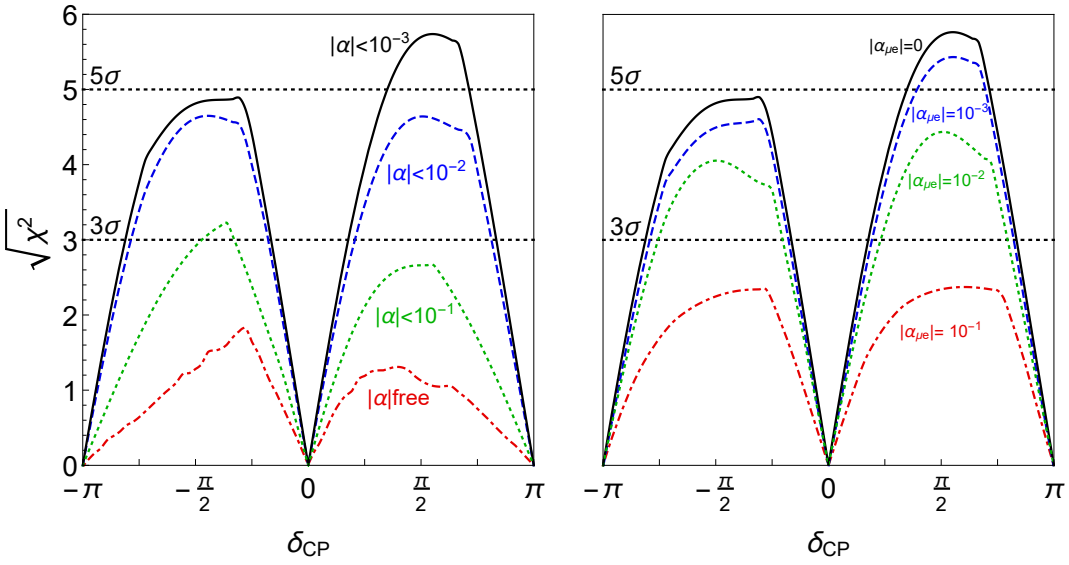

Figure 8.5: The impact of non-unitarity on the DUNE CPV discovery potential. See the text for details.

8.4.2.1 Conclusions

A non-unitary lepton mixing matrix, as generally expected from the most common extensions of the SM explaining neutrino masses, would affect the neutrino oscillations to be measured by DUNE.

The sensitivity that DUNE would provide to the non-unitarity parameters is comparable to that from present oscillation experiments, while not competitive to that from flavor and electroweak precision observables, which is roughly an order of magnitude more stringent. Conversely, the capability of DUNE to determine the standard oscillation parameters such as CPV from δ_{CP} or the octant or maximality of θ_{23} would be seriously compromised by unitarity deviations in the PMNS. This negative impact is however significantly reduced when priors on the size of these deviations from other oscillation experiments are considered and disappears altogether if the more stringent constraints from flavor and electroweak precision data are added instead.

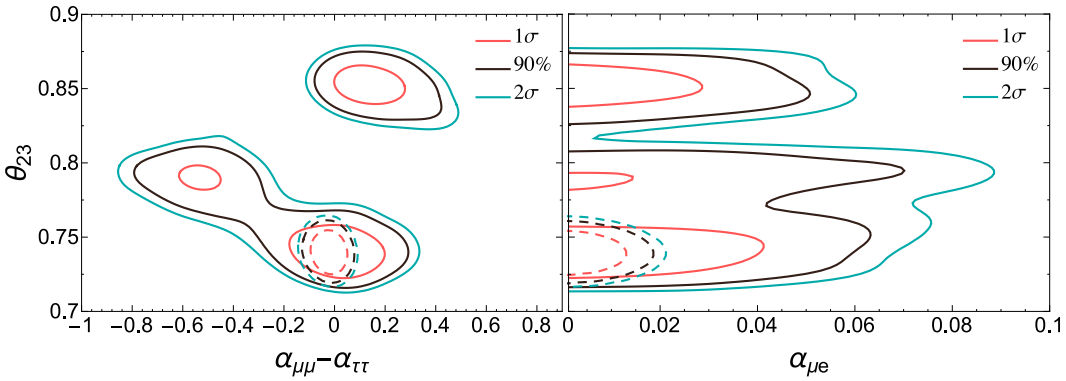

Figure 8.6: Expected frequentist allowed regions at the 1σ, 90% and 2σ CL for DUNE. All new physics parameters are assumed to be zero so as to obtain the expected non-unitarity sensitivities. The solid lines correspond to the analysis of DUNE data alone, while the dashed lines include the present constraints on non-unitarity.

8.5 Non-Standard Neutrino Interactions

NSI can significantly modify the data to be collected by DUNE as long as the new physics parameters are large enough. NSI may impact the determination of current unknowns such as CPV [384, 385], mass hierarchy [386] and octant of θ_{23} [387]. If the DUNE data are consistent with the standard oscillation for three massive neutrinos, NC NSI effects of order 0.1 G_F, affecting neutrino propagation through the Earth, can be ruled out at DUNE [388, 389]. We notice that DUNE might improve current constraints on $|\epsilon^m_{e\tau}|$ and $|\epsilon^m_{e\mu}|$ by a factor 2-5 [390, 391, 316]. New CC interactions can also lead to modifications in the production and the detection of neutrinos. The findings on source and detector NSI studies at DUNE are presented in [392, 393]. In particular, the simultaneous impact on the measurement of $\delta_{\rm CP}$ and θ_{23} is investigated in detail. Depending on the assumptions, such as the use of the ND and whether NSI at production and detection are the same, the impact of source/detector NSI at DUNE may be relevant. We are assuming the results from [392], in which DUNE does not have sensitivity to discover or to improve bounds on source/detector NSI, and focus our attention in the propagation.

8.5.1 NSI in propagation at DUNE

NC NSI can be understood as non-standard matter effects that are visible only in a FD at a sufficiently long baseline. They can be parameterized as new contributions to the Mikheyev-Smirnov-Wolfenstein effect (MSW) matrix in the neutrino-propagation Hamiltonian:

$$H = U \begin{pmatrix} 0 & & \\ & \Delta m^2_{21}/2E & \\ & & \Delta m^2_{31}/2E \end{pmatrix} U^\dagger + \tilde{V}_{\rm MSW}\,, \tag{8.7}$$

with

$$\tilde{V}_{\rm MSW} = \sqrt{2} G_F N_e \begin{pmatrix} 1+\epsilon^m_{ee} & \epsilon^m_{e\mu} & \epsilon^m_{e\tau} \\ \epsilon^{m*}_{e\mu} & \epsilon^m_{\mu\mu} & \epsilon^m_{\mu\tau} \\ \epsilon^{m*}_{e\tau} & \epsilon^{m*}_{\mu\tau} & \epsilon^m_{\tau\tau} \end{pmatrix} \tag{8.8}$$

Here, U is the standard PMNS leptonic mixing matrix, for which we use the standard parameterization found, e.g., in [78], and the ϵ-parameters give the magnitude of the NSI relative to standard weak interactions. For new physics scales of a few hundred GeV, a value of $|\epsilon|$ of the order 0.01 or less is expected [394, 395, 396]. The DUNE baseline provides an advantage in the detection of NSI relative to existing beam-based experiments with shorter baselines. Only atmospheric-neutrino experiments have longer baselines, but the sensitivity of these experiments to NSI is limited by systematic effects [7].

To assess DUNE sensitivity to NC NSI, the NSI discovery reach is defined in the following way: the expected event spectra are simulated using GLoBES [197, 198], assuming *true* values for the NSI parameters, and a fit is then attempted assuming no NSI. If the fit is incompatible with the simulated data at a given confidence level, the chosen *true* values of the NSI parameters are considered to be within the experimental discovery reach.

In this analysis, we use GLoBES with the Monte Carlo Utility Based Experiment Simulator (MonteCUBES) C library [383], a plugin that replaces the deterministic GLoBES minimizer by a Markov Chain Monte Carlo (MCMC) method that is able to handle higher dimensional parameter spaces. In the simulations we use the configuration for the DUNE CDR [200]. Each point scanned by the MCMC is stored and a frequentist χ^2 analysis is performed with the results. The analysis assumes an exposure of 300 kton.MW.year.

Considering that NSI exists, conducting the analysis with all the NSI parameters free to vary, we obtain the sensitivity regions in Figure 8.7. We omit the superscript m that appears in Eq. 8.8. The credible regions are shown for different confidence level intervals.

We note, however, that constraints on $\epsilon_{\tau\tau} - \epsilon_{\mu\mu}$ coming from global fit analysis [397, 391, 316, 398] can remove the left and right solutions of $\epsilon_{\tau\tau} - \epsilon_{\mu\mu}$ in Figure 8.7.

In order to constrain the standard oscillation parameters when NSI are present, we use the fit for

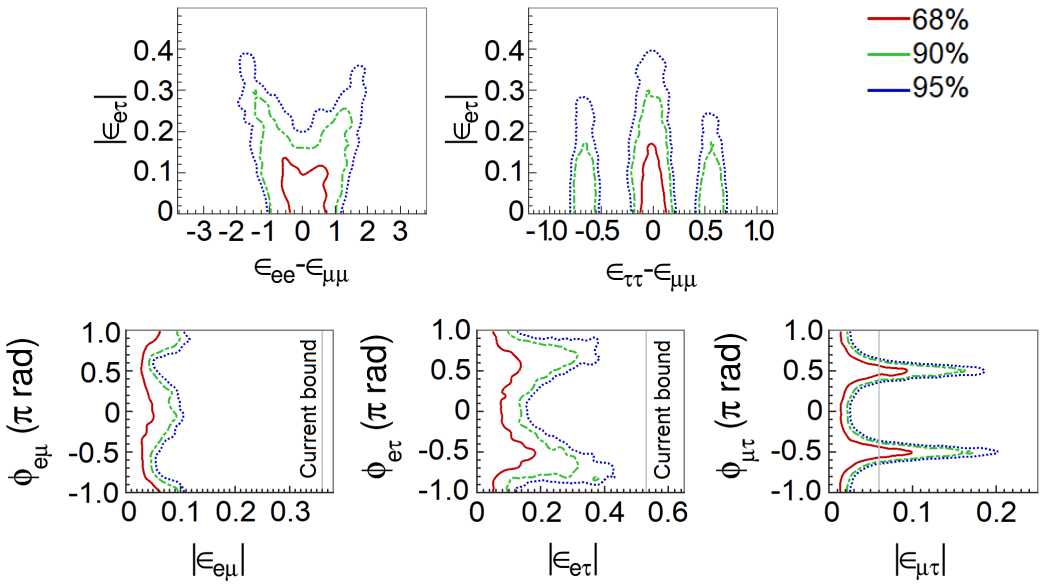

Figure 8.7: Allowed regions of the non-standard oscillation parameters in which we see important degeneracies (top) and the complex non-diagonal ones (bottom). We conduct the analysis considering all the NSI parameters as non-negligible. The sensitivity regions are for 68% CL [red line (left)], 90% CL [green dashed line (middle)], and 95% CL [blue dotted line (right)]. Current bounds are taken from [397].

three-neutrino mixing from [397] and implement prior constraints to restrict the region sampled by the MCMC. The sampling of the parameter space is explained in [389] and the priors that we use can be found in table 8.6.

Then we can observe the effects of NSI on the measurements of the standard oscillation parameters at DUNE. In Figure 8.8, we superpose the allowed regions with non-negligible NSI and the standard-only credible regions at 90% CL. An important degeneracy appears in the measurement of the mixing angle θ_{23}. We also see that the sensitivity of the CP phase is strongly affected.

8.5.2 Effects of baseline and matter-density variation on NSI measurements

The effects of matter density variation and its average along the beam path from Fermilab to SURF were studied considering the standard neutrino oscillation framework with three flavors [399, 400]. In order to obtain the results of Figures 8.7 and 8.8, we use a high-precision calculation for the baseline of 1284.9 km and the average density of 2.8482 g/cm^3 [399].

The DUNE collaboration has been using the so-called PREM [401, 402] density profile to consider matter density variation. With this assumption, the neutrino beam crosses a few constant density layers. However, a more detailed density map is available for the USA with more than 50 layers and 0.25 × 0.25 degree cells of latitude and longitude: The Shen-Ritzwoller or S.R. profile [403,

Table 8.6: Oscillation parameters and priors implemented in MCMC for calculation of Figure 8.7.

Parameter	Nominal	1σ Range ($\pm$)
θ_{12}	0.19π rad	2.29%
$\sin^2(2\theta_{13})$	0.08470	0.00292
$\sin^2(2\theta_{23})$	0.9860	0.0123
Δm^2_{21}	7.5 $\times 10^{-5}$eV^2	2.53%
Δm^2_{31}	2.524 $\times 10^{-3}$eV^2	free
$\delta_{\rm CP}$	1.45π rad	free

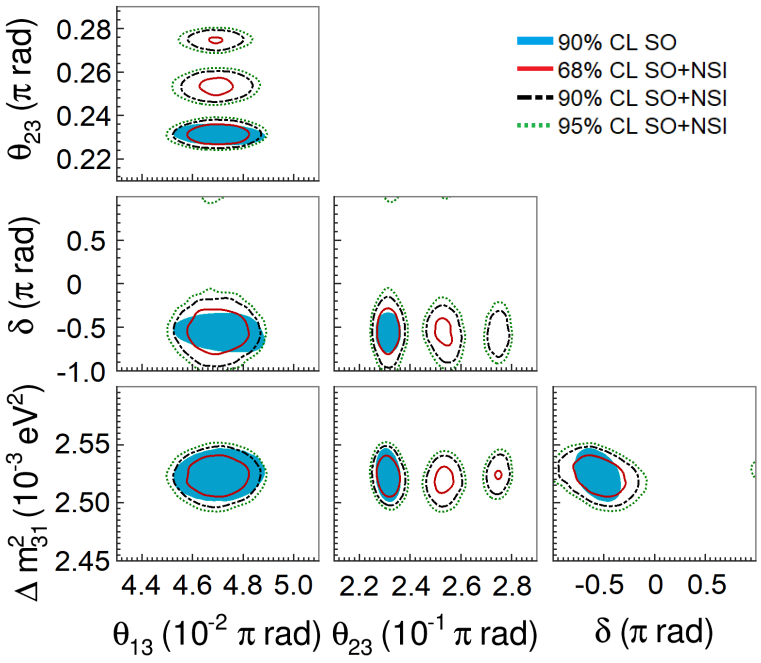

Figure 8.8: Projections of the standard oscillation parameters with nonzero NSI. The sensitivity regions are for 68%, 90%, and 95% CL. The allowed regions considering negligible NSI (standard oscillation (SO)) are superposed to the SO+NSI at 90% CL.

399]. Comparing the S.R. with the PREM profiles, Kelly and Parke [400] show that, in the standard oscillation paradigm, DUNE is not highly sensitive to the density profile and that the only oscillation parameter with its measurement slightly impacted by the average density true value is $\delta_{\rm CP}$. NSI, however, may be sensitive to the profile, particularly considering the phase $\phi_{e\tau}$ [404], to which DUNE will have a high sensitivity [390, 391, 388, 389, 316], as we also see in Figure 8.7.

In order to compare the results of our analysis predictions for DUNE with the constraints from other experiments we use the results from [316]. There are differences in the parameter nominal values used for calculating the χ^2 function and other assumptions. This is the reason why the regions in Figure 8.9 do not have the same central values, but this comparison gives a good view of how DUNE can substantially improve the bounds on, for example, $\varepsilon_{\tau\tau} - \varepsilon_{\mu\mu}$, Δm^2_{31}, and the non-diagonal NSI parameters.

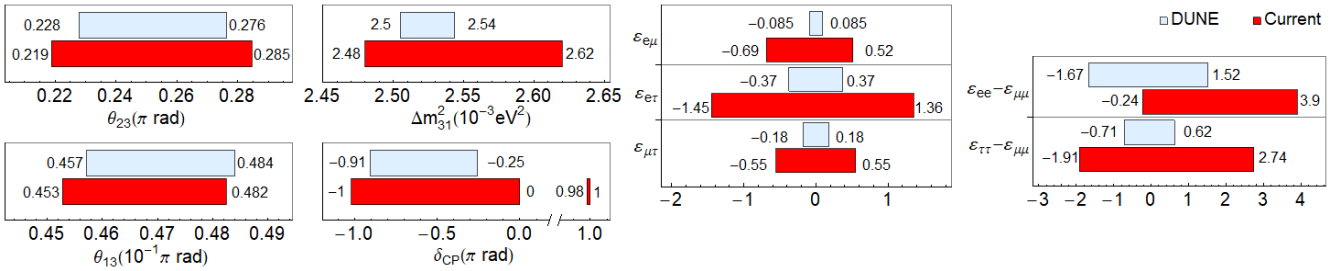

Figure 8.9: One-dimensional DUNE constraints compared with current constraints calculated in [316]. See text for details.

8.5.2.1 Conclusions and prospects

NSI can significantly impact the determination of current unknowns such as CPV and the octant of θ_{23}. Clean determination of the intrinsic CP phase at long-baseline experiments such as DUNE is a formidable task [405]. A feasible strategy to extricate physics scenarios at DUNE using high-energy beams was suggested in [406].

8.6 CPT Symmetry Violation

CPT symmetry, the combination of charge conjugation, parity and time reversal, is a cornerstone of our model-building strategy. DUNE can improve the present limits on Lorentz and CPT violation by several orders of magnitude [317, 318, 235, 240, 236, 319], contributing as a very important experiment to test these fundamental assumptions underlying quantum field theory.

CPT invariance is one of the predictions of major importance of local, relativistic quantum field theory. One of the predictions of CPT invariance is that particles and antiparticles have the same

masses and, if unstable, the same lifetimes. To prove the CPT theorem one needs only three ingredients [317]: Lorentz invariance, hermeticity of the Hamiltonian, and locality.

Experimental bounds on CPT invariance can be derived using the neutral kaon system [407]:

$$\frac{|m(K^0) - m(\overline{K}^0)|}{m_K} < 0.6 \times 10^{-18}\,. \tag{8.9}$$

This result, however, should be interpreted very carefully for two reasons. First, we do not have a complete theory of CPT violation, and it is therefore arbitrary to take the kaon-mass as a scale. Second, since kaons are bosons, the term entering the Lagrangian is the mass squared and not the mass itself. With this in mind, we can rewrite the previous bound as: $|m^2(K^0) - m^2(\overline{K}^0)| < 0.3\,\mathrm{eV}^2$. Here we see that neutrinos can test the predictions of the CPT theorem to an unprecedented extent and could, therefore, provide stronger limits than the ones regarded as the most stringent ones to date[3]. In the absence of a solid model of flavor, not to mention one of CPT violation, the spectrum of neutrinos and antineutrinos can differ both in the mass eigenstates themselves as well as in the flavor composition of each of these states. It is important to notice then that neutrino oscillation experiments can only test CPT in the mass differences and mixing angles. An overall shift between the neutrino and antineutrino spectra will be missed by oscillation experiments. Nevertheless, such a pattern can be bounded by cosmological data [408]. Unfortunately direct searches for neutrino mass (past, present, and future) involve only antineutrinos and hence cannot be used to draw any conclusion on CPT invariance on the absolute mass scale, either. Therefore, using neutrino oscillation data, we will compare the mass splittings and mixing angles of neutrinos with those of antineutrinos. Differences in the neutrino and antineutrino spectrum would imply the violation of the CPT theorem.

In Ref. [319] the authors derived the most up-to-date bounds on CPT invariance from the neutrino sector using the same data that was used in the global fit to neutrino oscillations in Ref. [142]. Of course, experiments that cannot distinguish between neutrinos and antineutrinos, such as atmospheric data from Super–Kamiokande [409], IceCube-DeepCore [410, 411] and ANTARES [412] were not included. The complete data set used, as well as the parameters to which they are sensitive, are (1) from solar neutrino data [298, 413, 414, 415, 416, 417, 418, 419, 420, 421]: θ_{12}, Δm^2_{21}, and θ_{13}; (2) from neutrino mode in long-baseline experiments K2K [422], MINOS [423, 424], T2K [425, 426], and NOνA [427, 428]: θ_{23}, Δm^2_{31}, and θ_{13}; (3) from KamLAND reactor antineutrino data [429]: $\overline{\theta}_{12}$, $\Delta\overline{m}^2_{21}$, and $\overline{\theta}_{13}$; (4) from short-baseline reactor antineutrino experiments Daya Bay [430], RENO [431], and Double Chooz [432]: $\overline{\theta}_{13}$ and $\Delta\overline{m}^2_{31}$; and (5) from antineutrino mode in long-baseline experiments MINOS [423, 424] and T2K [425, 426]: $\overline{\theta}_{23}$, $\Delta\overline{m}^2_{31}$, and $\overline{\theta}_{13}$[4].

From the analysis of all previous data samples, one can derive the most up-to-date bounds on CPT violation: $|\Delta m^2_{21} - \Delta\overline{m}^2_{21}| < 4.7\times10^{-5}\,\mathrm{eV}^2$, $|\Delta m^2_{31} - \Delta\overline{m}^2_{31}| < 3.7\times10^{-4}\,\mathrm{eV}^2$, $|\sin^2\theta_{12} - \sin^2\overline{\theta}_{12}| < 0.14$, $|\sin^2\theta_{13} - \sin^2\overline{\theta}_{13}| < 0.03$, and $|\sin^2\theta_{23} - \sin^2\overline{\theta}_{23}| < 0.32$.

At the moment it is not possible to set any bound on $|\delta - \overline{\delta}|$, since all possible values of δ or $\overline{\delta}$ are allowed by data. The preferred intervals of δ obtained in Ref. [142] can only be obtained after

[3] CPT was tested also using charged leptons. However, these measurements involve a combination of mass and charge and are not a direct CPT test. Only neutrinos can provide CPT tests on an elementary mass not contaminated by charge.

[4] The K2K experiment took data only in neutrino mode, while the NOvA experiment had not published data in the antineutrino mode when these bounds were calculated.

combining the neutrino and antineutrino data samples. The limits on $\Delta(\Delta m^2_{31})$ and $\Delta(\Delta m^2_{21})$ are already better than the one derived from the neutral kaon system and should be regarded as the best current bounds on CPT violation on the mass squared. Note that these results were derived assuming the same mass ordering for neutrinos and antineutrinos. If the ordering was different for neutrinos and antineutrinos, this would be an indication for CPT violation on its own. In the following we show how DUNE could improve this bound.

8.6.0.1 Sensitivity to CPT symmetry violation in the neutrino sector

Table 8.7: Oscillation parameters used to simulate neutrino and antineutrino data analyzed in Section 8.6.0.1.

Parameter	Value
Δm^2_{21}	$7.56 \times 10^{-5}\text{eV}^2$
Δm^2_{31}	$2.55 \times 10^{-3}\text{eV}^2$
$\sin^2\theta_{12}$	0.321
$\sin^2\theta_{23}$	0.43, 0.50, 0.60
$\sin^2\theta_{13}$	0.02155
δ	1.50π

Here we study the sensitivity of the DUNE experiment to measure CPT violation in the neutrino sector by analyzing neutrino and antineutrino oscillation parameters separately. We assume the neutrino oscillations being parameterized by the usual PMNS matrix U_{PMNS}, with parameters $\theta_{12}, \theta_{13}, \theta_{23}, \Delta m^2_{21}, \Delta m^2_{31}$, and δ, while the antineutrino oscillations are parameterized by a matrix $\overline{U}_{\text{PMNS}}$ with parameters $\overline{\theta}_{12}, \overline{\theta}_{13}, \overline{\theta}_{23}, \Delta\overline{m}^2_{21}, \Delta\overline{m}^2_{31}$, and $\overline{\delta}$. Hence, antineutrino oscillation is described by the same probability functions as neutrinos with the neutrino parameters replaced by their antineutrino counterparts[5]. To simulate the future neutrino data signal in DUNE, we assume the true values for neutrinos and antineutrinos to be as listed in Table 8.7. Then, in the statistical analysis, we vary freely all the oscillation parameters, except the solar ones, which are fixed to their best fit values throughout the simulations. Given the great precision in the determination of the reactor mixing angle by the short-baseline reactor experiments [430, 431, 432], in our analysis we use a prior on $\overline{\theta}_{13}$, but not on θ_{13}. We also consider three different values for the atmospheric angles, as indicated in Table 8.7. The exposure considered in the analysis corresponds to 300 kton.MW.year.

Therefore, to test the sensitivity at DUNE we perform the simulations assuming $\Delta x = |x - \overline{x}| = 0$, where x is any of the oscillation parameters. Then we estimate the sensitivity to $\Delta x \neq 0$. To do so

[5]Note that the antineutrino oscillation probabilities also include the standard change of sign in the CP phase.

we calculate two χ^2-grids, one for neutrinos and one for antineutrinos, varying the four parameters of interest. After minimizing over all parameters except x and $\overline{x}$, we calculate

$$\chi^2(\Delta x) = \chi^2(|x - \overline{x}|) = \chi^2(x) + \chi^2(\overline{x}), \tag{8.10}$$

where we have considered all the possible combinations of $|x - \overline{x}|$. The results are presented in Figure 8.10, where we plot three different lines, labeled as "high", "max" and "low." These refer to the assumed value for the atmospheric angle: in the lower octant (low), maximal mixing (max) or in the upper octant (high). Here we can see that there is sensitivity neither to $\Delta(\sin^2\theta_{13})$, where the 3σ bound would be of the same order as the current measured value for $\sin^2\overline{\theta}_{13}$, nor to $\Delta\delta$, where no single value of the parameter would be excluded at more than 2σ.

On the contrary, interesting results for $\Delta(\Delta m^2_{31})$ and $\Delta(\sin^2\theta_{23})$ are obtained. First, we see that DUNE can put stronger bounds on the difference of the atmospheric mass splittings, namely $\Delta(\Delta m^2_{31}) < 8.1 \times 10^{-5}$, improving the current neutrino bound by one order of magnitude. For the atmospheric angle, we obtain different results depending on the true value assumed in the simulation of DUNE data. In the lower right panel of Figure 8.10 we see the different behavior obtained for θ_{23} with the values of $\sin^2\theta_{23}$ from table 8.7, i.e., lying in the lower octant, being maximal, and lying in the upper octant. As one might expect, the sensitivity increases with $\Delta\sin^2\theta_{23}$ in the case of maximal mixing. However, if the true value lies in the lower or upper octant, a degenerate solution appears in the complementary octant.

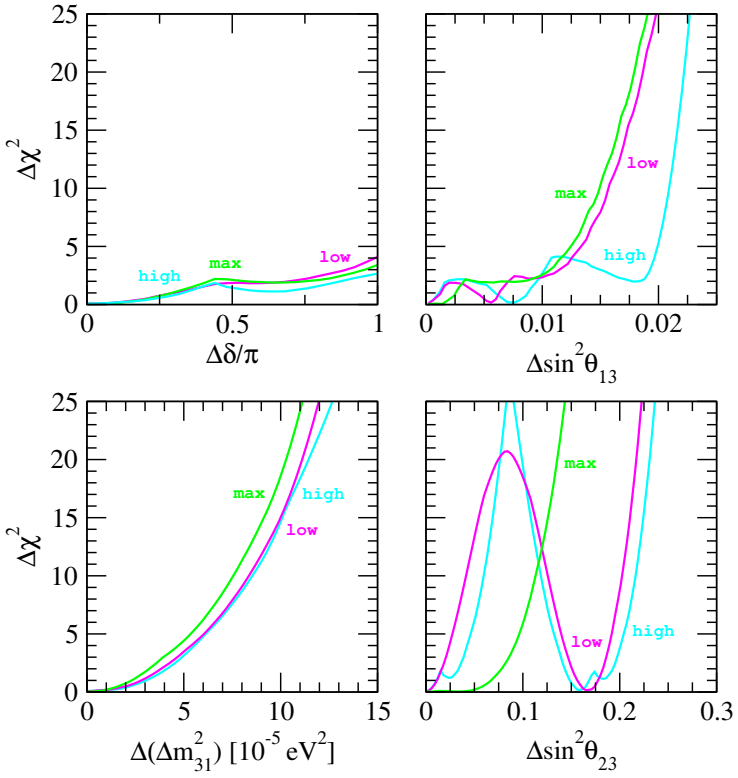

Figure 8.10: The sensitivities of DUNE to the difference of neutrino and antineutrino parameters: $\Delta\delta$, $\Delta(\Delta m^2_{31})$, $\Delta(\sin^2\theta_{13})$ and $\Delta(\sin^2\theta_{23})$ for the atmospheric angle in the lower octant (magenta line), in the upper octant (cyan line) and for maximal mixing (green line).

8.6.1 Imposter solutions

In some types of neutrino oscillation experiments, e.g., accelerator experiments, neutrino and antineutrino data are obtained in separate experimental runs. The usual procedure followed by the experimental collaborations, as well as the global oscillation fits as for example Ref. [142], assumes CPT invariance and analyzes the full data sample in a joint way. However, if CPT is violated in nature, the outcome of the joint data analysis might give rise to what we call an "imposter" solution, i.e., one that does not correspond to the true solution of any channel.

Under the assumption of CPT conservation, the χ^2 functions are computed according to

$$\chi^2_{\text{total}} = \chi^2(\nu) + \chi^2(\overline{\nu})\,, \tag{8.11}$$

and assuming that the same parameters describe neutrino and antineutrino flavor oscillations. In contrast, in Eq. (8.10) we first profiled over the parameters in neutrino and antineutrino mode separately and then added the profiles. Here, we shall assume CPT to be violated in nature, but perform our analysis as if it were conserved. As an example, we assume that the true value for the atmospheric neutrino mixing is $\sin^2\theta_{23} = 0.5$, while the antineutrino mixing angle is given by $\sin^2\overline{\theta}_{23} = 0.43$. The rest of the oscillation parameters are set to the values in Table 8.7. Performing the statistical analysis in the CPT-conserving way, as indicated in Eq. (8.11), we obtain the profile of the atmospheric mixing angle presented in Figure 8.11. The profiles for the individual reconstructed results (neutrino and antineutrino) are also shown in the figure for comparison. The result is a new best fit value at $\sin^2\theta_{23}^{\text{comb}} = 0.467$, disfavoring the true values for neutrino and antineutrino parameters at approximately 3σ and more than 5σ, respectively.

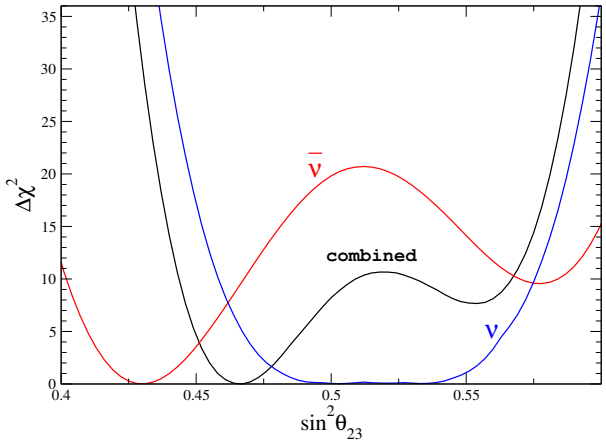

Figure 8.11: DUNE sensitivity to the atmospheric angle for neutrinos (blue), antineutrinos (red), and to the combination of both under the assumption of CPT conservation (black).

8.7 Search for Neutrino Tridents at the Near Detector

Neutrino trident production is a weak process in which a neutrino, scattering off the Coulomb field of a heavy nucleus, generates a pair of charged leptons, as shown in Fig. 8.12 [320, 321, 322, 323,

324, 325, 326]. Measurements of muonic neutrino tridents ($\nu_\mu \to \nu_\mu\mu^+\mu^-$) were carried out at the CHARM-II [433], CCFR [434] and NuTeV [435] experiments:

$$\frac{\sigma(\nu_\mu \to \nu_\mu\mu^+\mu^-)_{\rm exp}}{\sigma(\nu_\mu \to \nu_\mu\mu^+\mu^-)_{\rm SM}} = \begin{cases} 1.58 \pm 0.64 & \text{(CHARM-II)} \\ 0.82 \pm 0.28 & \text{(CCFR)} \\ 0.72^{+1.73}_{-0.72} & \text{(NuTeV)} \end{cases}$$

The high-intensity muon-neutrino beam at the DUNE ND will lead to a sizable production rate of trident events (see Table 8.8), offering excellent prospects to improve the above measurements [327, 328, 329]. A deviation from the event rate predicted by the SM could be an indication of new interactions mediated by the corresponding new gauge bosons [436].

The main challenge in obtaining a precise measurement of the muonic trident cross section will be the copious backgrounds, mainly consisting of CC single-pion production events, $\nu_\mu N \to \mu\pi N'$, as muon and pion tracks can be easily confused in LArTPC detectors. The discrimination power of the DUNE ND LArTPC was evaluated using large simulation datasets of signal and background. Each simulation event represents a different neutrino-argon interaction in the active volume of the detector. Signal events were generated using a standalone code [327] that simulates trident production of muons and electrons through the scattering of ν_μ and ν_e on argon nuclei (or iron nuclei, for comparison with CCFR and NuTeV results). The generator considers both the coherent scattering on the full nucleus (the dominant contribution) and the incoherent scattering on individual nucleons. Background events, consisting of several SM neutrino interactions, were generated using GENIE. Roughly 38% of the generated events have a charged pion in the final state, leading to two charged tracks with muon-like energy deposition pattern ($\mathrm{d}E/\mathrm{d}x$), as in our trident signal.

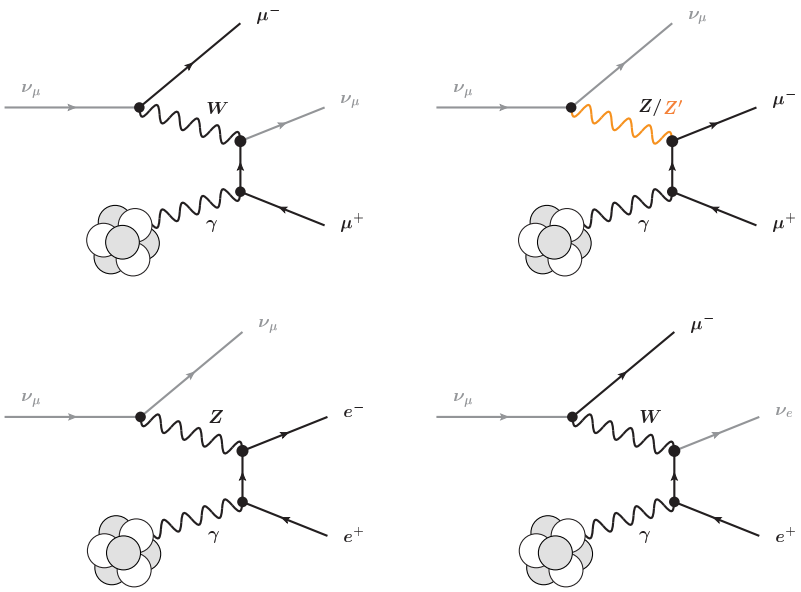

Figure 8.12: Example diagrams for muon-neutrino-induced trident processes in the Standard Model. A second set of diagrams where the photon couples to the negatively charged leptons is not shown. Analogous diagrams exist for processes induced by different neutrino flavors and by anti-neutrinos. A diagram illustrating trident interactions mediated by a new Z' gauge boson, discussed in the text, is shown on the top right.

Table 8.8: Expected number of SM ν_μ and $\bar{\nu}_\mu$-induced trident events at the LArTPC of the DUNE ND per metric ton of argon and year of operation.

Process	Coherent	Incoherent
$\nu_\mu \to \nu_\mu \mu^+ \mu^-$	1.17 ± 0.07	0.49 ± 0.15
$\nu_\mu \to \nu_\mu e^+ e^-$	2.84 ± 0.17	0.18 ± 0.06
$\nu_\mu \to \nu_e e^+ \mu^-$	9.8 ± 0.6	1.2 ± 0.4
$\nu_\mu \to \nu_e \mu^+ e^-$	0	0
$\bar{\nu}_\mu \to \bar{\nu}_\mu \mu^+ \mu^-$	0.72 ± 0.04	0.32 ± 0.10
$\bar{\nu}_\mu \to \bar{\nu}_\mu e^+ e^-$	2.21 ± 0.13	0.13 ± 0.04
$\bar{\nu}_\mu \to \bar{\nu}_e e^+ \mu^-$	0	0
$\bar{\nu}_\mu \to \bar{\nu}_e \mu^+ e^-$	7.0 ± 0.4	0.9 ± 0.3

All final-state particles produced in the interactions were propagated through the detector geometry using the Geant4-based [437, 438, 439] simulation of the DUNE ND. Charge collection and readout were not simulated, and possible inefficiencies due to misreconstruction effects or event pile-up were disregarded for simplicity.

Figure 8.13 shows the distribution (area normalized) for signal and background of the different kinematic variables used in our analysis for the discrimination between signal and background. As expected, background events tend to contain a higher number of tracks than the signal. The other distributions also show a clear discriminating power: the angle between the two tracks is typically much smaller in the signal than in the background. Moreover, the signal tracks (two muons) tend to be longer than tracks in the background (mainly one muon plus one pion).

8.7.1 Sensitivity to new physics

The sensitivity of neutrino tridents to heavy new physics (i.e., heavy compared to the momentum transfer in the process) can be parameterized in a model-independent way using a modification of the effective four-fermion interaction Hamiltonian. Focusing on the case of muon-neutrinos interacting with muons, the vector and axial-vector couplings can be written as

$$g^V_{\mu\mu\mu\mu} = 1 + 4\sin^2\theta_W + \Delta g^V_{\mu\mu\mu\mu} \quad \text{and} \quad g^A_{\mu\mu\mu\mu} = -1 + \Delta g^A_{\mu\mu\mu\mu} \ , \tag{8.12}$$

where $\Delta g^V_{\mu\mu\mu\mu}$ and $\Delta g^A_{\mu\mu\mu\mu}$ parameterize possible new physics contributions. Couplings involving other combinations of lepton flavors can be modified analogously. Note, however, that for interactions that involve electrons, very strong constraints can be derived from LEP bounds on

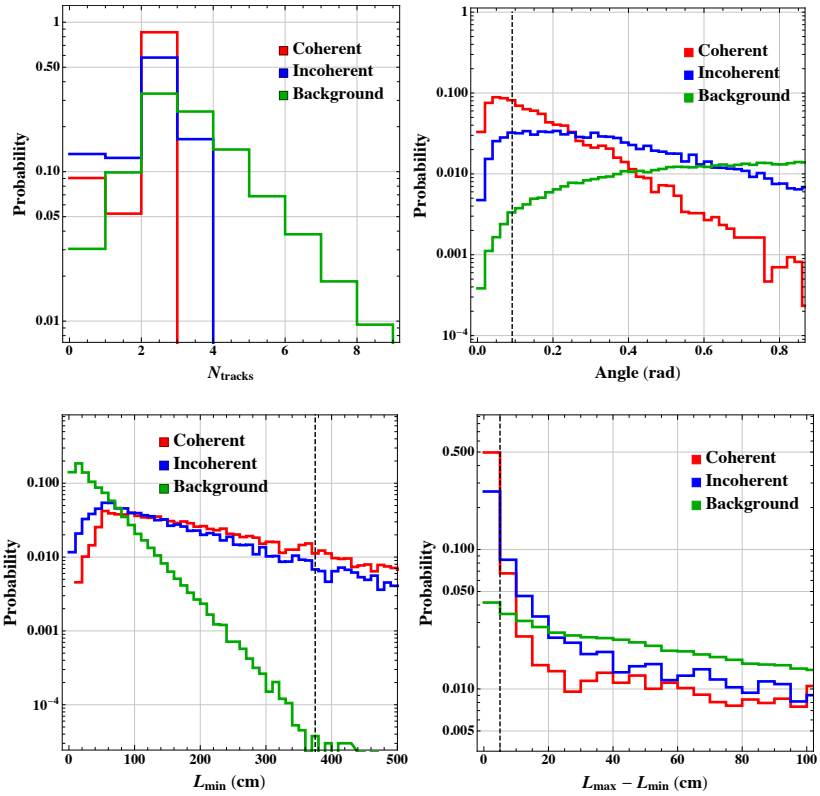

Figure 8.13: Event kinematic distributions of signal and background considered for the selection of muonic trident interactions in the ND LArTPC: number of tracks (top left), angle between the two main tracks (top right), length of the shortest track (bottom left), and the difference in length between the two main tracks (bottom right). The dashed, black vertical lines indicate the optimal cut values used in the analysis.

electron contact interactions [440]. The modified interactions of the muon-neutrinos with muons alter the cross section of the $\nu_\mu N \to \nu_\mu \mu^+ \mu^- N$ trident process. In Figure 8.14 we show the regions in the $\Delta g^V_{\mu\mu\mu\mu}$ vs. $\Delta g^A_{\mu\mu\mu\mu}$ plane that are excluded by the existing CCFR measurement $\sigma_{\text{CCFR}}/\sigma^{\text{SM}}_{\text{CCFR}} = 0.82 \pm 0.28$ [434] at the 95% CL in gray. A measurement of the $\nu_\mu N \to \nu_\mu \mu^+ \mu^- N$ cross section with 40% uncertainty at the DUNE ND could cover the blue hashed regions. Our baseline analysis does not extend the sensitivity into parameter space that is unconstrained by the CCFR measurement. However, It is likely that the use of a magnetized spectrometer, as it is being considered for the DUNE ND, able to identify the charge signal of the trident final state, along with a more sophisticated event selection (e.g. deep-learning-based), will significantly improve separation between neutrino trident interactions and backgrounds. Therefore, we also present the region that could be probed by a 25% measurement of the neutrino trident cross section at DUNE, which would extend the coverage of new physics parameter space substantially.

We consider a class of models that modify the trident cross section through the presence of an additional neutral gauge boson, Z', that couples to neutrinos and charged leptons. A consistent way of introducing such a Z' is to gauge an anomaly-free global symmetry of the SM. Of particular interest is the Z' that is based on gauging the difference of muon-number and tau-number, $L_\mu - L_\tau$ [55, 56]. Such a Z' is relatively weakly constrained and can for example address the longstanding discrepancy between SM prediction and measurement of the anomalous magnetic moment of the

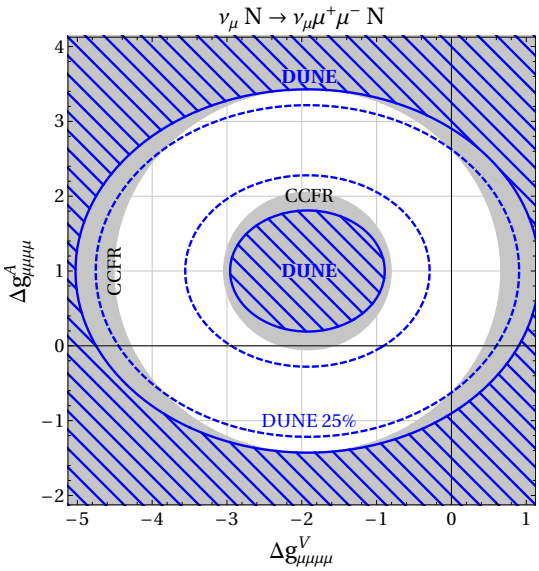

Figure 8.14: Projected sensitivity (95% CL) of a measurement of the $\nu_\mu N \to \nu_\mu\mu^+\mu^- N$ cross section at the DUNE ND to modifications of the vector and axial-vector couplings of muon-neutrinos to muons (blue hashed regions). The gray regions are excluded at 95% CL by existing measurements of the cross section by the CCFR collaboration. The intersection of the black lines indicates the SM point.

muon, $(g-2)_\mu$ [57, 58]. The $L_\mu - L_\tau$ Z' has also been used in models to explain B physics anomalies [441] and as a portal to DM [442, 443]. The $\nu_\mu N \to \nu_\mu\mu^+\mu^- N$ trident process has been identified as important probe of gauged $L_\mu - L_\tau$ models over a broad range of Z' masses [441, 436].

In Figure 8.15 we show the existing CCFR constraint on the model parameter space in the $m_{Z'}$ vs. g' plane and compare it to the region of parameter space where the anomaly in $(g-2)_\mu = 2a_\mu$ can be explained. The green region shows the 1σ and 2σ preferred parameter space corresponding to a shift $\Delta a_\mu = a_\mu^{\rm exp} - a_\mu^{\rm SM} = (2.71 \pm 0.73) \times 10^{-9}$ [452]. Shown are in addition constraints from LHC searches for the Z' in the $pp \to \mu^+\mu^- Z' \to \mu^+\mu^-\mu^+\mu^-$ process [444] (see also [436]), direct searches for the Z' at BaBar using the $e^+e^- \to \mu^+\mu^- Z' \to \mu^+\mu^-\mu^+\mu^-$ process [445], and constraints from LEP precision measurements of leptonic Z couplings [446, 441]. Also a Borexino bound on non-standard contributions to neutrino-electron scattering [448, 447, 449] has been used to constrain the $L_\mu - L_\tau$ gauge boson [451, 453, 454]. Our reproduction of the Borexino constraint is shown. For very light Z' masses of O(few MeV) and below, strong constraints from measurements of the effective number of relativistic degrees of freedom during big bang nucleosynthesis (BBN) apply [450, 451]. Taking into account all relevant constraints, parameter space to explain $(g-2)_\mu$ is left below the di-muon threshold $m_{Z'} \lesssim 210$ MeV.

8.8 Dark Matter Probes

Dark matter (DM) is a crucial ingredient to understand the cosmological history of the universe, and the most up-to-date measurements suggests the existence of DM with an abundance of 27% [31]. In light of this situation, a tremendous amount of experimental effort has gone into

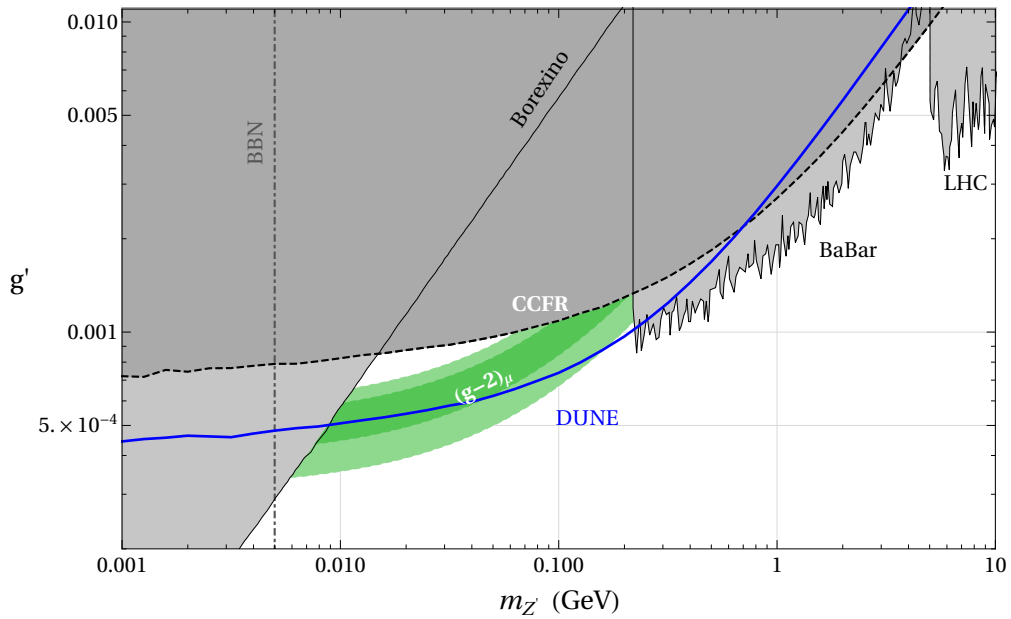

Figure 8.15: Existing constraints and projected DUNE sensitivity in the $L_\mu - L_\tau$ parameter space. Shown in green is the region where the $(g-2)_\mu$ anomaly can be explained at the 2σ level. The parameter regions already excluded by existing constraints are shaded in gray and correspond to a CMS search for $pp \to \mu^+\mu^- Z' \to \mu^+\mu^-\mu^+\mu^-$ [444] ("LHC"), a BaBar search for $e^+e^- \to \mu^+\mu^- Z' \to \mu^+\mu^-\mu^+\mu^-$ [445] ("BaBar"), precision measurements of $Z \to \ell^+\ell^-$ and $Z \to \nu\bar{\nu}$ couplings [446, 441] ("LEP"), a previous measurement of the trident cross section [434, 436] ("CCFR"), a measurement of the scattering rate of solar neutrinos on electrons [447, 448, 449] ("Borexino"), and bounds from big bang nucleosynthesis [450, 451] ("BBN"). The DUNE sensitivity shown by the solid blue line assumes a measurement of the trident cross section with 40% precision.

the search for DM-induced signatures, for example, DM direct and indirect detections and collider searches. However, no "smoking-gun" signals have been discovered thus far while more parameter space in relevant DM models is simply ruled out. It is noteworthy that most conventional DM search strategies are designed to be sensitive to signals from the WIMP, one of the well-motivated DM candidates, whose mass range is from a few GeV to tens of TeV. The null observation of DM via non-gravitational interactions actually motivates unconventional or alternative DM search schemes. One such possibility is a search for experimental signatures induced by boosted, hence relativistic, DM for which a mass range smaller than that of the weak scale is often motivated.

One of the possible ways to produce and then detect relativistic DM particles can be through accelerator experiments, for example, neutrino beam experiments [330, 331, 332, 199]. By construction, large signal statistics is expected so that this sort of search strategy can allow for significant sensitivity to DM-induced signals despite the feeble interaction of DM with SM particles. DUNE will perform a signal search in the relativistic scattering of LDM at the ND, as it is close enough to the beam source to sample a substantial level of DM flux, assuming that DM is produced.

Alternatively, it is possible that BDM particles are created in the universe under non-minimal dark-sector scenarios [78, 333], and can reach terrestrial detectors. For example, one can imagine a two-component DM scenario in which a lighter component is usually a subdominant relic with direct coupling to SM particles, while the heavier is the cosmological DM that pair-annihilates

directly to a lighter DM pair, not to SM particles. Other mechanisms such as semi-annihilation in which a DM particle pair-annihilates to a lighter DM particle and a dark sector particle that may decay away are also possible [455, 456, 335, 79, 80]. In typical cases, the BDM flux is not large and thus large-volume neutrino detectors are desirable to overcome the challenge in statistics (for an exception, see [81, 457]).

Indeed, a (full-fledged) DUNE FD with a fiducial mass of 40 kt and quality detector performance is expected to possess competitive sensitivity to BDM signals from various sources in the current universe such as the galactic halo [78, 84, 85, 458, 334, 336], the sun [335, 79, 80, 336], and dwarf spheroidal galaxies [83]. Furthermore, the ProtoDUNE detectors are operational, and we anticipate preliminary studies with their cosmic data. Interactions of BDM with electrons [78] and with hadrons (protons) [79], were investigated for Cherenkov detectors, such as Super–Kamiokande, which recently published a dedicated search for BDM in the electron channel [459]. However, in such detectors the BDM signal rate is shown to often be significantly attenuated due to Cherenkov threshold, in particular for hadronic channels. LAr detectors, such as DUNE's, have the potential to greatly improve the sensitivity for BDM compared to Cherenkov detectors. This is due to improved particle identification techniques, as well as a significantly lower energy threshold for proton detection. Earlier studies have shown an improvement with DUNE forBDM-electron interaction [83].

8.8.1 Benchmark Dark Matter Models

The benchmark "DM models" defined in this section describe only couplings of dark-sector states including LDM particles. We consider two example models: i) a vector portal-type scenario where a (massive) dark-sector photon V mixes with the SM photon and ii) a leptophobic Z' scenario. The former is used in Sections 8.8.2 and 8.8.3, while the latter features in Section 8.8.4. DM and other dark-sector particles are assumed to be fermionic for convenience.

Benchmark Model i) The relevant interaction Lagrangian is given by

$$\mathcal{L}_{\rm int} \supset -\frac{\epsilon}{2} V_{\mu\nu} F^{\mu\nu} + g_{11} \bar{\chi}_1 \gamma^\mu \chi_1 V_\mu + g_{12} \bar{\chi}_2 \gamma^\mu \chi_1 V_\mu + h.c.\,, \tag{8.13}$$

where $V^{\mu\nu}$ and $F^{\mu\nu}$ are the field strength tensors for the dark-sector photon and the SM photon, respectively. Here we have introduced the kinetic mixing parameter ϵ, while g_{11} and g_{12} parameterize the interaction strengths for flavor-conserving (second operator) and flavor-changing (third operator) couplings, respectively. Here χ_1 and χ_2 denote a dark matter particle and a heavier, *un*stable dark-sector state, respectively (i.e., $m_{\chi_2} > m_{\chi_1}$), and the third term allows (boosted) χ_1 to up-scatter to this χ_2 (i.e., an "inelastic" scattering process).

This model introduces five new free parameters that may be varied for our sensitivity analysis: dark photon mass m_V, DM mass m_{χ_1}, heavier dark-sector state mass m_{χ_2}, kinetic mixing parameter ϵ, dark-sector diagonal coupling $\alpha_{11} = g_{11}^2/(4\pi)$, and dark-sector off-diagonal coupling $\alpha_{12} = g_{12}^2/(4\pi)$. We shall perform our analyses with some of the parameters fixed to certain values for illustration.

Benchmark Model ii) This model employs a leptophobic Z' mediator for interactions with the nucleons. The interaction lagrangian for this model is

$$\mathcal{L}_{\rm int} \supset -g_{Z'} \sum_f Z'_\mu \bar{q}_f \gamma^\mu \gamma^5 q_f - g_{Z'} Z'_\mu \bar{\chi} \gamma^\mu \gamma^5 \chi - Q_\psi g_{Z'} Z'_\mu \bar{\psi} \gamma^\mu \gamma^5 \psi. \quad (8.14)$$

Here, all couplings are taken to be axial. f denotes the quark flavors in the SM sector. The dark matter states are denoted by χ and ψ with $m_\chi < m_\psi$. The coupling $g_{Z'}$ and the masses of the dark matter states are free parameters. Q_ψ is taken to be less than 1 and determines the abundance of dark matter in the universe. The hadronic interaction model study presented here is complementary to and has different phenomenology compared to others such as Benchmark Model i). The study of this benchmark model and the result are discussed in Section 8.8.4.

8.8.2 Search for Low-Mass Dark Mater at the Near Detector

8.8.2.1 Dark Matter Production and Detection

Here, we focus on Benchmark Model i) from Eq. (8.13), specifically where only one DM particle $\chi \equiv \chi_1$ exists. We also define the dark fine structure constant $\alpha_D \equiv g_{11}^2/4\pi$. We assume that χ is a fermionic thermal relic – in this case, the DM/dark photon masses and couplings will provide a target for which the relic abundance matches the observed abundance in the universe. Here, the largest flux of dark photons V and DM to reach the DUNE ND will come from the decays of light pseudoscalar mesons (specifically π^0 and η mesons) that are produced in the DUNE target, as well as proton bremsstrahlung processes $p + p \to p + p + V$. For the entirety of this analysis, we will fix $\alpha_D = 0.5$ and assume that the DM mass M_χ is lighter than half the mass of a pseudoscalar meson $\mathfrak{m}$ that is produced in the DUNE target. In this scenario, χ is produced via two decays, those of on-shell V and those of off-shell V. This production is depicted in Figure 8.16.

The flux of DM produced via meson decays – via on-shell V – may be estimated by[6]

$$N_\chi = 2 N_{\rm POT} c_{\mathfrak{m}} {\rm Br}(\mathfrak{m} \to \gamma\gamma) \left[2\varepsilon^2 \left(1 - \frac{M_V^2}{m_{\rm m}^2} \right)^3 \right] {\rm Br}(V \to \chi\bar{\chi}) g(M_\chi, M_V), \quad (8.15)$$

where $N_{\rm POT}$ is the number of protons on target delivered by the beam, $c_{\mathfrak{m}}$ is the average number of meson $\mathfrak{m}$ produced per POT, the term in braces is the relative branching fraction of $\mathfrak{m} \to \gamma V$ relative to $\gamma\gamma$, and $g(x, y)$ characterizes the geometrical acceptance fraction of DM reaching the DUNE ND. $g(x, y)$ is determined given model parameters using Monte Carlo techniques. For the range of dark photon and DM masses in which DUNE will set a competitive limit, the DM flux due to meson decays will dominate over the flux due to proton bremsstrahlung. Considering DM masses in the ∼1-300 MeV range, this will require production via the π^0 and η mesons. Our simulations using PYTHIA determine that $c_{\pi^0} \approx 4.5$ and $c_\eta \approx 0.5$.

If the DM reaches the near detector, it may scatter elastically off nucleons or electrons in the detector, via a t-channel dark photon. Due to its smaller backgrounds, we focus on scattering off

[6] See Ref. [460] for a complete derivation of these expressions, including those for meson decays via off-shell V.

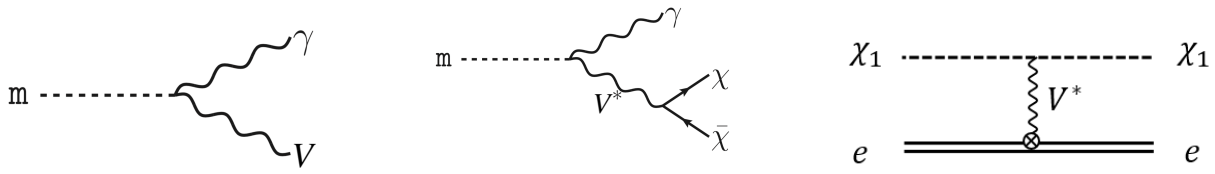

Figure 8.16: Production of fermionic DM via two-body pseudoscalar meson decay $\mathfrak{m} \to \gamma V$, when $M_V < m_{\mathfrak{m}}$ (left) or via three-body decay $\mathfrak{m} \to \gamma\chi\overline{\chi}$ (center) and DM-electron elastic scattering (right panel).

electrons, depicted in the right panel of Figure 8.16. The differential cross section of this scattering, as a function of the recoil energy of the electron E_e, is

$$\frac{d\sigma_{\chi e}}{dE_e} = 4\pi\epsilon^2\alpha_D\alpha_{EM}\frac{2m_eE_\chi^2 - (2m_eE_\chi + m_\chi^2)(E_e - m_e)}{(E_e^2 - m_\chi^2)(m_V^2 + 2m_eE_e - 2m_e^2)^2}\,, \tag{8.16}$$

where E_χ is the incoming DM χ energy. The signal is an event with only one recoil electron in the final state. We may use the scattering angle and energy of the electron to distinguish between signal and background (discussed in the following) events.

8.8.2.2 Background Considerations

The background to the process shown in the right panel of Figure 8.16 consists of any processes involving an electron recoil. As the ND is located near the surface, background events, in general, can be induced by cosmic rays as well as by neutrinos generated from the beam. Since majority of cosmic-induced, however, will be vetoed by triggers and timing information, the dominant background will be from neutrinos coming in the DUNE beam.

The two neutrino-related backgrounds are $\nu_\mu - e^-$ scattering, which looks nearly identical to the signal, and ν_e CCQE scattering, which does not. The latter has a much larger rate ($\sim$ 10 times higher) than the former, however, we expect that using the kinematical variable $E_e\theta_e^2$ of the final state, where θ_e is the direction of the outgoing electron relative to the beam direction, will allow the ν_e CCQE background to be vetoed effectively.

While spectral information regarding E_e could allow a search to distinguish between χe and $\nu_\mu e$ scattering, we expect that uncertainties in the ν_μ flux (both in terms of overall normalization and shape as a function of neutrino energy) will make such an analysis very complicated. For this reason, we include a normalization uncertainty of 10% on the expected background rate and perform a counting analysis. Studies are ongoing to determine how such an analysis may be improved.

For this analysis we have assumed 3.5 years of data collection each in neutrino and antineutrino modes, analyzing events that occur within the fiducial volume of the DUNE near detector. We compare results assuming either all data is collected with the ND on-axis, or data collection is divided equally among all off-axis positions, 0.7 yr at each position i, between 0 and 24 m transverse to the beam direction (in steps of 6 meters). We assume three sources of uncertainty:

statistical, correlated systematic, and an uncorrelated systematic in each bin. For a correlated systematic uncertainty, we include a nuisance parameter A that modifies the number of neutrino-related background events in all bins – an overall normalization uncertainty across all off-axis locations. We further include an additional term in our test statistic for A, a Gaussian probability with width $\sigma_A = 10\%$. We also include an uncorrelated uncertainty in each bin, which we assume to be much narrower than σ_A. We assume this uncertainty to be parameterized by a Gaussian with width $\sigma_{f_i} = 1\%$. After marginalizing over the corresponding uncorrelated nuisance parameters, the test statistic reads

$$-2\Delta\mathcal{L} = \sum_i \frac{r_i^m \left(\left(\frac{\varepsilon}{\varepsilon_0}\right)^4 N_i^\chi + (A-1)N_i^\nu \right)^2}{A\left(N_i^\nu + (\sigma_{f_i} N_i^\nu)^2\right)} + \frac{(A-1)^2}{\sigma_A^2}. \tag{8.17}$$

In Eq. (8.17), N_i^χ is the number of DM scattering events, calculated assuming ε is equal to some reference value $\varepsilon_0 \ll 1$. N_i^ν is the number of $\nu_\mu e^-$ scattering events expected in detector position i, and r_i^m is the number of years of data collection in detector position i during beam mode m (neutrino or antineutrino mode). If data are only collected on-axis, then this test statistic will be dominated by the systematic uncertainty associated with σ_A. If on- and off-axis measurements are combined, then the resulting sensitivity will improve significantly.

8.8.2.3 Sensitivity Calculation and Results

We compute the expected DUNE sensitivity assuming all data collected with the ND on-axis (DUNE On-axis) or equal times at each ND off-axis position (DUNE-PRISM). We present results in terms of the DM or dark photon mass and the parameter Y, where

$$Y \equiv \varepsilon^2 \alpha_D \left(\frac{M_\chi}{M_V}\right)^4. \tag{8.18}$$

Assuming $M_V \gg M_\chi$, this parameter determines the relic abundance of DM in the universe today, and sets a theoretical goal in terms of sensitivity reach. We present the 90% CL sensitivity reach of the DUNE ND in Figure 8.17. We assume $\alpha_D = 0.5$ in our simulations and we display the results fixing $M_V = 3M_\chi$ (left panel) and $M_\chi = 20$ MeV (right panel). We also compare the sensitivity reach of this analysis with other existing experiments, shown as grey shaded regions. We further show for comparison the sensitivity curve expected for a proposed dedicated experiment to search for LDM, LDMX-Phase I [461] (solid blue).

From our estimates, we see that DUNE can significantly improve the constraints from LSND [462] and the MiniBooNE-DM search [50], as well as BaBar [463] if $M_V \lesssim 200$ MeV. We also show limits in the right panel from beam-dump experiments (where the dark photon is assumed to decay visibly if $M_V < 2M_\chi$) [464, 465, 466, 467, 468, 469], as well as the lower limits obtained from matching the thermal relic abundance of χ with the observed one (black).

The features in the sensitivity curve in the right panel can be understood by looking at the DM production mechanism. For a fixed χ mass, as M_V grows, the DM production goes from off-shell to on-shell and back to off-shell. The first transition explains the strong feature near

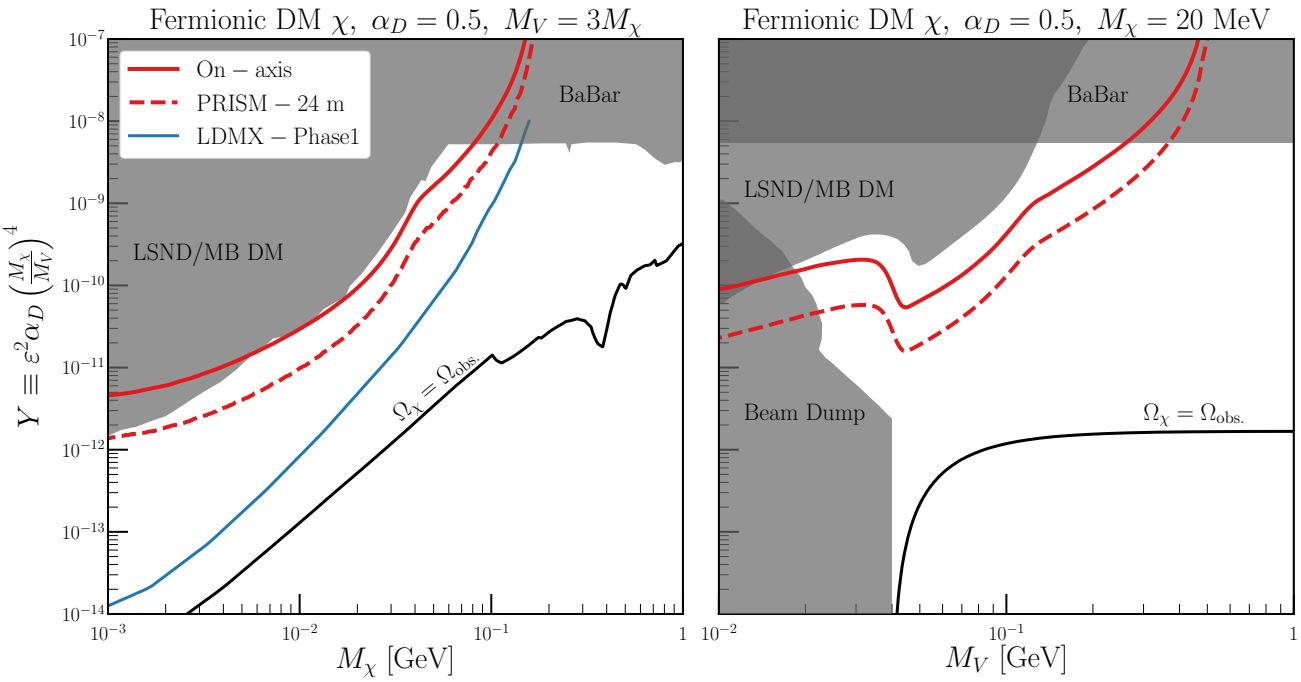

Figure 8.17: Expected DUNE On-axis (solid red) and PRISM (dashed red) sensitivity using $\chi e^- \to \chi e^-$ scattering. We assume $\alpha_D = 0.5$ in both panels, and $M_V = 3M_\chi$ ($M_\chi = 20$ MeV) in the left (right) panel, respectively. Existing constraints are shown in grey, and the relic density target is shown as a black line. We also show for comparison the sensitivity curve expected for LDMX-Phase I (solid blue) [461].

$M_V = 2M_\chi = 40$ MeV, while the second is the source for the slight kink around $M_V = m_{\pi^0}$ (which appears also in the left panel).

8.8.3 Inelastic Boosted Dark Matter Search at the DUNE FD

8.8.3.1 BDM Flux from the Galactic Halo

As we mentioned in Section 8.1, we look at an annihilating two-component DM scenario [333] in this study. The heavier DM (denoted χ_0) plays a role of cosmological DM and pair-annihilates to a pair of lighter DM particles (denoted χ_1) in the universe today. The expected flux near the Earth is given by [78, 458, 336]

$$\mathcal{F}_1 = \ 1.6 \times 10^{-6} \mathrm{cm}^{-2}\mathrm{s}^{-1} \times \left(\frac{\langle\sigma v\rangle_{0\to1}}{5\times10^{-26}\mathrm{cm}^3\mathrm{s}^{-1}}\right) \times \left(\frac{10\,\mathrm{GeV}}{m_{\chi_0}}\right)^2 , \tag{8.19}$$

where m_{χ_0} is the mass of χ_0 and $\langle\sigma v\rangle_{0\to1}$ stands for the velocity-averaged annihilation cross section of $\chi_0\bar{\chi}_0 \to \chi_1\bar{\chi}_1$ in the current universe. To evaluate the reference value shown as the first prefactor, we take $m_{\chi_0} = 10$ GeV and $\langle\sigma v\rangle_{0\to1} = 5 \times 10^{-26}\mathrm{cm}^3\mathrm{s}^{-1}$, the latter of which is consistent with the current observation of DM relic density assuming χ_0 and its anti-particle $\bar{\chi}_0$ are distinguishable. To integrate all relevant contributions over the entire galaxy, we assume the Navarro-Frenk-White

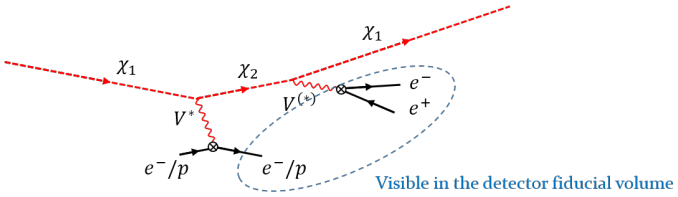

Figure 8.18: The inelastic BDM signal under consideration.

(NFW) DM halo profile [470, 471]. In this section we assume the BDM flux with a m_{χ_0} dependence given by Eq. (8.19) for the phenomenological analysis.

8.8.3.2 Experimental Signatures

The BDM that is created, e.g., at the galactic center, reaches the DUNE FD detectors and scatters off either electrons or protons energetically. In this study, we focus on electron scattering signatures for illustration, under Benchmark Model i) defined in Eq. (8.13). The overall process is summarized as follows:

$$\chi_1 + e^- \to e^- + \chi_2 (\to \chi_1 + V^{(*)} \to \chi_1 + e^+ + e^-)\,, \tag{8.20}$$

and a diagrammatic description is shown in Figure 8.18 where particles visible by the detector are circled in blue. In the final state, there exist three visible particles that usually leave sizable (e-like) tracks in the detectors. Note that we can replace e^- in the left-hand side and the first e^- in the right-hand side of the above process to p for the p-scattering case. In the basic model, Eq. (8.13), and given the source of BDM at the galactic center, the primary signature is quasi-elastic proton recoiling [472] in this case.

8.8.3.3 Background Estimation

As we have identified a possible iBDM signature, we are now in a position to discuss potential SM background events.

For the DUNE detector modules located $\sim$ 1480 m deep underground, the cosmic-induced background discussed earlier is not an issue. The most plausible scenario for background production is the creation of multiple pions that subsequently decay to electrons, positrons, and neutrinos. Relevant channels are the resonance production and/or deep inelastic scattering (DIS) by the CC ν_e or $\bar{\nu}_e$ scattering with a nucleon in the LAr target. Summing up all the resonance production and DIS events that are not only induced by ν_e or $\bar{\nu}_e$ but relevant to production of a few pions, we find that the total number of multi-pion production events is at most ~ 12 kt^{-1}yr^{-1} based on the neutrino flux in Ref. [247] and the cross section in Ref. [473]. In addition, the charged pions often leave appreciable tracks inside the detector so that the probability of misidentifying the $e^\pm$ from the decays of $\pi^\pm$ with the iBDM signal events would be very small. Hence, we conclude that it is fairly reasonable to assume that almost no background events exist.

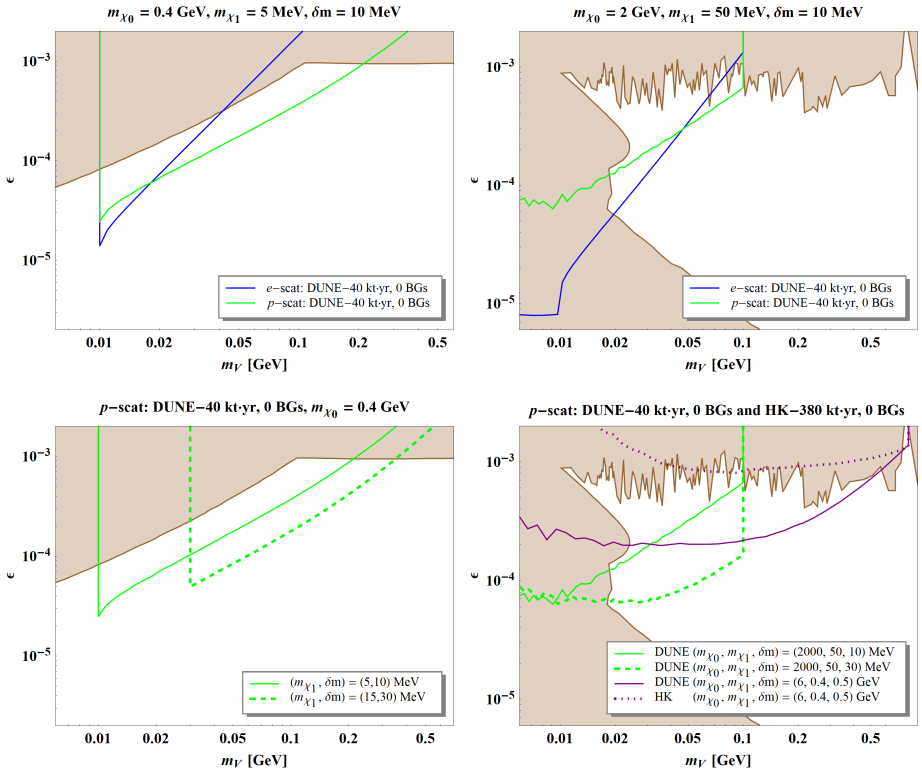

Figure 8.19: The experimental sensitivities in terms of reference model parameters $m_V - \epsilon$ for $m_{\chi_0} = 0.4$ GeV, $m_{\chi_1} = 5$ MeV, and $\delta m = m_{\chi_2} - m_{\chi_1} = 10$ MeV (upper-left panel) and $m_{\chi_0} = 2$ GeV, $m_{\chi_1} = 50$ MeV, and $\delta m = 10$ MeV (upper-right panel). The left panels are for Scenario 1 and the right ones are for Scenario 2. The lower panels compare different reference points in the p-scattering channel. See the text for the details.

8.8.3.4 Phenomenology

We finally present the expected experimental sensitivities at DUNE, in the searches for iBDM. We closely follow the strategies illustrated in Refs. [458, 334, 336] to represent phenomenological interpretations.

In displaying the results, we separate the signal categories into

- Scenario 1: $m_V > 2m_{\chi_1}$, experimental limits for $V \to$ invisible applied.
- Scenario 2: $m_V \leq 2m_{\chi_1}$, experimental limits for $V \to e^+e^-$ invisible applied.

The brown-shaded region shows the latest limits set by various experiments such as the fixed-target experiment NA64 at the CERN SPS and the B-factory experiment BaBar [474]. The blue solid line describes the experimental sensitivity[7] at DUNE FD under a zero background assumption. The associated exposure is $40\,\mathrm{kt} \cdot \mathrm{yr}$, i.e., a total fiducial volume of 40 kilo-ton times 1-year running time. For comparison, we also show the sensitivities of DUNE to the p-scattering signal as a green

[7] This is defined as the boundary of parameter space that can be probed by the dedicated search in a given experiment at 90% CL, practically obtained from Eq. (8.22).

solid line.

Inspired by this potential of searching for the proton scattering channel, we study another reference parameter and compare it with the original one in the lower-left panel of Figure 8.19. We see the reachable ϵ values rise, as m_V increases.

For Scenario 2 (the right panels of Figure 8.19), we choose a different reference parameter set: $m_{\chi_0} = 2$ GeV, $m_{\chi_1} = 50$ MeV, $\delta m = 10$ MeV. The current limits (brown shaded regions), from various fixed target experiments, B-factory experiments, and astrophysical observations, are taken from Ref. [475].

We next discuss model-independent experimental sensitivities. The experimental sensitivities are determined by the number of signal events excluded at 90% CL in the absence of an observed signal. The expected number of signal events, $N_{\rm sig}$, is given by

$$N_{\rm sig} = \sigma_\epsilon \mathcal{F} A(\ell_{\rm lab}) t_{\rm exp} N_T \,, \tag{8.21}$$

where T stands for the target that χ_1 scatters off, σ_ϵ is the cross section of the primary scattering $\chi_1 T \to \chi_2 T$, $\mathcal{F}$ is the flux of χ_1, $t_{\rm exp}$ is the exposure time, and $A(\ell_{\rm lab})$ is the acceptance that is defined as 1 if the event occurs within the fiducial volume and 0 otherwise. Here we determine the acceptance for an iBDM signal by the distance between the primary and secondary vertices in the laboratory frame, $\ell_{\rm lab}$, so $A(\ell_{\rm lab}) = 1$ when both the primary and secondary events occur inside the fiducial volume. (Given this definition, obviously, $A(\ell_{\rm lab}) = 1$ for elastic BDM.) Our notation σ_ϵ includes additional realistic effects from cuts, threshold energy, and the detector response, hence it can be understood as the fiducial cross section.

The 90% CL exclusion limit, N_s^{90}, can be obtained with a modified frequentist construction [476, 477]. We follow the methods in Refs. [478, 479, 480] in which the Poisson likelihood is assumed. An experiment becomes sensitive to the signal model independently if $N_{\rm sig} \geq N_s^{90}$. Plugging Eq. (8.21) here, we find the experimental sensitivity expressed by

$$\sigma_\epsilon \mathcal{F} \geq \frac{N_s^{90}}{A(\ell_{\rm lab}) t_{\rm exp} N_T} \,. \tag{8.22}$$

Since $\ell_{\rm lab}$ differs event-by-event, we take the maximally possible value of laboratory-frame mean decay length, i.e., $\bar{\ell}_{\rm lab}^{\rm max} \equiv \gamma_{\chi_2}^{\rm max} \bar{\ell}_{\rm rest}$ where $\gamma_{\chi_2}^{\rm max}$ is the maximum boost factor of χ_2 and $\bar{\ell}_{\rm rest}$ is the rest-frame mean decay length. We emphasize that this is a rather conservative approach, because the acceptance A is inversely proportional to $\ell_{\rm lab}$. We then show the experimental sensitivity of any kind of experiment for a given background expectation, exposure time, and number of targets, in the plane of $\bar{\ell}_{\rm lab}^{\rm max} - \sigma_\epsilon \cdot \mathcal{F}$. The left panel of Figure 8.20 demonstrates the expected model-independent sensitivities at the DUNE experiment. The green (blue) line is for the DUNE FD with a background-free assumption and 20 (40) kt·yr exposure.

The right panel of Figure 8.20 reports model-dependent sensitivities for $\bar{\ell}_{\rm lab}^{\rm max} = 0$ m and 100 m corresponding to the experiments in the left panel. Note that this method of presentation is reminiscent of the widely known scheme for showing the experimental reaches in various DM direct detection experiments, i.e., $m_{\rm DM} - \sigma_{\rm DM-target}$ where $m_{\rm DM}$ is the mass of DM and $\sigma_{\rm DM-target}$ is the cross section between the DM and target. For the case of non-relativistic DM scattering in the

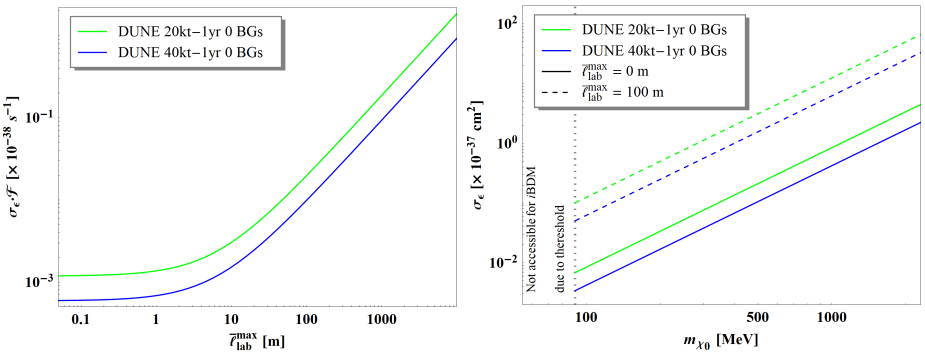

Figure 8.20: Left: model-independent experimental sensitivities of iBDM search in $\bar{\ell}^{\rm max}_{\rm lab} - \sigma_\epsilon \cdot \mathcal{F}$ plane. The reference experiments are DUNE 20kt (green), and DUNE 40kt (blue) with zero-background assumption for 1-year time exposure. Right: Experimental sensitivities of iBDM search in $m_{\chi_0} - \sigma_\epsilon$ plane. The sensitivities for $\bar{\ell}^{\rm max}_{\rm lab} = 0$ m and 100 m are shown as solid and dashed lines for each reference experiment in the left panel.

direct-detection experiments, $m_{\rm DM}$ determines the kinetic energy scale of the incoming DM, just like m_{χ_0} sets out the incoming energy of boosted χ_1 in the iBDM search.

8.8.4 Elastic Boosted Dark Matter from the Sun

8.8.4.1 Introduction and theoretical framework

In this section, we focus on the Benchmark Model ii) discussed in Section 8.8.1. This study represents the first assessment of sensitivity to this model in DUNE using DUNE's full event generation and detector simulation. We focus on BDM flux sourced by DM annihilation in the core of the sun. DM particles can be captured through their scattering with the nuclei within the sun, mostly hydrogen and helium. This makes the core of the sun a region with concentrated DM distribution. The BDM flux is

$$\Phi = f \frac{A}{4\pi D^2}, \tag{8.23}$$

where A is the annihilation rate, and $D = 1\,\text{AU}$ is the distance from the sun. f is a model-dependent parameter, where $f = 2$ for two-component DM as considered here.

For the parameter space of interest, assuming that the DM annihilation cross section is not too small, the DM distribution in the sun has reached an equilibrium between capture and annihilation. This helps to eliminate the annihilation cross section dependence in our study. The chain of processes involved in giving rise to the boosted DM signal from the Sun is illustrated in Fig. 8.21.

Two additional comments are in order. First, the DM particles cannot be too light, i.e., lighter than 4 GeV [481, 482], otherwise we will lose most of the captured DM through evaporation rather than annihilation; this would dramatically reduce the BDM flux. Additionally, one needs to check

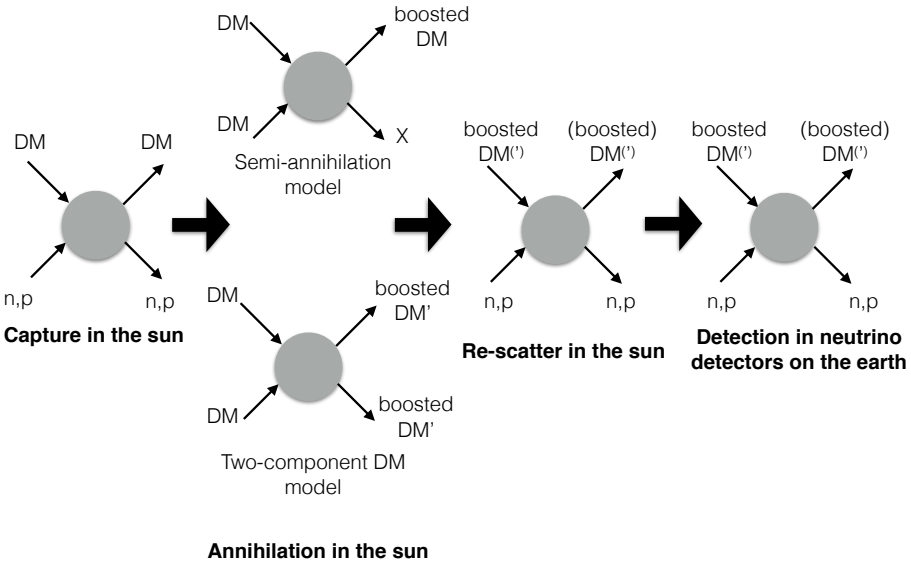

Figure 8.21: The chain of processes leading to boosted DM signal from the sun. The semi-annihilation and two-component DM models refer to the two examples of the non-minimal dark-sector scenarios introduced in the beginning of Section 8.8. DM' denotes the lighter DM in the two-component DM model. X is a lighter dark sector particle that may decay away.

that BDM particles cannot lose energy and potentially be recaptured by scattering with the solar material when they escape from the core region after production. Rescattering is found to be rare for the benchmark models considered in this study and we consider the BDM flux to be monochromatic at its production energy.

The event rate to be observed at DUNE is

$$R = \Phi \times \sigma_{\mathrm{SM}-\chi} \times \varepsilon \times N, \tag{8.24}$$

where Φ is the flux given by Eq. (8.23), $\sigma_{\mathrm{SM}-\chi}$ is the scattering cross section of the BDM off of SM particles, ε is the efficiency of the detection of such a process, and N is the number of target particles in DUNE. The computation of the flux of BDM from the sun can be found in [79].

The processes of typical BDM scattering in argon are illustrated in Fig. 8.22. We generate the signal events and calculate interaction cross sections in the detector using a newly developed BDM module [70, 176, 483] that includes elastic and deep inelastic scattering, as well as a range of nuclear effects. This conservative event generation neglects the dominant contributions from baryon resonances in the final state hadronic invariant mass range of 1.2 to 1.8 GeV, which should not have a major effect on our main results. The interactions are taken to be mediated by an axial, flavor-universal Z' coupling to both the BDM and with the quarks. The axial charge is taken to be 1. The events are generated for the 10 kt DUNE detector module [484], though we only study the dominant scattering off of the ^{40}Ar atoms therein. The method for determining the efficiency ε is described below. The number of target argon atoms is $N = 1.5 \times 10^{32}$ assuming a target mass of 10 kt.

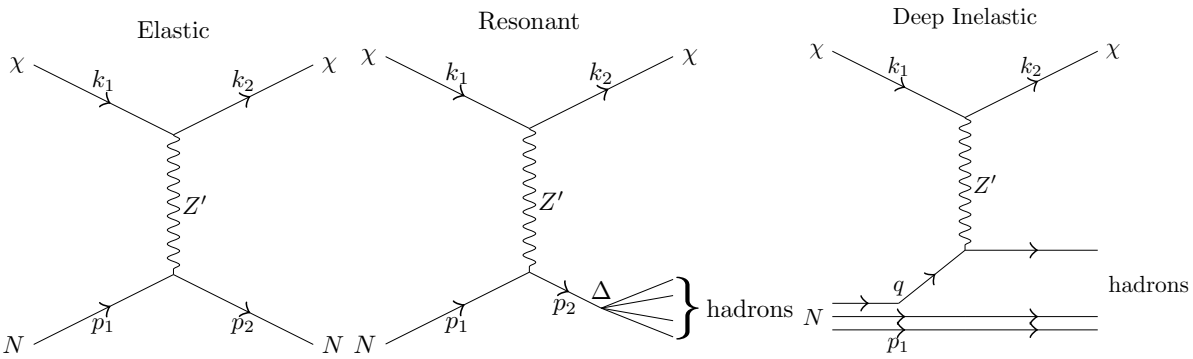

Figure 8.22: Diagram illustrating each of the three processes contributing to dark matter scattering in argon: elastic (left), baryon resonance (middle), and deep inelastic (right).

8.8.4.2 Background Estimation

The main background in this process comes from the NC interactions of atmospheric neutrinos and argon, as they share the features that the timing of events is unknown in advance, and that the interactions with argon produce hadronic activity in the detector. We use GENIE [70, 176] interfaced by the Liquid Argon Software (LArSoft) toolkit to generate the NC atmospheric neutrino events, and obtain 845 events in a 10 kt module for one year of exposure.

8.8.4.3 Detector Response

The finite detector resolution is taken into account by smearing the direction of the stable final state particles, including protons, neutrons, charged pions, muons, electrons, and photons, with the expected angular resolution, and by ignoring the ones with kinetic energy below detector threshold, using the parameters reported in the DUNE CDR [199]. We form as the observable the total momentum from all the stable final state particles, and obtain its angle with respect to the direction of the sun. The sun position is simulated with the SolTrack package [485] including the geographical coordinates of the DUNE FD [486]. We consider both the scenarios in which we can reconstruct neutrons and in which neutrons will not be reconstructed. Figure 8.23 shows the angular distributions of the BDM signals with mass of 10 GeV and different boost factors, and of the background events.

To increase the signal fraction in our samples, we select events with $\cos\theta > 0.6$, and obtain the selection efficiency ε for different BDM models. We predict that 104.0 ± 0.7 and 79.4 ± 0.6 background events per year, in the scenarios with and without neutrons respectively, survive the selection in a DUNE 10 kt module.

8.8.4.4 Results

The resulting expected sensitivity is presented in Figure 8.24 in terms of the DM mass and the Z' gauge coupling for potential DM boosts of $\gamma = 1.25, 2, 10$ and for a fixed mediator mass of

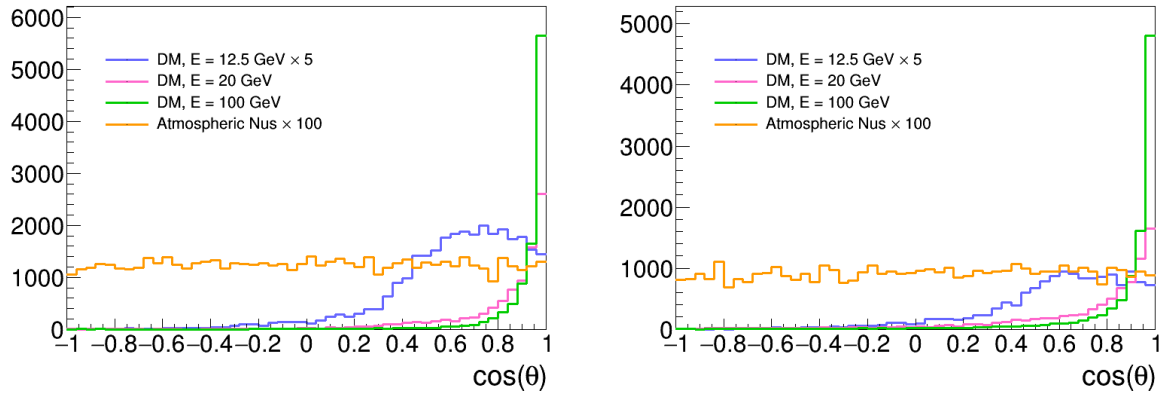

Figure 8.23: Angular distribution of the BDM signal events for a BDM mass of 10 GeV and different boosted factors, γ, and of the atmospheric neutrino NC background events. θ represents the angle of the sum over all the stable final state particles as detailed in the text. The amount of background represents one-year data collection, magnified by a factor 100, while the amount of signal reflects the detection efficiency of 10,000 Monte Carlo (MC) events, as described in this note. The left plot shows the scenario where neutrons can be reconstructed, while the right plot represents the scenario without neutrons.

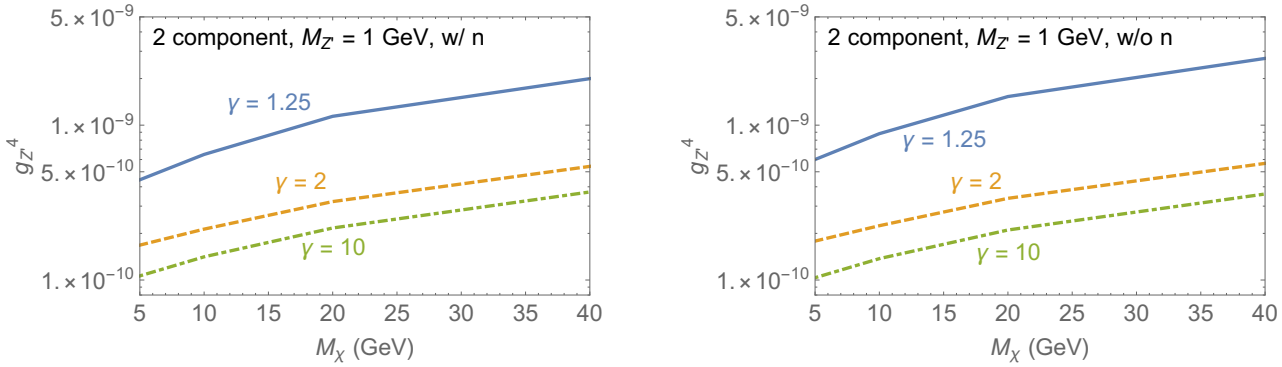

Figure 8.24: Expected 5σ discovery reach with one year of DUNE livetime for one 10 kt module including neutrons in reconstruction (left) and excluding neutrons (right).

$m_{Z'} = 1$ GeV. We assume a DUNE livetime of one year for one 10 kt module. The models presented here are currently unconstrained by direct detection searches if the thermal relic abundance of the DM is chosen to fit current observations. Figure 8.25 compares the sensitivity of 10 years of data collected in DUNE (40 kton) to re-analyses of the results from other experiments, including Super Kamiokande [487] and DM direct detection, PICO-60 [488] and PandaX [489].

8.8.5 Discussion and Conclusions

In this work, we have conducted simulation studies of the dark matter models described in Eqs. (8.13) and (8.14) in terms of their detection prospects at the DUNE ND and FD. Thanks to its relatively low threshold and strong particle identification capabilities, DUNE presents an opportunity to significantly advance the search for LDM and BDM beyond what has been possible

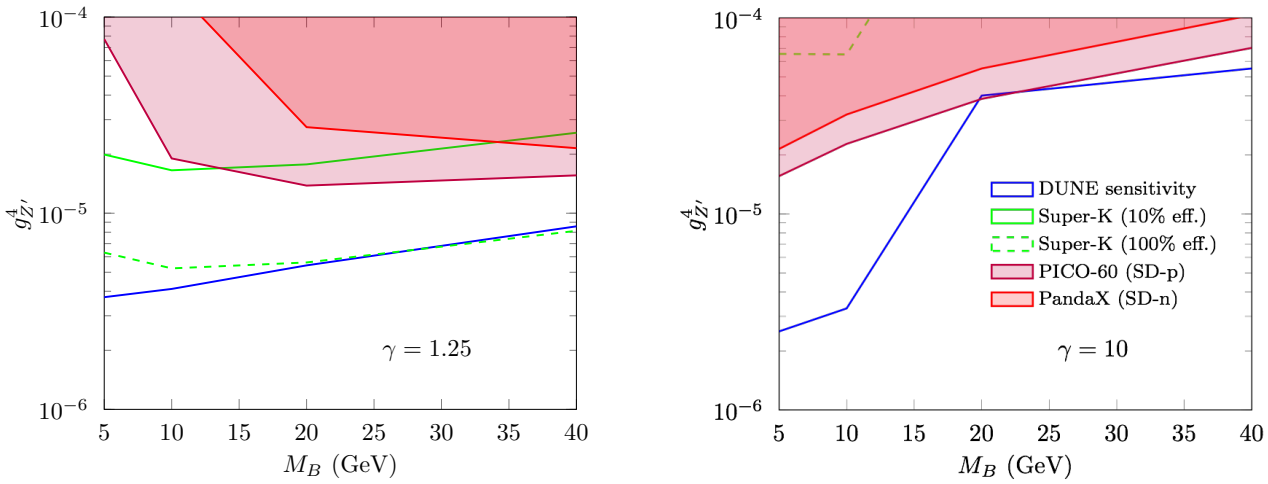

Figure 8.25: Comparison of sensitivity of DUNE for 10 years of data collection and 40 kton of detector mass with Super Kamiokande, assuming 10% and 100% of the selection efficiency on the atmospheric neutrino analysis in Ref. [487], and with the reinterpretations of the current results from PICO-60 [488] and PandaX [489]. The samples with two boosted factors, $\gamma = 1.25$ (left) and $\gamma = 10$ (right), are also presented.

with water Cherenkov detectors.

In the case of the ND, we assumed that the relativistic DM is being produced directly at the target and leaves an experimental signature through an elastic electron scattering. Using two constrained parameters of the light DM model and a range of two free parameters, a sensitivity map was produced. Within the context of the vector portal DM model and the chosen parameter constraints along with the electron scattering as the signal event, this result sets stringent limits on DM parameters that are comparable or even better than recent experimental bounds in the sub-GeV mass range.

By contrast, in the case of the FD modules, we assumed that the signal events are due to DM coming from the galactic halo and the sun with a significant boost factor. For the *in*elastic scattering case, the DM scatters off either an electron or proton in the detector material into a heavier unstable dark-sector state. The heavier state, by construction, decays back to DM and an electron-positron pair via a dark-photon exchange. Therefore, in the final state, a signal event comes with an electron or proton recoil plus an electron-positron pair. This distinctive signal feature enabled us to perform (almost) background-free analyses. As ProtoDUNE detectors are prototypes of DUNE FD modules, the same study was conducted and corresponding results were compared with the ones of the DUNE FD modules. We first investigated the experimental sensitivity in a dark-photon parameter space, dark-photon mass m_V versus kinetic mixing parameter ϵ. The results were shown separately for Scenario 1 and 2. They suggest that ProtoDUNE and DUNE FD modules would probe a broad range of unexplored regions; they would allow for reaching $\sim 1-2$ orders of magnitude smaller ϵ values than the current limits along MeV to sub-GeV-range dark photons. We also examined model-independent reaches at both ProtoDUNE detectors and DUNE FD modules, providing limits for models that assume the existence of iBDM (or iBDM-like) signals (i.e., a target recoil and a fermion pair).

For the elastic scattering case, we considered the case in which BDM comes from the sun. With one year of data, the 5σ sensitivity is expected to reach a coupling of $g^4_{Z'} = 9.57 \times 10^{-10}$ for a boost of 1.25 and $g^4_{Z'} = 1.49 \times 10^{-10}$ for a boost of 10 at a DM mass of 10 GeV without including neutrons in the reconstruction.

8.9 Other BSM Physics Opportunities

8.9.1 Tau Neutrino Appearance

With only 19 ν_τ-CC and $\bar{\nu}_\tau$-CC candidates detected with high purity, we have less direct experimental knowledge of tau neutrinos than of any other SM particle. Of these, nine ν_τ-CC and $\bar{\nu}_\tau$-CC candidate events with a background of 1.5 events, observed by the DONuT experiment [490, 491], were directly produced though D_S meson decays. The remaining 10 ν_τ-CC candidate events with an estimated background of two events, observed by the OPERA experiment [492, 493], were produced through the oscillation of a muon neutrino beam. From this sample, a 20% measurement of Δm^2_{32} was performed under the assumption that $\sin^2 2\theta_{23} = 1$. The Super–Kamiokande and IceCube experiments developed methods to statistically separate samples of ν_τ-CC and $\bar{\nu}_\tau$-CC events in atmospheric neutrinos to exclude the no-tau-neutrino appearance hypothesis at the 4.6σ level and 3.2σ level respectively [494, 495, 496], but limitations of Cherenkov detectors constrain the ability to select a high-purity sample and perform precision measurements.

The DUNE experiment has the possibility of significantly improving the experimental situation. Tau-neutrino appearance can potentially improve the discovery potential for sterile neutrinos, NC NSI, and non-unitarity. For model independence, the first goal should be measuring the atmospheric oscillation parameters in the ν_τ appearance channel and checking the consistency of this measurement with those performed using the ν_μ disappearance channel. A truth-level study of ν_τ selection in atmospheric neutrinos in a large, underground LArTPC detector suggested that ν_τ-CC interactions with hadronically decaying τ-leptons, which make up 65% of total τ-lepton decays [25], can be selected with high purity [497]. This analysis suggests that it may be possible to select up to 30% of ν_τ-CC events with hadronically decaying τ-leptons with minimal neutral current background. Under these assumptions, we expect to select $\sim$25 ν_τ-CC candidates per year using the CPV optimized beam. The physics reach of this sample has been studied in Ref. [498]. As shown in Figure 8.26 (left), this sample is sufficient to simultaneously constrain Δm^2_{31} and $\sin^2 2\theta_{23}$. Independent measurements of Δm^2_{31} and $\sin^2 2\theta_{23}$ in the ν_e appearance, ν_μ disappearance, and ν_τ appearance channels should allow DUNE to constrain $|U_{e3}|^2 + |U_{\mu 3}|^2 + |U_{\tau 3}|^2$ to 6% [498], a significant improvement over current constraints [53].

However, all of the events in the beam sample occur at energies higher than the first oscillation maximum due to kinematic constraints. Only seeing the tail of the oscillation maximum creates a partial degeneracy between the measurement of Δm^2_{31} and $\sin^2 2\theta_{23}$. Atmospheric neutrinos, due to sampling a much larger L/E range, allow for measuring both above and below the first oscillation maximum with ν_τ appearance. Although we only expect to select $\sim$70 ν_τ-CC and $\bar{\nu}_\tau$-CC candidates in 350 kt-year in the atmospheric sample, as shown in Figure 8.26 (right), a direct

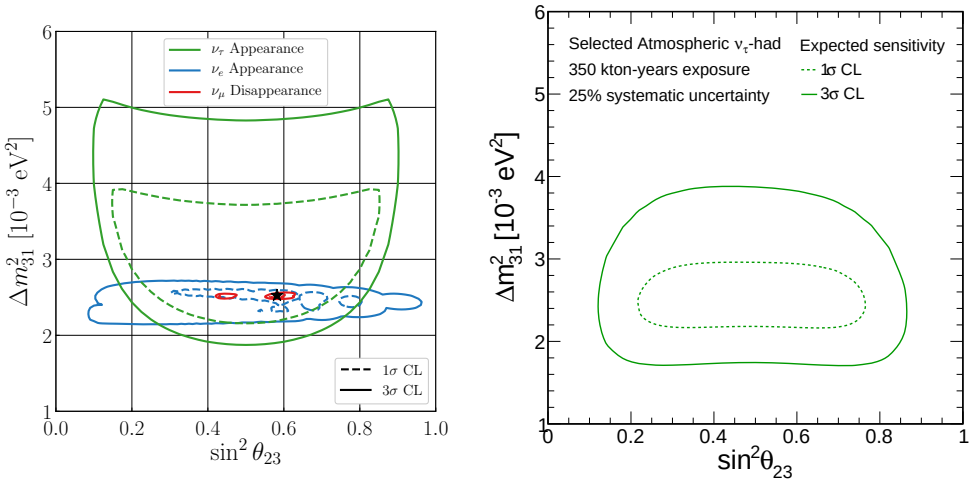

Figure 8.26: The 1σ (dashed) and 3σ (solid) expected sensitivity for measuring Δm^2_{31} and $\sin^2\theta_{23}$ using a variety of samples. Left: The expected sensitivity for seven years of beam data collection, assuming 3.5 years each in neutrino and antineutrino modes, measured independently using ν_e appearance (blue), ν_μ disappearance (red), and ν_τ appearance (green). Adapted from Ref. [498]. Right: The expected sensitivity for the ν_τ appearance channel using 350 kton-years of atmospheric exposure.

measurement of the oscillation maximum breaks the degeneracy seen in the beam sample. The complementary shapes of the beam and atmospheric constraints combine to reduce the uncertainty on $\sin^2\theta_{23}$, directly leading to improved unitarity constraints. Finally, a high-energy beam option optimized for ν_τ appearance should produce ~150 selected ν_τ-CC candidates in one year. These higher energy events are further in the tail of the first oscillation maximum, but they will permit a simultaneous measurement of the ν_τ cross section. When analyzed within the non-unitarity framework described in Section 8.4, the high-energy beam significantly improves constraints on the parameter α_{33} due to increased matter effects [498].

8.9.2 Large Extra-Dimensions

DUNE can search for or constrain the size of large extra-dimensions by looking for distortions of the oscillation pattern predicted by the three-flavor paradigm. These distortions arise through mixing between the right-handed neutrino Kaluza-Klein modes, which propagate in the compactified extra dimensions, and the active neutrinos, which exist only in the four-dimensional brane [499, 500, 501]. Such distortions are determined by two parameters in the model, specifically R, the radius of the circle where the extra-dimension is compactified, and m_0, defined as the lightest active neutrino mass (m_1 for normal mass ordering, and m_3 for inverted mass ordering). Searching for these distortions in, for instance, the ν_μ CC disappearance spectrum, should provide significantly enhanced sensitivity over existing results from the MINOS/MINOS+ experiment [502].

Figure 8.27 shows a comparison between the DUNE and MINOS [502] sensitivities to LED at 90% CL for two degrees of freedom represented by the solid and dashed lines, respectively. In the case of DUNE, an exposure of 300 kt MW year was assumed and spectral information from

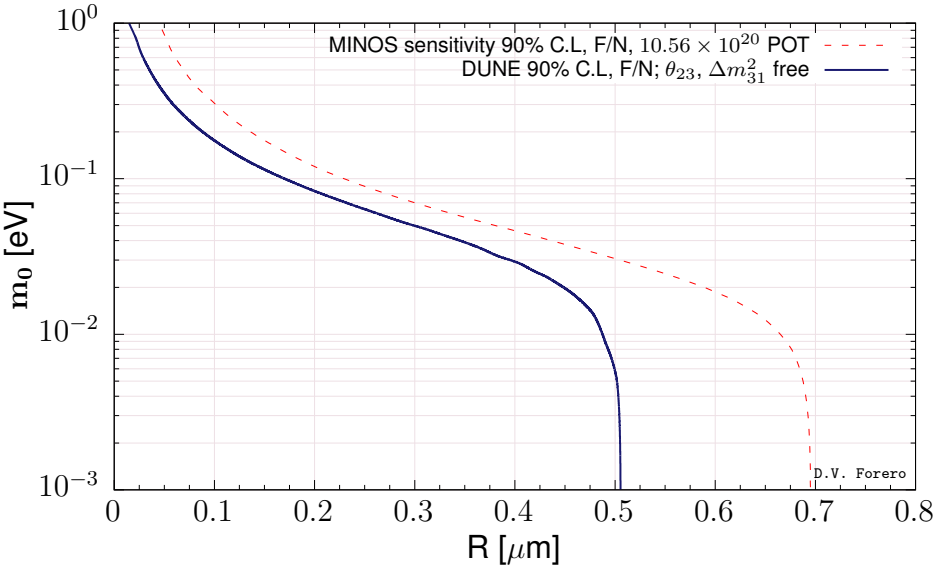

Figure 8.27: Sensitivity to the LED model in Ref. [499, 500, 501] through its impact on the neutrino oscillations expected at DUNE. For comparison, the MINOS sensitivity [502] is also shown.

the four oscillation channels, (anti)neutrino appearance and disappearance, were included in the analysis. The muon (anti)neutrino fluxes, cross sections for the neutrino interactions in argon, detector energy resolutions, efficiencies and systematical errors were taken into account by the use of GLoBES files prepared for the DUNE LBL studies. In the analysis, we assumed DUNE simulated data as compatible with the standard three neutrino hypothesis (which corresponds to the limit $R \to 0$) and we have tested the LED model. The solar parameters were kept fixed, and also the reactor mixing angle, while the atmospheric parameters were allowed to float free. In general, DUNE improves over the MINOS sensitivity for all values of m_0 and this is more noticeable for $m_0 \sim 10^{-3}$ eV, where the most conservative sensitivity limit to R is obtained.

8.9.3 Heavy Neutral Leptons

The high intensity of the LBNF neutrino beam and the production of charm and bottom mesons in the beam enables DUNE to search for a wide variety of lightweight long-lived, exotic particles, by looking for topologies of rare event interactions and decays in the fiducial volume of the DUNE ND. These particles include weakly interacting heavy neutral leptons (HNLs), such as right-handed partners of the active neutrinos, light super-symmetric particles, or vector, scalar, and/or axion portals to a Hidden Sector containing new interactions and new particles. Assuming these heavy neutral leptons are the lighter particles of their hidden sector, they will only decay into SM particles. The parameter space explored by the DUNE ND extends into the cosmologically relevant region complementary to the LHC heavy-mass dark-matter searches through missing energy and mono-jets.

Thanks to small mixing angles, the particles can be stable enough to travel from the baseline to the detector and decay inside the active region. It is worth noting that, differently from a light neutrino beam, an HNL beam is not polarized, due to their large mass. The correct description of

the helicity components in the beam is important for predicting the angular distributions of HNL decays, as they might depend on the initial helicity state. More specifically, there is a different phenomenology if the decaying HNL is a Majorana or a Dirac fermion [503, 504]. Typical decay channels are two-body decays into a charged lepton and a pseudo-scalar meson, or a vector meson if the mass allows it, two-body decays into neutral mesons, and three-body leptonic decays.

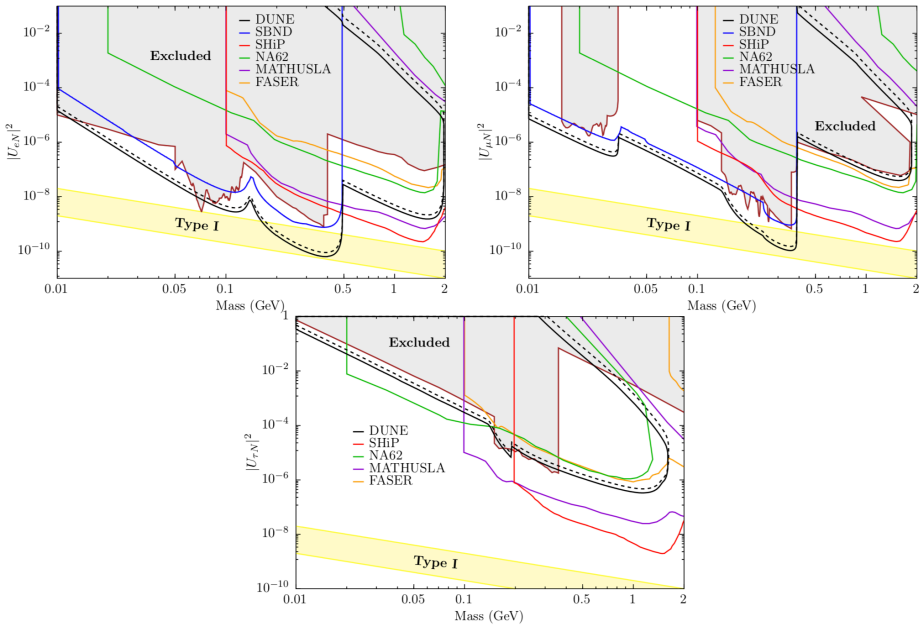

Figure 8.28: The 90 % CL sensitivity regions for dominant mixings $|U_{eN}|^2$ (top left), $|U_{\mu N}|^2$ (top right), and $|U_{\tau N}|^2$ (bottom) are presented for DUNE ND (black) [504]. The regions are a combination of the sensitivity to HNL decay channels with good detection prospects.These are $N \to \nu ee$, $\nu e\mu$, $\nu\mu\mu$, $\nu\pi^0$, $e\pi$, and $\mu\pi$.The study is performed for Majorana neutrinos (solid) and Dirac neutrinos (dashed), assuming no background. The region excluded by experimental constraints (grey/brown) is obtained by combining the results from PS191 [505, 506], peak searches [507, 508, 509, 510, 511], CHARM [512], NuTeV [513], DELPHI [514], and T2K [515]. The sensitivity for DUNE ND is compared to the predictions of future experiments, SBN [516] (blue), SHiP [517] (red), NA62 [518] (green), MATHUSLA [519] (purple), and the Phase II of FASER [520]. For reference, a band corresponding to the contribution light neutrino masses between 20 meV and 200 meV in a single generation see-saw type I model is shown (yellow). Larger values of the mixing angles are allowed if an extension to see-saw models is invoked, for instance, in an inverse or extended see-saw scheme.

A recent study illustrates the potential sensitivity for HNLs searches with the DUNE Near Detector [504]. The sensitivity for HNL particles with masses in the range of 10 MeV to 2 GeV, from decays of mesons produced in the proton beam dump that produces the pions for the neutrino beam production, was studied. The production of D_s mesons leads to access to high mass HNL production. The dominant HNL decay modes to SM particles have been included, and basic detector constraints as well as the dominant background process have been taking into account.

The experimental signature for these decays is a decay-in-flight event with no interaction vertex, typical of neutrino–nucleon scattering, and a rather forward direction with respect to the beam. The main background to this search comes from SM neutrino–nucleon scattering events in which

the hadronic activity at the vertex is below threshold. Charged current quasi-elastic events with pion emission from resonances are background to the semi-leptonic decay channels, whereas mis-identification of long pion tracks into muons can constitute a background to three-body leptonic decays. Neutral pions are often emitted in neutrino scattering events and can be a challenge for decays into neutral meson or channels with electrons in the final state.

We report in Fig. 8.28 the physics reach of the DUNE ND in its current configuration without backgrounds and for a Majorana and a Dirac HNL. The sensitivity was estimated assuming a total of 1.32 x 10^{22} POT, i.e. for a running scenario with 6 years with a 80 GeV proton beam of 1.2 MW, followed by six years of a beam with 2.4 MW, but using only the neutrino mode configuration, which corresponds to half of the total runtime. As a result, HNLs with masses up to 2 GeV can be searched for in all flavor-mixing channels.

The results show that DUNE will have an improved sensitivity to small values of the mixing parameters $|U_{\alpha N}|^2$, where $\alpha = e$, μ, τ, compared to the presently available experimental limits on mixing of HNLs with the three lepton flavors. At 90% CL sensitivity, DUNE can probe mixing parameters as low as $10^{-9} - 10^{-10}$ in the mass range of 300-500 MeV, for mixing with the electron or muon neutrino flavors. In the region above 500 MeV the sensitivity is reduced to 10^{-8} for eN mixing and 10^{-7} for μN mixing. The τN mixing sensitivity is weaker but still covering a new unexplored regime. A large fraction of the covered parameter space for all neutrino flavors falls in the region that is relevant for explaining the baryon asymmetry in the universe.

Studies are ongoing with full detector simulations to validate these encouraging results.

8.9.4 Dark Matter Annihilation in the Sun

DUNE's large FD LArTPC modules provide an excellent setting to conduct searches for neutrinos arising from DM annihilation in the core of the sun. These would typically result in a high-energy neutrino signal almost always accompanied by a low-energy neutrino component, which has its origin in a hadronic cascade that develops in the dense solar medium and produces large numbers of light long-lived mesons, such as π^+ and K^+ that then stop and decay at rest. The decay of each π^+ and K^+ will produce monoenergetic neutrinos with an energy 30 MeV or 236 MeV, respectively. The 236 MeV flux can be measured with the DUNE FD, thanks to its excellent energy resolution, and importantly, will benefit from directional information. By selecting neutrinos arriving from the direction of the sun, large reduction in backgrounds can be achieved. This directional resolution for sub-GeV neutrinos will enable DUNE to be competitive with experiments with even larger fiducial masses, but less precise angular information, such as Hyper-K [521].

8.10 Conclusions and Outlook

DUNE will be a powerful discovery tool on a variety of physics topics under very active exploration today, from the potential discovery of new particles beyond those predicted in the SM, to precision

neutrino measurements that may uncover deviations from the present three-flavor mixing paradigm and unveil new interactions and symmetries. The ND alone will offer excellent opportunities to search for light DM and mixing with light sterile neutrinos, and to measure rare processes such as neutrino trident interactions. Besides looking for deviations from the three-flavor oscillation paradigm such as nonstandard interactions, DUNE's massive high-resolution FD will probe the possible existence of BDM. The flexibility of the LBNF beamline enables planning for high-energy beam running, providing access to probing and measuring tau neutrino physics with unprecedented precision.

DUNE will offer a long-term privileged setting for collaboration between experimentalists and theorists in the domain areas of neutrino physics, astrophysics, and cosmology, and will provide the highest potential for breakthrough discoveries among the new near-term facilities projected to start operations during the next decade.

Glossary

35 ton prototype A prototype cryostat and single-phase (SP) detector built at Fermilab before the ProtoDUNE detectors. 113, 114

analog-to-digital converter (ADC) A sampling of a voltage resulting in a discrete integer count corresponding in some way to the input. 74, 76–79, 92, 93, 106

anode plane assembly (APA) A unit of the SP detector module containing the elements sensitive to ionization in the LAr. It contains two faces each of three planes of wires, and interfaces to the cold electronics and photon detection system. 28, 29, 32, 59–61, 83, 103, 114, 116, 120, 150, 245

ArgonCube The name of the core part of the Deep Underground Neutrino Experiment (DUNE) near detector (ND), a liquid argon time-projection chamber (LArTPC). 32, 33, 35

ArgoNeuT The ArgoNeuT test-beam experiment and LArTPC prototype at Fermi National Accelerator Laboratory (Fermilab). 28, 157

art A software framework implementing an event-based execution paradigm. 85

ASIC application-specific integrated circuit. 77

AU astronomical unit. 278

boosted dark matter (BDM) A new model that describes a relativistic dark matter particle boosted by the annihilation of heavier dark matter participles in the galactic center or the sun. 243, 244, 269, 270, 274–283, 288

boosted decision tree (BDT) A method of multivariate analysis. 89, 184, 199–201, 203, 204, 207, 208

baryon-number violating (BNV) Describing an interaction where baryon number is not conserved. 46, 47

BSM beyond the standard model. 52, 56, 72, 205, 213, 242, 244, 245, 283

Bugey Neutrino experiment that operated at the Bugey nuclear power plant in France. 55

CAFAna Common Analysis File Analysis. 160, 161

charged current (CC) Refers to an interaction between elementary particles where a charged weak force carrier (W^+ or W^-) is exchanged. 9, 70, 92, 98, 127, 129, 130, 145, 146, 149–156, 158, 162, 178, 179, 184, 198–200, 203, 208, 222, 223, 226, 242–244, 246, 247, 249, 250, 256, 265, 275, 283, 284

conceptual design report (CDR) A formal project document that describes the experiment at a conceptual level. 155, 159, 224, 249, 254, 257, 280

European Organization for Nuclear Research (CERN) The leading particle physics laboratory in Europe and home to the ProtoDUNEs. (In French, the Organisation Européenne pour la Recherche Nucléaire, derived from Conseil Européen pour la Recherche Nucléaire. 27, 122

conventional facilities (CF) Pertaining to construction and operation of buildings and conventional infrastructure, and for LBNF and DUNE project (LBNF/DUNE), CF includes the excavation caverns. 26

computational fluid dynamics (CFD) High performance computer-assisted modeling of fluid dynamical systems. 114

Cabibbo-Kobayashi-Maskawa matrix (CKM matrix) Refers to the matrix describing the mixing between mass and weak eigenstates of quarks. 126

confidence level (CL) Refers to a probability used to determine the value of a random variable given its distribution. 48, 192, 203, 205, 208, 210, 249–252, 254, 256, 259, 266, 268, 276, 277, 284, 286, 287

convolutional neural network (CNN) A deep learning technique most commonly applied to analyzing visual imagery. 78, 92, 152, 199, 200, 207, 210

carbon nitrogen oxygen (CNO) The CNO cycle (for carbon-nitrogen-oxygen) is one of the two known sets of fusion reactions by which stars convert hydrogen to helium, the other being the proton-proton chain reaction (pp-chain reaction). In the CNO cycle, four protons fuse, using carbon, nitrogen, and oxygen isotopes as catalysts, to produce one alpha particle, two positrons and two electron neutrinos. 239

charge parity (CP) Product of charge and parity transformations. 5, 9, 32, 62, 70, 122, 125, 212, 244, 254, 255, 259, 260, 262

cathode plane assembly (CPA) The component of the SP detector module that provides the drift HV cathode. 60, 103, 104, 114, 116, 150

charge, parity, and time reversal symmetry (CPT) product of charge, parity and time-reversal

transformations. 5, 213, 237, 238, 243, 260–264

charge-parity symmetry violation (CPV) Lack of symmetry in a system before and after charge and parity transformations are applied. For CP symmetry to hold, a particle turns into its corresponding antiparticle under a charge transformation, and a parity transformation inverts its space coordinates, i.e., produces the mirror image. 4, 5, 8, 9, 11, 15, 16, 39, 62, 110, 122, 124–126, 128, 159, 161, 165, 167, 171, 244, 254–256, 260, 283

charge-readout plane (CRP) In the dual-phase (DP) technology, a collection of electrodes in a planar arrangement placed at a particular voltage relative to some applied E field such that drifting electrons may be collected and their number and time may be measured. 29

central utility cavern (CUC) The utility cavern at the 4850L of Sanford Underground Research Facility (SURF) located between the two detector caverns. It contains utilities such as central cryogenics and other systems, and the underground data center and control room. 26

convolutional visual network (CVN) An algorithm for identifying neutrino interactions based on their topology and without the need for detailed reconstruction algorithms. 92, 151–156

data acquisition (DAQ) The data acquisition system accepts data from the detector front-end (FE) electronics, buffers the data, performs a trigger decision, builds events from the selected data and delivers the result to the offline secondary DAQ buffer. 115, 118, 121, 225, 241

Daya Bay a neutrino-oscillation experiment in Daya Bay, China, designed to measure the mixing angle Θ_{13} using antineutrinos produced by the reactors of the Daya Bay and Ling Ao nuclear power plants. 55

detector module The entire DUNE far detector is segmented into four modules, each with a nominal 10 kt fiducial mass. 26, 27, 30, 31, 60, 95, 112, 114, 116, 118, 119, 150, 275

deep inelastic scattering (DIS) Refers to the interaction of an elementary charged particle with a nucleus in an energy range where the interaction can be modeled as taking place with individual nucleons. 206, 275

dark matter (DM) The term given to the unknown matter or force that explains measurements of galaxy motion that are otherwise inconsistent with the amount of mass associated with the observed amount of photon production. 53, 72, 111, 243, 244, 267–274, 277, 278, 280–283, 287, 288

DOE U.S. Department of Energy. 24

dual-phase (DP) Distinguishes one of the DUNE far detector technologies by the fact that it operates using argon in both gas and liquid phases. 27, 29, 30, 109, 111, 245

DP module dual-phase DUNE far detector (FD) module. 27, 30, 31, 109, 115, 119, 241

diffuse supernova neutrino background (DSNB) The term describing the pervasive, constant flux of neutrinos due to all past supernova neutrino bursts. 240

Deep Underground Neutrino Experiment (DUNE) A leading-edge, international experiment for neutrino science and proton decay studies. 2, 24, 26–33, 35, 39, 109, 110, 122, 124, 125, 138, 142, 146, 148, 150, 152–154, 156, 159–162, 171, 178, 181, 187, 192, 193, 196, 198, 199, 204, 205, 207, 210–214

DUNE Precision Reaction-Independent Spectrum Measurement (DUNE-PRISM) a mobile near detector that can perform measurements over a range of angles off-axis from the neutrino beam direction in order to sample many different neutrino energy distributions. 32, 35

electromagnetic calorimeter (ECAL) A detector component that measures energy deposition of traversing particles (in the near detector conceptual design). 32, 33, 35, 143–145, 180

elastic scattering (ES) Events in which a neutrino elastically scatters off of another particle. 226, 228, 230

field cage (FC) The component of a LArTPC that contains and shapes the applied E field. 27, 29, 30, 109, 115

far detector (FD) The 70 kt total (40 kt fiducial) mass LArTPC DUNE detector, composed of four 17.5 kt total (10 kt fiducial) mass modules, to be installed at the far site at SURF in Lead, SD, USA. 2, 3, 7, 17, 20, 21, 24, 26, 29, 30, 32, 33, 59, 60, 62, 65, 70, 78, 82–84, 86, 88, 89, 94, 95, 105, 109–111, 115, 118, 127, 131, 132, 138, 142, 148–150, 152, 156–160, 162, 178, 181, 182, 184–189, 192, 193, 203, 204, 211, 212, 214, 242–252, 256, 269, 275–277, 280–282, 287, 288

front-end (FE) The front-end refers a point that is "upstream" of the data flow for a particular subsystem. For example the SP front-end electronics is where the cold electronics meet the sense wires of the TPC and the front-end data acquisition (DAQ) is where the DAQ meets the output of the electronics. 74, 76, 119

Fermi National Accelerator Laboratory (Fermilab) U.S. national laboratory in Batavia, IL. It is the laboratory that hosts DUNE and serves as its near site. 24, 26, 27, 127, 142

FHC forward horn current (ν_μ mode). 145, 146, 153, 154, 184, 188

final-state interactions (FSI) Refers to interactions between elementary or composite particles subsequent to the initial, fundamental particle interaction, such as may occur as the products exit a nucleus. 132, 137, 141, 150, 194, 196, 198, 200, 201, 205–207

gaseous argon time-projection chamber (GArTPC) A time projection chamber (TPC) filled with gaseous argon; a possible technology choice for the ND. 143, 157

geometry description markup language (GDML) An application-indepedent, geometry-description format based on XML. 245

Geant4 A software toolkit for the simulation of the passage of particles through matter using Monte Carlo (MC) methods. 73, 74, 127, 144, 150, 244

Generates Events for Neutrino Interaction Experiments (GENIE) Software providing an object-oriented neutrino interaction simulation resulting in kinematics of the products of the interaction. 71, 72, 127, 132–140, 142, 144, 150, 184, 187, 188, 193–196, 206, 207, 211, 244, 246, 265, 280

General Long-Baseline Experiment Simulator (GLoBES) A software package for simulating energy spectra of neutrino flux, interactions, and energy spectra measured after application of some model of a detector response). 159, 224, 245, 246, 248, 249, 254, 257

grand unified theory (GUT) A class of theories that unifies the electro-weak and strong forces. 47, 49, 191, 192

high-pressure gas (HPG) gas at high pressure to be used in a high-pressure gaseous argon TPC (HPgTPC). 144, 145, 180

high-pressure gaseous argon TPC (HPgTPC) A TPC filled with gaseous argon; a possible component of the DUNE ND. 32, 33

high voltage (HV) Generally describes a voltage applied to drive the motion of free electrons through some media, e.g., LAr. 27, 114, 116, 119

Hyper Kamiokande (HyperK) 260 kt water Cerenkov neutrino detector to begin construction at Kamiokande in 2020. 49

ICARUS A neutrino experiment that was located at the Laboratori Nazionali del Gran Sasso (LNGS) in Italy, then refurbished at European Organization for Nuclear Research (CERN) for re-use in the same neutrino beam from Fermilab used by the MiniBooNE, MicroBooNE and SBND experiments. The ICARUS detector is being reassembled at Fermilab. 27

inverted ordering (IO) Refers to the neutrino mass eigenstate ordering whereby the sign of the mass squared difference associated with the atmospheric neutrino problem is negative. 234, 236

liquid argon (LAr) Argon in its liquid phase; it is a cryogenic liquid with a boiling point of $-90\,^{\circ}\mathrm{C}$ (87 K) and density of 1.4 g/ml. 24, 26–28, 31–33, 109, 111, 115, 116, 118, 142–145, 148, 149, 157–159, 162, 179–182, 193, 197, 211, 221

LArIAT The repurposed ArgoNeuT LArTPC, modified for use in a charged particle beam, dedicated to the calibration and precise characterization of the output response of these detectors.

28, 157

Liquid Argon Software (LArSoft) A shared base of physics software across LArTPC experiments. 70, 72, 74, 85, 89, 92, 93, 222, 223, 225, 280

liquid argon time-projection chamber (LArTPC) A TPC filled with liquid argon; the basis for the DUNE FD modules. 2, 14, 24, 26–30, 32, 33, 35, 72, 88, 109, 113, 115, 118, 142, 148–150, 152–154, 156, 157, 191, 193, 194, 197, 204, 239, 240, 245, 267

long-baseline (LBL) Refers to the distance between the neutrino source and the FD. It can also refer to the distance between the near and far detectors. The "long" designation is an approximate and relative distinction. For DUNE, this distance (between Fermilab and SURF) is approximately 1300 km. 4, 65, 109–111, 116, 247

Long-Baseline Neutrino Facility (LBNF) The organizational entity responsible for developing the neutrino beam, the cryostats and cryogenics systems, and the conventional facilities for DUNE. 24, 26, 127, 128

light-mass dark matter (LDM) Refers to dark matter particles with mass values much lower than the electroweak scale, specifically below the 1 GeV level. 243, 269, 270, 273, 281

large electron multiplier (LEM) A micro-pattern detector suitable for use in ultra-pure argon vapor; LEMs consist of copper-clad PCB boards with sub-millimeter-size holes through which electrons undergo amplification. 27, 29

Liquid Scintilator Neutrino Detector (LSND) A scintillation detector and associated experiment located at Los Alamos National Laboratory. 54, 55, 252

Model of Argon Reaction Low Energy Yields (MARLEY) Developed at UC Davis, MARLEY is the first realistic model of neutrino electron interactions on argon for enegies less than 50 MeV. This includes the energy range important for supernova neutrino burst (SNB) neutrinos and also solar 8–boron neutrinos. 17, 222–225, 232

Monte Carlo (MC) Refers to a method of numerical integration that entails the statistical sampling of the integrand function. Forms the basis for some types of detector and physics simulations. 71, 72, 83, 98, 101–104, 106–108, 153, 160, 161, 194, 199, 218, 281

Monte Carlo Particle (MCParticle) Individual true simulated particle. 94–97

mass hierarchy (MH) Describes the separation between the mass squared differences related to the solar and atmospheric neutrino problems. 125

MicroBooNE The LArTPC-based MicroBooNE neutrino oscillation experiment at Fermilab. 27, 28, 88, 111, 112, 114, 116, 117, 157, 158

MINERvA The MINERvA neutrino cross sections experiment at Fermilab. 157, 158

MINOS A long-baseline neutrino experiment, with a near detector at Fermilab and a far detector in the Soudan mine in Minnesota, designed to observe the phenomena of neutrino oscillations (ended data runs in 2012). 156

MINOS+ The successor to the MINOS experiment, utilizing the same detectors and beam line, but operating at higher beam energy tune than MINOS, parasitic with NOvA. 55

minimum ionizing particle (MIP) Refers to a particle traversing some medium such that the particle's mean energy loss is near the minimum. 20, 114

multi-purpose detector (MPD) A component of the near detector conceptual design; it is a magnetized system consisting of a HPgTPC and a surrounding electromagnetic calorimeter (ECAL). 32, 33, 35, 142, 143, 145, 148, 157–159, 179, 181

Mikheyev-Smirnov-Wolfenstein effect (MSW) Explains the oscillatory behavior of neutrinos produced inside the sun as they traverse the solar matter. 211, 233, 234, 236, 237, 239, 256

neutral current (NC) Refers to an interaction between elementary particles where a neutrally charged weak force carrier (Z^0) is exchanged. 9, 92, 96, 111, 127, 130, 146, 150, 153, 155, 179, 206, 208, 222, 242, 244, 246, 247, 249–251, 256, 257, 280, 283

near detector (ND) Refers to the detector(s) installed close to the neutrino source at Fermilab. 24, 26, 32, 33, 35, 65, 68, 109, 120, 131, 132, 138, 142, 144, 148, 149, 156–159, 162, 163, 177, 178, 181, 182, 184–189, 242–245, 247–252, 256, 264–269, 271–273, 281, 282, 285, 288

neutrino interaction generator (NEUT) A neutrino interaction simulation program library for the studies of atmospheric accelerator neutrinos. 132

normal ordering (NO) Refers to the neutrino mass eigenstate ordering whereby the sign of the mass squared difference associated with the atmospheric neutrino problem is positive. 234, 236

NOvA The NOvA off-axis neutrino oscillation experiment at Fermilab. 152, 154, 157, 160

nonstandard interaction (NSI) A general class of theory of elementary particles other than the Standard Model. 243, 248, 256–260, 283

NuFIT 4.0 The NuFIT 4.0 global fit to neutrino oscillation data. 9, 125, 127, 162, 166, 168, 169, 172, 174, 179–181, 183, 184

NuWro neutrino interaction generator. 132, 133, 184

Pandora The Pandora multi-algorithm approach to pattern recognition. 78, 85–88, 94, 95, 97, 101–105, 151

principal component analysis (PCA) A statistical procedure that uses an orthogonal transfor-

mation to convert a set of observations of possibly correlated variables into a set of values of linearly uncorrelated variables called principal components (Wikipedia). 105, 162, 163

photon detector (PD) The detector elements involved in measurement of the number and arrival times of optical photons produced in a detector module. 27–29, 61, 73, 77, 78, 93, 94, 150

photon detection system (PD system) The detector subsystem sensitive to light produced in the LAr. 113, 118, 119, 204, 245

PDG Particle Data Group. 194, 214

particle flow particle (PFParticle) Each of the individual reconstructed particles in the hierarchy (or particle flow) describing the reconstructed event interaction. 85, 94, 95

particle ID (PID) Particle identification. 78, 110, 111, 197, 198, 200

Proton Improvement Plan II (PIP-II) A Fermilab project for improving the protons on target delivered delivered by the Long-Baseline Neutrino Facility (LBNF) neutrino production beam. This is version two of this plan and it is planned to be followed by a PIP-III. 26

Projection Matching Algorithm (PMA) A reconstruction algorithm that combines 2D reconstructed objects to form a 3D representation. 78, 89, 151, 196, 207

Pontecorvo-Maki-Nakagawa-Sakata (PMNS) A type of matrix that describes the mixing between mass and weak eigenstates of the neutrino. 122, 123, 126, 242, 253, 256, 257, 262

photomultiplier tube (PMT) A device that makes use of the photoelectric effect to produce an electrical signal from the arrival of optical photons. 30, 31

protons on target (POT) Typically used as a unit of normalization for the number of protons striking the neutrino production target. 6, 248

ProtoDUNE Either of the two DUNE prototype detectors constructed at CERN. One prototype implements SP technology and the other DP. 28, 31, 83, 107, 109–111, 113, 115, 119, 120, 157, 244, 270, 282

ProtoDUNE-DP The DP ProtoDUNE detector at CERN. 31

ProtoDUNE-SP The SP ProtoDUNE detector at CERN. 12, 31, 32, 76, 77, 79–81, 85, 88, 89, 91, 92, 94, 101, 106–108, 154

quasi-elastic (QE) Refers to interaction between elementary particles and a nucleus in an energy range where the interaction can be modeled as occurring between constituent quarks of one nucleon and resulting in no bulk recoil of the resulting nucleus. 198, 200

RHC reverse horn current ($\overline{\nu}_\mu$ mode). 152, 153, 184, 188

random phase approximation (RPA) an approximation method commonly used for describing the dynamic linear electronic response of electron systems (Wikipedia). 134

signal-to-noise (S/N) signal-to-noise ratio. 20, 27, 32

System for on-Axis Neutrino Detection (SAND) The beam monitor component of the near detector that remains on-axis at all times and serves as a dedicated neutrino spectrum monitor. 32, 34, 35, 142, 143, 179, 180

Short-Baseline Neutrino (SBN) A Fermilab program consisting of three collaborations, MicroBooNE, SBND, and ICARUS, to perform sensitive searches for ν_e appearance and ν_μ disappearance in the Booster Neutrino Beam. 252

SBND The Short-Baseline Near Detector experiment at Fermilab. 27

signal feedthrough chimney (SFT chimney) In the DP technology, a volume above the cryostat penetration used for a signal feedthrough. 30

silicon photomultiplier (SiPM) A solid-state avalanche photodiode sensitive to single photoelectron signals. 28, 73, 77, 93

standard model (SM) Refers to a theory describing the interaction of elementary particles. 46, 47, 56–58, 122, 123, 191, 242, 243, 253, 255, 265–270, 275, 279, 283, 285, 287

standard-model extension (SME) an effective field theory that contains the standard model (SM), general relativity, and all possible operators that break Lorentz symmetry (Wikipedia). 213, 214, 237

supernova neutrino burst (SNB) A prompt increase in the flux of low-energy neutrinos emitted in the first few seconds of a core-collapse supernova. It can also refer to a trigger command type that may be due to this phenomenon, or detector conditions that mimic its interaction signature. 4, 15, 17, 59, 70, 71, 109–111, 113, 116, 118, 119, 216

supernova neutrino burst and low energy (SNB/LE) Supernova neutrino burst and low-energy physics program. 216, 222

Sudbury Neutrino Observatory (SNO) The Sudbury Neutrino Observatory was a detector built 6800 feet under ground, in INCO's Creighton mine near Sudbury, Ontario, Canada. SNO was a heavy-water Cherenkov detector designed to detect neutrinos produced by fusion reactions in the sun. 239

SuperNova Observatories with GLoBES (SNOwGLoBES) From the official description [68]: SNOwGLoBES is public software for computing interaction rates and distributions of observed quantities for SNB neutrinos in common detector materials. 216, 221, 222, 224, 225, 231, 232

single-phase (SP) Distinguishes one of the DUNE far detector technologies by the fact that it operates using argon in its liquid phase only. 27–29, 109, 111, 119, 245

SP module single-phase DUNE FD module. 27–29, 31, 109, 119, 241

Super-Kamiokande Experiment sited in the Kamioka-mine, Hida-city, Gifu, Japan that uses a large water Cherenkov detector to study neutrino properties through the observation of solar neutrinos, atmospheric neutrinos and man-made neutrinos. 239

Sanford Underground Research Facility (SURF) The laboratory in South Dakota where the LBNF far site conventional facilities (FSCF) will be constructed and the DUNE FD will be installed and operated. 24–26

supersymmetry (SUSY) Theoretical symmetry between a fermion and a boson. 191

technical design report (TDR) A formal project document that describes the experiment at a technical level. 2, 15, 57, 71, 109, 115, 119, 181, 249

time projection chamber (TPC) A type of particle detector that uses an E field together with a sensitive volume of gas or liquid, e.g., liquid argon (LAr), to perform a 3D reconstruction of a particle trajectory or interaction. The activity is recorded by digitizing the waveforms of current induced on the anode as the distribution of ionization charge passes by or is collected on the electrode. 27, 28, 31–33, 118, 142–145, 149, 158, 162, 179, 180, 193, 196, 204, 222, 228, 239

VALOR A neutrino oscillation fitting framework that is used by T2K; the name stands for VALencia-Oxford-Rutherford, the original three institutions that developed it. 159

WA105 DP demonstrator The $3 \times 1 \times 1\,\mathrm{m}^3$ WA105 DP prototype detector at CERN. 27

weakly-interacting massive particle (WIMP) A hypothesized particle that may be a component of dark matter. 241, 243, 268

Wire-Cell A tomographic automated 3D neutrino event reconstruction method for LArTPCs. 78, 90

References

[1] Particle Physics Project Prioritization Panel, "Building for Discovery; Strategic Plan for U.S. Particle Physics in the Global Context," 2014. http://science.energy.gov/~/media/hep/hepap/pdf/May%202014/FINAL_P5_Report_Interactive_060214.pdf.

[2] I. Esteban, M. C. Gonzalez-Garcia, A. Hernàndez-Cabezudo, M. Maltoni, and T. Schwetz, "Global analysis of three-flavour neutrino oscillations: synergies and tensions in the determination of θ_{23}, δ_{CP}, and the mass ordering," arXiv:1811.05487 [hep-ph].

[3] "Nufit4.0." http://www.nu-fit.org/.

[4] **Super-Kamiokande** Collaboration, K. Abe *et al.*, "Search for proton decay via $p \to \nu K^+$ using 260 kiloton-year data of Super-Kamiokande," *Phys. Rev.* **D90** no. 7, (2014) 072005, arXiv:1408.1195 [hep-ex].

[5] R. Bionta, G. Blewitt, C. Bratton, D. Casper, A. Ciocio, *et al.*, "Observation of a Neutrino Burst in Coincidence with Supernova SN 1987a in the Large Magellanic Cloud," *Phys.Rev.Lett.* **58** (1987) 1494.

[6] **KAMIOKANDE-II** Collaboration, K. Hirata *et al.*, "Observation of a Neutrino Burst from the Supernova SN 1987a," *Phys.Rev.Lett.* **58** (1987) 1490–1493.

[7] **LBNE** Collaboration, C. Adams *et al.*, "The Long-Baseline Neutrino Experiment: Exploring Fundamental Symmetries of the Universe." arXiv:1307.7335 [hep-ex], 2013.

[8] "Final report of the LAGUNA-LBNO design of a pan-European infrastructure for large apparatus studying Grand Unification, Neutrino Astrophysics and Long Baseline Neutrino Oscillations (Funded by European Commission FP7 Research Infrastructures, grant agreement number: 284518)," *Annex* .

[9] **LAGUNA-LBNO** Collaboration, S. Agarwalla *et al.*, "Optimised sensitivity to leptonic CP violation from spectral information: the LBNO case at 2300 km baseline," arXiv:1412.0593 [hep-ph].

[10] **LBNE** Collaboration, M. Bass *et al.*, "Baseline optimization for the measurement of CP violation, mass hierarchy, and θ_{23} octant in a long-baseline neutrino oscillation

experiment," *Phys.Rev.* **D91** no. 5, (2015) 052015, arXiv:1311.0212 [hep-ex].

[11] A. Bernstein *et al.*, "Report on the Depth Requirements for a Massive Detector at Homestake (LBNE:DocDB-34)," arXiv:0907.4183 [hep-ex]. arXiv:0907.4183 [hep-ex].

[12] L. Whitehead, "DUNE Far Detector Task Force Final Report," DUNE doc 3384, 2018. https://docs.dunescience.org/cgi-bin/private/ShowDocument?docid=3384&asof=2019-11-1.

[13] "DUNE Far Detector Task Force Preliminary Report," DUNE doc 1752, 2016. https://docs.dunescience.org/cgi-bin/private/ShowDocument?docid=1752&asof=2019-11-1.

[14] **ArgoNeuT** Collaboration, R. Acciarri *et al.*, "First Observation of Low Energy Electron Neutrinos in a Liquid Argon Time Projection Chamber," *Phys. Rev.* **D95** no. 7, (2017) 072005, arXiv:1610.04102 [hep-ex].

[15] P. Derwent *et al.*, "Proton Improvement Plan-II." http://projectx-docdb.fnal.gov/cgi-bin/RetrieveFile?=1232&filename=1.2%20MW%20Report_Rev5.pdf&version=3, 2013.

[16] S. Amerio *et al.*, "Design, construction and tests of the ICARUS T600 detector," *Nucl. Instrum. Meth. A* no. 527, 329, (2004) .

[17] R. Acciarri *et al.*, "Design and construction of the microboone detector," *Journal of Instrumentation* **12** no. 02, (2017) P02017. http://stacks.iop.org/1748-0221/12/i=02/a=P02017.

[18] C. Anderson, M. Antonello, B. Baller, T. Bolton, C. Bromberg, *et al.*, "The ArgoNeuT Detector in the NuMI Low-Energy beam line at Fermilab," *JINST* **7** (2012) P10019, arXiv:1205.6747 [physics.ins-det].

[19] **LArIAT** Collaboration, F. Cavanna, M. Kordosky, J. Raaf, and B. Rebel, "LArIAT: Liquid Argon In A Testbeam." arXiv:1406.5560, 2014.

[20] **DUNE** Collaboration, B. Abi *et al.*, "The Single-Phase ProtoDUNE Technical Design Report," arXiv:1706.07081 [physics.ins-det].

[21] A. Machado and E. Segreto, "ARAPUCA a new device for liquid argon scintillation light detection," *JINST* **11** (2016) C02004.

[22] H. daMotta, A.A. Machado, L. Paulucci, E. Segreto, B. Gelli, M.R. Guzzo, G. Marques, D. Galante, V. Teixeira, W. Araujo, C. Ambrosio, M.Bissiano and F. Marinho, "ARAPUCA light trap for large liquid argon time projection chambers," *POS* (2017) . https://pos.sissa.it/295/153/pdf.

[23] E. Segreto *et al.*, "Liquid Argon test of the ARAPUCA device," *JINST* **13** no. 08, (2018) P08021, arXiv:1805.00382 [physics.ins-det].

[24] A. de Gouvêa, B. Kayser, and R. N. Mohapatra, "Manifest CP violation from Majorana phases," *Phys. Rev.* **D67** (2003) 053004, arXiv:hep-ph/0211394 [hep-ph].

[25] **Particle Data Group** Collaboration, M. Tanabashi *et al.*, "Review of Particle Physics," *Phys. Rev.* **D98** no. 3, (2018) 030001.

[26] **T2K** Collaboration, K. Abe *et al.*, "Constraint on the Matter-Antimatter Symmetry-Violating Phase in Neutrino Oscillations," arXiv:1910.03887 [hep-ex].

[27] **Belle-II** Collaboration, W. Altmannshofer *et al.*, "The Belle II Physics Book," arXiv:1808.10567 [hep-ex].

[28] S. Antusch, P. Huber, S. F. King, and T. Schwetz, "Neutrino mixing sum rules and oscillation experiments," *JHEP* **04** (2007) 060, arXiv:hep-ph/0702286 [HEP-PH].

[29] P. Ballett, S. F. King, C. Luhn, S. Pascoli, and M. A. Schmidt, "Testing atmospheric mixing sum rules at precision neutrino facilities," *Phys. Rev.* **D89** no. 1, (2014) 016016, arXiv:1308.4314 [hep-ph].

[30] M. Fukugita and T. Yanagida, "Baryogenesis Without Grand Unification," *Phys. Lett.* **B174** (1986) 45.

[31] **Planck** Collaboration, N. Aghanim *et al.*, "Planck 2018 results. VI. Cosmological parameters," arXiv:1807.06209 [astro-ph.CO].

[32] A. D. Sakharov, "Violation of CP Invariance, C asymmetry, and baryon asymmetry of the universe," *Pisma Zh. Eksp. Teor. Fiz.* **5** (1967) 32–35. [Usp. Fiz. Nauk161,no.5,61(1991)].

[33] P. Nath and P. Fileviez Perez, "Proton stability in grand unified theories, in strings and in branes," *Phys.Rept.* **441** (2007) 191–317, arXiv:hep-ph/0601023 [hep-ph].

[34] K. S. Babu *et al.*, "Working Group Report: Baryon Number Violation," in *Proceedings, 2013 Community Summer Study on the Future of U.S. Particle Physics: Snowmass on the Mississippi (CSS2013): Minneapolis, MN, USA, July 29-August 6, 2013*. 2013. arXiv:1311.5285 [hep-ph]. http://www.slac.stanford.edu/econf/C1307292/docs/IntensityFrontier/BaryonNo-13.pdf.

[35] **Super-Kamiokande** Collaboration, K. Abe *et al.*, "Search for nucleon decay into charged antilepton plus meson in 0.316 megaton·years exposure of the Super-Kamiokande water Cherenkov detector," *Phys. Rev.* **D96** no. 1, (2017) 012003, arXiv:1705.07221 [hep-ex].

[36] **Hyper-Kamiokande** Collaboration, K. Abe *et al.*, "Hyper-Kamiokande Design Report," arXiv:1805.04163 [physics.ins-det].

[37] **Super-Kamiokande** Collaboration, K. Abe *et al.*, "Search for proton decay via $p \to e^+\pi^0$ and $p \to \mu^+\pi^0$ in 0.31 megaton·years exposure of the Super-Kamiokande water Cherenkov detector," *Phys. Rev.* **D95** no. 1, (2017) 012004, arXiv:1610.03597 [hep-ex].

[38] **JUNO** Collaboration, Z. Djurcic *et al.*, "JUNO Conceptual Design Report," arXiv:1508.07166 [physics.ins-det].

[39] **JUNO** Collaboration, F. An *et al.*, "Neutrino Physics with JUNO," *J. Phys.* **G43** no. 3, (2016) 030401, arXiv:1507.05613 [physics.ins-det].

[40] D. N. Schramm and J. W. Truran, "New physics from Supernova SN1987A," *Phys. Rept.* **189** (1990) 89–126.

[41] F. Vissani, "Comparative analysis of SN1987A antineutrino fluence," *J. Phys.* **G42** (2015) 013001, arXiv:1409.4710 [astro-ph.HE].

[42] A. Mirizzi, I. Tamborra, H.-T. Janka, N. Saviano, K. Scholberg, R. Bollig, L. Hudepohl, and S. Chakraborty, "Supernova Neutrinos: Production, Oscillations and Detection," *Riv. Nuovo Cim.* **39** no. 1-2, (2016) 1–112, arXiv:1508.00785 [astro-ph.HE].

[43] S. Horiuchi and J. P. Kneller, "What can be learned from a future supernova neutrino detection?," *J. Phys.* **G45** no. 4, (2018) 043002, arXiv:1709.01515 [astro-ph.HE].

[44] K. Scholberg, "Supernova Neutrino Detection," *Ann.Rev.Nucl.Part.Sci.* **62** (2012) 81–103, arXiv:1205.6003 [astro-ph.IM].

[45] **GROND, SALT Group, OzGrav, DFN, INTEGRAL, Virgo, Insight-Hxmt, MAXI Team, Fermi-LAT, J-GEM, RATIR, IceCube, CAASTRO, LWA, ePESSTO, GRAWITA, RIMAS, SKA South Africa/MeerKAT, H.E.S.S., 1M2H Team, IKI-GW Follow-up, Fermi GBM, Pi of Sky, DWF (Deeper Wider Faster Program), Dark Energy Survey, MASTER, AstroSat Cadmium Zinc Telluride Imager Team, Swift, Pierre Auger, ASKAP, VINROUGE, JAGWAR, Chandra Team at McGill University, TTU-NRAO, GROWTH, AGILE Team, MWA, ATCA, AST3, TOROS, Pan-STARRS, NuSTAR, ATLAS Telescopes, BOOTES, CaltechNRAO, LIGO Scientific, High Time Resolution Universe Survey, Nordic Optical Telescope, Las Cumbres Observatory Group, TZAC Consortium, LOFAR, IPN, DLT40, Texas Tech University, HAWC, ANTARES, KU, Dark Energy Camera GW-EM, CALET, Euro VLBI Team, ALMA** Collaboration, B. P. Abbott *et al.*, "Multi-messenger Observations of a Binary Neutron Star Merger," *Astrophys. J.* **848** no. 2, (2017) L12, arXiv:1710.05833 [astro-ph.HE].

[46] P. Antonioli *et al.*, "SNEWS: The SuperNova Early Warning System," *New J. Phys.* **6** (2004) 114, arXiv:astro-ph/0406214.

[47] A. Ankowski *et al.*, "Supernova Physics at DUNE," in *Supernova Physics at DUNE Blacksburg, Virginia, USA, March 11-12, 2016*. 2016. arXiv:1608.07853 [hep-ex].

[48] J. Beacham *et al.*, "Physics Beyond Colliders at CERN: Beyond the Standard Model Working Group Report," arXiv:1901.09966 [hep-ex].

[49] C. A. Argüelles *et al.*, "White Paper on New Opportunities at the Next-Generation

Neutrino Experiments (Part 1: BSM Neutrino Physics and Dark Matter)," arXiv:1907.08311 [hep-ph].

[50] **MiniBooNE DM** Collaboration, A. A. Aguilar-Arevalo *et al.*, "Dark Matter Search in Nucleon, Pion, and Electron Channels from a Proton Beam Dump with MiniBooNE," *Phys. Rev.* **D98** no. 11, (2018) 112004, arXiv:1807.06137 [hep-ex].

[51] **MiniBooNE** Collaboration, A. A. Aguilar-Arevalo *et al.*, "Dark Matter Search in a Proton Beam Dump with MiniBooNE," *Phys. Rev. Lett.* **118** no. 22, (2017) 221803, arXiv:1702.02688 [hep-ex].

[52] M. Pospelov, A. Ritz, and M. B. Voloshin, "Secluded WIMP Dark Matter," *Phys. Lett.* **B662** (2008) 53–61, arXiv:0711.4866 [hep-ph].

[53] S. Parke and M. Ross-Lonergan, "Unitarity and the Three Flavour Neutrino Mixing Matrix," arXiv:1508.05095 [hep-ph].

[54] S. Gariazzo, C. Giunti, M. Laveder, Y. F. Li, and E. M. Zavanin, "Light sterile neutrinos," *J. Phys.* **G43** (2016) 033001, arXiv:1507.08204 [hep-ph].

[55] X. G. He, G. C. Joshi, H. Lew, and R. R. Volkas, "NEW Z-prime PHENOMENOLOGY," *Phys. Rev. D* **43** (1991) 22–24.

[56] X.-G. He, G. C. Joshi, H. Lew, and R. R. Volkas, "Simplest Z-prime model," *Phys. Rev. D* **44** (1991) 2118–2132.

[57] S. Baek, N. G. Deshpande, X. G. He, and P. Ko, "Muon anomalous g-2 and gauged L(muon)- L(tau) models," *Phys. Rev. D* **64** (2001) 055006, arXiv:hep-ph/0104141 [hep-ph].

[58] K. Harigaya, T. Igari, M. M. Nojiri, M. Takeuchi, and K. Tobe, "Muon g-2 and LHC phenomenology in the $L_\mu - L_\tau$ gauge symmetric model," *JHEP* **03** (2014) 105, arXiv:1311.0870 [hep-ph].

[59] **LBNF/DUNE** Collaboration, P. Adamson *et al.*, "Long-Baseline Neutrino Facility (LBNF)/DUNE Conceptual Design Report: Annex 3A_opt." https://docs.dunescience.org/cgi-bin/private/RetrieveFile?docid=4559&filename=CDR_Optimized_Beam_Oct02.pdf&version=12, 2017.

[60] M. Calviani, S. Di Luise, V. Galymov, and P. Velten, "Optimization of neutrino fluxes for future long baseline neutrino oscillation experiments," *Nucl. Part. Phys. Proc.* **273-275** (2016) 2681–2683, arXiv:1411.2418 [physics.ins-det].

[61] **DUNE** Collaboration, Fields, L. and Weber, A. for the Beam Optimization Task Force, "Beam Optimization Task Force Final Report," tech. rep., 2017. https://docs.dunescience.org/cgi-bin/private/ShowDocument?docid=2901.

[62] **MINERvA** Collaboration, L. Aliaga *et al.*, "Neutrino Flux Predictions for the NuMI Beam," *Phys. Rev.* **D94** no. 9, (2016) 092005, arXiv:1607.00704 [hep-ex]. [Addendum: Phys. Rev.D95,no.3,039903(2017)].

[63] L. Aliaga Soplin, *Neutrino Flux Prediction for the NuMI Beamline*. PhD thesis, William-Mary Coll., 2016. http://lss.fnal.gov/archive/thesis/2000/fermilab-thesis-2016-03.pdf.

[64] **NA49** Collaboration, M. Makariev, "Pion production in p + C collisions at 158-GeV/c beam momentum.," *AIP Conf.Proc.* **899** (2007) 203.

[65] K. E. Duffy, *Measurement of the neutrino oscillation parameters* $\sin 2\theta_{23}$, $\Delta m^2 i_{32}$, $\sin 2\theta_{13}$, *and* δ_{CP} *in neutrino and antineutrino oscillation at T2K*. PhD thesis, Oxford U., 2016.

[66] M. Bhattacharya *et al.*, "Neutrino absorption efficiency of an Ar-40 detector from the beta decay of Ti-40," *Phys. Rev.* **C58** (1998) 3677–3687.

[67] J. A. Cameron and B. Singh, "Nuclear Data Sheets for A=40," *Nucl. Data Sheets* **102** (2004) 293–513.

[68] http://www.phy.duke.edu/~schol/snowglobes.

[69] C. V. J. Gava, J. Kneller and G. C. McLaughlin *Phys. Rev. Lett.* **103** (2009) 071101. arXiv:0902.0317 [hep-ph].

[70] C. Andreopoulos *et al.*, "The GENIE Neutrino Monte Carlo Generator," *Nucl. Instrum. Meth.* **A614** (2010) 87–104, arXiv:0905.2517 [hep-ph].

[71] T. Yang, C. Andreopoulos, H. Gallagher, K. Hoffmann, and P. Kehayias, "A Hadronization Model for Few-GeV Neutrino Interactions," *Eur. Phys. J.* **C63** (2009) 1–10, arXiv:0904.4043 [hep-ph].

[72] S. Dytman, "GENIE final state interactions," *AIP Conf. Proc.* **1680** (2015) 020005.

[73] A. Bodek and J. L. Ritchie, "Further Studies of Fermi Motion Effects in Lepton Scattering from Nuclear Targets," *Phys. Rev.* **D24** (1981) 1400.

[74] C. H. Llewellyn Smith, "Neutrino Reactions at Accelerator Energies," *Phys. Rept.* **3** (1972) 261–379.

[75] J. W. Lightbody and J. S. O'Connell, "Modeling single arm electron scattering and nucleon production from nuclei by GeV electrons," *Comput. Phys.* **2** no. 3, (1988) 57.

[76] D. Rein and L. M. Sehgal, "Neutrino Excitation of Baryon Resonances and Single Pion Production," *Annals Phys.* **133** (1981) 79–153.

[77] A. Bodek and U. K. Yang, "Higher twist, xi(omega) scaling, and effective LO PDFs for

lepton scattering in the few GeV region," *J. Phys.* **G29** (2003) 1899–1906, arXiv:hep-ex/0210024 [hep-ex].

[78] K. Agashe, Y. Cui, L. Necib, and J. Thaler, "(In)direct Detection of Boosted Dark Matter," *JCAP* **1410** no. 10, (2014) 062, arXiv:1405.7370 [hep-ph].

[79] J. Berger, Y. Cui, and Y. Zhao, "Detecting Boosted Dark Matter from the Sun with Large Volume Neutrino Detectors," *JCAP* **1502** no. 02, (2015) 005, arXiv:1410.2246 [hep-ph].

[80] K. Kong, G. Mohlabeng, and J.-C. Park, "Boosted dark matter signals uplifted with self-interaction," *Phys. Lett.* **B743** (2015) 256–266, arXiv:1411.6632 [hep-ph].

[81] J. F. Cherry, M. T. Frandsen, and I. M. Shoemaker, "Direct Detection Phenomenology in Models Where the Products of Dark Matter Annihilation Interact with Nuclei," *Phys. Rev. Lett.* **114** (2015) 231303, arXiv:1501.03166 [hep-ph].

[82] J. Kopp, J. Liu, and X.-P. Wang, "Boosted Dark Matter in IceCube and at the Galactic Center," *JHEP* **04** (2015) 105, arXiv:1503.02669 [hep-ph].

[83] L. Necib, J. Moon, T. Wongjirad, and J. M. Conrad, "Boosted Dark Matter at Neutrino Experiments," *Phys. Rev.* **D95** no. 7, (2017) 075018, arXiv:1610.03486 [hep-ph].

[84] H. Alhazmi, K. Kong, G. Mohlabeng, and J.-C. Park, "Boosted Dark Matter at the Deep Underground Neutrino Experiment," *JHEP* **04** (2017) 158, arXiv:1611.09866 [hep-ph].

[85] D. Kim, J.-C. Park, and S. Shin, "Dark Matter 'Collider' from Inelastic Boosted Dark Matter," *Phys. Rev. Lett.* **119** no. 16, (2017) 161801, arXiv:1612.06867 [hep-ph].

[86] **ArgoNeuT** Collaboration, R. Acciarri *et al.*, "A study of electron recombination using highly ionizing particles in the ArgoNeuT Liquid Argon TPC," *JINST* **8** (2013) P08005, arXiv:1306.1712 [physics.ins-det].

[87] **ICARUS** Collaboration, S. Amoruso *et al.*, "Study of electron recombination in liquid argon with the ICARUS TPC," *Nucl. Instrum. Meth.* **A523** (2004) 275–286.

[88] Y. Li *et al.*, "Measurement of Longitudinal Electron Diffusion in Liquid Argon," *Nucl. Instrum. Meth.* **A816** (2016) 160–170, arXiv:1508.07059 [physics.ins-det].

[89] The Liquid Argon Technology @BNL, "Basic properties." https://lar.bnl.gov/properties/basic.html. Accessed Jan. 15, 2019.

[90] W. Shockley, "Currents to conductors induced by a moving point charge," *Journal of Applied Physics* **9** no. 10, (1938) 635–636.

[91] S. Ramo, "Currents induced by electron motion," *Proc. Ire.* **27** (1939) 584–585.

[92] R. Veenhof, "GARFIELD, recent developments," *Nucl. Instrum. Meth.* **A419** (1998)

726–730.

[93] **MicroBooNE** Collaboration, C. Adams *et al.*, "Ionization electron signal processing in single phase LArTPCs. Part I. Algorithm Description and quantitative evaluation with MicroBooNE simulation," *JINST* **13** no. 07, (2018) P07006, arXiv:1802.08709 [physics.ins-det].

[94] "Wire-Cell Toolkit." https://github.com/WireCell.

[95] B. Viren, "Full TPC Signal Simulation," tech. rep. https://indico.fnal.gov/event/10641/session/16/material/slides/0?contribId=31.

[96] **MicroBooNE** Collaboration, C. Adams *et al.*, "Ionization electron signal processing in single phase LArTPCs. Part II. Data/simulation comparison and performance in MicroBooNE," *JINST* **13** no. 07, (2018) P07007, arXiv:1804.02583 [physics.ins-det].

[97] L. W. Nagel and D. Pederson, "SPICE (Simulation Program with Integrated Circuit Emphasis),".

[98] **MicroBooNE** Collaboration, R. Acciarri *et al.*, "Noise Characterization and Filtering in the MicroBooNE Liquid Argon TPC," *JINST* **12** no. 08, (2017) P08003, arXiv:1705.07341 [physics.ins-det].

[99] D. Whittington, S. Mufson, and B. Howard, "Scintillation Light from Cosmic-Ray Muons in Liquid Argon," *JINST* **11** no. 05, (2016) P05016, arXiv:1408.1763 [physics.ins-det].

[100] B. Baller, "Liquid argon TPC signal formation, signal processing and reconstruction techniques," *JINST* **12** no. 07, (2017) P07010, arXiv:1703.04024 [physics.ins-det].

[101] W. Gu, "Wire-cell signal processing in protodune," tech. rep. https://indico.fnal.gov/event/19185/contribution/1/material/slides/1.pptx.

[102] Baller, Bruce https://cdcvs.fnal.gov/redmine/documents/727.

[103] Baller, Bruce https://cdcvs.fnal.gov/redmine/documents/1026.

[104] J. S. Marshall and M. A. Thomson, "The Pandora Software Development Kit for Pattern Recognition," *Eur. Phys. J.* **C75** no. 9, (2015) 439, arXiv:1506.05348 [physics.data-an].

[105] **MicroBooNE** Collaboration, R. Acciarri *et al.*, "The Pandora multi-algorithm approach to automated pattern recognition of cosmic-ray muon and neutrino events in the MicroBooNE detector," *Eur. Phys. J.* **C78** no. 1, (2018) 82, arXiv:1708.03135 [hep-ex].

[106] M. Antonello, B. Baibussinov, P. Benetti, E. Calligarich, N. Canci, *et al.*, "Precise 3D track reconstruction algorithm for the ICARUS T600 liquid argon time projection chamber detector," *Adv.High Energy Phys.* **2013** (2013) 260820, arXiv:1210.5089

[physics.ins-det].

[107] X. Qian, "Wire cell reconstruction," tech. rep. https://indico.fnal.gov/event/18523/session/5/contribution/7/material/slides/0.pptx.

[108] X. Qian, C. Zhang, B. Viren, and M. Diwan, "Three-dimensional Imaging for Large LArTPCs," *JINST* **13** no. 05, (2018) P05032, arXiv:1803.04850 [physics.ins-det].

[109] M. collaboration, "Tomographic event reconstruction with microboone data." MICROBOONE-NOTE-1040-PUB, http://microboone.fnal.gov/wp-content/uploads/MICROBOONE-NOTE-1040-PUB.pdf.

[110] "Bee 3d event display." https://www.phy.bnl.gov/twister/bee.

[111] C. Zhang, "Protodune web-based 3d event display bee," tech. rep. https://indico.fnal.gov/event/18110/contribution/3/material/slides/0.pdf.

[112] "Bee event display of an protodune event." https://drive.google.com/open?id=1GxBxj0S6ZSQAjKFUlIhkUU4nDDf9F0kC.

[113] Worcester, E., "Energy Systematics Studies," 2016. https://indico.fnal.gov/event/11718/contribution/4/material/slides/0.pdf.

[114] E. Conley, "Fitting supernova neutrino spectral parameters with the Deep Underground Neutrino Experiment," DUNE doc 14068, DUNE, 2019. https://docs.dunescience.org/cgi-bin/private/ShowDocument?docid=14068&asof=2019-11-1.

[115] **MicroBooNE** Collaboration, R. Acciarri *et al.*, "Michel Electron Reconstruction Using Cosmic-Ray Data from the MicroBooNE LArTPC," *JINST* **12** no. 09, (2017) P09014, arXiv:1704.02927 [physics.ins-det].

[116] M. Antonello, B. Baibussinov, P. Benetti, F. Boffelli, A. Bubak, *et al.*, "Experimental observation of an extremely high electron lifetime with the ICARUS-T600 LAr-TPC," *JINST* **9** no. 12, (2014) P12006, arXiv:1409.5592 [physics.ins-det].

[117] P. Cennini *et al.*, "Performance of a 3-ton liquid argon time projection chamber," *Nucl. Instrum. Meth.* **A345** (1994) 230–243.

[118] T. K. Warburton, *Simulations and Data analysis for the 35 ton Liquid Argon detector as a prototype for the DUNE experiment*. PhD thesis, Sheffield U., 2017. http://lss.fnal.gov/archive/thesis/2000/fermilab-thesis-2017-28.pdf.

[119] A. Ereditato, D. Goeldi, S. Janos, I. Kreslo, M. Luethi, C. Rudolf von Rohr, M. Schenk, T. Strauss, M. S. Weber, and M. Zeller, "Measurement of the drift field in the ARGONTUBE LAr TPC with 266 nm pulsed laser beams," *JINST* **9** no. 11, (2014) P11010, arXiv:1408.6635 [physics.ins-det].

[120] **MicroBooNE** Collaboration, R. Acciarri *et al.*, "Design and Construction of the MicroBooNE Detector," *JINST* **12** no. 02, (2017) P02017, arXiv:1612.05824 [physics.ins-det].

[121] M. Auger *et al.*, "A Novel Cosmic Ray Tagger System for Liquid Argon TPC Neutrino Detectors," *Instruments* **1** no. 1, (2017) 2, arXiv:1612.04614 [physics.ins-det].

[122] **ArgoNeuT** Collaboration, R. Acciarri *et al.*, "Measurement of ν_μ and $\bar{\nu}_\mu$ neutral current $\pi^0 \to \gamma\gamma$ production in the ArgoNeuT detector," *Phys. Rev.* **D96** no. 1, (2017) 012006, arXiv:1511.00941 [hep-ex].

[123] **MicroBooNE** Collaboration, "A Measurement of the Attenuation of Drifting Electrons in the MicroBooNE LArTPC," 2017. MICROBOONE-NOTE-1026-PUB,http://microboone.fnal.gov/wp-content/uploads/MICROBOONE-NOTE-1026-PUB.pdf.

[124] MicroBooNE Collaboration, "Study of Space Charge Effects in MicroBooNE," tech. rep., 2016. http://microboone.fnal.gov/wp-content/uploads/MICROBOONE-NOTE-1018-PUB.pdf. MICROBOONE-NOTE-1018-PUB.

[125] MicroBooNE Collaboration, "Establishing a Pure Sample of Side-Piercing Through-Going Cosmic-Ray Muons for LArTPC Calibration in MicroBooNE," tech. rep., 2017. http://microboone.fnal.gov/wp-content/uploads/MICROBOONE-NOTE-1028-PUB.pdf. MICROBOONE-NOTE-1028-PUB.

[126] **MicroBooNE** Collaboration, P. Abratenko *et al.*, "Determination of muon momentum in the MicroBooNE LArTPC using an improved model of multiple Coulomb scattering," *JINST* **12** no. 10, (2017) P10010, arXiv:1703.06187 [physics.ins-det].

[127] **ICARUS** Collaboration, A. Ankowski *et al.*, "Energy reconstruction of electromagnetic showers from pi0 decays with the ICARUS T600 Liquid Argon TPC," *Acta Phys. Polon.* **B41** (2010) 103–125, arXiv:0812.2373 [hep-ex].

[128] **ICARUS** Collaboration, A. Ankowski *et al.*, "Measurement of through-going particle momentum by means of multiple scattering with the ICARUS T600 TPC," *Eur.Phys.J.* **C48** (2006) 667–676, arXiv:hep-ex/0606006 [hep-ex].

[129] **ICARUS** Collaboration, M. Antonello *et al.*, "Muon momentum measurement in ICARUS-T600 LAr-TPC via multiple scattering in few-GeV range," *JINST* **12** no. 04, (2017) P04010, arXiv:1612.07715 [physics.ins-det].

[130] **CAPTAIN** Collaboration, B. Bhandari *et al.*, "First Measurement of the Total Neutron Cross Section on Argon Between 100 and 800 MeV," arXiv:1903.05276 [hep-ex].

[131] G. Cancelo, F. Cavanna, C. O. Escobar, E. Kemp, A. A. Machado, A. Para, E. Segreto, D. Totani, and D. Warner, "Increasing the efficiency of photon collection in LArTPCs: the ARAPUCA light trap," *JINST* **13** no. 03, (2018) C03040, arXiv:1802.09726

[physics.ins-det].

[132] Z. Moss, J. Moon, L. Bugel, J. M. Conrad, K. Sachdev, M. Toups, and T. Wongjirad, "A Factor of Four Increase in Attenuation Length of Dipped Lightguides for Liquid Argon TPCs Through Improved Coating," arXiv:1604.03103 [physics.ins-det].

[133] Z. Moss, L. Bugel, G. Collin, J. M. Conrad, B. J. P. Jones, J. Moon, M. Toups, and T. Wongjirad, "Improved TPB-coated Light Guides for Liquid Argon TPC Light Detection Systems," *JINST* **10** no. 08, (2015) P08017, arXiv:1410.6256 [physics.ins-det].

[134] MicroBooNE Collaboration, "Study of Reconstructed ^{39}Ar Beta Decays at the MicroBooNE Detector," tech. rep., 2018. http://microboone.fnal.gov/wp-content/uploads/MICROBOONE-NOTE-1050-PUB.pdf. MICROBOONE-NOTE-1050-PUB.

[135] M. Zeller *et al.*, "First measurements with ARGONTUBE, a 5m long drift Liquid Argon TPC," *Nucl. Instrum. Meth.* **A718** (2013) 454–458.

[136] A. Ereditato, I. Kreslo, M. Lüthi, C. Rudolf von Rohr, M. Schenk, T. Strauss, M. Weber, and M. Zeller, "A steerable UV laser system for the calibration of liquid argon time projection chambers," *JINST* **9** no. 11, (2014) T11007, arXiv:1406.6400 [physics.ins-det].

[137] **MicroBooNE** Collaboration, C. Adams *et al.*, "A Method to Determine the Electric Field of Liquid Argon Time Projection Chambers using a UV Laser System and its Application in MicroBooNE," *submitted to JINST* (2019) , arXiv:1910.01430 [physics.ins-det].

[138] **LAr1-ND, ICARUS-WA104, MicroBooNE** Collaboration, M. Antonello *et al.*, "A Proposal for a Three Detector Short-Baseline Neutrino Oscillation Program in the Fermilab Booster Neutrino Beam," arXiv:1503.01520 [physics.ins-det].

[139] **T2K ND280 TPC** Collaboration, N. Abgrall *et al.*, "Time Projection Chambers for the T2K Near Detectors," *Nucl. Instrum. Meth.* **A637** (2011) 25–46, arXiv:1012.0865 [physics.ins-det].

[140] V. Fischer *et al.*, "Measurement of the neutron capture cross-section on argon," arXiv:1902.00596 [nucl-ex].

[141] J. Schechter and J. Valle, "Neutrino Masses in SU(2) x U(1) Theories," *Phys.Rev.* **D22** (1980) 2227.

[142] P. F. de Salas, D. V. Forero, C. A. Ternes, M. Tortola, and J. W. F. Valle, "Status of neutrino oscillations 2018: 3σ hint for normal mass ordering and improved CP sensitivity," *Phys. Lett.* **B782** (2018) 633–640, arXiv:1708.01186 [hep-ph].

[143] F. Capozzi, E. Lisi, A. Marrone, D. Montanino, and A. Palazzo, "Status and prospects of global analyses of neutrino mass-mixing parameters," *J. Phys. Conf. Ser.* **888** no. 1, (2017)

012037.

[144] H. Nunokawa, S. J. Parke, and J. W. Valle, "CP Violation and Neutrino Oscillations," *Prog.Part.Nucl.Phys.* **60** (2008) 338–402, arXiv:0710.0554 [hep-ph].

[145] M. V. Diwan, "The Case for a super neutrino beam," *Frascati Phys. Ser.* **35** (2004) 89–109, arXiv:hep-ex/0407047 [hep-ex]. [,89(2004)].

[146] C. Jarlskog, "A Basis Independent Formulation of the Connection Between Quark Mass Matrices, CP Violation and Experiment," *Z.Phys.* **C29** (1985) 491–497.

[147] S. F. King, A. Merle, S. Morisi, Y. Shimizu, and M. Tanimoto, "Neutrino Mass and Mixing: from Theory to Experiment," *New J.Phys.* **16** (2014) 045018, arXiv:1402.4271 [hep-ph].

[148] **EMPHATIC** Collaboration, T. Akaishi *et al.*, "EMPHATIC: A Proposed Experiment to Measure Hadron Scattering and Production Cross Sections for Improved Neutrino Flux Predictions," arXiv:1912.08841 [hep-ex].

[149] T. Vladisavljevic, "Constraining the T2K Neutrino Flux Prediction with 2009 NA61/SHINE Replica-Target Data," in *Proceedings, Prospects in Neutrino Physics (NuPhys2017): London, UK, December 20-22, 2017*, pp. 189–193. 2018. arXiv:1804.00272 [physics.ins-det].

[150] **NA61/SHINE** Collaboration, A. Aduszkiewicz, "Report from the NA61/SHINE experiment at the CERN SPS," Tech. Rep. CERN-SPSC-2016-038. SPSC-SR-197, CERN, Geneva, Oct, 2016. https://cds.cern.ch/record/2222876.

[151] O. Benhar, A. Fabrocini, S. Fantoni, and I. Sick, "Spectral function of finite nuclei and scattering of GeV electrons," *Nucl. Phys.* **A579** (1994) 493–517.

[152] J. Nieves, J. E. Amaro, and M. Valverde, "Inclusive quasi-elastic neutrino reactions," *Phys. Rev.* **C70** (2004) 055503, arXiv:nucl-th/0408005 [nucl-th]. [Erratum: Phys. Rev.C72,019902(2005)].

[153] K. Gallmeister, U. Mosel, and J. Weil, "Neutrino-Induced Reactions on Nuclei," *Phys. Rev.* **C94** no. 3, (2016) 035502, arXiv:1605.09391 [nucl-th].

[154] V. Pandey, N. Jachowicz, T. Van Cuyck, J. Ryckebusch, and M. Martini, "Low-energy excitations and quasielastic contribution to electron-nucleus and neutrino-nucleus scattering in the continuum random-phase approximation," *Phys. Rev.* **C92** no. 2, (2015) 024606, arXiv:1412.4624 [nucl-th].

[155] J. E. Sobczyk, "Intercomparison of lepton-nucleus scattering models in the quasielastic region," *Phys. Rev.* **C96** no. 4, (2017) 045501, arXiv:1706.06739 [nucl-th].

[156] A. S. Meyer, M. Betancourt, R. Gran, and R. J. Hill, "Deuterium target data for precision neutrino-nucleus cross sections," *Phys. Rev.* **D93** no. 11, (2016) 113015,

arXiv:1603.03048 [hep-ph].

[157] J. Nieves, I. Ruiz Simo, and M. J. Vicente Vacas, "Inclusive Charged–Current Neutrino–Nucleus Reactions," *Phys. Rev.* **C83** (2011) 045501, arXiv:1102.2777 [hep-ph].

[158] R. Gran, J. Nieves, F. Sanchez, and M. J. Vicente Vacas, "Neutrino-nucleus quasi-elastic and 2p2h interactions up to 10 GeV," *Phys. Rev.* **D88** no. 11, (2013) 113007, arXiv:1307.8105 [hep-ph].

[159] F. Sanchez, "Private communication regarding RPA uncertainty parameterization.".

[160] R. Gran, "Model Uncertainties for Valencia RPA Effect for MINERvA," arXiv:1705.02932 [hep-ex].

[161] **T2K** Collaboration, K. Abe *et al.*, "Search for CP Violation in Neutrino and Antineutrino Oscillations by the T2K Experiment with 2.2×10^{21} Protons on Target," *Phys. Rev. Lett.* **121** no. 17, (2018) 171802, arXiv:1807.07891 [hep-ex].

[162] **MINERvA** Collaboration, P. A. Rodrigues *et al.*, "Identification of nuclear effects in neutrino-carbon interactions at low three-momentum transfer," *Phys. Rev. Lett.* **116** (2016) 071802, arXiv:1511.05944 [hep-ex].

[163] C. Colle, O. Hen, W. Cosyn, I. Korover, E. Piasetzky, J. Ryckebusch, and L. B. Weinstein, "Extracting the mass dependence and quantum numbers of short-range correlated pairs from $A(e, e'p)$ and $A(e, e'pp)$ scattering," *Phys. Rev.* **C92** no. 2, (2015) 024604, arXiv:1503.06050 [nucl-th].

[164] J. E. Amaro, M. B. Barbaro, J. A. Caballero, A. De Pace, T. W. Donnelly, G. D. Megias, and I. Ruiz Simo, "Density dependence of 2p-2h meson-exchange currents," *Phys. Rev.* **C95** no. 6, (2017) 065502, arXiv:1704.01539 [nucl-th].

[165] C. L. Smith, "Neutrino reactions at accelerator energies," *Physics Reports* **3** no. 5, (1972) 261 – 379, http://www.sciencedirect.com/science/article/pii/0370157372900105.

[166] P. Rodrigues, C. Wilkinson, and K. McFarland, "Constraining the GENIE model of neutrino-induced single pion production using reanalyzed bubble chamber data," *Eur. Phys. J.* **C76** no. 8, (2016) 474, arXiv:1601.01888 [hep-ex].

[167] **MINERvA** Collaboration, O. Altinok *et al.*, "Measurement of ν_μ charged-current single π^0 production on hydrocarbon in the few-GeV region using MINERvA," *Phys. Rev.* **D96** no. 7, (2017) 072003, arXiv:1708.03723 [hep-ex].

[168] **MINERvA** Collaboration, C. L. McGivern *et al.*, "Cross sections for ν_μ and $\bar{\nu}_\mu$ induced pion production on hydrocarbon in the few-GeV region using MINERvA," *Phys. Rev.* **D94** no. 5, (2016) 052005, arXiv:1606.07127 [hep-ex].

[169] **MINERvA** Collaboration, B. Eberly *et al.*, "Charged pion production in ν_μ interactions on hydrocarbon at $\langle E_\nu \rangle = 4.0$ GeV," *Phys. Rev.* **D92** no. 9, (2015) 092008, arXiv:1406.6415 [hep-ex].

[170] **MINOS** Collaboration, P. Adamson *et al.*, "Study of quasielastic scattering using charged-current ν_μ-iron interactions in the MINOS near detector," *Phys. Rev.* **D91** no. 1, (2015) 012005, arXiv:1410.8613 [hep-ex].

[171] M. Sanchez, "Nova results and prospects," in *XXVIII International Conference on Neutrino Physics and Astrophysics (Neutrino 2018)*. Zenodo, June, 2018. https://zenodo.org/record/1286758.

[172] P. Stowell. PhD thesis, University of Sheffield, 2018.

[173] M. Kabirnezhad, "Single pion production in neutrino-nucleon interactions," *Phys. Rev. D* **97** (Jan, 2018) 013002. https://link.aps.org/doi/10.1103/PhysRevD.97.013002.

[174] **MINERvA** Collaboration, A. Mislivec *et al.*, "Measurement of total and differential cross sections of neutrino and antineutrino coherent $\pi^\pm$ production on carbon," *Phys. Rev.* **D97** no. 3, (2018) 032014, arXiv:1711.01178 [hep-ex].

[175] M. Day and K. S. McFarland, "Differences in quasielastic cross sections of muon and electron neutrinos," *Phys. Rev. D* **86** (Sep, 2012) 053003. http://link.aps.org/doi/10.1103/PhysRevD.86.053003.

[176] C. Andreopoulos, C. Barry, S. Dytman, H. Gallagher, T. Golan, R. Hatcher, G. Perdue, and J. Yarba, "The GENIE Neutrino Monte Carlo Generator: Physics and User Manual," arXiv:1510.05494 [hep-ph].

[177] J. Asaadi *et al.*, "A pixelated charge readout for Liquid Argon Time Projection Chambers," *JINST* **13** no. 02, (2018) C02008.

[178] D. A. Dwyer *et al.*, "LArPix: Demonstration of low-power 3D pixelated charge readout for liquid argon time projection chambers," *JINST* **13** no. 10, (2018) P10007, arXiv:1808.02969 [physics.ins-det].

[179] M. Auger, Y. Chen, A. Ereditato, D. Goeldi, I. Kreslo, D. Lorca, M. Luethi, T. Mettler, J. R. Sinclair, and M. S. Weber, "ArCLight-A Compact Dielectric Large-Area Photon Detector," *Instruments* **2** no. 1, (2018) 3, arXiv:1711.11409 [physics.ins-det].

[180] A. Bross *et al.*, "High-Pressure Argon gas TPC Option for the DUNE Near Detector," DUNE doc 12388, DUNE, 2019. https://docs.dunescience.org/cgi-bin/private/ShowDocument?docid=12388&asof=2019-11-1.

[181] L. Emberger and F. Simon, "A highly granular calorimeter concept for long baseline near detectors," *J. Phys. Conf. Ser.* **1162** no. 1, (2019) 012033, arXiv:1810.03677 [physics.ins-det].

[182] A. Radovic, M. Williams, D. Rousseau, M. Kagan, D. Bonacorsi, A. Himmel, A. Aurisano, K. Terao, and T. Wongjirad, "Machine learning at the energy and intensity frontiers of particle physics," *Nature* **560** no. 7716, (2018) 41–48.

[183] A. Aurisano, A. Radovic, D. Rocco, A. Himmel, M. D. Messier, E. Niner, G. Pawloski, F. Psihas, A. Sousa, and P. Vahle, "A Convolutional Neural Network Neutrino Event Classifier," *JINST* **11** no. 09, (2016) P09001, arXiv:1604.01444 [hep-ex].

[184] C. Szegedy, W. Liu, Y. Jia, P. Sermanet, S. E. Reed, D. Anguelov, D. Erhan, V. Vanhoucke, and A. Rabinovich, "Going deeper with convolutions," *CoRR* **abs/1409.4842** (2014) , arXiv:1409.4842. http://arxiv.org/abs/1409.4842.

[185] K. He, X. Zhang, S. Ren, and J. Sun, "Deep residual learning for image recognition," *CoRR* **abs/1512.03385** (2015) , arXiv:1512.03385. http://arxiv.org/abs/1512.03385.

[186] J. Hu, L. Shen, and G. Sun, "Squeeze-and-excitation networks," *CoRR* **abs/1709.01507** (2017) , arXiv:1709.01507. http://arxiv.org/abs/1709.01507.

[187] K. Sachdev, *Muon Neutrino to Electron Neutrino Oscillation in NOνA*. PhD thesis, Minnesota U., 2015. http://lss.fnal.gov/archive/thesis/2000/fermilab-thesis-2015-20.pdf.

[188] **NOvA** Collaboration, R. P. Gandrajula and M. Groh, "Systematic Uncertainties and Cross-Checks for the NOvA Joint ν_μ+ν_e Analysis," 2018. arXiv:1808.10760 [hep-ex]. https://doi.org/10.5281/zenodo.1292418.

[189] J. A. A. Boehm, *Measurement of electron neutrino appearance with the MINOS experiment*. PhD thesis, Harvard U., 2009. http://lss.fnal.gov/cgi-bin/find_paper.pl?thesis-2009-17.

[190] **NOvA** Collaboration, M. A. Acero *et al.*, "New constraints on oscillation parameters from ν_e appearance and ν_μ disappearance in the NOvA experiment," *Phys. Rev.* **D98** (2018) 032012, arXiv:1806.00096 [hep-ex].

[191] **CAPTAIN** Collaboration, H. Berns *et al.*, "The CAPTAIN Detector and Physics Program." 2013.

[192] **ArgoNeuT** Collaboration, R. Acciarri *et al.*, "Demonstration of MeV-Scale Physics in Liquid Argon Time Projection Chambers Using ArgoNeuT," *Phys. Rev.* **D99** no. 1, (2019) 012002, arXiv:1810.06502 [hep-ex].

[193] **MINERvA** Collaboration, M. Elkins *et al.*, "Neutron measurements from anti-neutrino hydrocarbon reactions," arXiv:1901.04892 [hep-ex].

[194] **MicroBooNE** Collaboration, C. Adams *et al.*, "First Measurement of ν_μ Charged-Current π^0 Production on Argon with a LArTPC," arXiv:1811.02700 [hep-ex].

[195] X. Qian, A. Tan, W. Wang, J. Ling, R. McKeown, *et al.*, "Statistical Evaluation of Experimental Determinations of Neutrino Mass Hierarchy," *Phys.Rev.* **D86** (2012) 113011, arXiv:1210.3651 [hep-ph].

[196] M. Blennow, P. Coloma, P. Huber, and T. Schwetz, "Quantifying the sensitivity of oscillation experiments to the neutrino mass ordering," *JHEP* **1403** (2014) 028, arXiv:1311.1822 [hep-ph].

[197] P. Huber, M. Lindner, and W. Winter, "Simulation of long-baseline neutrino oscillation experiments with GLoBES (General Long Baseline Experiment Simulator)," *Comput.Phys.Commun.* **167** (2005) 195, arXiv:hep-ph/0407333 [hep-ph].

[198] P. Huber, J. Kopp, M. Lindner, M. Rolinec, and W. Winter, "New features in the simulation of neutrino oscillation experiments with GLoBES 3.0: General Long Baseline Experiment Simulator," *Comput.Phys.Commun.* **177** (2007) 432–438, arXiv:hep-ph/0701187 [hep-ph].

[199] **DUNE** Collaboration, R. Acciarri *et al.*, "Long-Baseline Neutrino Facility (LBNF) and Deep Underground Neutrino Experiment (DUNE)," arXiv:1512.06148 [physics.ins-det].

[200] **DUNE** Collaboration, T. Alion *et al.*, "Experiment Simulation Configurations Used in DUNE CDR," arXiv:1606.09550 [physics.ins-det].

[201] M. Bass, "Neutrino Oscillation Parameter Sensitivity in Future Long-Baseline Experiments,".

[202] "The valor neutrino fit group." https://valor.pp.rl.ac.uk/.

[203] NOvA Collaboration, ed., *NOvA-ART*, ch. CAFAna overview. Redmine, 2019. https://cdcvs.fnal.gov/redmine/projects/novaart/wiki/CAFAna_overview.

[204] F. James, "MINUIT Function Minimization and Error Analysis: Reference Manual Version 94.1." CERN-D-506, CERN-D506, 1994.

[205] J. C. Pati and A. Salam, "Is Baryon Number Conserved?," *Phys.Rev.Lett.* **31** (1973) 661–664.

[206] H. Georgi and S. Glashow, "Unity of All Elementary Particle Forces," *Phys.Rev.Lett.* **32** (1974) 438–441.

[207] S. Dimopoulos, S. Raby, and F. Wilczek, "Proton Decay in Supersymmetric Models," *Phys.Lett.* **B112** (1982) 133.

[208] P. Langacker, "Grand Unified Theories and Proton Decay," *Phys.Rept.* **72** (1981) 185.

[209] W. de Boer, "Grand unified theories and supersymmetry in particle physics and

cosmology," *Prog.Part.Nucl.Phys.* **33** (1994) 201–302, arXiv:hep-ph/9402266 [hep-ph].

[210] G. Altarelli and D. Meloni, "A non supersymmetric SO(10) grand unified model for all the physics below M_{GUT}," *JHEP* **08** (2013) 021, arXiv:1305.1001 [hep-ph].

[211] G. D. Barr, T. K. Gaisser, P. Lipari, S. Robbins, and T. Stanev, "A Three - dimensional calculation of atmospheric neutrinos," *Phys. Rev.* **D70** (2004) 023006, arXiv:astro-ph/0403630 [astro-ph].

[212] D. V. Bugg *et al.*, "Kaon-Nucleon Total Cross Sections from 0.6 to 2.65 GeV/c," *Phys. Rev.* **168** (1968) 1466–1475.

[213] E. Friedman *et al.*, "K+ nucleus reaction and total cross-sections: New analysis of transmission experiments," *Phys. Rev.* **C55** (1997) 1304–1311.

[214] **MINERvA** Collaboration, C. M. Marshall *et al.*, "Measurement of K^+ production in charged-current ν_μ interactions," *Phys. Rev.* **D94** no. 1, (2016) 012002, arXiv:1604.03920 [hep-ex].

[215] A. Hocker *et al.*, "TMVA - Toolkit for Multivariate Data Analysis," arXiv:physics/0703039 [physics.data-an].

[216] G. D. Barr, T. K. Gaisser, S. Robbins, and T. Stanev, "Uncertainties in Atmospheric Neutrino Fluxes," *Phys. Rev.* **D74** (2006) 094009, arXiv:astro-ph/0611266 [astro-ph].

[217] K. Mahn, C. Marshall, and C. Wilkinson, "Progress in Measurements of 0.1-10 GeV Neutrino-Nucleus Scattering and Anticipated Results from Future Experiments," *Ann. Rev. Nucl. Part. Sci.* **68** (2018) 105–129, arXiv:1803.08848 [hep-ex].

[218] **Frejus** Collaboration, C. Berger *et al.*, "Lifetime limits on (B-L) violating nucleon decay and dinucleon decay modes from the Frejus experiment," *Phys. Lett.* **B269** (1991) 227–233.

[219] D. G. Phillips, II *et al.*, "Neutron-Antineutron Oscillations: Theoretical Status and Experimental Prospects," *Phys. Rept.* **612** (2016) 1–45, arXiv:1410.1100 [hep-ex].

[220] S. Nussinov and R. Shrock, "N - anti-N oscillations in models with large extra dimensions," *Phys. Rev. Lett.* **88** (2002) 171601, arXiv:hep-ph/0112337 [hep-ph].

[221] M. Baldo-Ceolin *et al.*, "A New experimental limit on neutron - anti-neutron oscillations," *Z. Phys.* **C63** (1994) 409–416.

[222] **Super-Kamiokande** Collaboration, K. Abe *et al.*, "The Search for $n - \bar{n}$ oscillation in Super-Kamiokande I," *Phys. Rev.* **D91** (2015) 072006, arXiv:1109.4227 [hep-ex].

[223] J. E. T. Hewes, *Searches for Bound Neutron-Antineutron Oscillation in Liquid Argon Time Projection Chambers*. PhD thesis, Manchester U., 2017. http://lss.fnal.gov/archive/thesis/2000/fermilab-thesis-2017-27.pdf.

[224] E. Friedman and A. Gal, "Realistic calculations of nuclear disappearance lifetimes induced by n anti-n oscillations," *Phys. Rev.* **D78** (2008) 016002, arXiv:0803.3696 [hep-ph].

[225] A. Chatterjee, P. Mehta, D. Choudhury, and R. Gandhi, "Testing nonstandard neutrino matter interactions in atmospheric neutrino propagation," *Phys. Rev.* **D93** no. 9, (2016) 093017, arXiv:1409.8472 [hep-ph].

[226] **Super-Kamiokande** Collaboration, K. Abe *et al.*, "Search for Matter-Dependent Atmospheric Neutrino Oscillations in Super-Kamiokande," *Phys.Rev.* **D77** (2008) 052001, arXiv:0801.0776 [hep-ex].

[227] **Super-Kamiokande** Collaboration, K. Abe *et al.*, "Limits on sterile neutrino mixing using atmospheric neutrinos in Super-Kamiokande," *Phys. Rev.* **D91** (2015) 052019, arXiv:1410.2008 [hep-ex].

[228] K. J. Kelly, P. A. Machado, I. Martinez Soler, S. J. Parke, and Y. F. Perez Gonzalez, "Sub-GeV Atmospheric Neutrinos and CP-Violation in DUNE," arXiv:1904.02751 [hep-ph].

[229] V. A. Kostelecký and S. Samuel, "Spontaneous Breaking of Lorentz Symmetry in String Theory," *Phys. Rev.* **D39** (1989) 683.

[230] V. A. Kostelecký and R. Potting, "CPT and strings," *Nucl. Phys.* **B359** (1991) 545–570.

[231] V. A. Kostelecký and R. Potting, "CPT, strings, and meson factories," *Phys. Rev.* **D51** (1995) 3923–3935, arXiv:hep-ph/9501341 [hep-ph].

[232] D. Colladay and V. A. Kostelecký, "CPT violation and the standard model," *Phys.Rev.* **D55** (1997) 6760–6774, arXiv:hep-ph/9703464 [hep-ph].

[233] D. Colladay and V. A. Kostelecký, "Lorentz violating extension of the standard model," *Phys.Rev.* **D58** (1998) 116002, arXiv:hep-ph/9809521 [hep-ph].

[234] V. A. Kostelecký, "Gravity, Lorentz violation, and the standard model," *Phys.Rev.* **D69** (2004) 105009, arXiv:hep-th/0312310 [hep-th].

[235] V. A. Kostelecký and M. Mewes, "Lorentz and CPT violation in neutrinos," *Phys.Rev.* **D69** (2004) 016005, arXiv:hep-ph/0309025 [hep-ph].

[236] A. Kostelecký and M. Mewes, "Neutrinos with Lorentz-violating operators of arbitrary dimension," *Phys.Rev.* **D85** (2012) 096005, arXiv:1112.6395 [hep-ph].

[237] V. A. Kostelecký and N. Russell, "Data Tables for Lorentz and CPT Violation," *Rev. Mod. Phys.* **83** (2011) 11–31, arXiv:0801.0287 [hep-ph].

[238] V. A. Kostelecký and M. Mewes, "Lorentz and CPT violation in the neutrino sector," *Phys.Rev.* **D70** (2004) 031902, arXiv:hep-ph/0308300 [hep-ph].

[239] V. A. Kostelecký and M. Mewes, "Lorentz violation and short-baseline neutrino experiments," *Phys. Rev.* **D70** (2004) 076002, arXiv:hep-ph/0406255 [hep-ph].

[240] J. S. Diaz, V. A. Kostelecký, and M. Mewes, "Perturbative Lorentz and CPT violation for neutrino and antineutrino oscillations," *Phys.Rev.* **D80** (2009) 076007, arXiv:0908.1401 [hep-ph].

[241] J. S. Díaz, A. Kostelecký, and R. Lehnert, "Relativity violations and beta decay," *Phys. Rev.* **D88** no. 7, (2013) 071902, arXiv:1305.4636 [hep-ph].

[242] J. S. Díaz, A. Kostelecky, and M. Mewes, "Testing Relativity with High-Energy Astrophysical Neutrinos," *Phys. Rev.* **D89** no. 4, (2014) 043005, arXiv:1308.6344 [astro-ph.HE].

[243] **IceCube** Collaboration, R. Abbasi *et al.*, "Search for a Lorentz-violating sidereal signal with atmospheric neutrinos in IceCube," *Phys. Rev.* **D82** (2010) 112003, arXiv:1010.4096 [astro-ph.HE].

[244] **Super-Kamiokande** Collaboration, K. Abe *et al.*, "Test of Lorentz invariance with atmospheric neutrinos," *Phys. Rev.* **D91** no. 5, (2015) 052003, arXiv:1410.4267 [hep-ex].

[245] **IceCube** Collaboration, M. G. Aartsen *et al.*, "Neutrino Interferometry for High-Precision Tests of Lorentz Symmetry with IceCube," *Nature Phys.* **14** no. 9, (2018) 961–966, arXiv:1709.03434 [hep-ex].

[246] V. A. Kostelecký and M. Mewes, "Signals for Lorentz violation in electrodynamics," *Phys. Rev.* **D66** (2002) 056005, arXiv:hep-ph/0205211 [hep-ph].

[247] M. Honda, M. Sajjad Athar, T. Kajita, K. Kasahara, and S. Midorikawa, "Atmospheric neutrino flux calculation using the NRLMSISE-00 atmospheric model," *Phys. Rev.* **D92** no. 2, (2015) 023004, arXiv:1502.03916 [astro-ph.HE].

[248] J. Picone *et al.*, "NRLMSISE-00 empirical model of the atmosphere: Statistical comparisons and scientific issues," *J. Geophys. Res.* **107** no. A12, (2002) SIA 15–1.

[249] L. Hudepohl, B. Muller, H.-T. Janka, A. Marek, and G. Raffelt, "Neutrino Signal of Electron-Capture Supernovae from Core Collapse to Cooling," *Phys.Rev.Lett.* **104** (2010) 251101, arXiv:0912.0260 [astro-ph.SR].

[250] H. Minakata, H. Nunokawa, R. Tomas, and J. W. Valle, "Parameter Degeneracy in Flavor-Dependent Reconstruction of Supernova Neutrino Fluxes," *JCAP* **0812** (2008) 006, arXiv:0802.1489 [hep-ph].

[251] I. Tamborra, B. Muller, L. Hudepohl, H.-T. Janka, and G. Raffelt, "High-resolution supernova neutrino spectra represented by a simple fit," *Phys.Rev.* **D86** (2012) 125031, arXiv:1211.3920 [astro-ph.SR].

[252] A. Hayes. Private communication.

[253] I. Gil Botella and A. Rubbia, "Oscillation effects on supernova neutrino rates and spectra and detection of the shock breakout in a liquid argon TPC," *JCAP* **0310** (2003) 009, arXiv:hep-ph/0307244.

[254] S. Gardiner, B. Svoboda, C. Grant, and E. Pantic, "MARLEY (Model of Argon Reaction Low Energy Yields)." http://www.marleygen.org/.

[255] T. Totani, K. Sato, H. E. Dalhed, and J. R. Wilson, "Future detection of supernova neutrino burst and explosion mechanism," *Astrophys. J.* **496** (1998) 216–225, arXiv:astro-ph/9710203.

[256] J. Gava, J. Kneller, C. Volpe, and G. C. McLaughlin, "A dynamical collective calculation of supernova neutrino signals," *Phys. Rev. Lett.* **103** (2009) 071101, arXiv:0902.0317 [hep-ph].

[257] I. Tamborra, F. Hanke, H.-T. Janka, B. Mueller, G. G. Raffelt, *et al.*, "Self-sustained asymmetry of lepton-number emission: A new phenomenon during the supernova shock-accretion phase in three dimensions," *Astrophys.J.* **792** (2014) 96, arXiv:1402.5418 [astro-ph.SR].

[258] R. Laha and J. F. Beacom, "Gadolinium in water Cherenkov detectors improves detection of supernova ν_e," *Phys.Rev.* **D89** (2014) 063007, arXiv:1311.6407 [astro-ph.HE].

[259] R. Laha, J. F. Beacom, and S. K. Agarwalla, "New Power to Measure Supernova ν_e with Large Liquid Scintillator Detectors." arXiv:1412.8425 [hep-ph], 2014.

[260] C. S. Kochanek, J. F. Beacom, M. D. Kistler, J. L. Prieto, K. Z. Stanek, T. A. Thompson, and H. Yuksel, "A Survey About Nothing: Monitoring a Million Supergiants for Failed Supernovae," *Astrophys. J.* **684** (2008) 1336–1342, arXiv:0802.0456 [astro-ph].

[261] J. F. Cherry, J. Carlson, A. Friedland, G. M. Fuller, and A. Vlasenko, "Halo Modification of a Supernova Neutronization Neutrino Burst," *Phys.Rev.* **D87** (2013) 085037, arXiv:1302.1159 [astro-ph.HE].

[262] J. F. Beacom, R. Boyd, and A. Mezzacappa, "Black hole formation in core collapse supernovae and time-of-flight measurements of the neutrino masses," *Phys.Rev.* **D63** (2001) 073011, arXiv:astro-ph/0010398 [astro-ph].

[263] T. Fischer, S. C. Whitehouse, A. Mezzacappa, F. K. Thielemann, and M. Liebendorfer, "The neutrino signal from protoneutron star accretion and black hole formation," *Astron. Astrophys.* **499** (2009) 1, arXiv:0809.5129 [astro-ph].

[264] R. C. Schirato and G. M. Fuller, "Connection between supernova shocks, flavor transformation, and the neutrino signal," arXiv:astro-ph/0205390 [astro-ph].

[265] F. Hanke, A. Marek, B. Muller, and H.-T. Janka, "Is Strong SASI Activity the Key to Successful Neutrino-Driven Supernova Explosions?," *Astrophys.J.* **755** (2012) 138, arXiv:1108.4355 [astro-ph.SR].

[266] F. Hanke, B. Mueller, A. Wongwathanarat, A. Marek, and H.-T. Janka, "SASI Activity in Three-Dimensional Neutrino-Hydrodynamics Simulations of Supernova Cores," *Astrophys.J.* **770** (2013) 66, arXiv:1303.6269 [astro-ph.SR].

[267] A. Friedland and A. Gruzinov, "Neutrino signatures of supernova turbulence." 2006.

[268] T. Lund and J. P. Kneller, "Combining collective, MSW, and turbulence effects in supernova neutrino flavor evolution," *Phys. Rev.* **D88** no. 2, (2013) 023008, arXiv:1304.6372 [astro-ph.HE].

[269] N. Arnaud, M. Barsuglia, M.-A. Bizouard, V. Brisson, F. Cavalier, *et al.*, "Detection of a close supernova gravitational wave burst in a network of interferometers, neutrino and optical detectors," *Astropart.Phys.* **21** (2004) 201–221, arXiv:gr-qc/0307101 [gr-qc].

[270] C. Ott, E. O'Connor, S. Gossan, E. Abdikamalov, U. Gamma, *et al.*, "Core-Collapse Supernovae, Neutrinos, and Gravitational Waves," *Nucl.Phys.Proc.Suppl.* **235-236** (2013) 381–387, arXiv:1212.4250 [astro-ph.HE].

[271] B. Mueller, H.-T. Janka, and A. Marek, "A New Multi-Dimensional General Relativistic Neutrino Hydrodynamics Code of Core-Collapse Supernovae III. Gravitational Wave Signals from Supernova Explosion Models," *Astrophys.J.* **766** (2013) 43, arXiv:1210.6984 [astro-ph.SR].

[272] A. Nishizawa and T. Nakamura, "Measuring Speed of Gravitational Waves by Observations of Photons and Neutrinos from Compact Binary Mergers and Supernovae," *Phys.Rev.* **D90** no. 4, (2014) 044048, arXiv:1406.5544 [gr-qc].

[273] P. Antonioli *et al.*, "SNEWS: The SuperNova Early Warning System," *New J. Phys.* **6** (2004) 114, astro-ph/0406214.

[274] K. Scholberg, "The SuperNova Early Warning System," *Astron. Nachr.* **329** (2008) 337–339, arXiv:0803.0531 [astro-ph].

[275] A. Bueno, I. Gil Botella, and A. Rubbia, "Supernova neutrino detection in a liquid argon TPC." 2003.

[276] K. Nakazato, K. Sumiyoshi, H. Suzuki, T. Totani, H. Umeda, and S. Yamada, "Supernova Neutrino Light Curves and Spectra for Various Progenitor Stars: From Core Collapse to Proto-neutron Star Cooling," *Astrophys. J. Suppl.* **205** (2013) 2, arXiv:1210.6841 [astro-ph.HE].

[277] L. Huedepohl, *Neutrinos from the Formation, Cooling and Black Hole Collapse of Neutron Stars*. PhD thesis, Technische Universitat Munchen., 2014. https:

//wwwmpa.mpa-garching.mpg.de/ccsnarchive/data/Huedepohl2014_phd_thesis/.

[278] G. G. Raffelt, "Particle Physics from Stars," *Ann. Rev. Nucl. Part. Sci.* **49** (1999) 163–216, arXiv:hep-ph/9903472.

[279] H. Duan, G. M. Fuller, and Y.-Z. Qian, "Collective neutrino flavor transformation in supernovae," *Phys.Rev.* **D74** (2006) 123004, arXiv:astro-ph/0511275 [astro-ph].

[280] G. L. Fogli, E. Lisi, A. Marrone, and A. Mirizzi, "Collective neutrino flavor transitions in supernovae and the role of trajectory averaging," *JCAP* **0712** (2007) 010, arXiv:0707.1998 [hep-ph].

[281] G. G. Raffelt and A. Y. Smirnov, "Self-induced spectral splits in supernova neutrino fluxes," *Phys.Rev.* **D76** (2007) 081301, arXiv:0705.1830 [hep-ph].

[282] G. G. Raffelt and A. Y. Smirnov, "Adiabaticity and spectral splits in collective neutrino transformations," *Phys.Rev.* **D76** (2007) 125008, arXiv:0709.4641 [hep-ph].

[283] A. Esteban-Pretel, A. Mirizzi, S. Pastor, R. Tomas, G. Raffelt, *et al.*, "Role of dense matter in collective supernova neutrino transformations," *Phys.Rev.* **D78** (2008) 085012, arXiv:0807.0659 [astro-ph].

[284] H. Duan and J. P. Kneller, "Neutrino flavour transformation in supernovae," *J.Phys.G* **G36** (2009) 113201, arXiv:0904.0974 [astro-ph.HE].

[285] B. Dasgupta, A. Dighe, G. G. Raffelt, and A. Y. Smirnov, "Multiple Spectral Splits of Supernova Neutrinos," *Phys.Rev.Lett.* **103** (2009) 051105, arXiv:0904.3542 [hep-ph].

[286] H. Duan, G. M. Fuller, and Y.-Z. Qian, "Collective Neutrino Oscillations," *Ann.Rev.Nucl.Part.Sci.* **60** (2010) 569–594, arXiv:1001.2799 [hep-ph].

[287] H. Duan and A. Friedland, "Self-induced suppression of collective neutrino oscillations in a supernova," *Phys.Rev.Lett.* **106** (2011) 091101, arXiv:1006.2359 [hep-ph].

[288] M.-R. Wu, Y.-Z. Qian, G. Martinez-Pinedo, T. Fischer, and L. Huther, "Effects of neutrino oscillations on nucleosynthesis and neutrino signals for an 18 $M_\odot$ supernova model," *Phys.Rev.* **D91** no. 6, (2015) 065016, arXiv:1412.8587 [astro-ph.HE].

[289] K. Scholberg, "Supernova Signatures of Neutrino Mass Ordering," *J. Phys.* **G45** no. 1, (2018) 014002, arXiv:1707.06384 [hep-ex].

[290] V. A. KosteleckÃ¡ and M. Mewes, "Testing local Lorentz invariance with gravitational waves," *Phys. Lett.* **B757** (2016) 510–514, arXiv:1602.04782 [gr-qc].

[291] J. Diaz, V. Kostelecký, and M. Mewes. Private communication.

[292] F. Rossi-Torres, M. Guzzo, and E. Kemp, "Boundaries on Neutrino Mass from Supernovae

Neutronization Burst by Liquid Argon Experiments," arXiv:1501.00456 [hep-ph].

[293] P. Keranen, J. Maalampi, M. Myyrylainen, and J. Riittinen, "Sterile neutrino signals from supernovae," *Phys.Rev.* **D76** (2007) 125026, arXiv:0708.3337 [hep-ph].

[294] I. Tamborra, G. G. Raffelt, L. Hudepohl, and H.-T. Janka, "Impact of eV-mass sterile neutrinos on neutrino-driven supernova outflows," *JCAP* **1201** (2012) 013, arXiv:1110.2104 [astro-ph.SR].

[295] A. Esmaili, O. Peres, and P. D. Serpico, "Impact of sterile neutrinos on the early time flux from a galactic supernova," *Phys.Rev.* **D90** no. 3, (2014) 033013, arXiv:1402.1453 [hep-ph].

[296] **Super-Kamiokande** Collaboration, S. Fukuda *et al.*, "Solar B-8 and hep neutrino measurements from 1258 days of Super-Kamiokande data," *Phys.Rev.Lett.* **86** (2001) 5651–5655, arXiv:hep-ex/0103032 [hep-ex].

[297] **SNO** Collaboration, Q. Ahmad *et al.*, "Measurement of the rate of $nu_e + dtop + p + e^-$ interactions produced by B-8 solar neutrinos at the Sudbury Neutrino Observatory," *Phys.Rev.Lett.* **87** (2001) 071301, arXiv:nucl-ex/0106015 [nucl-ex].

[298] B. Cleveland, T. Daily, J. Davis, Raymond, J. R. Distel, K. Lande, *et al.*, "Measurement of the solar electron neutrino flux with the Homestake chlorine detector," *Astrophys.J.* **496** (1998) 505–526.

[299] F. Capozzi, S. W. Li, G. Zhu, and J. F. Beacom, "DUNE as the Next-Generation Solar Neutrino Experiment," arXiv:1808.08232 [hep-ph].

[300] J. F. Beacom, "The Diffuse Supernova Neutrino Background," *Ann.Rev.Nucl.Part.Sci.* **60** (2010) 439–462, arXiv:1004.3311 [astro-ph.HE].

[301] C. Lunardini and I. Tamborra, "Diffuse supernova neutrinos: oscillation effects, stellar cooling and progenitor mass dependence," *JCAP* **1207** (2012) 012, arXiv:1205.6292 [astro-ph.SR].

[302] K. Moeller, A. M. Suliga, I. Tamborra, and P. B. Denton, "Measuring the supernova unknowns at the next-generation neutrino telescopes through the diffuse neutrino background," *JCAP* **1805** no. 05, (2018) 066, arXiv:1804.03157 [astro-ph.HE].

[303] A. Cocco, A. Ereditato, G. Fiorillo, G. Mangano, and V. Pettorino, "Supernova relic neutrinos in liquid argon detectors," *JCAP* **0412** (2004) 002, arXiv:hep-ph/0408031 [hep-ph].

[304] W. P. Wright, J. P. Kneller, S. T. Ohlmann, F. K. Roepke, K. Scholberg, and I. R. Seitenzahl, "Neutrinos from type Ia supernovae: The gravitationally confined detonation scenario," *Phys. Rev.* **D95** no. 4, (2017) 043006, arXiv:1609.07403 [astro-ph.HE].

[305] W. P. Wright, G. Nagaraj, J. P. Kneller, K. Scholberg, and I. R. Seitenzahl, "Neutrinos from type Ia supernovae: The deflagration-to-detonation transition scenario," *Phys. Rev.* **D94** no. 2, (2016) 025026, arXiv:1605.01408 [astro-ph.HE].

[306] O. Caballero, G. McLaughlin, and R. Surman, "Neutrino Spectra from Accretion Disks: Neutrino General Relativistic Effects and the Consequences for Nucleosynthesis," *Astrophys.J.* **745** (2012) 170, arXiv:1105.6371 [astro-ph.HE].

[307] O. Caballero, G. McLaughlin, R. Surman, and R. Surman, "Detecting neutrinos from black hole neutron stars mergers," *Phys.Rev.* **D80** (2009) 123004, arXiv:0910.1385 [astro-ph.HE].

[308] C. Rott, J. Siegal-Gaskins, and J. F. Beacom, "New Sensitivity to Solar WIMP Annihilation using Low-Energy Neutrinos," *Phys.Rev.* **D88** (2013) 055005, arXiv:1208.0827 [astro-ph.HE].

[309] N. Bernal, J. Martín-Albo, and S. Palomares-Ruiz, "A novel way of constraining WIMPs annihilations in the Sun: MeV neutrinos," *JCAP* **1308** (2013) 011, arXiv:1208.0834 [hep-ph].

[310] M. Dentler, A. Hernández-Cabezudo, J. Kopp, P. A. N. Machado, M. Maltoni, I. Martinez-Soler, and T. Schwetz, "Updated Global Analysis of Neutrino Oscillations in the Presence of eV-Scale Sterile Neutrinos," *JHEP* **08** (2018) 010, arXiv:1803.10661 [hep-ph].

[311] S. Gariazzo, C. Giunti, M. Laveder, and Y. F. Li, "Updated Global 3+1 Analysis of Short-BaseLine Neutrino Oscillations," *JHEP* **06** (2017) 135, arXiv:1703.00860 [hep-ph].

[312] P. Minkowski, "$\mu \to e\gamma$ at a Rate of One Out of 10^9 Muon Decays?," *Phys. Lett.* **67B** (1977) 421–428.

[313] R. N. Mohapatra and G. Senjanovic, "Neutrino Mass and Spontaneous Parity Violation," *Phys. Rev. Lett.* **44** (1980) 912.

[314] T. Yanagida, "Horizontal Symmetry and Masses of Neutrinos," *Conf. Proc.* **C7902131** (1979) 95–99.

[315] M. Gell-Mann, P. Ramond, and R. Slansky, "Complex Spinors and Unified Theories," *Conf. Proc.* **C790927** (1979) 315–321, arXiv:1306.4669 [hep-th].

[316] Y. Farzan and M. Tortola, "Neutrino oscillations and Non-Standard Interactions," *Front.in Phys.* **6** (2018) 10, arXiv:1710.09360 [hep-ph].

[317] R. F. Streater and A. S. Wightman, *PCT, spin and statistics, and all that.* 1989.

[318] G. Barenboim and J. D. Lykken, "A Model of CPT violation for neutrinos," *Phys. Lett.*

B554 (2003) 73–80, arXiv:hep-ph/0210411 [hep-ph].

[319] G. Barenboim, C. A. Ternes, and M. Tortola, "Neutrinos, DUNE and the world best bound on CPT violation," arXiv:1712.01714 [hep-ph].

[320] W. Czyz, G. C. Sheppey, and J. D. Walecka, "Neutrino production of lepton pairs through the point four-fermion interaction," *Nuovo Cim.* **34** (1964) 404–435.

[321] J. Lovseth and M. Radomiski, "Kinematical distributions of neutrino-produced lepton triplets," *Phys. Rev. D* **3** (1971) 2686–2706.

[322] K. Fujikawa, "The self-coupling of weak lepton currents in high-energy neutrino and muon reactions," *Annals Phys.* **68** (1971) 102–162.

[323] K. Koike, M. Konuma, K. Kurata, and K. Sugano, "Neutrino production of lepton pairs. 1. -," *Prog. Theor. Phys.* **46** (1971) 1150–1169.

[324] K. Koike, M. Konuma, K. Kurata, and K. Sugano, "Neutrino production of lepton pairs. 2.," *Prog. Theor. Phys.* **46** (1971) 1799–1804.

[325] R. W. Brown, R. H. Hobbs, J. Smith, and N. Stanko, "Intermediate boson. iii. virtual-boson effects in neutrino trident production," *Phys. Rev. D* **6** (1972) 3273–3292.

[326] R. Belusevic and J. Smith, "W-Z Interference in Neutrino-Nucleus Scattering," *Phys. Rev. D* **37** (1988) 2419.

[327] W. Altmannshofer, S. Gori, J. Martín-Albo, A. Sousa, and M. Wallbank, "Neutrino tridents at DUNE," arXiv:1902.06765 [hep-ph].

[328] P. Ballett, M. Hostert, S. Pascoli, Y. F. Perez-Gonzalez, Z. Tabrizi, and R. Zukanovich Funchal, "Neutrino Trident Scattering at Near Detectors," arXiv:1807.10973 [hep-ph].

[329] P. Ballett, M. Hostert, S. Pascoli, Y. F. Perez-Gonzalez, and Z. Tabrizi, "Z's in neutrino scattering at DUNE," arXiv:1902.08579 [hep-ph].

[330] J. Alexander *et al.*, "Dark Sectors 2016 Workshop: Community Report," 2016. arXiv:1608.08632 [hep-ph]. http://inspirehep.net/record/1484628/files/arXiv:1608.08632.pdf.

[331] M. Battaglieri *et al.*, "US Cosmic Visions: New Ideas in Dark Matter 2017: Community Report," arXiv:1707.04591 [hep-ph].

[332] J. LoSecco, L. Sulak, R. Galik, J. Horstkotte, J. Knauer, H. H. Williams, A. Soukas, P. J. Wanderer, and W. Weng, "Limits on the Production of Neutral Penetrating States in a Beam Dump," *Phys. Lett.* **102B** (1981) 209–212.

[333] G. Belanger and J.-C. Park, "Assisted freeze-out," *JCAP* **1203** (2012) 038, arXiv:1112.4491 [hep-ph].

[334] A. Chatterjee, A. De Roeck, D. Kim, Z. G. Moghaddam, J.-C. Park, S. Shin, L. H. Whitehead, and J. Yu, "Search for Boosted Dark Matter at ProtoDUNE," arXiv:1803.03264 [hep-ph].

[335] J. Huang and Y. Zhao, "Dark Matter Induced Nucleon Decay: Model and Signatures," *JHEP* **02** (2014) 077, arXiv:1312.0011 [hep-ph].

[336] D. Kim, K. Kong, J.-C. Park, and S. Shin, "Boosted Dark Matter Quarrying at Surface Neutrino Detectors," *JHEP* **08** (2018) 155, arXiv:1804.07302 [hep-ph].

[337] P. Adamson *et al.*, "Long-Baseline Neutrino Facility (LBNF)/DUNE Conceptual Design Report: Annex 3A_opt," DUNE doc 4559, 2017. http://docs.dunescience.org/cgi-bin/ShowDocument?docid=4559&asof=2019-7-15.

[338] **LSND** Collaboration, A. A. Aguilar-Arevalo *et al.*, "Evidence for neutrino oscillations from the observation of anti-neutrino(electron) appearance in a anti-neutrino(muon) beam," *Phys. Rev.* **D64** (2001) 112007, arXiv:hep-ex/0104049 [hep-ex].

[339] **MiniBooNE** Collaboration, A. A. Aguilar-Arevalo *et al.*, "Improved Search for $\bar{\nu}_\mu \to \bar{\nu}_e$ Oscillations in the MiniBooNE Experiment," *Phys. Rev. Lett.* **110** (2013) 161801, arXiv:1303.2588 [hep-ex].

[340] M. A. Acero, C. Giunti, and M. Laveder, "Limits on nu(e) and anti-nu(e) disappearance from Gallium and reactor experiments," *Phys. Rev.* **D78** (2008) 073009, arXiv:0711.4222 [hep-ph].

[341] G. Mention, M. Fechner, T. Lasserre, T. A. Mueller, D. Lhuillier, M. Cribier, and A. Letourneau, "The Reactor Antineutrino Anomaly," *Phys. Rev.* **D83** (2011) 073006, arXiv:1101.2755 [hep-ex].

[342] D. Dutta, R. Gandhi, B. Kayser, M. Masud, and S. Prakash, "Capabilities of long-baseline experiments in the presence of a sterile neutrino," arXiv:1607.02152 [hep-ph].

[343] J. Kopp, "Sterile neutrinos and non-standard neutrino interactions in GLoBES," *https://www.mpi-hd.mpg.de/personalhomes/globes/tools/snu-1.0.pdf* (2010) .

[344] M. Blennow, E. Fernandez-Martinez, S. Rosauro-Alcaraz, A. Sousa, and J. Todd, "Tech Note - Search for Sterile Neutrinos in DUNE." https://docs.dunescience.org/cgi-bin/private/RetrieveFile?docid=12067&filename=DUNE_BSM_Sterile_Neutrinos_Tech_Note.pdf&version=3, 2018.

[345] **NOvA** Collaboration, P. Adamson *et al.*, "Search for active-sterile neutrino mixing using neutral-current interactions in NOvA," *Phys. Rev.* **D96** no. 7, (2017) 072006, arXiv:1706.04592 [hep-ex].

[346] **MINOS+** Collaboration, P. Adamson *et al.*, "Search for sterile neutrinos in MINOS and MINOS+ using a two-detector fit," *Phys. Rev. Lett.* **122** no. 9, (2019) 091803, arXiv:1710.06488 [hep-ex].

[347] **Super-Kamiokande** Collaboration, K. Abe *et al. Phys. Rev. D* **91** (2015) 052019.

[348] **IceCube** Collaboration, M. G. Aartsen *et al. Phys. Rev. Lett.* **117** (2016) 071801.

[349] **IceCube** Collaboration, M. G. Aartsen *et al.*, "Search for sterile neutrino mixing using three years of IceCube DeepCore data," *Phys. Rev. D* **95** no. 11, (2017) 112002.

[350] B. W. Lee and R. E. Shrock, "Natural Suppression of Symmetry Violation in Gauge Theories: Muon - Lepton and Electron Lepton Number Nonconservation," *Phys. Rev.* **D16** (1977) 1444.

[351] R. N. Mohapatra and J. W. F. Valle, "Neutrino Mass and Baryon Number Nonconservation in Superstring Models," *Phys. Rev.* **D34** (1986) 1642.

[352] E. K. Akhmedov, M. Lindner, E. Schnapka, and J. W. F. Valle, "Dynamical left-right symmetry breaking," *Phys. Rev.* **D53** (1996) 2752–2780, arXiv:hep-ph/9509255 [hep-ph].

[353] E. K. Akhmedov, M. Lindner, E. Schnapka, and J. W. F. Valle, "Left-right symmetry breaking in NJL approach," *Phys. Lett.* **B368** (1996) 270–280, arXiv:hep-ph/9507275 [hep-ph].

[354] M. Malinsky, J. C. Romao, and J. W. F. Valle, "Novel supersymmetric SO(10) seesaw mechanism," *Phys. Rev. Lett.* **95** (2005) 161801, arXiv:hep-ph/0506296 [hep-ph].

[355] M. Blennow, P. Coloma, E. Fernandez-Martinez, J. Hernandez-Garcia, and J. Lopez-Pavon, "Non-Unitarity, sterile neutrinos, and Non-Standard neutrino Interactions," *JHEP* **04** (2017) 153, arXiv:1609.08637 [hep-ph].

[356] F. J. Escrihuela, D. V. Forero, O. G. Miranda, M. Tortola, and J. W. F. Valle, "Probing CP violation with non-unitary mixing in long-baseline neutrino oscillation experiments: DUNE as a case study," *New J. Phys.* **19** no. 9, (2017) 093005, arXiv:1612.07377 [hep-ph].

[357] R. N. Mohapatra and P. B. Pal, "Massive neutrinos in physics and astrophysics. Second edition," *World Sci. Lect. Notes Phys.* **60** (1998) 1–397. [World Sci. Lect. Notes Phys.72,1(2004)].

[358] J. W. F. Valle and J. C. Romao, *Neutrinos in high energy and astroparticle physics.* Physics textbook. Wiley-VCH, Weinheim, 2015. http://eu.wiley.com/WileyCDA/WileyTitle/productCd-3527411976.html.

[359] M. Fukugita and T. Yanagida, *Physics of neutrinos and applications to astrophysics.* Berlin, Germany: Springer (2003) 593 p, 2003.

[360] F. J. Escrihuela, D. V. Forero, O. G. Miranda, M. Tortola, and J. W. F. Valle, "On the description of non-unitary neutrino mixing," *Phys. Rev.* **D92** no. 5, (2015) 053009, arXiv:1503.08879 [hep-ph].

[361] Z.-z. Xing, "Correlation between the Charged Current Interactions of Light and Heavy Majorana Neutrinos," *Phys. Lett.* **B660** (2008) 515–521, arXiv:0709.2220 [hep-ph].

[362] Z.-z. Xing, "A full parametrization of the 6 X 6 flavor mixing matrix in the presence of three light or heavy sterile neutrinos," *Phys. Rev.* **D85** (2012) 013008, arXiv:1110.0083 [hep-ph].

[363] R. E. Shrock, "New Tests For, and Bounds On, Neutrino Masses and Lepton Mixing," *Phys. Lett.* **B96** (1980) 159–164.

[364] R. E. Shrock, "General Theory of Weak Leptonic and Semileptonic Decays. 1. Leptonic Pseudoscalar Meson Decays, with Associated Tests For, and Bounds on, Neutrino Masses and Lepton Mixing," *Phys. Rev.* **D24** (1981) 1232.

[365] R. E. Shrock, "General Theory of Weak Processes Involving Neutrinos. 2. Pure Leptonic Decays," *Phys. Rev.* **D24** (1981) 1275.

[366] P. Langacker and D. London, "Mixing Between Ordinary and Exotic Fermions," *Phys.Rev.* **D38** (1988) 886.

[367] S. M. Bilenky and C. Giunti, "Seesaw type mixing and muon-neutrino to tau-neutrino oscillations," *Phys. Lett.* **B300** (1993) 137–140, arXiv:hep-ph/9211269 [hep-ph].

[368] E. Nardi, E. Roulet, and D. Tommasini, "Limits on neutrino mixing with new heavy particles," *Phys.Lett.* **B327** (1994) 319–326, arXiv:hep-ph/9402224 [hep-ph].

[369] D. Tommasini, G. Barenboim, J. Bernabeu, and C. Jarlskog, "Nondecoupling of heavy neutrinos and lepton flavor violation," *Nucl.Phys.* **B444** (1995) 451–467, arXiv:hep-ph/9503228 [hep-ph].

[370] S. Antusch, C. Biggio, E. Fernandez-Martinez, M. Gavela, and J. Lopez-Pavon, "Unitarity of the Leptonic Mixing Matrix," *JHEP* **0610** (2006) 084, arXiv:hep-ph/0607020 [hep-ph].

[371] E. Fernandez-Martinez, M. B. Gavela, J. Lopez-Pavon, and O. Yasuda, "CP-violation from non-unitary leptonic mixing," *Phys. Lett.* **B649** (2007) 427–435, arXiv:hep-ph/0703098.

[372] S. Antusch, J. P. Baumann, and E. Fernandez-Martinez, "Non-Standard Neutrino Interactions with Matter from Physics Beyond the Standard Model," *Nucl.Phys.* **B810** (2009) 369–388, arXiv:0807.1003 [hep-ph].

[373] C. Biggio, "The Contribution of fermionic seesaws to the anomalous magnetic moment of leptons," *Phys. Lett.* **B668** (2008) 378–384, arXiv:0806.2558 [hep-ph].

[374] S. Antusch, M. Blennow, E. Fernandez-Martinez, and J. Lopez-Pavon, "Probing non-unitary mixing and CP-violation at a Neutrino Factory," *Phys. Rev.* **D80** (2009) 033002, arXiv:0903.3986 [hep-ph].

[375] D. V. Forero, S. Morisi, M. Tortola, and J. W. F. Valle, "Lepton flavor violation and non-unitary lepton mixing in low-scale type-I seesaw," *JHEP* **09** (2011) 142, arXiv:1107.6009 [hep-ph].

[376] R. Alonso, M. Dhen, M. Gavela, and T. Hambye, "Muon conversion to electron in nuclei in type-I seesaw models," *JHEP* **1301** (2013) 118, arXiv:1209.2679 [hep-ph].

[377] S. Antusch and O. Fischer, "Non-unitarity of the leptonic mixing matrix: Present bounds and future sensitivities," *JHEP* **1410** (2014) 94, arXiv:1407.6607 [hep-ph].

[378] A. Abada and T. Toma, "Electric Dipole Moments of Charged Leptons with Sterile Fermions," *JHEP* **02** (2016) 174, arXiv:1511.03265 [hep-ph].

[379] E. Fernandez-Martinez, J. Hernandez-Garcia, J. Lopez-Pavon, and M. Lucente, "Loop level constraints on Seesaw neutrino mixing," *JHEP* **10** (2015) 130, arXiv:1508.03051 [hep-ph].

[380] O. G. Miranda, M. Tortola, and J. W. F. Valle, "New ambiguity in probing CP violation in neutrino oscillations," *Phys. Rev. Lett.* **117** no. 6, (2016) 061804, arXiv:1604.05690 [hep-ph].

[381] C. S. Fong, H. Minakata, and H. Nunokawa, "A framework for testing leptonic unitarity by neutrino oscillation experiments," *JHEP* **02** (2017) 114, arXiv:1609.08623 [hep-ph].

[382] E. Fernandez-Martinez, J. Hernandez-Garcia, and J. Lopez-Pavon, "Global constraints on heavy neutrino mixing," *JHEP* **08** (2016) 033, arXiv:1605.08774 [hep-ph].

[383] M. Blennow and E. Fernandez-Martinez, "Neutrino oscillation parameter sampling with MonteCUBES," *Comput. Phys. Commun.* **181** (2010) 227–231, arXiv:0903.3985 [hep-ph]. http://wwwth.mpp.mpg.de/members/blennow/montecubes/.

[384] M. Masud, A. Chatterjee, and P. Mehta, "Probing CP violation signal at DUNE in presence of non-standard neutrino interactions," *J. Phys.* **G43** no. 9, (2016) 095005, arXiv:1510.08261 [hep-ph].

[385] M. Masud and P. Mehta, "Nonstandard interactions spoiling the CP violation sensitivity at DUNE and other long baseline experiments," *Phys. Rev.* **D94** (2016) 013014, arXiv:1603.01380 [hep-ph].

[386] M. Masud and P. Mehta, "Nonstandard interactions and resolving the ordering of neutrino masses at DUNE and other long baseline experiments," *Phys. Rev.* **D94** no. 5, (2016) 053007, arXiv:1606.05662 [hep-ph].

[387] S. K. Agarwalla, S. S. Chatterjee, and A. Palazzo, "Degeneracy between θ_{23} octant and neutrino non-standard interactions at DUNE," arXiv:1607.01745 [hep-ph].

[388] A. de Gouvea and K. J. Kelly, "Non-standard Neutrino Interactions at DUNE," *Nucl. Phys.* **B908** (2016) 318–335, arXiv:1511.05562 [hep-ph].

[389] P. Coloma, "Non-Standard Interactions in propagation at the Deep Underground Neutrino Experiment," *JHEP* **03** (2016) 016, arXiv:1511.06357 [hep-ph].

[390] T. Ohlsson, "Status of non-standard neutrino interactions," *Rept. Prog. Phys.* **76** (2013) 044201, arXiv:1209.2710 [hep-ph].

[391] O. G. Miranda and H. Nunokawa, "Non standard neutrino interactions: current status and future prospects," *New J. Phys.* **17** no. 9, (2015) 095002, arXiv:1505.06254 [hep-ph].

[392] M. Blennow, S. Choubey, T. Ohlsson, D. Pramanik, and S. K. Raut, "A combined study of source, detector and matter non-standard neutrino interactions at DUNE," *JHEP* **08** (2016) 090, arXiv:1606.08851 [hep-ph].

[393] P. Bakhti, A. N. Khan, and W. Wang, "Sensitivities to charged-current nonstandard neutrino interactions at DUNE," *J. Phys.* **G44** no. 12, (2017) 125001, arXiv:1607.00065 [hep-ph].

[394] S. Davidson, C. Pena-Garay, N. Rius, and A. Santamaria, "Present and future bounds on nonstandard neutrino interactions," *JHEP* **0303** (2003) 011, arXiv:hep-ph/0302093 [hep-ph].

[395] M. Gonzalez-Garcia and M. Maltoni, "Phenomenology with Massive Neutrinos," *Phys.Rept.* **460** (2008) 1–129, arXiv:0704.1800 [hep-ph].

[396] C. Biggio, M. Blennow, and E. Fernandez-Martinez, "General bounds on non-standard neutrino interactions," *JHEP* **0908** (2009) 090, arXiv:0907.0097 [hep-ph].

[397] M. C. Gonzalez-Garcia and M. Maltoni, "Determination of matter potential from global analysis of neutrino oscillation data," *JHEP* **09** (2013) 152, arXiv:1307.3092 [hep-ph].

[398] I. Esteban, M. C. Gonzalez-Garcia, M. Maltoni, I. Martinez-Soler, and J. Salvado, "Updated Constraints on Non-Standard Interactions from Global Analysis of Oscillation Data," *JHEP* **08** (2018) 180, arXiv:1805.04530 [hep-ph].

[399] B. Roe, "Matter density versus distance for the neutrino beam from Fermilab to Lead, South Dakota, and comparison of oscillations with variable and constant density," *Phys. Rev.* **D95** no. 11, (2017) 113004, arXiv:1707.02322 [hep-ex].

[400] K. J. Kelly and S. J. Parke, "Matter Density Profile Shape Effects at DUNE," *Phys. Rev.* **D98** no. 1, (2018) 015025, arXiv:1802.06784 [hep-ph].

[401] A. M. Dziewonski and D. L. Anderson, "Preliminary reference earth model," *Phys. Earth Planet. Interiors* **25** (1981) 297–356.

[402] F. Stacey, *Physics of the earth*. Wiley, 2nd ed. ed., 1977.

[403] W. Shen and M. H. Ritzwoller, "Crustal and uppermost mantle structure beneath the United States," *J. Geophys. Res.: Solid Earth* **121** (2016) 4306.

[404] A. Chatterjee, F. Kamiya, C. A. Moura, and J. Yu, "Impact of Matter Density Profile Shape on Non-Standard Interactions at DUNE," arXiv:1809.09313 [hep-ph].

[405] J. Rout, M. Masud, and P. Mehta, "Can we probe intrinsic CP and T violations and nonunitarity at long baseline accelerator experiments?," *Phys. Rev.* **D95** no. 7, (2017) 075035, arXiv:1702.02163 [hep-ph].

[406] M. Masud, M. Bishai, and P. Mehta, "Extricating New Physics Scenarios at DUNE with High Energy Beams," arXiv:1704.08650 [hep-ph].

[407] B. Schwingenheuer *et al.*, "CPT tests in the neutral kaon system," *Phys. Rev. Lett.* **74** (1995) 4376–4379.

[408] G. Barenboim and J. Salvado, "Cosmology and CPT violating neutrinos," *Eur. Phys. J.* **C77** no. 11, (2017) 766, arXiv:1707.08155 [hep-ph].

[409] **Super-Kamiokande** Collaboration, K. Abe *et al.*, "Atmospheric neutrino oscillation analysis with external constraints in Super-Kamiokande I-IV," arXiv:1710.09126 [hep-ex].

[410] **IceCube** Collaboration, M. G. Aartsen *et al.*, "Determining neutrino oscillation parameters from atmospheric muon neutrino disappearance with three years of IceCube DeepCore data," *Phys. Rev.* **D91** no. 7, (2015) 072004, arXiv:1410.7227 [hep-ex].

[411] **IceCube** Collaboration, M. G. Aartsen *et al.*, "Measurement of Atmospheric Neutrino Oscillations at 6-56 GeV with IceCube DeepCore," *Phys. Rev. Lett.* **120** no. 7, (2018) 071801, arXiv:1707.07081 [hep-ex].

[412] **ANTARES** Collaboration, S. Adrian-Martinez *et al.*, "Measurement of Atmospheric Neutrino Oscillations with the ANTARES Neutrino Telescope," *Phys. Lett.* **B714** (2012) 224–230, arXiv:1206.0645 [hep-ex].

[413] F. Kaether, W. Hampel, G. Heusser, J. Kiko, and T. Kirsten, "Reanalysis of the GALLEX solar neutrino flux and source experiments," *Phys. Lett.* **B685** (2010) 47–54, arXiv:1001.2731 [hep-ex].

[414] **SAGE** Collaboration, J. N. Abdurashitov *et al.*, "Measurement of the solar neutrino capture rate with gallium metal. III: Results for the 2002–2007 data-taking period," *Phys. Rev.* **C80** (2009) 015807, arXiv:0901.2200 [nucl-ex].

[415] **Super-Kamiokande** Collaboration, J. Hosaka *et al.*, "Solar neutrino measurements in super-Kamiokande-I," *Phys. Rev.* **D73** (2006) 112001, arXiv:hep-ex/0508053 [hep-ex].

[416] **Super-Kamiokande** Collaboration, J. P. Cravens *et al.*, "Solar neutrino measurements in Super-Kamiokande-II," *Phys. Rev.* **D78** (2008) 032002, arXiv:0803.4312 [hep-ex].

[417] **Super-Kamiokande** Collaboration, K. Abe *et al.*, "Solar neutrino results in Super-Kamiokande-III," *Phys. Rev.* **D83** (2011) 052010, arXiv:1010.0118 [hep-ex].

[418] Y. Nakano, "PhD Thesis, University of Tokyo." http://www-sk.icrr.u-tokyo.ac.jp/sk/_pdf/articles/2016/doc_thesis_naknao.pdf, 2016.

[419] **SNO** Collaboration, B. Aharmim *et al.*, "An Independent Measurement of the Total Active B-8 Solar Neutrino Flux Using an Array of He-3 Proportional Counters at the Sudbury Neutrino Observatory," *Phys. Rev. Lett.* **101** (2008) 111301, arXiv:0806.0989 [nucl-ex].

[420] **SNO** Collaboration, B. Aharmim *et al.*, "Low Energy Threshold Analysis of the Phase I and Phase II Data Sets of the Sudbury Neutrino Observatory," *Phys. Rev.* **C81** (2010) 055504, arXiv:0910.2984 [nucl-ex].

[421] **Borexino** Collaboration, G. Bellini *et al.*, "Final results of Borexino Phase-I on low energy solar neutrino spectroscopy," *Phys. Rev.* **D89** no. 11, (2014) 112007, arXiv:1308.0443 [hep-ex].

[422] **K2K** Collaboration, M. H. Ahn *et al.*, "Measurement of Neutrino Oscillation by the K2K Experiment," *Phys. Rev.* **D74** (2006) 072003, arXiv:hep-ex/0606032 [hep-ex].

[423] **MINOS** Collaboration, P. Adamson *et al.*, "Measurement of Neutrino and Antineutrino Oscillations Using Beam and Atmospheric Data in MINOS," *Phys.Rev.Lett.* **110** no. 25, (2013) 251801, arXiv:1304.6335 [hep-ex].

[424] **MINOS** Collaboration, P. Adamson *et al.*, "Combined analysis of ν_μ disappearance and $\nu_\mu \to \nu_e$ appearance in MINOS using accelerator and atmospheric neutrinos," *Phys. Rev. Lett.* **112** (2014) 191801, arXiv:1403.0867 [hep-ex].

[425] **T2K** Collaboration, K. Abe *et al.*, "Combined Analysis of Neutrino and Antineutrino Oscillations at T2K," *Phys. Rev. Lett.* **118** no. 15, (2017) 151801, arXiv:1701.00432 [hep-ex].

[426] **T2K** Collaboration, K. Abe *et al.*, "Updated T2K measurements of muon neutrino and antineutrino disappearance using $1.5{\times}10^{21}$ protons on target," *Phys. Rev.* **D96** no. 1, (2017) 011102, arXiv:1704.06409 [hep-ex].

[427] **NOvA** Collaboration, P. Adamson *et al.*, "Measurement of the neutrino mixing angle θ_{23} in NOvA," *Phys. Rev. Lett.* **118** no. 15, (2017) 151802, arXiv:1701.05891 [hep-ex].

[428] **NOvA** Collaboration, P. Adamson *et al.*, "Constraints on Oscillation Parameters from ν_e Appearance and ν_μ Disappearance in NOvA," *Phys. Rev. Lett.* **118** no. 23, (2017) 231801, arXiv:1703.03328 [hep-ex].

[429] A. Gando *et al.*, "Constraints on θ_{13} from a Three-Flavor Oscillation Analysis of Reactor Antineutrinos at KamLAND," *Phys.Rev.D* **83** (2011) 052002. arXiv:1009.4771 [hep-ex].

[430] **Daya Bay** Collaboration, F. P. An *et al.*, "Measurement of electron antineutrino oscillation based on 1230 days of operation of the Daya Bay experiment," *Phys. Rev.* **D95** no. 7, (2017) 072006, arXiv:1610.04802 [hep-ex].

[431] **RENO** Collaboration, J. H. Choi *et al.*, "Observation of Energy and Baseline Dependent Reactor Antineutrino Disappearance in the RENO Experiment," *Phys. Rev. Lett.* **116** no. 21, (2016) 211801, arXiv:1511.05849 [hep-ex].

[432] **Double Chooz** Collaboration, Y. Abe *et al.*, "Improved measurements of the neutrino mixing angle θ_{13} with the Double Chooz detector," *JHEP* **10** (2014) 086, arXiv:1406.7763 [hep-ex]. [Erratum: JHEP02,074(2015)].

[433] **CHARM-II** Collaboration, D. Geiregat *et al.*, "First observation of neutrino trident production," *Phys. Lett.* **B245** (1990) 271–275.

[434] **CCFR** Collaboration, S. R. Mishra *et al.*, "Neutrino tridents and W Z interference," *Phys. Rev. Lett.* **66** (1991) 3117–3120.

[435] **NuTeV** Collaboration, T. Adams *et al.*, "Evidence for diffractive charm production in muon-neutrino Fe and anti-muon-neutrino Fe scattering at the Tevatron," *Phys. Rev. D* **61** (2000) 092001, arXiv:hep-ex/9909041 [hep-ex].

[436] W. Altmannshofer, S. Gori, M. Pospelov, and I. Yavin, "Neutrino Trident Production: A Powerful Probe of New Physics with Neutrino Beams," *Phys. Rev. Lett.* **113** (2014) 091801, arXiv:1406.2332 [hep-ph].

[437] **GEANT4** Collaboration, S. Agostinelli *et al.*, "GEANT4: A Simulation toolkit," *Nucl. Instrum. Meth. A* **506** (2003) 250–303.

[438] J. Allison *et al.*, "Geant4 developments and applications," *IEEE Trans. Nucl. Sci.* **53** (2006) 270.

[439] J. Allison *et al.*, "Recent developments in Geant4," *Nucl. Instrum. Meth.* **A835** (2016) 186–225.

[440] **DELPHI, OPAL, LEP Electroweak, ALEPH and L3 Collaborations** Collaboration, S. Schael *et al.*, "Electroweak Measurements in Electron-Positron Collisions at W-Boson-Pair Energies at LEP," *Phys. Rept.* **532** (2013) 119–244, arXiv:1302.3415 [hep-ex].

[441] W. Altmannshofer, S. Gori, M. Pospelov, and I. Yavin, "Quark flavor transitions in $L_\mu - L_\tau$ models," *Phys. Rev. D* **89** (2014) 095033, arXiv:1403.1269 [hep-ph].

[442] S. Baek and P. Ko, "Phenomenology of U(1)(L(mu)-L(tau)) charged dark matter at PAMELA and colliders," *JCAP* **0910** (2009) 011, arXiv:0811.1646 [hep-ph].

[443] W. Altmannshofer, S. Gori, S. Profumo, and F. S. Queiroz, "Explaining dark matter and B decay anomalies with an $L_\mu - L_\tau$ model," *JHEP* **12** (2016) 106, arXiv:1609.04026 [hep-ph].

[444] **CMS** Collaboration, A. M. Sirunyan *et al.*, "Search for an $L_\mu - L_\tau$ gauge boson using Z$\to 4\mu$ events in proton-proton collisions at $\sqrt{s} = 13$ TeV," *Submitted to: Phys. Lett.* (2018) , arXiv:1808.03684 [hep-ex].

[445] **BaBar** Collaboration, J. P. Lees *et al.*, "Search for a muonic dark force at BABAR," *Phys. Rev. D* **94** no. 1, (2016) 011102, arXiv:1606.03501 [hep-ex].

[446] **SLD Electroweak Group, DELPHI, ALEPH, SLD, SLD Heavy Flavour Group, OPAL, LEP Electroweak Working Group, L3** Collaboration, S. Schael *et al.*, "Precision electroweak measurements on the Z resonance," *Phys. Rept.* **427** (2006) 257–454, arXiv:hep-ex/0509008 [hep-ex].

[447] G. Bellini *et al.*, "Precision measurement of the 7Be solar neutrino interaction rate in Borexino," *Phys. Rev. Lett.* **107** (2011) 141302, arXiv:1104.1816 [hep-ex].

[448] R. Harnik, J. Kopp, and P. A. N. Machado, "Exploring nu Signals in Dark Matter Detectors," *JCAP* **1207** (2012) 026, arXiv:1202.6073 [hep-ph].

[449] **Borexino** Collaboration, M. Agostini *et al.*, "First Simultaneous Precision Spectroscopy of *pp*, ^{7}Be, and *pep* Solar Neutrinos with Borexino Phase-II," arXiv:1707.09279 [hep-ex].

[450] B. Ahlgren, T. Ohlsson, and S. Zhou, "Comment on 'Is Dark Matter with Long-Range Interactions a Solution to All Small-Scale Problems of Λ Cold Dark Matter Cosmology?'," *Phys. Rev. Lett.* **111** no. 19, (2013) 199001, arXiv:1309.0991 [hep-ph].

[451] A. Kamada and H.-B. Yu, "Coherent Propagation of PeV Neutrinos and the Dip in the Neutrino Spectrum at IceCube," *Phys. Rev. D* **92** no. 11, (2015) 113004, arXiv:1504.00711 [hep-ph].

[452] A. Keshavarzi, D. Nomura, and T. Teubner, "Muon $g-2$ and $\alpha(M_Z^2)$: a new data-based analysis," *Phys. Rev. D* **97** no. 11, (2018) 114025, arXiv:1802.02995 [hep-ph].

[453] T. Araki, F. Kaneko, T. Ota, J. Sato, and T. Shimomura, "MeV scale leptonic force for cosmic neutrino spectrum and muon anomalous magnetic moment," *Phys. Rev.* **D93** no. 1, (2016) 013014, arXiv:1508.07471 [hep-ph].

[454] A. Kamada, K. Kaneta, K. Yanagi, and H.-B. Yu, "Self-interacting dark matter and muon

$g-2$ in a gauged $U(1)_{L_\mu - L_\tau}$ model," *JHEP* **06** (2018) 117, arXiv:1805.00651 [hep-ph].

[455] E. D. Carlson, M. E. Machacek, and L. J. Hall, "Self-interacting dark matter," *Astrophys. J.* **398** (1992) 43–52.

[456] Y. Hochberg, E. Kuflik, T. Volansky, and J. G. Wacker, "Mechanism for Thermal Relic Dark Matter of Strongly Interacting Massive Particles," *Phys. Rev. Lett.* **113** (2014) 171301, arXiv:1402.5143 [hep-ph].

[457] Y. Cui, M. Pospelov, and J. Pradler, "Signatures of Dark Radiation in Neutrino and Dark Matter Detectors," *Phys. Rev.* **D97** no. 10, (2018) 103004, arXiv:1711.04531 [hep-ph].

[458] G. F. Giudice, D. Kim, J.-C. Park, and S. Shin, "Inelastic Boosted Dark Matter at Direct Detection Experiments," *Phys. Lett.* **B780** (2018) 543–552, arXiv:1712.07126 [hep-ph].

[459] **Super-Kamiokande** Collaboration, C. Kachulis *et al.*, "Search for Boosted Dark Matter Interacting With Electrons in Super-Kamiokande," *Phys. Rev. Lett.* **120** no. 22, (2018) 221301, arXiv:1711.05278 [hep-ex].

[460] V. De Romeri, K. J. Kelly, and P. A. N. Machado, "Hunting On- and Off-Axis for Light Dark Matter with DUNE-PRISM," arXiv:1903.10505 [hep-ph].

[461] **LDMX** Collaboration, T. Åkesson *et al.*, "Light Dark Matter eXperiment (LDMX)," arXiv:1808.05219 [hep-ex].

[462] P. deNiverville and C. Frugiuele, "Hunting sub-GeV dark matter with the NOνA near detector," *Phys. Rev.* **D99** no. 5, (2019) 051701, arXiv:1807.06501 [hep-ph].

[463] **BaBar** Collaboration, J. P. Lees *et al.*, "Search for Invisible Decays of a Dark Photon Produced in e^+e^- Collisions at BaBar," *Phys. Rev. Lett.* **119** no. 13, (2017) 131804, arXiv:1702.03327 [hep-ex].

[464] M. Davier and H. Nguyen Ngoc, "An Unambiguous Search for a Light Higgs Boson," *Phys. Lett.* **B229** (1989) 150–155.

[465] **NA48/2** Collaboration, J. R. Batley *et al.*, "Search for the dark photon in π^0 decays," *Phys. Lett.* **B746** (2015) 178–185, arXiv:1504.00607 [hep-ex].

[466] J. D. Bjorken, S. Ecklund, W. R. Nelson, A. Abashian, C. Church, B. Lu, L. W. Mo, T. A. Nunamaker, and P. Rassmann, "Search for Neutral Metastable Penetrating Particles Produced in the SLAC Beam Dump," *Phys. Rev.* **D38** (1988) 3375.

[467] E. M. Riordan *et al.*, "A Search for Short Lived Axions in an Electron Beam Dump Experiment," *Phys. Rev. Lett.* **59** (1987) 755.

[468] J. D. Bjorken, R. Essig, P. Schuster, and N. Toro, "New Fixed-Target Experiments to Search for Dark Gauge Forces," *Phys. Rev.* **D80** (2009) 075018, arXiv:0906.0580

[hep-ph].

[469] A. Bross, M. Crisler, S. H. Pordes, J. Volk, S. Errede, and J. Wrbanek, "A Search for Shortlived Particles Produced in an Electron Beam Dump," *Phys. Rev. Lett.* **67** (1991) 2942–2945.

[470] J. F. Navarro, C. S. Frenk, and S. D. M. White, "The Structure of cold dark matter halos," *Astrophys. J.* **462** (1996) 563–575, arXiv:astro-ph/9508025 [astro-ph].

[471] J. F. Navarro, C. S. Frenk, and S. D. M. White, "A Universal density profile from hierarchical clustering," *Astrophys. J.* **490** (1997) 493–508, arXiv:astro-ph/9611107 [astro-ph].

[472] D. Kim, P. A. N. Machado, J.-C. Park, and S. Shin, "Work in progress,".

[473] J. A. Formaggio and G. P. Zeller, "From eV to EeV: Neutrino Cross Sections Across Energy Scales," *Rev. Mod. Phys.* **84** (2012) 1307–1341, arXiv:1305.7513 [hep-ex].

[474] **NA64** Collaboration, D. Banerjee *et al.*, "Search for vector mediator of Dark Matter production in invisible decay mode," *Phys. Rev.* **D97** no. 7, (2018) 072002, arXiv:1710.00971 [hep-ex].

[475] **NA64** Collaboration, D. Banerjee *et al.*, "Search for a Hypothetical 16.7 MeV Gauge Boson and Dark Photons in the NA64 Experiment at CERN," *Phys. Rev. Lett.* **120** no. 23, (2018) 231802, arXiv:1803.07748 [hep-ex].

[476] A. L. Read, "Modified frequentist analysis of search results (the cl(s) method)," in *Workshop on confidence limits, CERN, Geneva, Switzerland, 17-18 Jan 2000: Proceedings*, pp. 81–101. 2000. http://weblib.cern.ch/abstract?CERN-OPEN-2000-205.

[477] **ATLAS, CMS, LHC Higgs Combination Group** Collaboration, "Procedure for the LHC Higgs boson search combination in summer 2011,".

[478] R. Dermisek, J. P. Hall, E. Lunghi, and S. Shin, "A New Avenue to Charged Higgs Discovery in Multi-Higgs Models," *JHEP* **04** (2014) 140, arXiv:1311.7208 [hep-ph].

[479] R. Dermisek, J. P. Hall, E. Lunghi, and S. Shin, "Limits on Vectorlike Leptons from Searches for Anomalous Production of Multi-Lepton Events," *JHEP* **12** (2014) 013, arXiv:1408.3123 [hep-ph].

[480] R. Dermisek, E. Lunghi, and S. Shin, "New constraints and discovery potential for Higgs to Higgs cascade decays through vectorlike leptons," *JHEP* **10** (2016) 081, arXiv:1608.00662 [hep-ph].

[481] K. Griest and D. Seckel, "Cosmic Asymmetry, Neutrinos and the Sun," *Nucl. Phys.* **B283** (1987) 681–705. [Erratum: Nucl. Phys.B296,1034(1988)].

[482] A. Gould, "WIMP Distribution in and Evaporation From the Sun," *Astrophys. J.* **321** (1987) 560.

[483] J. Berger, "A module for boosted dark matter event generation in genie," `Forthcoming`.

[484] *https://cdcvs.fnal.gov/redmine/projects/dunetpc* .

[485] *http://soltrack.sourceforge.net* .

[486] J. Yacknowitz, "Long baseline neutrino facility – far site conventional facilities – buildings, site and infrastructure design," *DUNE DocDB 136* (2015) .

[487] **Super-Kamiokande** Collaboration, M. Fechner *et al.*, "Kinematic reconstruction of atmospheric neutrino events in a large water Cherenkov detector with proton identification," *Phys. Rev.* **D79** (2009) 112010, `arXiv:0901.1645 [hep-ex]`.

[488] **PICO** Collaboration, C. Amole *et al.*, "Dark Matter Search Results from the Complete Exposure of the PICO-60 C_3F_8 Bubble Chamber," `arXiv:1902.04031 [astro-ph.CO]`.

[489] **PandaX-II** Collaboration, J. Xia *et al.*, "PandaX-II Constraints on Spin-Dependent WIMP-Nucleon Effective Interactions," *Phys. Lett.* **B792** (2019) 193–198, `arXiv:1807.01936 [hep-ex]`.

[490] **DONUT** Collaboration, K. Kodama *et al.*, "Observation of tau neutrino interactions," *Phys. Lett.* **B504** (2001) 218–224, `arXiv:hep-ex/0012035 [hep-ex]`.

[491] **DONuT** Collaboration, K. Kodama *et al.*, "Final tau-neutrino results from the DONuT experiment," *Phys. Rev.* **D78** (2008) 052002, `arXiv:0711.0728 [hep-ex]`.

[492] **OPERA** Collaboration, M. Guler *et al.*, "OPERA: An appearance experiment to search for $\nu_\mu \leftrightarrow \nu_\tau$ oscillations in the CNGS beam. Experimental proposal,".

[493] **OPERA** Collaboration, N. Agafonova *et al.*, "Final Results of the OPERA Experiment on ν_τ Appearance in the CNGS Neutrino Beam," *Phys. Rev. Lett.* **120** no. 21, (2018) 211801, `arXiv:1804.04912 [hep-ex]`. [Erratum: Phys. Rev. Lett.121,no.13,139901(2018)].

[494] **Super-Kamiokande** Collaboration, K. Abe *et al.*, "Evidence for the Appearance of Atmospheric Tau Neutrinos in Super-Kamiokande," *Phys. Rev. Lett.* **110** no. 18, (2013) 181802, `arXiv:1206.0328 [hep-ex]`.

[495] **Super-Kamiokande** Collaboration, Z. Li *et al.*, "Measurement of the tau neutrino cross section in atmospheric neutrino oscillations with Super-Kamiokande," *Phys. Rev.* **D98** no. 5, (2018) 052006, `arXiv:1711.09436 [hep-ex]`.

[496] **IceCube** Collaboration, M. G. Aartsen *et al.*, "Measurement of Atmospheric Tau Neutrino Appearance with IceCube DeepCore," *Phys. Rev.* **D99** no. 3, (2019) 032007, `arXiv:1901.05366 [hep-ex]`.

[497] J. Conrad *et al.*, "Atmospheric tau neutrinos in a multi-kiloton liquid argon detector,". arXiv:1008.2984/hep-ph.

[498] A. De Gouvêa, K. J. Kelly, G. V. Stenico, and P. Pasquini, "Physics with Beam Tau-Neutrino Appearance at DUNE," arXiv:1904.07265 [hep-ph].

[499] K. R. Dienes, E. Dudas, and T. Gherghetta, "Neutrino oscillations without neutrino masses or heavy mass scales: A Higher dimensional seesaw mechanism," *Nucl. Phys.* **B557** (1999) 25, arXiv:hep-ph/9811428 [hep-ph].

[500] N. Arkani-Hamed, S. Dimopoulos, G. R. Dvali, and J. March-Russell, "Neutrino masses from large extra dimensions," *Phys. Rev.* **D65** (2001) 024032, arXiv:hep-ph/9811448 [hep-ph].

[501] H. Davoudiasl, P. Langacker, and M. Perelstein, "Constraints on large extra dimensions from neutrino oscillation experiments," *Phys. Rev.* **D65** (2002) 105015, arXiv:hep-ph/0201128 [hep-ph].

[502] **MINOS** Collaboration, P. Adamson *et al.*, "Constraints on Large Extra Dimensions from the MINOS Experiment," *Phys. Rev.* **D94** no. 11, (2016) 111101, arXiv:1608.06964 [hep-ex].

[503] A. B. Balantekin, A. de Gouvêa, and B. Kayser, "Addressing the Majorana vs. Dirac Question with Neutrino Decays," *Phys. Lett.* **B789** (2019) 488–495, arXiv:1808.10518 [hep-ph].

[504] P. Ballett, T. Boschi, and S. Pascoli, "Heavy Neutral Leptons from low-scale seesaws at the DUNE Near Detector," arXiv:1905.00284 [hep-ph].

[505] G. Bernardi *et al.*, "Search for Neutrino Decay," *Phys. Lett.* **166B** (1986) 479–483.

[506] G. Bernardi *et al.*, "Further Limits on Heavy Neutrino Couplings," *Phys. Lett.* **B203** (1988) 332–334.

[507] **E949** Collaboration, A. V. Artamonov *et al.*, "Search for heavy neutrinos in $K^+ \to \mu^+ \nu_H$ decays," *Phys. Rev.* **D91** no. 5, (2015) 052001, arXiv:1411.3963 [hep-ex]. [Erratum: Phys. Rev.D91,no.5,059903(2015)].

[508] D. I. Britton *et al.*, "Measurement of the $\pi^+ \to e^+ \nu$ branching ratio," *Phys. Rev. Lett.* **68** (1992) 3000–3003.

[509] D. I. Britton *et al.*, "Improved search for massive neutrinos in $\pi^+ \to e^+ \nu$ decay," *Phys. Rev.* **D46** (1992) R885–R887.

[510] **PIENU** Collaboration, A. Aguilar-Arevalo *et al.*, "Improved search for heavy neutrinos in the decay $\pi \to e\nu$," *Phys. Rev.* **D97** no. 7, (2018) 072012, arXiv:1712.03275 [hep-ex].

[511] **PIENU** Collaboration, A. Aguilar-Arevalo *et al.*, "Search for Heavy Neutrinos in $\pi \to \mu\nu$ Decay," arXiv:1904.03269 [hep-ex].

[512] **CHARM II** Collaboration, P. Vilain *et al.*, "Search for heavy isosinglet neutrinos," *Phys. Lett.* **B343** (1995) 453–458. [Phys. Lett.B351,387(1995)].

[513] **NuTeV, E815** Collaboration, A. Vaitaitis *et al.*, "Search for neutral heavy leptons in a high-energy neutrino beam," *Phys. Rev. Lett.* **83** (1999) 4943–4946, arXiv:hep-ex/9908011 [hep-ex].

[514] **DELPHI** Collaboration, P. Abreu *et al.*, "Search for neutral heavy leptons produced in Z decays," *Z. Phys.* **C74** (1997) 57–71. [Erratum: Z. Phys.C75,580(1997)].

[515] **T2K** Collaboration, K. Abe *et al.*, "Search for heavy neutrinos with the T2K near detector ND280," arXiv:1902.07598 [hep-ex].

[516] P. Ballett, S. Pascoli, and M. Ross-Lonergan, "MeV-scale sterile neutrino decays at the Fermilab Short-Baseline Neutrino program," *JHEP* **04** (2017) 102, arXiv:1610.08512 [hep-ph].

[517] S. Alekhin *et al.*, "A facility to Search for Hidden Particles at the CERN SPS: the SHiP physics case," *Rept. Prog. Phys.* **79** no. 12, (2016) 124201, arXiv:1504.04855 [hep-ph].

[518] M. Drewes, J. Hajer, J. Klaric, and G. Lanfranchi, "NA62 sensitivity to heavy neutral leptons in the low scale seesaw model," *JHEP* **07** (2018) 105, arXiv:1801.04207 [hep-ph].

[519] D. Curtin *et al.*, "Long-Lived Particles at the Energy Frontier: The MATHUSLA Physics Case," arXiv:1806.07396 [hep-ph].

[520] F. Kling and S. Trojanowski, "Heavy Neutral Leptons at FASER," *Phys. Rev.* **D97** no. 9, (2018) 095016, arXiv:1801.08947 [hep-ph].

[521] C. Rott, S. In, J. Kumar, and D. Yaylali, "Directional Searches at DUNE for Sub-GeV Monoenergetic Neutrinos Arising from Dark Matter Annihilation in the Sun," *JCAP* **1701** no. 01, (2017) 016, arXiv:1609.04876 [hep-ph].